THE MINISTRY OF SCIENCE AND HIGHER EDUCATION OF THE RUSSIAN FEDERATION

ST. PETERSBURG STATE POLYTECHNICAL UNIVERSITY

JOURNAL

Physics and Mathematics

VOLUME 17, No.3.1, 2024

Peter the Great St. Petersburg
Polytechnic University
2024

ST. PETERSBURG STATE POLYTECHNICAL UNIVERSITY JOURNAL.
PHYSICS AND MATHEMATICS

The journal is included in the List of leading peer-reviewed scientific journals and other editions to publish major findings of theses for the research degrees of Doctor of Sciences and Candidate of Sciences.

The publications are presented in the VINITI RAS Abstract Journal and Ulrich's Periodical Directory International Database.

The journal is published since 2008 as part of the periodical edition 'Nauchno-tekhnicheskie vedomosti SPb-GPU'.

The journal is registered with the Federal Service for Supervision in the Sphere of Telecom, Information Technologies and Mass Communications (ROSKOMNADZOR). Certificate ПИ № ФС77-52144 issued December 11, 2012.

The journal is distributed through the CIS countries catalogue, the «Press of Russia» joint catalogue and the «Press by subscription» Internet catalogue. The subscription index is 71823.

The journal is in the **Web of Science** (Emerging Sources Citation Index), **Scopus,** the **Russian Science Citation Index** (RSCI) and the **Directory of Open Access Journals** (DOAJ) databases.

Address: 195251 Politekhnicheskaya St. 29, St. Petersburg, Russia.

Phone: (812) 294-22-85.

http://ntv.spbstu.ru/physics

PREFACE

11th International School and Conference on Optoelectronics, Photonics, Engineering and Nanostructures (SPb OPEN – 2024) / 11-я Международная школа-конференция по оптоэлектронике, фотонике, инженерии и наноструктурам

The 11th International School and Conference on Optoelectronics, Photonics, Engineering and Nanostructures (Saint-Petersburg OPEN 2024) was held from May 14 to May 17, 2024. It continues the annual schools and seminars for young scientists on physics and technology of nanostructures, organized since 2009, spearheaded by Zhores Alferov, RAS Academician and winner of the 2000 Nobel Prize in Physics.

The School was organized by the St. Petersburg Higher School of Economics, Peter the Great St. Petersburg Polytechnic University, the World-Class Research Center for Advanced Digital Technologies and the Alferov University with the support of Photonics Russia, Special Systems Photonics LLC and OOO "Aktivnaia Fotonika".

The Program Committee of the School and Conference selected 281 papers by young scientists, graduate and undergraduate students from 25 cities in Russia. The same as last year, the average age of the attendees was under 27 years old, 78% of the reports were presented by attendees under 30.

Presentations were given in six panels:
- Synthesis and structural properties of semiconductor materials and nanostructures,
- Lasers, solar cells, other optoelectronic devices,
- Nanophotonics, spectroscopy, microresonators, optical properties, plasmonics,
- Biophysics, nanobiotechnology, biophotonics
- Electrical, magnetic and microwave characteristics and devices,
- Other aspects of nanotechnology.

The highest percentage of reports (26%) were given in the section "Nanophotonics...", closely followed by "Synthesis..." with 23% of reports.

In addition to poster presentations from young scientists, the programme included a series of keynote speeches by prominent researchers, outlining the main advances and challenges in various fields of physics and technology. In total, 89 leading scientists participated in the conference. The keynote speakers included:
- Victor Soyfer (Samara University, Samara)
- Anatoly Pushkarev (ITMO University, St. Petersburg)
- Vladimir Drachev (Skoltech, Skolkovo)
- Alexander Vul' (Ioffe Institute, St. Petersburg)
- Vitaly Shchukin (VI Systems, Germany)
- Anton Krivtsov (Peter the Great St. Petersburg Polytechnic University, St. Petersburg)
- Evgenii Lutsenko (B.I. Stepanov Institute of Physics, National Academy of Sciences of Belarus)
- Yuriy Dedkov (Shanghai University, China)
- Pavel Frantsuzov (Institute of Chemical Kinetics and Combustion, Novosibirsk)
- Evgeny Viktorov (ITMO University, St. Petersburg)

The same as last year, the peer-reviewed reports from the conference are published in St. Petersburg State Polytechnical University Journal: Physics and Mathematics. The Programme Committee of SPbOPEN-2024 hopes that the range of subjects presented at the conference will be of interest to the journal's audience. We would like to thank the journal for giving us the opportunity to publish the proceedings, and thank the reviewers for useful recommendations and constructive criticism. We of course express our gratitude to all participants of the conference.

We invite young scientists, graduate and undergraduate students to take part in the next Saint Petersburg OPEN School and Conference in 2025. Please visit https://spb.hse.ru/spbopen/ for more details.

Alexey Zhukov
Higher School of Economics, St. Petersburg
St. Petersburg School of Physics, Mathematics, and Computer Science
aezhukov@hse.ru

Contents

Condensed matter physics

Simulation of physical processes

Atom physics and physics of clusters and nanostructures

Experimental technique and devices

Physical electronics

Physical optics

Physical materials technology

Biophysics and medical physics

Mathematical physics

Mechanics

Radiophysics

Theoretical physics

CONDENSED MATTER PHYSICS

Conference materials
UDC 537.533.331
DOI: https://doi.org/10.18721/JPM.173.101

Effect of the electrostatic focusing lens voltage on structures size in 3D printing by charged Au nanoparticles

A.N. Patarashvili [1] ✉, A.A. Efimov [1], M.S. Ivanov [1],
M.R. Ghorbani Fard [1], D.V. Maslennikov [1], V.V. Ivanov [1]

[1] Moscow Institute of Physics and Technology (National Research University), Dolgoprudny, Russia
✉ patarashvili@phystech.edu

Abstract. The paper demonstrates a method for three-dimensional aerosol printing of charged nanoparticles using electrostatic focusing through a conductive matrix lens. The study showcases the successful printing of narrow and highly conductive structures on a silicon substrate, utilizing 20–180 nm gold nanoparticles and alternating voltage on a stainless-steel lens. The results indicate that structures significantly smaller than the lens holes were achieved, and an experimental relationship between the structure width and lens voltage was established.

Keywords: focusing nanoparticles, microstructure, inkjet printing, aerosol charging, additive manufacturing

Funding: Russian Science Foundation grant No. 22-79-10127.

Citation: Patarashvili A.N., Efimov A.A., Ivanov M.S., Ghorbani Fard M.R., Maslennikov D.V., Ivanov V.V., Effect of the electrostatic focusing lens voltage on structures size in 3D printing by charged Au nanoparticles, St. Petersburg State Polytechnical University Journal. Physics and Mathematics. 17 (3.1) (2024) 10–13. DOI: https://doi.org/10.18721/JPM.173.101

Материалы конференции
УДК 537.533.331
DOI: https://doi.org/10.18721/JPM.173.101

Влияние напряжения электростатической фокусирующей линзы на размер структур при 3D-печати заряженными наночастицами золота

А.Н. Патарашвили [1] ✉, А.А. Ефимов [1], М.С. Иванов [1],
М.Р. Горбани Фард [1], Д.В. Масленников [1], В.В. Иванов [1]

[1] Московский физико-технический институт (национальный исследовательский университет), г. Долгопрудный, Россия
✉ patarashvili@phystech.edu

Аннотация. В статье демонстрируется метод трехмерной аэрозольной печати заряженных наночастиц золота размером 20–180 нм на кремниевой подложке с использованием электростатической фокусировки через матричную проводящую линзу. В результате эксперимента была установлена экспериментальная зависимость между шириной структуры и напряжением на линзе. Также получены структуры до 20 раз меньшего размера, чем отверстие в линзе.

Ключевые слова: фокусировка наночастиц, микроструктура, струйная печать, аэрозольная зарядка, аддитивное производство

Финансирование: Российский научный фонд, грант № 22-79-10127.

Ссылка при цитировании: Патарашвили А.Н., Ефимов А.А., Иванов М.С., Горбани Фард М.Р., Масленников Д.В., Иванов В.В. Влияние напряжения электростатической фокусирующей линзы на размер структур при 3D-печати заряженными наночастицами золота // Научно-технические ведомости СПбГПУ. Физико-математические науки. 2024. Т. 17. № 3.1. С. 10–13. DOI: https://doi.org/10.18721/JPM.173.101

Introduction

Creating narrow and conductive microstructures is a challenging yet promising field of study within printed electronics. These structures have potential applications as transparent electrode arrays, 3D interconnects, transparent heaters, optical metamaterials for light absorption or reflection, and photonic crystals. Various methods exist for focusing nanoparticles using physical forces like electrostatic [1, 2], magnetic [3], or capillary [4]. This study outlines an experimental setup for generating conductive structures through electrostatic focusing.

Materials and Methods

The process of synthesizing aerosol nanoparticles involved the electrical erosion of gold (Au) electrodes within an air-controlled environment, where the relative humidity was maintained at $34 \pm 4\%$ and the temperature at 23 ± 3 °C [5]. The airflow rate was recorded at 1 lpm. Next, the nanoparticles were sintered into spheres during the passage of a tubular furnace at a temperature of 985 °C for one second. Post-sintering, the nanoparticles were negatively charged via a unipolar charger. These charged nanoparticles were then introduced into the printing chamber for the deposition experiment, as depicted in Figure 1 of the experimental setup. The nanoparticles exhibited a log-normal size distribution, with mean size 62 nm, a GSD = 1.45, and a total number concentration of 2.8×10^6 cm^{-3}. The experimental design provided for a gap of 25 mm between the copper plate and the substrate with a dielectric layer thickness of 0.18 mm.

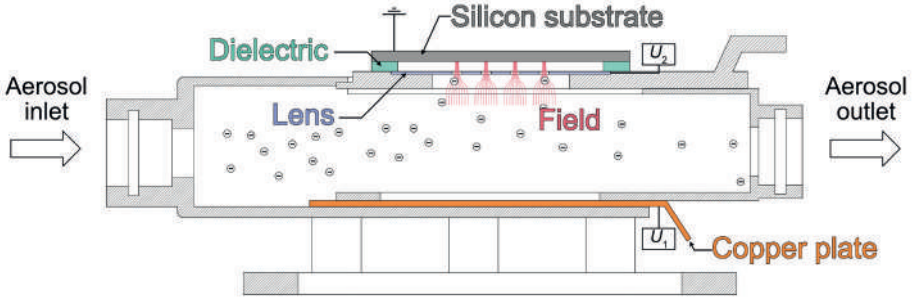

Fig. 1. The schematic of the experimental setup

The trajectory of charged nanoparticles within the focusing process is governed by a combination of forces, prominently including the Brownian force ($\overline{F_B}$), which arises from stochastic interactions with surrounding gas molecules. Additionally, the particles experience the Lorentz force ($\overline{F_L}$) and the drag force ($\overline{F_{Drag}}$) (presented in equation (1)). These forces are quantitatively represented in the Langevin equation, a fundamental mathematical model that elucidates the motion and aggregation behavior of nanoparticles under the influence of these forces during the focusing operation.

$$m\frac{d\overline{V_p}}{dt} = \overline{F_B} + \overline{F_{Drag}} + \overline{F_L} \quad (1)$$

In equation (1), m represents the nanoparticle mass, and $\overline{V_p}$ represents the nanoparticle velocity.

Results and Discussion

The experimental outcomes showcase the ability to manipulate the dimensions of the printed structures by varying the voltage applied to the lens, designated as U_2. This control over size is quantitatively captured in Table, which summarizes the experimental data. The visual representation of this relationship is further depicted in Figure 2, offering a graphical interpretation of the effect of the applied voltage on the resulting structure size.

Table

The effect of lens voltage on the structure size

Plate voltage U_1, V	Lens voltage U_2, V	Lens hole size d_L, μm	Structure size d_S, μm
–25	–5	280	100
	–10		82
	–15		70
	–20		61
	–25		52
	–30		37
	–35		18
	–37		14

a) *b*)

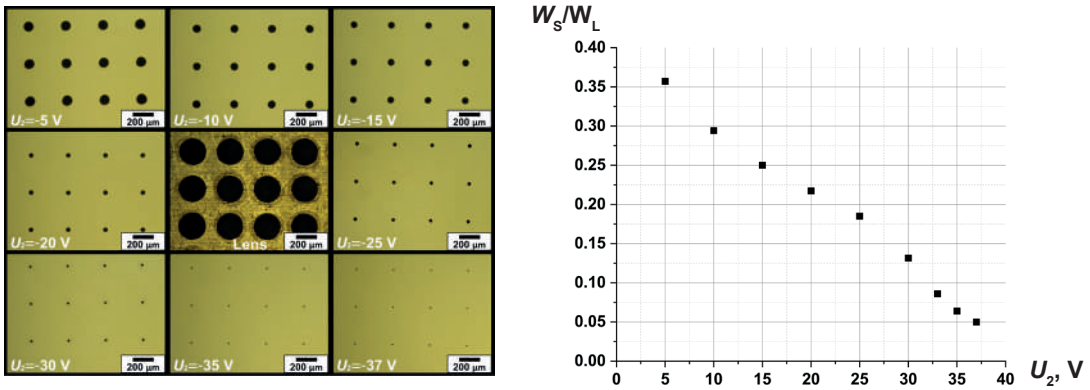

Fig. 2. Images of structures obtained at various lens voltage U_2 (image of the lens in the center) (*a*); Experimental dependence relative size of the structure on the absolute value of the lens voltage U_2 (*b*)

Elevating the voltage U_2 results in a heightened repulsive force acting on the nanoparticles at the periphery of the lens, altering the electric field distribution within the printing chamber. Notably, when the absolute voltage U_2 exceeds 30V, a marked reduction in printing velocity is observed, culminating in a complete cessation of printing at voltages surpassing 37V. This phenomenon is attributed to the nanoparticles being repelled from the lens surface towards the copper plate, thereby augmenting their distance from the substrate.

Conclusion

The paper discusses a test chamber designed for printing charged nanoparticles, featuring an optimal geometry that enables control over the size of the d_S structure. By adjusting the voltage on the U_2 electrostatic lens from −5 V to −37 V and maintaining a lens hole size of d_L = 280 μm, the size of the structure can be varied from 100 μm to 14 μm.

REFERENCES

1. **Jung, W., Jung, YH., Pikhitsa, P.V. et al.,** Three-dimensional nanoprinting via charged aerosol jets, Nature. (592) (2021) 54–59.

2. **Liu S., Ai J., Zhang Y., Feng J.,** Programmable and Parallel 3D Nanoprinting Using Configured Electric Fields, Advanced Functional Materials. (2023) 2308734.

3. **Wolf H., Birringer R.,** Pattern formation in an array of magnetic nanoscale rods mimics magnetic-dipole interaction-driven spinodal decomposition, Journal of Applied Physics. 98 (7) (2005) 74303.

4. **Lutfurakhmanov A., Loken G.K., Schulz D.L. and Akhatov I.S.,** Capillary-based Applied Physics Letters. 97 (12) (2010) 124107.

5. **Kornyushin D., Musaev A., Patarashvili A., Buchnev A., Arsenov P., Ivanov M., Vershinina O., Kameneva E., Volkov I., Efimov A., et al.,** Effect of the Gas Temperature on Agglomeration of Au Nanoparticles Synthesized by Spark Discharge and Their Application in Surface-Enhanced Raman Spectroscopy. Metals. 13 (301) (2023).

THE AUTHORS

PATARASHVILI Anton N.
patarashvili@phystech.edu
ORCID: 0009-0001-2673-6580

GHORBANI FARD Mohammad Reza
gorbani.fm@phystech.edu
ORCID: 0000-0002-5788-5159

EFIMOV Alexey A.
efimov.aa@mipt.ru
ORCID: 0000-0003-3276-0277

MASLENNIKOV Dmitry V.
maslennikov.dv@phystech.edu
ORCID: 0009-0005-1810-956X

IVANOV Matthey S.
ms.ivanov@phystech.edu
ORCID: 0009-0003-6861-3401

IVANOV Victor V.
ivanov.vv@mipt.ru
ORCID: 0000-0002-9149-0468

Received 05.07.2024. Approved after reviewing 29.07.2024. Accepted 29.07.2024.

Conference materials
UDC 538.9
DOI: https://doi.org/10.18721/JPM.173.102

Development of semitransparent Perovskite Solar Cells with double electron transport layer and modified top electrode

V.S. Ivanov [1] ✉, D. Sapori [1]

[1] ITMO University, St. Petersburg, Russia

✉ vladimir.ivanov@metalab.ifmo.ru

Abstract. In this work we report on semitransparent perovskite solar cell fabrication using double electron transport layer and double top electrode. Such devices may be used in tandem solar cells which are made to overcome Shockley-Queisser limit for one junction solar cell and improve efficiency of the device. One of the main issues of this task is to make transparent top electrode since it is usually made of metal. In this work the combination of ITO/Ag is used in which silver is deposited via special mask to improve conductivity. Top ITO electrode was deposited via magnetron sputtering – the process was optimized for room temperatures to avoid perovskite and organic degradation. ZnO nanoparticles are incorporated in device as second electron transport layer to protect all below layers from ITO sputtering damage. This layer was deposited via spin-coating process, which is much easier and faster than atomic layer deposition, which is usually used for ZnO deposition. The best semitransparent perovskite solar cell made with these modifications showed 11.5% efficiency with high V_{OC} value of 1.1 V.

Keywords: Perovskite solar cells, photovoltaics, tandem solar cells, semitransparent electrode, double electron transport layer

Funding: This study was funded by Russian Science Foundation, grant number 23-73-00060.

Citation: Ivanov V.S., Sapori D., Development of semitransparent Perovskite Solar Cells with double electron transport layer and modified top electrode, St. Petersburg State Polytechnical University Journal. Physics and Mathematics. 17 (3.1) (2024) 14–18. DOI: https://doi.org/10.18721/JPM.173.102

Материалы конференции
УДК 538.9
DOI: https://doi.org/10.18721/JPM.173.102

Разработка полупрозрачных перовскитных солнечных элементов с двойным электронным транспортным слоем и модифицированным верхним электродом

В.С. Иванов [1] ✉, Д. Сапори [1]

[1] Университет ИТМО, Санкт-Петербург, Россия

✉ vladimir.ivanov@metalab.ifmo.ru

Аннотация. В данной работе был получен полупрозрачный перовскитный солнечный элемент с двойным электронным транспортным слоем и двойным верхним электродом. Такое устройство может быть использовано в тандемном солнечном элементе. Основной сложностью в процессе синтеза полупрозрачных устройств является замена непрозрачного верхнего электрода на прозрачный. В данной работе для этой цели использовалась комбинация ITO/Ag, серебро напылялось через специальную маску, чтобы увеличить проводимость. Нанесение верхнего слоя ITO проводилось с помощью магнетронного напыления, процесс был оптимизирован для работы в условиях комнатной температуры для защиты перовскита и органики от термического разложения. Наночастицы ZnO использовались как дополнительный электронный транспортный слой для защиты

всех нижних слоев от ионов в процессе напыления ITO. Этот слой был нанесен с помощью метода центрифугирования, который значительно проще и быстрее атомно слоевого осаждения, которым обычно получают пленки ZnO. Лучшее полупрозрачное устройство, полученное в таких условиях, обладало 11,5% эффективности и высоким значением $V_{x.x.}$, равным 1,1 В.

Ключевые слова: перовскитные солнечные элементы, фотовольтаика, тандемные солнечные элементы, полупрозрачный электрод, двойной электронный транспортный слой

Финансирование: Исследование выполнено за счет гранта Российского научного фонда (проект № 23–73–00060).

Ссылка при цитировании: Иванов В.С., Сапори Д. Разработка полупрозрачных перовскитных солнечных элементов с двойным электронным транспортным слоем и модифицированным верхним электродом // Научно-технические ведомости СПбГПУ. Физико-математические науки. 2024. Т. 17. № 3.1. С. 14–18. DOI: https://doi.org/10.18721/JPM.173.102

Introduction

Nowadays perovskite solar cells (PSCs) are the most promising photovoltaic devices. The first working cell was produced in 2009 [1], and in only fifteen years the power conversion efficiency has reached the value more that 26.1% [2]. Such fast development is possible due to excellent physical properties of perovskite material. Perovskite is originally $CaTiO_3$, but now the whole class of artificial materials with crystal structure ABX_3 is referred to perovskites. The ability of bandgap tuning with composition changing is the key advantage of these materials, the whole visible plus IR and UV parts of spectrum may be obtained using different combinations of A-cations or X-halides [3].

There is a theoretical limit of efficiency of one-junction solar cell named Shockley-Queisser limit [4], and in case of perovskite solar cells its value is around 33%. Therefore, tandem systems with two or more active materials should be produced to overcome this efficiency value. Materials with certain bandgap values should be combined to obtain the highest possible power conversion efficiency (PCE). Since the most common perovskite material $CH_3NH_3PbI_3$ ($MAPbI_3$) has bandgap of 1.55 eV, it is possible to obtain ~40% PCE when combining it with ~1.1 eV cell [5]. This value matches well with Si or CIGS cells; hence, highly efficient tandem systems Si/perovskite and CIGS/perovskite may be produced.

Since perovskite material has greater bandgap that Si or CIGS, this cell is used as top cell, and it should be therefore semitransparent to pass the light to the bottom cell. The main problem here is top electrode which is usually made of metal. It is possible to use thin metals [6] or another materials such as carbon nanotubes [7], PEDOT:PSS and indium tin oxide (ITO). The last one is the most popular transparent electrode, which is usually used as bottom electrode in PSCs. It is usually deposited via magnetron sputtering technique under high (> 200 °C) temperature, and in case of perovskite devices such conditions may damage all organic and active layers. Also, there are high energy ions while this process, and all below layers should be protected from them with some inorganic film. Therefore, there are two main problems which should be solved to have semitransparent perovskite solar cell with ITO as top electrode: the problem of perovskite degradation under high temperature, and the problem of sputtering damage to organic transport layers.

In this work, the process of ITO sputtering was optimized to room temperature. ZnO nanoparticles were incorporated in structure to protect organic electron transport layer from ion damage while sputtering.

Materials and Methods

Perovskite solar cells in this work had the following *p-i-n* structure: ITO/PTAA/perovskite/PCBM/ZnO/ITO/Ag. All layers except ITO and Ag were deposited via spin-coating process,

classical $MAPbI_3$ was used as perovskite, solution was obtained combining MAI and PbI_2 salts in DMF/DMSO. Top ITO film was sputtered, and Ag was thermally evaporated. JV curves under dark and light conditions were measured to characterize the devices, in case of ITO films transparency spectrum, resistivity and thickness were measured while optimization work.

Results and Discussion

ZnO nanoparticles were spun onto the PCBM to protect it from sputtering damage, such combination works as double electron transport layer (ETL), enhancing transport properties compared to the single ETL. The first step of the work was to optimize the ZnO incorporation process. Device with PCBM/BCP double ETL was used as reference having the best efficiency of 16.9%. Different parameters of spin-coating process or annealing were changed during the experimental work. After the optimization, the champion device with ZnO showed high PCE value of 17.2% (Fig. 1), which can be used as base device for next ITO deposition.

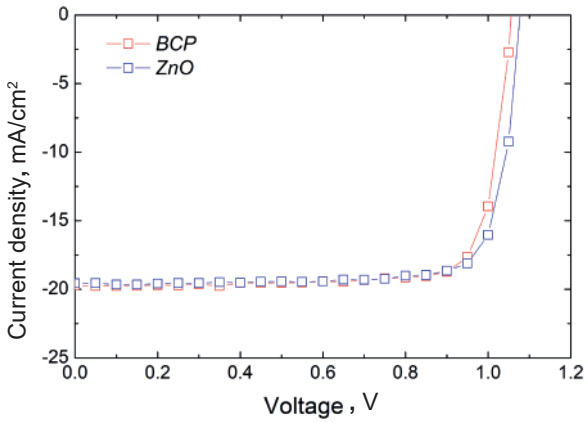

Fig. 1. JV curves of reference devices with BCP and ZnO layers

Since protective double ETL in perovskite solar cells was achieved, work on optimization of ITO sputtering under room temperature has begun. There are several parameters, which can be tuned in this process: flux of the gases (Ar and O_2), target power, process time etc. First main goal was to achieve ITO film under room temperature with low resistivity and high transparency. If O_2 flux was equal to 5 sccm, resistivity was found to be 109 Ohm/sq, almost transparent yellowish films were obtained. In such conditions the first semitransparent devices were made, and PCE of only 6.2% was obtained (Fig. 2). Spatial silver frame was used to improve the conductivity, it was deposited on the edges of the pixel, therefore there are still semitransparent ITO windows.

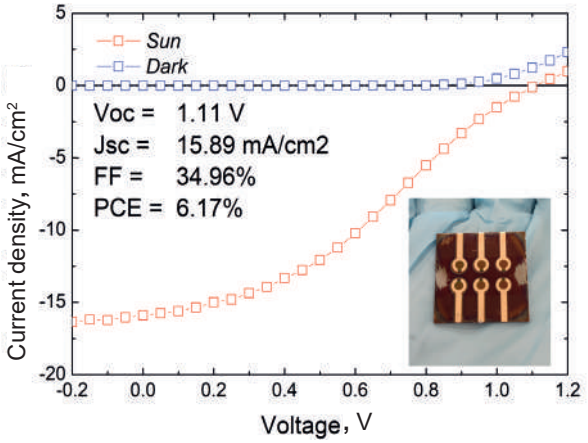

Fig. 2. JV curves of the first semitransparent device and photo of the device (inset)

However, fill factor (FF) of the device was too law – only 35%, while V_{OC} had normal value of 1.1 V. The reason of low FF is high series resistance in the device, which occurred due to additional ITO film. After this, the work on ITO film improvement was done. It was found that changing O_2 flux value may affect the resistivity of the film, 11 sccm led to only 38 Ohm/sq, *T* spectrum showed also better transparency (Fig. 3, *a*). In such conditions champion semitransparent device with PCE of 11.6% was achieved with high FF value of 62% (Fig 3, *b*).

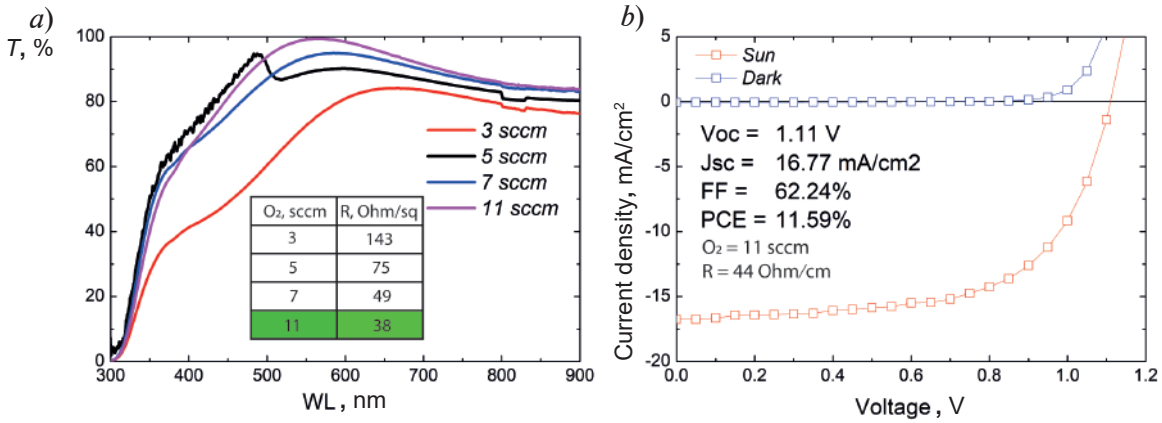

Fig. 3. *T* spectrum of different ITO films (*a*) and JV curves of the best semitransparent device (*b*)

In order to incorporate such solar cell in tandem with narrow bandgap material, the device should be transparent in IR part of spectrum. Transmittance was measured for a pixel from semitransparent window of the device (Fig. 4).

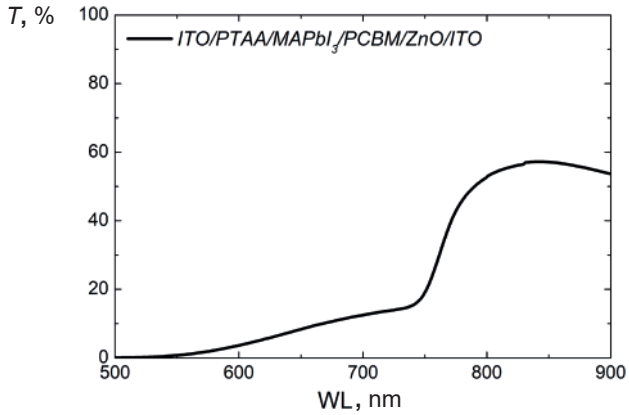

Fig. 4. T spectrum of the whole device measured through ITO window

It can be seen from the spectrum that obtained device passes radiation of IR part through itself. There are losses and *T* value is not high, but this device already may be used in experimental tandem systems with Si solar cells since it is semitransparent for long wavelengths.

Conclusion

In this work, semitransparent perovskite solar cells with double ETL and electrode were fabricated. High V_{OC} value of 1.1 V and FF of 62% led to PCE of 11.6%. Protective inorganic ZnO nanoparticles were spun onto PCBM to avoid high energy ion damage while sputtering process. Changing gas flux under room temperature conditions led to low resistance and high transparency of ITO films. Further optimization of ITO sputtering process should be done to improve J_{SC} of the semitransparent device, and after tandem solar cells of Si/perovskite or CIGS/perovskite may be produced.

Acknowledgments

This study was funded by Russian Science Foundation, grant number 23-73-00060.

REFERENCES

1. **Kojima A., Teshima K., Shirai Y., Miyasaka T.,** Organometal halide perovskites as visible-light sensitizers for photovoltaic cells. Journal of the American chemical society. 131 (2009) 6050–6051.

2. **Szabo G., Park N.-G., Angelis F., Kamat P.,** Are Perovskite Solar Cells Reaching the Efficiency and Voltage Limits?. ACS Energy Lett., 8, 9 (2023) 3829–3831.

3. **Unger E.L., Kegelmann L., Suchan K., Sorell D., Korte L., Albrecht S.,** Roadmap and roadblocks for the band gap tunability of metal halide perovskites. Journal of Materials Chemistry A. (2017) 11401–11409.

4. **Shockley W., Queisser H.J.,** Detailed Balance Limit of Efficiency of p-n Junction Solar Cells. J. Appl. Phys. 32 (1961) 510–519.

5. PVEducation. URL: https://www.pveducation.org/pvcdrom/tandem-cells. Accessed March 25, 2024.

6. **Lee H.-J., Cho S.-P., Na S.-I., Kim S.-S.,** Thin metal top electrode and interface engineering for efficient and air-stable semitransparent perovskite solar cells. Journal of Alloys and Compounds. 797 (2019) 65–73.

7. **Li Z., Kulkarni S.A., Boix P.P., Shi E., Cao A., Fu K., Batabyal S.K., Zhang J., Xiong Q., Wong L.H., Mathews N., Mhaisalkar S.G.,** Laminated Carbon Nanotube Networks for Metal Electrode-Free Efficient Perovskite Solar Cells. ACS Nano. 8, 7 (2014) 6797–6804.

THE AUTHORS

IVANOV Vladimir S.
vladimir.ivanov@metalab.ifmo.ru
ORCID: 0009-0005-0242-4784

SAPORI Daniel
daniel.sapori@gmail.com
ORCID: 0000-0002-9381-9650

Received 08.07.2024. Approved after reviewing 29.07.2024. Accepted 29.07.2024.

Conference materials
UDC 29.19.22
DOI: https://doi.org/10.18721/JPM.173.103

Thermal and electrical conductivity of grain boundaries in metals with bcc and fcc crystal lattices

E.V. Morozova [1] ✉, D.A. Timkaeva [1]

[1] Ulyanovsk State University, Ulyanovsk, Russia

✉ kat-valezhanina@yandex.ru

Abstract. This study employs first-principles calculation methods to investigate the thermoelectric properties of high-angle grain boundaries in metals (iron, titanium, copper, and nickel) with symmetric tilt boundaries of two types of crystal lattice: body-centered cubic and face-centered cubic. Grain boundaries play a significant role in carrier and phonon transport in materials. Altering geometric parameters is one of the simplest ways to control thermoelectric characteristics. By varying the grain rotation axis, rotation angle, and grain self-orientation, we derived the dependence of the electrical and thermal conductivity of studied materials on the geometry of the modeled device at room temperature. The results presented in the work can give an idea of the effect of this type of surface defect on thermal and electrical conductivity.

Keywords: grain boundary, electrical conductivity, thermal conductivity

Funding: This study was funded by the Russian Science Foundation under the grant number 22-11-00036.

Citation: Morozova E.V., Timkaeva D.A., Thermal and electrical conductivity of grain boundaries in metals with bcc and fcc crystal lattices, St. Petersburg State Polytechnical University Journal. Physics and Mathematics. 17 (3.1) (2024) 19–22. DOI: https://doi.org/10.18721/JPM.173.103

Материалы конференции
УДК 29.19.22
DOI: https://doi.org/10.18721/JPM.173.103

Тепло- и электропроводность границ зерен в металлах с ОЦК и ГЦК кристаллическими решетками

Е.В. Морозова [1] ✉, Д.А. Тимкаева [1]

[1] Ульяновский государственный университет, г. Ульяновск, Россия

✉ kat-valezhanina@yandex.ru

Аннотация. В данной работе использованы первопринципные методы расчета для исследования переноса электронов и фононов в высокоугловых границах зерен металлов (железо, титан, медь и никель) с симметричным наклоном границы двух типов кристаллической решетки: объемоцентрированная и гранецентрированная кубическая. Варьируя ось вращения зерен, угол поворота и собственную ориентацию зерен, мы получили зависимость транспорта электронов и фононов от геометрии моделируемого устройства. Результаты, приведенные в работе, могут дать представление о влиянии такого типа поверхностного дефекта на тепло- и электропроводность.

Ключевые слова: граница зерна, электрическая проводимость, теплопроводность

Финансирование: Исследование выполнено при финансовой поддержке Российского научного фонда по гранту № 22-11-00036.

Ссылка при цитировании: Морозова Е.В., Тимкаева Д.А. Тепло- и электропроводность границ зерен в металлах с ОЦК и ГЦК кристаллическими решетками // Научно-технические ведомости СПбГПУ. Физико-математические науки. 2024. Т. 17. № 3.1. С. 19–22. DOI: https://doi.org/10.18721/JPM.173.103

Introduction

The grain boundary (GB) is a two-dimensional (surface) defect in the atomic structure, separating two differently oriented grains (crystallites). Typically, it is a disordered multi-atom system with a wide variety of forms. GBs play a significant role in carrier and phonon transport in materials [1–2]. Various studies indicate that GBs are an active element of the material's defect structure, affecting properties such as plasticity, diffusion, fracture, and deformation at elevated temperatures, among others. The bonding at GBs differs from that in a regular crystalline lattice. Due to the formation of a specific structure at the grain contact region different from the perfect crystal structure, the properties of boundaries can differ from those of the bulk material [3–7].

At low temperatures, the resistivity of metals depends on the scattering of electrons on defects in the crystal lattice, and the contribution of thermal vibrations of lattice atoms should tend to zero. Metals are good conductors of electricity. Typically, such materials are also good heat conductors. In this regard, we will consider the electrical conductivity and thermal conductivity of nano-sized metallic materials with a defect in the form of a grain boundary.

The present study investigates the influence of a surface defect such as GB on the thermoelectric properties of grains of transition metals (iron, copper, titanium, nickel) and semiconductors (silicon carbide, boron nitride) with face-centered cubic and body-centered cubic lattices.

Materials and Methods

The calculations were carried out within the framework of the Slater-Koster method using the Density Functional Based Tight Binding (DFTB) formalism for electronic properties and molecular dynamics for thermal characteristics. The system, simulating the device, was divided into three regions: the left and right semi-infinite electrode regions and the central part. Transport coefficients were calculated using the non-equilibrium Green's function (NEGF) method, density functional theory (DFT), and non-equilibrium molecular dynamics. The studied parameters were computed using the following relationships:

$$G_{\mathrm{e}} = \left.\frac{dI}{dV_{\mathrm{bias}}}\right|_{dT=0}, \quad S = -\left.\frac{dV_{\mathrm{bias}}}{dT}\right|_{I=0}, \quad \lambda_{\mathrm{e}} = \left.\frac{dI_Q}{dT}\right|_{I=0}, \quad \Pi = \left.\frac{I_Q}{I}\right|_{dT=0} = SV_{\mathrm{bias}}. \tag{1}$$

Here, S is the Seebeck coefficient, G_{e} is electrical conductivity, T is absolute temperature, λ is thermal conductivity, which is equal to the sum of electronic λ_{e} and phonon λ_{ph} thermal conductivity, $I_Q = \mathrm{d}Q/\mathrm{d}T$ is the electronic component of the heat flux.

Results and Discussion

In our work, to obtain the dependences of electrical and thermal conductivity, we changed such geometric parameters of symmetrical grain boundaries as the rotation axis of the grains, the rotation angle, and the proper orientation of the grain boundary in space. Structure parameters are indicated in the Table. Examples of the calculation results are presented in Figures 1 and 2.

Near the Fermi level, the maximum thermal conductivity of nickel is greater than that of copper by 1.7. A similar relationship is observed for electrical conductivity.

The maximum conductivity of iron is achieved at grain rotation axes [001] and exceeds the minimum conductivity of 1.4 near the Fermi level.

Table

Characteristics of symmetrical inclined grain boundaries of metals

Axis of rotation	Name sample	Grain boundary	Disorientation angle	Lattice type
[001]	Fe	Σ 5(–2–10)	53.13°	bcc
[011]	Fe	Σ 3(11–1)	70.53°	bcc
[111]	Fe	Σ 3(–12–1)	60°	bcc
[111]	Ti	Σ 3(–12–1)	60°	bcc
[111]	Cu	Σ 3(–12–1)	60°	fcc
[111]	Ni	Σ 3(–12–1)	60°	fcc

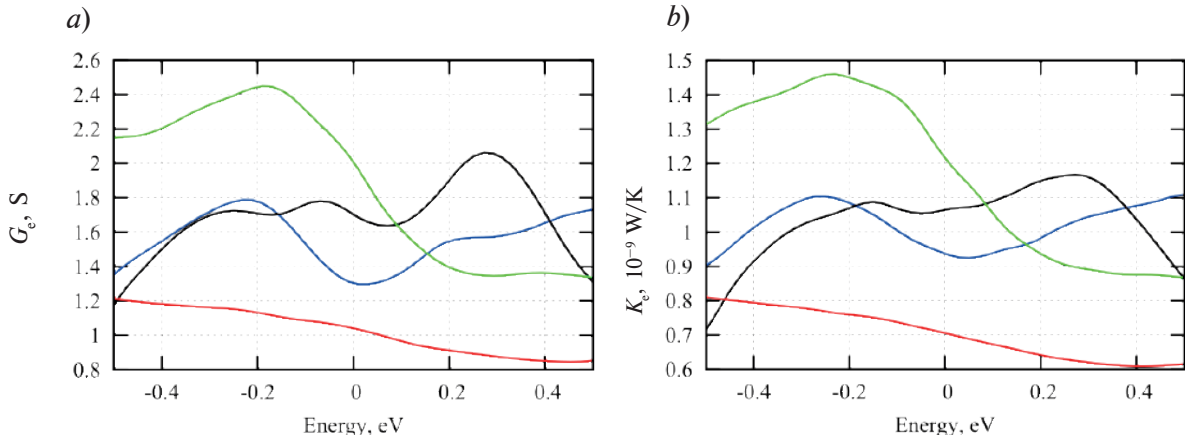

Fig. 1. Electrical conductivity (*a*) and thermal conductivity (*b*) coefficients for symmetric grain boundaries in metals with a [111] rotation axis: Fe – blue curve, Ti – black curve, Cu – red curve, Ni – green curve

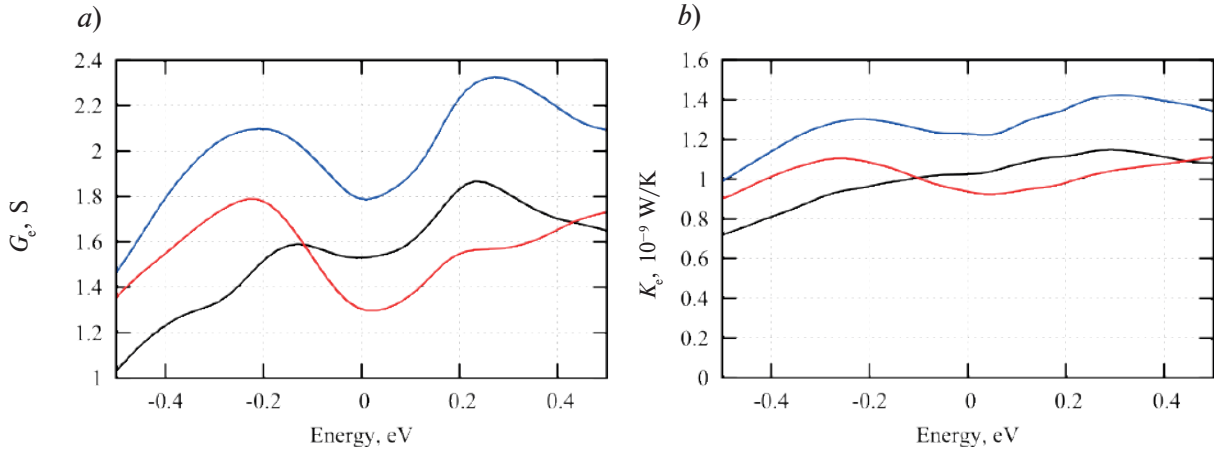

Fig. 2. Electrical conductivity (*a*) and thermal conductivity (*b*) coefficients for the symmetric grain boundary of iron with rotation axes [001] (blue curve), [011] (red curve), and [111] (black curve) are provided

Conclusion

Based on the results obtained, it can be concluded that the grain rotation axis and misorientation angle affect the conductivity parameters of the device to varying degrees for each material. For instance, metals with a face-centered cubic lattice will exhibit the highest electrical conductivity coefficient with grain rotation axes [001] and [011].

Contrary to the statement that highly conductive materials should conduct heat well, in low-dimensional metal structures, namely iron, titanium, nickel and copper, we observe low thermal conductivity (on the order of 0.7 to 2 nW/K) with comparatively high electrical conductivity (up to 2 Ohm^{-1} units). Then concludes that the grain boundary defect in metals can be used in nanostructured materials for thermal insulation applications.

REFERENCES

1. **Gottstein G.,** Physical foundations of materials science, Vol. 3, Berlin: Springer. 2004.

2. **Singh R., Schneibel J.H., Divinski S., Wilde G.,** Grain boundary diffusion of Fe in ultrafinegrained nanocluster-strengthened ferritic steel. Acta Materialia. 59 (4) (2011) 1346–1353.

3. **Wachowicz E., Kiejna A.,** Effect of impurities on grain boundary cohesion in bcc iron. Computational Materials Science. 43 (4) (2008) 736–743.

4. **Sutton A.P., Balluffi R.W.,** Interfaces in crystalline solids. Oxford: Clarendon. (1995) 856.

5. **Kodama T., et al.,** Modulation of thermal and thermoelectric transport in individual carbon nanotubes by fullerene encapsulation. Nature materials. 16 (9) (2017) 892–897.

6. **Sibatov R.T.,** Anomalous grain boundary diffusion: Fractional calculus approach. Advances in Mathematical Physics. 2019 (1) (2019) 8017363.

7. **L'vov P.E., Sibatov R.T.,** Phase-field model of grain boundary diffusion in nanocrystalline solids: Anisotropic fluctuations, anomalous diffusion, and precipitation. Journal of Applied Physics. 132 (12) (2002).

THE AUTHORS

MOROZOVA Ekaterina V.
kat-valezhanina@yandex.ru
ORCID: 0000-0002-7530-3933

TIMKAEVA Diana A.
dianatimkaeva@mail.ru
ORCID: 0000-0003-3748-0696

Received 11.07.2024. Approved after reviewing 27.08.2024. Accepted 28.08.2024.

Conference materials
UDC 621.315.592.3
DOI: https://doi.org/10.18721/JPM.173.104

The effect of the rate of temperature change on the thermomigration of liquid inclusions in silicon

B.M. Seredin [1] ✉, V.P. Popov [1], A.V. Malibashev [1], A.D. Stepchenko [1]

[1] Platov South-Russian State Polytechnic University (NPI), Novocherkassk, Russia;
✉ seredinboris@gmail.com

Abstract. The influence of the rate of temperature change of the composition on the consistency of the processes of dissolution, crystallization and atomic transfer in a liquid inclusion and at its boundaries, characteristic of stationary conditions of thermomigration, is theoretically estimated. Using the example of the silicon-aluminum system, the effect of stepwise and smooth temperature changes on the processes determining thermal migration and the velocity of movement of the liquid inclusion is established. A critical rate of temperature change has been found, above which thermomigration becomes impossible.

Keywords: thermomigration, silicon, crystallization, dissolution

Funding: This study was funded by the Ministry of Education and Science of the Russian Federation within the framework of the state assignment to the South Russian State Polytechnic University (NPI) named after M.I. Platov on the topic FENN-2023-0005.

Citation: Seredin B.M., Popov V.P., Malibashev A.V., Stepchenko A.D., The effect of the rate of temperature change on the thermomigration of liquid inclusions in silicon, St. Petersburg State Polytechnical University Journal. Physics and Mathematics. 17 (3.1) (2024) 23–27. DOI: https://doi.org/10.18721/JPM.173.104

Материалы конференции
УДК 621.315.592.3
DOI: https://doi.org/10.18721/JPM.173.104

Влияние скорости изменения температуры на термомиграцию жидких включений в кремнии

Б.М. Середин [1] ✉, В.П. Попов [1], А.В. Малибашев [1], А.Д. Степченко [1]

[1] Южно-Российский государственный политехнический университет (НПИ) им. М.И. Платова, г. Новочеркасск, Россия
✉ seredinboris@gmail.com

Аннотация. Теоретически оценено влияние скорости изменения температуры композиции на характерную для стационарных условий термомиграции согласованность процессов растворения, кристаллизации и атомарного переноса в жидком включении и на его границах. На примере системы кремний-алюминий установлено влияние ступенчатого и плавного изменения температуры на процессы, определяющие термомиграцию и скорость движения жидкого включения. Найдена критическая скорость изменения температуры, выше которой термомиграция становится невозможной.

Ключевые слова: термомиграция, кремний, скорость нагрева, скорость охлаждения, скорость миграции

Финансирование: Работа выполнена при поддержке Минобрнауки России в рамках государственного задания Южно-Российскому государственному политехническому университету (НПИ) имени М.И. Платова по теме FENN-2023-0005.

Ссылка при цитировании: Середин Б.М., Попов В.П., Малибашев А.В., Степченко А.Д. Влияние скорости изменения температуры на термомиграцию жидких включений в кремнии // Научно-технические ведомости СПбГПУ. Физико-математические науки. 2024. Т. 17. № 3.1. С. 23–27. DOI: https://doi.org/10.18721/JPM.173.104

Introduction

Thermomigration (TM) of liquid inclusions (zones) in solids under the action of a temperature gradient is used in physico-chemical studies and for the formation of electrically heterogeneous structures in a silicon wafer [1–4]. The movement of the zones is caused by the recrystallization of silicon through a metal-based solvent zone, which lowers the temperature of formation of the liquid phase. The rate of TM under stationary conditions is determined by three self-consistent processes: dissolution at the "hot" boundary of the zone, diffusion transfer of atoms through the zone and crystallization at the "cold" boundary. The advantage of the TM method is the high recrystallization rate, which is 3–4 orders of magnitude higher than the rate of solid-state diffusion. This makes it possible to form channels not only on the surface, but also in the volume of the wafer.

In stationary TM conditions, the temperature of the zone increases as it migrates in the direction of the temperature gradient and usually does not exceed several degrees. This ensures quasi-isothermal conditions of the process, which is important for the uniformity and crystal perfection of the formed structures. The temperature of the zone can be changed by regulating the power of the heating device, which inevitably occurs when the composition is heated before entering stationary mode and when cooled after TM. Moreover, the heating or cooling time is commensurate with the time of the stationary mode. In particular, the temperature change causing supersaturation or undersaturation of the melt solution is an additional driving force for the crystallization and dissolution processes at TM, which has not been studied. The effects of abrupt (stepwise) and smooth (slow) temperature changes on the processes occurring in the zone are different. Previously, the influence of only small temperature fluctuations in the TM process was considered in the literature [5]. The rate of temperature change can affect the interrelated processes of dissolution, crystallization and atomic transfer in the zone, which determine the velocity and shape of the liquid zone. The aim of the work is theoretically assess this effect using the example of the silicon-aluminum system.

Stepwise temperature change

The temperature T in the zone is established much faster than the concentration of components in the melt solution, since the coefficients of thermal conductivity and diffusion differ by about three orders of magnitude. Therefore, with a stepwise temperature change, the establishment of the concentration distribution necessary for TM in the zone is delayed for some time.

Let's estimate the value of τ using a one—dimensional numerical model of mass transfer based on the diffusion equation

$$\frac{\partial C}{\partial t} = D\frac{\partial^2 C}{\partial x^2},$$

where $D(T)$ and $C(x,t)$ are the diffusion coefficient and the silicon concentration in the zone, t is current time, x is coordinate in the direction of the temperature gradient G (Fig. 1, *a*).

The initial distribution of the concentration $C(x, 0)$ corresponding to the stationary regime of TM is shown on curve *1* (Fig. 1, *b*), which shows the temperature differences at the boundaries of the zone necessary for the continuous processes of dissolution and crystallization. A stepwise change in temperature causes a change in the concentration of silicon at both boundaries of the zone according to the phase diagram of the system. In this case, the thickness of the zone increases or decreases proportionally if the temperature jump is positive or negative. The time of equilibrium of concentration at the boundaries of the zone is neglected, since the temperature

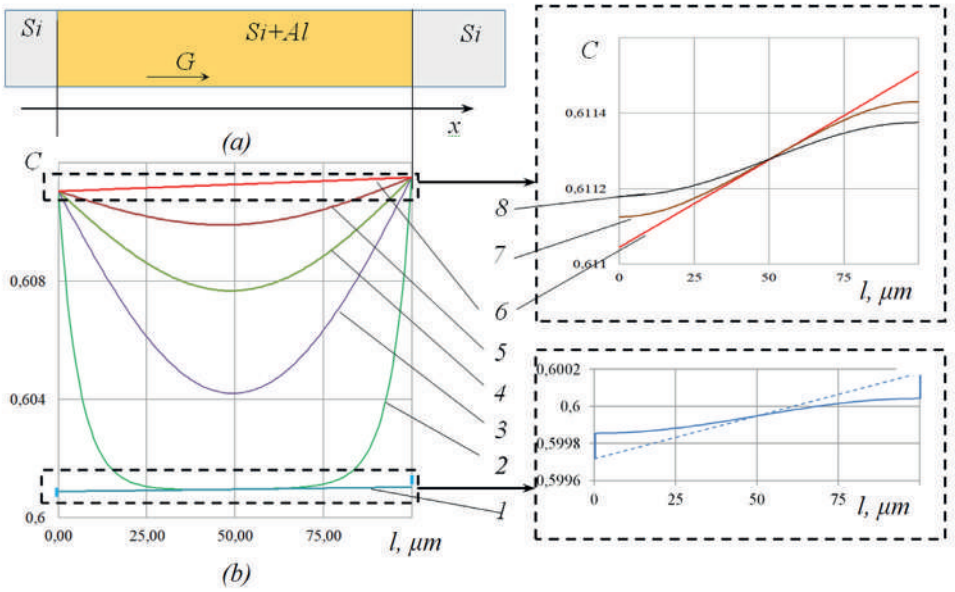

Fig. 1. Diagram of the liquid zone motion model (*a*) and the distribution of silicon concentration in the liquid phase at $t = 0$; 0.003; 0.06; 0.12; 0.21; 0.9; 0.95; 1 s (curves *1* – *8*) (*b*)

jump is greater than the temperature drop in the zone. Fig. 1, *b* shows as an example the calculated curves (*2* – *8*) of the distribution of silicon concentration in the zone for different time points at an initial temperature $T = 1373$ K, $G = 40$ K/cm, $l = 100$ microns for a temperature jump of 10 K. Upon reaching the concentration distribution (curve *6*, Fig. 1, *b*) in the boundary conditions of the diffusion problem, deviations of concentration from equilibrium values were taken into account, which is necessary for the implementation of atomic kinetic processes at both boundaries of the zone (Fig. 1, *b*).

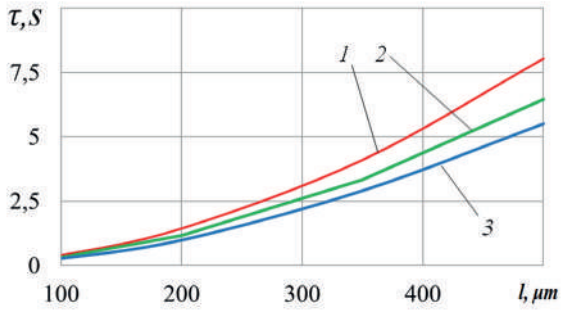

Fig. 2. Dependence of the time of establishment of the stationary regime on the thickness of the flat zone at different values of the TM temperature
1 – $T = 1173$ K, *2* – $T = 1373$ K, *3* – $T = 1573$ K

During the simulation, it was assumed that the concentration differences in the zone necessary for the coordinated processes of crystallization, dissolution and diffusion have the same values. The variation of these differences had a slight (within 5%) effect on the time of establishing a stationary concentration distribution. The total setting time was 0.5 — 8 s for typical TM conditions. The value of τ depended most sharply on l, less sharply on T (Fig. 2) and practically did not depend on the value of temperature jump. During this period of time, the zone stopped, and then continued to migrate at a constant rate corresponding to the new temperature value.

Smooth temperature change

Such a temperature change affects the atomic kinetic processes of dissolution or crystallization and causes inhibition or blocking of boundary movement. An increase in temperature inhibits

crystallization at the "cold" boundary of the zone and promotes dissolution at the "hot" one. Lowering the temperature makes it difficult or blocks dissolution at the "hot" boundary and promotes crystallization at the "cold" one. Blocking any of these processes stops the movement of the zone.

We find the critical velocity of the acr blocking the movement of the zone, based on the thicknesses of the layers grown (or dissolved) due to thermal migration of h_G and cooling (or heating) h_T at one of the boundaries of the zone in a short period of time Δt: $h_G = \upsilon \Delta t$ and $h_T = 0.5\, \Delta C\, l$. Here υ — speed of movement of the zone, ΔC — change in silicon concentration with a temperature change by ΔT during Δt: $\Delta C = \dfrac{dC}{dT}\Delta T$, where dC/dT — cotangent of the angle of inclination of the liquidus line of the system state diagram, $\Delta T = a_{cr}\, \Delta t$. The change in the volume of silicon during the phase transition is small and it is not taken into account. Equating h_G and h_T, we obtain the formula for the critical rate of temperature change $a_{cr} = 2\upsilon/l$. The numerical value of a_{cr} for typical TM conditions was 1 – 10 K/s (Fig. 3).

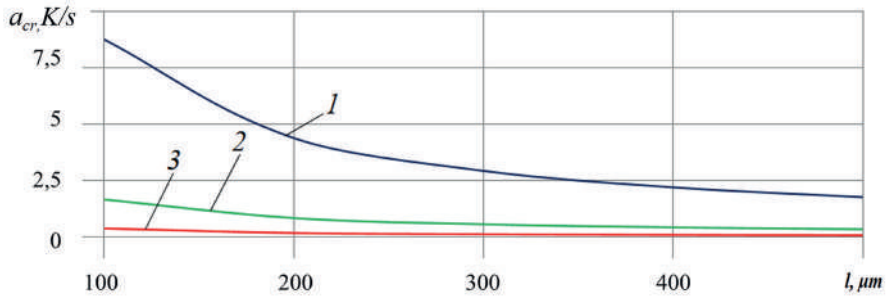

Fig. 3. Dependence of the critical rate of temperature change on the thickness of the flat zone at different temperature values
1 – T = 1173 K, *2* – T = 1373 K, *3* – T = 1573 K

If the actual rate of temperature change is greater than the critical one, then the movement of the zone is impossible due to the blocking of one of the two processes at the boundary of the zone, depending on the heating or cooling of the composition. At $a < a_{cr}$, the velocity of movement of the zone can both decrease and increase. The decrease υ corresponds to the same difficulty of crystallization and dissolution processes. However, dissolution is more difficult for the Si-Al system [1], which leads to deformation (compression) of the zone in the direction of movement. By adjusting the heating rate during the TM process, it is possible to relax the restrictions at the dissolution boundary, while maintaining an acceptable crystallization rate. In this case, an increase in the velocity and a decrease in the degree of deformation of the zone is achievable.

Conclusion

A stepwise change in the temperature of the composition at TM stops the movement of the zone for a short time, and with a smooth change in temperature, the velocity of the zone can both decrease and increase at heating or cooling speeds lower than the found critical value. When the temperature change rates exceed the critical one, the movement of the zone becomes impossible. In the area of speeds lower than the critical one, temperature changes in the TM process can control the deformation of the zone.

REFERENCES

1. **Lozovskii V.N., Lunin L.S., Popov V.P.,** Zonnaya perekristallizaciya gradientom temperatury poluprovodnikovyh materialov, Metallurgiya. Moscow. 1987.

2. **Cline H.E., Anthony T.R.,** Thermomigration of aluminum-rich liquid wires through silicon, J Appl. Phys. 47 (6) (1976) 2332–2336.

3. **Morillon B., Dilhac J.-M., Ganibal C., Anceau C.,** Study of aluminum thermomigration as a low thermal budget technique for innovative power devices, Microelectronics Reliability. 43 (4) (2003) 565–569.

4. **Poluhin A.,** Issledovanie tekhnologicheskih faktorov processa termomigracii, Silovaya elektronika. 2 (2009) 90–92.

5. **Gershanov V.Y., Garmashov S.I.,** Nelinejnye nestacionarnye effekty v processah massoperenosa, Izdatel'stvo YUFU, Rostov-on-Don, 2014.

THE AUTHORS

SEREDIN Boris M.
seredinboris@gmail.com
ORCID: 0000-0002-1405-5745

MALIBASHEV Alexander V.
a_malib@mail.ru
ORCID: 0000-0001-9534-2246

POPOV Victor P.
popovnpi@gmail.com
ORCID: 0000-0001-6561-4319

STEPCHENKO Artem D.
Stepchenko.A.D@yandex.ru
ORCID: 0009-0008-9843-6553

Received 10.07.2024. Approved after reviewing 01.08.2024. Accepted 01.08.2024.

Conference materials
UDC 538.975
DOI: https://doi.org/10.18721/JPM.173.105

Control of properties and geometric characteristics of selectively formed GaAs nanowires within the FIB treatment area on Si(111)

N.A. Shandyba [1] ✉, M.M. Eremenko [1], V.A. Sharov [2, 3],
S.V. Balakirev [1], M.S. Solodovnik [1]

[1] Southern Federal University, Taganrog, Russia;
[2] Alferov University, St. Petersburg, Russia;
[3] Ioffe Institute, St. Petersburg, Russia
✉ shandyba@sfedu.ru

Abstract. In this paper we present the results of experimental studies on the selective formation of GaAs nanowire arrays on the Si(111) substrate surface and the control of their properties. It has been shown that pre-treatment of the Si(111) surface with a native oxide layer by a focused Ga-ion beam with further low-temperature annealing and high-temperature growth allows the formation of selective GaAs nanowire arrays with a different set of parameters that can be controlled by changing the dose of ion-beam treatment. We also demonstrated the possibility of obtaining arrays with a yield of vertically oriented nanowires at the level of almost 100% and very high density (up to 8 μm^{-2}). At the same time outside the modified areas, the formation of nanowires was almost completely suppressed. Moreover, based on Raman spectroscopy study we have found that our approach allows to obtain nanowire arrays with clear zinc-blende crystal phase in wide range of nanostructure sizes.

Keywords: nanowires, gallium arsenide, focused ion beam, molecular beam epitaxy, A3B5

Funding: This work was funded by the Ministry of Science and Higher Education of the Russian Federation: Grant No. FENW-2022-0034 and Grant № FSRM-2023-0007.

Citation: Shandyba N.A., Eremenko M.M., Sharov V.A., Balakirev S.V., Solodovnik M.S., Control of properties and geometric characteristics of selectively formed GaAs nanowires within the FIB treatment area on Si(111), St. Petersburg State Polytechnical University Journal. Physics and Mathematics. 17 (3.1) (2024) 28–33. DOI: https://doi.org/10.18721/JPM.173.105

Материалы конференции
УДК 538.975
DOI: https://doi.org/10.18721/JPM.173.105

Управление свойствами и геометрическими характеристиками селективно сформированных нитевидных нанокристаллов GaAs в области обработки ФИП на подложке Si(111)

Н.А. Шандыба [1] ✉, М.М. Ерёменко [1], В.А. Шаров [2, 3],
С.В. Балакирев [1], М.С. Солодовник [1]

[1] Южный федеральный университет, г. Таганрог, Россия;
[2] Алферовский университет, Санкт-Петербург, Россия;
[3] Физико-технический институт им. А.Ф. Иоффе РАН, Санкт-Петербург, Россия
✉ shandyba@sfedu.ru

Аннотация. В данной работе представлены результаты экспериментальных исследований селективного формирования массивов нитевидных нанокристаллов GaAs

на поверхности подложки Si(111) и их свойств. Было показано, что предварительная обработка поверхности Si(111) со слоем естественного оксида фокусированным пучком ионов Ga с последующим низкотемпературным отжигом и высокотемпературным ростом позволяет локально формировать массивы нитевидных нанокристаллов GaAs с различным набором параметров, которыми можно управлять, изменяя дозу ионно-лучевой обработки. Продемонстрирована возможность получения массивов с выходом вертикально ориентированных нитевидных нанокристаллов на уровне практически 100% и очень высокой плотностью (до 8 мкм$^{-2}$). При этом вне области обработки образование нитевидных нанокристаллов было практически полностью подавлено. Результаты анализа образцов спектроскопией комбинационного рассеяния света показали возможность получения массивов нитевидных нанокристаллов со структурой цинковой обманки в широком диапазоне размеров наноструктур.

Ключевые слова: нанопроволоки, арсенид галлия, фокусированный ионный пучок, молекулярно-лучевая эпитаксия, A3B5

Финансирование: Работа выполнена при финансовой поддержке Министерства науки и высшего образования Российской Федерации: грант № FENW-2022-0034 и № FSRM-2023-0007.

Ссылка при цитировании: Шандыба Н.А., Ерёменко М.М., Шаров В.А., Балакирев С.В., Солодовник М.С. Управление свойствами и геометрическими характеристиками селективно сформированных нитевидных нанокристаллов GaAs в области обработки ФИП на подложке Si(111) // Научно-технические ведомости СПбГПУ. Физико-математические науки. 2024. Т. 17. № 3.1. С. 28–33. DOI: https://doi.org/10.18721/JPM.173.105

Introduction

Currently, A3B5 nanowires (NWs) are of great interest as key elements for creating promising photonic and nanoelectronic devices [1, 2]. The availability of technology capable of precisely controlling the NW position and their various properties and geometric parameters is required for the creation of various devices [3]. To date, one of the most perspective technologies for this purpose is focused ion beam (FIB) treatment of the substrate surface prior to NW growth [4–7]. However, the processes of NW epitaxial growth on the surface prepared in this way, as well as the influence of substrate processing parameters by the FIB method on the resulting characteristics of the formed NW arrays remain poorly understood and require additional research. In this paper, we study the selective growth of GaAs NW arrays within the FIB treatment area on the Si(111) surface with a native oxide layer at a high growth temperature and the dose effect on their properties and geometric characteristics.

Materials and Methods

Experimental studies were carried out on Si(111) p-type epi-ready substrate with a native oxide layer. The Ga ions were implanted into the substrate at an accelerating voltage of 30 kV according to a template consisting of several 5×5 μm square areas in which the dose ranged from 0.052–52 pC/μm^2. Then annealing was performed at a temperature of 600 °C for 1 hour. After that, the NW growth was carried out with substrate temperature of 750 °C with a nominal deposition rate of 0.25 ML/s for 48 minutes by the MBE method. The sample was analyzed by SEM and Raman spectroscopy methods. The Raman spectra were measured at room temperature using a Horiba LabRam HR800 setup equipped with a 532 nm laser.

Results and Discussion

SEM images analysis of the surface after NW growth shows that GaAs NW arrays selectively form within areas treated with an ion beam (Fig. 1). At the same time, their growth is practically

suppressed outside the modification area and only the formation of low-density GaAs crystallites is observed (Fig. 1, *d*). It is also seen that changing the dose allows to control key NW morphological characteristics, such as: density, length, diameter and yield of vertical NWs (Fig. 1, *a*, *b*, *c*). The character of the dose effect on the NW parameters is presented through the dependences plotted based on SEM images statistical processing (Fig. 2, *a*, *b*).

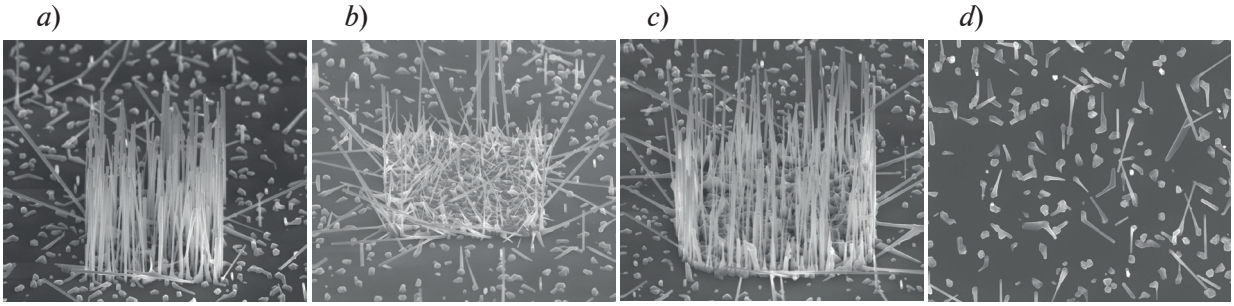

Fig. 1. Tilted SEM-images of modified areas after GaAs nanowire growth for ion doses: 0.052 (*a*), 5.2 (*b*), 52 (*c*) pC/μm^2 and for unmodified area (*d*). The size of the SEM images is 10×10 μm

The analysis of the obtained dependences shows that the curves change character from the FIB dose is rather complex and nonlinear. So, selective formation of an NW array with almost 100% verticality value is observed at the beginning of the ion dose range (0.052 pC/μm^2 see Fig. 1, *a*, 2, *a*). This is an unexpected result considering that the growth occurs on the substrate surface with a native oxide layer [8]. The value of the NW density in this case is ~ 5 μm^{-2}. The deviation of some NWs within the array from the vertical position (angle less than 90° between the surface and the NW itself) is due to the fact that this NWs were formed in the transition area between the FIB surface treatment and the reference region without modification. Such NWs were categorized as non-vertical. A slight deviation and connection between neighboring NWs near their top are due to the impact of the electron beam on them in the process of SEM surface analysis [9]. It is also worth noting that in the whole range of considered ion doses, only for a certain dose value (0.052 pC/μm^2) the NW formation with maximum average values of length (3.6 ± 0.25 μm) and diameter (65 ± 4 nm) within the array is observed (Fig. 2, *b*). At the same time, the NW diameter is practically equal to the reference values (71 ± 4 nm) whereas the length is 2.25 times greater than that outside the processing area (1.6 ± 0.2 μm). Then, as the ion dose rises, the NW density slightly increases (up to ~ 7 μm^{-2}) and the values of the NW verticality, length and diameter begin to decrease (Fig. 2, *a*, *b*). However, the verticality also remains in the region of high values (about 80% for 0.52 pC/μm^2) compared to the unmodified area (20%). A further increase in the dose leads to a sharp decrease and stabilization of all key NW characteristics in the region of minimum values within the dose range of 1.56 – 26 pC/μm^2. The values stabilize at: 5.4 μm^{-2} for density, 10% for verticality, 29 ± 2 nm and 0.7 ± 0.12 μm for diameter and length, respectively (Fig. 2, *a*, *b*). This can be attributed to the formation of a GaAs polycrystalline base (Fig. 1, *b*) that changes the conditions and mechanism of NW growth on the surface within the treatment area [10]. Meanwhile, it is also interesting to note that this stabilization is aborted by a subsequent increase in ion dose (52 pC/μm^2). This leads to a sharp increase in all NW characteristics and the formation of an array with a maximum density (Fig. 1, *c*) equal to 8 μm^{-2} which is 20 times greater than that outside the treatment area (0.42 μm^{-2}). It is also worth noting that the curves of the length, diameter and verticality of NWs show a similar character of dependence on the FIB dose. The density values, in contrast, change slightly and fluctuate mainly in the range from 5 to 7 μm^{-2}, except for the last point in the considered dose range. Mechanisms underlying the FIB dose effect on the NW parameters is reflected in [11].

Furthermore, it is important to mention that the technology developed and applied in this work, on the one hand, allows to obtain high-density NW arrays with 100% verticality and, on the other hand, allows to obtain arrays with high selectivity on the silicon surface with native oxide layer. An important feature of this approach is the absence of the need for templates, masks and the use of complex lithographic techniques for surface preparation before growth. We assume that such selectivity is achieved primarily by the by using a combination of low-temperature

annealing and high-temperature growth. This allows to reduce the number of pores formed on the substrate surface in the native oxide layer outside the modification area during the annealing stage. Simultaneously, this temperature facilitates their formation within the ion beam treatment area through the chemical interaction of embedded Ga ions diffusing to the substrate surface with oxide atoms [11]. The high growth temperature reduces the probability of nucleation outside the modification area while increasing it within the FIB treatment area due to the abundance of nanopores and active diffusion of Ga atoms over the Si surface.

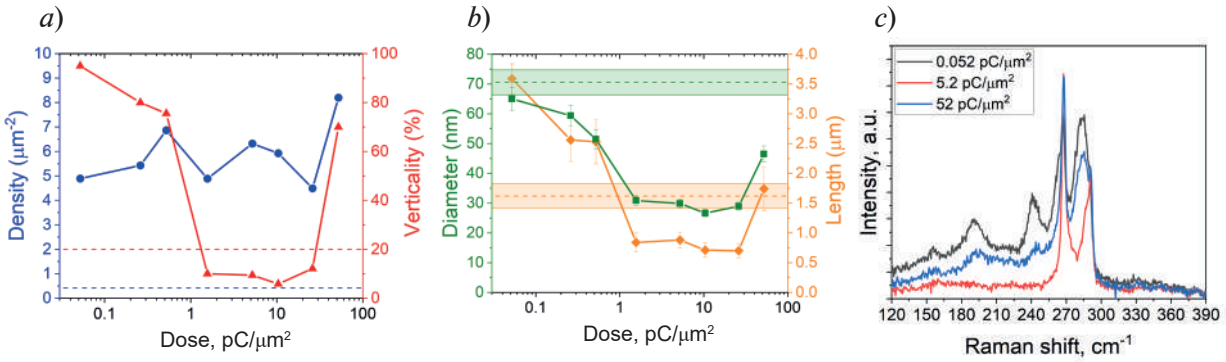

Fig. 2. Dependence of the NW density and verticality (*a*) and diameter and length (*b*) on Ga ion dose. Dash lines correspond to values for unmodified area. Raman spectra from NW arrays formed within the area with different FIB dose (*c*)

The obtained results analysis of NW arrays structural studies by Raman spectroscopy shows the presence of the main intense peaks at frequencies 267 cm^{-1} and 291 cm^{-1} in the whole ion dose range (Fig. 2, *c*). These peaks are typical for transverse (TO) and longitudinal (LO) optical phonons, respectively, in a GaAs bulk crystal with a cubic zinc-blende (ZB) lattice [12]. We can also distinguish the peak formation (low-frequency shift in the LO mode region) with the maximum value of its intensity varying with increasing ion dose in the range of 281 – 287 cm^{-1}. This peak is associated with surface optical (SO) phonons in the ZB lattice of GaAs [13]. The SO peak position dependence on the ion dose is related to the change in the NW geometrical characteristics (Fig. 2, *b*) as the dose increases [14]. It is important to note that the peaks described above are typical only for the cubic crystal lattice of GaAs. The presence of wurtzite (WZ) hexagonal insertions in ZB GaAs NW (polytypism) is usually determined by the presence of an additional peak on the spectra located in the region of 258 cm^{-1} (E2 mode) [15]. As can be seen from the spectra in Figure 2, *c*, the peak responsible for the E2 mode is completely absent in this frequency region which generally indicates that the NW arrays formation occurs in a single ZB crystalline phase of sphalerite, regardless of the FIB dose applied.

Conclusion

Thus, it was shown that the developed approach based on the preliminary preparation of Si(111) surface with a native oxide layer by focused Ga ion beam in combination with optimal annealing and growth parameters allows to form selective GaAs NW arrays and to control their characteristics within a wide range by changing the ion dose. At the same time, for certain dose values the vertical NW yield can be maintained above 80% and increased up to almost 100%. Based on the results of Raman spectroscopy it was also revealed that the developed technique allows to form NWs with a single zinc-blende crystalline phase regardless of the applied FIB dose. It is worth noting that this approach does not require the use of additional templates, masks, resist and chemical etchants and allows to perform all necessary operations in a single technological cycle. This makes this technology fully compatible with vacuum equipment and relatively simple and cheap which is an extremely important factor in the creation of the integrated photonics element base.

REFERENCES

1. **Quan L.N., Kang J., Ning C.Z., Yang P.,** Nanowires for Photonics, Chem. Rev. 119 (2019) 9153–9169.

2. **Barrigyn E., Heurlin M., Bi Z., Monemar B., Samuelson L.,** Synthesis and Applications of III–V Nanowires, Chem. Rev. 119 (2019) 9170–9220.

3. **Demontis V., Zannier V., Sorba L., Rossella F.,** Surface Nano-Patterning for the Bottom-Up Growth of III-V Semiconductor Nanowire Ordered Arrays, Nanomaterials. 11 (2021) 2079.

4. **Shandyba N., Balakirev S., Sharov V., Chernenko N., Kirichenko D., Solodovnik M.,** Effect of Si(111) Surface Modification by Ga Focused Ion Beam at 30 kV on GaAs Nanowire Growth, Int. J. Mol. Sci. 24 (2023) 224.

5. **Bahrami D., Mostafavi Kashani S. M., Al Hassan A., Davtyan A., Pietsch U.,** High yield of self-catalyzed GaAs nanowire growth on silicon (111) substrate templated by focused ion beam patterning, Nanotechnology. 31 (2020) 185302.

6. **Shandyba N., Kirichenko D., Chernenko N., Eremenko M., Balakirev S., Solodovnik M.,** Effect of FIB-modification of Si(111) surface on GaAs nanowire growth, St. Petersbg. State Polytech. Univ. Journal. Phys. Math. 15 (2022) 36–41.

7. **Shandyba N.A., Kirichenko D.V., Chernenko N.E., Sharov V.A., Balakirev S.V., Solodovnik M.S.,** Effect of ion dose and accelerating voltage during Si(111) surface FIB treatment on GaAs nanowires growth, St. Petersbg. State Polytech. Univ. Journal. Phys. Math. 16 (2023) 79–83.

8. **Bastiman F., Кьpers H., Somaschini C., Geelhaar L.,** Growth map for Ga-assisted growth of GaAs nanowires on Si(111) substrates by molecular beam epitaxy, Nanotechnology. 27 (2016) 095601.

9. **Dai X., Dayeh S.A., Veeramuthu V., Larrue A., Wang J., Su H., Soci C.,** Tailoring the Vapor–Liquid–Solid Growth toward the Self-Assembly of GaAs Nanowire Junctions, Nano Lett. 11 (2011) 4947–4952.

10. **Shandyba N.A., Chernenko N.E., Balakirev S.V., Eremenko M.M., Kirichenko D.V., Solodovnik M.S.,** Investigation of the influence of the ion-beam treatment dose of the Si(111) surface on the GaAs nanowires growth processes, Semiconductors. 56 (2022) 541.

11. **Shandyba N.A., Kirichenko D.V., Sharov V.A., Chernenko N.E., Balakirev S.V., Solodovnik M.S.,** Modulation of GaAs nanowire growth by pre-treatment of Si substrate using a Ga focused ion beam, Nanotechnology. 34 (2023) 465603.

12. **Spirkoska D., Arbiol J., Gustafsson A., Conesa-Boj S., Glas F., Zardo I., Heigoldt M., Gass M.H., Bleloch A. L., Estrade S., Kaniber M., Rossler J., Peiro F., Morante J.R., Abstreiter G., Samuelson L.,** Fontcuberta i Morral A., Structural and optical properties of high-quality zinc-blende/wurtzite GaAs nanowire heterostructures, Phys. Rev. B. 80 (2009) 245325.

13. **Spirkoska D., Abstreiter G., Fontcuberta i Morral A.,** Size and environment dependence of surface phonon modes of gallium arsenide nanowires as measured by Raman spectroscopy, Nanotechnology. 19 (2008) 435704.

14. **Spirkoska D., Abstreiter G., Fontcuberta i Morral A.,** GaAs nanowires and related prismatic heterostructures, Semicond. Sci. Technol. 24 (2009) 113001.

15. **Ramsteiner M., Brandt O., Kusch P., Breuer S., Reich S., Geelhaar L.,** Quenching of the E2 phonon line in the Raman spectra of wurtzite GaAs nanowires caused by the dielectric polarization contrast, Appl. Phys. Lett. 103 (2013).

THE AUTHORS

SHANDYBA Nikita A.
shandyba@sfedu.ru
ORCID: 0000-0001-8488-9932

BALAKIREV Sergey V.
sbalakirev@sfedu.ru
ORCID: 0000-0003-2566-7840

EREMENKO Mikhail M.
eryomenko@sfedu.ru
ORCID: 0000-0002-7987-0695

SOLODOVNIK Maxim S.
solodovnikms@sfedu.ru
ORCID: 0000-0002-0557-5909

SHAROV Vladislav A.
vl_sharov@mail.ru
ORCID: 0000-0001-9693-5748

Received 09.07.2024. Approved after reviewing 19.07.2024. Accepted 19.07.2024.

Conference materials
UDC 538.958; 538.975
DOI: https://doi.org/10.18721/JPM.173.106

Photoluminescence of self-induced InAs nanowires diluted with nitrogen

M.S. Ruzhevich [1] ✉, K.D. Mynbaev [2], N.L. Bazhenov [2], A.K. Kaveev [2],
A.V. Pavlov [3], V.V. Fedorov [3, 4], I.S. Mukhin [3]

[1] ITMO University, St. Petersburg, Russia;
[2] Ioffe Institute, St. Petersburg, Russia;
[3] Peter the Great St. Petersburg Polytechnic University, St. Petersburg, Russia;
[4] Alferov University, St. Petersburg, Russia
✉ max.ruzhevich@niuitmo.ru

Abstract. Photoluminescence of arrays of self-induced nanowires consisting of pure InAs and of InAs diluted with nitrogen was studied in the 4.2–300 K temperature range. Formation of the hexagonal wurtzite (nanowires) and cubic sphalerite (mostly parasitic islands) crystal structure modifications was observed on a Si substrate used for the growth of the nanowires. A decrease in the band gap of both crystalline phases due to the introduction of nitrogen was established.

Keywords: InAs, nanowires, photoluminescence, crystal structure

Funding: This study was funded by the Russian Scientific Foundation (RSF project [22-19-00494]) for epitaxial growth of the nanowires.

Citation: Ruzhevich M.S., Mynbaev K.D., Bazhenov N.L., Kaveev A.K., Pavlov A.V., Fedorov V.V., Mukhin I.S., Photoluminescence of self-induced InAs nanowires diluted with nitrogen, St. Petersburg State Polytechnical University Journal. Physics and Mathematics. 17 (3.1) (2024) 34–37. DOI: https://doi.org/10.18721/JPM.173.106

Материалы конференции
УДК 538.958; 538.975
DOI: https://doi.org/10.18721/JPM.173.106

Фотолюминесценция самоиндуцированных нитевидных нанокристаллов InAs, разбавленных азотом

М.С. Ружевич [1] ✉, К.Д. Мынбаев [2], Н.Л. Баженов [2], А.К. Кавеев [2],
А.В. Павлов [3], В.В. Федоров [3, 4], И.С. Мухин [3]

[1] Университет ИТМО, Санкт-Петербург, Россия;
[2] Физико-технический институт им. А.Ф. Иоффе РАН, Санкт-Петербург, Россия;
[3] Санкт-Петербургский политехнический университет Петра Великого, Санкт-Петербург, Россия;
[4] Академический университет им. Ж.И. Алфёрова РАН, Санкт-Петербург, Россия
✉ max.ruzhevich@niuitmo.ru

Аннотация. В интервале температур 4,2–300 K исследована фотолюминесценция массивов самоиндуцированных нитевидных нанокристаллов из чистого InAs и InAs, разбавленного азотом. Наблюдалось формирование как гексагональной типа вюрцита (нитевидные нанокристаллы), так и кубической типа сфалерита (преимущественно паразитные островки) фаз кристаллической структуры материала на подложке Si,

использовавшейся для роста нанокристаллов. Установлено уменьшение ширины запрещенной зоны обеих кристаллических фаз при введении в материал азота.

Ключевые слова: InAs, нитевидные нанокристаллы, фотолюминесценция, кристаллическая структура

Финансирование: Работа поддержана грантом РНФ [22-19-00494] в части эпитаксиального роста нанокристаллов.

Ссылка при цитировании: Ружевич М.С., Мынбаев К.Д., Баженов Н.Л., Кавеев А.К., Павлов А.В., Федоров В.В., Мухин И.С. Фотолюминесценция самоиндуцированных нитевидных нанокристаллов InAs, разбавленных азотом // Научно-технические ведомости СПбГПУ. Физико-математические науки. 2024. Т. 17. № 3.1. С. 34–37. DOI: https://doi.org/10.18721/JPM.173.106

Introduction

InAs compound semiconductor has a direct band gap and high electron mobility, and is widely used in infrared (IR) optoelectronics. The bulk InAs material has a cubic crystal lattice of the sphalerite (zinc blende, ZB) type with a band gap E_g ~0.35 eV at the temperature T = 300 K. Recently, interest has been growing in InAs-based nanowires (NWs); these can be used for the fabrication of photodetectors and emitters operating in the mid-IR spectral region (wavelength $\lambda = 3–6$ μm) [1–3]. The transition to NW geometry provides an efficient method for electrical and optical confinement, which can improve the efficiency of photo- and optoelectronic devices. However, the growth of low-dimensional InAs structures allows for the formation of both cubic ZB and hexagonal wurtzite (WZ) type structures [4], with E_g of the latter being ~0.4 eV at 300 K. In this work, we studied the influence of the morphology and crystal structure modifications on the InAs NW photoluminescence (PL) spectra. In addition, we used the PL method to study the nitrogen dilution in NWs. Introduction of nitrogen can reduce optical E_g, and thus, extend the working range of the devices to longer wavelengths. This effect is believed to originate in the changes of electronic structure of the material through the interaction between localized N levels and the InAs band states [5].

Materials and Methods

Arrays of NWs (120–150 nm in diameter and 1–2.5 μm in height) made of pure InAs and InAs diluted with nitrogen (InAsN) were grown by plasma-assisted molecular beam epitaxy (PA-MBE) using a Veeco GEN III MBE system on Si(111) substrates using the method described elsewhere [6]. With the method, NW formation occurs without the use of third-party catalysts; it proceeds in a self-induced mode at pinhole defects formed in the SiO_x layer under high temperature annealing performed after wet substrate oxidation. According to scanning electron microscopy studies, besides NWs, additional parasitic islands were formed on the SiO_x surface outside of the pinhole defects due to the tendency of nitrogen to react with SiO_x.

PL spectra were recorded in the T = 4.2–300 K temperature range using MDR-23 grating monochromator and excitation by a pulsed (1 kHz, 2 μs) semiconductor laser with $\lambda = 1.03$ μm. PL signal was detected with a lock-in amplifier using a cooled InSb photodiode.

Results and Discussion

Structural studies with X-ray diffractometry with reciprocal space mapping (XRD-RSM) and transmission electron microscopy showed the domination of the wurtzite structure in the NWs with clear presence of numerous stacking faults (SFs) along the [0001] growth direction.

PL spectra of the NWs recorded at low temperatures (not shown) contained two bands. At T = 4.2 K these PL bands peaked at energies ~413 meV and ~456 meV for a pure InAs sample, and ~400 meV and ~443 meV for an InAsN sample, respectively. The full-widths at half maxima (FWHM) of the high-energy (HE) peaks were ~37 meV for the InAs sample and ~45 meV for

the InAsN sample. For the low-energy (LE) peaks, the FWHMs equaled ~38 meV and ~29 meV, respectively. At $T = 274$ K, the FWHM of the HE peaks equaled ~85 meV for the InAs sample and ~51 meV for the InAsN sample. Comparison of the PL and XRD-RSM data suggested that the high-intensity HE peaks originated in the NWs with the WZ structure, while the less intense LE peaks were from the parasitic islands with the ZB structure. For the InAsN sample, a ~13 meV shift of the PL spectrum to longer wavelengths relative to that of the pure InAs sample was observed for both PL peaks.

Figure 1 shows temperature dependences of the PL peak energy position E_{PL} for the studied samples. As can be seen in Fig. 1, *a*, the $E_{PL}(T)$ dependence for the LE peak from the sample with NWs made of InAs (symbols *1*) is very similar to that for the interband transitions in a commercially available ('MeGa SM') bulk (100)InAs sample; the latter dependence was recorded under similar conditions using the same experimental setup (symbols *4*). Both these dependences agree very well with the $E_g(T)$ curve calculated for ZB InAs (curve *3*). The LE peaks were observed in the spectra up to $T = 125$ K for the sample with NWs made of InAs (Fig. 1, *a*) and up to $T = 50$ K for the sample with NWs made of InAsN (Fig. 1, *b*). HE peaks (symbols *2*) showed no pronounced $E_{PL}(T)$ dependence up to about 50 K. With temperature increasing further, the slope of $E_{PL}(T)$ dependence for these peaks approached that of the $E_g(T)$ dependence for InAs. At $T = 4.2$ K, the E_{PL} for the HE peak for InAs NWs (~456 meV) was smaller than the known (both from calculations and experiments, see, e.g., refs. [6, 7]) band gap of WZ InAs (~477 meV). This can be explained by the above-mentioned presence of SFs, as those lead to a red-shift of the PL peak compared to the calculated WZ band gap value [6].

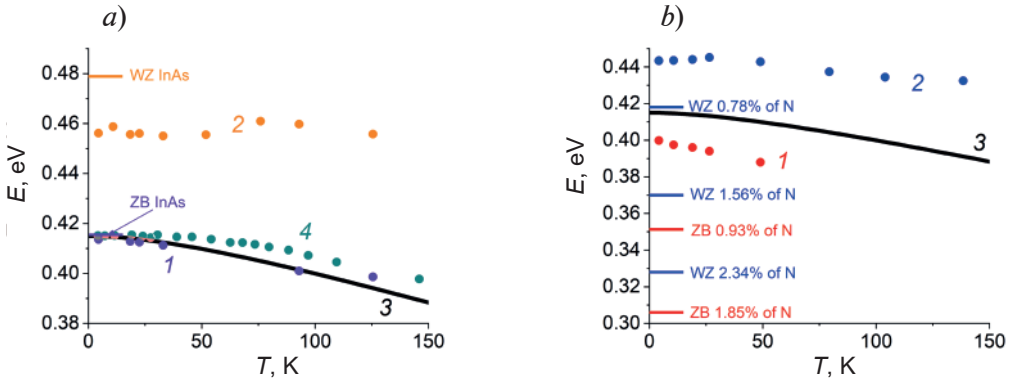

Fig. 1. Temperature dependences of the energy: of LE (*1*) and HE (*2*) PL peaks for the sample with InAs NWs (*a*) and for the sample with InAsN NWs (*b*). Solid curves *3* show calculated $E_g(T)$ dependence for ZB InAs. Dots (*4*) show interband PL peaks for bulk InAs (*a*). Dashes show calculated E_g values for WZ and ZB InAs (*a*) and WZ and ZB InAsN (*b*)

To estimate the amount of nitrogen incorporated in the material, WZ InAs and InAsN band structures were calculated using density functional theory (DFT) with GPAW software package [8]. A quasi-random structure (SQS) approach [9], which allows for emulating a random distribution of impurities in semiconductor alloys, was used to find the dependence of the E_g of InAsN on nitrogen concentration. The calculations were performed for two SQS constructed from the WZ InAs unit cell, with 192 and 256 atoms, corresponding to 4×4×3 and 4×4×4 supercells, respectively, and for one SQS constructed from ZB InAs cell with 216 atoms, corresponding to a 3×3×3 supercell. Dashes in Fig. 1, *b* show the results of the DFT calculations for InAsN with various nitrogen concentrations. As can be seen, the band gap energy calculated for these concentrations appear to be significantly smaller than the energy of PL peaks observed in the experiment. Thus, to assess the actual amount of nitrogen in the material, a linear approximation for the dependence of calculated E_g on nitrogen concentration (in %) was used. For ZB InAsN structure, this approximation yielded −55 meV/% slope and the amount of nitrogen in the parasitic islands in the studied sample was estimated as 0.5%. For WZ InAsN structure, at low nitrogen concentrations (up to 1%), the calculated slope appeared to be steeper (−77 meV/%); also, the effect of the SFs, which reduced HE E_{PL} in the pure InAs NWs, had to be considered. The resulting amount of nitrogen in the material constituting NWs made of InAsN was estimated to be 0.7%.

Conclusion

In conclusion, we have studied photoluminescence of arrays of self-induced NWs grown by PA-MBE on Si substrates and consisting of pure InAs and InAs diluted with nitrogen. In the PL spectra, we observed optical transitions in both the NWs with the WZ structure and parasitic islands with the ZB-type structure, the latter being formed as a by-product of the growth. Introduction of nitrogen lead to the red shift of the PL response from both the NWs and the islands by ~13 meV. On the basis of this data, the nitrogen concentration in the InAsN material was assessed as 0.5–0.7%.

REFERENCES

1. **Chen H., Li J., Cao S., Deng W., Zhang Y.,** InAs nanowire visible-infrared detector photoresponse engineering, Infrared Physics & Technology. 133 (2023) 104785.

2. **Xu T., Wang H., Chen X., Luo M., Zhang L., Wang Y., Chen F., Shan C., Yu C.,** Recent progress on infrared photodetectors based on InAs and InAsSb nanowires, Nanotechnology. 31 (2020) 294004.

3. **Alhodaib A., Noori Y., Krier A., Marshall A.R.J.,** Nanowires for Room-Temperature Mid-Infrared Emission, Chapter 4 in: Nanowires – Synthesis, Properties and Applications. IntechOpen. 2019. Available at: http://dx.doi.org/10.5772/intechopen.79463. Accessed May 24, 2024.

4. **Dick K. A., Thelander C., Samuelson L., Caroff P.,** Crystal phase engineering in single InAs nanowires, Nano Letters. 10 (9) (2010) 3494–3499.

5. **Wu J., Shan W., Walukiewicz W.,** Band anticrossing in highly mismatched III-V semiconductor alloys, Semiconductor Science and Technology. 17 (8) (2002) 860–869.

6. **Fedorov V., Vinnichenko M., Ustimenko R., Kirilenko D., Pirogov E., Pavlov A., Polozkov R., Sharov V., Kaveev A., Miniv D., Dvoretckaia L., Firsov D., Mozharov A., Mukhin I.,** Non-Uniformly Strained Core–Shell InAs/InP Nanowires for Mid-Infrared Photonic Applications, ACS Applied Nano Materials. 6 (7) (2023) 5460–5468.

7. **Rota M.B., Ameruddin A.S., Fonseka H.A., Gao Q., Mura F., Polimeni A., Miriametro A., Tan H.H., Jagadish C., Capizzi M.,** Bandgap Energy of Wurtzite InAs Nanowires, Nano Letters. 16 (8) (2016) 5197–5203.

8. **Enkovaara J., Rostgaard C., Mortensen J.J., et al.,** Electronic Structure Calculations with GPAW: A Real-Space Implementation of the Projector Augmented-Wave Method, Journal of Physics Condensed Matter. 22 (25) (2010) 253202.

9. **Zunger A., Wei S.-H., Ferreira L.G., Bernard J.E.,** Special Quasirandom Structures, Physical Review Letters. 65 (3) (1990) 353–356.

THE AUTHORS

RUZHEVICH Maxim S.
max.ruzhevich@niuitmo.ru
ORCID: 0000-0002-4513-6345

MYNBAEV Karim D.
mynkad@mail.ioffe.ru
ORCID: 0000-0002-9853-8874

BAZHENOV Nicolay L.
bazhnil.ivom@mail.ioffe.ru
ORCID: 0000-0002-3019-2280

KAVEEV Andrey K.
kaveev@mail.ioffe.ru

PAVLOV Alexander V.
a.pavlov@physics.spbstu.ru

FEDOROV Vladimir V.
fedorov_vv@spbstu.ru
ORCID: 0000-0001-5547-9387

MUKHIN Ivan S.
imukhin@yandex.ru

Received 10.07.2024. Approved after reviewing 23.07.2024. Accepted 23.07.2024.

Conference materials
UDC 538.9
DOI: https://doi.org/10.18721/JPM.173.107

Quantum dots formation by InGaAs decomposition onto a patterned GaAs surface

N.E. Chernenko [1] ✉, I.S. Makhov [2], I.A. Melnichenko [2], K.D. Yakunina [1],
S.V. Balakirev [1], N.V. Kryzhanovskaya [2], M.S. Solodovnik [1]

[1] Southern Federal University, Taganrog, Russia;
[2] National Research University Higher School of Economics, St. Petersburg branch, St. Petersburg, Russia
✉ nchernenko@sfedu.ru

Abstract. In this work, we present the results of experimental studies of the formation processes and optical properties of ordered arrays of InGaAs nanostructures obtained by deposition of quantum well material layer on the nanopatterned GaAs surface. For GaAs nanopatterning we used our original technique based on the combination of focused ion beam treatment and local droplet etching which allows to create regular arrays of nanoholes with different morphology. Using room-temperature photoluminescence (PL) intensity mapping we have shown that quantum well material localizes inside the created holes but position of corresponding PL peak (960–970 nm) is independent of morphology and is determined only by the chemical composition of the deposited material. Based on low-temperature (5 K) PL measurements we conclude that inside the holes quantum well decomposes due to the difference in a mobility of Ga and In adatoms during its material deposition with formation a "quantum well + quantum dot" system. While the quantum well PL peak locates approximately at 920 nm, the quantum dot lines lie in the wavelength range of 930–950 nm.

Keywords: quantum dots, A3B5, decomposition, structuring, molecular beam epitaxy, nanostructures, nanopatterning

Funding: This work was supported by the Russian Science Foundation Grant No. 22-79-10251 at the Southern Federal University.

Citation: Chernenko N.E., Makhov I.S., Melnichenko I.A., Yakunina K.D., Balakirev S.V., Kryzhanovskaya N.V., Solodovnik M.S., Quantum dots formation by InGaAs decomposition onto a patterned GaAs surface, St. Petersburg State Polytechnical University Journal. Physics and Mathematics. 17 (3.1) (2024) 38–42. DOI: https://doi.org/10.18721/JPM.173.107

Материалы конференции
УДК 538.9
DOI: https://doi.org/10.18721/JPM.173.107

Формирование квантовых точек путем осаждения InGaAs на структурированную поверхность GaAs

Н.Е. Черненко [1] ✉, И.С. Махов [2], И.А. Мельниченко [2], К.Д. Якунина [1],
С.В. Балакирев [1], Н.В. Крыжановская [2], М.С. Солодовник [1]

[1] Южный федеральный университет, г. Таганрог, Россия;
[2] Национальный исследовательский университет «Высшая школа экономики», Санкт-Петербургский филиал, Санкт-Петербург, Россия
✉ nchernenko@sfedu.ru

Аннотация. В данной работе представлены результаты экспериментальных исследований процессов формирования и оптических свойств упорядоченных массивов наноструктур InGaAs, полученных методом осаждения слоя материала квантовой ямы на структурированную поверхность GaAs. Для структурирования GaAs использовалась оригинальная методика на основе комбинации технологий сфокусированного ионного пучка и локального капельного травления, которая позволяет формировать массивы углублений на поверхности с различной морфологией. Анализ карт распределения интенсивности фотолюминесценции (ФЛ) при комнатной температуре показал, что материал квантовой ямы локализуется внутри сформированных на поверхности углублений. Было показано, что положение пика ФЛ локализованных наноструктур (960–970 нм) не зависит от морфологии и определяется только химическим составом осажденного материала. Анализ спектров микрофотолюминесценции при 5 K показал, что внутри углублений квантовая яма распадается, предположительно, из-за разницы в подвижности адатомов Ga и In при осаждении материала с образованием системы «квантовая яма + квантовая точка». При этом спектре ФЛ квантовой яме соответствует пик на 920 нм, а линии квантовых точек лежат в диапазоне длин волн 930–950 нм.

Ключевые слова: квантовые точки, A3B5, распад, структурирование, молекулярно-лучевая эпитаксия, наноструктуры, модификация

Финансирование: Работа выполнена при поддержке гранта Российского научного фонда № 22-79-10251 в Южном федеральном университете.

Ссылка при цитировании: Черненко Н.Е., Махов И.С., Мельниченко И.А., Якунина К.Д., Балакирев С.В., Крыжановская Н.В., Солодовник М.С. Формирование квантовых точек путем осаждения InGaAs на структурированную поверхность GaAs // Научно-технические ведомости СПбГПУ. Физико-математические науки. 2024. Т. 17. № 3.1. С. 38–42. DOI: https://doi.org/10.18721/JPM.173.107

Introduction

Great interest in quantum dots (QD) is due not only to their unique electronic and optical properties, but also to the need to create highly efficient compact (micro- and nano-sized) light sources including non-classical sources of single [1] and entangled photons [2] based on them. Since the properties of QDs largely depend on their structural characteristics [3–5], the requirements for the accuracy of their control increase as the size of devices based on them decreases. And despite the long history of studying QDs, the development of effective methods for controlling their properties, including the position of individual dots in an array [6, 7], remains an urgent task. One of the most promising methods of QD control is the preliminary structuring of the surface by creating holes (or recesses) of various geometries [8, 9], which are the preferred sites for the nucleation and growth of self-organized nanostructures [10, 11]. This paper presents the results of studies on the possibility of forming InGaAs QDs and their ordered arrays by deposition of quantum well (QW) material onto a nanostructured GaAs surface.

Materials and Methods

Preliminary nanopatterning of GaAs surface was carried out on GaAs/AlGaAs heterostructure using a focused ion beam (FIB) etching. As a result, square arrays of holes with different geometric characteristics were formed. The ion beam accelerating voltage was 5 kV, and the distance L between the holes in the array was 0.5 and 1 μm. The number of ion beam passes N varied from 1 to 60. Then pre-growth treatment was carried out using the original local droplet etching technique [8], because of which pyramidal-shaped holes with lateral sizes varied from ~ 100 to ~ 300 nm were formed at every point of ion beam exposure. Then a 10 nm thick InGaAs layer with an indium content of 17% was deposited on the patterned surface. This layer was placed in the center of the optical cavity formed by the AlGaAs/GaAs/AlGaAs heterostructure. After formation sample were studied by photoluminescence spectroscopy at 5 and 300 K.

Results and Discussion

The results of experimental studies showed that when 10 nm InGaAs is deposited on the nanostructured surface, the epitaxial material is localized in the region of the holes (Fig. 1, *a*). PL intensity distribution maps (300 K) show the dependence of the PL signal intensity in the wavelength range 900–1050 nm on the initial morphology specified by the parameters of nanopatterning. PL measurements at different points of the signal maximum showed that the position of the long-wavelength peak corresponding to InGaAs is unchanged for all points and locates in the spectral region of 960–970 nm, regardless of the initial morphology. Such wavelength corresponds to the emission of InGaAs/GaAs QWs with the same composition on non-patterned surfaces.

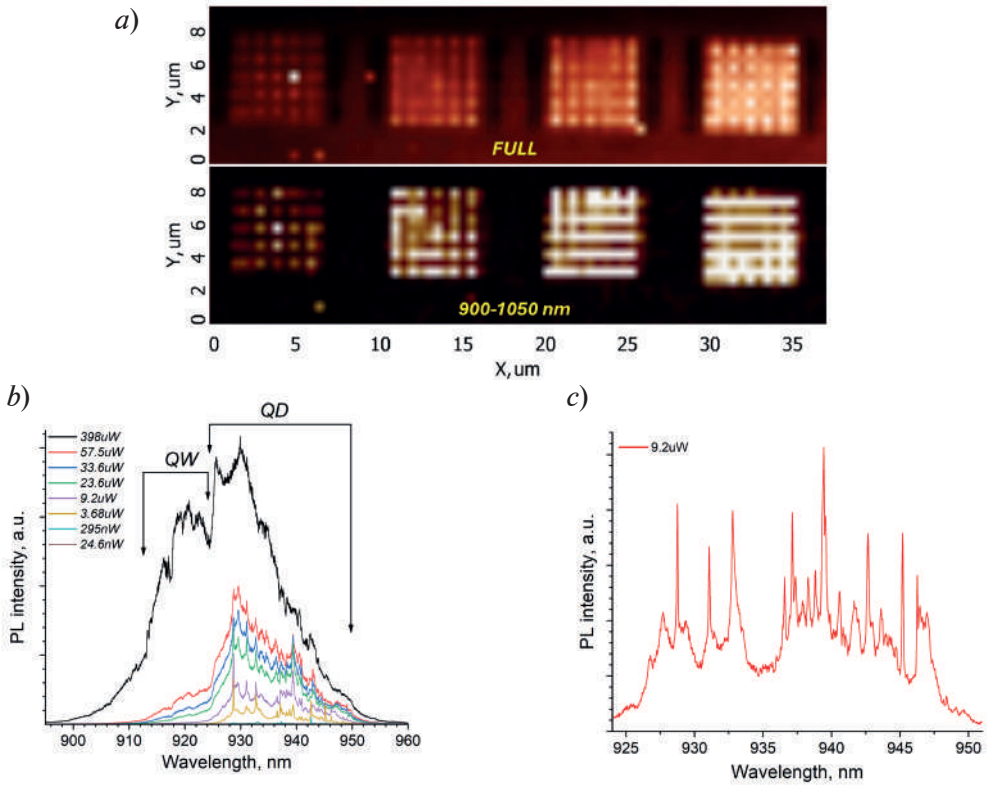

Fig. 1. PL spectra in patterned areas: PL intensity distribution map at 300 K for arrays with $L = 1.0$ μm and N varied from 20 (left array) to 60 (right array) passes (upper panel – full spectra; lower panel – spectra in the wavelength range 900 – 1050 nm) (*a*); spectra at different excitation powers for an array with $L = 0.5$ μm and $N = 40$ passes; *c*) high resolution PL spectra of the same arrays with individual QDs lines (*b*)

Analysis of the PL spectra at 5 K (Fig. 1, *b*) showed that localized InGaAs nanostructures emit in the broad wavelength range of 900–950 nm. At low temperature as the excitation power decreases, the peak splits into short- (900–925 nm) and long-wavelength (930–950 nm) components. Moreover from Fig. 1, *b* we can clearly see that as the pump power decreases, the maximum intensity shifts to the long-wavelength region due to the rapid decay of the short-wavelength shoulder. At the same time, the long-wavelength part of the spectrum breaks up into separate lines corresponding to the radiation of individual quantum dots. This is especially clearly visible in the high-resolution spectrum shown in the Fig. 1, *c*.

Analysis of the presented data allows us to assume that two types of nanostructures are formed in the nanoholes – a quantum well and a quantum dot, forming a coupled quantum-size system. In this case, the position of the emission lines of quantum wells and quantum dots does not depend on geometric characteristics of nanoholes. At the same time, the overall emission intensity of the InGaAs nanostructures shows a positive correlation with the sizes of the corresponding holes (Fig. 1). We associate this with the redistribution of QW and QD contributions to the PL

spectrum when the morphological parameters of growth surface are changed. Based on this we conclude that inside the holes QW decomposes due to the difference in a mobility of Ga and In adatoms during its material deposition with formation a “quantum well + quantum dot” system.

Conclusion

Thus, we conducted studies on the possibility of forming In(Ga)As QDs on a structured GaAs surface by filling the nanoholes with InGaAs quantum well material. The results of studying the obtained samples using the PL method showed a high degree of localization of the quantum well material in the holes. We found that the PL intensity of the structures is directly proportional to the size of the initial nanoholes. Analysis of PL at low temperatures showed the formation of QDs emitting in the longer wavelength range in the holes. This suggests that the QDs are enriched in indium, which leads to the formation of a dot-in-well type structure inside the nanoholes. We attribute this to the decomposition of the quantum well material at the initial stage of epitaxial growth, caused by different diffusion lengths of the metal (Ga and In) components. Since the QD wavelength does not depend on the morphology, we can assume that the process is self-regulating and is determined by the balance of elastic strains in the “quantum dot + quantum well” system.

REFERENCES

1. **Senellart P., Solomon G., White A.,** High-performance semiconductor quantum-dot single-photon sources, Nat. Nanotechnol. 12 (11) (2017) 1026–1039.

2. **Schimpf C., Reindl M., Basso Basset F., Jöns K. D., Trotta R., Rastelli A.,** Quantum dots as potential sources of strongly entangled photons: Perspectives and challenges for applications in quantum networks, Appl. Phys. Lett. 118 (10) (2021).

3. **Yeo H.S., Lee K., Cho J.H., Park S.H., Cho Y.H.,** Control of the 3-Fold Symmetric Shape of Group III-Nitride Quantum Dots: Suppression of Fine-Structure Splitting, Nano Lett. 20 (12) (2020) 8461–8468.

4. **Balakirev S., Kirichnenko D., Chernenko N., Shandyba N., Komarov S., Dragunova A., Kryzhanovskaya N., Zhukov A., Solodovnik M.,** Influence of the arsenic pressure during rapid overgrowth of InAs/GaAs quantum dots on their photoluminescence properties, Crystals. 13 (9) (2023) 1358.

5. **Balakirev S., Nadtochiy A., Kryzhanovskaya N., Kirichenko D., Chernenko N., Shandyba N., Komarov S., Dragunova A., Zhukov A., Solodovnik M.,** Role of arsenic vapor pressure in transformation of InAs quantum dots during overgrowth by a GaAs capping layer, J. Lumin. 272 (2024) 120621.

6. **Shih C., et al.,** Self-Aligned Photonic Defect Microcavity Lasers with Site-Controlled Quantum Dots, Laser Photon. Rev. (2024).

7. **Balakirev S.V., Kirichenko D.V., Shandyba N.A., Chernenko N.E., Solodovnik M.S.,** Droplet epitaxy of site-controlled In/GaAs(001) nanostructures with a variable distance: experiments and simulations, St. Petersburg. State Polytech. Univ. J. Phys. Math. 16 (3.1) (2023) 41–46.

8. **Chernenko N.E., Kirichenko D.V., Shandyba N.A., Balakirev S.V., Eremenko M.M., Solodovnik M.S.,** Experimental study of nanoholes formation using local droplet etching of FIB-modified GaAs (001) surface, St. Petersburg. State Polytech. Univ. J. Phys. Math. 15 (3.3) (2022) 48–53.

9. **Lakhina E.A., Shandyba N.A., Chernenko N.E., Kirichenko D.V., Balakirev S.V., Solodovnik M.S.,** Formation of symmetrical nanoholes by local droplet etching for site-controlled growth of single quantum dots, St. Petersburg. State Polytech. Univ. J. Phys. Math. 16 (3.1) (2023) 53–58.

10. **Cheng C. C., Meneou K., Cheng K. Y.,** High optical quality InAs site-controlled quantum dots grown on soft photocurable nanoimprint lithography patterned GaAs substrates, Appl. Phys. Lett. 95 (17) (2009).

11. **Chernenko N.E., Makhov I.S., Balakirev S.V., Kirichenko D.V., Shandyba N.A., Kryzhanovskaya N.V., Solodovnik M.S.,** Study of InAs/GaAs quantum dots formation in subcritical growth modes on patterned substrates, St. Petersburg State Polytechnical University Journal. Physics and Mathematics. 16 (3.1) (2023) 64–68.

THE AUTHORS

CHERNENKO Natalia E.
nchernenko@sfedu.ru
ORCID: 0000-0001-8468-7425

BALAKIREV Sergey V.
sbalakirev@sfedu.ru
ORCID: 0000-0003-2566-7840

MAKHOV Ivan S.
imahov@hse.ru
ORCID: 0000-0003-4527-1958

KRYZHANOVSKAYA Natalia V.
nkryzhanovskaya@hse.ru
ORCID: 0000-0002-4945-9803

MELNICHENKO Ivan A.
imelnichenko@hse.ru
ORCID: 0000-0003-3542-6776

SOLODOVNIK Maxim S.
solodovnikms@mail.ru
ORCID: 0000-0002-0557-5909

YAKUNINA Ksenia D.
iakunina@sfedu.ru
ORCID: 0009-0003-3518-8402

Received 11.07.2024. Approved after reviewing 19.07.2024. Accepted 19.07.2024.

Conference materials
UDC 533.924
DOI: https://doi.org/10.18721/JPM.173.108

Formation of nanocones on the surface of $Pb_{0.4}Sn_{0.6}Te$ films during ion-plasma treatment with argon ions with an energy of 140 eV

Y.D. Belov [1] ✉, S.P. Zimin [1, 2], I.I. Amirov [1], L.A. Mazaletskiy [1, 2]

[1] Yaroslavl Branch of the Valiev Institute of Physics and Technology, RAS, Yaroslavl, Russia;
[2] P.G. Demidov Yaroslavl State University, Yaroslavl, Russia
✉ yadbelov@gmail.com

Abstract. The article studies the modification of the surface of $Pb_{0.4}Sn_{0.6}Te$ epitaxial films during ion-plasma treatment in argon plasma. Lead-tin telluride films with a thickness of 2 μm were grown on BaF_2 (111) substrates by molecular beam epitaxy. Ion-plasma treatment was carried out in a dense argon plasma of a high-frequency inductive discharge at an ion energy of ~140 eV. The duration of the process is 60 and 120 s. The parameters of an ensemble of nanocones are studied, the evolution of the height of the cones, their lateral dimensions and surface density is described while maintaining the processing time.

Keywords: argon plasma, lead-tin telluride, nanostructuring

Funding: This study was funded by ministry of Science and Higher Education of Russia for Valiev Institute of Physics and Technology number FFNN-2022-0017of RAS.

Citation: Belov Y.D., Zimin S.P., Amirov I.I., Mazaletskiy L.A., Formation of nanocones on the surface of $Pb_{0.4}Sn_{0.6}Te$ films during ion-plasma treatment with argon ions with an energy of 140 eV, St. Petersburg State Polytechnical University Journal. Physics and Mathematics. 17 (3.1) (2024) 43–46. DOI: https://doi.org/10.18721/JPM.173.108

Материалы конференции
УДК 533.924
DOI: https://doi.org/10.18721/JPM.173.108

Формирование наноконусов на поверхности пленок $Pb_{0.4}Sn_{0.6}Te$ при ионно-плазменной обработке ионами аргона с энергией 140 эВ

Я.Д. Белов [1] ✉, С.П. Зимин [1, 2], И.И. Амиров [1], Л.А. Мазалецкий [1, 2]

[1] Филиал Физико-технологического института РАН, г. Ярославль, Россия;
[2] Ярославский университет им. П.Г. Демидова, г. Ярославль, Россия
✉ yadbelov@gmail.com

Аннотация. В статье исследована модификация поверхности эпитаксиальных пленок $Pb_{0.4}Sn_{0.6}Te$ при ионно-плазменной обработке в аргоновой плазме. Пленки теллурида свинца-олова толщиной 2 мкм были выращены на подложках BaF_2 (111) методом молекулярно-лучевой эпитаксии. Ионно-плазменная обработка проводилась в плотной аргоновой плазме ВЧ индукционного разряде при энергии ионов ~140 эВ. Продолжительность процесса составляла 60 и 120 с. Изучены параметры ансамбля наноконусов, описана эволюция высоты конусов, их поперечных размеров и поверхностной плотности при изменении времени обработки.

Ключевые слова: аргоновая плазма, теллурид свинца-олова, наноструктурирование

Финансирование: Исследование выполнено при финансовой поддержке Минобрнауки России для Физико-технологического института имени Валиева номер FFNN-2022-0017 РАН.

Ссылка при цитировании: Белов Я.Д., Зимин С.П., Амиров И.И., Мазалецкий Л.А. Формирование наноконусов на поверхности пленок $Pb_{0.4}Sn_{0.6}Te$ при ионно-плазменной обработке ионами аргона с энергией 140 эВ // Научно-технические ведомости СПбГПУ. Физико-математические науки. 2024. Т. 17. № 3.1. С. 43–46. DOI: https://doi.org/10.18721/JPM.173.108

Introduction

Interest in lead-tin telluride is associated with the possibility of manufacturing optoelectronic devices in the infrared region of the spectrum based on it [1]. Currently, among the methods for modifying the surface of IV–VI semiconductors, ion-plasma processing methods stand out favorably, which make it possible to control the architecture and parameters of the created micro- and nanostructures within a wide range by varying the ion energy and duration of treatment [2–6]. In particular, it was shown in [5] that during ion-plasma treatment, lead-tin telluride nanocones can grow according to a modified vapor-liquid-solid (VLS) mechanism with plasma self-formation of catalyst metal nanodroplets. The purpose of this work was to study the nanostructures that appear on the surface of $Pb_{0.4}Sn_{0.6}Te$ epitaxial films during ion-plasma treatment with an argon ion energy of 140 eV, intermediate between the previous experiments of 25 [3], 75 [4] and 200 [5] eV. The results of works [3–5] show the diversity of the architecture of the created nanostructures. Analysis of the results obtained allows us to hope that at an ion energy of 140 eV and at certain values of treatment time, we should expect the appearance of an ensemble of nanocones on the surface for all $Pb_{1-x}Sn_xTe$ compositions from lead telluride to tin telluride, which is promising for modifying the optical properties of lead-tin telluride. As part of this work, studies were carried out on $Pb_{0.4}Sn_{0.6}Te$, films, for which (in accordance with the phase diagram for the Pb-Sn alloy) metal nanodroplets will have a minimum melting point.

Materials and Methods

$Pb_{0.4}Sn_{0.6}Te$ films were grown by molecular beam epitaxy using a Riber 32 P installation (INPE, Brazil) on BaF_2 (111) substrates by the authors of [7]. Ion-plasma treatment of the samples was carried out in an argon plasma reactor of a high-frequency induction discharge (13.56 MHz, 800 W) [2]. The treatment was carried out at an ion energy of 140 eV; the treatment duration was 60 and 120 s. Surface morphology studies were carried out using scanning electron microscopy (SEM) on a Zeiss Supra-40 microscope.

Results and Discussion

The initial samples had a smooth surface with the presence of dislocation pits. During plasma treatment of $Pb_{0.4}Sn_{0.6}Te$ films in argon plasma with an energy of 140 eV, the formation of ensembles of cone-shaped structures shown in Fig. 1 was observed. 1. After processing for 60 s, the cones were ~70 nm high with quasi-spherical caps at the top. The physical nature of the formation of metal caps is described in [4, 5]. It is important to note that the formation of such nanocones under similar conditions of processing $Pb_{1-x}Sn_xTe$ films with $0.6 < x < 0.6$ was not observed. As the processing time increased to 120 s, the height of the structures increased to ~80 nm. In this case, the lateral dimensions of the bases of the nanocones were ~60 nm for 60 s and ~65 nm for 120 s. The surface density of the structures after 60 s of treatment was ~8·109 cm^{-2}; with an increase in treatment time to 120 s, the density decreased to ~$7 \cdot 10^9$ cm^{-2}.

Figure 2 shows the quantitative characteristics of the parameters of nanocones, including the dimensions of the heights with a cap, the diameters of the caps, and the lateral dimensions at the surface. From an examination of the histograms it follows that the sizes of the structures change insignificantly. On average, the heights and diameters of the caps increase by 20%, while the dimensions of the structures at the base of the cones practically do not change. At the same time (Fig. 1), there is an increase in the lateral dimensions of the cones under the cap. Based on the geometric dimensions of the caps and the parameters of truncated cones, the volumes of cone ensembles were determined for processing times of 60 and 120 s. The results of these calculations showed that the volume of material

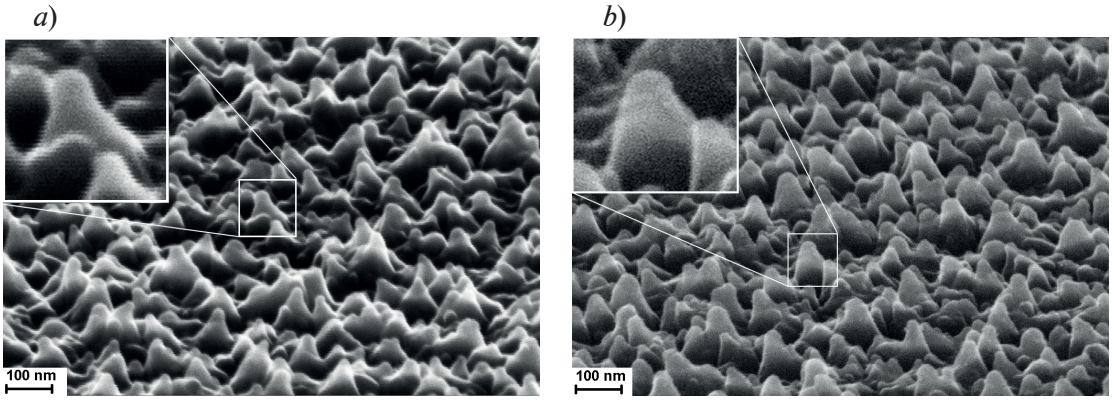

Fig. 1 Modification of the surface of the $Pb_{0.4}Sn_{0.6}Te$ film after treatment in argon plasma with an ion energy of 140 eV for 60 (*a*) and 120 (*b*) s. View at an angle of 70°

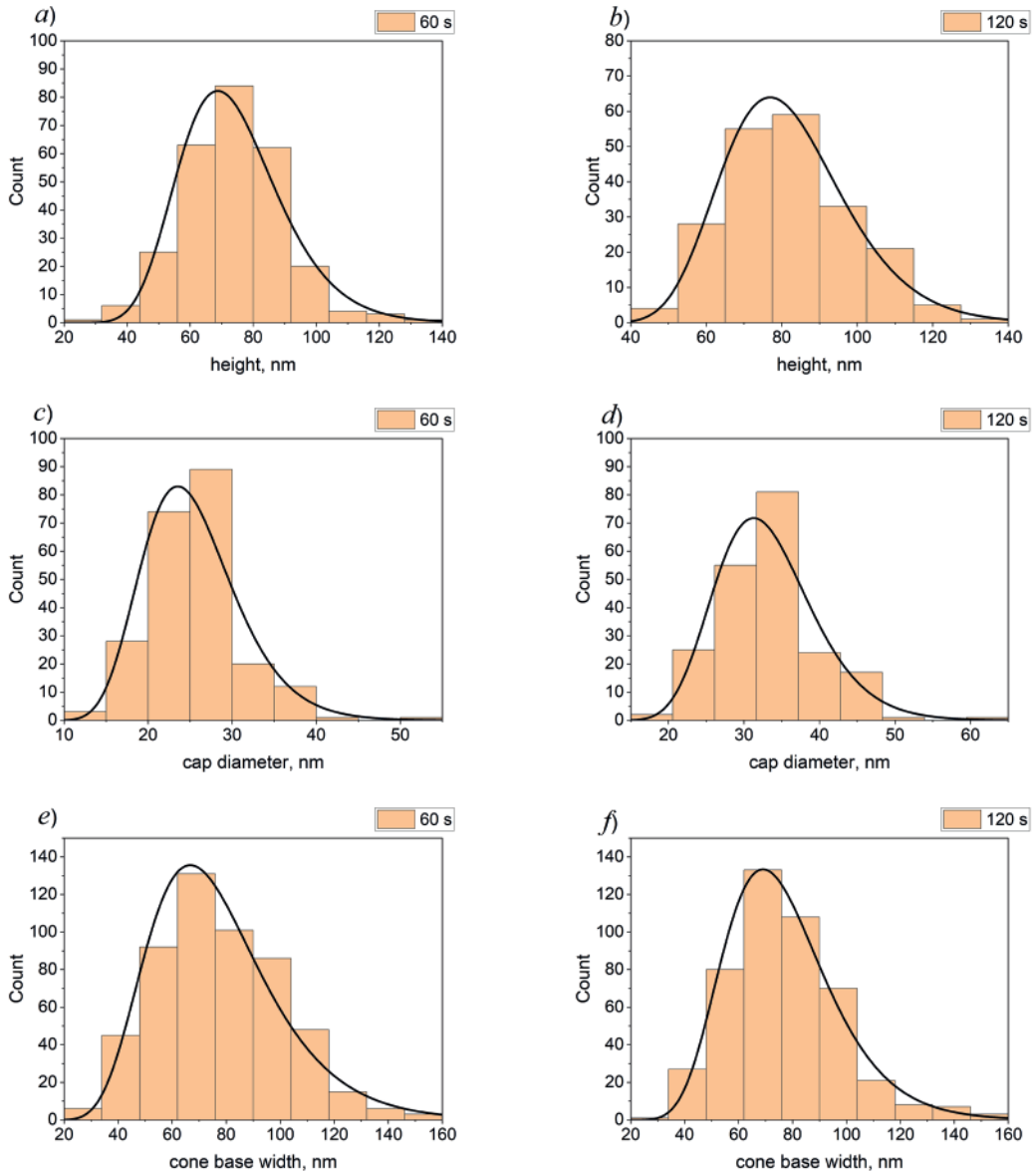

Fig. 2 Histograms of the distribution of heights of cone-shaped structures after treatment for 60 (*a*) and 120 (*b*) s. Histograms of size distribution for cap diameter (*c*, *d*) and lateral dimensions at the base on the cones (*e*, *f*) for treatment 60 (*c*, *e*) and 120 (*d*, *f*) s

increases by approximately 1.7 times, which correlates with the total volume of sputtering material during plasma treatment. The material is redeposited onto the walls of the cones from saturated steam, forming a thickening with a slight increase in the height of the cones.

Conclusion

For $Pb_{0.4}Sn_{0.6}Te$ films, the growth of nanocones was demonstrated during treatment with argon ions with an energy of 140 eV for 60 and 120 s. The results of the work made it possible to establish new experimental patterns in the model of the formation of ensembles of nanocones according to the "vapor-liquid-solid" mechanism with a parallel process of ion sputtering. It is shown that a homogeneous ensemble of truncated cones (similar to the structures obtained in previous experiments [3–5]) of lead-tin telluride with a metal cap on the top, when the processing time changes from 60 to 120 s, slightly increases in height and does not change its lateral dimensions on the surface. Changes occur in the upper part of the nanocones, where there is an increase in the lateral dimensions of the cones under the quasi-spherical caps.

Acknowledgments

SEM investigations were carried out at the Facilities Sharing Centre "Diagnostics of Micro- and Nanostructures" with the support of the Ministry of Science and Higher Education of Russian Federation. Authors are grateful to E. Abramof, P.H.O. Rappl for the provided samples. The investigation was supported by the program no. FFNN-2022-0017.

REFERENCES

1. **Ishida A., Naruse K., Nakashima S., Takano Y., Du S., Hirakawa K.,** Interband absorption in PbTe/PbSnTe-based type-II superlattices, Appl. Phys. Lett. 113 (2018) 072103.

2. **Zimin S.P., Gorlachev E.S., Amirov I.I.,** Inductively Coupled Plasma Sputtering: Structure of IV-VI Semiconductors. In Encyclopedia of Plasma Technology 1st ed. J L Shohet. (2017) 679–691.

3. **Zimin S.P., Amirov I.I., Naumov V.V., Belov Y.D., Abramof E., Rappl P.H.O.,** Surface modification of lead–tin telluride films with low-energy argon ions, J. Surf. Invest.: X-Ray Synchrotron Neutron Tech. 10 (1) (2022) 66–74.

4. **Belov Y.D., Zimin S.P., Amirov I.I., Naumov V.V., Abramof E., Rappl P.H.O,** Formation of Pb-Sn Janus particles on the surface of lead-tin telluride films during ion-plasma sputtering, St. Petersburg State Polytechnical University Journal. Physics and Mathematics. 15 (3.3) (2022) 13–17.

5. **Zimin S.P., Gorlachev E.S., Amirov I.I., Naumov V.V., Juskenas R., Skapas M., Abramof E., Rappl P.H.O.,** Plasma-assisted surface nanostructuring of epitaxial $Pb_{1-x}Sn_xTe$ ($0 \leq x \leq 1$) films, Semiconductor Science and Technology. 34 (9) (2019) 095001.

6. **Zimin S.P., Gorlachev E.S., Amirov I.I., Gerke M.N.,** Submicrometer-and nanometer-structure formation on the surface of epitaxial IV–VI semiconductor films by Ar-plasma treatment. Russian Microelectronics. 37 (3) (2008) 175–186.

7. **Rappl P.H.O., Closs H., Ferreira S.O., Abramof E., Boschetti C., Motisuke P., Ueta A.Y., Bandeira I. N.,** Molecular beam epitaxial growth of high quality $Pb_{1-x}Sn_xTe$ layers with $0 \leq x \leq 1$, Journal of Crystal Growth. 191(3) (1998) 466–471.

THE AUTHORS

BELOV Yaroslav D.
yadbelov@gmail.com
ORCID: 0000-0001-9226-8108

AMIROV Ildar I.
ildamirov@yandex.ru
ORCID: 0000-0001-5273-3298

ZIMIN Sergey P.
zimin@uniyar.ac.ru

MAZALETSKIY Leonid A.
l.mazaletskiy@uniyar.ac.ru
ORCID: 0000-0003-2413-9528

Received 11.07.2024. Approved after reviewing 12.08.2024. Accepted 12.08.2024.

Conference materials
UDC 535.016
DOI: https://doi.org/10.18721/JPM.173.109

Ion exchange method for obtaining second-order nonlinearity in glass

G. Kan [1, 2] ✉, I.V. Reshetov [1, 2], A.N. Terpitskiy [1],
S.A. Scherbak [1, 2], A.A. Lipovskii [1, 2]

[1] Alferov University, St. Petersburg, Russia;
[2] Peter the Great St. Petersburg Polytechnic University, St. Petersburg, Russia
✉ kan@spbau.ru

Abstract. In this work, we propose two-step process to create a second-order nonlinearity in glasses. First, we use the ion exchange method to form a region of an ion concentration and, consequently, conductivity gradient in glass. Afterwards, we apply DC voltage to the specimen at room temperature. This causes formation of non-equilibrium charge and inner electrostatic field, which induces effective second-order optical nonlinearity of the glass that exceeds one of thermally poled glass sample. After turning the voltage off, the effect gradually degrades within a few hundreds of seconds. Comparison of silver-for-sodium and potassium-for-sodium ion exchanges shows that in the latter case the result nonlinearity has longer relaxation time.

Keywords: glass, ion-exchange, Maxwell-Wagner effect, EFISH, second harmonic generation

Funding: The study was funded by the Ministry of Science and Higher Education of Russian Federation, project FSRM-2023-0009.

Citation: Kan G., Reshetov I.V., Terpitskiy A.N., Scherbak S.A., Lipovskii A.A., Ion exchange method for obtaining second-order nonlinearity in glass, St. Petersburg State Polytechnical University Journal. Physics and Mathematics. 17 (3.1) (2024) 47–51. DOI: https://doi.org/10.18721/JPM.173.109

Материалы конференции
УДК 535.016
DOI: https://doi.org/10.18721/JPM.173.109

Метод ионного обмена для получения нелинейности второго порядка в стекле

Г. Кан [1, 2] ✉, И.В. Решетов [1, 2], А.Н. Терпицкий [1],
С.А. Щербак [1, 2], А.А. Липовский [1, 2]

[1] Академический университет им. Ж.И. Алфёрова РАН, Санкт-Петербург, Россия;
[2] Санкт-Петербургский политехнический университет Петра Великого, Санкт-Петербург, Россия
✉ kan@spbau.ru

Аннотация. Мы представляем двухэтапный процесс создания нелинейности второго порядка в стеклах. На первом этапе используется ионный обмен в стекле для формирования градиента концентрации подвижных ионов и, следовательно, градиента проводимости. На втором этапе прикладывается постоянное напряжение, наводящее неравновесный электрический заряд и внутреннее электростатическое поле, которое индуцирует в стекле эффективную оптическую нелинейность второго порядка, превышающую нелинейность термически поляризованного стекла. После отключения напряжения этот эффект постепенно затухает в течение нескольких сотен секунд. Сравнение ионного обмена серебро-натрий и калий-натрий показывает, что во втором случае время релаксации полученной нелинейности больше.

Ключевые слова: стекло, ионный обмен, эффект Максвелла-Вагнера, EFISH, генерация второй гармоники

Финансирование: Работа выполнена в рамках Государственного задания FSRM-2023-0009.

Ссылка при цитировании: Кан Г., Решетов И.В., Терпицкий А.Н., Щербак С.А., Липовский А.А. Метод ионного обмена для получения нелинейности второго порядка в стекле // Научно-технические ведомости СПбГПУ. Физико-математические науки. 2024. Т. 17. № 3.1. С. 47–51. DOI: https://doi.org/10.18721/JPM.173.109

Introduction

It is well known that glass, due to its amorphous nature, is isotropic. However, modification of glass by thermal poling (TP) can break the isotropy in the near-surface layer [1]. The process involves heating a plate of glass, applying a constant voltage, and cooling under the voltage. Compositional analysis shows that the voltage forces mobile alkali ions of the glass to migrate from the sub-anode region. Differing in mobility hydrogen/hydronium ions from atmosphere compensate the deficit of electric charge in the depleted region. Therefore, regions with different conductivities are formed in glass. Current flow through them causes the accumulation of a non-equilibrium charge. That is known as the Maxwell-Wagner (M-W) effect [2]. Upon cooling, the charge "freezes" and forms an inner electrostatic field. The higher the dielectric constant of a material and the lower its conductivity, the longer the relaxation time of the non-equilibrium charge and electric field. This field mixed with the third-order optical nonlinearity of the glass leads to the appearance of an effective second-order nonlinearity (SON) and allows for second optical harmonic generation in glass, which is known as EFISH (Electric-Field Induced Second-Harmonic) effect [3].

We propose two-step process, alternative to TP, to create a second-order nonlinearity in glasses. At the first stage, we modify the glass by ion exchange (IE) [4] which allows creating a conductivity gradient where non-equilibrium charge accumulation is possible due to the M-W effect. In the second stage, we apply a DC voltage to the ion-exchanged samples. This results in electric charge accumulation and creating an effective SON.

Materials and Methods

For this study, we use a 1 mm thick soda-lime microscopic slide (Menzel) containing 14.3 wt.% of sodium oxide [5]. Potassium-to-sodium (K-Na) IE was carried out in a KNO_3 melt for 8 h at 365 °C, and silver-to-sodium (Ag-Na) IE – in a mixture of 5%/95% $AgNO_3/NaNO_3$ for 20 min at 325 °C. To confirm the presence of a concentration gradient in the samples, the potassium, silver and sodium concentration profiles across the sample were characterized using an Ultim Max 100 EDX spectroscopy (Oxford Instruments, UK) setup combined with a Supra 25 scanning electron microscope (Zeiss, Germany).

After, electric current flowing through the samples was characterized. In experiments, the samples were pressed between stainless steel electrodes, a DC voltage (1.3 kV) was applied and the current was measured using an A2-4 picoammeter (MNIPI, Belarus). A discharge of the accumulated electric charge was performed by short-circuiting the sides of the sample through the picoammeter. The charge/discharge of the samples were followed by the characterization of the second harmonic (SH) signal. The setup consisted of a Nano L ns-pulsed laser with an emission wavelength of 1.064 μm (Litron, UK), filters, a collecting lens and a photodetector. Also, we used ITO film electrodes transparent to the fundamental and second harmonic wavelength for simultaneous charge/discharge of the specimen and characterization of its SH signal. An incident angle of the radiation corresponded to the maximum of the SH signal from the sample. Note, preliminarily studies showed that ITO did not contribute to the SH signal. More details of the optical setup can be found elsewhere [6].

Results and Discussion

The concentration profiles of K-Na IE 8h-365 °C and Ag-Na IE 20min-325 °C samples obtained by EDX spectroscopy are shown in Figure 1, *a*, *b*, respectively. The profiles are ratiometrically normalized so that the sum of the ion concentrations equals to one. Figure 1 demonstrates that concentration gradients in the near-surface region have been formed. Depths of the profiles are ~6 and ~7 μm, respectively.

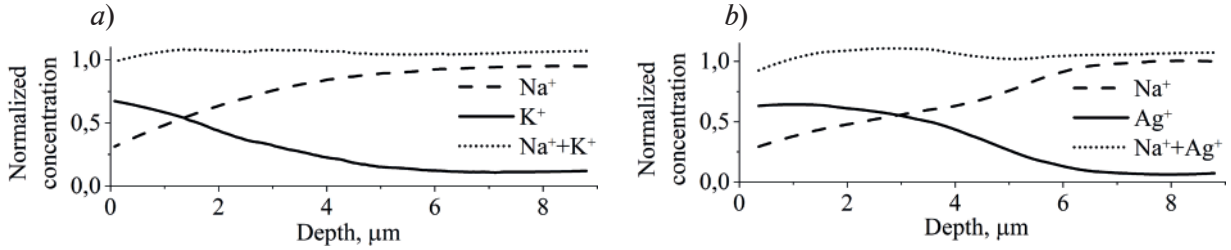

Fig. 1. Normalized concentration profiles of K-Na IE for 8 h-365 °C (*a*) and Ag-Na IE for 20 min-325 °C (*b*) measured by EDX spectroscopy

Then, the voltage was applied to the formed structures. The resulting graph of the current temporal dependence is demonstrated in Fig. 2, *a*. One can conclude that the presence of potassium gradient leads to the accumulation of non-equilibrium charge within 30 min. The Ag-Na IE sample charges much faster (~3 min). The same relates to the samples when discharging.

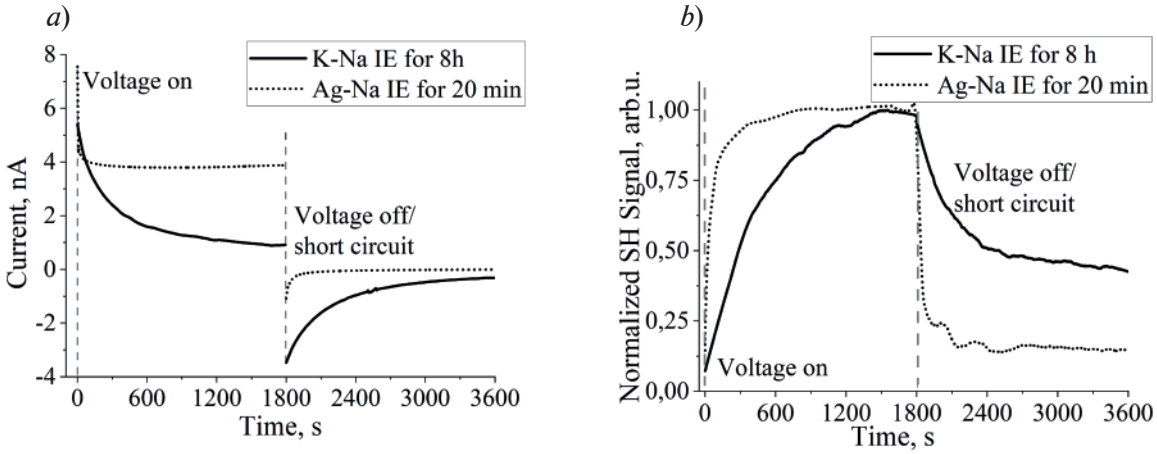

Fig. 2. Temporal dependences of the current (*a*) and normalized SH signal (*b*) with voltage on and off after 30 min

A similar estimation can be made from measuring the second harmonic dynamics (Fig. 2, *b*). The SH signal from Ag-Na IE sample saturates and relaxes much faster than one from the K-Na IE sample, and the characteristic discharge times correspond to those mentioned above. Besides, the discharge of K-Na IE sample takes longer than expected, and this needs further investigation.

This behavior can be explained by ionic mobility (see Table) and, respectively, the conductivity, which is inversely proportional to the relaxation time in the Maxwell-Wagner effect. Injection of less mobile potassium ions in glass leads to longer time of charge accumulation and dissolution, while more mobile silver ions fasten the processes.

Table

Mobility of ion species in soda-lime glass at T = 300 K

Ion species	Na^+	Ag^+	K^+
Mobility at T = 300 K, $m^2/(V \cdot s)$	$1.4 \cdot 10^{-20}$	$1.7 \cdot 10^{-21}$	$1.7 \cdot 10^{-22}$

The SH signal of the IE glasses can be compared with the one of thermally poled sample using Maker Fringe technique that is measuring SH intensity dependence on the incidence angle. For this purpose, K-Na IE glass sample was used, since Ag-Na IE one discharges faster than the measurement duration. Also, by restricting the access of the salt melt to one side, a single-side K-Na IE sample was obtained. TP was carried out using DC electric discharge in air gap [7]: DC voltage of 1.3 kV, temperature of 250 °C for 20 min. The result is shown in Fig. 3 for the single-side K-Na IE sample and the TP sample compared to the double side one. The SH intensity was normalized to the maximum of the SH value from the double-side sample.

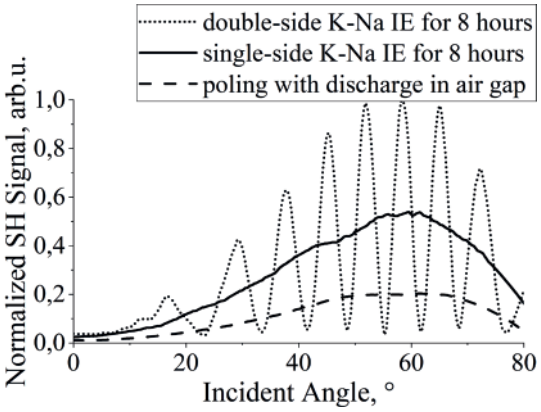

Fig. 3. Maker's Fringe pattern of double-side K-Na IE for 8h-365°C (dotted line), single-side K-Na IE for 8h-365°C (solid line) and sample poled using electric discharge in air gap (dashed line)

The fringes of dotted curve (double-side IE specimen) in Fig. 3 indicate interference between the SH signals from the two opposite sides of the glass slide. Two other curves (single-side IE and TP specimens) correspond to the signal generated only at one side. The single-side K-Na IE sample is given for direct comparison to TP. The SH intensity obtained from the single-side sample is ~2.5 times higher than that of the TP.

Conclusion

Thus, we demonstrate the formation of ion concentration and, consequently, conductivity gradient in glass after ion exchange that is sufficient for Maxwell-Wagner effect. This effect manifests in accumulation of electric charge and formation of inner electric field in the subsurface region of the glass upon DC voltage application. We registered it via measurements of optical second harmonic signal, which arises due to the EFISH effect. After turning the voltage off, the accumulated charge and corresponding electric field gradually dissolve within a few hundreds of seconds. We demonstrate that relaxation time varies depending on ion species used in IE.

Thus, ion exchange and subsequent room temperature voltage treatment is a new approach to induce and control optical nonlinearity of glasses that is comparable to one obtained by thermal poling.

Acknowledgments

The authors thank V.P. Kaasik for the assistance in the second harmonic measurements.

REFERENCES

1. **Myers R.A., Mukherjee N., Brueck S.R.J.,** Large second-order nonlinearity in poled fused silica. Optics Letters. 16 (22) (1991) 1732.

2. **Iwamoto M.,** Maxwell–Wagner Effect, Encyclopedia of Nanotechnology. Springer Netherlands, Dordrecht. (2014) 1–13.

3. **Driscoll T.J.,** Optically encoded second-harmonic generation in bulk silica-based glasses. JOSA B. 11 (2) (1994) 355–371.

4. **Gy R.,** Ion exchange for glass strengthening. Materials Science and Engineering: B. 149 (2) (2008) 159–165.

5. High Quality Microscope Slides. URL: https://www.agarscientific.com/high-quality-microscope-slides. Accessed Jun. 18, 2024.

6. **Reshetov I.V, Zhurikhina V.V, Lipovskii A.A., Scherbak S.A.,** Second harmonic generation by surface of poled glasses: modeling and measurement of Maker fringes. St. Petersburg State Polytechnical University Journal. Physics and Mathematics. 14 (4) (2021) 95–113.

7. **Scherbak S.A., Kaasik V.P., Zhurikhina V.V., Lipovskii A.A.,** Poling of Glasses Using Resistive Barrier Discharge Plasma. Materials. 15 (23) (2022) 8620.

THE AUTHORS

KAN Gennadiy
gennadiykang@gmail.com
ORCID: 0009-0007-3942-7908

SCHERBAK Sergey A.
sergeygtn@yandex.ru
ORCID: 0000-0002-0507-5621

RESHETOV Ilya V.
reshetov_iv@spbstu.ru
ORCID: 0000-0002-8661-3654

LIPOVSKII Andrey A.
lipovskii@gmail.com
ORCID: 0000-0001-9472-9190

TERPITSKIY Aleksey N.
terpiczkij@mail.ru
ORCID: 0000-0002-1744-5976

Received 11.07.2024. Approved after reviewing 01.08.2024. Accepted 01.08.2024.

Conference materials
UDC 538.958, 54.057
DOI: https://doi.org/10.18721/JPM.173.110

Quantum size effect in cadmium sulphide films after plasma treatment

A.V. Stanchik [1, 2] ✉, K.P. Buskis [1], V.F. Gremenok [1, 2], A.V. Kabyliatski [1],
V.V. Khoroshko [2], S.P. Zimin [3, 4], I.I. Amirov [3]

[1] Scientific-Practical Materials Research Centre of the National Academy of Sciences of Belarus, Minsk, Belarus;
[2] Belarussian State University of Informatics and Radioelectronics, Minsk, Belarus;
[3] Valiev Institute of Physics and Technology of RAS, Yaroslavl Branch, Yaroslavl, Russia;
[4] P.G. Demidov Yaroslavl State University, Yaroslavl, Russia
✉ stanchik@physics.by

Abstract. In this work, the optical properties of nanocrystalline CdS films in the initial state and after ion-plasma treatment have been studied. The chemical bath deposition technique was used to prepare CdS films with thickness 80–115 nm on glass substrates. The ion-plasma treatment was carried out in argon plasma in a high-density low-pressure radio frequency inductively coupled plasma reactor at an argon ion energy of 25 eV for 30–50 s. It has been established that ion-plasma treatment leads to a decrease in film thickness by 10–15% of the initial one and the formation of new nanostructures on its surface. The results showed that the sizes of coherent scattering regions during plasma treatment decreased for a series of studied samples from 8.2–10.0 nm to 6.3–7.7 nm. This led to an increase in the band gap energy of the for nanocrystalline CdS films from 2.53–2.78 eV to 2.95–3.11 eV.

Keywords: cadmium sulphide, thin films, chemical bath deposition, plasma treatment, transmission spectra, band gap energy

Funding: This study was funded by the Belarusian Republican Foundation for Fundamental Research grant number T23RNFM-029. This work supported by the Ministry of Higher Education and Science of the Russian Federation was performed in the framework of the state task of the Yaroslavl Branch of K. A. Valiev Institute of Physics and Technology, Russian Academy of Sciences (FFNN-2022-0017).

Citation: Stanchik A.V., Buskis K.P., Gremenok V.F., Kabyliatski A.V., Khoroshko V.V., Zimin S.P., Amirov I.I., Quantum size effect in cadmium sulphide films after plasma treatment, St. Petersburg State Polytechnical University Journal. Physics and Mathematics. 17 (3.1) (2024) 52–57. DOI: https://doi.org/10.18721/JPM.173.110

Материалы конференции
УДК 538.958, 54.057
DOI: https://doi.org/10.18721/JPM.173.110

Квантовый размерный эффект в пленках сульфида кадмия после плазменной обработки

А.В. Станчик [1, 2] ✉, К.П. Бускис [1], В.Ф. Гременок [1, 2], А.В. Кобыляцкий [1],
В.В. Хорошко [2], С.П. Зимин [3, 4], И.И. Амиров [3]

[1] Научно-практический центр Национальной академии наук Беларуси по материаловедению, г. Минск, Беларусь;
[2] Белорусский государственный университет информатики и радиоэлектроники, г. Минск, Беларусь;
[3] Ярославский филиал Физико-Технологического института РАН им. К.А. Валиева, г. Ярославль, Россия;

[4] Ярославский государственный университет им. П.Г. Демидова, г. Ярославль, Россия
✉ stanchik@physics.by

Аннотация. В данной работе исследовано влияние плазменной обработки на оптические свойства нанокристаллических пленок CdS толщиной 80–115 нм, полученных на стеклянных подложках методом осаждения из химической ванны. Результаты показали, что плазменная обработка пленок CdS при 25 эВ в течение 30–50 с приводит к увеличению оптической ширины запрещенной зоны с 2,53–2,78 эВ до 2,95–3,11 эВ. Такое увеличение значений ширины запрещенной зоны пленок связано с уменьшением размеров областей когерентного рассеяния (размера кристаллитов) с 8,2–10,0 нм до 6,3–7,7 нм.

Ключевые слова: сульфид кадмия, тонкие пленки, химическое осаждение в ванне, плазменная обработка, спектры пропускания, энергия запрещенной зоны

Финансирование: Работа выполнена при поддержке Белорусского республиканского фонда фундаментальных исследований (грант Т23РНФМ-029), Министерства высшего образования и науки Российской Федерации в рамках государственного задания Ярославского филиала Физико-технического института им. К.А. Валиева Российской академии наук (FFNN-2022-0017).

Ссылка при цитировании: Станчик А.В., Бускис К.П., Гременок В.Ф., Кобыляцкий А.В., Хорошко В.В., Зимин С.П., Амиров И.И. Квантовый размерный эффект в пленках сульфида кадмия после плазменной обработки // Научно-технические ведомости СПбГПУ. Физико-математические науки. 2024. Т. 17. № 3.1. С. 52–57. DOI: https://doi.org/10.18721/JPM.173.110

Introduction

Cadmium sulphide (CdS) is an important semiconductor of II-VI group with a band gap of 2.42 eV for the hexagonal modification, which has potential application in nanoelectronic and optoelectronic systems, in particular thin-film solar cells and photocathodes. Today, improving the efficiency of thin-film solar cells and photocathodes is a current research problem.

In solar cells, films of CdS are used as a buffer layer between the transparent conductive oxide (ZnO) and the light-absorbing layer to improve their interface. The buffer layer should have minimal absorption losses, low surface recombination, and minimal electrical resistance during the transport of photogenerated carriers. The CdS films is the most preferred among the known materials, but it has optical absorption losses, especially in the shortwave range. As noted in the literature, the photogeneration of charge carriers can be maximized using buffer materials with minimal recombination losses by a wider extension of the space charge region in the absorbing layer [1]. Therefore, the development of methods for controlling surface properties is of absolute relevance. And, an actual direction of CdS research in recent years is the formation and study of nanostructured materials with controllable properties. One of the effective methods of nanostructuring is the method of ion-plasma treatment [2]. Its effect is generally due to both the introduction of impurity atoms and various processes associated with the action of an ion beam (ion etching, ion-stimulated diffusion, the formation of disordered regions due to the accumulation of point defects, etc.). For example in [3], it was shown that oxygen plasma treatment of CdS allows to reduce parasitic absorption of the device and leads to an increase in the short-circuit current density of $Sb_2(S,Se)_3$ solar cells. It was found that Ar-plasma treatment of thermally evaporated In_2S_3 thin films, which are also used as a buffer layer in solar cells, leads to the formation of an array of metallic indium nanostructures on their surface and an increase in optical absorption, but the band gap width decreases by 0.21 eV [4]. Such metallic nanostructures on the semiconductor surface can form a Schottky barrier, which acts as an electron trap and, accordingly, can effectively prevent the recombination of photo-generated electron-hole pairs [4]. In [5] showed that the electrochemically deposited CdS films after cold plasma-surface modification change their surface from hydrophobic to hydrophilic, and have a

long average lifetime with a rapid reduction time constant, indicating a high quality films with low trap density. In [6], in order to improve the photovoltaic characteristics of Sb_2Se_3 films for application as photocathodes for H_2 generation via solar-driven water splitting, an approach to plasma treatment of N_2 and ambient air was developed. After plasma treatment, the surface of Sb_2Se_3 films also changed from hydrophobic to hydrophilic, which provided a significant increase in photocurrent density by 3-fold compared to the untreated film and improved H_2 generation via light-driven water splitting. Thus, plasma treatment can be an effective way to form an intrinsic nanostructure for chalcogenide materials.

The aim of this work was to study the effect of ion plasma treatment on the optical characteristics of CdS films obtained by chemical bath deposition for further modification of the physical properties of various devices based on this material.

Materials and Methods

In our experiments the chemical bath deposition (CBD) technique was used to prepare CdS thin films (80–115 nm). The resulting solution in the bath used for CdS preparation, composed of 90 ml deionized water, 30 ml NH_4OH (wt 25%), 40 ml 0.0096M $CdSO_4$ as a source of cadmium and 40 ml 0.8M $CS(NH_2)_2$ as a source of sulphide [7]. The deposition is performed at a bath temperature of 50–70 °C for 5–20 min onto pre-cleaned glass substrates. The ion-plasma treatment was carried out in Ar plasma in a high-density low-pressure radio frequency inductively coupled plasma reactor at an Ar ion energy of 25 eV for 30–50 s [8]. The elemental composition was obtained using energy-dispersive X-ray spectroscopy (EDS) on AZtecLive Advanced with Ultim Max 40 (Oxford Instruments). The structural properties of films were studied by using Ultima IV X-ray diffractometer (Rigaku) in grazing incidence X-ray diffraction geometry at 1 degree with CuK_α radiation source (λ = 1.5418 Å). Morphological of films was analyzed using an H-800 scanning electron micro-scope (SEM, Hitachi) with a resolution of 0.2 nm. The transmission and reflection spectra of the films were obtained using Photon RT (Essent Optics) spectrophotometer with spectral resolution better than 4 nm using unpolarized light at room temperature.

Results and Discussion

The elemental composition of the deposited CdS films on glass substrate is sulphur 42.5–50.0 at.% and cadmium 50.0–57.5 at.%. It did not change after ion-plasma treatment.

Figure 1 shows typical the X-ray diffraction patterns of the synthesized CdS films in initial state and after plasma treatment. The three peaks observed in the XRD pattern of the deposited CdS films: a strong reflection at (111) and two minor peaks at (220) and (311), correspond to a cubic structure of the space group $F\bar{4}3m$ according to the Powder Diffraction File for CdS (PDF no. 75-1546). The cubic crystal structure of the synthesized CdS films is retained after plasma treatment no matter of its duration (30–50 s) at an ion energy of 25 eV. Moreover, for the plasma-treated films, no additional diffraction peaks concerning the formation of secondary phases or the hexagonal phase of CdS have been identified. It is known that the most common phase of the bulk CdS crystal is the hexagonal structure, while the cubic phase of CdS is metastable and appears in low-dimensional structures [9]. This indicates the nanocrystalline nature of the CdS

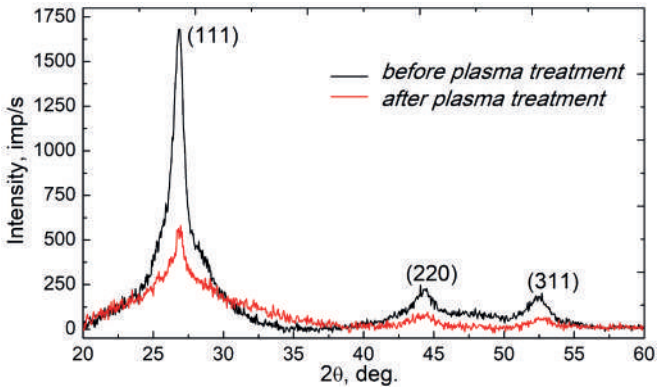

Fig. 1. Typical X-ray diffraction patterns of the CdS film before and after plasma treatment

thin films in the initial state and after ion bombardment. The presence of a broad diffraction peaks is probably due to small grain size and/or a thin layer of CdS presenting a broad noisy background [9].

After plasma treatment of CdS films, the intensity of all peaks on the X-ray pattern is significantly reduced, while the predominant orientation still remains in the direction of the (111) plane (Fig. 1). The Full Width at Half Maximum values of the main diffraction peak for the deposited films are about 1.9, which increases to ~5.4 after plasma treatment. At the same time, a shift of the main diffraction peak towards higher diffraction angle values (0.19°) compared to that of the untreated films and a slightly decrease in the interplanar spacing from 0.334 to 0.331 nm according to the Bragg's equation ($2d_{hkl} \sin\theta = \lambda$) are observed. The calculated value of the interplanar spacing for the deposited films is less than the theoretical value (d = 0.33601 nm, PDF no. 75-1546), indicating the appearance of compressive strain in the crystal lattice, which increases after ion bombardment of films. It is the explanation for the decrease in intensity, broadening and shift of the diffraction peaks in the X-ray pattern for the plasma-treated films. An average size of coherent scattering regions (crystallite sizes), calculated using the Scherrer equation, decreased from 8.2–10.0 nm to 6.3–7.7 nm during plasma treatment for a series of studied CdS films.

It was found that ion-plasma treatment leads to modification of morphology of nanocrystalline CdS films (Fig. 2).

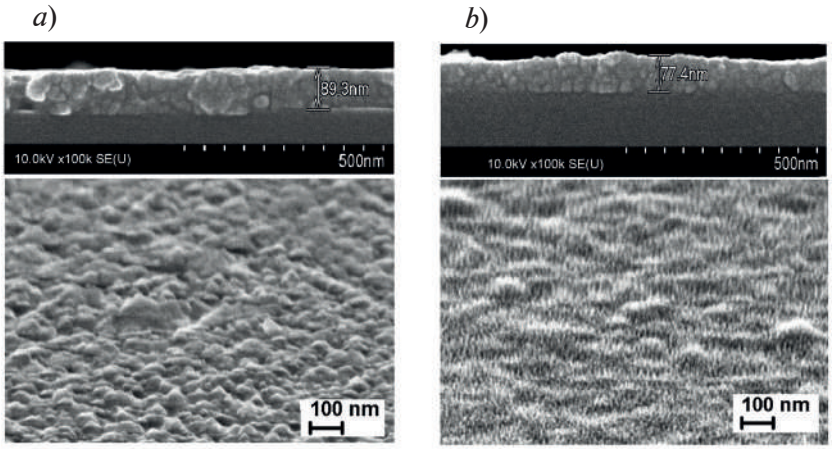

Fig. 2. Typical SEM top view and cross-sectional image of CdS thin film before (*a*) and after plasma treatment (*b*)

In the process of ion sputtering, a decrease in the film thickness by 10–15% of the initial one and the appearance of new nanostructures on their surface are observed. It is the result of the etching in plasma. As an example, the cross-section SEM images of CdS films shown in Fig. 2 demonstrate the reduction in film thickness after plasma treatment, and it is also seen that the cadmium sulphide layer becomes denser with smaller crystals. The surface of the initial deposited films is a collection of spherical CdS nanoparticles with sizes ranging from 30 to 100 nm (Fig. 2, *a*). Whereas ion-plasma treatment leads to nanostructuring of the surface in the form of formation of a homogeneous ensemble of vertical nanorods up to 20–30 nm high with lateral dimensions at the base of less than 15 nm (Fig. 2, *b*), the surface density of which is about $2 \cdot 10^{11}$ cm^{-2}.

Changing the structural parameters and morphology of the CdS films leads to a change in their optical properties, which is shown on the example of one of the samples in Fig. 3. The presented optical spectra show that plasma treatment of the films results in a slight increase in transmission and, accordingly, a decrease in reflection (Fig. 3, *a*). All CdS films before and after plasma treatment were characterized by a sloping fundamental absorption edge, which shifts to high energies (smallest wavelength) as a result of ion bombardment.

Based on the analysis of the transmission and reflection spectra, the values of the band gap energy (E_g) were determined (Fig. 3, *b*). The obtained value of E_g = 2.53–2.78 eV for deposited CdS films differs from the reported values for the hexagonal (2.42 eV) and cubic (2.34–2.58 eV)

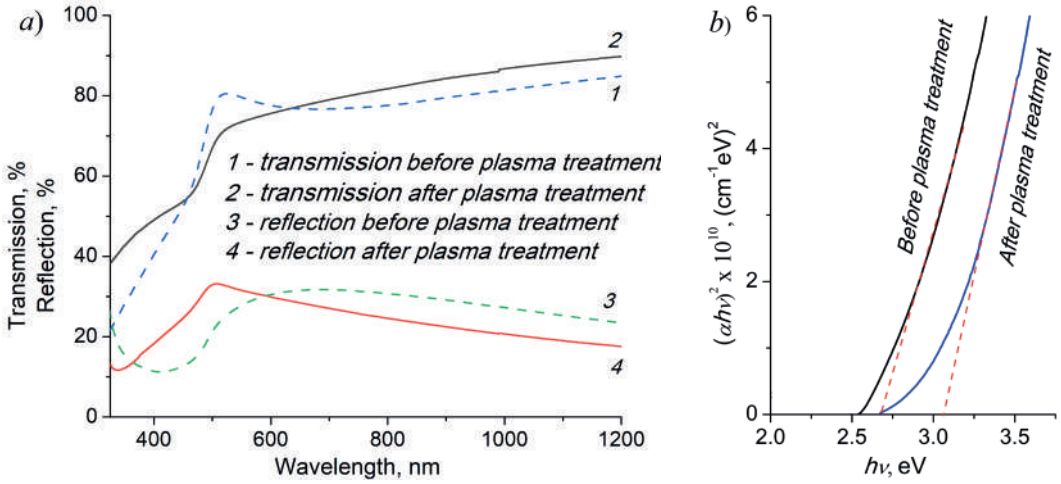

Fig. 3. Reflection and transmission spectra for CdS film before and after plasma treatment (*a*). Tauc plots and band gap values evaluation for as prepared and after plasma treatment CdS (*b*)

phases of CdS [7,9]. An increase in the E_g from 2.53–2.78 to 2.95–3.11 eV was observed for all samples after ion-plasma treatment. An increase in E_g as a result of plasma treatment is due to the manifestation of the quantum-size effect (the quantum confinement of carriers inside the grains) [10, 11]. For example, Cortes et al. report a clear increase in the band gap with decreasing grain size in CdS films, which is associated with quantum confinement and confirm by calculations of an inverse square dependence of the shifting band gap energy with grain sizes [9]. In our case, as noted above, during the ion bombardment of the CdS films, the grain sizes decrease and new nanostructures are formed on the surface of films in the form of ensembles of nanorods, smaller in size compared to the nanocrystals before plasma treatment. For example, such an increase in the optical band gap of the CdS films is useful for thin-films solar cells, where it is used as a buffer layer. An increasing the band gap energy of CdS minimizes optical absorption losses in the buffer layer, especially in the shortwave range. This will lead to increased current generation at lower wavelengths and, accordingly, can improve the efficiency of solar cells [12].

Conclusion

The results of this work showed that ion-plasma treatment of nanocrystalline films of cadmium sulphide with 80–115 nm thickness promotes the formation of nanostructures of smaller sizes, which provides an increase in the band gap energy due to the realization of quantum size effects. The report compares the obtained data with literature data and analyzes the physical reasons for the changes in the structural parameters of films during ion-plasma treatment.

REFERENCES

1. **Ruiz-Ortega R.C., Esquivel-Mendez L.A., Gonzalez-Trujillo M.A., Hernandez-Vasquez C., Matsumoto Y., Albor-Aguilera M.L.,** Comprehensive Analysis of CdS Ultrathin Films Modified by the Substrate Position inside the Reactor Container Using the CBD Technique, ACS Omega. 8 (2023) 31725–31737.

2. **Levchenko I., Ostrikov K.,** Nanostructures of various dimensionalities from plasma and neutral fluxes, J. Phys. D: Appl. Phys. 40 (8) (2007) 2308–2319.

3. **Zang R., Wang H., Peng X., Li K., Gu Y., Dong Y., Yan Z., Cai Z., Gao H., Sheng S., Tang R., Chen T.,** Effect of substrate temperature and oxygen plasma treatment on the properties of magnetron-sputtered CdS for solar cell applications, JUSTC. 54 (6) (2024) 0604.

4. **Rasool S., Saritha K., Ramakrishna Reddy K.T., Tivanov M.S., Korolik O.V., Gremenok V.F., Zimin S.P., Amirov I.I.,** Effect of Ar-plasma treatment and annealing on thermally evaporated β-In2S3 thin films, Adv. Nat. Sci.: Nanosci. Nanotechnol. 14 (2023) 025010.

5. **Khadayeira A.A., Najima F.A., Wanasa A.H.,** Modification in morphological, structural, photoluminescence and antibacterial properties of SnS and CdS thin films by cold plasma treatment, Chalcogenide Letters. 18 (7) (2021) 385–396.

6. **Costa M.B., Araujo M.A., Paiva R., Cruz S.A., Mascaro L.H.,** Plasma treatment of electrodeposited Sb_2Se_3 thin films for improvement of solar-driven hydrogen evolution reaction, Chemical Engineering Journal. 485 (2024) 149526.

7. **Gremenok V.F., Zaretskaya E.P., Stanchik A.V., Buskis K.P., Pashayan S.T., Tokmajya A.S., Musayelyan A.S., Petrosyan S.G.,** Study of structural and optical properties of CdS thin films depending on chemical deposition time, Optics and Spectroscopy. 132 (2024) 161–168. (in Russian).

8. **Zimin S., Gorlachev E., Amirov I.,** Inductively Coupled Plasma Sputtering: Structure of IV-VI Semiconductors, Encyclopedia of Plasma Technology, CRC Press, New York, 2017.

9. **Cortes A., Gomez H., Marotti R.E., Riveros G., Dalchiele E.A.,** Grain size dependence of the bandgap in chemical bath deposited CdS thin films, Solar Energy Materials & Solar Cells. 82 (2004) 21–34.

10. **Brus L.,** Electronic wave functions in semiconductor clusters: experiment and theory, J. Phys. Chem. 90 (12) (1986) 2555–2560.

11. **Yoffe A.D.,** Low-dimensional systems: quantum size effects and electronic properties of semiconductor microcrystallites (zero-dimensional systems) and some quasi-two-dimensional systems, Advances in Physics. 42 (2) (1993) 173–262.

12. **Siebentritt S.,** Alternative buffers for chalcopyrite solar cells, Solar Energy. 77 (2004) 767–775.

THE AUTHORS

STANCHIK Aliona V.
alena.stanchik@bk.ru
ORCID: 0000-0001-8222-8030

BUSKIS Konstantin P.
konstantinbuskis@gmail.com
ORCID: 0000-0001-9920-8159

GREMENOK Valery F.
gremenok@physics.by
ORCID: 0000-0002-3442-5299

KABYLIATSKI Aliaksandr V.
kobylyackiy.sasha@mail.ru

KHOROSHKO Vitaliy V.
khoroshko1986@gmail.com

ZIMIN Sergey P.
zimin@uniyar.ac.ru

AMIROV Ildar I.
ildamirov@yandex.ru
ORCID: 0000-0001-5273-3298

Received 12.07.2024. Approved after reviewing 29.07.2024. Accepted 30.07.2024.

Conference materials
UDC 538.9
DOI: https://doi.org/10.18721/JPM.173.111

Influence of annealing conditions on the characteristics of nanoholes formed by focused ion beams on the GaAs(111) surface

E.A. Lakhina [1] ✉, N.E. Chernenko [1], N.A. Shandyba [1],
D.V. Kirichenko [1], S.V. Balakirev [1], M.S. Solodovnik [1]

[1] Southern Federal University, Taganrog, Russia
✉ lakhina@sfedu.ru

Abstract. In this paper, we study the effect of annealing of GaAs(111) substrates under various conditions on the morphological characteristics of nanoholes formed by focused ion beams. In the absence of annealing and when annealing in the absence of the arsenic flux, the depth and lateral size of nanoholes increase with the number of ion beam passes. In the case of annealing of the substrates in the arsenic flux, the dependences of the hole depth and lateral size on the number of beam passes is non-monotonic, which is attributed to the competition of the processes of surface etching by gallium droplets during thermal oxide removal and droplet crystallization in the arsenic flux. We demonstrate technological conditions enabling formation of highly symmetric nanoholes in the form of triangular pyramids.

Keywords: focused ion beams, annealing, local droplet etching, GaAs(111)

Funding: This study was funded by the Russian Science Foundation Grant No. 23-79-10313, https://rscf.ru/project/23-79-10313/, at the Southern Federal University.

Citation: Lakhina E.A., Chernenko N.E., Shandyba N.A., Kirichenko D.V., Balakirev S.V., Solodovnik M.S., Influence of annealing conditions on the characteristics of nanoholes formed by focused ion beams on the GaAs(111) surface, St. Petersburg State Polytechnical University Journal. Physics and Mathematics. 17 (3.1) (2024) 58–62. DOI: https://doi.org/10.18721/JPM.173.111

Материалы конференции
УДК 538.9.
DOI: https://doi.org/10.18721/JPM.173.111

Влияние условий отжига на характеристики наноуглублений, формируемых фокусированными ионными пучками на поверхности GaAs(111)

Е.А. Лахина [1] ✉, Н.Е. Черненко [1], Н.А. Шандыба [1],
Д.В. Кириченко [1], С.В. Балакирев [1], М.С. Солодовник [1]

[1] Южный федеральный университет, г. Таганрог, Россия
✉ lakhina@sfedu.ru

Аннотация. В работе представлены результаты исследования влияния отжига подложек GaAs(111) при различных условиях на морфологические характеристики наноуглублений, формируемых фокусированными ионными пучками. В отсутствие отжига и при отжиге в отсутствие потока мышьяка глубина и латеральный размер углублений возрастают с числом проходов ионного пучка. В случае отжига подложек в потоке мышьяка зависимости глубины и латерального размера углублений от числа проходов немонотонны, что связано с конкуренцией процессов травления поверхности

каплями галлия во время термического сгона окисла и процессов кристаллизации капель в потоке мышьяка. Продемонстрированы технологические режимы, позволяющие формировать высокосимметричные наноуглубления в форме треугольных пирамид.

Ключевые слова: фокусированные ионные пучки, отжиг, локальное капельное травление, GaAs(111)

Финансирование: Исследование выполнено за счет гранта Российского научного фонда № 23-79-10313, https://rscf.ru/project/23-79-10313/, в Южном федеральном университете.

Ссылка при цитировании: Лахина Е.А., Черненко Н.Е., Шандыба Н.А., Кириченко Д.В., Балакирев С.В., Солодовник М.С. Влияние условий отжига на характеристики наноуглублений, формируемых фокусированными ионными пучками на поверхности GaAs(111) // Научно-технические ведомости СПбГПУ. Физико-математические науки. 2024. Т. 17. № 3.1. С. 58–62. DOI: https://doi.org/10.18721/JPM.173.111

Introduction

Emitters of single and entangled photons have recently attracted increased interest due to the possibility of their use in quantum information devices [1, 2]. A good candidate for these emitters is an epitaxially grown InAs quantum dot (QD) formed at a specified site of the GaAs surface [3]. QDs with C3v symmetry are particularly important and can be grown on surfaces with (111) orientation [4]. Because of their symmetry, such QDs demonstrate vanishing fine structure splitting, which favors a high degree of entanglement of photon pairs [5]. Despite the increased interest in this topic, the results of studies of the formation of nanoholes on the GaAs(111) surface – QD nucleation centers – by focused ion beams (FIB) followed by annealing in a molecular beam epitaxy (MBE) chamber to restore the disturbed crystalline regions have not been presented so far.

In this paper, the influence of FIB and MBE technological conditions on the characteristics of nanoholes formed on the GaAs(111) surface are investigated and formation of nanoholes with high C_{3v} symmetry is achieved. The results of the study of the dependence of the shape, depth and lateral size of nanoholes obtained directly after FIB treatment and after subsequent annealing under different conditions on the number of ion beam passes are also presented.

Materials and Methods

FIB treatment of the GaAs(111) surfaces was carried out on a FEI Nova NanoLab 600 scanning electron microscope (SEM) equipped with a FIB column (with Ga^+ ion source) at an accelerating voltage of 5 kV. FIB treatment point arrays of 4×4 μm in size with 2 μm spacing between the points and the number of ion beam passes (N) from 1 to 60 were used. In the next step, the FIB treated substrates were placed in a SemiTEq STE 35 MBE unit for annealing under different conditions to transform the nanoholes. Sample 1 was not annealed in the MBE chamber, samples 2 and 3 were annealed until the oxide removal at 600 °C without and with the arsenic flux, respectively, and then both samples were additionally annealed in the arsenic flux for 60 min.

The obtained samples were examined using a FEI Nova NanoLab 600 SEM and an NT-MDT Ntegra atomic force microscope (AFM) in a semi-contact mode. The average depth and lateral size of the nanoholes were estimated using the built-in tool of the Image Analysis software package designed for AFM image processing.

Thermodynamic analysis of chemical reactions in the Ga-As-O system was carried out in the FactSage 6.3 software package (using EquiSage, Reactions and PhaseSage modules). The package allows estimating the probability of chemical reactions in the considered system on the basis of the dependence of the Gibbs free energy change on the temperature.

Results and Discussion

AFM images of nanoholes formed by FIB without subsequent annealing demonstrate that FIB treatment leads to the formation of a shallow hole surrounded by a halo of swelled and redeposited substrate material (Fig.1, *a*, *b*). An increase in the number of FIB passes leads to deepening of nanoholes at their almost constant lateral size (diameter) and a decrease in the height of surrounding halos (Fig. 1, *c*).

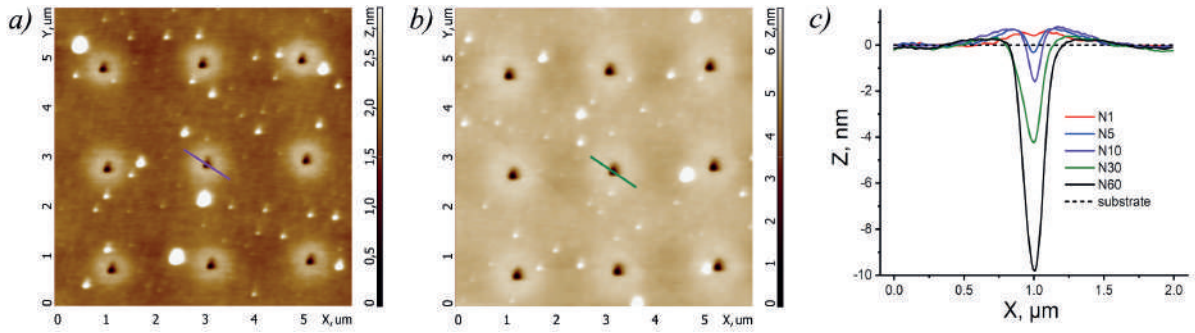

Fig. 1. AFM images of arrays of nanoholes formed after FIB treatment of the surface with various number of ion beam passes: 10 (*a*), 30 (*b*) and AFM cross sections of nanoholes located in the array centers (*c*)

An increase in the number of FIB passes leads to a monotonous increase both in the depth and diameter of nanoholes (Fig. 2, *a*). Annealing of the FIB-modified substrate results in the local droplet etching (LDE) of the GaAs(111) surface by Ga droplets [6, 7] and the formation of nanoholes with a shape of close-to-regular triangular pyramids (Fig. 3, *a*, *c*). The effect of LDE is particularly pronounced on the nanoholes obtained after 1 FIB pass and annealing under the arsenic flux: the average nanohole depth and lateral size, which are 0.2 and 70 nm immediately after the FIB treatment (Fig. 2, *a*), increase to 156 and 367 nm, respectively (Fig. 2, *b*). In the absence of arsenic flux, the surface is etched much less intensively (Fig. 3, *b*). However, an increase in the number of FIB passes to 10 and subsequent annealing without As results in the formation of an ordered array of uniformly sized nanoholes in the form of complete triangular pyramids (Fig. 3, *c*), as opposed to truncated ones in Figure 3, *a*. A further increase in the number of FIB passes up to 60 leads to an increase in the nanohole depth and reappearance of a flat base on its bottom in the case of As-free annealing and to the formation of complete triangular pyramids after the As-supplied annealing.

While both the depth and lateral size of nanoholes increases almost monotonically with the number of FIB passes for substrates with annealing in the As-free atmosphere (Fig. 2, *c*), the presence of arsenic leads to rises and dips in the dependences of hole size on the number of FIB

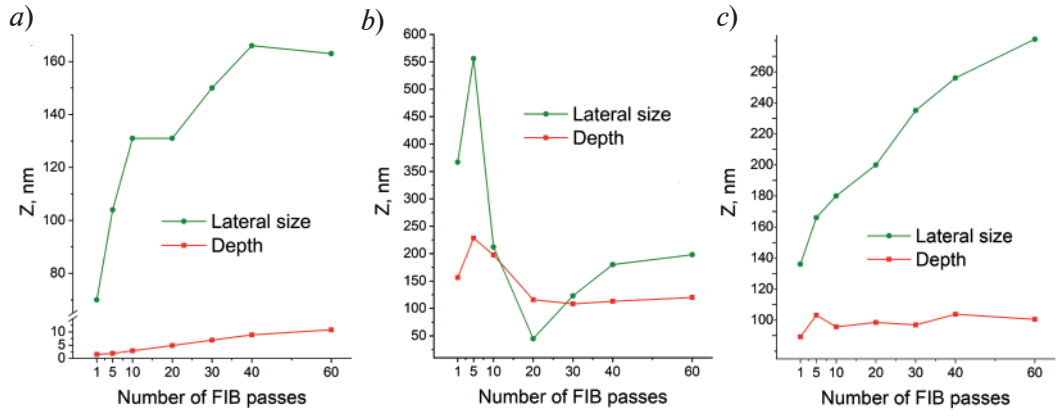

Fig. 2. Dependences of the lateral size and depth of nanoholes on the number of FIB passes in the FIB-treated areas before annealing (*a*), after annealing in the As flux (*b*) and without the As flux (*c*)

passes (Fig. 2, *b*). This behavior can be explained by the competition of the processes of surface etching by gallium droplets and droplet crystallization in the arsenic flux.

Although a standard procedure of the oxide removal from GaAs substrates is carried out in the absence of arsenic flux, the results of our studies demonstrate that its presence leads, first, to an increase in the size of nanoholes on the surface areas not treated by FIB and second, to an increase in the size and degree of symmetry of nanoholes at a small number of FIB passes (Fig. 3, *a*, *b*). When the number of passes is increased, the difference between the sizes of nanoholes obtained after annealing in the arsenic flux and in its absence becomes less noticeable.

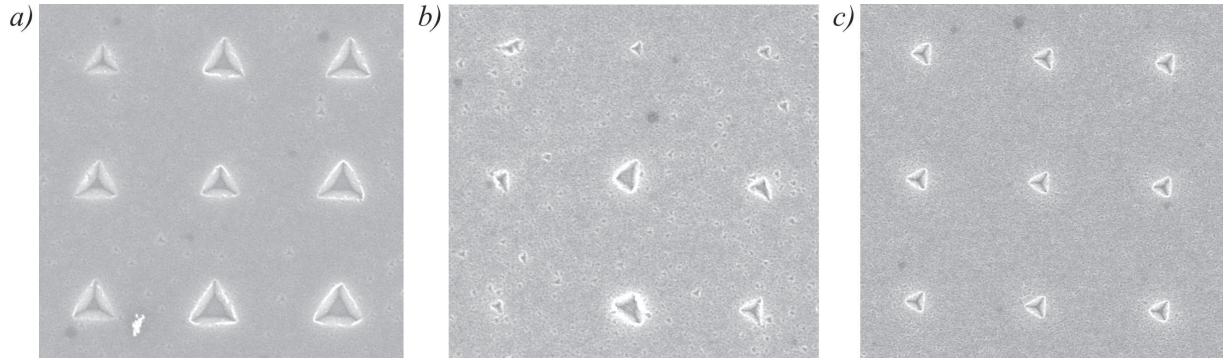

Fig. 3. SEM images of arrays of nanoholes formed after FIB treatment of the surface with various number of ion beam passes: 1 (*a*, *b*), 10 (*c*) – after annealing under different conditions: in the As flux (*a*), without the As flux (*b*, *c*)

Thermodynamic analysis of chemical reactions occurring in the Ga-As-O system (interaction of arsenic and gallium oxides with the underlying GaAs layer, as well as decomposition of GaAs and arsenic oxides) showed that gallium oxide Ga_2O_3 remains on the surface during heating longer than As_2O_3 and As_2O_5 arsenic oxides and serves as a kind of mask protecting gallium accumulating under it from crystallization in the arsenic flux. At the same time, arsenic stabilizing the GaAs surface serves as a drain for gallium atoms under the surface areas covered with stable Ga_2O_3-containing oxides. In this regard, an increase in the arsenic flux leads to enhancement of LDE, resulting in the formation of large nanoholes with pronounced crystal faceting. In turn, in the absence of the arsenic flux, gallium predominantly remains under the oxide and crystallizes after its removal, preventing etching of the substrate and the formation of pyramidal nanoholes.

Conclusion

Thus, the arsenic flux has a significant effect on the transformation of nanoholes formed by the FIB method, leading to an increase in their size at a small number of FIB passes and to its decrease at a large number of FIB passes. Highly symmetrical and uniformly sized nanoholes in the form of triangular pyramids were obtained after As-supplied annealing of the GaAs(111) substrate with arrays of FIB impact points formed after 60 ion beam passes and after 10 ion beam passes in the case of annealing in the As-free atmosphere.

REFERENCES

1. **Valeri M., Barigelli P., Polacchi B., Rodari G., De Santis G., Giordani T., Carvacho G., Spagnolo N., Sciarrino F.,** Generation and characterization of polarization-entangled states using quantum dot single-photon sources, Quantum Science and Technology. 9 (2) (2024) 025002.

2. **Vajner D.A., Holewa P., Zięba-Ostyj E., Wasiluk M., von Helversen M., Sakanas A., Huck A., Yvind K., Gregersen N., Musiał A., Syperek M., Semenova E., Heindel T.,** On-Demand Generation of Indistinguishable Photons in the Telecom C-Band Using Quantum Dot Devices, ACS Photonics. 11 (2) (2024) 339–347.

3. **Zeuner K.D., Jцns K.D., Schweickert L., Hedlund C.R., Lobato C.N., Lettner T., Wang K., Gyger S., Schöll E., Steinhauer S., Hammar M., Zwiller V.,** On-Demand Generation of Entangled Photon Pairs in the Telecom C-Band with InAs Quantum Dots, ACS Photonics. 8 (8) (2021) 2337–2344.

4. **Mano T., Ohtake A., Kuroda T.,** Lattice-Mismatched Epitaxy of InAs on (111)A-Oriented Substrate: Metamorphic Layer Growth and Self-Assembly of Quantum Dots, Physica Status Solidi. (2024) 2300767.

5. **Tuktamyshev A., Fedorov A., Bietti S., Vichi S., Zeuner K. D., Jцns K. D., Chrastina D., Tsukamoto S., Zwiller V., Gurioli M., Sanguinetti S.,** Telecom-wavelength InAs QDs with low fine structure splitting grown by droplet epitaxy on GaAs(111)A vicinal substrates, Applied Physics Letters. 118 (13) (2021).

6. **Wang Z.M., Liang B.L., Sablon K.A., Salamo G.J.,** Nanoholes fabricated by self-assembled gallium nanodrill on GaAs(100), Applied Physics Letters. 90 (11) (2007) 113120.

7. **Heyn C., Stemmann A., Klingbeil M., Strelow Ch., Köppen T., Mendach S., Hansen W.,** Mechanism and applications of local droplet etching, Journal of Crystal Growth. 323 (1) (2011) 263–266.

THE AUTHORS

LAKHINA Ekaterina A.
lakhina@sfedu.ru
ORCID: 0000-0002-9326-2418

KIRICHENKO Danil V.
dankir@sfedu.ru
ORCID: 0000-0001-7476-2778

CHERNENKO Natalia E.
nchernenko@sfedu.ru
ORCID: 0000-0001-8468-7425

BALAKIREV Sergey V.
sbalakirev@sfedu.ru
ORCID: 0000-0003-2566-7840

SHANDYBA Nikita A.
shandyba.nikita@gmail.com
ORCID: 0000-0001-8488-9932

SOLODOVNIK Maxim S.
solodovnikms@sfedu.ru
ORCID: 0000-0002-0557-5909

Received 11.07.2024. Approved after reviewing 01.08.2024. Accepted 12.08.2024.

Conference materials
UDC 538.9
DOI: https://doi.org/10.18721/JPM.173.112

Pressure and temperature sensing via ZnO-PDMS based membrane for wearable electronic applications

A.V. Nikolaeva [1, 2, 3] ✉, V.M. Kondratev [2, 3], S.A. Kadinskaya [2, 3], D.E. Kolesina [2, 4], F.I. Zubov [2], F.M. Kochetkov [2], L.N. Dvoretckaia [2], V.V. Lendyashova [1, 2], V.O. Gridchin [1, 6], A.O. Monastyrenko [2], A.D. Bolshakov [2, 3, 5]

[1] St. Petersburg State University, St. Petersburg, Russia;
[2] Alferov University, Saint Petersburg, Russia;
[3] Moscow Institute of Physics and Technology, Moscow, Russia;
[4] Peter the Great St. Petersburg Polytechnic University, Russia;
[5] Laboratory of Advanced Functional Materials, Yerevan State University, Armenia;
[6] Institute for Analytical Instrumentation of the Russian Academy of Sciences, Russia
✉ nikalex2000@bk.ru

Abstract. In this work, we have grown vertically oriented ZnO microstructures via low-temperature hydrothermal method using microsphere photolithography and followed by etching to prepare the growth substrate and establish ZnO nucleation areas. The synthesized structures were rod-shaped ZnO microcrystals with a height of 5 μm and a diameter of about 400 nm. Such structures were encapsulated in polydimethylsiloxane (PDMS) for ZnO-PDMS membrane formation. Based on this membrane, flexible and solid pressure sensors were fabricated. All sensors have been studied using electrical impedance spectroscopy in terms of the change in resistance and electrical capacitance when pressure is applied. A correlation between the electrical characteristics of such sensors and an applied mechanical pressure was demonstrated. One of such sensors shows the possibility of synchronous measurement of pressure and temperatures in the range of 25 °C – 100 °C was demonstrated. Fabricated sensors can find their application in the field of personalized healthcare and for the advancement of electronic skin (E-skin).

Keywords: ZnO, PDMS, sensor

Funding: The Ministry of Science and Higher Education of the Russian Federation (agreement 075-03-2023-106, project FSMG-2021-0005; project FSRM-2023-0010). Russian Science Foundation (Grant 24-12-00225). For the substrates preparation for the samples growth the authors acknowledge Saint-Petersburg State University for a research project 87465891.

Citation: Nikolaeva A.V., Kondratev V.M., Kadinskaya S.A., Kolesina D.E., Zubov F.I., Kochetkov F.M., Dvoretckaia L.N., Lendyashova V.V., Gridchin V.O., Monastyrenko A.O., Bolshakov A.D., Pressure and temperature sensing via ZnO-PDMS based membrane for wearable electronic applications, St. Petersburg State Polytechnical University Journal. Physics and Mathematics. 17 (3.1) (2024) 63–67. DOI: https://doi.org/10.18721/JPM.173.112

Материалы конференции
УДК 538.9
DOI: https://doi.org/10.18721/JPM.173.112

Сенсоры давления и температуры на основе мембраны ZnO-ПДМС для носимой электроники

А.В. Николаева [1, 2, 3] ✉, В.М. Кондратьев [2, 3], С.А. Кадинская [2, 3], Д.Е. Колесина [2, 4], Ф.И. Зубов [2], Ф.М. Кочетков [2], Л.Н. Дворецкая [2], В.В. Лендяшова [1, 2],

В.О. Гридчин [1, 6], А.О. Монастыренко [2], А.Д. Большаков [2, 3, 5]

[1] Санкт-Петербургский государственный университет, Санкт-Петербург, Россия;

[2] Академический университет им. Ж.И. Алфёрова РАН, Санкт-Петербург, Россия;

[3] Московский физико-технический институт (национальный исследовательский университет), г. Долгопрудный, Россия;

[4] Санкт-Петербургский политехнический университет Петра Великого, Санкт-Петербург, Россия;

[5] Ереванский государственный университет, Ереван, Армения;

[6] Институт аналитического приборостроения Российской академии наук, Россия

✉ nikalex2000@bk.ru

Аннотация. В данной работе была продемонстрирована корреляция между электрическими характеристиками сенсоров на базе гидротермальных микроструктур ZnO, инкапсулированных в гибкую ПДМС матрицу, и приложенным механическим давлением, а также температурой. Сенсоры демонстрируют возможность синхронного измерения давления и температуры в диапазоне 0.2 – 1.8 Мпа и 25 °C – 100 °C, соответственно. Изготовленные сенсоры могут быть эффективно использованы для решения задач персонифицированной медицины и для создания электронной кожи (E-skin).

Ключевые слова: ZnO, ПДМС, сенсор

Финансирование: Министерство науки и высшего образования Российской Федерации (соглашение 075-03-2023-106, проект ФСМГ-2021-0005; проект ФСРМ-2023-0010). Российский научный фонд (грант 24-12-00225). За подготовку подложек для выращивания образцов авторы выражают благодарность Санкт-Петербургскому государственному университету за научный проект 87465891.

Ссылка при цитировании: Николаева А.В., Кондратьев В.М., Кадинская С.А., Колесина Д.Е., Зубов Ф.И., Кочетков Ф.М., Дворецкая Л.Н., Лендяшова В.В., Гридчин В. О., Монастыренко А.О., Большаков А.Д. Сенсоры давления и температуры на основе мембраны ZnO-ПДМС для носимой электроники // Научно-технические ведомости СПбГПУ. Физико-математические науки. 2024. Т. 17. № 3.1. С. 63–67. DOI: https://doi.org/10.18721/JPM.173.112

Introduction

Micro- and nanoscale structures of various materials [1] found broad applications in sensorics [2, 3], electronics and photonics [4, 5]. The miniaturization of microelectronics-based sensors has played an influential role in the development of flexible wearable devices that can be repeatedly bent and subjected to mechanical deformation without degradation of functionality and even with the ability to self-heal. In addition, flexible sensors can find their application in personalized healthcare for measuring pressure, heart rate, and temperature.

An array of ZnO microcrystals encapsulated in a PDMS polymer matrix is a material that has both piezoelectric and semiconductor properties, as well as flexibility and resistance to deformation. The advantages of such a sensor also include the simplicity and low cost of synthesizing ZnO by hydrothermal method [6–8], which makes it easy to scale up the production technology of such a device.

This work is devoted to the synthesis of ZnO microstructures by low-temperature hydrothermal method using microsphere photolithography, fabrication and study of biocompatible, potentially flexible, wearable, miniature mechanical pressure sensors with the possibility of parallel temperature measurement.

Materials and Methods

The ZnO growth substrates were pre-processed using a photolithography technique with quartz spheres, 1.5 μm in diameter, on a silicon (Si) substrate in a 30 nm thick silicon oxide (SiO_2)

layer followed by etching in KOH to obtain an ordered array of 400 nm diameter holes. The ZnO microwires (MWs) were synthesized via low-temperature hydrothermal method which involves the oriented growth of zinc oxide microstructures in an aqueous solution of growth precursors. Zinc oxide crystals were encapsulated in PDMS by g-coating method. The ZnO-PDMS membrane was separated from the substrate to fabricate a flexible pressure sensor with carbon nanotubes (CNT) as electrodes. The flexible sensor was studied in the pressure range 40–300 kPa.

For measuring pressures in the order of MPa and temperature sensing in the range of 25–100 °C, a solid sensor based on the ZnO-PDMS membrane was fabricated using Al_2O_3 ceramic substrates with counter-pinned gold contacts. All sensors were studied by electrical impedance spectroscopy technique (EIS) using impedance meter Z500P (Elins Ltd., Russia) in the frequency range 0.5–500 kHz with amplitude 100 mV and bias voltage 2 V.

Results and Discussion

The sensor's resistance and capacitance response r as a function of the applied pressure was calculated as:

$$r_X(p) = \frac{|X(p) - X_0|}{X_0} \cdot 100\%, \quad (1)$$

where $X(p)$ is the resistance or capacitance when pressure p is applied and X_0 is the resistance or capacitance of the sensors in the absence of a load. Flexible and solid sensors based on the ZnO-PDMS membrane showed a response in electrical capacitance (r_C) and in resistance (r_R) with increasing pressure (Fig. 1, *a*, *d*). The increase in the electrical capacity of the sensors (C) can be explained in terms of the piezoelectric effect that occurs in an array of ZnO microcrystals under mechanical deformation. The decrease in sensor resistance (R) is associated with the establishment of contact between the top electrode and the tops of the microcrystals when pressure is applied.

Moreover, the observed step-like character in the flexible sensor's response is believed to be due to the consecutive connection of crystals to the top and bottom CNT contacts with increasing applied pressure (Fig. 1, *d*).

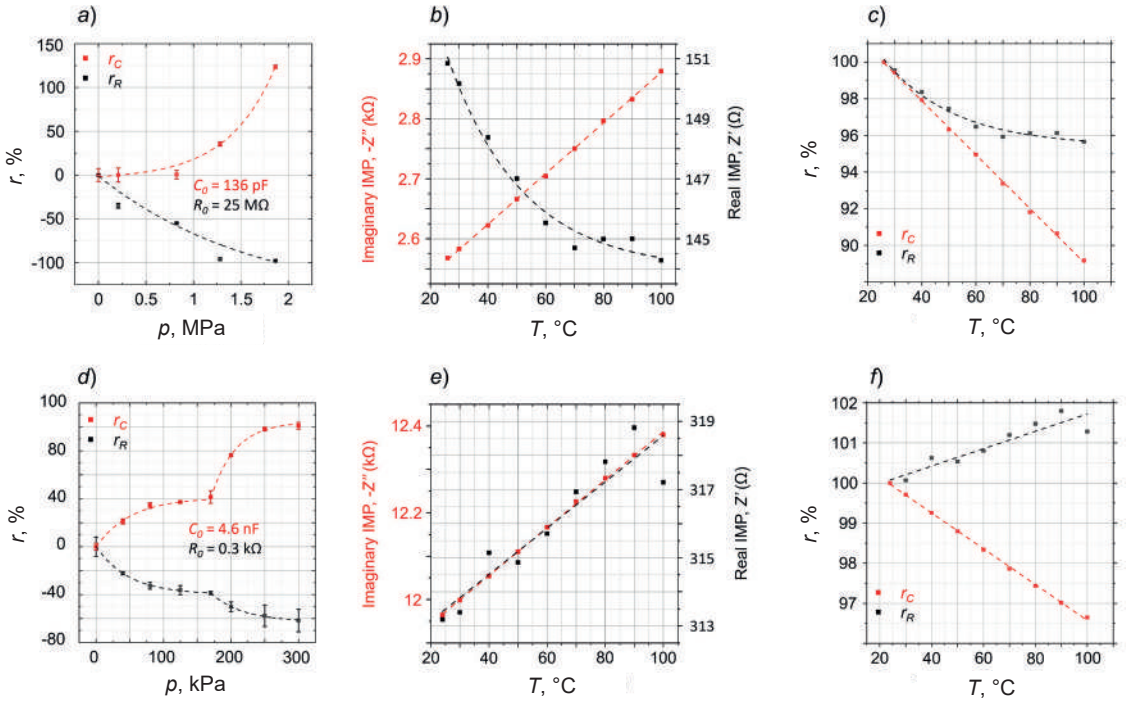

Fig. 1. Sensory response in the pressure range 0.2 – 1.8 MPa for solid sensor (*a*) and 40 – 300 kPa for flexible sensor (*d*). Dependence of the real and imaginary parts of the impedance on temperature in the range of 25 °C – 100 °C for solid sensor (*b*) and reference sample (*e*). Temperature sensory responses for solid sensor (*c*) and reference sample (*f*)

To expand the understanding of the functionality of the fabricated devices, a series of EIS measurements were conducted on solid and reference sample within the temperature range of 25 °C to 100 °C. These measurements were carried out at a frequency of 500 kHz. The results of these measurements are illustrated in (Fig. 1, *b*, *c*, *e*, *f*), depicting the variations in the impedance components with temperature. It is observed that as the temperature increases, the imaginary part of the impedance Z'' for solid sensor rises, while the real part of the impedance Z' decreases. Similar measurements were carried out on the reference sample. In this case, both the real and imaginary components of the impedance demonstrate increase with rising temperature, as shown in (Fig. 1, *e*). The increase in the imaginary part of the impedance Z'' as temperature rises can be attributed to the thermal expansion of PDMS, leading to an increase in electrode spacing d. This, in turn according to the flat capacitor approximation:

$$C = \frac{\varepsilon_0 \cdot \varepsilon \cdot S}{d}, \tag{2}$$

where ε_0 is the dielectric constant ($8.854 \cdot 10^{-12}$ F·m), ε is the relative permittivity and S is the shell area, results in a decrease in electrical capacitance inversely proportional to Z''. Yet the decrease in the real part of impedance (Z'), which is associated with resistance (R), with increasing temperature can be attributed to the semiconducting properties of ZnO.

Noteworthy, an increase in the imaginary part corresponds to a decrease in the capacitance, so an increase in temperature in solid sensor (Fig. 1, *b*) induces a simultaneous drop in resistance and capacitance. This behaviour is different from the response upon a change in a mechanical load. The latter stimulates different resistive and capacitive responses (Fig. 1, *a*). As such, the fabricated sensor allows for simultaneous pressure and temperature monitoring. It exhibits a 4% and 10% change in the real part and imaginary parts of the impedance, respectively, when the temperature is altered by 75 °C (Fig. 1, *c*). The reference sample shows a twofold weaker response of 2% and 3% change in resistive and capacitive characteristics, respectively, for the same temperature range (Fig. 1, *f*).

Conclusion

Thus, the flexible sensor for low-pressure measurements and a solid sensor for high-pressure measurements were established.

The innovative fabricated sensors demonstrated the potential capability of simultaneous measurement of pressure and temperature by electrical impedance spectroscopy, which is a universal measurement method for multifunctional sensors that can be used in the advanced flexible wearable electronics for personalized healthcare and in the development of electronic skin applications.

REFERENCES

1. **Aubekerov K., Punegova K.N., Sergeenko R., Kuznetsov A., Kondratev V.M., Kadinskaya S.A., Nalimova S.S., Moshnikov V.A.,** Synthesis and study of gas sensitive $ZnFe_2O_4$ – modified ZnO nanowires. 2227 (2022) 012014.

2. **Kondratev V.M., Morozov I.A., Vyacheslavova E.A., Kirilenko D.A., Kuznetsov A., Kadinskaya S.A., Nalimova S.S., Moshnikov V.A., Gudovskikh A.S., Bolshakov A.D.,** Silicon Nanowire-Based Room-Temperature Multi-environment Ammonia Detection, ACS Appl Nano Mater. 5 (2022) 9940–9949.

3. **Kondratev V.M., Vyacheslavova E.A., Shugabaev T., Kirilenko D.A., Kuznetsov A., Kadinskaya S.A., Shomakhov Z.V., Baranov A.I., Nalimova S.S, Moshnikov V.A., Gudovskikh A.S., Bolshakov A.D.,** Si Nanowire-Based Schottky Sensors for Selective Sensing of NH_3 and HCl via Impedance Spectroscopy, ACS Appl Nano Mater. 6 (2023) 11513–11523.

4. **Kuznetsov A., Roy P., Grudinin D.V., Kondratev V.M., Kadinskaya S.A., Vorobyev A.A., Kotlyar K.P., Ubyivovk E.V., Fedorov V.V., Cirlin G.E., Mukhin I.S., Arsenin A.V., Volkov V.S., Bolshakov A.D.,** Self-assembled photonic structure: a Ga optical antenna on GaP nanowires, Nanoscale. 15 (2023) 2332–2339.

5. **Kuznetsov A., Moiseev E., Abramov A.N., Fominykh N., Sharov V.A., Kondratev V.M., Shishkin I.I., Kotlyar K.P., Kirilenko D.A., Fedorov V.V., Kadinskaya S.A., Vorobyev A.A., Mukhin I.S., Arsenin A.V., Volkov V.S., Kravtsov V., Bolshakov A.D.,** Elastic Gallium Phosphide Nanowire Optical Waveguides – Versatile Subwavelength Platform for Integrated Photonics. 19 (2023).

6. **Levkevich E.A., Maksimov A.I., Kirillova S.A., Nalimova S.S., Kondratev V.M., Semenova A.A.,** Synthesis, Investigation and Gas Sensitivity of Zinc Stannate Layers, in: 2020 IEEE Conference of Russian Young Researchers in Electrical and Electronic Engineering (EIConRus), IEEE. (2020) 984–986.

7. **Kadinskaya S.A., Kondratev V.M., Kindyushov I.K., Kuznetsov A., Punegova K.N.,** Hydrothermal ZnO-based Nanostructures: Geometry Control and Narrow Band UV Emission, in: 2022 Conference of Russian Young Researchers in Electrical and Electronic Engineering (ElConRus), IEEE. (2022) 958–961.

8. **Kadinskaya S., Kondratev V., Kindyushov I., Koval O., Yakubovsky D., Kusnetsov A., Lihachev A., Nashchekin A., Akopyan I., Serov A., Labzovskaya M., Mikushev S., Novikov B., Shtrom I., Bolshakov A.,** Deep-Level Emission Tailoring in ZnO Nanostructures Grown via Hydrothermal Synthesis, Nanomaterials. 13 (58) (2022).

THE AUTHORS

NIKOLAEVA Aleksandra V.
nikalex2000@bk.ru
ORCID: 0009-0008-4344-4863

DVORETCKAIA Liliia N.
Liliyabutler@gmail.com
ORCID: 0000-0002-4172-940X

KONDRATEV Valeriy M.
kvm_96@mail.ru
ORCID: 0000-0002-3469-5897

LENDYASHOVA Vera V.
erilerican@gmail.com
ORCID: 0000-0001-8192-7614

KADINSKAYA Svetlana A.
skadinskaya@bk.ru
ORCID: 0000-0003-2508-2244

GRIDCHIN Vladislav O.
gridchinvo@gmail.com
ORCID: 0000-0002-6522-3673

KOLESINA Diana E.
diana666167@gmail.com
ORCID: 0009-0007-9013-7973

MONASTYRENKO Anatoliy O.
monas@spbau.ru
ORCID: 0009-0009-7051-8458

ZUBOV Fedor I.
fedyazu@mail.ru
ORCID: 0000-0002-3926-8675

BOLSHAKOV Alexey D.
acr1235@mail.ru
ORCID: 0000-0001-7223-7232

KOCHETKOV Fedor M.
azemerat@rambler.ru
ORCID: 0000-0002-2209-6483

Received 16.07.2024. Approved after reviewing 12.08.2024. Accepted 14.08.2024.

Conference materials
UDC [621.793+544.164]::681.787.22
DOI: https://doi.org/10.18721/JPM.173.113

Change in the carbon nanotube thin layer refractive index after water and ammonia molecules adsorption

A.V. Romashkin [1] ✉, R.Yu. Rozanov [2], A.V. Lashkov [1], A.S. Vishnevskiy [3], A.E. Mitrofanova [2, 4], D.D. Levin [2], V.V. Svetikov [2, 5]

[1] National Research University of Electronic Technology, Zelenograd, Moscow, Russia;
[2] JSC "Zelenograd Nanotechnology Center", Zelenograd, Moscow, Russia;
[3] MIREA – Russian Technological University, Moscow, Russia;
[4] Moscow Institute of Physics and Technology, Dolgoprudny, Moscow Region, Russia;
[5] Prokhorov General Physics Institute of the RAS, Moscow, Russia
✉ romaleval@gmail.com

Abstract. Spray-deposited carboxylated carbon nanotube (CNT) layers were characterized using AFM, Raman, and spectroscopic ellipsometry. The layers' thickness, diameters and band gap of CNTs, as well as the changes in the CNT layer refractive index at 1319 nm and 2010 nm after H_2O and NH_3 adsorption in air and H_2O in N_2 were analyzed. Refractive index changes and modeling the necessary length of the modified interferometer arm for a $\pi/2$ phase shift allow us to propose the use of such CNT layers for integrated interferometric sensors and gas recognition.

Keywords: carbon nanotube, ellipsometry, integrated optics, interferometer, sensor

Funding: This research was supported by the Ministry of Science and Higher Education of the Russian Federation in the framework of state tasks FSMR-2023-0002 (spray deposition, post-processing, AFM, Raman study, CNT layers ellipsometry data analysis) and partially FSFZ-2023-0005 (RTU MIREA: CNT layer ellipsometry in N_2 with H_2O or 2-propanol vapors).

Citation: Romashkin A.V., Rozanov R.Yu., Lashkov A.V., Vishnevskiy A.S., Mitrofanova A.E., Levin D.D., Svetikov V.V., Change in the carbon nanotube thin layer refractive index after water and ammonia molecules adsorption, St. Petersburg State Polytechnical University Journal. Physics and Mathematics. 17 (3.1) (2024) 68–74. DOI: https://doi.org/10.18721/JPM.173.113

Материалы конференции
УДК [621.793+544.164]::681.787.22
DOI: https://doi.org/10.18721/JPM.173.113

Изменение показателя преломления тонкого слоя углеродных нанотрубок при адсорбции молекул воды и аммиака

А.В. Ромашкин [1] ✉, Р.Ю. Розанов [2], А.В. Лашков [1], А.С. Вишневский [3], А.Е. Митрофанова [2, 4], Д.Д. Левин [2], В.В. Светиков [2, 5]

[1] Национальный исследовательский университет «МИЭТ», г. Зеленоград, Москва, Россия;
[2] АО «Зеленоградский нанотехнологический центр», г. Зеленоград, Москва, Россия;
[3] МИРЭА – Российский технологический университет, Москва, Россия;
[4] Московский физико-технический институт (национальный исследовательский университет), г. Долгопрудный, Россия;
[5] Институт общей физики им. А. М. Прохорова РАН, Москва, Россия
✉ romaleval@gmail.com

Аннотация. Карбоксилированные углеродные нанотрубки (УНТ), нанесенные аэрозольным распылением, исследовались с помощью АСМ, комбинационного рассеяния света и спектроскопической эллипсометрии. Проанализированы толщина слоев, диаметры и запрещенная зона УНТ, изменение показателя преломления слоев в ИК диапазоне после адсорбции H_2O и NH_3 на воздухе и H_2O в N_2. Расчеты длины модифицированного плеча интерферометра для $\pi/2$ фазового сдвига позволяют предложить такие слои УНТ для изготовления интегральных интерферометрических датчиков и распознавания газов.

Ключевые слова: углеродная нанотрубка, эллипсометрия, интегральная оптика, интерферометр, сенсор

Финансирование: Работа выполнена при поддержке Минобрнауки России в рамках государственного задания FSMR-2023-0002 (нанесение, постобработка, АСМ, КР спектроскопия, анализ эллипсометрии слоев УНТ) и частично FSFZ-2023-0005 (РТУ МИРЭА: эллипсометрия слоев УНТ в сухом N_2 с парами H_2O, 2-пропанола).

Ссылка при цитировании: Ромашкин А.В., Розанов Р.Ю., Лашков А.В., Вишневский А.С., Митрофанова А.Е., Левин Д.Д., Светиков В.В. Изменение показателя преломления тонкого слоя углеродных нанотрубок при адсорбции молекул воды и аммиака // Научно-технические ведомости СПбГПУ. Физико-математические науки. 2024. Т. 17. № 3.1. С. 68–74. DOI: https://doi.org/10.18721/JPM.173.113

Introduction

Recently, instead of using a complex system with various wavelengths to detect gases based on their absorption peaks, multisensor interferometric systems for gas recognition have been demonstrated [1]. To achieve their high sensitivity, it is important to develop thin modifying layers that significantly alter their own refractive index (n) upon analyte adsorption. Sensitivity at the ppb-level (for agrunitrile), as well as recognition of volatile organic compounds using the sensor array, have already been shown [1]. High selectivity and ppm-level sensitivity for H_2S by one sensor have also been shown [2]. The development of such layers is also relevant for interferometric biosensors [3]. Modified nanocarbon materials are promising for these tasks and forming the sensor array. Carboxylation of carbon nanotubes (CNTs) provides a significant increase in the response to ammonia [4]. Also, they are capable of significantly changing their electronic structure when the adsorbed molecules change [5]. However, identifying the magnitude and mechanisms of change in the optical parameters for functionalized CNTs, such as n at different wavelengths (λ) during the various molecules adsorption, remains a relevant task and is the goal of this work. Previously, only non-functionalized CNTs were studied using ellipsometry to obtain the $n(\lambda)$ graph, without studying the effect of adsorption on $n(\lambda)$ [6, 7].

Materials and methods

We studied three samples of carboxylated CNTs (P3-SWNT, Carbon Solutions, USA [8]) with different layer thicknesses, measured by AFM (NT-MDT, Russia). The CNT diameter was evaluated [9] from the RBM-band Raman (532 nm laser, Nano Scan Technology, Russia). CNTs were spray deposited from a dispersion [10] onto a Si substrate with native oxide, followed by the residual solvent removal [11] at 90 °C. The absorption of the CNT layer was evaluated by the suppression of Raman of Si by the CNT layer at points in 1×1 mm areas. AFM and ellipsometry were performed in the same areas. Spectroscopic ellipsometry (SENTECH Instruments, Germany) was performed at angles of incidence of 75°, 70°, 65° at λ: 371–2300 nm for the layer after exposure in a chamber with H_2O at ~12500 ppm (relative humidity (RH) change from 30% to ~75%) or NH_3 at ~2000 ppm and after 25 min of desorption under normal conditions at the same sample area, but different for each analyte. Exposure to H_2O or 2-propanol (IPA) in N_2 was realized in situ during ellipsometry, only at 70°, with a 0.3 L/min flow rate, managed by gas-flow controllers. The values of n, extinction coefficient (k), and carrier concentration (p) in the

layer were estimated from the found Drude–Lorentz model parameters obtained by fitting [7] the experimental ellipsometry data. Eight oscillators were used: two pairs each to describe the E_{11} or E_{22} to describe the CNT differences in the layer; one for M_{11} and the remaining to describe the onset (over 2.5–3 eV) of the π-plasmon peak CNT [6] and an increase in absorption with photon energy [12]. The band gap of the semiconductor CNT (E_{11}), the E_{22} and M_{11} transitions were estimated from the $k(\lambda)$ graph obtained from ellipsometry data [6, 7]. E_{11} was also evaluated based on the CNT diameter estimated from Raman [9], without considering the CNT chirality indices [13]. Numerical modeling (Beam Propagation Method, RSoft CAD) was carried out to evaluate the CNT modified arm length (L_{mod}) required to achieve a $\pi/2$ phase shift in the 900×350 nm Si_3N_4 waveguide Mach–Zehnder interferometer (MZI). The electric field distribution was calculated using the EME method (ANSYS Lumerical MODE).

Results and Discussion

Spray-deposited CNTs used have functional groups and contain residual solvent before post-treatment (Fig. 1, *a*). Therefore even their resulting concentration in the layer (Fig. 1, *b*, *c*) is ca. 3 times lower than in other work [6], which determines the higher slope of the thickness on absorbance dependence (Fig. 1, *d*). The layer thicknesses were 3 nm, 17 nm, 35.5 nm (Fig. 1, *b*).

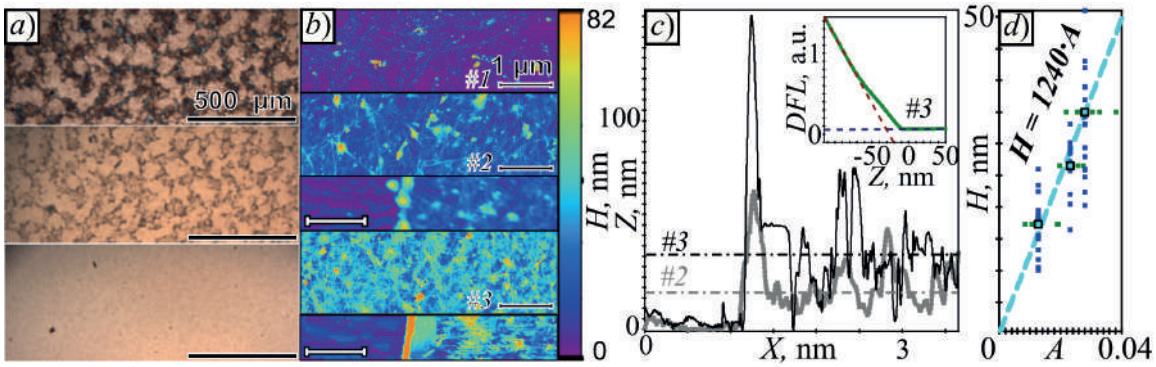

Fig. 1. Optical images of iterative residual solvent removal from the CNT layer (*a*); AFM (*b*) with cross sections, inset: force – distance curve (*c*); graph of thickness (H) versus absorbance (A) at $\lambda \approx 550$ nm (*d*)

The results of applying the Drude–Lorentz model to describe the experimental data of Ψ and Δ are shown in Fig. 2. Estimates of the n are slightly different (Fig. 2, *a*) due to the layer thickness non-uniformity (~10 %) while the thickness is the same in the model for each analyte. E_{11}, E_{22}, M_{11} evaluated from $k(\lambda)$ were 0.70, 1.31, 2.05 eV respectively, which are higher than in another work [6], due to the smaller CNT diameter. A larger M_{11} peak relative to E_{11} distinguishes functionalized CNTs [6, 12]. When exposed to H_2O in air, n increased (Fig. 2, *a*, *c*, *f*) from 1.653 to 1.661 at $\lambda = 1319$ nm (Nd:YAG laser) and from 1.890 to 1.907 at $\lambda = 2010$ nm (Tm:YAG laser). The latter λ corresponds to the photon energy, similar to E_{11} and to the estimate of the CNT band gap (E_g). Approximately 70% of the RBM Raman region (140–195 cm^{-1}) corresponds to CNT diameters of 1.6, 1.44, 1.3 nm [9] with Eg energies of about 0.67, 0.74 (~40 %), 0.81 eV [13] respectively (Fig. 2, *a* inset). The charge carrier concentration (p) decreased slightly from $5.75 \cdot 10^{19}$ cm^{-3} to $5.72 \cdot 10^{19}$ cm^{-3} when exposed to H_2O in air, which corresponds to the low resistive response of a high-density CNT network [10]. When exposed to NH_3, n dropped from 1.586 to 1.584 at $\lambda = 1319$ nm, but increased from 1.815 to 1.847 at $\lambda = 2010$ nm (Fig. 2, *a*, *d*, *g*); and p was dropped from $7.31 \cdot 10^{19}$ cm^{-3} to $7.28 \cdot 10^{19}$ cm^{-3}, which also corresponded to the low resistive response [10]. Considering the differences in the concentrations of H_2O and NH_3, the measurement results indicate a change in the electronic structure of CNTs during adsorption, and are not associated with filling the pores of the layer. This is further supported by the nature of the n response changes when the carrier gas is altered. H_2O adsorption led to an increase in the n under air conditions, but a decrease in the n when the carrier gas was dry N_2 (Fig. 2), the same as for IPA in N_2. The p values increased with the adsorption of H_2O in N_2, and for RH of 0%, 32%, 64%, 85% they were $7.55 \cdot 10^{19}$, $7.69 \cdot 10^{19}$, $7.89 \cdot 10^{19}$, $8.06 \cdot 10^{19}$ cm^{-3}. This effect is presumably

related to a charge carriers type change: from holes in air conditions to electrons in dry N_2 [6], and H_2O and NH_3 are donors for CNTs (ca. 0.03 *e*/molecule) opposed to O_2 and NO_2, both of which are charge acceptors (ca. −0.09 *e*/molecule) [14]. Thus, in air, H_2O and NH_3 reduce the concentration of CNT carriers and increase resistivity [10, 12], but in the absence of oxygen, the opposite occurs. The values of the *n*, determined after cycles of exposure to H_2O followed by N_2 purging before applying the next concentration of vapor, almost return to the initial value at 0% RH: 1.464. The values of *n* at λ = 1319 nm during exposure (subsequent purging) were: 1.453 (1.459), 1.446 (1.457), 1.431 (1.454). The incomplete return is due to incomplete desorption during 20-minute low-flow N_2 purge, which is typical for CNTs [10].

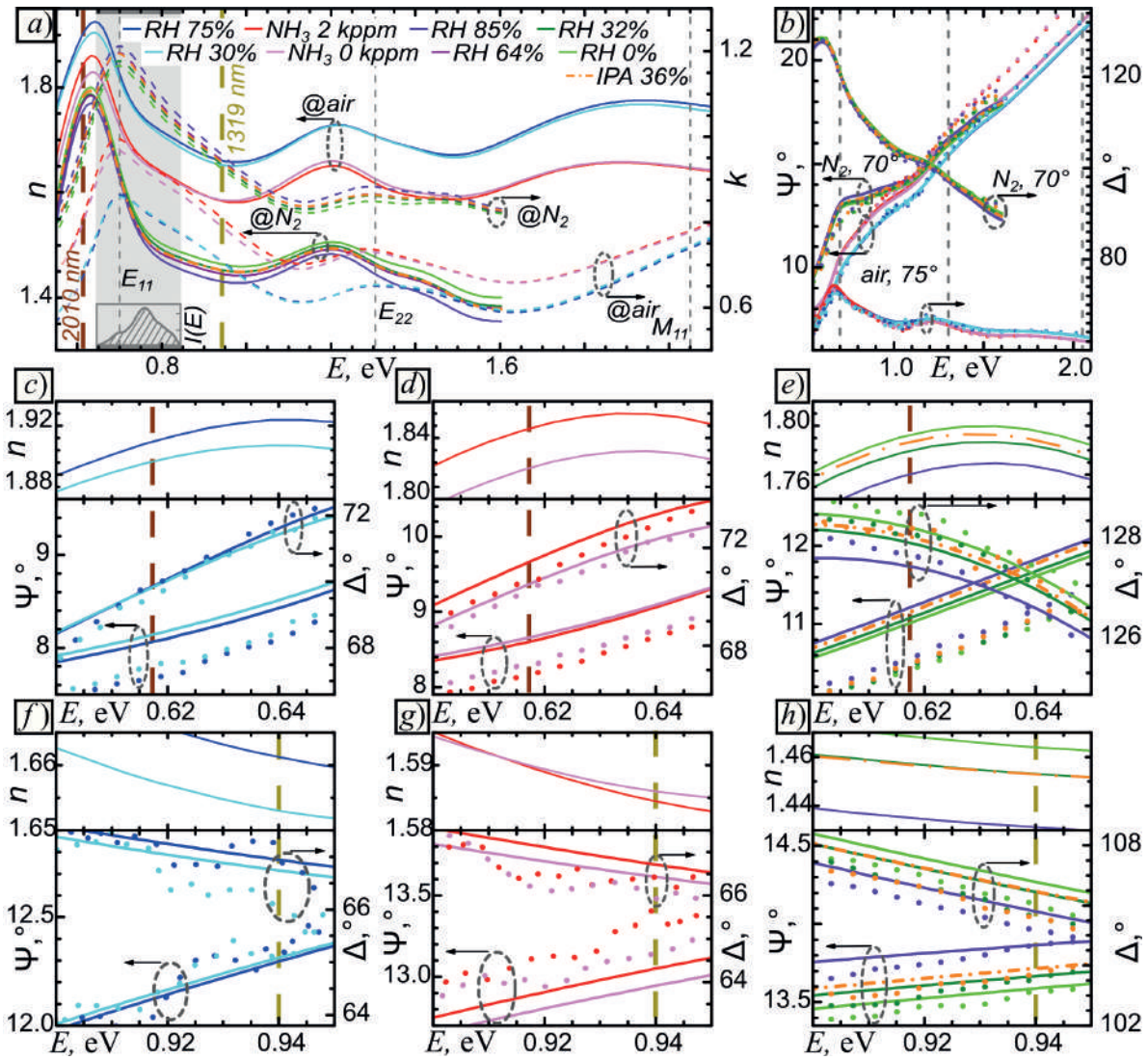

Fig. 2. Application of the Drude−Lorentz model to obtain a graph of *n* and *k* on photon energy: $n(E)$, $k(E)$; inset − fraction of CNT (*I*) with different E_g (*a*); to describe the experimental data of Ψ and Δ (*b*), and enlarged sections in the regions of λ = 2010 nm and λ = 1319 nm for the adsorption of H_2O (*c*, *f*) and NH_3 in air (*d*, *g*), H_2O and IPA in N_2 (*e*, *h*)

Numerical modeling showed that the single-mode regime is realized in the MZI (Fig. 3, *a*, *b*). Stronger differences in the change in *n* during NH_3 adsorption at λ = 2010 nm, compared to λ = 1319 nm (Fig. 2), determine the shorter required L_{mod} of the MZI arm: 700 μm at λ = 2010 nm instead of 7700 μm at λ = 1319 nm. Similar behavior exists for H_2O in air (Fig. 3, *c*). These obtained values are in agreement with other studies [15]. However, for H_2O vapor in N_2, more significant changes in the *n* occur in the region of 0.8−1.2 eV compared to 0.62−0.7 eV.

This enables the implementation of a π/2 phase shift using a shorter Lmod of the MZI arm: 700 μm for λ = 1319 nm instead of 780 μm at λ = 2010 nm. This is apparently due to the greater changes in the electronic structure of CNTs not near the band gap and at its edges (E_{11} region in Fig. 2 and inset), but in more distant energy regions of the CNT density of states spectrum, up to E_{22}. In turn, this can be explained by the absence of oxygen on the CNT during measurements in N_2. The absence of oxygen can alter the band structure through molecule adsorption not only the vicinity of the band gap edges but also in the region of Van Hove singularities of CNTs [16]. It apparently leads to significant changes in the $n(\lambda)$ not only in the E_{11} region but also at photon energies of 0.8–1.2 eV (Fig. 2, *a*, for NH_3 in air and H_2O in N_2), exceeding the CNT E_g energy. This corresponds to changes in the density of states no longer so much inside or near the edges of the CNT band gap but far from them, as is the case, for example, with the adsorption of NH_3 and H_2S [14, 17]. A similar behavior apparently occurs during the adsorption of H_2O in N_2. Such opposing or different changes in *n* after the adsorption of H_2O or NH_3 allow the recognition of analytes in the pair of NH_3 and H_2O in air or H_2O in air and H_2O in N_2 using the MZI configuration with two outputs by analyzing the opposing intensity changes. The intensity on each in the absence of analyte adsorption is equal to 0.5 of the sum of inputs in the signal loss absence, which sets a convenient zero point (Fig. 3, *d*, *e*).

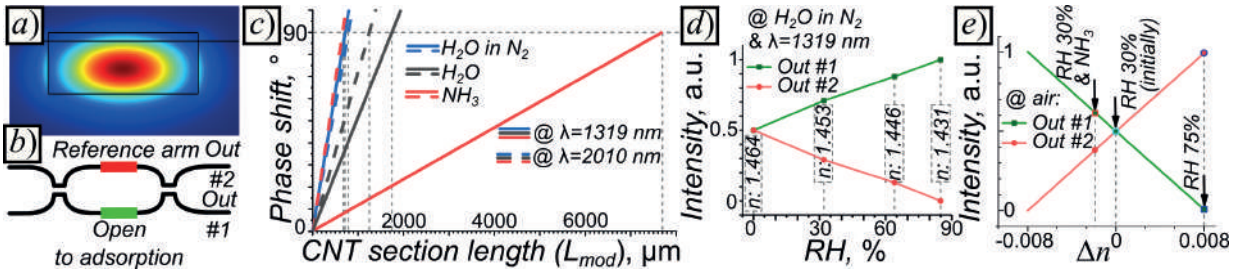

Fig. 3. Waveguide electric field distribution (*a*); MZI scheme (*b*); modified section length (L_{mod}) for π/2 phase shift (*c*); output intensities after exposure to H_2O in N_2 ($_d$), H_2O or NH_3 in air (*e*) for selected L_{mod}

The changes in the *n* were grown when the photon energy became close to E_g (Fig. 2, *c*, *f*), thus the required L_{mod} was decreased (Fig. 3, *c*). However, due to the *n* of the CNTs becomes close to Si_3N_4, the losses in the waveguide with CNT increase (4% at λ = 1319 nm, 12% at λ = 2010 nm). The differences in the response behavior of the interferometric sensor to implement the recognition of NH_3 against the H_2O background should be noticeable already in the λ range of 1.3–1.65 μm. Based on the typical noise level in such structures of about 0.2° [1] and an estimate of the sensitivity derived from modeling and ellipsometry data of 0.045°/ppm, assuming a linear dependence of the response on concentration, we can theoretically estimate the detection limit of the proposed MZI sensor to be 4.5 ppm. This is higher than for the CNT resistive sensors [10]. However, as the CNT network density decreases, the changes in the CNT layer properties during adsorption can increase. If in resistive sensors this leads to an increase in noise that limits detection [10], in the proposed MZI sensor, high resistivity is not a limitation.

Conclusions

Spray-deposited CNT layers with subsequent solvent residual removal can be used to modify the surface of waveguides in integrated interferometric sensors. CNT layers provide high sensitivity and selectivity with maintaining an acceptable length of the interferometer arms and refractive index changes following analyte adsorption. Recognition can be realized for the NH_3 and H_2O pair in air or for the H_2O in air and H_2O in N_2 pair in the MZI configuration with two outputs, due to the opposite changes in the *n* after the adsorption of molecules in these pairs. The ability of the CNT refractive index to be changed at photon energy not near CNT band gap energy, but corresponding to the change in density of states in the CNT band structure far from the edges of the band gap with analyte adsorption opens up new additional mechanisms for increasing the sensor response and its selectivity. This can be used for the development of optical, rather than resistive,

gas sensors based on functionalized carbon nanomaterials. The low electrical conductivity of the waveguide modifying layer is not a limiting factor for the proposed MZI optical sensor. This expands the range of materials that can be used in such integrated optical sensors and potentially improves the detection limit.

REFERENCES

1. **Laplatine L., Fournier M., Gaignebet N., Hou Y., Mathey R., Herrier C., Liu J., Descloux D., Gautheron B., Livache T.,** Silicon photonic olfactory sensor based on an array of 64 biofunctionalized Mach-Zehnder interferometers, Opt. Express. 30 (19) (2022) 33955–33968.

2. **Huang G., Li Y., Chen C., Yue Z., Zhai W., Li M., Yang B.,** Hydrogen sulfide gas sensor based on titanium dioxide/amino-functionalized graphene quantum dots coated photonic crystal fiber, Journal of Physics D: Applied Physics. 53 (32) (2020) 325102.

3. **Nekrasov N., Yakunina N., Pushkarev A.V., Orlov A.V., Gadjanski I., Pesquera A., Centeno A., Zurutuza A., Nikitin P. I., Bobrinetskiy I.,** Spectral-phase interferometry detection of ochratoxin a via aptamer-functionalized graphene coated glass. Nanomaterials. 11 (1) (2021) 226.

4. **Hannon A., Lu Y., Hong H., Li J., Meyyappan M.,** Functionalized-carbon nanotube sensor for room temperature ammonia detection. Sensor Lett. 12 (10) (2014) 1469–1476.

5. **Avouris P., Martel R., Derycke V., Appenzeller J.,** Carbon nanotube transistors and logic circuits, Physica B: Condensed Matter. 323 (1–4) (2002) 6–14.

6. **Ermolaev G.A., Tsapenko A.P., Volkov V.S., Anisimov A.S., Gladush Y.G., Nasibulin A.G.,** Express determination of thickness and dielectric function of single-walled carbon nanotube films, Appl. Phys. Lett. 116 (23) (2020) 231103.

7. **Barnes T.M., Van de Lagemaat J., Levi D., Rumbles G., Coutts T.J., Weeks C.L., Britz D.A., Levitsky I., Peltola J., Glatkowski P.,** Optical characterization of highly conductive single-wall carbon-nanotube transparent electrodes, Phys. Rev. B. 75 (23) (2007) 235410.

8. **Itkis M.E., Perea D.E., Niyogi S., Rickard S.M., Hamon M.A., Hu H., Zhao B., Haddon R.C.,** Purity evaluation of as-prepared single-walled carbon nanotube soot by use of solution-phase near-IR spectroscopy, Nano Lett. 3 (3) (2003) 309–314.

9. **Zhang D., Yang J., Yang F., Li R., Li M., Ji D., Li Y.,** (n, m) Assignments and quantification for single-walled carbon nanotubes on SiO_2/Si substrates by resonant Raman spectroscopy. Nanoscale. 7 (24) (2015) 10719–10727.

10. **Romashkin A.V., Lashkov A.V., Sysoev V.V., Struchkov N.S., Alexandrov E.V., Levin D.D.,** Energy-Efficient Chemiresistive Sensor Array Based on SWCNT Networks, WO_3 Nanochannels and SWCNT-Pt Heterojunctions for NH_3 Detection against the Background Humidity, Chemosensors. 10 (11) (2022) 476.

11. **Polikarpov Y.A., Romashkin A.V., Struchkov N.S., Levin D.D.,** High uniform carbon nanotube thin films spray deposition on substrates with patterned structures having height difference, In: Proceedings of the IEEE Conference of Russian Young Researchers in Electrical and Electronic Engineering, St. Petersburg, Russia, 28–31 January 2019; IEEE. (2019) 1980.

12. **Anoshkin I.V., Nasibulin A.G., Mudimela P.R., He M., Ermolov V., Kauppinen E.I.,** Single-walled carbon nanotube networks for ethanol vapor sensing applications, Nano Research. 6 (2013) 77–86.

13. **Gelao G., Marani R., Perri A.G.,** A formula to determine energy band gap in semiconducting carbon nanotubes, ECS J. Solid State Sci. Technol. 8 (2) (2019) M19.

14. **Zhao J., Buldum A., Han J., Lu J.P.,** Gas molecule adsorption in carbon nanotubes and nanotube bundles, Nanotechnology. 13 (2) (2002) 195–200.

15. **Tseng S. Y., Fuentes-Hernandez C., Owens D., Kippelen B.,** Variable splitting ratio 2×2 MMI couplers using multimode waveguide holograms, Opt. Express. 15 (14) (2007) 9015–9021.

16. **Kroes J. M., Pietrucci F., Curioni A., Jaafar R., Gruning O., Andreoni W.,** Atomic oxygen chemisorption on carbon nanotubes revisited with theory and experiment, The Journal of Physical Chemistry C. 117 (4) (2013) 1948–1954.

17. **Tang X., Zhao Y., Liang X., Fang Z., Li X., He Y., Li H.,** Density Functional Theory Study of Adsorption and Selection Behavior of Harmful Gas Molecules on the Surface of SWNTs: Implications for Gas Sensing, ACS Appl. Nano Mater. 6 (21) (2023) 19786–19796.

THE AUTHORS

ROMASHKIN Alexey V.
romaleval@gmail.com
ORCID: 0000-0002-0101-6122

ROZANOV Roman Yu.
roman-roz@yandex.ru
ORCID: 0000-0001-5063-1669

LASHKOV Andrey V.
lav.lab-sm.sstu@rambler.ru
ORCID: 0000-0001-6794-8523

VISHNEVSKIY Alexey S.
alexeysw@mail.ru
ORCID: 0000-0002-4024-5411

MITROFANOVA Anastasia E.
mitrofanova.ae@phystech.edu
ORCID: 0009-0004-5306-278X

LEVIN Denis D.
skaldd@yandex.ru
ORCID: 0000-0002-8414-6191

SVETIKOV Vladimir V.
svetikov@nsc.gpi.ru

Received 16.07.2024. Approved after reviewing 19.07.2024. Accepted 20.07.2024.

Conference materials
UDC 538.9
DOI: https://doi.org/10.18721/JPM.173.114

Combined approach of patterning on SiO_2/Si substrate using ion beam and chemical wet etching

M.M. Eremenko [1] ✉, N.A. Shandyba [1], N.E. Chernenko [1],
J.Y. Jityaeva [1], S.V. Balakirev [1], M.S. Solodovnik [1]

[1] Southern Federal University, Taganrog, Russia;
✉ eryomenko@sfedu.ru

Abstract. In this work, we studied the influence of combined processing of SiO_2/Si(001) substrates using focused ion beams (FIB) and wet chemical etching on the possibility of forming pyramidal cavities and their geometric parameters. It has been shown that etching FIB-modified samples only in KOH leads to the formation of pyramidal cavities covered with a shell, possibly made of porous silicon layer. We have shown that the use of an isotropic etchant before anisotropic etching allows to remove a porous silicon layer. An increase in the implantation dose led not only to an increase in the depth of the cavities, but also to an increase in the undercut of the oxide layer.

Keywords: wet chemical etching, silicon, monolithic integration, focused ion beam, nanopatterning

Funding: This work was funded by the Ministry of Science and Higher Education of the Russian Federation; project No. FENW-2022-0001 and No FENW-2022-0034.

Citation: Eremenko M.M., Shandyba N.A., Chernenko N.E., Jityaeva J.Y., Balakirev S.V., Solodovnik M.S., Combined approach of patterning on SiO_2/Si substrate using ion beam and chemical wet etching, St. Petersburg State Polytechnical University Journal. Physics and Mathematics. 17 (3.1) (2024) 75–78. DOI: https://doi.org/10.18721/JPM.173.114

Материалы конференции
УДК 538.9
DOI: https://doi.org/10.18721/JPM.173.114

Комбинированный подход к созданию шаблона на подложке SiO_2/Si с использованием ионных пучков и жидкостного травления

М.М. Ерёменко [1] ✉, Н.А. Шандыба [1], Н.Е. Черненко [1],
Ю.Ю. Житяева [1], С.В. Балакирев [1], М.С. Солодовник [1]

[1] Южный федеральный университет, г. Таганрог, Россия;
✉ eryomenko@sfedu.ru

Аннотация. В данной работе представлены результаты исследований влияния обработки подложек SiO_2/Si(001) с помощью комбинации методов фокусированных ионных пучков (ФИП) и жидкостного травления на возможность формирования в подложке пирамидальных углублений и их геометрические характеристики. Показано, что травление образцов, модифицированных ФИП, только в КОН приводит к образованию пирамидальных углублений, прикрытых сверху слоем, предположительно, пористого кремния, формирующего замкнутые полости. Было продемонстрировано, что использование изотропного травителя для кремния перед анизотропным травлением позволяет избежать формирования слоя с пористым кремнием.

Ключевые слова: жидкостное травление, кремний, монолитная интеграция, фокусированные ионные пучки, нанопрофилирование

Финансирование: Работа выполнена при финансовой поддержке Министерства науки и высшего образования Российской Федерации; государственное задание в области научной деятельности № FENW-2022-0001 и № FENW-2022-0034.

Ссылка при цитировании: Ерёменко М.М., Шандыба Н.А., Черненко Н.Е., Житяева Ю.Ю., Балакирев С.В., Солодовник М.С. Комбинированный подход к созданию шаблона на подложке SiO_2/Si с использованием ионных пучков и жидкостного травления // Научно-технические ведомости СПбГПУ. Физико-математические науки. 2024. Т. 17. № 3.1. С. 75–78. DOI: https://doi.org/10.18721/JPM.173.114

Introduction

Patterning semiconductor Si substrates using various lithography methods is currently one of the promising approaches in monolithic integration of GaAs on Si in particular using selective area growth techniques [1–3]. However, submicron lithographic surface patterning processes are labor-intensive and very expensive. On the other hand, the method of surface modification with focused ion beams (FIB) makes it possible to simplify the procedure for forming nano- and submicron-sized patterns on the surface, and also eliminate the step of using photoresist and physical templates for patterning. Early studies of clear Si surface modification using the FIB method with subsequent GaAs growth showed (despite high spatial selectivity) polycrystalline growth within modified area [4–6]. Therefore, it is necessary to improve the approach to the creation of new templates for monolithic integration of GaAs on Si substrates. A combination of focused ion beam and wet chemical etching techniques may be the answer to these problems. Treatment with focused ion beams is expected to allow localization of the wet etching process and subsequent epitaxial growth. Treatment of the Si substrate in the anisotropic etchant (KOH) will in turn lead to the creation of nano-sized pyramidal cavities. The shape and form of the pyramidal cavities will make it possible to localize defects on their faces that arise during the epitaxial growth of GaAs on Si [7–9].

Thus, in this work, we propose to use a combination of FIB surface modification and wet chemical etching for nanopatterning of SiO_2/Si(001) substrate that can act as a template for subsequent direct growth of GaAs by selective area epitaxy.

Materials and Methods

At the first stage, Si(001) substrates with a 200 nm thick SiO_2 layer were etched by the Ga^+ FIB. SiO_2 was used as a protective layer of the Si surface from wet chemical etching processes. FIB-modification was carried out by processing of substrate square areas with sizes varying from 0.25×0.25 to 1×1 μm. The accelerating voltage was 30 kV, and the ion beam passes varied in the range from 1 to 1000. Next, the part of samples was placed in isotropic silicon etchant HNO_3:H_2O:NH_4F for 30 seconds. And then all samples were etched in 30% KOH at 80 °C for 1 minute to form pyramidal cavities. The obtained samples were examined by scanning electron microscopy (SEM).

Results and Discussion

The results of sample treatment in 30% KOH (only) after FIB processing are shown on Figure 1. It was shown that during etching a porous film formed on the surface of the modified area (Fig. 1, *a*, *b*). Moreover, etching of the sample led to the formation of a pyramidal cavity under the film. We suppose that this film is a near-surface layer of silicon with gallium ions implanted during FIB treatment which is etched much more slowly than crystalline silicon. However, under certain FIB-modification conditions, pyramidal cavities were formed (Fig. 1, *c*). Apparently, the oxide was greatly thinned during FIB treatment, but was not completely removed

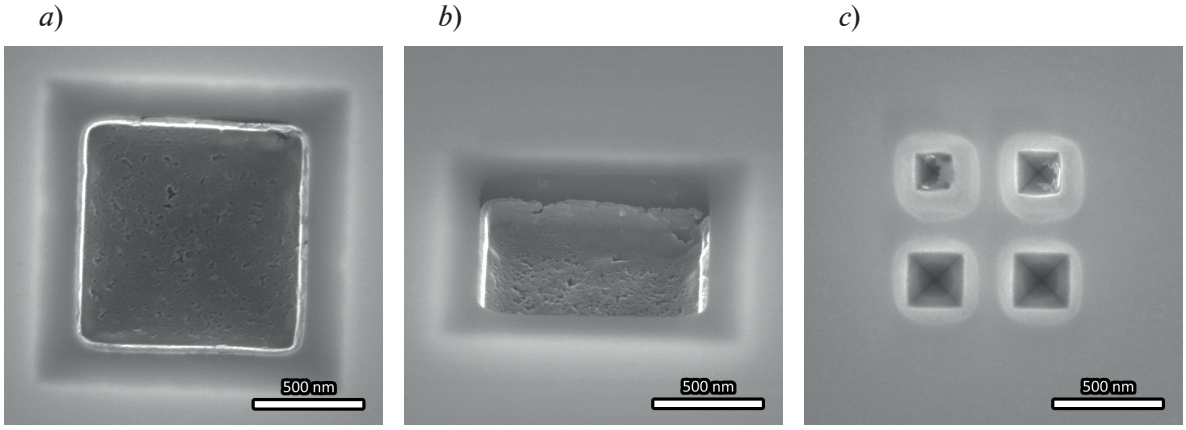

Fig. 1. SEM-images of FIB-modified SiO2/Si areas after etching in 30% KOH. FIB beam passes: (*a*, *b*) 500, (*c*) 250,. Initial size of FIB-modification areas: (*a*, *b*) 1×1 μm, (*c*) 0.25×0.25 μm

and was removed after etching in KOH. This resulted in the exposed area of the silicon substrate being subjected to normal anisotropic etching, since the silicon did not contain implanted Ga^+. Although pyramidal cavities were obtained, for a reproducible result and subsequent epitaxial growth it is still necessary to remove a thin film of silicon with Ga^+.

The nature and type of etching changes when an isotropic silicon etchant is used at the first stage of chemical treatment of the sample (Fig. 2, *a*, *b*). According to the results obtained, it is clear that pyramidal cavities without any film were formed in the FIB modified areas. Apparently, an isotropic silicon etchant also prevents the formation of porous silicon layers.

The geometric characteristics of the resulting cavities also depend on the FIB processing modes. Increasing the number of ion beam passes during FIB treatment increases the depth of the modified area, which in turn increases the amount of undercut after etching in KOH (Fig. 2, *c*).

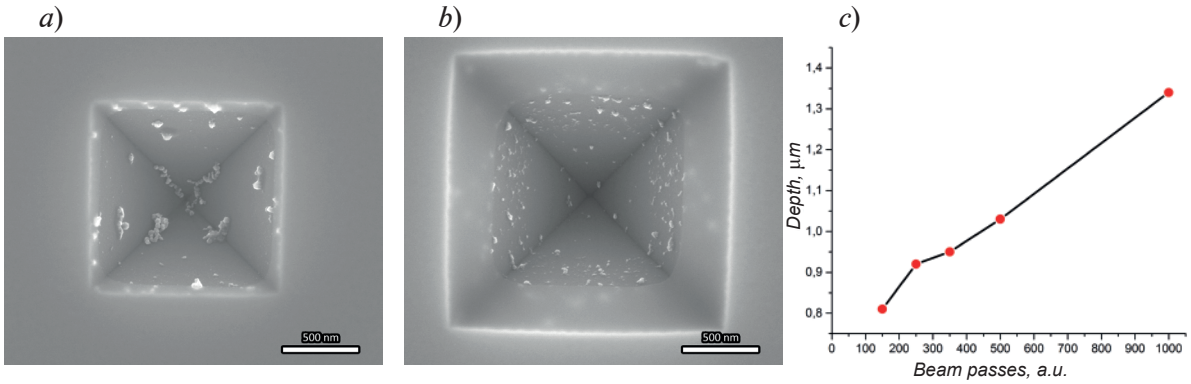

Fig. 2. SEM-images of FIB-modified SiO_2/Si areas after etching in isotropic silicon etchant and 30% KOH. FIB beam passes: (*a*) 250, (*b*) 1000. (*c*) Dependence of the influence of the number of beam passes on the depth of cavities obtained after wet chemical etching of structures 1×1 μm in size

Thus, by changing the FIB processing mode, we can adjust the size of the cavities in the required range. As can be seen from the obtained results, the SiO_2 film remains hanging over the edges of the etched area in each of the obtained results with pyramidal cavities (Fig. 2, a, b). In the future, we plan to determine the optimal parameters of FIB and wet chemical etching to ensure the absence of undercut. On the other hand, this allows us, without changing the topology of FIB and wet chemical etching processing, to vary both the size of the resulting cavities and the depth of the undercut.

It is worth noting that the use of FIB modes with a number of passes below 150 resulted in the absence of Si substrate wet chemical etching due to the remaining unetched oxide layer.

Conclusion

In conclusion, we have proposed a new approach to forming a submicron template on SiO_2/Si(001) substrates for monolithic integration of GaAs on Si. It is expected that this approach will increase the selectivity of growth processes and will also make it possible to obtain nanostructures with high crystalline perfection due to the possibility of localizing defects on the faces of etched cavities.

REFERENCES

1. **Tiwari P., Trivino N.V., Schmid H., Moselund K.E.,** Review: III–V infrared emitters on Si: fabrication concepts, device architectures and down-scaling with a focus on template-assisted selective epitaxy, Semiconductor Science and Technology. 38 (2023) 053001.

2. **Han Y., Lau K.M.,** III–V lasers selectively grown on (001) silicon, Journal of Applied Physics. 128 (2020) 200901.

3. **Zhou Z., Yin B., Michel J.,** On-chip light sources for silicon photonics, Light: Science & Applications. 4 (2015) e358.

4. **Eremenko M.M., Shandyba N.A., Chernenko N.E., Balakirev S.V., Solodovnik M.S., Ageev O.A.,** Investigation of GaAs MBE growth on FIB-modified Si(100), Proceedings of SPIE. 12157 (2022).

5. **Eremenko M.M., Shandyba N.A., Chernenko N.E., Solodovnik M.S., Balakirev S.V., Ageev O.A.,** Study of the initial stage of GaAs growth on FIB-modified silicon substrates, Journal of Physics: Conference Series. 2086 (2021) 012007.

6. **Balakirev S.V., Eremenko M.M., Lakhina E.A., Kirichenko D.V., Shandyba N.A., Chernenko N.E., Ageev O.A., Solodovnik M.S.,** Study of GaAs epitaxial growth on Si substrates modified by focused ion beams, Physics of the Solid State. 64 (6) (2022) 595–600.

7. **Viazmitinov D. V., Berdnikov Y., Kadkhodazadeh S., Dragunova A., Sibirev N., Kryzhanovskaya N., Radko I., Huck A., Yvind K., Semenova E.,** Monolithic integration of InP on Si by molten alloy driven selective area epitaxial growth, Nanoscale. 12 (2020) 23780–23788.

8. **Shi B., Han Y., Li Q., Lau K. M.,** 1.55 μm lasers epitaxially grown on silicon, IEEE Journal of Selected Topics in Quantum Electronics. 25 (6) (2019) 1–11.

9. **Park J.-S., Tang. M., Chen S., Liu H.,** Heteroepitaxial Growth of III-V Semiconductors on Silicon, Crystals. 10 (2020) 1163.

THE AUTHORS

EREMENKO Mikhail M.
eryomenko@sfedu.ru
ORCID: 0000-0002-7987-0695

CHERNENKO Natalia E.
nchernenko@sfedu.ru
ORCID: 0000-0001-8468-7425

JITYAEVA Julia Y.
zhityaeva@sfedu.ru
ORCID: 0000-0002-5961-407X

BALAKIREV Sergey V.
sbalakirev@sfedu.ru
ORCID: 0000-0003-2566-7840

SHANDYBA Nikita A.
shandyba@sfedu.ru
ORCID: 0000-0001-8488-9932

SOLODOVNIK Maxim S.
solodovnikms@sfedu.ru
ORCID: 0000-0002-0557-5909

Received 17.07.2024. Approved after reviewing 22.07.2024. Accepted 27.07.2024.

Conference materials
UDC 538.9
DOI: https://doi.org/10.18721/JPM.173.115

Study of the photoluminescence properties of subcritical InAs/GaAs quantum dots formed onto structured substrates

D.V. Kirichenko [1] ✉, I.S. Makhov [2], S.V. Balakirev [1],
N.V. Kryzhanovskaya [2], M.S. Solodovnik [1]

[1] Southern Federal University, Taganrog, Russia;
[2] National Research University Higher School of Economics, St. Petersburg branch, St. Petersburg, Russia
✉ dankir@sfedu.ru

Abstract. In this work we study the optical properties of InAs quantum dots grown on the GaAs(001) nanostructured surfaces at sub-critical thickness of deposition. For substrate nanostructuring we used technique based on two-stage thermal desorption of native GaAs oxide under molecular arsenic flux. The results of experimental studies showed the possibility of quantum dots formation on structured surfaces at equivalent deposition thicknesses in the range of 0.5–1.5 ML. In this case, quantum dots are formed predominantly in nanoholes on the surface and are high inhomogeneous in size. At the same time measurements by photoluminescence spectroscopy showed broad (900–1100 nm) emission spectrum for quantum dot only for sample with 1.5 ML of InAs. We hypothesize that at smaller thicknesses, the formed quantum dots become smaller than the minimum acceptable sizes due to segregation effects during overgrowth. The use of a structured surface also makes it possible to suppress the wetting layer formation – in the photoluminescence spectra there are only lines of platelets, apparently formed on morphological inhomogeneities outside the holes.

Keywords: native oxide, quantum dots, A3B5, molecular beam epitaxy, nanopatterning

Funding: This work was supported by the Russian Science Foundation Grant No. 22-79-10251 at the Southern Federal University.

Citation: Kirichenko D.V., Makhov I.S., Balakirev S.V., Kryzhanovskaya N.V., Solodovnik M.S., Study of the photoluminescence properties of subcritical InAs/GaAs quantum dots formed onto structured substrates, St. Petersburg State Polytechnical University Journal. Physics and Mathematics. 17 (3.1) (2024) 79–83. DOI: https://doi.org/10.18721/JPM.173.115

Материалы конференции
УДК 538.9
DOI: https://doi.org/10.18721/JPM.173.115

Исследование фотолюминесцентных свойств докритических квантовых точек InAs/GaAs, сформированных на структурированных подложках

Д.В. Кириченко [1] ✉, И.С. Махов [2], С.В. Балакирев [1],
Н.В. Крыжановская [2], М.С. Солодовник [1]

[1] Южный федеральный университет, г. Таганрог, Россия;
[2] Национальный исследовательский университет «Высшая школа экономики», Санкт-Петербургский филиал, Санкт-Петербург, Россия
✉ dankir@sfedu.ru

Аннотация. В данной работе проведены исследования оптических свойств квантовых точек InAs, полученных путем осаждения докритических толщин на наноструктурированную поверхность GaAs(001). Для наноструктурирования подложки была использована методика, основанная на двухстадийной термодесорбции собственного оксида GaAs в потоке молекулярного мышьяка. Результаты экспериментальных исследований показали возможность формирования квантовых точек на структурированных поверхностях при эквивалентных толщинах осаждения в диапазоне 0,5–1,5 МС. В этом случае квантовые точки формируются преимущественно в сформированных на поверхности углублениях и имеют высокую неоднородность размеров. Измерения методом фотолюминесцентной спектроскопии показали наличие квантовых точек, излучающих в широком диапазоне длин волн (900–1100 нм), только для образца с эквивалентной толщиной осаждения 1,5 МС InAs. Мы предполагаем, что при меньших толщинах образующиеся квантовые точки становятся меньше минимально допустимых размеров, в т.ч. из-за эффектов сегрегации при заращивании. Результаты исследования также показали, что использование структурированной поверхности позволяет подавить образование смачивающего слоя – в спектрах фотолюминесценции присутствуют только пик, отвечающий излучению локальных двумерных структур, по-видимому, образовавшихся на морфологических неоднородностях вне отверстий.

Ключевые слова: собственный оксид, квантовые точки, A3B5, молекулярно-лучевая эпитаксия, наноструктурирование

Финансирование: Работа выполнена при поддержке гранта Российского научного фонда № 22-79-10251 в Южном Федеральном Университете.

Ссылка при цитировании: Кириченко Д.В., Махов И.С., Балакирев С.В., Крыжановская Н.В., Солодовник М.С. Исследование фотолюминесцентных свойств докритических квантовых точек InAs/GaAs, сформированных на структурированных подложках // Научно-технические ведомости СПбГПУ. Физико-математические науки. 2024. Т. 17. № 3.1. С. 79–83. DOI: https://doi.org/10.18721/JPM.173.115

Introduction

The production of low-density quantum dots (QD) is becoming increasingly popular since they underlie the sources of single and entangled photons that act as the elemental basis for quantum communications and computing [1, 2]. One of the directions for obtaining low density quantum dots is the use of preliminary structuring of the growth surface with subsequent deposition of the quantum dot material [3–5]. In this case, the nanoholes formed on the surface subsequently act as nucleation centers for self-organizing nanostructures [6–8]. Today, surface structuring methods have a number of limitations that affect the optical qualities of subsequently formed quantum structures, mainly due to contamination of the growth surface. Therefore, the search for alternative methods of surface nanostructuring and growth technique for subsequent localized formation of quantum dots remains relevant. One of the candidate for this role can be controlled decomposition of the substrate surface at the stage of thermal removal of GaAs native oxide [3].

In this work we experimentally demonstrate the possibility of obtaining relatively low-density self-organizing InAs/GaAs quantum dots obtained on the GaAs(001) nanostructured surfaces at sub-critical thickness of deposition with an emission range of up to 1100 nm.

Materials and Methods

For experimental studies, we used GaAs(001) substrates with a pre-grown GaAs/AlGaAs structure, on the surface of which native oxide film was then formed in air. To form nano-sized holes, we used the original technique based on two-stage thermal desorption of native GaAs oxide under molecular arsenic flux. As a result, an array of inhomogeneous symmetrical holes was formed on the surface. The average values of the diameter and depth of which were 60 and 4 nm, respectively. Control of oxide removal was carried out in-situ using an integrated

RHEED system. At the next stage, an InAs layer with an equivalent thickness in the range of 0.5–1.5 ML was deposited. To study the optical properties, a GaAs/AlGaAs heterostructure was grown on top of the structures prepared in this way. In addition, we repeated the same heterostructure, where the active region was a 1.5 ML InAs wetting layer on an atomically flat surface without nanostructuring which we used as a reference sample. Uncapped structures were analyzed using scanning electron (SEM) and atomic force (AFM) microscopy. The optical properties were analyzed using photoluminescence spectroscopy (PL).

Results and Discussion

SEM-analysis (Fig. 1, *a*, *b*, *c*) of the surface of the uncapped samples showed that for all samples deposited material accumulates in the nano-sized holes formed at the nanopatterning stage, thereby forming an array of inhomogeneous QDs. In this case, decreasing the amount of InAs from 1.5 ML to 1.0 ML leads to a pronounced decrease in their size. And it was found that the structures do not assemble into obvious 3D objects after deposition of 0.5 ML. However, according to AFM data (Fig. 1, *d*), a decrease in the hole depth was observed, which indicates their filling with deposited material and the localization of nanostructures within them. However, relevant assessment of the size of such structures is difficult using AFM or SEM.

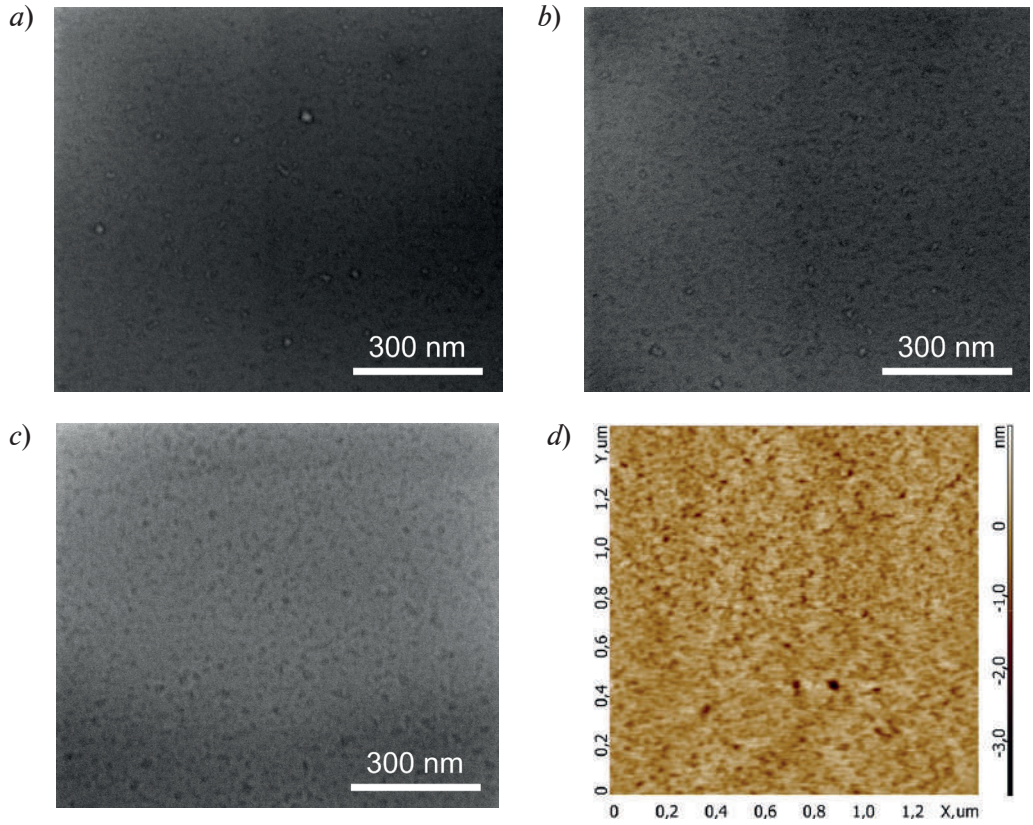

Fig. 1. SEM images of the nanostructured GaAs surface after deposition of (*a*) 1.5 ML, (*b*) 1.0 ML and (*c*) 0.5 ML InAs; (*d*) AFM images of the surface of (*c*)

PL spectra for samples with different equivalent layer thicknesses InAs are shown in Figure 2, *a*. The signal from the QDs (broad band in the range of 870–1100 nm) is only present on the 1.5 ML InAs sample. In addition, there is no peak of the wetting layer in the spectrum, which indicates the suppression of its formation during deposition on a structured surface. On samples with smaller thicknesses (1.0 and 0.5 ML), the PL spectra do not have any features characteristic of QD. This may be due to the fact that during the overgrowth process, part of the QD material segregates, which leads to a decrease in their effective size below the limit at which an electronic level exists in a quantum-sized system.

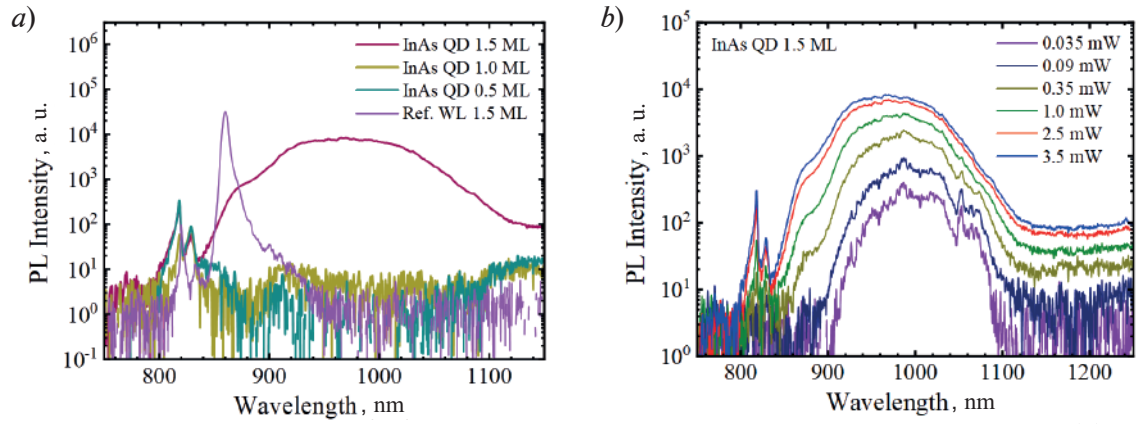

Fig. 2. PL spectra for the samples with different equivalent thickness of InAs deposition (*a*) and for the sample with 1.5 ML InAs deposition at different excitation powers (*b*)

Figure 2, *b* shows the photoluminescence spectra at different excitation powers for a sample with 1.5 ML of InAs. Analysis of the PL spectra of this sample shows that with increasing excitation power, in addition to the QD peaks (900–1100 nm), a low-intensity short-wavelength shoulder (850–900 nm) appears in the spectrum. The same type of structures is responsible for the formation of the long-wavelength shoulder in the spectrum of the reference sample in the Figure 2, *a*. We associate this feature with the emission of so-called platelets – two-dimensional structures formed on morphological inhomogeneities in the spaces between the hole with QDs.

Conclusion

Thus, studies have been carried out on the formation and optical properties of subcritical InAs/GaAs quantum dots on structured substrates. The possibility of obtaining subcritical QDs of low density, emitting in the range of 900–1100 nm, has been demonstrated. The emission wavelength of the obtained QDs is significantly longer compared to alternative methods for forming near-critical QDs (about 950 nm). The results obtained can be used to develop a technological process for the formation of low-density InAs QDs in the O- and, in the future, C-bands without a wetting layer.

REFERENCES

1. **Lu C.-Y., Pan J.-W.,** Quantum-dot single-photon sources for the quantum internet, Nat. Nanotechnol. 16 (2021) 1294–1296.

2. **Schimpf C., Reindl M., Huber D., Lehner B., Covre Da Silva S.F., Manna S., Vyvlecka M., Walther P., Rastelli A.,** Quantum cryptography with highly entangled photons from semiconductor quantum dots, Sci. Adv. 7 (2021).

3. **Kirichenko D.V., Chernenko N.E., Shandyba N.A., Balakirev S.V., Solodovnik M.S.,** Study of arsenic flux effect on thermal desorption of GaAs native oxide and surface morphology, St. Petersburg State Polytechnical University Journal. Physics and Mathematics. 16 (3.1) (2023) 74–78.

4. **Lakhina E.A., Shandyba N.A., Chernenko N.E., Kirichenko D.V., Balakirev S.V., Solodovnik M.S.,** Formation of symmetrical nanoholes by local droplet etching for site-controlled growth of single quantum dots, St. Petersburg State Polytechnical University Journal. Physics and Mathematics. 16 (3.1) (2023) 53–58.

5. **Chernenko N.E., Makhov I.S., Balakirev S.V., Kirichenko D.V., Shandyba N.A., Kryzhanovskaya N.V., Solodovnik M.S.,** Study of InAs/GaAs quantum dots formation in subcritical growth modes on patterned substrates, St. Petersburg State Polytechnical University Journal. Physics and Mathematics. 16 (3.1) (2023) 64–68.

6. **McCabe L.N., Wang Y., Doty M.F., Zide J.M.O.,** Low-density patterned InAs quantum dot arrays, J. Vac. Sci. Technol. B 38 (2020) 022803.

7. **Tommila J., Tukiainen A., Viheriälä J., Schramm A., Hakkarainen T., Aho A., Stenberg P., Dumitrescu M., Guina M.,** Nanoimprint lithography patterned GaAs templates for site-controlled InAs quantum dots, J. Cryst. Growth. 323 (2011) 183–186.

8. **Balakirev S.V., Kirichenko D.V., Shandyba N.A., Chernenko N.E., Solodovnik M.S.,** Droplet epitaxy of site-controlled In/GaAs(001) nanostructures with a variable distance: experiments and simulations, St. Petersburg State Polytechnical University Journal. Physics and Mathematics. 16 (3.1) (2023) 41–46.

THE AUTHORS

KIRICHENKO Danil V.
dankir@sfedu.ru
ORCID: 0000-0001-7476-2778

KRYZHANOVSKAYA Natalia V.
nkryzhanovskaya@hse.ru
ORCID: 0000-0002-4945-9803

MAKHOV Ivan S.
imahov@hse.ru
ORCID: 0000-0003-4527-1958

SOLODOVNIK Maxim S.
solodovnikms@sfedu.ru
ORCID: 0000-0002-0557-5909

BALAKIREV Sergey V.
sbalakirev@sfedu.ru
ORCID: 0000-0003-2566-7840

Received 19.07.2024. Approved after reviewing 01.08.2024. Accepted 08.08.2024.

SIMULATION OF PHYSICAL PROCESSES

Conference materials
UDC 536.331; 536.421.5
DOI: https://doi.org/10.18721/JPM.173.116

Modeling of the scanning track formation in the selective laser melting process of 316L steel

A.A. Gajna [1] ✉, A.A. Mozhayko [1, 2], V.V. Davydov [1, 3]

[1] Peter the Great St. Petersburg Polytechnic University, St. Petersburg, Russia;
[2] NRC "Kurchatov Institute" - CRISM "Prometey", St. Petersburg, Russia;
[3] Bonch-Bruevich Saint-Petersburg State University of Telecommunications, St. Petersburg, Russia
✉ gajna.aa@edu.spbstu.ru

Abstract. Selective laser melting (SLM) is a promising additive manufacturing method that uses metal powder materials and heats them with a laser beam to the melting temperature in such a way that the metal powder layer completely melts. This paper presents a study of SLM process for austenitic 316L steel. The study focuses on single laser track formation and the effects of laser radiation parameters on melt pool size. The research aims to investigate the effects of various laser radiation parameters on the melt pool dimensions in a sample. These parameters include laser power, scanning speed, and laser focal spot diameter. A computational model, created using the COMSOL Multiphysics finite element software, is used to simulate the behavior of the sample under different processing conditions and determine the optimal processing parameters. Results show that the melt width, length and depth depend on above laser parameters. This research contributes to our understanding of SLM processes and provides valuable insights into optimizing processing parameters for achieving desired sample properties.

Keywords: selective laser melting, heat transfer modeling, finite element method, austenitic steel, melt pool

Citation: Gajna A.A., Mozhayko A.A., Davydov V.V., Modeling of the scanning track formation in the selective laser melting process of 316L steel, St. Petersburg State Polytechnical University Journal. Physics and Mathematics. 17 (3.1) (2024) 84–88. DOI: https://doi.org/10.18721/JPM.173.116

Материалы конференции
УДК 536.331; 536.421.5
DOI: https://doi.org/10.18721/JPM.173.116

Моделирование формирования дорожки сканирования в процессе селективного лазерного сплавления стали 316L

А.А. Гайна [1] ✉, А.А. Можайко [1, 2], В.В. Давыдов [1, 3]

[1] Санкт-Петербургский политехнический университет Петра Великого, Санкт-Петербург, Россия;
[2] НИЦ «Курчатовский институт» - ЦНИИ КМ «Прометей», Санкт-Петербург, Россия;
[3] Санкт-Петербургский государственный университет телекоммуникаций им. проф. М.А. Бонч-Бруевича, Санкт-Петербург, Россия;
✉ gajna.aa@edu.spbstu.ru

Аннотация. Селективное лазерное плавление (SLM) - это перспективная технология аддитивного производства, в которой используется лазерный луч для нагрева

металлического порошка до температуры плавления, что приводит к полному его расплавлению в виде нового слоя. В этой работе мы исследуем процесс SLM на примере аустенитной стали 316L. Целью данного исследования является изучение влияния различных параметров лазерного излучения, включая мощность, скорость сканирования и диаметр фокусного пятна, на размеры расплавленной ванны внутри образца. Мы используем программное обеспечение COMSOL Multiphysics для моделирования поведения образца в различных условиях и определения оптимальных параметров обработки. Результаты моделирования показывают, что ширина, длина и глубина расплава зависят от этих изменяемых параметров лазера. Это исследование расширяет наше понимание процессов SLM и дает ценные рекомендации по оптимизации параметров обработки для достижения желаемых свойств образцов.

Ключевые слова: селективное лазерное сплавление, моделирование теплопередачи, метод конечных элементов, аустенитная сталь, ванна расплава

Ссылка при цитировании: Гайна А.А., Можайко А.А., Давыдов В.В. Моделирование формирования дорожки сканирования в процессе селективного лазерного сплавления стали 316L // Научно-технические ведомости СПбГПУ. Физико-математические науки. 2024. Т. 17. № 3.1. С. 84–88. DOI: https://doi.org/10.18721/JPM.173.116

Introduction

Among the various technologies of additive manufacturing, selective laser melting (SLM) is one of the most widely used for the construction of metal parts [1]. The SLM process involves the layer-by-layer fusion of metal powders using laser radiation. During melting, a melt pool is formed, and the morphology of this pool affects the final microstructure of the product [2]. Products manufactured using SLM are widely used in various industries, including biomedical, aerospace, energy, and automotive [3, 4]. The quality of these parts is influenced by numerous parameters and managing them can be time-consuming. Computer modeling is used to reduce time resources.

The thermal physico-mathematical model of the SLM was developed by the authors, and with its help, a number of studies were conducted to investigate the influence of various parameters of the SLM process on the melt pool size [5–8]. In [5], it was found that with a reduction in the scanning speed, the depth of melt pool increases. A change in energy density had a greater effect on both the length and the depth of the melt pool, while the width varied slightly. In [8], different types of scanning strategies (circular and bidirectional) were examined for SLM processing of 316L steel.

Of particular interest is the study of the impact of laser radiation parameters, such as power, scan speed, and focal spot diameter, on the melt pool size. To date, several studies have been conducted in this area. These studies indicate that laser power is one of the most influential process parameters that must be taken into account. An increase in laser power and a decrease in scanning speed lead to an increase in temperature and melt pool size [9]. When using a larger laser diameter, surface quality may be compromised due to defects caused by incomplete melting of powder layers. Additionally, a smaller beam diameter can cause metal evaporation and “keyhole mode” [10].

This article investigates a wider range of laser radiation parameter values and uses modern modeling software. The aim of this work is to determine the dependence of melt pool size on laser radiation parameters such as power, scan speed, and focal spot diameter. The COMSOL Multiphysics software was used to model [11, 12] the system. The model defines all the necessary parameters of the samples (dimensions, materials, and environment conditions), as well as laser radiation parameters (scanning strategy, power, speed, focal spot size), and the thermal effects of laser radiation on the surface of the sample. Based on these simulations, a temperature distribution in the sample is obtained.

Materials and methods

The COMSOL Multiphysics finite element package was selected as the primary tool for simulating the SLM process. A 6×3×2 mm sample was constructed. 316L stainless steel was chosen as the material for the model. This alloy has improved anti-corrosion, creep resistance, and durability properties, making it suitable for use in challenging environments.

In the simulation, the thermal properties of the steel, such as its thermal conductivity and heat capacity, were set to vary with temperature. Heat transfer was modeled using the equation for thermal conductivity, and conditions for convective and radiative heat transfer were specified at the boundary of the sample. When the boiling point was reached, a flow of steam was simulated from the surface. A more in-depth mathematical description of the simulation can be found in previous publications [5, 8].

Various modes were modeled: with a laser power in the range from 100 to 800 W at a constant scanning speed of 800 mm/s and a focal spot diameter of 100 microns, with a scanning speed in the range from 100 to 800 mm/s at a constant power of 400 W and a spot diameter of 100 microns, with a focal spot diameter in the range of 50 to 300 microns at a constant power of 200 W and a scanning speed of 800 mm/s.

Results and discussion

Figure 1 shows the relationship between melt pool size and laser power. As the power increases, so does the size of the pool. This is because that the material is heated more intensely. However, further increases in the laser power lead to a decrease in the dependence on the pool size, which may be caused by boiling and subsequent evaporation of the material within the pool.

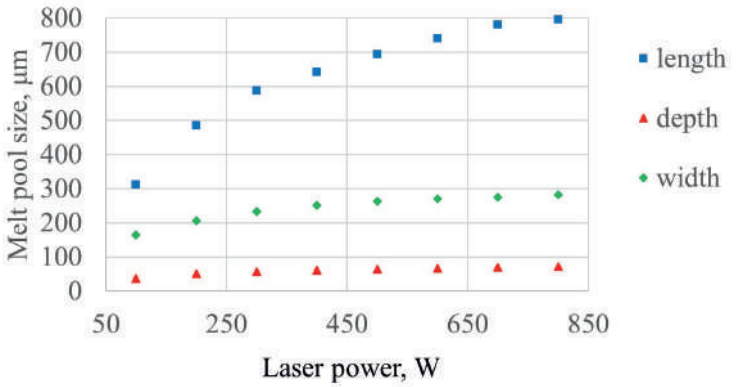

Fig. 1. Dependences of the length, width and depth of the melt pool on the laser power

Figure 2 illustrates the relationship between the size of the melt pool and the scanning speed. The low scanning speed ensures a more complete melting of the powder material. Consequently, the width and depth of the melt pool decrease with increasing scanning speed, while the length of the melt pool due to a lower solidification rate compared to the scanning speed.

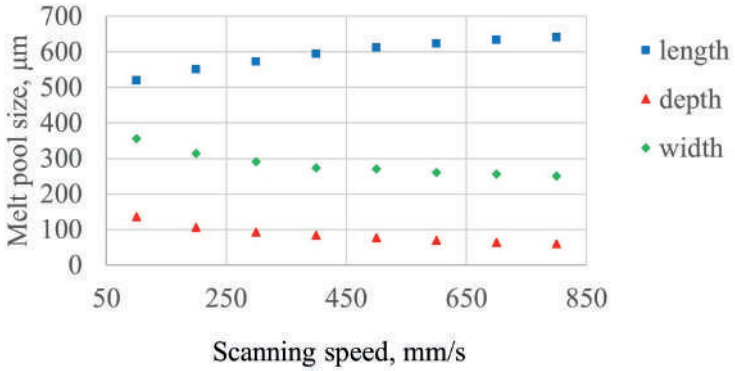

Fig. 2. Dependences of the length, width, and depth of the melt pool on scanning speed

Figure 3 shows the relationship between the size of the melted pool and the laser focal spot diameter. As the diameter of the laser beam increases (up to 200 microns), the width and length of the melted zone increase mainly due to an increase in the impact area and a slight change in energy concentration. However, the melt pool depth remains relatively constant, which can be explained by boiling of the material. Subsequently, as the diameter of the focus increases, all dimensions of the melted pool decrease due to a reduction in energy density.

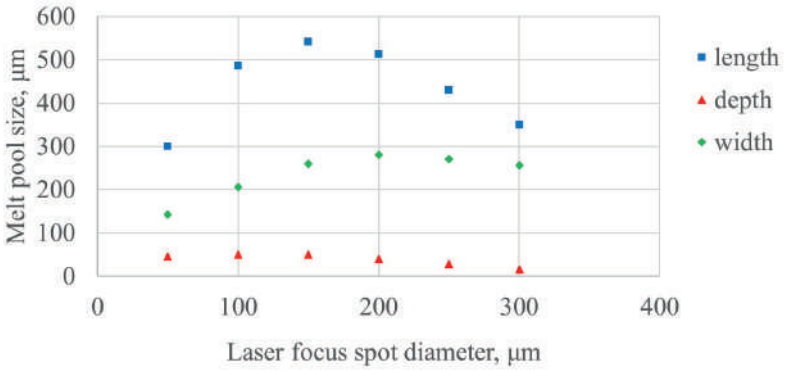

Fig. 1. Dependences of the length, width and depth of the melt pool on the laser power

Conclusion

In this article, we investigate the process of forming a scanning track during selective laser melting of 316L steel using numerical modeling. The size of the melt pool is determined by changing the laser power, scan speed, and laser focal spot diameter. Based on this study, several conclusions were drawn. Increasing laser power leads to an increase in all dimensions of the melt pool. Increasing scanning speed leads to a reduction in the width and depth of the pool, as well as an increase in its length. Minor changes in the focal spot size result in proportional changes in width and length, while depth remains relatively constant due to boiling effects. More significant changes in spot size reduce the melt pool size.

REFERENCES

1. **Gatoes D., Alves R., Alves B., Vieira M.T.,** Selective Laser Melting and Mechanical Properties of Stainless Steels, Materials. 15(21) (2022) 7575.

2. **Caffrey T., Campbell I., Wohlers T.,** Report 2016-3D Printing and Additive Manufacturing State of the Industry. Annual Worldwide Progress Report, Wohlers Associates, Fort Collins, 2016.

3. **Bahl S., Mishra S., Yazar K.U., Kola I.R., Chatterjee K., Suwas S.,** Non-equilibrium microstructure, crystallographic texture and morphological texture synergistically result in unusual mechanical properties of 3D printed 316L stainless steel, Additive Manufacturing. 28 (2019) 65–77.

4. **Prashanth K. G., Scudino S., Maity T., Das J., Eckert J.,** Is the energy density a reliable parameter for materials synthesis by selective laser melting?, Materials Research Letters. 5(6) (2017) 386–390.

5. **Kuznetsov P., Mozhayko A., Shakirov I., Bobyr V., Staritsyn M., Zhukov A.,** Modeling of LPBF Scanning Strategy and its Correlation with the Metallic 316 L, 321, and Alnico Magnets Samples Structure, Advanced Additive Manufacturing. 1 (2022) 187–193.

6. **Mozhayko A.A., Gerashchenkov D.A., Staritsyn M.V.,** Experimental and theoretical investigation of the formation of the surface layer highly alloyed with aluminum. Voprosy Materialovedeniya. 2 (110) (2022) 44–57.

7. **Mozhayko A.A., Manninen S.A., Davydov V.V., Rud V.Yu.,** Modeling of physical processes of interaction of ultrasonic wave with metal structures for detection of defects, Journal of Physics: Conference Series. 1745(1) (2021) 012046.

8. **Kuznetsov P.A., Shakirov I.V., Mozhayko A.A., Zhukov A.S., Bobyr V.V.,** Comparison of sequential and circular scanning thermal fields and their influence on microstructure of Alnico alloy produced by laser powder bed fusion. Journal of Physics: Conference Series. 1967 (1) (2021) 012064.

9. **Kazemi Z., Soleimani M., Rokhgireh H., Nayebi A.,** Melting pool simulation of 316L samples manufactured by Selective Laser Melting method, comparison with experimental results, International Journal of Thermal Sciences. 176 (2022) 107538.

10. **Zamindar N.,** Thermal simulation of selective laser melting made components. Diss. Politecnico di Torino. (2021).

11. The official website of COMSOL. URL: https://www.comsol.com. Accessed Apr 26, 2024.

12. **Bayat M., Mohanty S., Hattel J.H.,** Thermo-Fluid-Metallurgical Modelling of Laser-Based Powder Bed Fusion Process, COMSOL Conference, 2018.

THE AUTHORS

GAJNA Anna A.
gajna.aa@edu.spbstu.ru
ORCID: 0009-0002-2923-804X

DAVYDOV Vadim V.
davydov_vadim66@mail.ru
ORCID: 0000-0001-9530-4805

MOZHAYKO Anna A.
annaanna-1996@mail.ru
ORCID: 0000-0002-9146-4286

Received 09.07.2024. Approved after reviewing 02.08.2024. Accepted 02.08.2024.

Conference materials
UDC 533.9.02
DOI: https://doi.org/10.18721/JPM.173.117

The role of ectons in the vacuum breakdown process

V.Yu. Kozhevnikov [1] ✉, A.V. Kozyrev [1], A.O. Kokovin [1]

[1] Institute of High Current Electronics SB RAS, Tomsk, Russia

✉ Vasily.Y.Kozhevnikov@ieee.org

Abstract. This paper presents a valuable addition to the kinetic theory regarding vacuum breakdown formation in a planar vacuum gap, specifically focusing on the cathode plasma emission known as the 'ectonic' (pulse-periodic quasi-particle) nature. We investigate the contributions of ectonic and continuous types of emission from the cathode in terms of their effects on the mechanism of anomalous ion acceleration and cathode plasma expansion during a short-term switching of the emission current corresponding to the death and birth of ectons.

Keywords: vacuum breakdown, Vlasov-Poisson equations, ectons

Funding: The work was carried out within the framework of the State Task of the Ministry of Science and Higher Education of the Russian Federation on themes FWRM-2021-0007 and FWRM-2021-0014.

Citation: Kozhevnikov V.Yu., Kozyrev A.V., Kokovin A.O., The role of ectons in the vacuum breakdown process, St. Petersburg State Polytechnical University Journal. Physics and Mathematics. 17 (3.1) (2024) 89–94. DOI: https://doi.org/10.18721/JPM.173.117

Материалы конференции
УДК 533.9.02
DOI: https://doi.org/10.18721/JPM.173.117

Роль эктонов в процессе вакуумного пробоя

В.Ю. Кожевников [1] ✉, А.В. Козырев [1], А.О. Коковин [1]

[1] Институт сильноточной электроники СО РАН, г. Томск, Россия

✉ Vasily.Y.Kozhevnikov@ieee.org

Аннотация. Статья представляет собой дополнение кинетической теории образования вакуумного пробоя в плоском вакуумном зазоре, в котором особое внимание уделяется эмиссии катодной плазмы в т.н. эктонном (импульсно-периодическом) режиме. Исследовано влияние эктонной эмиссии на механизм аномального ускорения ионов и расширения двухкомпонентной катодной плазмы.

Ключевые слова: вакуумный пробой, уравнения Власова-Пуассона, эктоны

Финансирование: Работа выполнена в рамках государственного задания Министерства науки и высшего образования Российской Федерации по темам № FWRM-2021-0007, FWRM-2021-0014.

Ссылка при цитировании: Кожевников В.Ю., Козырев А.В., Коковин А.О. Роль эктонов в процессе вакуумного пробоя // Научно-технические ведомости СПбГПУ. Физико-математические науки. 2024. Т. 17. № 3.1. С. 89–94. DOI: https://doi.org/10.18721/JPM.173.117

Introduction

Between 2021 and 2023, in a series of theoretical papers by the Laboratory of Theoretical Physics of the Institute of High-Current Electronics SB RAS employees, the first self-consistent collisionless kinetic theory of cathode plasma expansion was formulated [1–3]. It opened up the possibility to explain the physical nature of the plasma expansion phenomenon in vacuum discharge in detail. It allowed us to predict the average speed of a cathode plasma expansion in the vacuum diodes of various designs. It was shown that in a vacuum gap, the key physical mechanism for the plasma expansion, regardless of the diode geometry and the connected electrical circuit, is the collisionless electrodynamic mechanism. It lies in the fact that the peripheral region of a dense cathode plasma in an external electric field acquires an excess negative volume charge, leading to the appearance of a "virtual cathode" of amplitude $\Delta\varphi < 0$. The presence of this region ensures the influence of accelerating electrodynamic forces on ions near the emission center at the cathode, due to which the ions start to move towards the anode and acquire "anomalously" high values of kinetic energy $\varepsilon_i > qU_0$. The possibility of the so-called "deep potential well" near the cathode $|\Delta\varphi| > U_0$ existence has also been predicted by the proposed theory. This effect is entirely assured by the emission center parameters and does not depend on the voltage amplitude U_0 applied to the diode.

In this study, we expand our research experience to investigate the influence of the ectonic mechanism of cathode plasma emission on the phenomenon of anomalous ion acceleration, which results in the expansion of the cathode plasma. Building upon the kinetic theory established previously, we elucidate the mechanism of plasma emission from the cathode and present the results of numerical solutions of the kinetic equations for the model of a planar vacuum diode, considering the periodic variation in the emission current density. Our proposed approach demonstrates that the previously identified collisionless mechanism remains fundamentally significant even when the emission operates in a pulsed regime. Specifically, one ecton's death is followed by another's emergence, leading to the interception of the discharge current throughout the vacuum discharge.

Materials and Methods

As a basic version of the calculations in this work, we use a mathematical model described in more detail in [1]. Here, we also consider a flat one-dimensional vacuum diode formed by a vacuum gap of length D with a cross-sectional area S. Three independent variables parameterize the electron distribution functions (EDF) and ions (IDF): the Cartesian coordinate x, the collinear momentum component p_x and time t. The EDF/IDF parameterized in this way also obeys the collisionless nonrelativistic kinetic equations:

$$\begin{cases} \dfrac{\partial f_e}{\partial t} + \dfrac{p_x}{m_e}\dfrac{\partial f_e}{\partial x} - qE_x\dfrac{\partial f_e}{\partial p_x} = 0, \\ \dfrac{\partial f_i^+}{\partial t} + \dfrac{p_x}{m_i}\dfrac{\partial f_i^+}{\partial x} + qE_x\dfrac{\partial f_i^+}{\partial p_x} = 0, \end{cases} \tag{1}$$

where q is the elementary charge, E_x is the component of the electric field strength along the x-coordinate axis, and m_e and m_i are the rest of the mass of the electron and ion, respectively. Following the methodology [1–3], the model is collisionless, i.e., on the right side of equations (1), there are no integrals of elastic and inelastic collisions. For simplicity of analysis, we will assume that the cathode plasma consists only of electrons and ions of the same type. This is a reasonable assumption for lithium, carbon, bismuth cathodes and some other materials [4]. The modeling proposed below assumes that the cathode material is antimony Sb (m_i = 121 a.m.u.), for which a two-component plasma is also justified.

In line with the comprehensive analogy with work [1], the kinetic equations system (1) is enhanced with the Poisson equation to compute a vacuum diode's electrostatic potential φ and

electric field E_x. This enables us to control the dynamics of the space charge of ions and electrons, offering exciting possibilities for innovation and advancement.

$$\frac{\partial^2 \varphi}{\partial x^2} = -\frac{q}{\varepsilon_0}\left(n_+ - n_e\right), \quad E_x = -\frac{\partial \varphi}{\partial x}, \tag{2}$$

where ε_0 is the dielectric constant of vacuum, n_+ is the ion number density, and n_e is the electron number density:

$$n_e(x,t) = \int_{-\infty}^{\infty} f_e(x,p_x,t)\,dp_x, \quad n_+(x,t) = \int_{-\infty}^{\infty} f_i^+(x,p_x,t)\,dp_x. \tag{3}$$

At the initial time $t = 0$, we assume that the vacuum gap is empty $f_e(t=0) = f_i^+(t=0) \equiv 0$. However, in contrast to the boundary conditions of continuous emission used in [10] to model ectonic periodic processes, in this work, the following boundary conditions for EDF/FRI are used:

$$f_e(x=0,p_x,t) = \frac{n_0\chi(t)}{\sqrt{2\pi m_e T_e}} e^{-\frac{p_x^2}{2m_e T_e}}, \quad f_i^+(x=0,p_x,t) = \frac{n_o\chi(t)}{\sqrt{2\pi m_i T_i}} e^{-\frac{p_x^2}{2m_i T_i}}, \tag{4}$$

where T_e and T_i are the thermodynamic temperatures of electrons and ions of the cathode plasma, respectively, the values of which are close to the parameters of the explosive emission plasma $T_e \sim 5$ eV and $T_i \sim 1$ eV [5], n_0 is the quasineutral plasma number density at the emission center. The function of a pulse-periodic signal with unit amplitude $\chi(t)$ characterizing non-stationary emission is shown in Fig. 1, where t_{rise} is the duration of the rising/falling edge of the signal, t_{width} is the duration of the signal at the base, T is the period of the signal.

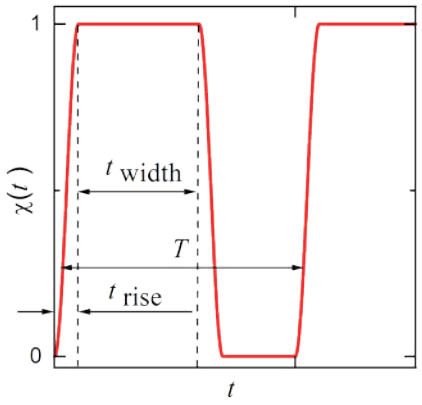

Fig. 1 Cathode plasma number density time profile for the ecton emission regime

The numerical algorithm used in this study is based on the approach described in [6]. To solve the Vlasov equations, we employed the semi-Lagrangian numerical method for solving kinetic equations (semi-Lagrangian method), which utilizes high-order interpolation by cubic splines. The computational algorithm was programmed using the OpenMP and GNU Scientific Library libraries in GNU C language.

Results and Discussion

To investigate the vacuum breakdown of a planar gap, a scenario was modeled (Fig. 2) in which a voltage $U(t)$ from an external source with a rise time of $t_{rise} = 0.1$ ns and an amplitude of $U_0 = 2$ kV is applied through a ballast resistor. The interelectrode distance was chosen to be $D = 1$ cm, and the product of the ballast resistance R and the cross-sectional area S was $RS = 200$ Ω·cm^2. The significant difference was that a pulsed-periodic function with a baseline plasma number density of $n_0 = 10^{22}$ m^{-3} was chosen as the boundary condition for plasma emission.

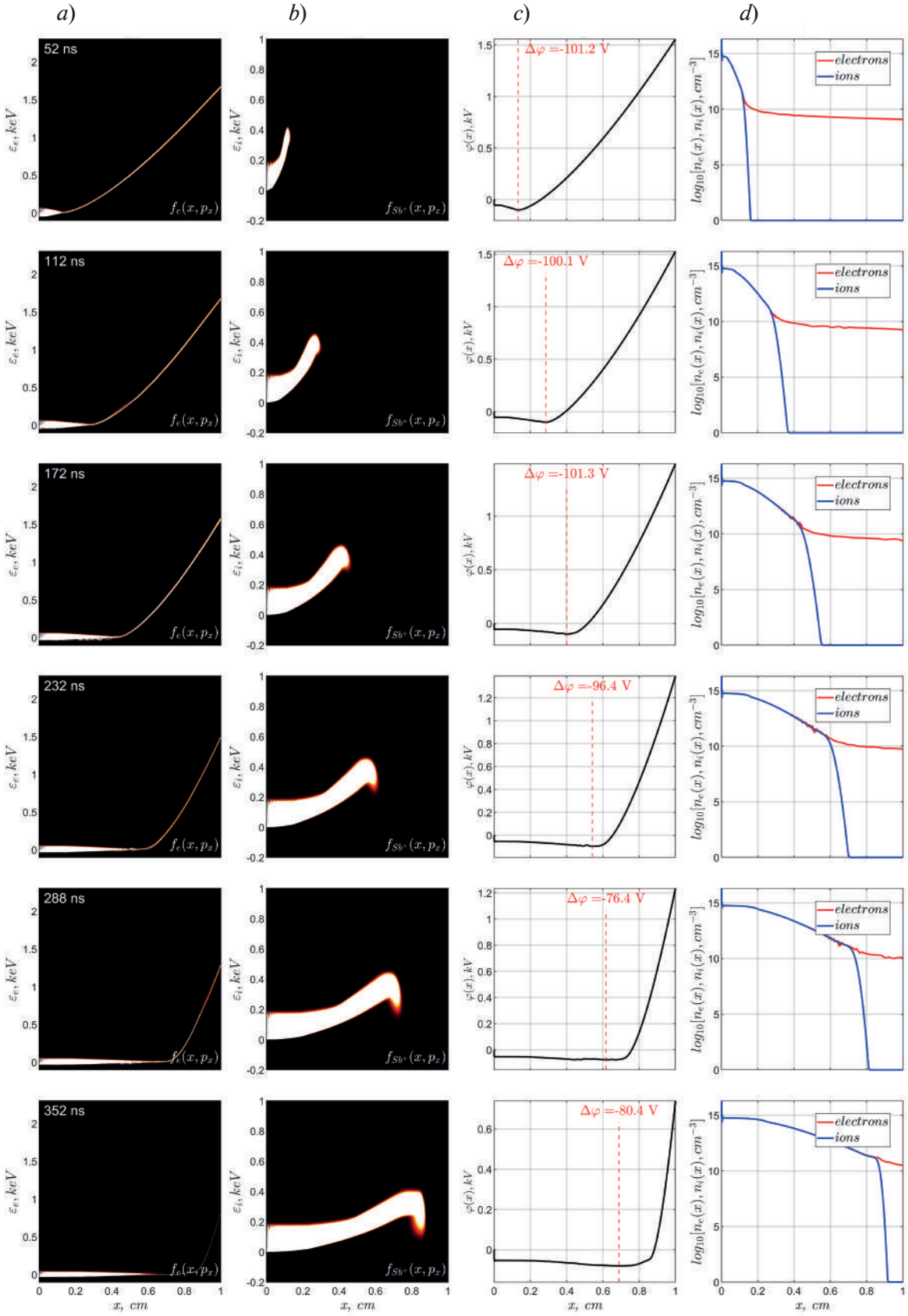

Fig. 2 Temporal dynamics of plasma during the vacuum breakdown stage across a 1 cm gap in the ecton emission mode of plasma from the cathode. (*a*) – EDF, (*b*) – IDF, (*c*) – electrostatic potential distribution, (*d*) – number density distribution of the expanding cathode plasma

The following values were used as parameters for the function: t_{rise} = 0.1 ns, t_{width} = 3 ns, and T = 5 ns. These parameters model the pulsating emission from the cathode so that the average emission current is approximately equivalent to that of continuous emission [1–3], thereby ensuring the high emission capability of the cathode.

The macroscopic picture of plasma expansion in the ecton emission mode does not differ from the case of continuous emission [1]. As lighter and thermalized particles, electrons shift from their initial state even without an external field, forming a negative space charge at the edges of the cluster, the magnitude of which is determined by the number density n_0. Thus, the initial short emission pulse (ecton) at the moment t = 0 initiates the expansion mechanism of the cathode plasma. At the time points when the emission current density is at its maximum, the characteristic value of the virtual cathode amplitude, Δφ, reaches −100 V. The shape of the electric potential distribution and the concentrations of charged particles are also approximately the same in both cases. The difference in plasma expansion modes lies in the somewhat lower average velocity of the ion component in the ecton emission mechanism. The average velocity in this case is approximately ~$2.2 \cdot 10^6$ cm/s, which is closer to the parameters of the cathode plume plasma observed in experiments [5]. This is because, during ecton emission, there is typically an interval between two successive pulses during which the cathode completely loses its emission capability.

More information about the influence of the ecton emission mechanism is provided by the detailed construction of electric potential distributions over one full period T (Fig. 3, *a*). Fig. 3, *b* shows the potential distributions at time points corresponding to points *1–6* and *1′* on the emission pulse's temporal profile. From time point 1, when the emission current begins to enter the gap, until the end of the emission, the potential distribution changes significantly. At time point *4*, the ecton terminates, meaning plasma emission from the cathode completely stops. Therefore, in the subsequent moments *5–6*, corresponding to the "dead time" between pulses, the virtual cathode (Δφ = −3.7 V) rapidly smooths out, the plasma discharges, and then the birth of a new ecton at point 6 (resumption of emission) continues the process described above.

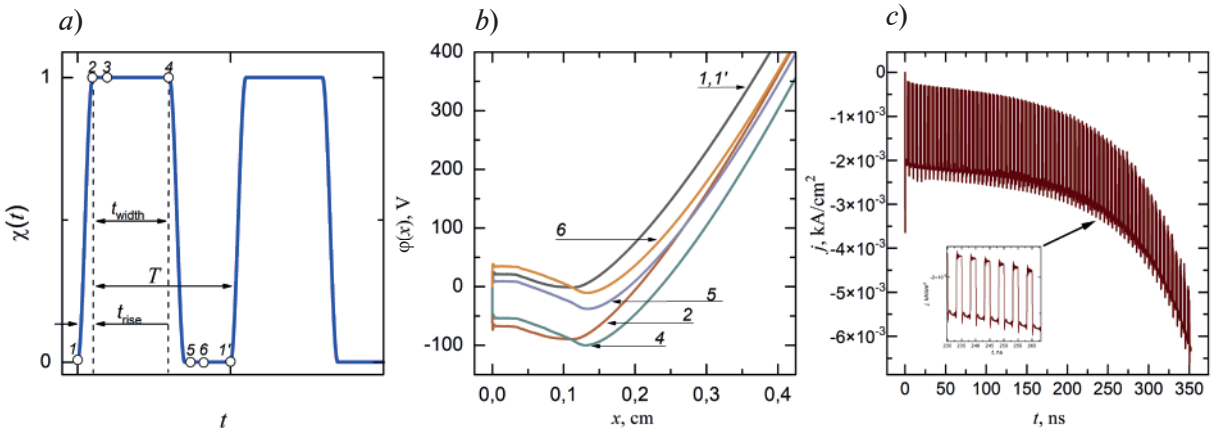

Fig. 3. The emission function profile (*a*), the corresponding electric potential distribution (*b*) and the time-dependent full current density profile in the vacuum diode in the near-to-cathode region

The rise and fall of the emission current due to the birth and death of ectons lead to oscillations of the space charge in the gap. In summary, the fluctuations in space charge caused by pulse-periodic ecton emission are evident in the time-varying current flow through the diode. (Fig. 3, *c*) illustrates the total current density in the vacuum diode within the power supply circuit, which includes a ballast resistance of R = 200 Ω. It can be seen that throughout the entire vacuum breakdown process, the total current density in the diode exhibits a curve with noticeable frequency modulation. The modulation amplitude (Fig. 3, *c*) is small (< 5%). Still, its presence shows the influence of the ecton emission mechanism on the current flow, as the volume charge oscillations have a period T that matches the modulation period and the period of the χ(t) function.

Conclusion

When comparing the results of numerical simulations of vacuum breakdown phenomena in a planar diode gap with a continuous cathode emission mechanism to those of a similar breakdown

simulation with an ecton emission mechanism, it was demonstrated that in both cases, the mechanism of cathode plasma expansion constitutes an electro-field collisionless process. Detailed kinetic modeling of vacuum breakdown in the simplest one-dimensional configuration of a planar diode utilizing the ecton mechanism revealed the following findings:

· The establishment of the initial cathode potential drop is characterized by durations significantly shorter than the typical ecton nucleation times. Hence, plasma expansion from the cathode jet commences at the first ecton's emergence.

· The cessation of one ecton and the interval preceding the emergence of the subsequent ecton cause a temporary vanishing of the virtual cathode region ($\Delta\varphi \sim 0$), yet it does not impede the plasma expansion from the cathode to the anode.

· Plasma expansion occurs at the outer emission boundary of the quasi-neutral expanding plasma during the intervals between bursts of emission current. For ions, this expansion is fueled by the inertia of the ion component, attributed to its kinetic energy acquired during the ecton existence (emission) periods.

· The appearance of each successive ecton triggers the formation of a new virtual cathode at the outer emission boundary. It accelerates a fresh portion of the plasma's ion component along the declining section of the electrostatic potential.

REFERENCES

1. **Kozhevnikov V., Kozyrev A., Kokovin A., Semeniuk N.,** The Electrodynamic Mechanism of Collisionless Multicomponent Plasma Expansion in Vacuum Discharges: From Estimates to Kinetic Theory., Energies. 14 (22) (2021) 7608.

2. **Kozhevnikov V.Yu., Kozyrev A.V., Kokovin A.O., Semeniuk N.S.,** The kinetic simulation in vacuum electronics: uncovering the fundamental nature of non-Maxwellian distribution function effects., St. Petersburg State Polytechnical University Journal: Physics and Mathematics. 15 (3.3) (2022) 76–81.

3. **Kozyrev A., Kozhevnikov V., Semeniuk N.S., Kokovin A.O.,** Initial kinetics of electrons, ions and electric field in planar vacuum diode with plasma cathode., Plasma Sources Science and Technology. 32 (10) (2023) 105010.

4. **Anders A.,** Ion charge state distributions of vacuum arc plasmas: The origin of species., Physical Review E. 55 (1) (1997) 969.

5. **Mesyats G.A.,** Explosive electron emission. Moscow, Fizmatlit, 2011. 280 p.

6. **Kozhevnikov V.Yu., Kozyrev A.V., Semeniuk N.S.,** Modeling of Space Charge Effects in Intense Electron Beams: Kinetic Equation Method vs PIC-method., IEEE Transactions on Plasma Science. 45 (10) (2017) 2762.

THE AUTHORS

KOZHEVNIKOV Vasily Yu.
Vasily.Y.Kozhevnikov@ieee.org
ORCID: 0000-0001-7499-0578

KOKOVIN Aleksandr O.
kokovin@to.hcei.tsc.ru
ORCID: 0000-0003-2068-7674

KOZYREV Andrey V.
kozyrev@to.hcei.tsc.ru
ORCID: 0000-0002-7078-7991

Received 08.07.2024. Approved after reviewing 29.07.2024. Accepted 03.08.2024.

Conference materials
UDC 616-71
DOI: https://doi.org/10.18721/JPM.173.118

Options for implementing electrical impedance tomography for diagnostics blood clots and bruises

A.I. Levin [1] ✉, E.A. Pecherskaya [1], J.V. Shepeleva [1],
V.V. Antipenko [1], D.V. Yakushov [1], D.V. Artamonov [2]

[1] Penza State University, Penza, Russia;
[2] Penza State University of Architecture and Construction, Penza, Russia
✉ levin.alescha2013@ yandex.ru

Abstract. The possibility of detecting and diagnosing bruises, blockages of veins or arteries and blood clots based on electroimpedance tomography is being considered. The advantages of electroimpedance tomography compared to other similar methods are substantiated. Physical principles are presented, implementation options for the electrical impedance tomography method are systematized; the basics of the clinical application of this diagnostic method including the capabilities of both classical and portable installation options are outlined.

Keywords: electroimpedance tomography, non-invasive diagnosis, bioimpedance, biological tissue, electrode

Citation: Levin A.I., Pecherskaya E.A., Shepeleva J.V., Antipenko V.V., Yakushov D.V., Artamonov D.V., Options for implementing electrical impedance tomography for diagnostics blood clots and bruises, St. Petersburg State Polytechnical University Journal. Physics and Mathematics. 17 (3.1) (2024) 95–99. DOI: https://doi.org/10.18721/JPM.173.118

Материалы конференции
УДК 616-71
DOI: https://doi.org/10.18721/JPM.173.118

Возможности применения электроимпедансной томографии для диагностики тромбов и гематом

А.И. Левин [1] ✉, Е.А. Печерская [1], Ю.В. Шепелева [1],
В.В. Антипенко [1], Д.В. Якушов [1], Д.В. Артамонов [2]

[1] Пензенский государственный университет, г. Пенза, Россия;
[2] Пензенский государственный университет архитектуры и строительства, г. Пенза, Россия
✉ levin.alescha2013@yandex.ru

Аннотация. Рассмотрена возможность обнаружения и диагностики гематом, закупорок вен или артерий и тромбов на основе электроимпедансной томографии. Обоснованы преимущества электроимпедансной томографии по сравнению с другими аналогичными методами. Представлены физические принципы, систематизированы варианты реализации метода электроимпедансной томографии; Изложены основы клинического применения этого метода диагностики, включая возможности как классического, так и портативного варианта установки.

Ключевые слова: электроимпедансная томография, неинвазивная диагностика, биоимпеданс, биологическая ткань, электрод

Ссылка при цитировании: Левин А.И., Печерская Е.А., Шепелева Ю.В., Антипенко В.В., Якушов Д.В., Артамонов Д.В. Возможности применения

электроимпедансной томографии для диагностики тромбов и гематом // Научно-технические ведомости СПбГПУ. Физико-математические науки. 2024. Т. 17. № 3.1. С. 95–99. DOI: https://doi.org/10.18721/JPM.173.118

Introduction

The principle of the electroimpedance tomography (EIT) method is to supply an electric current or voltage through electrodes that are located on the body of the person being examined. Thanks to this method, the impedance distribution of human tissues is visualized. The method is based on measuring the potential difference between the electrodes and the electric currents flowing through the electrodes [1]. The method of electroimpedance tomography has a number of advantages over other similar diagnostic methods, which, first of all, include ultrasound (ultrasound), magnetic resonance imaging, as well as computed tomography. The EIT positive functional characteristics include the fact that the method has high resolution and is non-invasive [2]. In addition, the method is also promising in terms of technical and economic indicators, since it is characterized by low cost, the small weight and overall dimensions of the equipment allow it to be portable, which opens up prospects for real-time monitoring. Technical limitations of the EIT method are associated with the inability to reconstruct the image slice by slice, since a change in conductivity anywhere in the region affects the measurement results in various areas, and not just for a specific slice [3]. The possibility of developing wearable portable devices based on EIT expanded the prospects for using this tomography method, which is essentially a unique portable imaging method.

Options for implementing EIT in practice

EIT with time-stretched measurements is useful for monitoring changing physiological phenomena (for example, 24-hour monitoring after surgery), but it is only applicable in special cases where changes occur over time, such as ventilation and perfusion. In contrast, EIT with a varying frequency of the current or voltage probing signal influences various tissue impedance characteristics, allowing image reconstruction if it is necessary to make measurements in a shorter time frame. Various modifications of the EIT imaging method are summarized in Table.

When implementing a method based on impedance measurement, single measurements, which are used to restore the distribution of absolute impedance across the tissues of the human body are performed. Despite the theoretical elaboration, in practice a number of uncertainties, which include errors in the location and accuracy of the electrodes on the surface of biological tissues, as well as other sources of systematic errors lead to errors in image reconstruction. Possible directions for solving this drawback are widely discussed in a number of scientific papers [2–3].

The current supply can be implemented in different ways depending on the specific purpose. A modification of the method is possible, in which an electric current is supplied between two adjacent electrodes, and the voltage is recorded between all remaining pairs of adjacent electrodes. This is the most common method. In another variant, it is possible to supply the current with two electrodes located at an angle of 180° relative to each other. In this case, the measurement of the electric voltage is carried out in pairs between each of the electrodes and the reference electrode [5]. One of the most common ways of such an arrangement of electrodes is the method of electroimpedance tomography in the study of the brain. The diagonal or cross arrangement of the electrodes is due to the fact that one electrode is used to measure voltage as a reference, and the current is set alternately between different combinations of electrode pairs.

Further, the following approaches to the implementation of electrical impedance tomography in practice are considered:

- EIT in voltage mode consists of applying a given voltage to biological tissues through electrodes and measuring induced currents;
- EIT in current mode means supplying specified values of electric currents and measuring voltages generated on the human body surface.

Table

The effect of lens voltage on the structure size

Area of application	Measurements based on the modification of the EIT method	Measured parameter
Computer modeling of tissues bioimpedance distribution	Impedance measurement	Bioimpedance
Study of the processes dynamics occurring in the body	Measuring dynamically changing impedance	Time dependence of bioimpedance
Identification of various types of biological tissues	Measuring impedance with a changing frequency of the measuring signal	Frequency dependence of bioimpedance

The so-called trigonometric modification of the method of arranging electrodes is based on the supply of electric current to all electrodes simultaneously. In this case, the electrical voltage is measured relatively to the reference electrode. The specified implementation of the method involves performing multiple independent measurements, due to a significant reduction in the random component of the measurement error is achieved.

The so-called trigonometric modification of the electrodes arrangement method is based on supplying an electric current simultaneously to all electrodes. In this case, the electrical voltage is measured relative to the reference electrode. The specified implementation of the method implies the performance of multiple independent measurements, thereby achieving a significant reduction in the random component of the measurement error [6–9].

The frequency of the flowing current depends on the bioimpedance and dielectric constant of the analyzed biological tissue. The standard frequency at which measurements are performed is 50 kHz, but some devices analyze several frequencies (10 Hz–10 MHz) to improve image quality and analyze various tissues. However, frequencies above 1 MHz are complex, primarily due to parasitic impedances that distort signals; thus, special high-performance circuit components and data acquisition modules are required [9–10].

Due to the fact that the conductivity of the human body has different numerical values in different areas, in addition, the measurement of conductivity is not always possible due to the technical capabilities of electrical impedance tomography, it is advisable to use the EIT to diagnose clots and bruises in the extremities and abdominal cavity, limbs, neck and head. Blood clots and bruises have reduced conductivity, unlike whole blood, as they are formed due to clots of blood components, lipids and proteins. To detect their accumulation or presence in a specific desired area, it is required to conduct an EIT under normal conditions, introduce a marker into the circulatory system in the form of a sodium chloride solution to improve blood conduction and re-examine the EIT [11–12].

We assume that the best EIT application is the diagnosis of pulmonary thromboembolism. There are several factors associated with it. Firstly, the belt of injecting-diagnostic electrodes can be positioned quite well precisely on the chest, where, in fact, the lungs and the small circulatory circle are located. This arrangement of the electrodes contributes both to the tight mechanical fixation of the electrodes and to the location of the electrodes at a distance from each other. Due to it, the mutual influence of the electrodes on each other is minimized and the parasitic capacitive component of measuring the potential difference on paired electrodes is minimized. Secondly, since pulmonary thromboembolism is caused by blood clots that form more often in the large veins of the lower extremities or pelvis, it is necessary to monitor changes in blood flow to the lower extremities, which can be done using the rheography method in tandem with an EIT. In addition, the flow of blood fluid by rheography can be measured between the upper extremities in order to already deal with hemodynamic characteristics during the EIT.

There are various methods for determining the hemodynamic parameters of the circulatory system. The most common are the stroke volume of the heart (SVH) according to the Kubichek, Tishchenko method and now patented by the domestic specialist Zabolotskikh I.B.

According to the latest method, the stroke volume of the heart in patients without heart defects is determined according to the following expression:

$$US = \left(90.97 + 0.54 \cdot PD - 0.57 \cdot AD - 0.61 \cdot V\right) \cdot k.$$

To calculate the stroke volume of patients with heart disease, the expression is used:

$$US = \left(90.97 + 0.54 \cdot PD - 0.57 \cdot AD - 0.61 \cdot B\right) / k,$$

where US is the stroke volume of the heart, PD is pulse pressure, AD is diastolic pressure, V is age in years, k is the entered coefficient depending on the patient.age.

To calculate the blood volume per minute (VB), the following formula was used:

$$\mathrm{VB} = \mathrm{UOS} \cdot \mathrm{FS} / 1000,$$

where UOS is the stroke volume of the heart, FS is the heart rate.

Pulse pressure is the difference between systolic and diastolic blood pressure, which can be determined using a tonometer using a hydrojet [13, 14].

Thus, it is possible to make an entire system based on rheography, EIT and tonometer, monitoring the hemodynamic parameters of a person and in monitoring mode (for example, during the day) determine a person's predisposition to thromboly in the early stages.

Conclusions

When implementing electroimpedance tomography, the bioimpedance distribution is analyzed based on the measurement of electric current and potential difference at the electrodes. The solution of the specified problem of reconstruction of the impedance distribution is nonlinear. In contrast, in the case of X-ray computed tomography, photons travel along rectilinear trajectories. In the case of EIT, the current depends on the bioimpedance values in different parts of the object. This imposes limitations on the task of image reconstruction using electroimpedance tomography. To increase the EIT modeling accuracy, it is necessary to take into account the anatomically realistic geometry of the body, heterogeneity, filling of living tissues with blood and other fluids, and the flow rate of fluids in the body.

REFERENCES

1. **Ke X.Y., Hou W., Huang Q., et al.,** Advances in electrical impedance tomography-based brain imaging, Military Med Res. 9 (1) (2022).

2. **Shi Y., Yang Z., Xie F., Ren S., Xu S.,** The Research Progress of Electrical Impedance Tomography for Lung Monitoring, Front Bioeng Biotechnol. 9 (726652) (2021).

3. **Cappellini I., Campiglia L., Zamidei L., Consales G.,** Electrical Impedance Tomography (EIT) to Optimize Ventilatory Management in Critically Ill Patients: A Report of Two Cases, Anesthesia Research. 1 (1) (2024) 3–7.

4. **Pennati F., Angelucci A., Morelli L., Bardini S., Barzanti E., Cavallini F., Conelli A., Di Federico G., Paganelli C., Aliverti A.,** Electrical Impedance Tomography: From the Traditional Design to the Novel Frontier of Wearables, Sensors. 23 (3) (2023) 1182.

5. **Levin A.I., Pecherskaya E.A., Varenik Yu.A., Shepeleva J.V.,** Implementation of electrical impedance tomography, St. Petersburg State Polytechnical University Journal. Physics and Mathematics. 16 (3.2) (2023) 288–293.

6. **Feitosa A.R.S., Ribeiro R.R., Barbosa V.A.F., Souza de R.E., Santos dos W.P.,** Reconstruction of electrical impedance tomography images using chaotic ring-topology particle swarm optimization and non-blind search, 2014 IEEE International Conference on Systems, Man, and Cybernetics (SMC). (2014) 2618–2623.

7. **Hannan S., Faulkner M., Aristovich K., Avery J., Walker M.C., and Holder D.S.,** In vivo imaging of deep neural activity from the cortical surface during hippocampal epileptiform events in the rat brain using electrical impedance tomography, Neuroimage. 209 (2020) 116525.

8. **Zhao Z., Fu F., Frerichs I.,** Thoracic electrical impedance tomography in Chinese hospitals: A review of clinical research and daily applications, Physiol. Meas. 41 (4) (2020).

9. **Halter R. J., et al.,** Real-time electrical impedance variations in women with and without breast cancer, IEEE Trans. Med. Imaging. 34 (1) (2015) 38–48.

10. **Hamilton S.J., Lionheart W.R.B., Adler A.,** Comparing D-bar and common regularization-based methods for electrical impedance tomography, Physiol. Meas. 40 (4) (2019) 44004.

11. **Heines S.J.H., Strauch U., Poll van de M.C.G., Roekaerts P.M.H.J., Bergmans D.C.J.J.,** Clinical implementation of electric impedance tomography in the treatment of ARDS: a single centre experience, J. Clin. Monit. Comput. 33 (2) (2019) 291–300.

12. **Putensen C., Hentze B., Muenster S., Muders T.,** Electrical Impedance Tomography for Cardio-Pulmonary Monitoring, J. Clin. Med. 8 (8) (2019) 1176.

13. **Karnaukhov V.V., Akishina E.S., Gerashchenko S.M.,** Investigation of the Process of Pressure Transfer From the Artery to the Cuff, Taking into Account the Soft Tissues of the Shoulder Tissue, 2023 IEEE Ural-Siberian Conference on Computational Technologies in Cognitive Science, Genomics and Biomedicine (CSGB), Novosibirsk, Russian Federation. (2023) 64–68.

14. **Antipenko V.V., Pecherskaya E.A., Zinchenko T.O., Melnikov O.A., Fimin A.V., Zaryvahina S.A.,** Analysis of methodological errors in measuring a digital automated bio-impedance meter, Journal of Physics: Conference Series. 1695 (1) (2020) 012051.

THE AUTHORS

LEVIN Alexis I.
levin.alescha2013@yandex.ru
ORCID: 0000-0003-0428-2319

ANTIPENKO Vladimir V.
v.antipenko7@yandex.ru
ORCID: 0000-0003-0274-7004

PECHERSKAYA Ekaterina A.
pea1@list.ru
ORCID: 0000-0001-5657-9128

YAKUSHOV Dmitriy V.
hammer.fate@yandex.ru
ORCID: 0009-0005-0892-312X

SHEPELEVA Juliya V.
eduard.shepelev.67@mail.ru
ORCID: 0000-0001-5075-2727

ARTAMONOV Dmitriy V.
dmitrartamon@yandex.ru
ORCID: 0000-0002-3240-7222

Received 09.07.2024. Approved after reviewing 01.08.2024. Accepted 06.08.2024.

Conference materials
UDC 538.9
DOI: https://doi.org/10.18721/JPM.173.119

Ab initio study of In adsorption on $Al_xGa_{1-x}As$ substrates at the first stages of droplet epitaxy

D.D. Dukhan [1] ✉, S.V. Balakirev [1], E.N. Voloshina [2], M.S. Solodovnik [1]

[1] Southern Federal University, Rostov-on-Don, Russia;
[2] Shanghai University, Shanghai, China
✉ duhan@sfedu.ru

Abstract. In this work we study the adsorption of In on $Al_xGa_{1-x}As$ substrates at the first stage of droplet epitaxy with goal of explaining the anomalous behavior observed in previous experiments where an increase in the content of chemically active Al in $Al_xGa_{1-x}As$ substrates led to an increase in the surface mobility of In adatoms affecting the final distribution of InAs quantum dots. DFT simulations showed that when In adatoms directly interact with As-terminated substrates, there is no deviation from normal behavior, but when In binds with a fully formed In wetting layer, the results are in agreement with those observed in our experiments – increasing Al content led to a decrease in adsorption energy, which means that surface mobility of adatoms has increased. We assume that this specific effect of droplet epitaxy is caused by lack of a stabilizing As layer, allowing the formation of In dimer rows and direct interaction of adatoms with them.

Keywords: density functional theory, III-V, indium, surface mobility, quantum dots, droplet epitaxy, molecular beam epitaxy

Funding: RNF grant: A3B5 droplet epitaxy for quantum technologies. No. 22-79-10251

Citation: Dukhan D.D., Balakirev S.V., Voloshina E.N., Solodovnik M.S., Ab initio study of In adsorption on $Al_xGa_{1-x}As$ substrates at the first stages of droplet epitaxy. St. Petersburg State Polytechnical University Journal. Physics and Mathematics. 17 (3.1) (2024) 100–104. DOI: https://doi.org/10.18721/JPM.173.119

Материалы конференции
УДК 538.9
DOI: https://doi.org/10.18721/JPM.173.119

Моделирование адсорбции In на подложках $Al_xGa_{1-x}As$ в течение первых стадий капельной эпитаксии

Д.Д. Духан [1] ✉, С.В. Балакирев [1], Е.Н. Волошина [2], М.С. Солодовник [1]

[1] Южный федеральный университет, г. Ростов-на-Дону, Россия;
[2] Шанхайский Университет, г. Шанхай, Китай
✉ duhan@sfedu.ru

Аннотация. В данной работе проведены исследования адсорбции In на подложках $Al_xGa_{1-x}As$ на начальной стадии процесса капельной эпитаксии с целью объяснить аномальное поведение, наблюдающееся при росте квантовых точек этим методом – увеличение содержания химически активного Al в подложках $Al_xGa_{1-x}As$ приводит не к уменьшению, а к увеличению подвижности адатомов In, влияя на конечное распределение квантовых точек InAs. DFT моделирование показало, что при взаимодействии адатомов In непосредственно с подложкой, Al снижает поверхностную подвижность адатомов, тогда как формирование промежуточного смачивающего слоя In между подложкой и адатомами приводит к изменению зависимости на противоположную – увеличение

содержания Al приводит к уменьшению энергии адсорбции. Мы предполагаем, что данный эффект проявляется в капельной эпитаксии ввиду смены типа поверхностной структуры с As- на Me-стабилизированную, что приводит к непосредственному взаимодействию адатомов In с образовавшимся реконструированным смачивающим слоем.

Ключевые слова: теория функционала плотности, A3B5, индий, поверхностная подвижность, квантовые точки, капельная эпитаксия, молекулярно-лучевая эпитаксия

Финансирование: Грант РНФ: Капельная эпитаксия A3B5 для квантовых технологий. №22-79-10251.

Ссылка при цитировании: Духан Д.Д., Балакирев С.В., Волошина Е.Н., Солодовник М.С. Моделирование адсорбции In на подложках $Al_xGa_{1-x}As$ в течение первых стадий капельной эпитаксии // Научно-технические ведомости СПбГПУ. Физико-математические науки. 2024. Т. 17. № 3.1. С. 100–104. DOI: https://doi.org/10.18721/JPM.173.119

Introduction

Use of InAs/AlGaAs quantum dots for single-photon emission requires low density (< 10^8 cm^{-2}), high uniformity and reproducibility of the size, shape and distribution of quantum dots (QD). When growing QDs in the Stranski-Krastanov (S-K) mode on the surfaces of Al containing substrates, it is expected that high chemical activity of Al will inhibit the adsorbates mobility, allowing the adsorbates to form stronger bonds with the surface [1]. This means that increase in the Al content leads to an increase in the QD density, which means that the adatom mobility decreases.

At the same time, in droplet epitaxy (DE) the effect is the opposite – as shown in our previous work [2, 3], an increase in the Al content leads to a decrease in the droplet density, which means that the adatom mobility during the wetting layer formation [4] increases. At low growth temperatures (less than 300 °C), the influence of the substrate composition is relatively small: the average diameter of the droplet structures increases from 16 to 21 nm at 150 °C and from 35 to 41 nm at 200 °C with an increase in the aluminum fraction from 0 to 1. The density decreases by 1.5 – 2 times: from $3 \cdot 10^{10}$ cm^{-2} to $2 \cdot 10^{10}$ cm^{-2} at 150 °C and from $3 \cdot 10^{9}$ cm^{-2} to $1.7 \cdot 10^{9}$ cm^{-2} at 200 °C (Fig. 1).

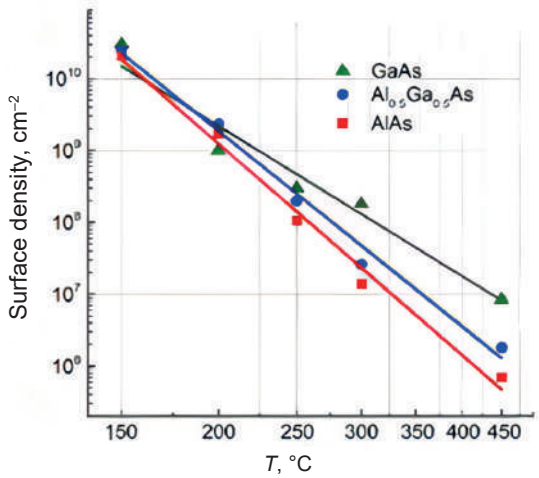

Fig. 1. Surface density of nanostructures obtained by droplet epitaxy after deposition of 3 ML of In on the GaAs, $Al_{0.5}Ga_{0.5}As$ and AlAs surfaces at different substrate temperatures

In the region of relatively high growth temperatures (high for droplet epitaxy of indium), the effect of the Al content is more pronounced. The density of indium droplet structures decreases by an order of magnitude: from $1.8 \cdot 10^8$ cm^{-2} down to $1.4 \cdot 10^7$ cm^{-2} at a substrate temperature of 300 °C and from $8.5 \cdot 10^6$ cm^{-2} to $7 \cdot 10^5$ cm^{-2} at 450 °C. In this case, the average size of droplet nanostructures doubles: from 98 to 176 nm at 300 °C and from 230 to 437 nm at 450 °C.

To see if this effect can be detected from first principles calculations, we modeled GaAs, $Al_{0.5}Ga_{0.5}As$ and AlAs covered by 0.25 ML and 1.25 ML of In (coverages representative of the first stages of droplet epitaxy), and calculated the resulting adsorption energies, which describe strength of bonding between the substrate and adatoms moving over it. The adsorption energy directly affects the adatom mobility, since the stronger the bond the adatom forms with the surface, the more difficult it becomes for it to move, which leads to a proportional decrease in the adatom mobility.

Methods

The adsorption energy was obtained using formula (1)

$$Eads_{0.25ML(1.25ML)} = E_{A3B5(+InML)+In} - E_{A3B5(+InML)} - E_{In}, \quad (1)$$

where $E_{A3B5(+InML)+In}$ is the total free energy of GaAs (covered with 1 ML of In) with an In atom on top, $E_{A3B5(+InML)}$ is the energy of GaAs (covered with 1 ML of In), and E_{In} is the energy of an indium atom in vacuum. A more negative value of *Eads* means a stronger bond between the adsorbate and the surface, which suppresses the adatom mobility, resulting in a higher density of nanostructures.

Ab initio calculations of the slab models were carried out using density functional theory (DFT). It was applied using the Vienna ab initio simulation package [5] with the projector augmented wave potential construction. For approximating the exchange-correlation functional we used Perdew's generalized-gradient-approximation (PBE) [6]. DFT+U method based on Dudarev's approach [7] was used to properly describe the interactions of p-band electrons. Simulation of parameters affected by random distribution of atoms in $Al_{0.5}Ga_{0.5}As$ alloy was achieved by use of special quasirandom structures [8]. After convergence testing K-point sampling density and cutoff energy values were set to 6x6x1 and 400 eV with higher values giving energy difference of less than 0.001 eV.

Since *Eads* would be different at different points of the surface, we calculated a potential energy surface (PES) plot, showing an approximate map of *Eads* obtained by interpolating the results of calculations over the surface on a uniform 5×5 grid. In the case of the 0.25 ML coverage calculations (Fig. 2 upper row), we put a single In adatom at grid coordinates over the As-terminated surfaces (which relax by forming As-dimer rows). In the case of a 1.25 ML coverage (Fig. 2 lower row), we study the interaction of the In adatom with the existing wetting layer (WL). This In WL also forms dimer rows during relaxation.

Results and discussion

Figure 2 shows the highest adsorption energy (which corresponds to the most favorable adsorption position) found after placing In adatoms at adsorption points forming a uniform 5×5 grid over the substrate surface for all coverages and substrates. Upper row of PES plots shows that max *Eads* changes with Al content at a low coverage of 0.25 ML. An increase in Al content leads to an increase in max *Eads* from −3.453 up to −3.823 eV for GaAs and AlAs, respectively, which means that adatom mobility decreases. This dependance matches the one seen in the S-K growth mode.

However, calculations at completely metal stabilized 1.25 ML coverage (Fig. 2 lower row), have shown that when In directly interacts with the dimer rows of the reconstructed In wetting layer (the relaxation step during the calculation results in the formation of dimer rows consisting of In adatoms), the behavior changes to one seen in our droplet epitaxy experiments, where an increase in the content of chemically active Al leads to a decrease in the adsorption energy from −4.289 down to −3.989 eV and consequently higher surface mobility. This shows that the observations obtained in our experiments are in good agreement with theory and can be explained by the nature of droplet epitaxy, in which an In wetting layer forms in the absence of a stabilizing As flux.

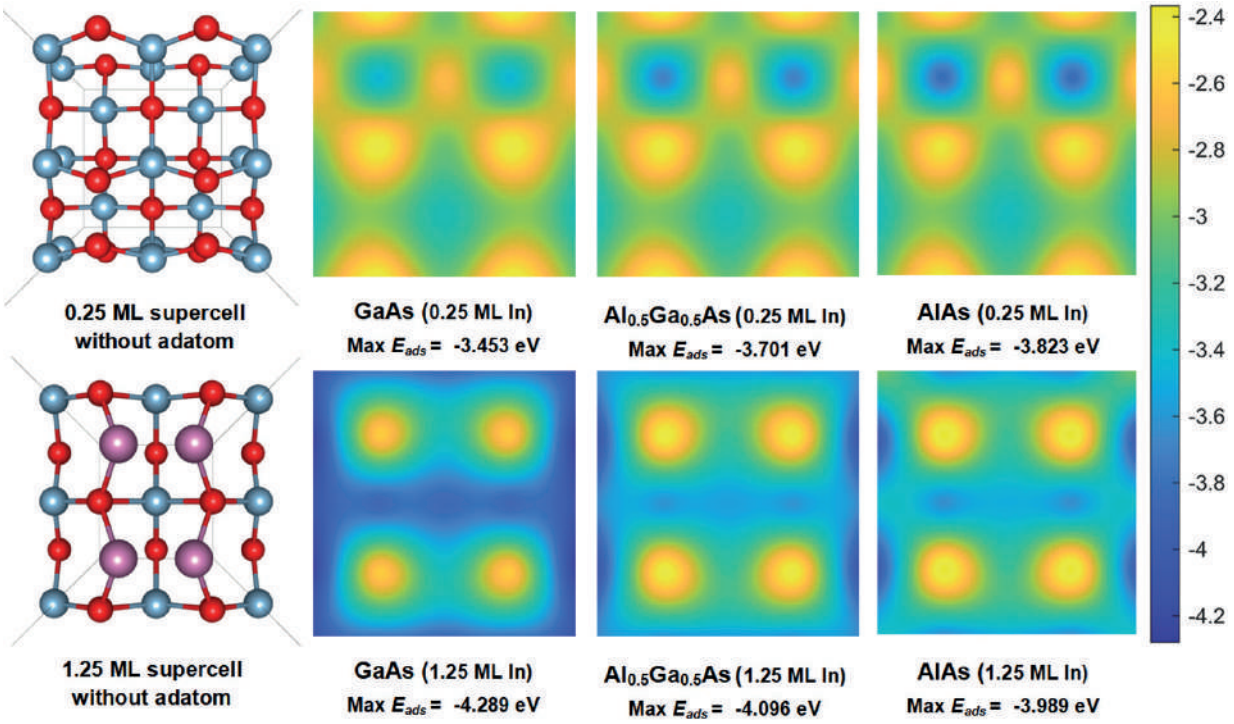

Fig. 2. PES plots showing *Eads* of In adatom on surfaces of $Al_xGa_{1-x}As$ substrates at 0.25 ML (1 In adatom) and 1.25 ML (4 In WL atoms + 1 In adatom) wetting layer coverage

This means that the change in the dependance of adatom mobility on Al content can be explained by the absence of a stabilizing As layer, which usually prevents the formation of In dimer rows and does not allow direct bonding of In adatoms to the already formed In wetting layer. These differences in the droplet epitaxy and S-K growth can be responsible for the studied effect, making them the subject of our future studies.

REFERENCES

1. **Andrews A. M., et al.,** Independent control of InAs quantum dot density and size on $Al_xGa_{1-x}As$ surfaces. Journal of Materials Science: Materials in Electronics. 19 (2008) 714–719.

2. **Balakirev S.V., et al.,** Anomalous behavior of In adatoms during droplet epitaxy on the AlGaAs surfaces. Nanotechnology. (31) (48) (2020) 485604.

3. **Chernenko N.E., et al.,** Effect of the Al content in the substrate on the In nanodroplets growth by droplet epitaxy. Journal of Physics: Conference Series. (1695) (1) (202).

4. **Dukhan D.D., Balakirev S.V., Voloshina E.N., Solodovnik M.S.,** Ab initio modelling of In wetting layer formation on As-stabilized GaAs during first stages of droplet epitaxy, St. Petersburg State Polytechnical University Journal. Physics and Mathematics. 16 (3.1) (2023) 193–197.

5. **Kresse G., Furthmüller J.,** Efficient iterative schemes for ab initio total-energy calculations using a plane-wave basis set. Physical review B. 54 (16) (1996) 11169.

6. **Perdew J.P., Burke K., Ernzerhof M.,** Generalized gradient approximation made simple. Physical review letters. 77 (18) (1996) 3865.

7. **Dudarev S.L., Botton G.A., Savrasov S.Y., Humphreys C.J., Sutton A.P.,** Electron-energy-loss spectra and the structural stability of nickel oxide: An LSDA+ U study. Physical Review B. 57 (3) (1998) 1505.

8. **Mäder K.A., Zunger A.,** Short-and long-range-order effects on the electronic properties of III-V semiconductor alloys. Physical Review B. (51) (16) (1995) 10462.

THE AUTHORS

DUKHAN Denis D.
duhan@sfedu.ru
ORCID: 0000-0002-6762-2053

BALAKIREV Sergey V.
sbalakirev@sfedu.ru
ORCID: 0000-0003-2566-7840

VOLOSHINA Elena N.
elena.voloshina@icloud.com
ORCID: 0000-0002-1799-1125

SOLODOVNIK Maxim S.
solodovnikms@sfedu.ru
ORCID: 0000-0002-0557-5909

Received 09.07.2024. Approved after reviewing 19.07.2024. Accepted 22.08.2024.

Conference materials
UDC 537.876
DOI: https://doi.org/10.18721/JPM.173.120

Simulation of an all-optical logical comparator based on a GaAs photonic crystal operating at a wavelength of 1.3 μm

M. Pleninger [1] ✉, S.V. Balakirev [1], M.S. Solodovnik [1]

[1] Southern Federal University, Taganrog, Russia

✉ pleninger@sfedu.ru

Abstract. This paper presents the results of simulation of a compact all-optical logical comparator based on a GaAs photonic crystal. The influence of geometric parameters of structural elements of the photonic crystal on characteristics of the comparator was studied in order to establish the optimal diameter of GaAs columns and the distance between them (period) for operation at a wavelength of 1.3 μm. Simulations of the dependences of the ratio of signal intensities at the input and output of the comparator show that it decreases with increasing diameter, both with one and both open channels. Calculating the difference between these ratios, we reveal that an optimal diameter of the photonic crystal columns is equal to 155 nm. After a similar study for the distance between the GaAs columns, we determine its optimal value as 600 nm.

Keywords: photonic crystal, logical comparator, GaAs

Funding: This work was funded by the Ministry of Science and Higher Education of the Russian Federation; the state task in the field of scientific activity No. FENW-2022-0034.

Citation: Pleninger M., Balakirev S.V., Solodovnik M.S., Simulation of an all-optical logical comparator based on a GaAs photonic crystal operating at a wavelength of 1.3 μm, St. Petersburg State Polytechnical University Journal. Physics and Mathematics. 17 (3.1) (2024) 105–109. DOI: https://doi.org/10.18721/JPM.173.120

Материалы конференции
УДК 537.876
DOI: https://doi.org/10.18721/JPM.173.120

Моделирование полностью оптического логического компаратора на основе фотонного кристалла GaAs, работающего на длине волны 1.3 мкм

М. Пленингер [1] ✉, С.В. Балакирев [1], М.С. Солодовник [1]

[1] Южный федеральный университет, г. Таганрог, Россия

✉ pleninger@sfedu.ru

Аннотация. В данной работе представлены результаты моделирования компактного полностью оптического логического компаратора на основе фотонного кристалла GaAs, работающего на длине волны 1.3 мкм. Исследовано влияние геометрических параметров структурных элементов фотонного кристалла на характеристики оптического компаратора. Показано, что наилучшие результаты достигаются при диаметре столбиков 155 нм и периоде между ними 600 нм.

Ключевые слова: фотонный кристалл, логический компаратор, GaAs

Финансирование: Работа выполнена при поддержке проекта Минобрнауки № FENW-2022-0034.

Ссылка при цитировании: Пленингер М., Балакирев С.В., Солодовник М.С. Моделирование полностью оптического логического компаратора на основе фотонного кристалла GaAs, работающего на длине волны 1.3 мкм // Научно-технические ведомости СПбГПУ. Физико-математические науки. 2024. Т. 17. № 3.1. С. 105–109. DOI: https://doi.org/10.18721/JPM.173.120

Introduction

Photonic crystals are a new class of inhomogeneous optical materials which are characterized by the presence of spatial periodic modulation of the dielectric constant with a period on the order of the light wavelength and photonic band gap in the spectrum of the crystal's own electromagnetic states [1]. A photonic bandgap (total or partial) is a frequency range within which light propagating in certain directions decays exponentially. In this case, the light incident on the photonic crystal is completely reflected. The emergence of a complete photonic band gap consists of the overlap of Bragg band gaps (stop bands) in all directions [2].

Photonic crystals have numerous practical and theoretical applications [3–6]. They are widely used in optical integrated circuits and light modulation. An important area of research on photonic crystals is the development of logical elements of photonic integrated circuits based on them. In particular, "NAND", "NOR", and "XNOR" logical gates based on photonic crystals were recently developed [7–8]. A logical comparator based on a GaAs photonic crystal was also simulated [9]. However, there is still a lack of studies devoted to the photonic crystals operating at a practically valuable wavelength of 1.3 μm.

In this work, we simulate the distribution of electric field strength (E) in an all-optical logical comparator based on a GaAs columnar photonic crystal operating at a wavelength of 1.3 μm. The choice of this wavelength is due to the fact that it is in the range of the second transparency window of the optical fiber and has zero dispersion [10]. Furthermore, widely used and highly manufacturable InGaAs quantum dots emit at this wavelength [11].

Model Description

The simulations were carried out using COMSOL Multiphysics 6.1. The optical comparator has two input and two output channels. When radiation is introduced into both input channels, the light propagating along the waveguides is almost completely extinguished at the point of their intersection. When radiation is introduced only into the first or second channel, the light passes through the waveguide with minimal losses.

The present study was carried out for a photonic crystal with a hexagonal lattice. A hexagonal lattice is the preferred structure option because it allows maximum reflection of radiation with a frequency belonging to the photonic band gap [12]. The structure consists of 15 horizontal columns and 13 vertical columns. The length of the structure is 8.4 μm, the width is 7.2 μm. Some columns were removed so as to form two intersecting waveguides through which the applied signal passes. The diameter of the GaAs columns (d) varied from 130 to 170 nm. Columns with a smaller diameter of 83 nm (1 column) and 62 nm (4 columns), respectively, were also added to the structure to provide light attenuation at the point where the waveguides intersect. The distance between the columns of the photonic crystal (a), which affects the penetration depth of electromagnetic radiation, varied in the range of 450–750 nm.

Results and Discussion

Figure 1 visualizes the distribution of the electric field strength depending on the columns diameter and spacing. Figures 1, *a* and 1, *b* show the operation of the comparator with one and two working channels, respectively. The columns diameter and spacing in Figures 1, *a* and 1, *b* is 130 and 600 nm, respectively. One can see that the comparator works incorrectly in this case because the radiation is practically not reflected at the intersection of the waveguides but continues to pass through them with small losses (Fig. 1, *b*).

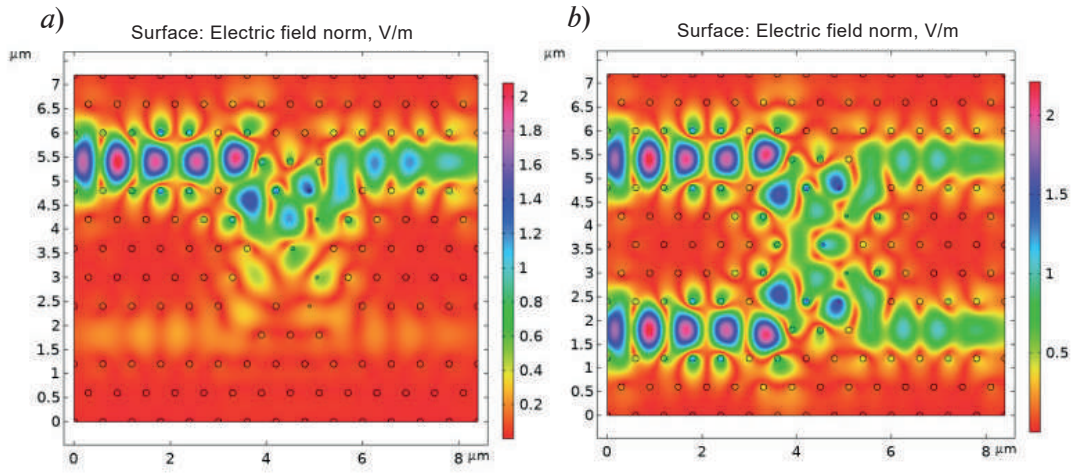

Fig. 1. Distribution of the electric field strength (color bar, V/m) in the logical comparator with one (*a*) and two (*b*) open channels: d = 130 nm, a = 600 nm

Figures 2, *a* and 2, *b* also present the results of simulation of the logical comparator with a column diameter of 155 nm and a structure period of 500 nm with one and two open channels, respectively. When both channels are opened, the radiation is almost completely attenuated at the intersection of the waveguides (Fig. 2, *b*), which meets the requirements of a photonic comparator [13]. However, with one channel open (upper waveguide, Fig. 2, *a*), there is a significant reflection of light at the intersection, which prevents the signal from propagating to the comparator output.

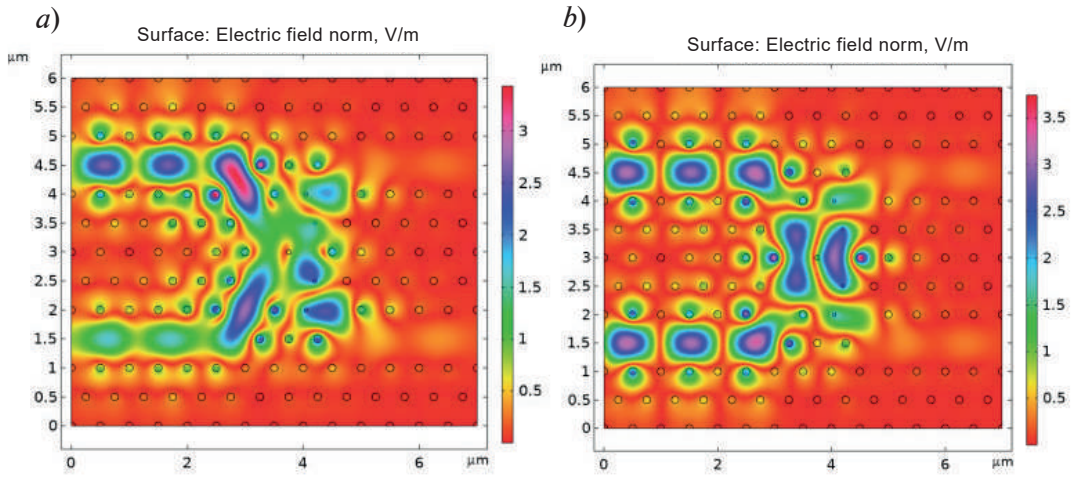

Fig. 2. Distribution of the electric field strength (color bar, V/m) in the logical comparator with one (*a*) and two (*b*) open channels: d = 155 nm, a = 500 nm

Next, the simulation of the electrical field strength distribution in the comparator with a column diameter of 155 nm and a period of 600 nm was carried out. Figure 3 demonstrates that this geometry meets the requirement for the operation of a logical comparator. With one open channel (Fig. 3, *a*), the radiation passes through the channel with minimal losses, but with both open channels (Fig. 3, *b*), it is attenuated at the intersection of the waveguides.

For better visualization, a ratio of the signal intensities (electric field strengths) at the input and the output of the comparator was plotted against the diameter of GaAs columns (Fig. 4, *a*) and their spacing (Fig. 4, *b*). A red curve with round markers in Figure 4 indicates the output/input (O/I) signal ratio in the case of one open channel. The value of this ratio should be as high as possible to provide low attenuation of the signal. The blue curve with square markers indicates the O/I signal ratio in the case of two open channels. In contrast, this value should be as small as possible to provide the signal attenuation at the intersection of the two waveguides. Therefore,

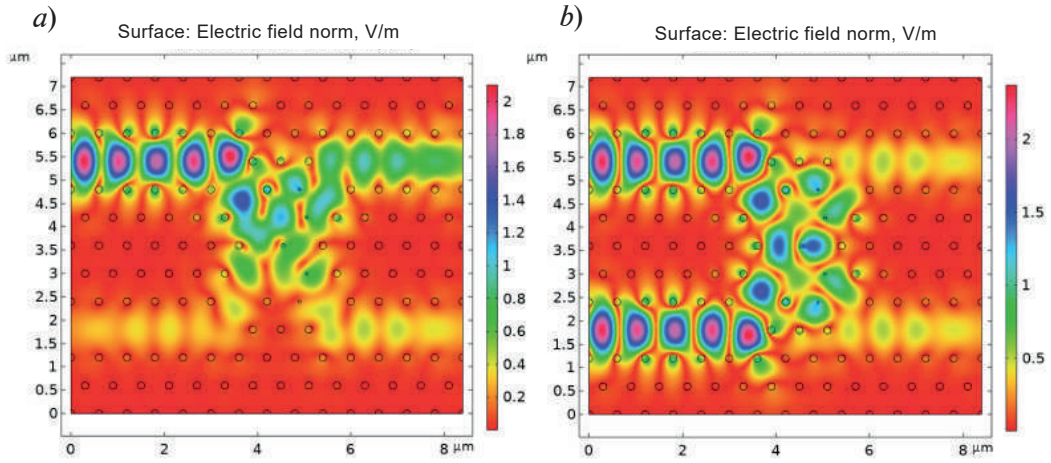

Fig. 3. Distribution of the electric field strength (color bar, V/m) in the logical comparator with one (*a*) and two (*b*) open channels: $d = 155$ nm, $a = 600$ nm

the difference between these two values (black curve with triangular markers) should be high to achieve the optimal comparator performance. The green dashed circles mark the optimal values for the diameter of the GaAs columns and the distance between them.

As one can see in Figure 4, *a*, the maximum value of the difference between the O/I signal intensity ratios is achieved at a column diameter of 155 nm. Similarly, the optimal distance between GaAs columns was found to be 600 nm (Fig. 4, *b*).

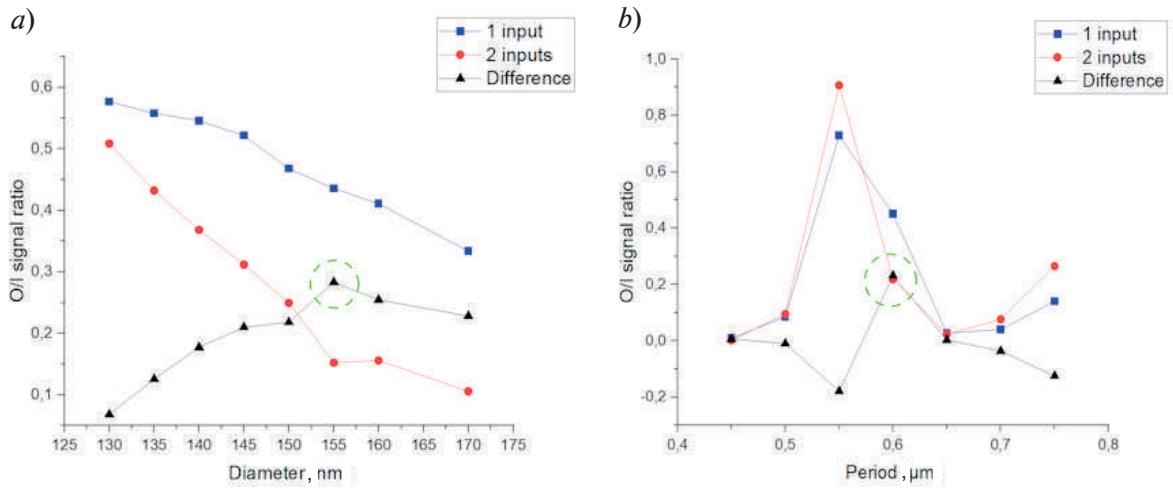

Fig. 4. Dependence of the output/input (O/I) signal intensity ratios and their difference on the diameter of GaAs columns (*a*) and their spacing (*b*)

Conclusion

This paper presented the results of simulation of the propagation of electromagnetic radiation in the optical comparator. This comparator used a two-dimensional photonic crystal with a hexagonal crystal lattice. To reflect radiation in a photonic crystal, columns of GaAs were built into its structure. By removing several GaAs columns, two intersecting waveguides were created. It was established that the optimal diameter of GaAs columns for the propagation of radiation with a wavelength of 1.3 μm is 155 nm, and the period is 600 nm.

REFERENCES

1. **Yablonovitch E.,** Inhibited Spontaneous Emission in Solid-State Physics and Electronics, Phys. Rev. Lett. 58 (20) (1987) 2059–2062.

2. **Dyachenko P.N., Miklyaev Y.V., Dmitrienko V.E.,** Three-dimensional photonic quasicrystal with a complete band gap, JETP Lett. 86 (4) (2007) 240–243.

3. **Zheltikov A.M.,** Nonlinear optics of microstructure fibers, Uspekhi Fiz. Nauk. 174 (1) (2004) 73.

4. **Sychov M.D., Kiselev I.L., Dronov S.P., Khvostovoi V.V., Frolova O.G., Sukovatykh B.S., Shatalov G.V., Vyacheslav Kuznetsov, Zviagin I.N.,** Substantiation Study of Using Immobilized Cytostatics in Management of Tumors with Peritoneal Canceromatosis, Vestn. Exp. Clin. Surg. 8 (1) (2015) 82–86.

5. **Hassan S., Chack D., Pavesi L.,** High extinction ratio thermo-optic based reconfigurable optical logic gates for programmable PICs. 12 (5) (2022) 055304.

6. **Olyaee S., Naraghi A., Ahmadi V.,** High sensitivity evanescent-field gas sensor based on modified photonic crystal fiber for gas condensate and air pollution monitoring, Optik (Stuttg). 125 (1) (2014) 596–600.

7. **Tamer A. Moniem.,** All-optical XNOR gate based on 2D photonic-crystal ring resonators, Quantum Electronics. 47 (2) (2017) 169–172.

8. **Sun Xiao-Wen., Yang Xiu-Lun., Meng Xiang-Feng., Ji-Nan Zhang.,** Design and analysis of logic NOR, NAND and XNOR gates based on interference effect, Quantum Electronics. 48 (2) (2018) 178–183.

9. **Parandin F.,** Ultra-compact terahertz all-optical logic comparator on GaAs photonic crystal platform, Opt. Laser Techbol. 144 (2021) 169–172.

10. **Brès C.-S., Alberto Della Torre., Davide Grassani., Victor Brasch., Christian Grillet., Christelle Monat.,** Supercontinuum in integrated photonics: generation, applications, challenges, and perspectives, Nanophotonics. 12 (7) (2023) 1199–1244.

11. **García de Arquer F.P., Dmitri V. Talapin., Victor Klimov., Yasuhiko Arakawa., Manfred Bayer., Edward H. Sargent.,** Semiconductor quantum dots: Technological progress and future challenges. 373 (6555) (2021) 8541.

12. **Gorbatsevich A.A., Freeman A.V., Gorelik B.C.,** Two-dimensional hexagonal photonic crystal with a new element geometry, Brief communications on physics of the Lebedev Physical Institute. 6 (2014) 37–38.

13. **Parandin F., Olyaee S., Kamarian R., Jomour M.,** Design and Simulation of Linear All-Optical Comparator Based on Square-Lattice Photonic Crystals. 9 (7) (2022) 459.

THE AUTHORS

PLENINGER Maximilian
pleninger@sfedu.ru

BALAKIREV Sergey V.
sbalakirev@sfedu.ru
ORCID: 0000-0003-2566-7840

SOLODOVNIK Maxim S.
solodovnikms@sfedu.ru
ORCID: 0000-0002-0557-5909

Received 11.07.2024. Approved after reviewing 31.07.2024. Accepted 31.07.2024.

Conference materials
UDC 535
DOI: https://doi.org/10.18721/JPM.173.121

Resonant scattering of silicon nanopillars for nonlinear optics

V.M. Kondratev [1, 2] ✉, A. Kuznetsov [1, 2], E.S. Zavyalova [1, 2],
M.A. Anikina [1, 2], A.D. Bolshakov [1, 2, 3]

[1] Alferov University, St. Petersburg, Russia;
[2] Moscow Institute of Physics and Technology, Dolgoprudny, Russia;
[3] St. Petersburg State University, St. Petersburg, Russia
✉ kvm_96@mail.ru

Abstract. This article summarizes the findings of a study on resonant scattering from single silicon nanopillars on a native substrate in the visible and near infrared spectral ranges. The study utilizes numerical simulation finite-difference time-domain method to investigate the effects of lateral and vertical dimensions of the pillars on their scattering behavior. The results show that manipulating the dimensions can shift resonance modes and enhance scattering intensity. Various pillars design variations are explored, including different lengths and radii, with the aim of optimizing scattering intensity for up-conversion devices.

Keywords: resonant scattering, silicon pillars, nonlinear optics

Funding: Ministry of Science and Higher Education of the Russian Federation (Grant FSRM-2023-0009).

Citation: Kondratev V.M., Kuznetsov A., Zavyalova E.S., Anikina M.A., Bolshakov A.D., Resonant scattering of silicon nanopillars for nonlinear optics, St. Petersburg State Polytechnical University Journal. Physics and Mathematics. 17 (3.1) (2024) 110–114. DOI: https://doi.org/10.18721/JPM.173.121

Материалы конференции
УДК 535
DOI: https://doi.org/10.18721/JPM.173.121

Резонансное рассеяние одиночных кремниевых наностолбиков для нелинейной оптики

В.М. Кондратьев [1, 2] ✉, А. Кузнецов [1, 2], Е.С. Завьялова [1, 2],
М.А. Аникина [1, 2], А.Д. Большаков [1, 2, 3]

[1] Академический университет им. Ж.И. Алферова, Санкт-Петербург, Россия;
[2] Московский физико-технический институт (национальный исследовательский университет), г. Долгопрудный, Россия;
[3] Санкт-Петербургский государственный университет, Санкт-Петербург, Россия
✉ kvm_96@mail.ru

Аннотация. Данная работа посвящена исследованию резонансного рассеяния одиночных кремниевых наностолбиков для решения задач нелинейной оптики. Показаны оптимальные геометрии кремниевых столбиков, обладающие максимальной интенсивностью рассеяния, которые могут быть использованы для создания устройств нанофотоники.

Ключевые слова: резонансное рассеяние, кремниевый столбик, нелинейная оптика

Финансирование: Министерство науки и высшего образования Российской Федерации (грант № FSRM-2023-0009).

Ссылка при цитировании: Кондратьев В.М., Кузнецов А., Завьялова Е.С., Аникина М.А., Большаков А.Д. Резонансное рассеяние одиночных кремниевых наностолбиков для нелинейной оптики // Научно-технические ведомости СПбГПУ. Физико-математические науки. 2024. Т. 17. № 3.1. С. 110–114. DOI: https://doi.org/10.18721/JPM.173.121

Introduction

Silicon micro- and nanostructures, such as pillars and wires [1, 2], are commonly employed in photonics and sensor applications [3–8]. Resonant scattering from silicon pillars on a substrate in the visible and near infrared spectral ranges is of particular interest for developing nonlinear optical devices. This study focuses on investigation of the resonant scattering of individual silicon columns to address challenges in the field of nonlinear optics. We use numerical modeling to study the interaction between light and silicon nanopillars with the goal of optimizing the structures' geometry to enhance the second harmonic (SH) response. By carefully analyzing the impact of various parameters on the nanopillar structures, we were able to determine the optimal geometry. Our results demonstrate the importance of precise control over the geometry of the nanopillars in order to achieve enhanced SH generation. These findings have important implications for the development of efficient photonic devices and applications.

Materials and Methods

To optimize the second harmonic generation (SHG) in Si pillars the numerical simulation was utilized. The calculations were carried out with an aid of finite-difference time-domain method (FDTD) according to Yee algorithm in Ansys Lumerical software. Single pillars were modeled as cylinders of different height and radius on native Si substrate. The spatial mesh step was 5 nm and the boundary conditions were absorptive (perfectly-matched layer, PML) to avoid artificial reflection in the simulation region. The excitation was simulated by the broadband plane wave source located at a 1-micron distance from the pillar edge directed perpendicularly to the substrate. To achieve more precise evaluation of the scattered field it was monitored only above the structure to be in agreement with the dark-field spectroscopy experimental setup collecting backscattered signal. The calculations were provided in 500–1300 nm spectral range. Geometry of the problem is demonstrated in Fig. 1.

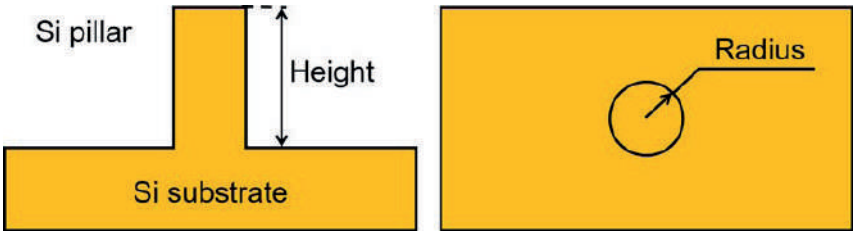

Fig. 1. Schematic of the single Si pillar for simulation

Results and Discussion

In this work we investigated the possibility of the SHG from single Si pillars. Si lattice is known to posses the inversion symmetry and second-order dielectric permeability equals zero. But, on the other hand, in the vicinity of the surface the symmetry is no longer preserved so, that is why we can achieve second-order nonlinear response. Also, according to the experimental works [4–7] such types of structures are synthesized by etching which affects the surface layers

which undergo amorphization breaking the inversion symmetry. The first step to analyze the possibility of the SHG in single nanostructures and metasurfaces is to calculate its scattering spectra and its dependencies from the geometry. The main goal is to match scattering peaks with pump and SHG spectral position [8]. For the structure under consideration, we estimate the SHG signal at 550 nm. To find resonant modes we calculated scattering spectra in 500–1300 nm spectral range for pillars height of 0.35, 0.4, 0.45, 0.5, 1.2, 1.4, 1.6, 1.8 and 2 μm in the range of radii 50–600 nm. In Fig. 2 the scattering spectra intensity maps for different diameters and heights of 0.45 and 1.8 μm are demonstrated.

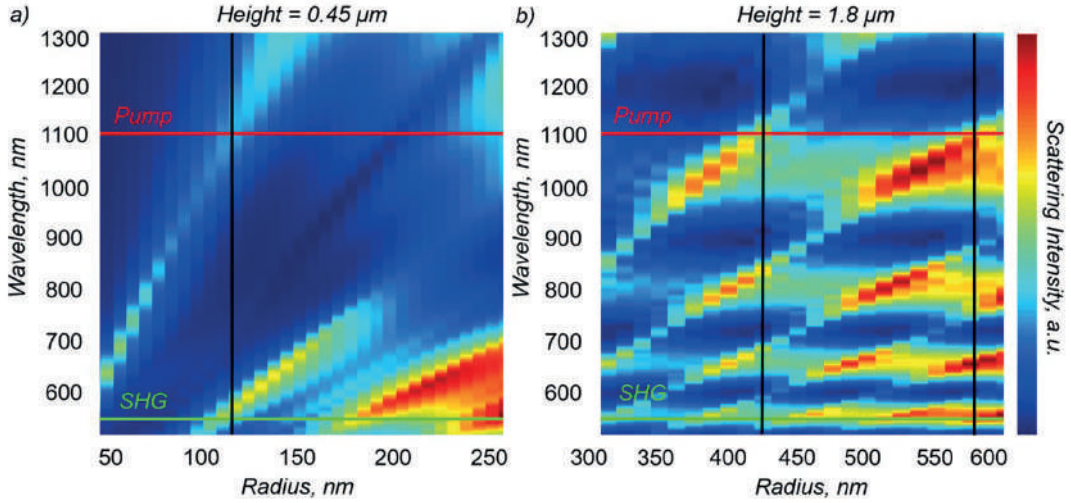

Fig. 2. Scattering spectra of the single Si pillars of different radii (*a*) 0.45 μm and (*b*) 1.8 μm tall

In Fig. 2 we can see scattering modes evolution with increase of the pillars radius. Two degrees of freedom (radius and height) allow us to precisely control the number of resonant modes and its spectral position. For example, using the pillar with the radius of 112.5 nm and the height of 0.45 μm provides the perfect match of two scattered modes with pump and SHG spectral lines. Instead of utilizing very small pillars which fabrication could be challenging it is evident from (Fig. 2, *b*) that we can achieve prominent resonant response from pillars higher than 1 μm and thicker than 300 nm (radius). In this case we achieve one order higher scattering intensity but the number of modes drastically increases with the increase of pillars height (Fig. 3). Additional longitudinal modes can affect the energy redistribution between them and decrease the SHG response intensity.

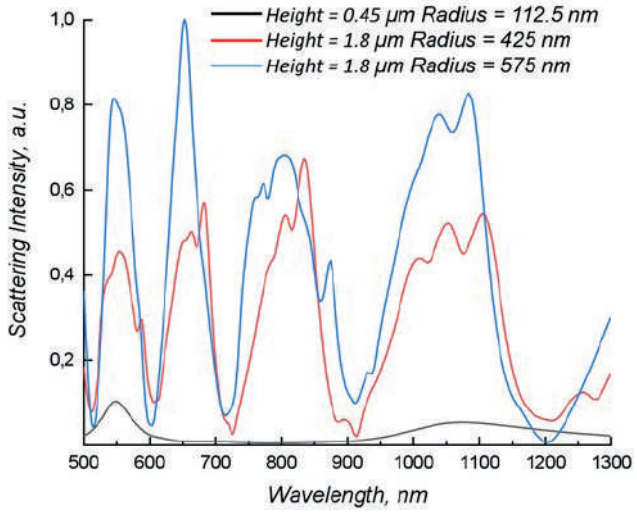

Fig. 3. Scattering spectra of the single Si pillars 0.45, 1.80 μm high and with the radii of 112.5, 425.0 and 575.0 nm

Conclusion

To sum up we demonstrate resonant scattering from the single Si pillars on the native substrate in the visible and near IR spectral ranges using numerical simulation finite-difference time-domain method. Precise control of the pillars lateral and longitudinal dimensions drastically affect the scattering behaviour of the pillar by shifting the resonant modes and changing their number. We demonstrate that there are several pillar designs having resonant features in the range of pump (1100 nm) and SHG (550 nm) lines with heights of 0.45 and 1.8 μm and radii of 112.5, 425 and 575 nm. More precise optimization should be carried out to achieve the structure with maximum scattering intensity in the spectral range of interest and it will open up the new pathways in design of the CMOS-compatible resonant up-conversion devices.

Acknowledgments

Authors thanks the Ministry of Science and Higher Education of the Russian Federation (Grant FSRM-2023-0009) for their support of the studies on the nonlinear response of silicon pillars and the identification of the underlying nature of this response.

REFERENCES

1. **Bolshakov A.D., Mozharov A.M., Sapunov G.A., Fedorov V.V., Dvoretckaia L.N., Mukhin I.S.,** Theoretical modeling of the self-catalyzed nanowire growth: nucleation-and adsorption-limited regimes. Materials Research Express. 4 (12) (2017) 125027.

2. **Dubrovskii V.G., Bolshakov A.D., Williams B.L., Durose K.,** Growth modeling of CdTe nanowires. Nanotechnology. 23(48) (2012) 485607.

3. **Bolshakov A.D., Shishkin I., Machnev A., Petrov M., Kirilenko D.A., Fedorov V.V., Ginzburg P.,** Single GaP nanowire nonlinear characterization with the aid of an optical trap. Nanoscale. 14 (3) (2022) 993–1000.

4. **Hsu C.M., Connor S.T., Tang M.X., Cui Y.,** Wafer-scale silicon nanopillars and nanocones by Langmuir-Blodgett assembly and etching, Appl Phys Lett 93 (2008).

5. **Chen W., Ahmed H.,** Fabrication of high aspect ratio silicon pillars of <10 nm diameter, Appl Phys Lett 63 (1993).

6. **Kondratev V.M., Morozov I.A., Vyacheslavova E.A., Kirilenko D.A., Kuznetsov A., Kadinskaya S.A., Nalimova S.S., Moshnikov V.A., Gudovskikh A.S., Bolshakov A.D.,** Silicon Nanowire-Based Room-Temperature Multi-environment Ammonia Detection, ACS Appl Nano Mater 5 (2022) 9940–9949.

7. **Kondratev V.M., Vyacheslavova E.A., Shugabaev T., Kirilenko D.A., Kuznetsov A., Kadinskaya S.A., Shomakhov Z.V., Baranov A.I., Nalimova S.S., Moshnikov V.A., Gudovskikh A.S., Bolshakov A.D.,** Si Nanowire-Based Schottky Sensors for Selective Sensing of NH3 and HCl via Impedance Spectroscopy, ACS Appl Nano Mater 6 (2023) 11513–11523.

8. **Makarov S.V., Petrov M.I., Zywietz U., Milichko V., Zuev D., Lopanitsyna N., Kuksin A., Mukhin I., Zograf G., Ubyivovk E., Smirnova D.A., Starikov S., Chichkov B.N., Kivshar Y.S.,** Efficient Second-Harmonic Generation in Nanocrystalline Silicon Nanoparticles, Nano Lett 17 (2017).

THE AUTHORS

KONDRATEV Valeriy M.
kvm_96@mail.ru
ORCID: 0000-0002-3469-5897

ANIKINA Maria A.
anikina_mar@spbau.ru
ORCID: 0000-0002-5522-5026

KUZNETSOV Alexey A.
alkuznetsov1998@gmail.com
ORCID: 0000-0001-7143-6686

BOLSHAKOV Alexey D.
acr1235@mail.ru
ORCID: 0000-0001-7223-7232

ZAVYALOVA Eseniya S.
ladieseniya@gmail.com
ORCID: 0009-0003-5049-538X

Received 12.07.2024. Approved after reviewing 02.08.2024. Accepted 02.08.2024.

Conference materials
UDC 535.3
DOI: https://doi.org/10.18721/JPM.173.122

Numerical modal analysis of GaP optical microcavity

A.S. Funtikova [1, 2] ✉, A.M. Mozharov [1, 2], V.V.Fedorov [1, 2],
V.A.Sharov [1, 3], I.S. Mukhin [1, 2]

[1] Alferov University, St. Petersburg, Russia;
[2] Saint-Petersburg Polytechnic University, St. Petersburg, Russia;
[3] Ioffe Institute, St. Petersburg, Russia
✉ n.fn@mail.com

Abstract. Despite the highly developed level of the silicon technology, efficiency of silicon-based photon devices is limited by material properties. In contrast, III-V materials are mostly applicable to make such type of devices as well as fabricating them in nanowire (NW) form provides compatibility with silicon technology. GaP(NAs) is a useful material system for optoelectronics because of tunable bandgap with controllable directivity and high refractive index. The eigenmodes of the Fabry-Perot resonator based on GaP NWs have been investigated. The simulation results showed that raise in diameter leads to the increase in the number of optical modes having different light distribution due to transverse mode type. Quality factor analysis shows growth in its values with the increase in structures' diameters.

Keywords: nanowires, gallium phosphide, Fabry-Perot resonance, waveguide modes

Funding: This study was funded by the Ministry of Science and Higher Education grant number FSEG-2024-0017.

Citation: Funtikova A.S., Mozharov A.M., Fedorov V.V., Sharov V.A., Mukhin I.S., Numerical modal analysis of GaP optical microcavity, St. Petersburg State Polytechnical University Journal. Physics and Mathematics. 17 (3.1) (2024) 115–119. DOI: https://doi.org/10.18721/JPM.173.122

Материалы конференции
УДК 535.3
DOI: https://doi.org/10.18721/JPM.173.122

Модовый анализ оптических микрорезонаторов GaP

А.С. Фунтикова [1, 2] ✉, А.М. Можаров [1, 2], В.В. Федоров [1, 2],
В.А. Шаров [1, 3], И.С. Мухин [1, 2]

[1] Академический университет им. Ж.И. Алфёрова РАН, Санкт-Петербург, Россия;
[2] Санкт-Петербургский политехнический университет Петра Великого, Санкт-Петербург, Россия;
[3] Физико-технический институт им. А.Ф. Иоффе РАН, Санкт-Петербург, Россия;
✉ n.fn@mail.ru

Аннотация. Несмотря на высокий уровень развития кремниевой технологии, эффективность фотонных устройств на основе кремния ограничена свойствами материала. Материалы группы III-V более применимы для создания устройств такого типа, а их изготовление в форме нитевидных нанокристаллов (ННК) обеспечивает совместимость с кремниевой технологией. GaP(NAs), благодаря перестраиваемой запрещенной зоне и высокому показателю преломления, является перспективной

системой для оптоэлектроники. В работе был исследован модовый состав резонатора Фабри-Перо на основе ННК GaP. Результаты моделирования показали, что увеличение диаметра приводит к росту числа оптических мод с различным распределением света за счет поперечного типа моды. Анализ коэффициента добротности показывает рост его значений с увеличением диаметра структур.

Ключевые слова: нитевидные нанокристаллы, фосфид галлия, резонанс Фабри-Перо, волноводные моды

Финансирование: Работа выполнена при финансовой поддержке Министерства науки и высшего образования (грант государственного задания FSEG-2024-0017).

Ссылка при цитировании: Фунтикова А.С., Можаров А.М., Федоров В.В., Шаров В.А., Мухин И.С. Модовый анализ оптических микрорезонаторов GaP // Научно-технические ведомости СПбГПУ. Физико-математические науки. 2024. Т. 17. № 3.1. С. 115–119. DOI: https://doi.org/10.18721/JPM.173.122

Introduction

Increase in the amount of transmitted information leads to enhancing data transfer speed which requires new technological and conceptual solutions for transmissive circuits. One of the promising approaches to achieve high-speed on-chip systems is based on using integrated optics instead of metal conductors. Passive optical elements can be made with well-known silicon technology, but it requires not only special IR light sources, but IR detectors. On the other hand to employ Si detectors SiNx technology can be used to work in visible or near IR spectrum range, but its low refractive index limits minimal size of photonic elements not to mention the requirement of light sources.

Other perspective materials are III-V semiconductors, including gallium phosphide. Good quality crystals can be grown on Si substrate due to the good lattice matching. High refractive index [1] and transparency in wide visible and infrared range [2], thus, small optical losses in this part of the spectrum, make GaP structures very promising for use in photonic integrated circuits. In general, gallium phosphide has indirect band gap, but it is possible to make it direct with As and N doping [3], which make them interesting not only for passive circuits' elements, but also active, such as lasers, light-emitting diodes, waveguides and nanoantennas. But in case of small sized light sources the planar technology approves oneself unfit due to required etching that leads to the appearance of free lateral surface, which can cause additional losses and reduce efficiency.

The solution can be III-V nanowires (NWs). They demonstrate high crystallinity and can also be grown on Si substrate, so, can be compatible with silicon technology [4] and efficiently used in nanophotonics due to their size. NWs lateral surfaces that have mirror-like quality also can be passivated by growing core-shell structures. It is important to mention that selective area growth methods can be used for element's construction in a predetermined location and solve the problem of placing and adjusting light sources with passive elements.

In optical integrated photonics, precise control over the direction of light distribution and mode structure is crucial for achieving high performance and functionality in photonic devices. This control affects several important aspects of photonics, including signal integrity, wavelength-division multiplexing, interconnect efficiency, and the performance of optical sensors. Selection of NWs parameters can help in optical alignment with other elements. Effective management of light paths improves signal routing, multichannel processing capabilities, and the ability to integrate complex functions into smaller chip areas. This enhances the development of compact, fast, and energy-efficient optical systems.

In this work numerical modal analysis of different size microcavities based on GaP NWs was done. The main goal of the work was to obtain correlation between NW size, wavelength and the NW's optical modal structure to specify optimal conditions for use GaP(NAs) NW as a small size optical source for integrated photonic circuits.

Materials and Methods

In our study COMSOL Multiphysics was used to simulate the necessary phenomenon. The MUMPS (multifrontal massively parallel sparse direct solver) was used to obtain the solutions. Also we use parametric sweeps to change diameter and length of the structure to analyze all necessary configurations. To get rid of any interference phenomena, a perfect matched layer (PML) on external boundaries was used. Refractive and extinction indexes for GaP, used for our calculations, were taken from [5]. Environment was declared as air with refractive index $n = 1$ and no extinction.

Results and Discussion

Due to the high refractive index and atomically smooth surfaces GaP NWs are able to localize electromagnetic waves and act as a resonator. NW's geometry has high asymmetry and, in consideration with general oscillations theory, one can expect a high level separation of the modal structure into groups, where the behavior within and between groups corresponds to a change in the order of resonance along or across the NW axis. Resonance appearance in the system caused by the fulfillment of the constructive interference conditions. Numerically it means that the product of wave vector and geometrical size of the system must equals defined discrete values. Wave vector in turn usually has an unknown value, and for system characterization a new parameter with close physical meaning is convenient in use. This parameter represents the ratio between geometrical size and wavelength. For the considered system a numerical calculation of modal structure was held and quality factor dependence on the size parameter $x = d/\lambda$ (d is NW diameter, λ is operating wavelength), which is shown on (Fig. 1, *a*), was built. Each point on this graph represents a resonance.

It can be seen that the increase in size parameter (this corresponds to rise in NW diameters or usage of more short-wave light) leads to the appearance of higher order resonant modes. Such stepwise nature of the dependence can be explained with the distribution possibility of resonant modes of different transverse order. Since increasing the x parameter the transverse

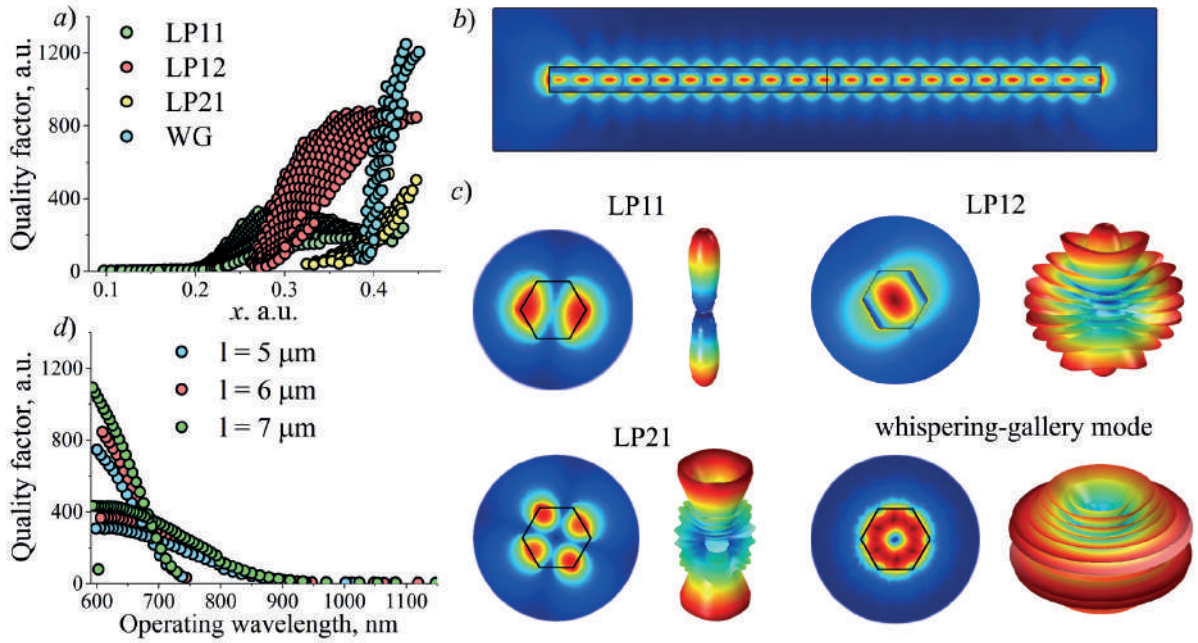

Fig. 1. Q-factor dependence on size parameters (NW length is 5 μm) for different modes in GaP NWs (*a*). Typical electric field distribution along the structure (*b*). Electric field distribution across the NW and far fields for some first transverse modes (*c*). Q-factor dependence on NW lengths (d = 200 nm) for different modes in GaP NWs (*d*)

wave vector increases too. It leads to the achievement of the next constant, representing the fulfillment of the constructive interference conditions for the next higher order transverse resonance. Likewise, within each group resonances are related to the changes in constructive interference conditions along NW. Based on the type of electric field distribution along the NW (Fig. 1, *b*), it can be concluded that the establishment of resonance conditions is associated with reflection from the NW's end surfaces and interference of electromagnetic wave. This fact suggests that the longitudinal component of the wave vector is represented by Fabry-Pérot resonances. Meanwhile in contradiction with typical Fabry-Pérot resonances behaviour, there is no plane wave in NW cross section, but the set of the transverse field distribution patterns (Fig. 1, *c*). It is related to spatial limitations for the wave by NW lateral surfaces. Thorough analysis of the transverse field distribution patterns shows that the main resonances set in the range of $x < 0.39$ is presented with transverse to the NW axis electromagnetic waves with linear electric polarization of increasing from 1 to 2 radial and azimuthal order, which changes with rise in size parameter. However, beginning with some value ($x = 0.39$) high quality whispering-gallery modes with azimuthal order equal to 3 can be detected. Typical Fabry-Pérot resonances have only longitudinal component of the wave vector. But in the considered system transverse component also can be detected and it was necessary to study the direction of light distribution, so the far field for the GaP NW is represented (Fig. 1, *c*). One of typical characteristic features is clearly seen on the far field diagrams: the end faces of the NWs for Fabry-Pérot modes are the largest sources of losses. Here we can see that LP11 mode is more directed than others: this corresponds to the minimal value of the wave vector transverse component.

Initially, it was expected to observe on (Fig. 1, *a*) distinct curves corresponding to each possible mode; however, instead of discrete curves, the graph displays "zones". These zones likely result from changes in the effective refractive index due to presence of the material dispersion. Growth of the q-factor with decrease in wavelength can be detected due to the rising of energy quantity that can stay in the resonator.

Also the dependence of q-factor on NW length was investigated (Fig. 1, *d*). Increase in NW length, as wavelength decreases, leads to growth in energy that can distribute in the resonator. But the end faces of the NW, which, as have been mentioned above, are the largest source of optical losses, don't increase in this process. These two reasons lead to the slight increase in modes' q-factor with rise in NW length.

Conclusion

We have demonstrated results of the numerical study of the GaP nanowires with different geometry configurations, which can fully describe the modal structure of these objects. The results of this calculation can be used for growing GaP NWs with known characteristics for integration into photonic circuits as lasers, light-emitting diodes, waveguides, etc.

Acknowledgments

The work was supported by the Ministry of Science and Higher Education (state assignment grant FSEG-2024-0017).

REFERENCES

1. **Khmelevskaia D., Markina D.I., Fedorov V.V., Ermolaev G.A., Arsenin A.V., Volkov V.S., Goltaev A.S., Zadiranov Yu.M., Tzibizov I.A., Pushkarev A.P., Samusev A.K., Shcherbakov A.A., Belov P.A., Mukhin I.S., Makarov S.V.,** Directly grown crystalline gallium phosphide on sapphire for nonlinear all-dielectric nanophotonics. Applied Physics Letters. 118 (20) (2021) 201101.

2. **Parsons D. F., Coleman P. D.,** Far Infrared Optical Constants of Gallium Phosphide. Appl. Opt. (10) (1971) 1683–1685.

3. **Geisz J.F., Friedman D.J., Kurtz S.,** [IEEE Conference Record of the Twenty-Ninth IEEE Photovoltaic Specialists Conference 2002 - New Orleans, LA, USA (19-24 May 2002)] Conference Record of the Twenty-Ninth IEEE Photovoltaic Specialists Conference, 2002. - GaNPAs solar cells lattice-matched to GaP. (0) (2002) 864–867.

4. **Zhang G., Tateno K., Sogawa T., Nakano H.,** Growth and characterization of GaP nanowires on Si substrate. Journal of Applied Physics. 103 (1) (2008) 014301.

5. **Adachi S.,** Optical dispersion relations for GaP, GaAs, GaSb, InP, InAs, InSb, $Al_xGa_{1-x}As$, and $In_{1-x}Ga_xAs_yP_{1-y}$. Journal of Applied Physics. 66 (12) (1989) 6030–6040.

THE AUTHORS

FUNTIKOVA Anastasiia S.
n.fn@mail.ru
ORCID: 0009-0000-3147-6974

SHAROV Vladislav A.
vl_sharov@mail.ru
ORCID: 0000-0001-9693-5748

MOZHAROV Alexey M.
mozharov@spbau.ru
ORCID: 0000-0002-8661-4083

MUKHIN Ivan S.
imukhin@yandex.ru
ORCID: 0000-0001-9792-045X

FEDOROV Vladimir V.
burunduk.uk@gmail.com
ORCID: 0000-0001-5547-9387

Received 22.07.2024. Approved after reviewing 07.08.2024. Accepted 08.08.2024.

ATOM PHYSICS AND PHYSICS OF CLUSTERS AND NANOSTRUCTURES

Conference materials
UDC 544.478-03
DOI: https://doi.org/10.18721/JPM.173.123

Nanostructured bimetallic PtNi catalyst for electrochemical systems with solid polymer electrolyte

M.D. Novichkov [1] ✉, S.A. Gurin [1], A.E. Shepeleva [1],
E.A. Pecherskaya [2], D.V. Agafonov [1], V.A. Ilyin [1]

[1] Joint Stock Company "Research Institute of Electronic and Mechanical Devices", Penza, Russia;
[2] Penza State University, Penza, Russia
✉ novichkov1998maks@gmail.com

Abstract. A method for forming a nanostructured bimetallic PtNi catalyst on the surface of a solid polymer electrolyte is presented. Nickel particles, on which the bulk of the platinum catalyst is grown by chemical deposition, are obtained by magnetron sputtering. The resulting system has high catalytic activity and temporary stability.

Keywords: bimetallic catalyst, solid polymer electrolyte, catalytic layer, magnetron sputtering, chemical deposition

Funding: The work was supported by the grant of the Ministry of Science and Higher Education of the Russian Federation "Synthesis and research of promising nanomaterials, coatings and electronics devices" (No. 124041700069-0).

Citation: Novichkov M.D., Gurin S.A., Shepeleva A.E., Pecherskaya E.A., Agafonov D.V., Ilyin V.A., Nanostructured bimetallic PtNi catalyst for electrochemical systems with solid polymer electrolyte, St. Petersburg State Polytechnical University Journal. Physics and Mathematics. 17 (3.1) (2024) 120–123. DOI: https://doi.org/10.18721/JPM.173.123

Материалы конференции
УДК 544.478-03
DOI: https://doi.org/10.18721/JPM.173.123

Наноструктурированный биметаллический катализатор PtNi электрохимических систем с твердополимерным электролитом

М.Д. Новичков [1] ✉, С.А. Гурин [1], А.Э. Шепелева [1],
Е.А. Печерская [2], Д.В. Агафонов [1], В.А. Ильин [1]

[1] АО «Научно-исследовательский институт электронно-механических приборов», г. Пенза, Россия;
[2] Пензенский государственный университет, г. Пенза, Россия
✉ novichkov1998maks@gmail.com

Аннотация. Представлен метод формирования наноструктурированного биметаллического катализатора PtNi на поверхности твердополимерного электролита. Частицы никеля получены методом магнетронного распыления, на которых химическим осаждением выращивается основной объем платинового катализатора. Полученная система имеет высокую каталитическую активность и временную стабильность.

Ключевые слова: биметаллический катализатор, твердополимерный электролит, каталитический слой, магнетронное распыление, химическое осаждение

Финансирование: Работа выполнена при поддержке гранта Министерства науки и высшего образования Российской Федерации «Синтез и исследование перспективных наноматериалов, покрытий и электронных устройств» (№ 124041700069-0).

Ссылка при цитировании: Новичков М.Д., Гурин С.А., Шепелева А.Э., Печерская Е.А., Агафонов Д.В., Ильин В.А. Наноструктурированный биметаллический катализатор PtNi электрохимических систем с твердополимерным электролитом // Научно-технические ведомости СПбГПУ. Физико-математические науки. 2024. Т. 17. № 3.1. С. 120–123. DOI: https://doi.org/10.18721/JPM.173.123

Introduction

Modern hydrogen-oxygen fuel cells typically consist of two electrodes, an anode and a cathode, separated by a polymer electrolytic membrane (PEM) [1]. The PEM use in its original form in fuel cells shows low productivity, which requires the introduction of a catalyst into the reaction area [2]. The most active in the hydrogen oxidation are catalysts based on highly dispersed platinum clusters, the properties and structure of which significantly determine the degree of the electrolytic process intensification [3, 4]. Therefore, the development of methods for the formation of nanostructured platinum-based catalysts with the required functional properties is an urgent task.

Materials and Methods

The PtNi bimetallic catalysts synthesis was carried out in two stages. At the first stage, adsorption centers were obtained on the surface of a solid polymer electrolyte (Nafion) using magnetron sputtering of a nickel target. Before sputtering, the pressure in the chamber was set to 5×10^{-5} Pa, after which the working gas – argon was supplied and a magnetron discharge with a power of 200 Watts was ignited.

Next, by chemical precipitation from a solution of H_2PtCl_6 – 2 g/l, N_2H_4 – 1.0 g/l, NH_4OH (conc.) – 200 ml/l, the main catalyst volume was formed to form a shell-core structure of platinum on nickel on the PEM surface. A membrane electrode block with an electrode area of 7 cm^2 was made on the basis of a membrane with the resulting catalyst, which was installed in a test bench (Fig. 1) for testing as part of a water electrolyzer and a fuel cell.

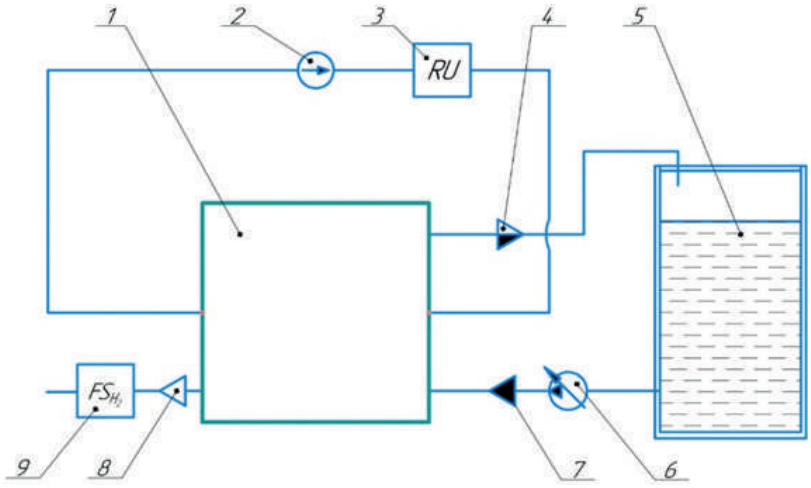

Fig .1. Scheme of the test bench. *1* – electrolytic cell; *2* – current source; *3* – registration block (including ammeter); *4* – tube output of the water-oxygen mixture; *5* –container with water; *6* – pump; *7* – tube for supplying water to the EC; *8* – output channel H_2; *9* – flow measurement sensor H_2

Results and Discussion

The study of membranes obtained by the combined method showed that the catalytic layer has a porous structure that does not interfere with proton transport to the membrane surface. The surface area of the membrane manufactured using a combined technology, fixed on the SEM, is shown in Fig. 2.

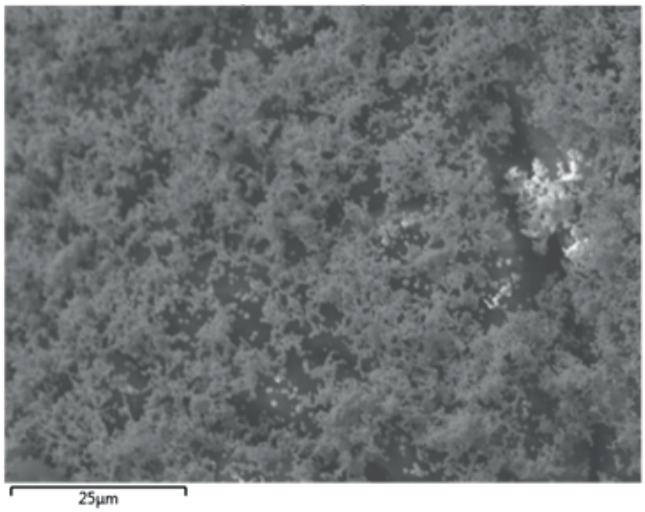

Fig. 2. SEM image of an ion exchange membrane with a nanostructured catalyst layer obtained by magnetron sputtering followed by chemical deposition

The study of the current-voltage characteristics of the obtained MEUs was carried out in comparison with MEUs based on a membrane with a catalyst synthesized only by a chemical method (Fig. 3).

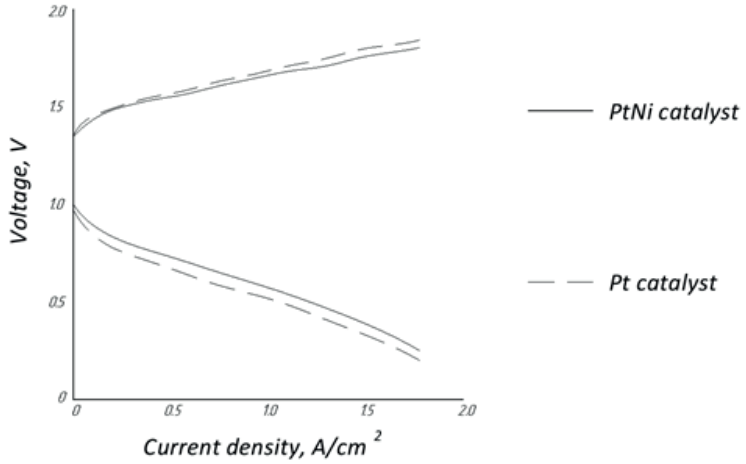

Fig. 3. Current-voltage characteristics of the MEU

The characteristics of bimetallic catalysts are higher, which is explained by electronic effects (lowering the energy of vacant d orbitals). Thus, the water electrolysis voltage is 0.03 V less at a current density of 1 A/cm^2, while the fuel cell voltage at the same current density is 0.05 V higher than the value for a MEU with a catalyst obtained by a chemical method.

It is also worth noting that the high energy of deposited particles during magnetron sputtering (10–20 eV) leads to energetic activation of the condensation process of particles on the substrate and, as a consequence, high coupling between the catalyst and the substrate [5], thereby having a positive effect on the MEU characteristics stability.

Conclusion

The use of a combination of magnetron sputtering and chemical deposition to form nickel and platinum layers, respectively, makes it possible to obtain bimetallic catalysts on the surface of solid polymer electrolytes characterized by high functional characteristics and their stability. The resulting catalyst is characterized by corrosion and morphological stability due to its strong bond with the substrate, as well as high catalytic activity, which is explained by electronic effects (lowering the energy of vacant d-orbitals).

REFERENCES

1. **Yaroslavtsev A.B., Dobrovolsky Y.A., Shaglaeva N.S., Frolova L.A., Gerasimova E.V., Sanginov E.A.,** Advances in Chemistry. 81 (3) (2012) 191–220.

2. **Grigoriev S.A., Fedotov A.A., Murzin V. Yu., Khramov E.V.,** Study of nanostructured electrocatalysts synthesized by magnetron-ion sputtering of platinum on a metallized nanocarbon carrier. Electrochemistry. Publishing House of the Russian Academy of Sciences. 51 (9) (2015) 915–929.

3. **Hodnik M., Zorko M., Bele M., Hocevar S.,** Gaberscek M., Identical location scanning electron microscopy: a case study of electrochemical degradation of PtNi nanoparticles using a new nondestructive method, J. Phys. Chem. 116 (40) (2012) 21326–21333.

4. **Rabis A., Rodriguez P., Schmidt T.J.,** Electrocatalysis for Polymer Electrolyte Fuel Cells: Recent Achievements and Future Challenges. ACS Catalysis. 2 (2012) 864–890.

5. **Fateev V.N., Alekseeva O.K., Porembskii V.I., Mikhalev A.I., Nikitin S.M.,** Corrosion-resistant electrodes/current collectors for anodes of electrolysis cells with solid polymer electrolyte. International Scientific Journal "Alternative Energy and Ecology" (ISJAEE). (25–27) (2017) 88–99.

THE AUTHORS

NOVICHKOV Maksim D.
novichkov1998maks@gmail.com
ORCID: 0000-0001-9319-2475

PECHERSKAYA Ekaterina A.
pea1@list.ru
ORCID: 0000-0001-5657-9128

GURIN Sergey A.
teslananoel@rambler.ru
ORCID: 0000-0001-9602-7221

AGAFONOV Dmitry V.
dmitryagafonov@list.ru
ORCID: 0009-0009-4548-3724

SHEPELEVA Anastasiya E.
anastasiya.shepeleva.01@mail.ru
ORCID: 0000-0002-8600-084X

ILYIN Vitaly A.
Mile_of_clay@bk.ru

Received 03.07.2024. Approved after reviewing 31.07.2024. Accepted 31.07.2024.

Conference materials
UDC 537.5
DOI: https://doi.org/10.18721/JPM.173.124

Formation of silver nanoparticles in glass by vacuum thermal poling

I.V. Reshetov [1, 2] ✉, E.S. Babich [1, 2], A.A. Lipovskii [1, 2],
V.G. Melehin [3], A.V. Nashchekin [3]

[1] Alferov University, St. Petersburg, Russia;
[2] Peter the Great St. Petersburg Polytechnic University, St. Petersburg, Russia;
[3] Ioffe Institute of Russia Academy of Sciences, St. Petersburg, Russia
✉ reshetov_iv@spbstu.ru

Abstract. It is shown that the vacuum poling of soda-lime silicate glass followed by silver-for-sodium ion exchange results in the formation of silver nanoparticles (NPs) in subcathode region of the glass. The latter was confirmed by the presence of silver NPs' localized surface plasmon resonance peak in optical absorption spectra of the samples. The NPs had grown in 2 μm thick subsurface region of the glass, which was confirmed by etching the cathode side of the sample. The possibility of forming a 2D-structured pattern from silver NPs that repeats the relief of the cathode electrode used for poling, has also been demonstrated. A hypothesis about the reduction of silver ions during the ion exchange by sodium atoms penetrated the glass from the cathode during poling in vacuum is proposed.

Keywords: soda-lime glass, thermal poling, silver nanoparticles

Funding: This study has been supported by the Ministry of Science and Education of Russian Federation, project FSRM-2023-0009.

Citation: Reshetov I.V., Babich E.S., Lipovskii A.A., Melehin V.G., Nashchekin A.V., Formation of silver nanoparticles in glass by vacuum thermal poling, St. Petersburg State Polytechnical University Journal. Physics and Mathematics. 17 (3.1) (2024) 124–128. DOI: https://doi.org/10.18721/JPM.173.124

Материалы конференции
УДК 537.5
DOI: https://doi.org/10.18721/JPM.173.124

Образование серебряных наночастиц в стекле с помощью термического полинга в вакууме

И.В. Решетов [1, 2] ✉, Е.С. Бабич [1, 2], А.А. Липовский [1, 2],
В.Г. Мелехин [3], А.В. Нащекин [3]

[1] Академический университет им. Ж.И. Алфёрова РАН, Санкт-Петербург, Россия;
[2] Санкт-Петербургский политехнический университет Петра Великого, Санкт-Петербург, Россия;
[3] Физико-технический институт им. А.Ф. Иоффе Российской академии наук, Санкт-Петербург, Россия
✉ reshetov_iv@spbstu.ru

Аннотация. Показано, что вакуумный полинг щелочно-силикатного стекла и последующий серебряно-натриевый обмен приводят к образованию серебряных наночастиц (НЧ) в подкатодной области стекла. Продемонстрирована возможность создания 2D-структурированных паттернов, образованных серебряными НЧ, повторяющих рельеф катодного электрода, используемого при полинге. Предложена гипотеза о восстановлении ионов серебра в процессе ионного обмена атомами натрия, проникшими в стекло с катодной стороны в процессе вакуумного полинга.

Ключевые слова: щелочно-силикатное стекло, термический полинг, серебряные наночастицы

Финансирование: Работа поддержана Министерством науки и высшего образования Российской Федерации, проект FSRM-2023-0009.

Ссылка при цитировании: Решетов И.В., Бабич Е.С., Липовский А.А., Мелехин В.Г., Нащекин А.В. Образование серебряных наночастиц в стекле с помощью термического полинга в вакууме // Научно-технические ведомости СПбГПУ. Физико-математические науки. 2023. Т. 17. № 3.1. С. 124–128. DOI: https://doi.org/10.18721/JPM.173.124

Introduction

Thermal poling of glasses consists in the application of a DC voltage to a heated glass plate. This process leads to compositional [1] and structural [2, 3] changes in the subanode layer of a glass and, accordingly, alternates physical properties of such layer. When soda-lime glass is poled in air, electric current through the sample occurs due to the influx of positive hydrogen/hydronium ions (H_3O^+) from atmosphere [4]. This results in a displacement of alkaline ions contained in it towards the bulk of the glass and the formation of alkaline-depleted and hydronium-enriched layer in the subanode region of the glass, which significantly slows down or even prevents ionic exchange [5]. This allows creating 2D-structured pattern from silver NPs in the subanode layer of the glass by poling silver-for-sodium exchanged glass with structured (relief) anode electrode and subsequent thermal treatment in reducing atmosphere. However, recent studies have also shown that the thermal poling of silver-for-sodium exchanged glasses being performed in air leads to the growth of silver dendrites in the subcathode layer of the glasses without the use of reducing atmosphere [6]. This allows us to conclude that poling itself creates reducing centers there. Indeed, when poled soda-lime glass in vacuum, we recorded an electric current through the glass, despite the absence of the penetration of positive species into it, the current being only several times less compared to the case of air-poling. This current arises partly because of the reduction of sodium ions near the cathode side of glass. Sodium ions drift is possible due to the local repolymerization of glassy network in subanode layer that compensate negative subanode charge [7]. We hypothesized that formed sodium atoms can act as reducing agents for silver ions, and we tested their presence in the subcathode layer of soda-lime glass poled in vacuum by performing silver-for sodium ion exchange. This work is devoted to the description of related experiments and demonstration of the possibility to form 2D-structured patterns from silver NPs by combination of vacuum thermal poling and silver-for-sodium ion exchange without using additional thermal treatment.

Experimental and results

In the experiments we used slides of a soda-lime glass, which composition in wt.% is: 72.2% SiO_2, 14.3% Na_2O, 6.4% CaO, 4.3% MgO, 1.2% K_2O, 1.2% Al_2O_3 and 0.4% other oxides. 1 mm thick glass slides were placed between two electrodes, heated to 300 °C and subjected to 800 V DC voltage in a vacuum chamber at about 2×10^{-5} mmHg pressure. After poling, we performed silver-for-sodium ion exchange by immersion the samples for 20 min in $Ag_{0.05}Na_{0.95}NO_3$ (in wt.%) melt heated to 325 °C.

To characterize quantity and depth distribution of silver nanoparticles we etched in several stages one of the samples in a solution of 80 ml H_2O, 10 ml NH_4F and 10 μl HF and measured the optical absorption at each stage. Evaluated etching rate was ~ 90 nm per min. The corresponding spectra are shown in Figure 1. The presence of localized surface plasmon (LSP) peak at ~ 410 nm confirmed the formation of silver NPs in poled glasses after the ion exchange [8]. From the dependence of integral absorbance (330–483 nm) on the etching depth we calculated the depth distribution of silver nanoparticles, which is shown in Figure 2.

This allowed us to assume that vacuum poling with structured cathode electrode should result

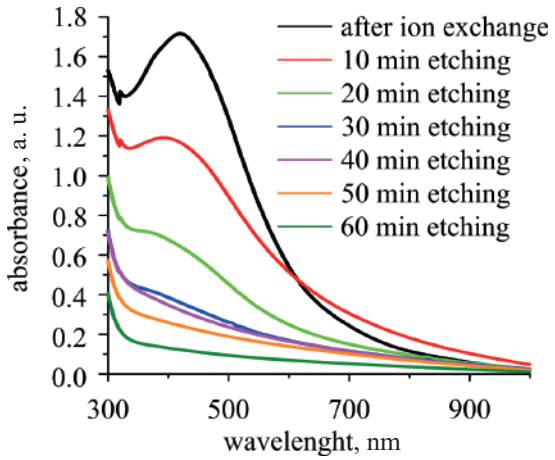

Fig. 1. Optical absorption spectra before and after etching of soda-lime glass after vacuum thermal poling and silver-for-sodium ion exchange

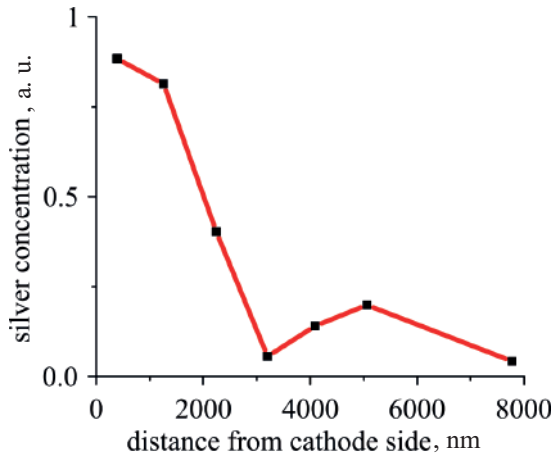

Fig. 2. Depth distribution of silver in soda-lime glass after vacuum thermal poling and silver-for-sodium ion exchange

in the formation of 2D patterns from silver NPs. The result of poling experiment with a bronze grid pressed to the glass slide and used as cathode electrode is shown in Figure 3. One can see that the dark strips, which correspond to the glass regions containing silver NPs, replicate the structure of the cathode electrode.

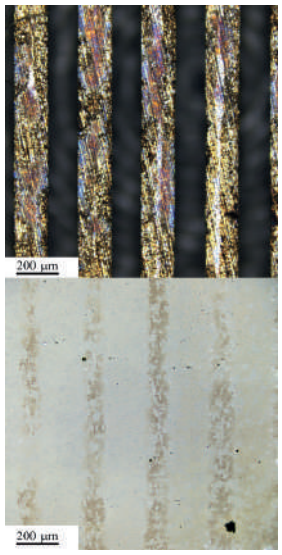

Fig. 3. Photos of the cathode electrode (top) and its replica formed by silver NPs in the subcathode layer of a sample (bottom)

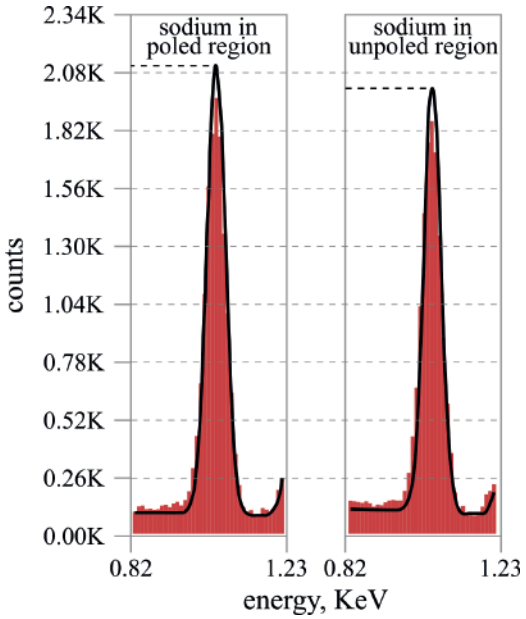

Fig. 4. EDX spectra in poled and unpoled regions of soda-lime glass

To interpret the difference the formation of nanoparticles in the subcathode layer of soda-lime glass poled in vacuum we measured sodium concentration in poled and unpoled regions under the cathode surface of the sample using energy-dispersive X-ray spectroscopy (EDX). The thickness of the analyzed region was about 1 μm. The corresponding data is shown in Figure 4. Calculated weight percentage gave 10.91 wt.% of sodium in poled region and 10.50 wt.% of sodium in unpoled region of the sample that is excess sodium in the poled subcathode region.

Discussion

According to figure 1, 40 min etching results in the complete degradation of LSP resonance that is to the removal of silver nanoparticles. Thus, the first peak in figure 2 mainly corresponds to silver NPs while the second – to ionic silver.

The correlation between the formation of silver nanoparticles in the poled region, that is, the reduction of silver ions, and the detected excess sodium suggested that it is responsible for the reduction.

In poling, atomic sodium forms at the cathode because of reduction of Na^+ ions. In the case of poling in air, neutral sodium immediately oxidizes and forms NaOH because of atmospheric humidity, while in vacuum poling it can preserve in atomic state at the cathode. Then, in a vacuum, sodium can be desorbed directly from the cathode surface into the glass either through vapor or even from a liquid layer between the glass and the cathode, the layer being formed due to the low melting temperature of sodium 98 °C. Thus, we suppose that the portion of sodium atoms not intercalated at the cathode penetrates from the cathode into the glass (the diffusion of sodium atoms into glass up to a depth of 10 microns was recorded [9]. Then penetrated sodium atoms serve as a reducing agent for silver ions against the background of conventional ion exchange:

$$Na^0 + ...Si\text{-}O\text{-}Ag^+ \rightarrow ...Si\text{-}O\text{-}Na^+ + Ag^0.$$

The possibility of the existence of neutral atoms and even sodium nanoparticles in glass has been confirmed experimentally [10, 11]. Reduced silver atoms, in turn, are clustering in silver nanoparticles at the temperature of the ion exchange (300 °C):

$$nAg \rightarrow Ag_n.$$

Conclusion

We demonstrate that vacuum poling of a soda-lime glass and subsequent silver-for-sodium ion exchange results in the formation of silver nanoparticles in the subcathode layer within 2 microns. This approach can be used to create 2D-structured glass metal composites without using thermal treatment in reducing atmosphere. A hypothesis about the reduction of silver ions during the ion exchange by sodium atoms penetrated the glass from the cathode during poling in vacuum is proposed.

REFERENCES

1. **Lepienski C.M., Giacometti J.A., Ferreira G.L., Freire Jr F.L., Achete C.A.,** Electric field disctribution and near-surface modifications in soda-lime glass submitted to a dc potential, Journal of Non-Crystalline Solids. 159 (3) (1993) 204–212.

2. **An H., Fleming S.,** Second-order optical nonlinearity and accompanying near-surface structural modifications in thermally poled soda-lime silicate glasses, JOSA B. 23 (11) (2006) 2303–2309.

3. **Ziemath E.C., Araujo V.D., Escanhoela C.A.,** Compositional and structural changes at the anodic surface of thermally poled soda-lime float glass, Journal of Applied Physics. 104 (5) (2008).

4. **Doremus R.H.,** Mechanism of electrical polarization of silica glass, Applied Physics Letters. 87 (23) (2005) 1–2.

5. **Babich E., Reduto I., Redkov A., Reshetov I., Zhurikhina V, Lipovskii A.,** Thermal poling of glasses to fabricate masks for ion exchange, Journal of Physics: Conference Series. 1695 (1) (2020) 012107.

6. **Brunkov P.N., Lipovskii A.A., Melehin V.G., Red'kov A.V., Statsenko V.V.,** Formation of silver fractal structures in ion-exchange under poling, Technical Physics. 60 (2015) 270–274.

7. **Redkov A.V., Melehin V.G., Lipovskii A.A.,** How Does Thermal Poling Produce Interstitial Molecular Oxygen in Silicate Glasses, The Journal of Physical Chemistry C. 119 (30) (2015) 17298–17307.

8. **Hlaing M., Gebear-Eigzabher B., Roa A., Marcano A., Radu D., Lai C.Y.,** Absorption and scattering cross-section extinction values of silver nanoparticles. 58 (2016) 439–444.

9. **Samuneva B., Djambaski P., Avramova K.,** Interaction between glasses and alkali metal vapours. Journal of Non-Crystalline Solids. 112 (1989) 385–391.

10. **Iliescu B., Enculescu I., Pera I., Alexe G., Polosan S., Stanculescu A.,** Chemical composition of structures obtained inside quartz crystal by sodium electrodiffusion, Crystal Research and Technology. 36 (4-5) (2001) 403–410.

11. **Bochkareva E.S., Nikonorov N.V., Podsvirov O.A., Prosnikov M.A., Sidorov A.I.,** The Formation of Sodium Nanoparticles in Alkali-Silicate Glass Under the Action of the Electron Beam and Thermal Treatments, Plasmonics. 11 (2016) 241–246.

THE AUTHORS

RESHETOV Ilya V.
reshetov_iv@spbstu.ru
ORCID: 0000-0002-8661-3654

BABICH Ekaterina S.
esbabich@inbox.ru
ORCID: 0000-0003-4970-2591

LIPOVSKII Andrey A.
lipovskii@mail.ru
ORCID: 0000-0001-9472-9190

MELEHIN Vladimir G.
melekhin1952@gmail.com
ORCID: 0000-0003-3741-3936

NASHCHEKIN Alexey V.
nashchekin@mail.ioffe.ru
ORCID: 0000-0002-2542-7364

Received 09.07.2024. Approved after reviewing 23.07.2024. Accepted 23.07.2024.

Conference materials
UDC 621.315.529
DOI: https://doi.org/10.18721/JPM.173.125

Heterostructure design features for 975 nm high-power laser diodes

E.V. Ershov [1] ✉, A.V. Fomin [1], M.V. Lupachev [1], O.A. Rogachkov [1], A.A. Naidin [1]

[1] Russian Federal Nuclear Center - Zababakhin All - Russia Research Institute of technical Physics, Snezhinsk, Chelyabinsk region, Russia

✉ sneg.ershov@mail.ru

Abstract. The heterostructure design has been optimized to achieve high radiation output power and high conversion efficiency of 970–980 nm laser diodes. The influence of active layer geometry and waveguide layer doping on the output electrical and optical LD chip parameters has been studied. As a result of the optimization, operating LD output of 11.6 W has been achieved at a current of 12 A. The maximum conversion efficiency was 65% at a pump current of 5A.

Keywords: laser diode, laser cavity, heterostructure, quantum well

Citation: Ershov E.V., Fomin A.V., Lupachev M.V., Rogachkov O.A., Naidin A.A., Heterostructure design features for 975 nm high-power laser diodes, St. Petersburg State Polytechnical University Journal. Physics and Mathematics. 17 (3.1) (2024) 129–133. DOI: https://doi.org/10.18721/JPM.173.125

Материалы конференции
УДК 621.315.529
DOI: https://doi.org/10.18721/JPM.173.125

Особенности конструкции гетероструктур для мощных лазерных диодов спектрального диапазона 975 нм

Е.В. Ершов [1] ✉, А.В. Фомин [1], М.В. Лупачев [1], О.А. Рогачков [1], А.А. Найдин [1]

[1] Российский Федеральный Ядерный Центр – Всероссийский научно-исследовательский институт технической физики им. академ. Е.И. Забабахина, г. Снежинск, Челябинская обл., Россия

✉ sneg.ershov@mail.ru

Аннотация. С целью достижения высокой выходной мощности излучения и КПД лазерных диодов спектрального диапазона 970–980 нм проведена оптимизация конструкции гетероструктуры. При оптимизации исследовано влияние геометрических параметров слоев активной области, а также легирования волноводных слоев гетероструктуры на выходные электрооптические характеристики чипов ЛД. Проведенная оптимизация позволила достичь рабочую выходную мощность излучения лазерных диодов 11,6 Вт при токе 12 А. Максимальный КПД при этом составил 65%, при токе накачки лазера 5 А.

Ключевые слова: лазерный диод, резонатор, гетероструктура, квантовая яма

Ссылка при цитировании: Ершов Е.В., Фомин А.В., Лупачев М.В., Рогачков О.А., Найдин А.А. Особенности конструкции гетероструктур для мощных лазерных диодов спектрального диапазона 975 нм // Научно-технические ведомости СПбГПУ. Физико-математические науки. 2024. Т. 17. № 3.1. С. 129–133. DOI: https://doi.org/10.18721/JPM.173.125

Introduction

Laser diodes (LDs) based on InGaAs/AlGaAs/GaAs with radiation wavelength λ_{rad} = 975 nm are widely used for fiber laser pumping. Specific requirements to heterostructure (HS) design are imposed by high optical output and operation modes of such lasers. The ways to improve LD output are intensively investigated by domestic and foreign scientific communities [1–3] while heterostructure design is constantly refined. Thus, output power is increased by 1) optimizing quantum well (QW) parameters, and 2) doping profile of HS waveguide layers. Therefore, the research aimed at optimizing the HS design with an extended waveguide is of high interest since it allows achieving high optical output and high conversion efficiency of LD chips.

Materials and Methods

For the research, InGaAs/GaAs/AlGaAs HSs were grown by MOCVD. The HS design for samples 1–8 is presented in Table.

Table

Design and composition of HS layers

Layer	Composition	Thickness
n-substrate	GaAs(001)	625±25 μm
buffer	GaAs:Si	1–2 μm
n-cladding	$Al_{1.75 \cdot x}Ga_{(1.75 \cdot x)-1}As$:Si	1.5 μm
waveguide	$Al_xGa_{1-x}As$	1.2 μm
active region	$In_yGa_{1-y}As$/(Al)GaAs	5–9 nm /10 nm
waveguide	$Al_xGa_{1-x}As$	0.5 μm
p-cladding	$Al_{1.75 \cdot x}Ga_{(1.75 \cdot x)-1}As$:Zn	1.0 μm
contact p-layer	GaAs:Zn	0.15–0.20 μm

The samples 1–8 were used to manufacture LDs with a cavity length of 4 mm and an emitting stripe width of 100 μm using the developed planar technology. The LD chips end facets were anti-reflective and reflective coated. The LD chips were soldered p-side down on a heat-conducting submount with vacuum Au-Sn eutectic solder coating. Light-current and voltage-current characteristics of LD chips were measured using the equipment for electrical and optical measurements in CW laser generation mode at the currents from 0 A to 12 A.

Results and Discussion

At the first stage of the work, the effect of QW thickness, d, and QW number on the LD chip output power, P_{max}, was investigated. Heterostructures with a single QW were grown with varying QW thickness from 5 nm to 9 nm. In those experiments with varying QW thickness, In molar fraction was selected so that the peak photoluminescence (PL) wavelength for a heterostructure would be 955 ± 2 nm at normal conditions. The above PL wavelength allows obtaining the radiation wavelength λ_{rad} = 975 ± 1 nm for LD chips in CW laser generation mode at the currents of 10–12 A. The dependencies of P_{max} on QW thickness and QW number are shown in Figure 1.

Figure 1 shows that P_{max} = 8.7 W was reached for the LD chips with a QW thickness of 6.0 nm. The radiation output decreased with varying the QW thickness. Note that the obtained optimal QW thickness agrees with the data in [4] where the dependency of internal quantum HS photoluminescence output on QW thickness was studied. The radiation output decreased from 8.6 W down to 8.0 W with double quantum well 6 nm thick due to the increase in the threshold current density, J_{th}, from 125 A/cm^2 up to 180 A/cm^2. Therefore, the HS design should contain a single QW with a thickness of ~ 6 nm to achieve high radiation output.

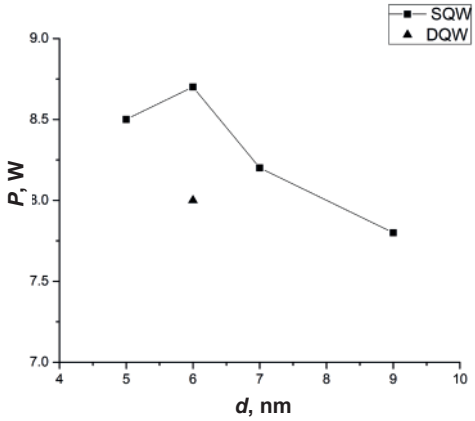

Fig. 1. Optical absorption spectra before and after etching of soda-lime glass after vacuum thermal poling and silver-for-sodium ion exchange

At the second stage, the effect of QW energy depth on the LD output characteristics was studied. For this, HS samples with an extended undoped waveguide were grown with varying Al molar fraction in $(Al_x)Ga_{1-x}As$ barrier layers from 0% to 20%. Those were grown with a single QW 6 nm thick to maintain high radiation output.

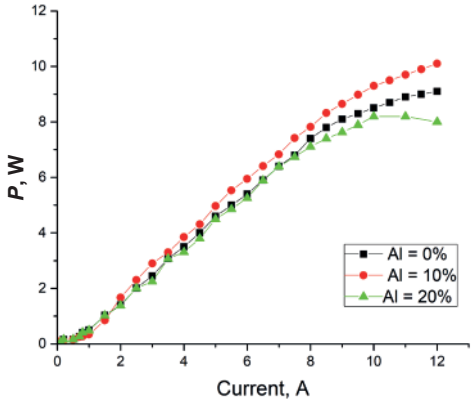

Fig. 2. Light-current characteristics of the LD chips from HSs with different Al molar fractions in InGaAs/$(Al_x)Ga_{1-x}As$ barrier layers of the active region

The measured light-current characteristics (Fig. 2) show that P_{max} of 10.1 W was achieved for the LD chips with Al molar fraction of 10% at a current of 12 A. Besides, saturation of light-current characteristics was observed for all LDs preventing radiation output from growing further. At that, the operating voltage, U, was 1.88 V at a current of 12 A. Saturation of light-current characteristics and high values of voltage-current characteristics are typical for LD chips with an extended undoped waveguide. Such waveguide design enables reducing internal optical loss, thus, increasing differential quantum efficiency, and allows using lasers with an extended cavity length. Moreover, HSs with an extended waveguide induce the decrease in laser radiation density on the cavity mirrors while shifting down the threshold of critical optical degradation of the mirrors. However, the extended undoped waveguide increases both thermal and electrical series resistance of the structure, thus, resulting in the increase in heat release, which affects laser conversion efficiency and constrains their maximum achievable output [5].

Additionally, the influence of doping HS waveguide layers on LD light-current and voltage-current characteristics was investigated to reduce thermal and electrical series resistance. For this, HS samples with $Al_{0.1}Ga_{0.9}As$ barrier layers were grown where the waveguide regions adjacent to n-cladding and p-cladding were doped with Si and Zn, respectively. The waveguide region adjacent to the quantum well remained undoped to keep the optical loss below 1 cm^{-1}. The zone energy diagram of such an HS is given in Figure 3.

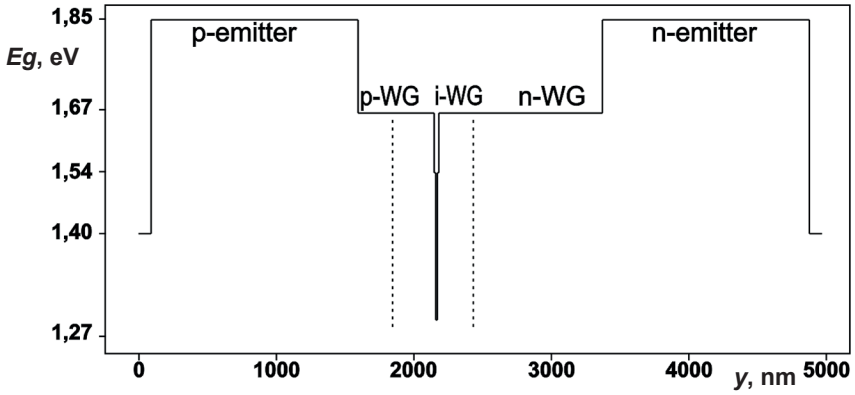

Fig. 3. Zone diagram of a doped-waveguide heterostructure

The measured light-current characteristics (Fig. 4, *a*) for the LD chips manufactured from doped-waveguide HSs showed the increase in the output power, P_{max}, up to 11.6 W at an operating current of 12 A. No saturation of light-current characteristics within an operating current range from 1 A to 12 A was observed. The voltage-current characteristics (Fig. 4, *b*) showed the decrease in the operating voltage, *U*, from 1.88 V down to 1.74 V at an operating current of 12 A for doped-waveguide chips. The LD chip conversion efficiency was 56% at an operating pump current of 12 A. The maximum conversion efficiency of 65% for the LD chips manufactured from doped-waveguide HSs was achieved at 5 A.

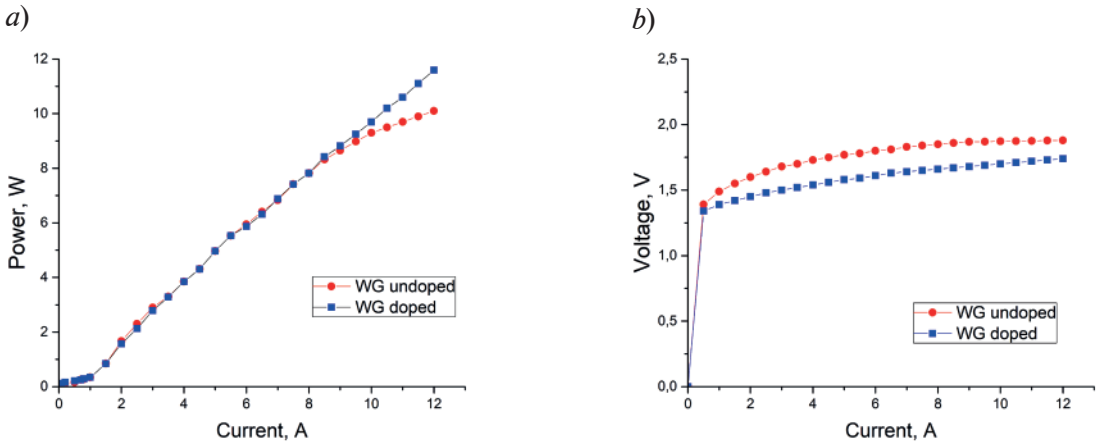

Fig. 4. Light-current and voltage-current LD chip characteristics manufactured from HS with doped and undoped waveguide layers

Conclusion

The HS design with an extended asymmetric waveguide has been optimized to obtain high radiation output power and high conversion efficiency of 970–980 nm LD chips. The influence of HS layer doping and the geometry of active-region layers on electrical and optical LD output characteristics has been investigated. As a result, the LD operating output power of 11.6 W at a current of 12 A. The maximum conversion efficiency of 65% have been achieved at a current of 5 A. It should be noted that authors of [5] achieved maximum conversion efficiency of 70–72% due to doping and decreased molar fraction of aluminum in AlGaAs waveguide layers.

REFERENCES

1. **Danilov I.A., Ivanov A.V., Konyaev V.P., Kurnyavko Yu.V., et al.,** Semiconductor lasers with improved emitting characteristics. Quantum Electronics (in Russian). 52 (12) (2022) 1079–1087.

2. **Wang X., Crump P., Wenzel H., Liero A., Hoffmann T. et. al.,** IEEE J. Quantum Electronics. 46 (5) 658 (2010).

3. **Liang Wang, Hongwei Qu, Aiyi Qi, Xuyan Zhou, Wanhua Zheng.,** High-power laser diode at 9xx nm with 81,10% efficiency // Optics Letters. 47 (13/1) 3231–32–34.

4. **Vinokurov D.A., Vasilieva V.V., Kapitonov V.A., Lyutetskii A.V., et al.,** The influence of active region thickness on the characteristics of semiconductor lasers based on AlGaAs/GaAs/InGaAs asymmetric heterostructures with an extended waveguide. Semiconductor Physics and Engineering (in Russian). 44 (2) (2010) 246–250.

5. **Volkov N.A., Bagaev T.A., Sabitov D.R., Andreev A.Yu., Yarotskaya I.V., Padalitsa A.A., et al.,** InGaAs/AlGaAs/GaAs semiconductor lasers (λ = 900–920nm) with asymmetric waveguide and enhanced voltage-current characteristic. Quantum Electronics (in Russian). 51 (10) 2021) 905–908.

THE AUTHORS

ERSHOV Evgenii V.
sneg.ershov@mail.ru

FOMIN Aleksei V.
a.v.fomin@vniitf.ru

LUPACHEV Maksim V.
Dep5@vniitf.ru

ROGACHKOV Oleg A.
roa_jr@mail.ru

NAIDIN Andrei A.
naydin_andrey@mail.ru

Received 20.07.2024. Approved after reviewing 12.08.2024. Accepted 12.08.2024.

Conference materials
UDC 621.311.243
DOI: https://doi.org/10.18721/JPM173.126

Effect of light incidence angle on the characteristics of silicon solar cells with different texturing

E.Y. Yarchuk [1] ✉, E.A. Vyacheslavova [2], A.O. Monastyrenko [2], A.S. Gudovskikh [2]

[1] St. Petersburg Electrotechnical University "LETI", St. Petersburg, Russia;
[2] Alferov University, St. Petersburg, Russia
✉ ernst_yarchuk@mail.ru

Abstract. The influence of the angle of incidence of the light flux on the photovoltaic performance of two types *a*-Si:H/*c*-Si heterojunction solar cells is investigated: KOH textured with a pyramidal surface, and black silicon with a nanostructured surface. Current-voltage characteristics and power depending on the angle of incidence of the solar flux – from 14 mW/cm^2 to 3 mW/cm^2 for pyramidal surface and from 9 mW/cm^2 to 2 mW/cm^2 for black silicon in the angle range 0–75° were obtained. Solar cell based on black silicon retains its characteristics 6% better as the angle of incidence of light increases to 75°.

Keywords: black silicon, amorphous silicon, heterojunction solar cell, current-voltage characteristic, angle of incidence

Funding: The research was supported by the RFBR research project No. 21-58-46001.

Citation: Yarchuk E.Y., Vyacheslavova E.A., Monastyrenko A.O., Gudovskikh A.S., Effect of light incidence angle on the characteristics of silicon solar cells with different texturing, St. Petersburg State Polytechnical University Journal. Physics and Mathematics. 17 (3.1) (2024) 134–137. DOI: https://doi.org/10.18721/JPM.173.126

Материалы конференции
УДК 621.311.243
DOI: https://doi.org/10.18721/JPM.173.126

Влияние угла падения света на характеристики кремниевых солнечных элементов с различным текстурированием

Э.Я. Ярчук [1] ✉, Е.А. Вячеславова [2], А.О. Монастыренко [2], А.С. Гудовских [2]

[1] Санкт-Петербургский государственный электротехнический университет «ЛЭТИ» им. В.И.Ульянова (Ленина), Санкт-Петербург, Россия;
[2] Академический университет им. Ж.И. Алфёрова РАН, Санкт-Петербург, Россия
✉ ernst_yarchuk@mail.ru

Аннотация. Исследовано влияние угла падения светового потока на фотоэлектрические характеристики двух типов солнечных элементов с гетеропереходом *a*-Si:H/*c*-Si: текстурированного KOH с пирамидальной поверхностью и черного кремния с наноструктурированной поверхностью. Вольтамперные характеристики и мощность в зависимости от угла падения солнечного потока – от 14 мВт/см^2 до 3 мВт/см^2 для образца с пирамидальной поверхностью и от 9 мВт/см^2 до 2 мВт/см^2 для черного кремния в диапазоне углов 0–75°. Солнечный элемент на основе черного кремния сохраняет свои характеристики на 6% лучше при увеличении угла падения света до 75°.

Ключевые слова: черный кремний, аморфный кремний, гетеропереходный солнечный элемент, вольтамперная характеристика, угол падения

Финансирование: Проект РФФИ № 21-58-46001 «Разработка высокоэффективных двухсторонних гетероструктурных солнечных элементов на основе черного кремния».

Ссылка при цитировании: Ярчук Э.Я., Вячеславова Е.А., Монастыренко А.О., Гудовских А.С. Влияние угла падения света на характеристики кремниевых солнечных элементов с различным текстурированием // Научно-технические ведомости СПбГПУ. Физико-математические науки. 2024. Т. 17. № 3.1. С. 134–137. DOI: https://doi.org/10.18721/JPM.173.126

Introduction

One of the solutions to the issue of electricity availability is solar energy, which is actively developing now. It is estimated that the increase in electricity generation in this area will reach 260 GW by 2026 [1]. Understanding the dependence of the current-voltage characteristics (I-V curves) of a solar cell (SC) at different angles of its inclination relative to the incident light flux allows us to take conclusions about changes of electricity generation during daylight hours and evaluate its efficiency. Silicon solar cells dominate among photovoltaic cells, as they are relatively cheap, accessible and durable.

The most promising concept of silicon SC is heterojunction *a*-Si:H/*c*-Si (HJT) technology [2] with anti-reflection coatings and a pyramidal textured surface to reduce optical losses [3, 4]. Also promising is black silicon (*b*-Si), which has minimal reflection in a wide range of waves [5] and retains these properties at high angles of light incidence on it.

In this article the influence of the angle of incidence of the light flux on the silicon solar cells on their current-voltage characteristics is considered.

Materials and Methods

Figure 1 shows two types of heterojunction (HJT) silicon *a*-Si:H/*c*-Si solar cells with an area of 1 cm^2 taken for the research: HJT based on black silicon (*b*-Si) with a nanotextured surface (Fig. 1, *a*) and HJT with conventional pyramidal structure (*pyr*-Si) (Fig. 1, *b*).

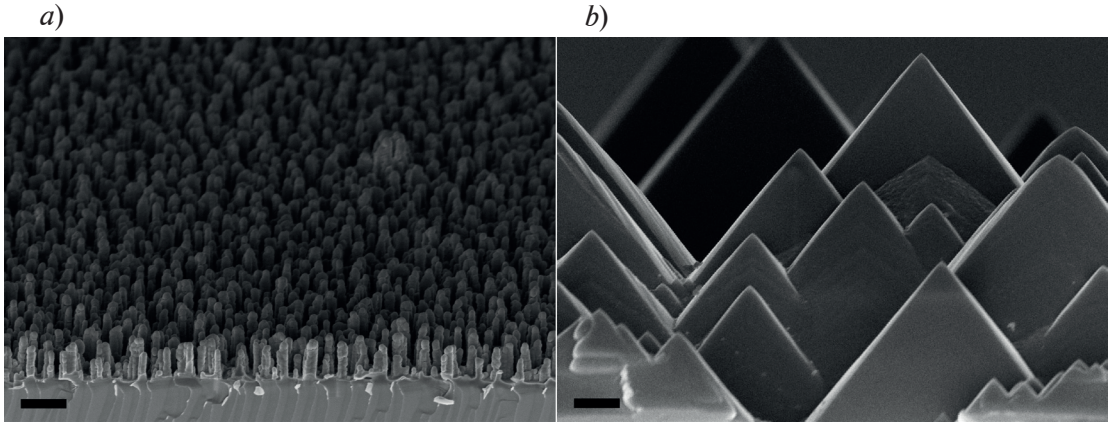

Fig. 1. SEM-images of the samples: *b*-Si (*a*), pyr-Si (*b*). The bare scale is 1000 nm

Comparison of the performance of *b*-Si and *pyr*-Si HJT allows us to evaluate the impact of different types of surface texturing on solar cell efficiency. This is important for determining the optimal type of structure for the development of more efficient photovoltaic devices.

To study the angular dependences of the current-voltage characteristics, a rotating sample holder was made and shown in Figure 2.

It is a tilt-adjustable platform that allows the solar cell to be precisely positioned relative to the beam of the solar simulator. The design of the stand eliminates the appearance of shadows, which ensures accurate measurement of the I-V curves at different angles of light incidence.

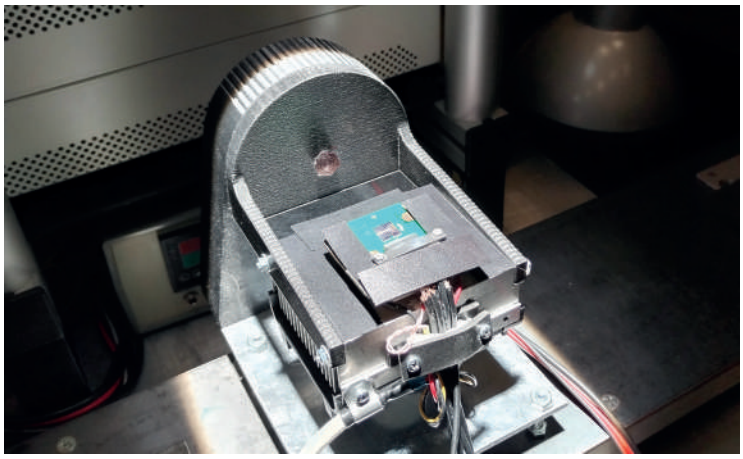

Fig. 2. Rotating sample holder designed for the research

Using a rotating stand allows us to study with high accuracy the effect of the angle of incidence of light on the efficiency of a solar battery. This allows to optimize the placement of solar panels to achieve maximum energy production throughout the day. Unlike standard methods for measuring current-voltage characteristics, which are often limited to several fixed angles, the use of a rotating stand allows to obtain a complete picture of the angular dependences of the current-voltage characteristics, which is especially important for assessing the performance of solar panels under conditions of changing insolation during the day.

Results and Discussion

The dependences of the I-V curves for these samples at angles of light incidence on them from 0° to 75°, the short circuit current and their power characteristics are shown in Figure 3.

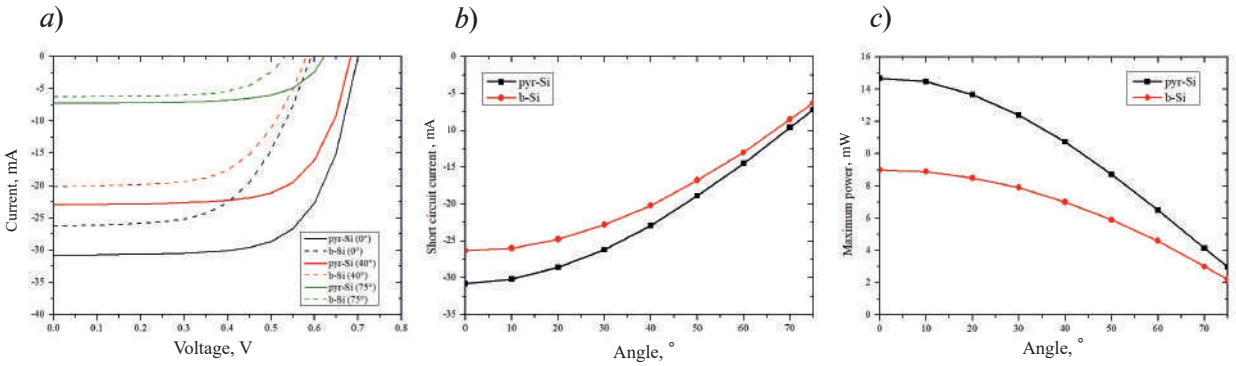

Fig. 3. I-V curves for samples *pyr*-Si (solid lines) and *b*-Si (dashed lines) for angles of 0° (black lines), 40° (red) and 75° (green) (*a*), angular dependences of short circuit current (*b*) and points of maximum power (*c*) for samples *pyr*-Si (black lines) and *b*-Si (red)

The maximum power is observed at light incidence angles of 0–20° and decreases with increasing angle. The *pyr*-Si demonstrates better perfomance (from 14.4 mW/cm^2 to 3 mW/cm^2, weakening is 79.2%), but at the same time characteristics more strongly decrease with increasing light incidence angle than the *b*-Si sample, which at more modest absolute values (from 9 mW/cm^2 to 2.3 mW/cm^2, weakening is 74.5%, 6% better), remains more stable at large angles, which explained by the structure of its surface.

Conclusion

The influence of the angle of incidence of the light flux on the current-voltage characteristics of heterostructure solar cells with different surfaces was studied. As the angle of incidence of light increases, the characteristics of solar cells deteriorate by reflection losses, but the nature of these changes is different. Thus, the *b*-Si shows more stability, while *pyr*-Si significantly loses its

effective power with increasing angle. This shows the potential of black silicon research, and the need to improve black silicon production technologies.

Acknowledgments

The research was supported by the RFBR research project No. 21-58-46001.

REFERENCES

1. A report by the International Energy Agency. Renewable electricity – Renewables 2021 – Analysis and key findings.

2. **Taguchi M., Yano A., Tohoda S., Matsuyama K., Nakamura Yu., Nishiwaki T., Kazunori F., Maruyama E.,** 24.7% Record efficiency HIT solar cell on thin silicon wafer, IEEE J. of Photovoltaics. 4 (1) (2014) 96–99.

3. **Chuchvaga N.A., Kislyakova N.M., Tokmoldin N.S. Rakymetov B.A., Serikkanov A.S.,** Problems arising from using KOH-IPA etchant to texture silicon wafers, Technical Physics. 65 (10) (2020) 1685–1689.

4. **Atobaev O.K., Terukov E.I., Shelopin G.G., Kabulov R.R.,** Wet Chemical Treatment of Monocrytalline Silicon Wafer Surfaces, Applied Solar Energy. 57 (2021) 363–369.

5. **Liu X., Coxon P.R., Peters M., Hoex B., Cole J.M., Fray D.J.,** Black silicon: fabrication methods, properties and solar energy applications, Energy & Environmental Science. 7 (10) (2014) 3223–3263.

THE AUTHORS

YARCHUK Ernst Y.
ernst_yarchuk@mail.ru
ORCID: 0009-0005-9558-4583

MONASTYRENKO Anatoliy O.
monas@spbau.ru
ORCID: 0009-0009-7051-8458

VYACHESLAVOVA Ekaterina A.
cate.viacheslavova@yandex.ru
ORCID: 0000-0001-6869-1213

GUDOVSKIKH Aleksander S.
gudovskikh@spbau.ru
ORCID: 0000-0002-7632-3194

Received 28.07.2024. Approved after reviewing 05.08.2024. Accepted 09.08.2024.

EXPERIMENTAL TECHNIQUE AND DEVICES

Conference materials
UDC 681.7.068
DOI: https://doi.org/10.18721/JPM.173.127

Microlenses formation by electric arc at the end of optical fibres, preserving the polarization of optical radiation

A.S. Pankov [1] ✉, R.S. Ponomarev [1]

[1] Perm State University, Perm, Russia

✉ lab.photon.psu@gmail.com

Abstract. In this paper, the use of tapered optical fibers with preservation of radiation polarization for the fabrication of microlenses is considered. The contraction of the fibers is achieved by stretching optical fiber under the influence of the electric arc the splicing machine. This method allows to fabricate microlenses with a mode field diameter at the focal point of up to 2 μm and with a polarization extinction ratio (PER) coefficient of radiation at the output of the microlens of up to 40 dB. At the same time, the drop in the PER coefficient in the microlens is no more than 3 dB.

Keywords: fiber microlens, tapered fiber, fiber with preservation of polarization, polarization extinction ratio, focal length, mode field diameter

Funding: The work was carried out within the framework of the State task "Development of the element base of photonic systems for telecommunications and sensor applications" (topic code [FSNF-2024-0001]).

Citation: Pankov A.S., Ponomarev R.S., Microlenses formation by electric arc at the end of optical fibres, preserving the polarization of optical radiation, St. Petersburg State Polytechnical University Journal. Physics and Mathematics. 17 (3.1) (2023) 138–141. DOI: https://doi.org/10.18721/JPM.173.127

Материалы конференции
УДК 681.7.068
DOI: https://doi.org/10.18721/JPM.173.127

Формирование микролинз с помощью электрической дуги на торце оптических волокон, сохраняющих поляризацию оптического излучения

А.С. Паньков [1] ✉, Р.С. Пономарев [1]

[1] Пермский государственный национальный исследовательский университет, г. Пермь, Россия

✉ lab.photon.psu@gmail.com

Аннотация. В настоящей работе рассматривается применение суженых конических оптических волокон с сохранением поляризации излучения для формирования микролинз. Сужение волокон достигается путем растяжения оптического волокна под воздействием электрической дуги сварочного аппарата. Данный способ позволяет получать микролинзы с диаметром поля моды в точке фокуса до 2 мкм и с коэффициентом поляризационного затухания излучения на выходе из микролинзы до 40 дБ. При этом падение коэффициента поляризационного затухания в микролинзе составляет не более 3 дБ.

Ключевые слова: волоконная микролинза, коническое волокно, волокно с сохранением поляризации, коэффициент поляризационного затухания, фокусное расстояние, диаметр поля моды

Финансирование: Работа выполнена в рамках госзадания Министерства науки и высшего образования РФ № 121101300016-2.

Ссылка при цитировании: Паньков А.С., Пономарев Р.С. Формирование микролинз с помощью электрической дуги на торце оптических волокон, сохраняющих поляризацию оптического излучения // Научно-технические ведомости СПбГПУ. Физико-математические науки. 2023. Т. 17. № 3.1. С. 138–141. DOI: https://doi.org/10.18721/JPM.173.127

Introduction

Optical constrictions, in the form of tapered fibers, are of great interest for a variety of applications. One of the first applications for such fibers was the creation of fiber-optic splitters and connectors. Over time, tapered fibers began to be used in medicine, chemical and biological sensing, construction, and engineering industries as sensors for physical quantities [1].

Currently, optical constrictions are produced using two main methods: chemical etching [2, 3] and thermal methods [4]. Chemical etching with hydrofluoric acid allows you to achieve the desired geometry by controlling several parameters, including the percentage concentration of the acid, the temperature during the etching process, the time of etching, and the amount of acid applied to the surface being etched. The main disadvantages of this method are the negative effects of acid on human health, as well as the requirement for special equipment for chemical etching.

The thermal method of producing tapered conical fibers is one of the most commonly used. This method involves an electric arc the fiber fusion splicer to soften the glass of the optical fiber. The advantages of this method include the high speed of producing the elements and their relatively low final cost. In this method, the following parameters are controlled: the power and duration of the electric arc, the rate of fiber stretching, and the time over which the stretching process occurs. In this paper, a method for the fabrication and measurement of microlenses parameters using optical constrictions on fibers while maintaining the polarization of optical radiation is proposed [5].

Fabrication method

The Fujikura FSM-100P the fiber fusion splicer is used to create microlenses using optical constriction. This device is designed for splicing optical fibers in laboratory conditions. As an additional option, it is possible to create optical constrictions with different geometric dimensions. The general process of creating fiber microlenses is illustrated in Fig. 1.

At the first stage, the cleaned optical fiber is placed in the fiber fusion splicer. Using the standard Fujikura FSM-100P mode, the next step is to fabricate a constriction (Fig. 1, *a*). The formation of an optical constriction is a process that involves several steps. First, the two ends of the fiber are connected by splicing. Then, with continuous exposure to an electric arc, the fiber is softened and stretched until a constriction with the desired geometric parameters is achieved. In the absence of an electric arc, a rupture occurs in the tapered area of the constriction. The result of the rupture is two segments of optical fiber with conical ends (Fig. 1, *b*). To form a hemispherical surface from two segments, one of the segments is chosen that does not contain a splicing site for the two fibers. The resulting tapered surface at the end of the fiber is additionally melted by the electric arc of the fiber fusion splicer. The fused section of the optical fiber, under the action of surface tension forces, forms a symmetrical convex surface that acts as a microlens (Fig. 1, *c*).

Measurement of microlenses characteristics

The focal length is the distance between the end of the lensed fiber and the point where the light beam focuses. The microlens converts the outgoing Gaussian beam into a converging beam at a certain distance, which is known as a necking. The focal length is directly related to the

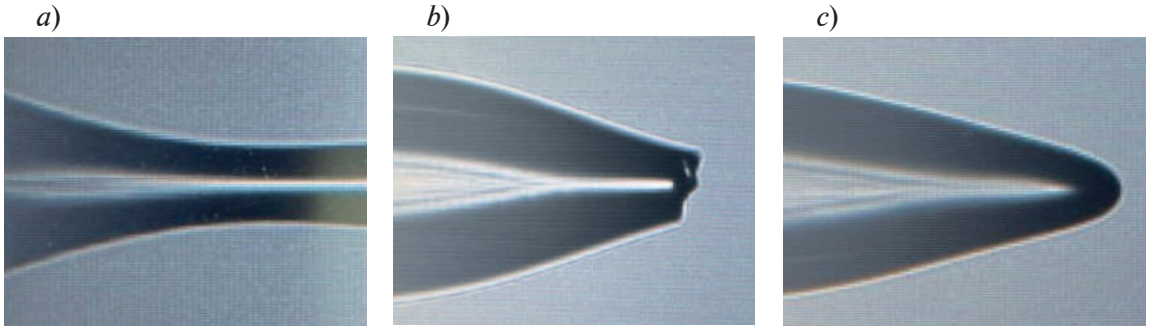

Fig. 1. Process of creating fiber microlenses: fabrication a constriction (*a*); rupture in the tapered area (*b*); fiber microlens (*c*)

length of the necking formed. The most widely used precision method for measuring focal length is the Fabry-Perot method [6], in which an outgoing beam of optical radiation is reflected from a mirror and returns back to the fiber, while experiencing interference. The value of the output power is fixed, and as a result, an optical power distribution is achieved, which depends on the length of the Fabry-Perot cavity.

The mode field diameter (MFD) in an optical fiber determines the area through which the main part of the optical radiation energy is transmitted. The MFD, for a fiber with a microlens at the end, is located in the area of the constriction formed at the focal length from the edge of the lens. An infrared profilometer is used to quickly and relatively accurately estimate the size of the MFD fiber microlens. It is a high-resolution infrared camera that uses a lens to capture images and a software suite to process the recorded signals. Measurement of the MFD of a fiber microlens is performed by image processing with power distribution of the optical signal coming out of it.

The polarization extinction ratio coefficient is the most important parameter for optical fiber-based microlenses while maintaining radiation polarization. The numerical value of this coefficient is used to evaluate the ability of the microlens to maintain the polarization of radiation. To date, the method of cross-polarization of PER measurement is known [7, 8]. It is based on the principle that polarized light is guided into the core of a single-mode optical fiber through a polarizer. The axis of polarization of the polarizer is aligned with one of the principal axes of the fiber, ensuring that the polarization of the radiation is maintained. The light that comes out of the fiber passes through the analyzer, where the proportion of output signal power is measured. This power is linearly polarized along two axes, called the fast (P_{max}) and slow (P_{min}) axes. The PER coefficient value is calculated using the formula:

$$\mathrm{PER} = 10\lg\left(\frac{P_{max}}{P_{min}}\right) \quad (1)$$

In this paper, a meter FIBERPRO ERM 2200 is used to evaluate the PER coefficient fiber microlenses. This device allows you to measure the numerical value of PER coifficient in real-time. The decrease in the PER coefficient of the lensed fiber is the difference between its value at the microlens entrance and its value at the exit.

Results and Discussion

Produced domestically optical fibers with polarization preservation of radiation were used to create a small batch of fiber microlenses. Unlike foreign analogues, these fibers have the property of preserving the PER coefficient up to 40 dB. During the manufacturing process, 10 lensed fibers were obtained and the repeatability of their parameters was evaluated.

The focal length of the obtained fiber microlenses varied in the range from 20 to 26 microns. The values of the mode field diameter at the focus point ranged from 2.0 to 2.5 microns. The optical losses introduced by a single microlens were no more than 3 dB. With all the above characteristics, the resulting products retained the radiation polarization. The decrease in the PER coefficient was not more than 3 dB. Based on the numerical values of the key characteristics of the microlenses obtained, it can be concluded that using an electric arc for creating batches up to 10 units is acceptable.

Conclusion

In this article, the use of optical constrictions for the formation of fiber microlenses while maintaining radiation polarization was considered. Using the electric arc of the fiber fusion splicer, lenses were formed using optical fibers with a spot size of 2 microns at the focal point. This method allows us to obtain microlenses with a PER coefficient of up to 40 dB at the output and a polarization drop of no more than 3 dB in the lens.

Acknowledgments

The work was carried out with the support of the Ministry of Science and Higher Education of the Russian Federation topic No. 121101300016-2.

REFERENCES

1. **Guzowski B., Lakomski M., Peczek K., Melka M.,** Evaluation of the tapered optical fiber geometry repeatability in arc-discharge method fabrication, Social Science Research Network. 17 (2023) 1–6.

2. **Haddock H.S., Shankar P.M., Mutharasan R.,** Fabrication of bioconical tapered optical fibers using hydrofluoric acid, Materials Science and Engineering. 97 (1) (2003) 87–93.

3. **Chenari Z., Latifi H., Ghamari S., Hashemi R.S., Doroodmand F.,** Adiabatic tapered optical fiberfabrication in twoo step etching, Optics & Laser Technoology. 76 (2016) 91–95.

4. **Karimi-Alavjeh H., Taslimi A., Maghsoudian M.H., Poorghadiri M.H., Kazemzadeh M.,** Fabrication of low-loss adiabatic optical microfibers using an attainable arc-discharge fiber tapering setup, Optics communications. 522(1) (2022) 128669.

5. **Jung Y., Brambilla G., Richardson D.J.,** Polarization-maintaining optical microfiber, Optics letters. 35 (12) (2010) 2034–2036.

6. **Li E.,** Characterization of a fiber lens, Optics letters. 31 (2006) 169–171.

7. **Penninckx D., Beck N.,** Definition, meaning, and measurement of the polarization extinction ratio of fiber-based devices, Applied Optics. 44 (36) (2005) 7773-7779.

8. **Aalto T., Harjanne M., Kapulainen M.,** Method for the rotational aligment of polarization-maintaining optical fibers and waveguides, Optical engineering. 42 (10) (2003) 2861–2867.

THE AUTHORS

PANKOV Anatoliy S.
lab.photon.psu@gmail.com

PONOMAREV Roman S.
rsponomarev@gmail.com
ORCID: 0000-0001-9729-628X

Received 22.07.2024. Approved after reviewing 23.07.2024. Accepted 23.07.2024.

Conference materials
UDC 004.942
DOI: https://doi.org/10.18721/JPM.173.128

Determination of the equivalent electric circuit parameters of a galvanic cell in the micro-arc oxidation process

P.E. Golubkov [1] ✉, E.A. Pecherskaya [1], D.V. Yakushov [1],
A.E. Shepeleva [1], G.V. Kozlov [1], A.V. Pecherskiy [1]

[1] Penza State University, Penza, Russia
✉ golpavpnz@yandex.ru

Abstract. A method for determining the thickness of microarc coatings based on the use of electrochemical impedance spectroscopy during the microarc oxidation process is proposed. To obtain the studied oxide coatings, a silicate-alkaline electrolyte was used in the following technological modes: sinusoidal electric current in the anode-cathode mode at a current density of 11 A/dm^2. The frequency range of electrochemical impedance spectroscopy ranges from 20 Hz to 2 MHz. During the study, the structure was revealed and the elements values of the electrical circuit of the galvanic cell were determined, taking into account electrochemical impedances by parametric optimization. The proposed equivalent electrical circuit takes into account the processes of ion diffusion through the oxide layer and the imperfection of the electrical capacitance of the coating, which is due to its porous structure. A regression and correlation analysis of the experimental data obtained was performed, during which the strong inverse correlation of the proportionality factor of the constant phase element of electrical circuit of the galvanic cell with the thickness of the formed coatings was found. The method of indirect measurement of the thickness of oxide coatings has satisfactory accuracy and can be used for laboratory studies. With an increase in the accuracy and speed of measuring operations, industrial application of this method is also possible. The proposed galvanic cell equivalent electrical circuit can be implemented in the decision support subsystem of an intelligent microarc oxidation system.

Keywords: microarc oxidation process, electrochemical impedance spectroscopy, electrical substitution circuit, galvanic cell, parametric identification, digital twin

Funding: The work was supported by the grant of the Ministry of Science and Higher Education of the Russian Federation "Fundamentals of the digital twin of the technological process of forming oxide coatings with specified properties by microarc oxidation" (No. 123091800009-1).

Citation: Golubkov P.E., Pecherskaya E.A., Yakushov D.V., Shepeleva A.E., Kozlov G.V., Pecherskiy A.V., Determination of the equivalent electric circuit parameters of a galvanic cell in the micro-arc oxidation process, St. Petersburg State Polytechnical University Journal. Physics and Mathematics. 17 (3.1) (2024) 142–146. DOI: https://doi.org/10.18721/JPM.173.128

Материалы конференции
УДК 004.942
DOI: https://doi.org/10.18721/JPM.173.128

Определение параметров схемы замещения гальванической ячейки в процессе микродугового оксидирования

П.Е. Голубков [1] ✉, Е.А. Печерская [1], Д.В. Якушов [1],
А.Э. Шепелева [1], Г.В. Козлов [1], А.В. Печерский [1]

[1] Пензенский государственный университет, г. Пенза, Россия
✉ golpavpnz@yandex.ru

Аннотация. В работе исследуется возможность применения метода электрохимической импедансной спектроскопии для определения толщины оксидных покрытий в процессе микродугового оксидирования. В ходе исследования выявлена структура и определены значения элементов электрической схемы замещения гальванической ячейки с учетом электрохимических импедансов методом параметрической оптимизации. Предложенная схема замещения учитывает процессы диффузии ионов через оксидный слой и неидеальность электрической емкости покрытия, которая обусловлена его пористой структурой. В результате регрессионного и корреляционного анализа полученных экспериментальных данных обнаружена сильная обратная корреляция фактора пропорциональности элемента постоянной фазы схемы замещения гальванической ячейки с толщиной формируемых покрытий. Метод определения толщины оксидных покрытий имеет удовлетворительную точность и может быть использован для лабораторных исследований. Предложенная схема замещения гальванической ячейки может быть использована для разработки цифрового двойника процесса микродугового оксидирования.

Ключевые слова: процесс микродугового оксидирования, электрохимическая импедансная спектроскопия, электрическая схема замещения, гальваническая ячейка, параметрическая идентификация, цифровой двойник

Финансирование: Работа выполнена при поддержке гранта Министерства науки и высшего образования Российской Федерации «Основы цифрового двойника технологического процесса формирования оксидных покрытий с заданными свойствами методом микродугового оксидирования» (№ 123091800009-1).

Ссылка при цитировании: Голубков П.Е., Печерская Е.А., Якушов Д.В., Шепелева А.Э., Козлов Г.В., Печерский А.В. Определение параметров схемы замещения гальванической ячейки в процессе микродугового оксидирования // Научно-технические ведомости СПбГПУ. Физико-математические науки. 2024. Т. 17. № 3.1. С. 142–146. DOI: https://doi.org/10.18721/JPM.173.128

Introduction

The task of creating a digital twin is related to the choice of a mathematical model that adequately describes the object of research. For the micro-arc oxidation (MAO) process, the object of the study is a galvanic cell, which is advisable to analyze a metal-oxide-electrolyte type system. For the analysis of electrophysical processes, systems of this type are presented in the form of an electrical replacement circuit. For example, in [1] a model of a galvanic cell based on a substitution circuit is presented, which includes active (resistance) and reactive (capacitance) elements. This substitution circuit does not take into account some features of the research object, as a result of which the model has limited accuracy. As a rule, electrical equivalent circuits for modeling electrochemical systems contain idealized elements characterizing physical and chemical processes in the metal-oxide-electrolyte type system (Warburg impedance *W*, constant phase element *CPE*, etc.) [2–4], while the structure of the electrical equivalent circuit may be different. However, this approach is currently used mainly to study the corrosion resistance of finished samples of oxide coatings. Therefore, it seems urgent to analyze the mathematical model of the microarc oxide coating process and refine it taking into account the electrochemical impedance.

Materials and Methods

To obtain the studied samples of oxide coatings by microarc oxidation, the surface of 10 bars of aluminum alloy AD31 with dimensions of 20×15×2 mm was developed. The processed sample is placed in the galvanic cell as an anode, the cathode is made of stainless steel. The process current source generates a symmetrical sinusoidal current with a density of 11 A/dm^2 in the anode-cathode mode. The following electrolyte was used: 2 g/l NaOH and 9 g/l Na_2SiO_3.

The microarc oxidation process was carried out over the following time: 30, 60, 120, 300, 600, 960 s. Measurements of the real and imaginary components of the complex impedance of the galvanic cell of each test sample were performed before the start of the technological process and at the above-mentioned time points. Measurements were made using the Keysight E4980A LCR meter in the frequency range from 20 Hz to 2 MHz. Before measuring the impedance, the galvanic cell was disconnected from the MAO installation, maintained for 5 minutes and discharged by closing the anode to the cathode for 30 seconds. Based on the results of the experiment, the Nyquist plots of the galvanic cell impedance were plotted for each sample. The structure selection and determination of the elements parameters of the galvanic cell equivalent electrical circuit were performed using the EIS Spectrum Analyser software [5] by parametric optimization using the Powell method. The coatings thickness was determined using a point autofocus probe surface texture measuring instrument Mitaka PF-60. Statistical processing of measurement results, including regression and correlation analysis, was performed using the STATISTICA 10 program.

Results and Discussion

Fig.1, *a* shows the impedance Nyquist plots obtained as a result of experiments. The galvanic cell equivalent electrical circuit, which satisfactorily approximates the impedance Nyquist plots (the model adequacy error does not exceed ± 2%), is shown in Fig. 1, *b*. The elements values of the galvanic cell equivalent electrical circuit are given in Table.

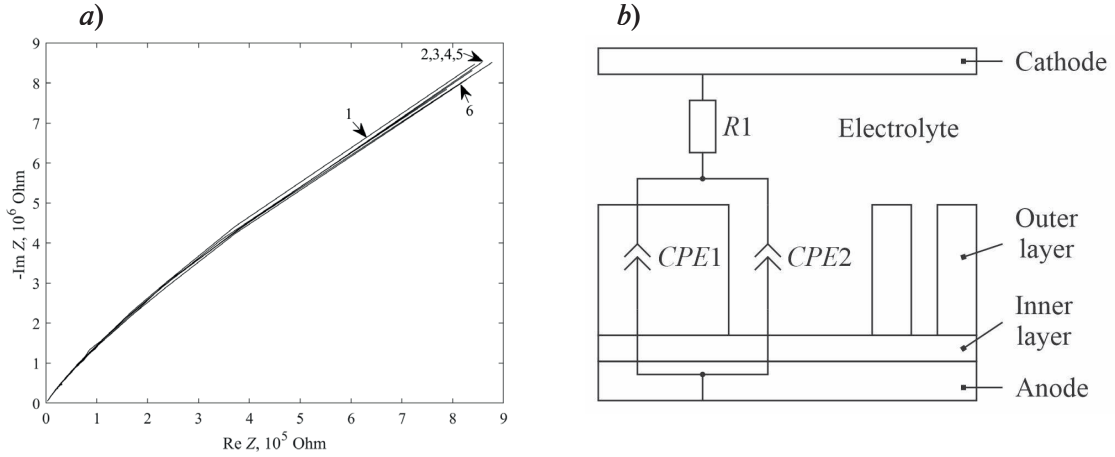

Fig. 1. Nyquist plots of the galvanic cell impedance (*a*) and equivalent electrical circuits of the galvanic cell (*b*): 1 – MAO treatment time of 30 s, 2 – 60 s, 3 – 120 s, 4 – 300 s, 5 – 600 s, 6 – 960 s; *R*1 – electrolyte resistance, *CPE*1 – imperfect capacitance of coating, *CPE*2 – imperfect Warburg impedance

Table

The elements values of the galvanic cell equivalent electrical circuit

Time, s	*R*1, Ohm	P_1	n_1	P_2	n_2
30	504.73	$2.64 \cdot 10^{-12}$	0.97	$6.20 \cdot 10^{-11}$	0.46
60	455.82	$2.48 \cdot 10^{-12}$	0.97	$5.37 \cdot 10^{-11}$	0.46
120	470.62	$2.44 \cdot 10^{-12}$	0.97	$4.88 \cdot 10^{-11}$	0.49
300	551.40	$2.40 \cdot 10^{-12}$	0.97	$4.40 \cdot 10^{-11}$	0.49
600	583.66	$2.39 \cdot 10^{-12}$	0.97	$2.88 \cdot 10^{-11}$	0.53
960	914.19	$1.73 \cdot 10^{-12}$	0.99	$6.06 \cdot 10^{-12}$	0.76

P_1, P_2 are proportionality factors; n_1, n_2 are exponents showing phase deviation. The error in determining the parameters of the galvanic cell equivalent electrical circuit and measuring error of the MAO coating thickness are ± 2% and ± 2.5% respectively.

The analysis of the data in Table, taking into account the available data on the MAO coatings structure [6, 7], allows us to interpret the physical meaning of the elements of the galvanic cell equivalent electrical circuit as follows. The resistor $R1$ represents the electrolyte resistance; the constant phase element $CPE1$ is an almost ideal capacitor ($n_1 \approx 1$) and represents the capacitance of the coating (barrier layer, working layer and porous layer, except for the pore area). The constant phase element $CPE2$ is the Warburg impedance ($n_2 \approx 0.5$), which in this case simulates the diffusion of oxygen and aluminum ions through the oxide layer; in this case, the parameter P_2 makes sense of the diffusion coefficient. The structure of the galvanic cell equivalent electrical circuit has some similarities with the one presented in [8].

The effect of the technological process time on the thickness of the oxide coating is shown in Fig. 2, *a*. It can be seen that this dependence is linear in nature, which is consistent with the results of [9–11]. The scattering diagram (Fig. 2, *b*) allows to analyze the relationship between the thickness of the synthesized coating and the coefficient P_1, which characterizes the electrical capacitance of the coating. It can be seen that with a confidence probability of 95%, the points in Fig. 2, *b* are within the confidence interval (curve *2* corresponds to the approximating curve, curves *1* and *3* correspond to the upper and lower boundaries of the confidence interval). The results of statistical processing confirmed the presence of an inverse correlation between the coating thickness and the coefficient P_1 (correlation coefficient $\rho = -0.89$). The above conclusions confirm the possibility of indirectly determining the thickness of the oxide coating using the parameter P_1.

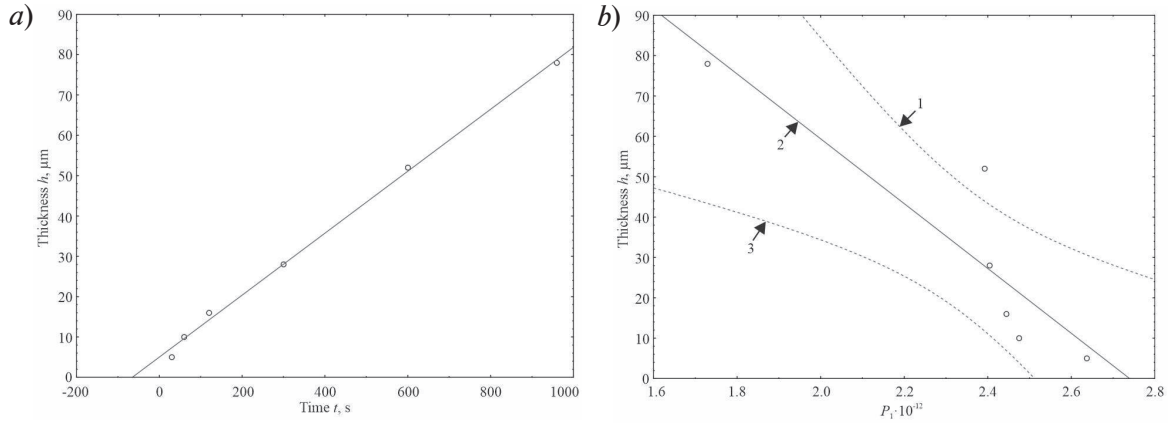

Fig. 2. Functional dependence showing the effect of the duration of the technological process t on the thickness of the coating h (*a*) and a scattering diagram reflecting the correlation between the coating thickness h and the coefficient $P1$ (*b*). Solid lines show approximating curves, dashed lines show the boundaries of the confidence interval

Conclusion

Thus, the revealed structure of the equivalent electrical circuit and the values of its elements obtained by parametric optimization adequately describe the behavior of the galvanic cell in the MAO process, taking into account the ions diffusion through the oxide layer and the imperfect capacitance of the coating having leakage through the pores. The model makes it possible to predict the change in coating thickness during the MAO process using the parameter $P1$ of the constant phase element $CPE1$, which has a physical meaning of electrical capacitance. The proposed thickness measurement method can be used for laboratory studies, since obtaining electrochemical impedance spectra suitable for analysis requires careful experimental preparation and takes a long time. In addition, the methods of parametric optimization used are not ideal and may give different results depending on the initial conditions, as a result of which the correct interpretation of the electrochemical impedance spectra is possible only with a deep understanding of the physical processes underlying the phenomena under consideration. Automation of measurement operations and improvement of parametric optimization methods will partially eliminate these disadvantages, which will make it possible for industrial use of the proposed method for determining the MAO coatings thickness.

REFERENCES

1. **Semenov A., Pecherskaya E., Golubkov P., Gurin S., Artamonov D., Shepeleva Y.,** Parametric identification of the mathematical model of the micro-arc oxidation process, Heliyon. (9) (2023) e19995.

2. **Kaseem M., Zehra T., Dikici B, Dafali A., Yang H.W., Ko Y.G.,** Improving the electrochemical stability of AZ31 Mg alloy in a 3.5wt.% NaCl solution via the surface functionalization of plasma electrolytic oxidation coating, Journal of Magnesium and Alloys. (10) (2022) 1311–1325.

3. **Almashhadani H.A., Khadom A.A., Khadhim M.M.,** Effect of Polyeugenol coating on surface treatment of grade 23 titanium alloy by micro arc technique for dental application, Results in Chemistry. (4) (2022) 100555.

4. **Hafili F., Chaharmahali R., Babaei K., Fattah-Alhosseini A.,** Duty cycle influence on the corrosion behavior of coatings created by plasma electrolytic oxidation on AZ31B magnesium alloy in simulated body fluid, Corrosion Communications. (3) (2021) 62–70.

5. **Bondarenko A.S., Ragoisha G.A.,** In Progress in Chemometrics Research, Pomerantsev A.L., Ed., Nova Science Publishers, New York. (2005) 89–102.

6. **Rogov A.B., Huang Y., Shore D., Matthews A., Yerokhin A.,** Toward rational design of ceramic coatings generated on valve metals by plasma electrolytic oxidation: The role of cathodic polarization, Ceramics International. (47) (2021) 34137–34158.

7. **Kaseem M., Fatimah S., Nashrah N., Ko Y.G.,** Recent progress in surface modification of metals coated by plasma electrolytic oxidation: Principle, structure, and performance, Progress in Materials Science. (117) (29) (2020) 100735.

8. **Jiang S., Zhang Zh., Wang D., Wen Y., Peng N., Shang W.,** ZIF-8-based micro-arc oxidation composite coatings enhanced the corrosion resistance and superhydrophobicity of a Mg alloy, Journal of Magnesium and Alloys. (11) (2023) 1367–1380.

9. **Rakoch A.G., Monakhova E.P., Khabibullina Z.V., Serdechnova M., Blawert C., Zheludkevich M.L., Gladkova A.A.,** Plasma electrolytic oxidation of AZ31 and AZ91 magnesium alloys: Comparison of coatings formation mechanism, Journal of Magnesium and Alloys. (8) (2020) 587–600.

10. **Pecherskaya E.A., Semenov A.D., Golubkov P.E.,** Simulation of electrical parameters of a galvanic cell in the process of microarc oxidation, Frontier Materials and Technologies. (4) (2023) 73–85.

11. **Rogov A. B., Matthews A., Yerokhin A.,** Role of cathodic current in plasma electrolytic oxidation of Al: A quantitative approach to in-situ evaluation of cathodically induced effects, Electrochimica Acta. (317) (2019) 221–231.

THE AUTHORS

GOLUBKOV Pavel E.
golpavpnz@yandex.ru
ORCID: 0000-0002-4387-3181

SHEPELEVA Anastasiya E.
anastasiya.shepeleva.01@mail.ru
ORCID: 0000-0002-8600-084X

PECHERSKAYA Ekaterina A.
pea1@list.ru
ORCID: 0000-0001-5657-9128

KOZLOV Gennadiy V.
gvk17@yandex.ru
ORCID: 0000-0002-5113-1305

YAKUSHOV Dmitriy V.
hammer.fate@yandex.ru
ORCID: 0009-0005-0892-312X

PECHERSKIY Anatoliy V.
ura258@yandex.ru
ORCID: 0000-0002-6692-1692

Received 03.07.2024. Approved after reviewing 31.07.2024. Accepted 31.07.2024.

Conference materials
UDC 621.317.42
DOI: https://doi.org/10.18721/JPM.173.129

Digital signal processing during measurement of magnetic materials parameters

A.V. Volik [1] ✉, E.A. Pecherskaya [1], A.M. Metalnikov [1],
P.E. Golubkov [1], G.V. Kozlov [1], U. S. Chikhrina [1]

[1] Penza State University, Penza, Russia

✉ nauka-fpite@mail.ru

Abstract. The principles of digital signal processing in the form of electrical voltage, which contain the information necessary for indirect measurement of magnetic induction, magnetic field strength, magnetic permeability and other parameters of magnetic materials are outlined. The structure of the processor module is presented, which implements the technique for measuring the parameters of magnetic materials and monitors the serviceability of the measuring installation. An interface has been developed that allows remote control of an information-measuring system for measuring the parameters of magnetic materials.

Keywords: magnetic materials, digital processing, magnetic induction, coercive force, measurement, processor module

Funding: The work was supported by the grant of the Ministry of Science and Higher Education of the Russian Federation «Synthesis and research of promising nanomaterials, coatings and electronics devices» (No. 124041700069-0).

Citation: Volik A.V., Pecherskaya E.A., Metalnikov A.M., Golubkov P.E., Kozlov G.V., Chikhrina U.S., Digital signal processing during measurement of magnetic materials parameters, St. Petersburg State Polytechnical University Journal. Physics and Mathematics. 17 (3.1) (2024) 147–152. DOI: https://doi.org/10.18721/JPM.173.129

Материалы конференции
УДК 621.317.42
DOI: https://doi.org/10.18721/JPM.173.129

Цифровая обработка сигналов в процессе измерения параметров магнитных материалов

А.В. Волик [1] ✉, Е.А. Печерская [1], А.М. Метальников [1],
П.Е. Голубков [1], Г.В. Козлов [1], У.С. Чихрина [1]

[1] Пензенский государственный университет, г. Пенза, Россия

✉ nauka-fpite@mail.ru

Аннотация. Изложены принципы цифровой обработки сигналов виде электрического напряжения, которые содержат информацию, необходимую для косвенного измерения магнитной индукции, напряженности магнитного поля, магнитной проницаемости и других параметров магнитных материалов. Представлена структура процессорного модуля, который реализует методику измерения параметров магнитных материалов и осуществляет контроль исправности измерительной установки. Разработан интерфейс, позволяющий осуществить дистанционное управление информационно-измерительной системой для измерения параметров магнитных материалов.

Ключевые слова: магнитные материалы, цифровая обработка, магнитная индукция, коэрцитивная сила, измерение, процессорный модуль

Финансирование: работа выполнена при поддержке Министерства науки и высшего образования РФ, проект «Синтез и исследование перспективных наноматериалов, покрытий и устройств электроники» (№ 124041700069-0).

Ссылка при цитировании: Волик А.В., Печерская Е.А., Метальников А.М., Голубков П.Е., Козлов Г.В., Чихрина У.С. Цифровая обработка сигналов в процессе измерения параметров магнитных материалов // Научно-технические ведомости СПбГПУ. Физико-математические науки. 2024. Т. 17. № 3.1. С. 147–152. DOI: https://doi.org/10.18721/JPM.173.129

Introduction

Modern electronics is developing towards the widespread use of digital signal processing, which is performed in various ways and methods: using general-purpose microcontrollers, programmable logic integrated circuits (FPGAs), digital controllers (DSP) [1, 2].

Digital signal processing methods are the most effective, as they provide more stable temperature and time parameters and allow changing the coefficients of transfer functions. Digital signal processing methods have less impact on the signal output parameters [3]. This is due to the absence of parasitic parameters inherent in passive components, such as capacitors and resistors, which are one of the components of analog integrator circuits [4].

Integrating circuits are used in various functional units: voltage-frequency converters, frequency-voltage converters, analog-to-digital converters, control units in automatic control systems, pulse generators, active analog filters [5]. As the device operates, it is necessary to change its parameters in the integrating circuit, namely the time constant, that is, to rebuild it. In turn, it is accompanied by transition processes that influence the result of integration [6].

The developed automated information-measuring system (IMS) for studying the parameters of magnetic materials is based on indirect measurements of magnetic induction and coercive force by integrating the secondary winding voltage and magnetizing current, respectively [7].

Materials and Methods

During the development process, it is possible to expand the functionality of the installation due to the modularity of the design. The main functional blocks of the measuring installation are: a standby power supply (provides power to the auxiliary units of the installation, i.e. a board with a microprocessor, operational amplifiers in the measuring channel, a board with a hardware integration module), a switching power supply (generates voltages for the magnetizing winding of the test sample), a processor module, integration module performing numerical integration in hardware (under development).

The processor module is based on an STM32F429 microcontroller. Figure 1 shows the block diagram of the processor module.

The processor module includes: SPI modules for interaction with the TFT display, UART and Ethernet for user interaction, built-in memory controller for data exchange with an external SDRAM chip, an analog-to-digital converter (ADC) using 4 channels, and a digital-to-analog converter (DAC) to set a code proportional to the magnetizing current value. Service and user information is stored in an external EEPROM memory chip. Channel 1 of the ADC is used to diagnose the power supply. Channel 2 receives readings from the current sensor of the current shaper, which sets the magnetic field strength. In channel 3, the EMF proportional to the magnetic induction is measured.

The relationship between electromotive force and magnetic induction B is described by the following expression:

$$B = \frac{\int \varepsilon(t)dt}{S \cdot n_{II}},$$

where S is the cross–sectional area of the core; n_{II} is the number of turns of the magnetizing winding; ε- the electromotive force of the measuring winding, which is converted into a digital code by means of an analog-to-digital converter.

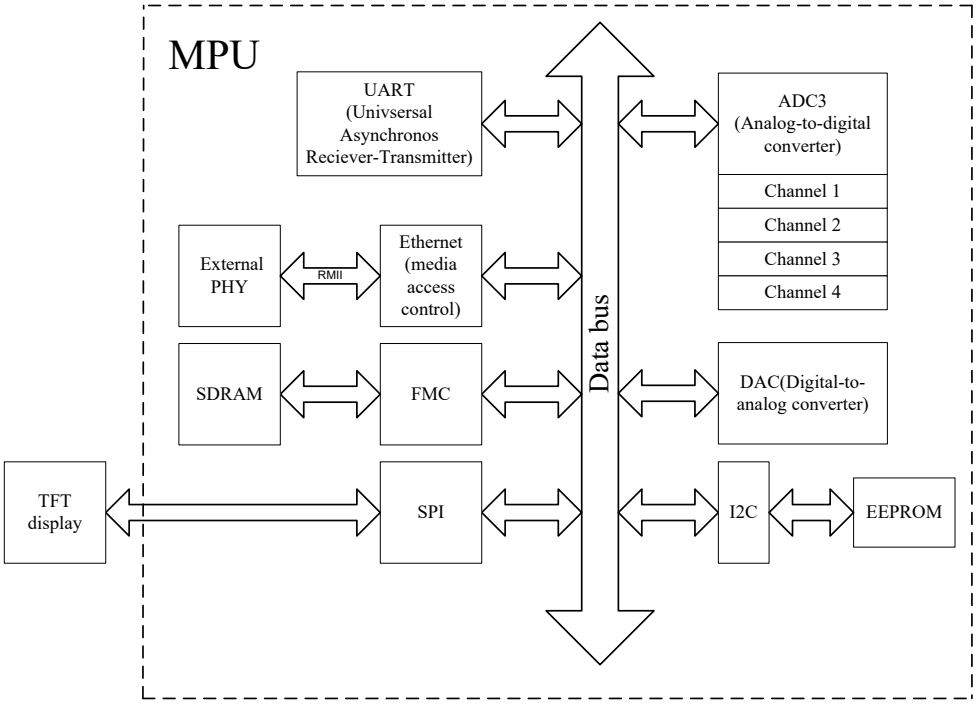

Fig. 1. Structure of the processor module

The use of two interfaces allows to expand the functionality of the installation. Using the RS232 interface, you can configure installation parameters (setting Ethernet network parameters). Thanks to a special client application, measurement results are displayed on the monitor. The disadvantage of this approach is the dependence on the target platform on which the client application must be deployed. The Web Interface does not have this drawback, access to which is provided by the Ethernet interface. For its work, the current version of the web browser must be installed on the client computer. Based on the use of Web Interface, remote work with the measuring installation, which is advisable to use both for educational purposes when performing remote laboratory work, and in scientific research of magnetic materials and structures based on them is organized.

The appearance of the printed circuit board of the processor module is shown in Figures 2 and 3.

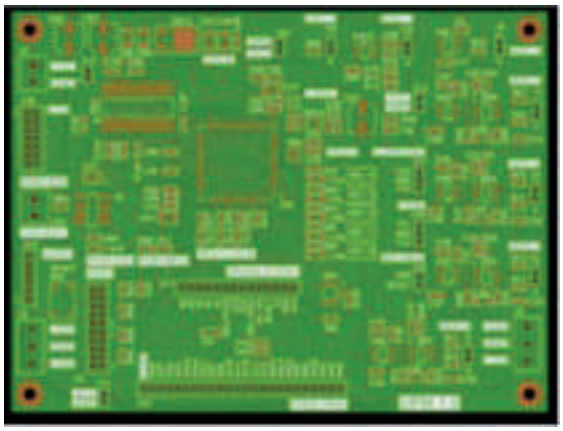

Fig. 2. The printed circuit board of the processor module, top view

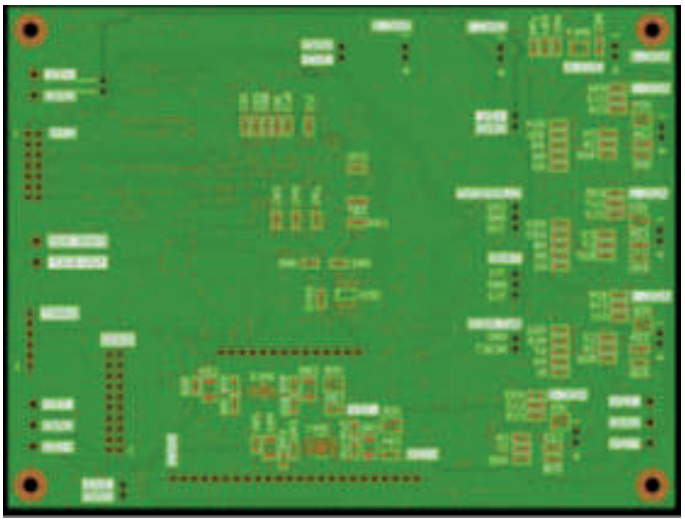

Fig. 3. Printed circuit board of the processor module, bottom view

The control program of the processor module includes a real-time operating system (RTOS). The tasks of the operating system include servicing data transmission via the UART interface, exchanging information with external devices and interacting with the TCP/IP stack necessary for the web interface implementation.

The TCP/IP protocol stack is implemented using the open source lwIP library. The lwIP stack is responsible for data generation, routing, and transmission.

This model includes four levels of abstraction, which are used to sort all related protocols according to the volume of the network used. Figure 4 shows the lwIP model architecture from the lowest to the highest layer:

- The channel layer contains communication technologies for one network segment (channel) of the local network.
- The Internet Layer (IP) connects independent networks, thereby establishing interconnection.
- The transport layer handles data exchange between hosts.
- The application layer contains all protocols for specific data transfer services at the interprocess level.

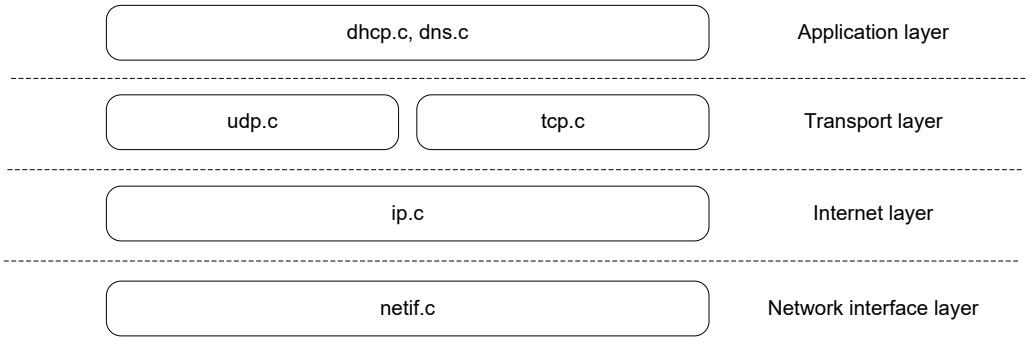

Fig. 4. lwIP Architecture

The firmware of the processor module implements three measurement modes.

The first mode consists in removing the voltage proportional to the magnetic induction from the operational amplifier. In this mode, an analog integrator circuit, which provides high performance is used. It is recommended to use this mode during rapid analysis, which is typical for conducting input control of ferrite products. The measurement error in this case depends on the variation of the operational amplifier parameters, which is reflected in the measurement result.

The second measurement mode is the oscilloscope mode. The voltage measured by an analog-to-digital converter (ADC) is transmitted directly from the measuring winding to the computer.

The third measurement mode uses a digital integrator, which is a separate module. The digital integrator communicates with the processor module via the SPI interface. The digital integrator board has its own ADC, which receives the reference points of the measuring pulse, and a programmable integrated logic circuit (FPGA) implementing a numerical integration method. The values obtained by the FPGA from the ADC are accumulated in the internal structure. Upon completion of the integration process, the FPGA informs the processor module with a strobing bit that it is ready to transmit data, then the read data from the FPGA is transmitted to the computer by the processor module.

Figure 5 shows the appearance of the web interface and the result of the measurements performed in graphical mode.

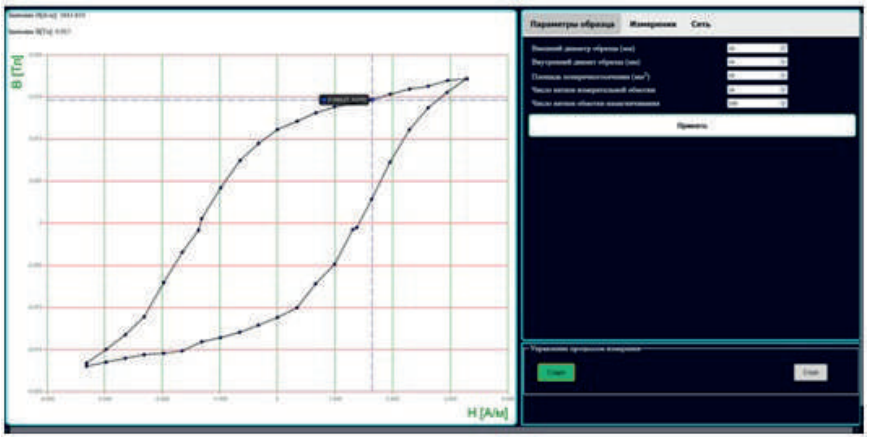

Fig. 5. The interface window with the measurement results performed by the processor module

Conclusion

The presented processor module, which is part of an information and measurement system for studying the parameters of magnetic materials, provides automation of the measurement process of ferrite products. The hardware and software complex allow you to reduce the operational time spent on performing measurement tasks. The number of operations performed by the operator is reduced by at least 3 times compared to non-automated measuring instruments. The presence of two interfaces allows you to increase the system reliability. The UART interface, in addition to measuring tasks, performs the function of a debugging interface that allows you to configure the measuring installation and display the parameters on the computer screen or the installation display. Remote access to the installation is possible via the Ethernet interface and using the web interface. The use of Ethernet technology makes it possible to include the installation in an automated production control circuit.

REFERENCES

1. **Varfolomeev V.I., Zhenishek E.Yu, Lupin A.V., Minaev V., Sakharov N.V., Babaritskiy P.A.,** Temperature control system for the electromagnetic system of the Globus-M2 tokamak, Technical Physics Letters. 48 (2022) 33.

2. **Wickenbrock A., Tricot F., Renzoni F.,** Magnetic induction measurements using an all-optical 87Rb atomic magnetometer, Applied Physics Letters. 103 (2013) 243503.

3. **Min S.-H., Seo Ch.-S., Lapushin S., Carastro L., Dalmia S., White G., Swaminathan M.,** Parasitic-Aware RF Design via Parameterization of Embedded Passives on Multilayer Organic Substrates, IEEE Electrical Performance of Electronic Packaging, Atlanta, GA, USA. (2007) 107–110.

4. **Lopez-Madrigal, J.E. et al.,** Magnetic Induction Spectroscopy for DNA Quantification: Preliminary Results. In: Flores Cuautle, J.d.J.A., et al. XLVI Mexican Conference on Biomedical Engineering. (96) (2023).

5. **Wolf L., Orozco A.,** Design, Development and Application of a Modular Electromagnetic Induction (EMI) Sensor for Near-Surface Geophysical Surveys. (2024).

6. **Pecherskaya E.A., Artamonov D.V., Kondrashin V.I., Golubkov P.E., Karpanin O.V., Zinchenko T.O.,** Software – Hardware Complex for Measurement and Control of Ferroelectrics Parameters, IOP Conference Series: Materials Science and Engineering. 225 (1) (2017) 012254.

7. **Volik A.V., Pecherskaya E.A., Varenik Y.A., Zinchenko T.O., Artamonov D.V., Timohina O.A.,** Metrological aspects of an automated method for measuring electrophysical parameters of soft magnetic materials Journal of Physics: Conference Series. 2086 (1) (2021) 012072.

THE AUTHORS

VOLIK Artem V.
minor401@gmail.com
ORCID: 0009-0004-3480-5322

PECHERSKAYA Ekaterina A.
pea1@list.ru
ORCID: 0000-0001-5657-9128

METALNIKOV Aleksey M.
metalnikovam@gmail.com
ORCID: 0009-0009-4904-7874

GOLUBKOV Pavel E.
golpavpnz@yandex.ru
ORCID: 0000-0002-4387-3181

KOZLOV Gennadiy V.
gvk17@yandex.ru
ORCID: 0000-0002-5113-1305

CHIKHRINA Ulyana S.
chikhulyana@yandex.ru
ORCID:0009-0000-3725-7326

Received 03.07.2024. Approved after reviewing 31.07.2024. Accepted 31.07.2024.

Conference materials
UDC 681.7
DOI: https://doi.org/10.18721/JPM.173.130

Development of an experimental device for measuring the internal stresses of single crystal diamond plates

I.O. Podoylov [1] ✉, A.A. Kharlamova [1]

[1] Northern (Arctic) Federal University named after M.V. Lomonosov,
Arkhangelsk, Russia
✉ i.podojlov@narfu.ru

Abstract. The paper presents a stand for measuring the internal stresses of monocrystalline diamond plates. The device is necessary to assess the quality of single crystal diamond plates as promising materials for quantum sensing. The use of diamond plates in engineering and instrumentation is limited by their quality. The device under development is used to assess the quality of the diamond plate according to the internal voltage indicator. The resulting device is an optical microscope with a modified polarizer system based on the phenomenon of double refraction and capable of detecting changes in the anisotropy coefficient of the sample under study. Also, software was developed for the stand that allows analyzing the received data. The result of the work of the stand is a map of the internal stress distributions in the test sample. The stand was tested on monocrystalline diamond plates with various anisotropy indicators. The results showed the effectiveness of the developed device, which recorded the internal stresses in the plates in all areas of graphitization, in places of cracks, etc.

Keywords: Anisotropy, polarizers, internal stresses, diamonds, optical microscope

Funding: The research was carried out with the support of the state assignment of the Russian Federation No. FSRU-2024 -0005 and the Russian Science Foundation, project No. 23-12-20014.

Citation: Podoylov I.O., Kharlamova A.A., Development of an experimental device for measuring the internal stresses of single crystal diamond plates, St. Petersburg State Polytechnical University Journal. Physics and Mathematics. 17 (3.1) (2024) 153–156. DOI: https://doi.org/10.18721/JPM.173.130

Материалы конференции
УДК 681.7
DOI: https://doi.org/10.18721/JPM.173.130

Разработка экспериментального устройства для измерения внутренних напряжений в монокристаллических алмазных пластинах

И.О. Подойлов [1] ✉, А. А. Харламова [1, 2]

[1] Северный (Арктический) федеральный университет им. М.В. Ломоносова,
г. Архангельск, Россия;
✉ i.podojlov@narfu.ru

Аннотация. В статье представлен стенд для измерения внутренних напряжений в монокристаллических алмазных пластинах. Прибор необходим для оценки качества монокристаллических алмазных пластин как перспективных материалов для квантового зондирования. Результаты показали эффективность разработанного прибора, который регистрировал внутренние напряжения в пластинах во всех зонах графитизации, в местах появления трещин и т.д.

Ключевые слова: анизотропия, поляризаторы, внутренние напряжения, алмазы, оптический микроскоп

Финансирование: Работа выполнена в рамках Государственного задания FSRU-2024-0005 и Государственного задания 23-12-20014.

Ссылка при цитировании: Подойлов И.О., Харламова А.А. Разработка экспериментального устройства для измерения внутренних напряжений в монокристаллических алмазных пластинах статьи // Научно-технические ведомости СПбГПУ. Физико-математические науки. 2024. Т. 17. № 3.1. С. 153–156. DOI: https://doi.org/10.18721/JPM.173.130

Introduction

Sensors made on the basis of synthetic diamonds are of great interest in the field of quantum technologies today. Monocrystalline diamond plates are becoming the main material for high-power electronics and advanced fields such as communications, energy, semiconductors and aerospace. Diamond single crystal is considered the most promising material for the manufacture of high-power, high-frequency, high-temperature electronic devices of a new generation with low power losses. But when they are used in the production of high-tech devices, careful quality control of monocrystalline plates is required. The most important parameter for evaluating the quality of the plate is the presence of internal stresses. In the process of growing diamond plates and processing them, internal stresses may occur, which lead to problems during the operation of the material [1–5].

Materials and Methods

The principle of operation of the developed stand is based on the phenomenon of double refraction. Diamond plates have the optical property of anisotropy, i.e. the refractive index of such a material depends on the direction of light propagation.

It is known that it is possible to detect double refraction on a sample using simple methods of polarization microscopy. When polarized light passes through a birefringent sample, a phase difference δ occurs between an ordinary and an extraordinary beam. By fixing the intensity of the light that passed through the sample, we can find δ. Knowing the phase difference, the thickness of the sample and the wavelength, we get the difference in the refractive indices of an ordinary and an extraordinary ray Δn. The dependence is expressed by the following formula (1):

$$\delta = \frac{2\pi}{\lambda}\Delta nL, \tag{1}$$

where λ is the wavelength of the light, L is the thickness of the sample and $\Delta n = n_1 - n_2$. The value ΔnL is known as the optical difference in the course of the rays.

By the magnitude of the optical anisotropy δ, one can judge the degree of internal stresses of the diamond plate, the nature of which indicates various deformations of the crystal structure and the presence of defects in it.

In this paper, a device is presented that registers the change in anisotropy. The developed stand is based on the Levenhuk MD 30 T optical microscope, modified by a rotating linear and circular polarizer system. Additionally, an electronic 2D positioning system was developed that allows moving the slide table with the sample under study. The developed device consists of the following main parts: a monochromatic light source (an LED and a light filter are used), a system of rotating polarizers, a quarter-wave plate (Fig. 1).

The signal received by the photo sensor is described by the following function

$$I = \frac{1}{2}I_0 + \frac{1}{2}I_0 \sin\delta \cdot \cos 2\varphi \cdot \sin 2\omega t - \frac{1}{2}I_0 \sin\delta \cdot \sin 2\varphi \cdot \cos 2\omega t, \tag{2}$$

Fig. 1. The device and its optical scheme

where is the signal intensity I_0, δ is the anisotropy, ω is the rotation frequency of the polarizer, φ is the optical orientation. The output of the quantities of interest is achieved using the least squares fitting procedure to the equation:

$$y(x) = a_0 + a_1 \sin x + a_2 \cos x, \tag{3}$$

the parameters a_0, a_1, a_2 can be found as:

$$a_0 = \sum_{i=1}^{N} \frac{1}{N} y_i, \; a_1 = \sum_{i=1}^{N} \frac{2}{N} y_i \sin x_i, \; a_2 = \sum_{i=1}^{N} \frac{2}{N} y_i \cos x_i, \tag{4}$$

where N is the number of polarizer steps. From equation (2), after substituting the coefficients, the amplitude corresponding to the optical anisotropy is determined:

$$\left|\sin \delta\right| = \frac{\sqrt{a_1^2 + a_2^2}}{a_0}. \tag{5}$$

Next, the phase shift of ordinary and extraordinary rays is determined, corresponding to the optical orientation:

$$\varphi = \frac{1}{2} \arcsin\left(-\frac{a_2}{\sqrt{a_1^2 + a_2^2}} \right). \tag{6}$$

Results and Discussion

The device gives an estimate of the magnitude of the anisotropy and shows the value of the difference in the refractive index of ordinary and extraordinary rays. The result of the stand is a snapshot of internal stresses in a color code, each color of which corresponds to a certain indicator of anisotropy (Fig. 2).

As can be seen from the map, the anisotropy coefficient in the center is 0.6 (Fig. 3, *a*), which shows the presence of large internal stresses. Graphitization grains are on the second plate. The device also shows a change in the anisotropy coefficient (Fig. 3, *b*).

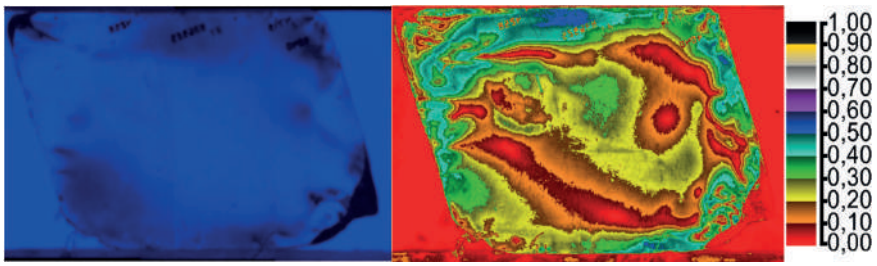

Fig. 2. The results of the device operation: (*a*) Diamond plate, image under a microscope; (*b*) Internal stress distribution map of the diamond plate

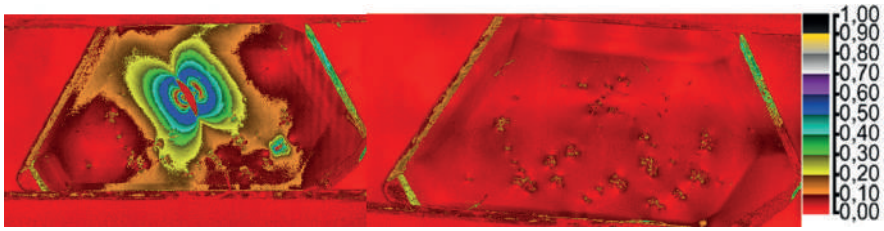

Fig. 3. The results of the device operation: (*a*) Internal stress distribution map on a cracked diamond plate; (*b*) A map of the distribution of internal stresses on a plate with growth defects

Conclusion

As a result, a stand for measuring internal stresses in diamond plates was developed and successfully tested. The removal of the anisotropy index of the crystal sinδ, the optical orientation φ of the difference in the refractive index of ordinary and extraordinary rays is ensured Δn. The measurement results prove the operability of the stand and its ability to record changes in the crystal structure of the sample.

Acknowledgments

The authors express their gratitude to AGD DIAMONDS for the resources provided during the development of the stand.

REFERENCES

1. **Glazer A.M., Lewis J.G., Kaminsky. W.,** An Automatic Optical Imaging System for Birefringent Media: Mathematical, Physical and Engineering Sciences. 452 (1996) 2751–2765.

2. **Howell. D.,** Strain-induced birefringence in natural diamond: a review: European Journal of Mineralogy. 24 (2012) 575–585.

3. **Howell. D., Wood I.G.,** Quantifying strain birefringence halos around inclusions in diamond, Contributions to Mineralogy and Petrology. 162 (2013) 1113–1113.

4. **Bulanova G.P., Griffin W.L., Ryan C.G.,** Nucleation environment of diamonds from Yakutian kimberlites: Mineral. Mag. 62 (1998) 409–419.

5. **Howell D., Woods I.G., Nestola F., Nimis P., Nasdala L.,** Inclusions under remnant pressure in diamond: A multi-technique approach, Eur. J. Mineral. 24 (2012) 563–573.

THE AUTHORS

PODOYLOV Igor O.
i.podojlov@narfu.ru
ORCID: 0009-0006-2002-0959

KHARLAMOVA Anastasya A.
kharlamova.anastasya2015@yandex.ru
ORCID: 0000-0002-8192-615X

Received 05.07.2024. Approved after reviewing 01.08.2024. Accepted 01.08.2024.

Conference materials
UDC 621.396.2
DOI: https://doi.org/10.18721/JPM.173.131

Experimental study of a broadband optical source with hybrid amplification

A.A. Pozdnyakov [1] ✉, E.I. Andreeva [1]

[1] St. Petersburg State University of Telecommunications. prof. M.A. Bonch-Bruevich, St. Petersburg, Russia

✉ me022@mail.ru

Abstract. The possibility of jointly using concentrated erbium and distributed Raman amplifiers to obtain a broadband optical radiation source has been demonstrated experimentally. Computer modeling was carried out using the OptiSystem program. The results of computer modeling and experimental research are in good agreement with each other.

Keywords: fiber-optic communication system, Raman amplifier, erbium amplifier, optical fiber, nonlinear effects

Citation: Pozdnyakov A.A., Andreeva E.I., Experimental study of a broadband optical source with hybrid amplification, St. Petersburg State Polytechnical University Journal. Physics and Mathematics. 17 (3.1) (2024) 157–160. DOI: https://doi.org/10.18721/JPM.173.131

Материалы конференции
УДК 621.396.2
DOI: https://doi.org/10.18721/JPM.173.131

Экспериментальное исследование широкополосного оптического источника с гибридным усилением

А.А. Поздняков [1] ✉, Е.И. Андреева [1]

[1] Санкт-Петербургский государственный университет телекоммуникаций им. проф. М.А. Бонч-Бруевича, Санкт-Петербург, Россия

✉ me022@mail.ru

Аннотация. Экспериментально продемонстрирована возможность совместного использования сосредоточенного оптического усилителя на волокне, легированном ионами эрбия, и распределенного комбинационного усиления для получения широкополосного источника оптического излучения. Проведено численное моделирование в программе OptiSystem. Результаты компьютерного моделирования и экспериментального исследования находятся в хорошем соответствии друг с другом.

Ключевые слова: волоконно-оптическая система связи, комбинационный усилитель, эрбиевый усилитель, волоконный световод, нелинейные эффекты

Ссылка при цитировании: Поздняков А.А., Андреева Е.И. Экспериментальное исследование широкополосного оптического источника с гибридным усилением // Научно-технические ведомости СПбГПУ. Физико-математические науки. 2024. Т. 17. № 3.1. С. 157–160. DOI: https://doi.org/10.18721/JPM.173.131

Introduction

Expanding the spectral range of operating wavelengths of fiber optic links requires the development of new measuring radiation sources for testing the spectral-selective components of such systems. The use of nonlinear effects in optical fibers makes it possible to create broadband measuring sources for systems operating in an extended spectral range [1–7]. The measuring source must meet the following requirements. Firstly, uniform distribution of radiation power over the entire wavelength range of interest. If the spectral characteristic of the source is not flat, then it should be as smooth as possible. Secondly, Possibility of inputting high optical power into optical fiber. Third, there should be no spurious back-reflections from the system under test, including the passive component itself.

Changing the spectrum of an optical signal transmitted along the optical fiber is of ever-increasing interest for creating systems for generating ultrashort high-power optical pulses and creating broadband radiation sources, including supercontinuum sources. The use of standard WDM components to produce broadband powerful radiation sources is of particular interest.

An experimental study of the possibility of creating a broadband healing source showed the feasibility of hybrid (local + distributed) signal amplification in optical fiber.

The aim of this work is to study the possibility of creating the broadband measuring source using the semiconductor laser and the nonlinear properties of the optical fiber.

Computer simulation

Computer simulation was carried out in OpiSystem program. As the source, the laser with the narrow spectral lasing line was chosen. The optical signal was amplified using the Er-amplifier and the Raman amplifier.

Nonlinear transformation of the optical signal spectrum occurred in standard single mode optical fiber (SSMF). For SSMF typically the group velocity dispersion $\beta_2 = 20$ ps^2/km, the nonlinear parameter $\gamma = 1.2$ W^{-1}km^{-1}, the optical loss $\alpha = 0.023$ km^{-1}. The simulation results are presented in Fig. 1.

Computer simulation confirms the possibility of significantly broadening the spectrum of the optical signal with hybrid amplification.

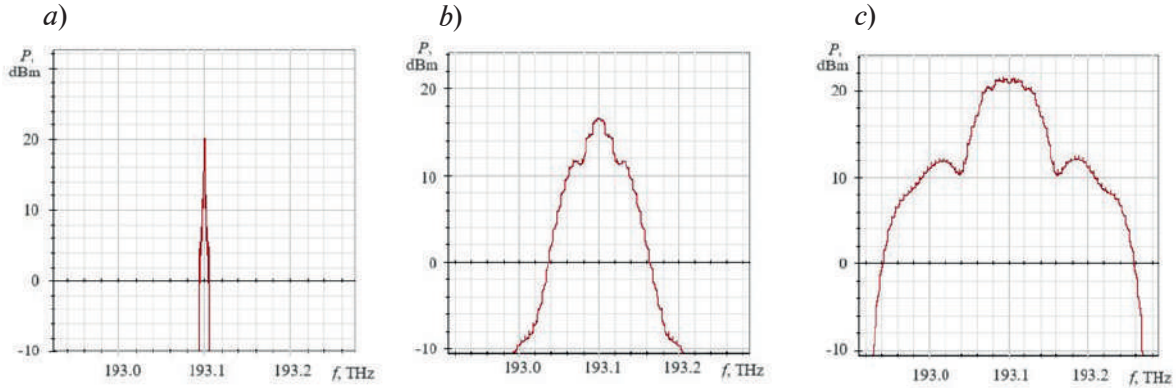

Fig. 1. Spectrum of the optical signal without an amplifier (*a*), with an Er-amplifier (*b*) and a hybrid Er and Raman amplifier (*c*)

Experimental Results and Discussion

To increase the efficiency of nonlinear effects in optical fiber, it is necessary to ensure the highest spectral energy density of optical signal [1]. So, the laser with a narrow spectral lasing line was chosen as the master oscillator.

To amplify the optical signal, the Er-amplifier with bidirectional (co-propagating and counter-propagating) pumping was used. The output power of the optical signal at the amplifier output reached 23 dBm.

A further increase in optical signal power was achieved using the Raman amplifier [7]. The high amplification efficiency was achieved using 4 pump diodes.

The block diagram of the experimental setup is shown in Fig. 2. The optical signal from the narrow-band laser *1* enters the input of the erbium amplifier *3*. Amplification occurs practically without changing the spectral characteristics. In the optical fiber *4* pumped simultaneously with the signal from *4* lasers in such a way that the frequency range and possible polarization mismatch are completely covered. As a result, the optical signal is further amplified and its spectrum is broadened.

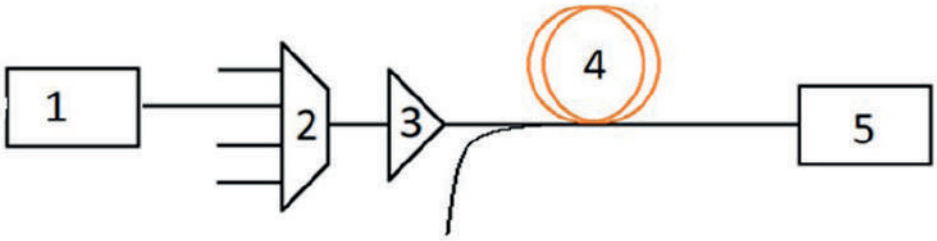

Fig. 2. Block diagram of the experimental study: *1* – optical pulse source, *2* – filter, *3* – Er optical amplifier, *4* – optical fiber, *5* – OSA

The results of measuring the signal spectrum at the input to fiber optic line *1*, using only erbium amplifier *2* and with additional Raman amplification *3* are shown in Fig. 3.

To enhance this effect, additional pump lasers and/or a dispersion-shifted fiber can be used.

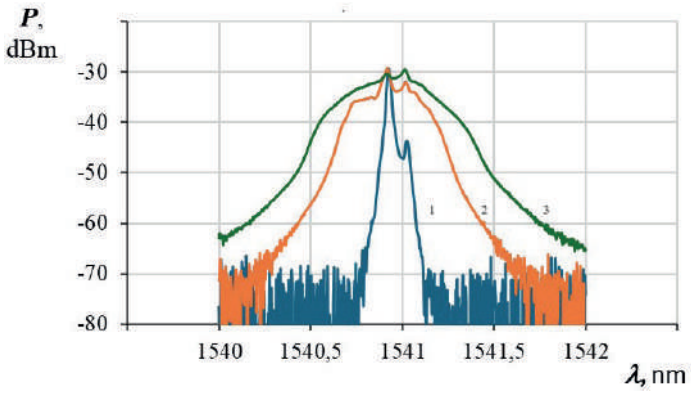

Fig. 3. The optical signal spectrum at the input to the optical fiber (*1*), at the output of the optical fiber using only erbium amplifier (*2*) and with additional Raman amplification (*3*)

Conclusion

Thus, the possibility of broadening the spectrum of an optical signal in the optical fiber using standard components has been demonstrated. To enhance the effect, the optical fiber with shifted (reduced) dispersion can be used.

REFERENCES

1. **Agrawal G.,** Nonlinear Fiber Optics, 6th Edition, Elsevier, 2019.

2. **Isupov A., Andreev D., Andreeva E.,** The broadband light source modeling using the optical fiber nonlinearity, Proc. of ITNT-2023, Samara. (2023) 10922.

3. **Agrawal G.,** Fiber-Optics Communication Systems, 5th Edition - New York, 2021.

4. **Kivshar Y.S.,** Optical Solitons. From fibers to Photonic Crystals, New York: Academic Press. (2003) 540.

5. **Zhluktova I.V., Kamynin V.A., Korobko D.A.,** Broadband Supercontinuum Generation in Dispersion Decreasing Fibers in the Spectral Range 900–2400 nm, Photonics. (9) (2022) 773.

6. **Rahman T., Okonkwo C., Waardt H., Rafique D., Napoli A., Spinnler B.,** 1.28Tb/s long-haul superchannel transmission employing EDFA-Raman amplification. Opto-Electronics and Communications Conference (OECC), Shanghai, China. (2015).

7. **Carena A., Curri V., Poggiolini P.,** On the optimization of hybrid Raman/erbium-doped fiber amplifiers, in IEEE Photonics Technology Letters. 13 (11) (2001) 1170–1172.

THE AUTHORS

POZDNYAKOV Artem A.
me022@mail.ru
ORCID: 0009-0009-6606-6807

ANDREEVA Elena I.
me022@mail.ru
ORCID: 0000-0002-1945-1050

Received 06.07.2024. Approved after reviewing 05.08.2024. Accepted 06.08.2024.

Conference materials
UDC 621.357.77; 620.22; 621.9.04
DOI: https://doi.org/10.18721/JPM.173.132

Methods and instruments for measuring surface morphology and mechanical parameters of oxide coatings

A.A. Maksov [1] ✉, S.A. Gurin [1], P.E. Golubkov [1], E.A. Pecherskaya [1],
J.V. Shepeleva [1], D.V. Artamonov [1]

[1] Penza State University, Penza, Russia
✉ maksov.01@mail.ru

Abstract. Morphological studies of coatings were carried out on aluminum samples obtained by microarc oxidation. The sinusoidal current density in the anodic and anode-cathode modes was 15 A/dm^2, and the processing time varied from 120 s to 960 s. The formation of oxide coatings occurred in a silicate-alkaline electrolyte. Studies of the surface topology and mechanical parameters of oxide coatings were carried out using an SEM, a laser profilometer and a universal electrical strength meter, which, in turn, made it possible to establish a relationship between the properties of the coatings and the sample processing time. Thus, an increase in the processing time during the micro-arc oxidation of products made of valve group alloys leads to a complication of the surface morphology, as well as an increase in the size and number of pores. In addition, the coating roughness increases in the anode and anode-cathode modes. Electrical strength tests showed that all samples with the resulting coatings withstood a voltage of 600 V. Multifunctional coatings obtained using the developed technological modes are multilayer structures. They consist of a base layer with excellent adhesion, an intermediate layer with porous structure and a top layer with high porosity and actively functioning surface. The changes revealed during morphological studies are characteristic of the plasma growth model of coatings. The results of the conducted morphological studies of coatings can be implemented in the development of a digital twin of the microarc oxidation process.

Keywords: micro-arc oxidation, digital twin, surface morphology, roughness, electrical strength, porosity

Funding: The work was supported by the grant of the Ministry of Science and Higher Education of the Russian Federation "Fundamentals of the digital twin of the technological process of forming oxide coatings with specified properties by microarc oxidation" (No. 123091800009-1).

Citation: Maksov A.A., Gurin S.A., Golubkov P.E., Pecherskaya E.A., Shepeleva J.V., Artamonov D.V., Methods and instruments for measuring surface morphology and mechanical parameters of oxide coatings, St. Petersburg State Polytechnical University Journal. Physics and Mathematics. 17 (3.1) (2024) 161–167. DOI: https://doi.org/10.18721/JPM.173.132

Материалы конференции
УДК 621.357.77; 620.22; 621.9.04
DOI: https://doi.org/10.18721/JPM.173.132

Методы и средства измерений морфологии поверхности и механических параметров оксидных покрытий

А.А. Максов [1] ✉, С.А. Гурин [1], П.Е. Голубков [1], Е.А. Печерска [1],
Ю.В. Шепелева [1], Д.В. Артамонов [1]

[1] Пензенский государственный университет, г. Пенза, Россия
✉ maksov.01@mail.ru

Аннотация. Проведены морфологические исследования покрытий на образцах алюминия, полученных микродуговым оксидированием. Плотность синусоидального тока в анодном и анодно-катодном режимах составляла 15 А/дм^2, а время обработки варьировалось от 120 с до 960 с. Формирование оксидных покрытий происходило в силикатно-щелочном электролите. Исследования топологии поверхности и механических параметров оксидных покрытий проводились посредством применения СЭМ, лазерного профилометра и универсального измерителя электрической прочности, что, в свою очередь, позволило установить взаимосвязь между свойствами покрытий и временем обработки образца. Так, увеличение длительности обработки в процессе микродугового оксидирования изделий из сплавов вентильной группы приводит к усложнению морфологии поверхности, а также увеличению размера и количества пор. Кроме того, в анодном и анодно-катодном режимах увеличивается шероховатость покрытия. Испытания на электрическую прочность показали, что все образцы с полученными покрытиями выдержали напряжение 600 В. Многофункциональные покрытия, полученные с использованием разработанных технологических режимов, представляют собой многослойные структуры. Они состоят из базового слоя с отличной адгезией, промежуточного слоя с пористой структурой и верхнего слоя с высокой пористостью и активно функционирующей поверхностью. Изменения, выявленные в ходе морфологических исследований, характерны для модели плазменного роста покрытий. Результаты проведенных морфологических исследований покрытий могут быть внедрены при разработке цифрового двойника процесса микродугового оксидирования.

Ключевые слова: микродуговое оксидирование, цифровой двойник, морфология поверхности, шероховатость, электрическая прочность, пористость, плазма

Финансирование: работа выполнена при поддержке Министерства науки и высшего образования РФ, проект «Фундаментальные основы цифрового двойника технологического процесса формирования оксидных покрытий с заданными свойствами методом микродугового оксидирования», № 123091800009-1.

Ссылка при цитировании: Максов А. А., Гурин С. А., Голубков П. Е., Печерская Е.А., Шепелева Ю.В. Методы и средства измерений морфологии поверхности и механических параметров оксидных покрытий // Научно-технические ведомости СПбГПУ. Физико-математические науки. 2024. Т. 17. № 3.1. С. 161–167. DOI: https://doi.org/10.18721/JPM.173.132

Introduction

Nowadays, most studies are aimed at studying the influence of heterogeneous factors of the microarc oxidation (MAO) process on the properties of the formed coatings, including mechanical ones. For example, the study in [1] demonstrates that increasing the number of plasma discharges at low current densities increases the porosity and roughness of the coating. According to the data from [2], electron microscopy revealed that the porosity of coatings decreases during time treatment, but the roughness increases. Adding TiO_2 nanoparticles to the electrolyte is also achieved by the increase porosity, thickness and surface roughness coating [3]. In [4] it is shown that that adding glycerol to the electrolyte leads to an increase in the number of pores and reducing their size, which reduces surface roughness. These studies are not unified, since they were carried out on different technological equipment under different processing modes and do not allow compare the results of experiments with each other, which limits their use as training data for the digital twin of the micro-arc process oxidation [5].

In addition, there is a need for a deeper study and understanding of the processes and phenomena occurring during micro-arc oxidation. In turn, it will allow us to investigate the modification of the coatings structure during their formation. In accordance with the studies of coatings obtained by the MAO method and described in [6], a plasma growth model was created for a specific coating, the structure of which includes a barrier layer, an inner layer with numerous closed pores and an outer layer with a rough surface.

Materials and methods

To study surface morphology and mechanical parameters of MAO coatings, 8 aluminum samples, presented in the form plates measuring 20×15×2 mm (surface area 0.05971 dm^2) and whose surface was previously brought to a roughness R_a in the range from 0.1 to 0.2 μm were selected. At the first stage, the samples were milled on a universal machine; at the second stage were polished on a manual grinding – polishing machine MP-100S MTDI (Korea) by sequentially sorting sandpapers with grades from P240 to P2000 (ISO6344 marking) and final polishing with a felt cloth using paste GOI. The treated samples were placed in a galvanic bath with silivate-alkaline electrolyte. Coatings were obtained using a MAO installation [7, 8] at a sinusoidal current (current density 15 A/dm^2), anode (A) and anode-cathode (AC) current modes) for 120 s, 240 s, 480 s, 960 s, respectively. Table 1 shows the technological parameters and oxidation time for each test sample.

Table 1

Technological parameters and process time of the studied samples

Sample No.	Mode	J, A/dm^2	t, s
1	A	15	120
2	A	15	240
3	A	15	480
4	A	15	960
5	AC	15	120
6	AC	15	240
7	AC	15	480
8	AC	15	960

Notations: A – anode mode; AC – anode-cathode mode; J – current density, A/dm^2; t – oxidation time, s.

Then, the topography of the surface of the selected samples was studied using a VEGA 3 scanning electron microscope, coating roughness measurements were carried out using a Mitaka FS150 3D laser contourograph, and the characteristics of the electrical parameters of MAO coatings were studied using a universal electrical strength meter. To do this, aluminum contacts were sprayed onto the samples at the UVN-71 P3 vacuum spraying unit, as shown in Fig. 1. Two electrodes were connected to the middle and one of the extreme contacts, between which a gradually increasing electrical voltage was created. The electrical strength was determined by the magnitude of the voltage at which the dielectric breakdown of the coating occurred.

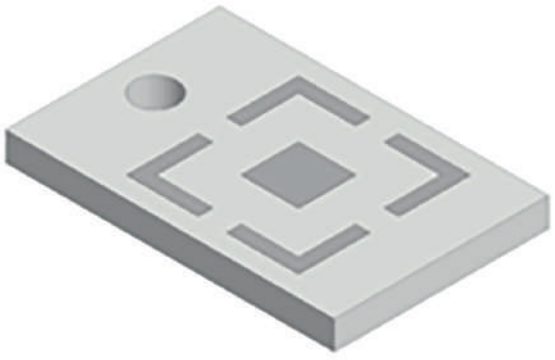

Fig. 1. The sample on which the MAO coating and metal contacts were sprayed

Results and discussion

Fig. 2 and 3 show topological images of the formed MAO coatings obtained using a VEGA 3 scanning electron microscope. Coatings on the samples were formed at a current density of 15 A/dm^2 in the anode and anode-cathode modes, depending on the oxidation time.

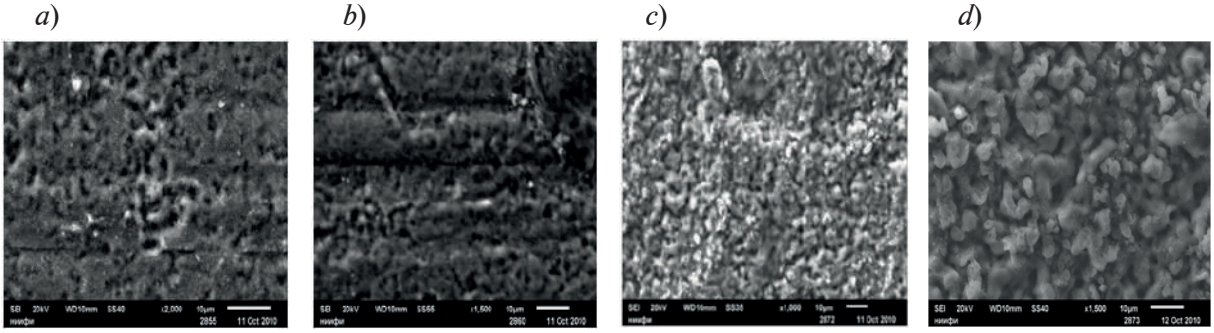

Fig. 2. Morphology of the surface of MAO coatings obtained at current density 15 A/dm^2 in anode mode for 120 s (*a*), 240 s (*b*), 480 s (*c*), 960 s (*d*)

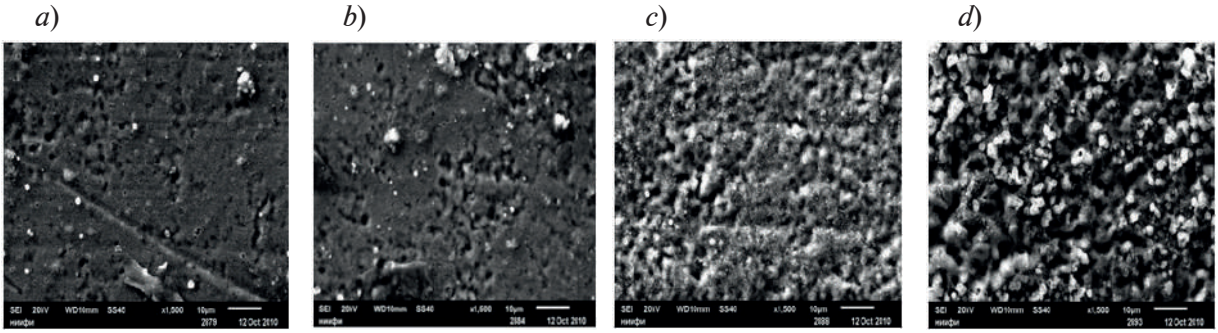

Fig. 3. Morphology of the MAO coatings surface obtained at current density 15 A/dm^2 in anode-cathode mode for 120 s (*a*), 240 s (*b*), 480 s (*c*), 960 s (*d*)

Analysis of morphology of the surface of samples with MAO coating (Fig. 2), as well as those obtained using the anode mode with current density 15 A/dm^2, confirmed that with increasing processing time of aluminum plates, the surface development, the size and number of pores increase. Thus, we can talk about the multilayering of the resulting ceramic coating. From the analysis It also follows that the first sample (Fig. 2, *a*), processed for the minimum time, is not porous and repeats the substrate structure. Such a coating can be attributed to the basic adhesive sub layer. Further exposure time leads to the appearance of small pores, and the coating

Table 2

The roughness of the MAO coatings samples obtained in the anode mode

Sample No.	Parameter	Side 1	Side 2
1	R_z, μm	2.62	2.33
	R_{max}, μm	3.72	3.00
	R_a, μm	0.17	0.32
2	R_z, μm	2.24	1.19
	R_{max}, μm	3.20	1.66
	R_a, μm	0.32	0.18
3	R_z, μm	2.56	12.90
	R_{max}, μm	3.55	55.00
	R_a, μm	0.35	0.68
4	R_z, μm	4.92	4.44
	R_{max}, μm	7.64	6.88
	R_a, μm	0.55	0.43

Notations: R_z – the height of the irregularities at ten points, μm; R_{max} – maximum height of irregularities, μm; R_a – the arithmetic mean deviation, μm.

structure gradually develops. Such layers have a well-developed structure. Thus, the fourth sample (Fig. 2, *d*) has a highly porous and developed structure.

For further analysis of the MAO process, the roughness of the samples surface was studied on a 3D laser conturograph profilometer. Table 2 contains the results of the measurements taken.

As a result of studying the values of the arithmetic mean deviation R_a, it was found that samples 1 (Fig. 2, *a*), 2 (Fig. 2, *b*) have them in the range from 0.1 to 0.3 μm. The information provided demonstrates that the coatings in the initial stages of growth have the same structure as the substrate due to the same surface roughness. Over time, the roughness of the samples gradually increases due to an increase in porosity and relief. Roughness values range from 0.1 to 0.7 μm.

At the second stage of the research, the following 4 aluminum plates were subjected to the MAO process in the mode of anode-cathode current (AC) with current density 15 A/dm^2.

Having analyzed the images of the surfaces of MAO coatings obtained using the anodic-cathode mode (Fig. 3), one can reveal a similar picture as in the anodic current mode. An increase in the processing time of aluminum plates leads to a complication of the surface structure of the formed coatings; accordingly, an increase in the size and number of pores is observed. Therefore, coatings obtained according to these modes can be considered multilayer, with a base adhesive coating, an intermediate porous and highly porous layer with a developed surface. In order to identify differences in the modes of obtaining coatings of the MAO process, an analysis of surface roughness was performed on a 3D laser conturograph profilometer. The obtained results of roughness measurements are presented in Table 3.

Table 3

Roughness of MAO coatings samples obtained in the anode-cathode mode

Sample No.	Parameter	Side 1	Side 2
5	R_z, μm	8.05	2.10
	R_{max}, μm	15.10	2.38
	R_a, μm	0.41	0.32
6	R_z, μm	3.10	2.32
	R_{max}, μm	5.78	2.63
	R_a, μm	0.32	0.34
7	R_z, μm	2.87	2.50
	R_{max}, μm	3.56	3.36
	R_a, μm	0.40	0.25
8	R_z, μm	2.58	2.40
	R_{max}, μm	3.23	2.83
	R_a, μm	0.59	0.43

Notations: R_z – the height of the irregularities at ten points, μm; R_{max} – maximum height of irregularities, μm; R_a – the arithmetic mean deviation, μm.

Analyzing the data given in Table 3, we can conclude that with increasing time of MAO treatment in the anode-cathode mode, the surface roughness increases, according to the arithmetic mean deviation Ra. The values of the first two samples (Fig. 3, *a*, *b*) are within 0.3 μm. The second two samples (Fig. 3, *c*, *d*) have values from 0.2 to 0.6 μm. The results obtained differ somewhat from the anode current mode. This is most likely due to plate defects. But we should not forget that the technological process itself contributes to the formation of oxide coatings.

Thus, the changes identified at the first and second stages of surface morphology studies are characteristic of the plasma coating growth model.

MAO coatings obtained using technological modes can be considered multilayer. They consist of a base layer with good adhesive properties, an intermediate porous layer and a top layer with high porosity and an actively functioning surface.

According to the results of data analysis, it can be concluded that with increasing the time of MAO process in anodic and anode-cathode modes, there is an increase in surface roughness determined by the values of arithmetic mean deviation R_a.

All samples with the obtained coatings, during the electrical strength tests, withstood a voltage of 600 V.

The process is characterized by high reproducibility and is also traceable dependence of coating properties (roughness, porosity, electrical strength) on processing time.

Conclusion

The topology of the MAO coatings surface on aluminum alloy samples, as well as their mechanical parameters, were studied. It has been revealed that an increase in the time of MAO treatment in the anode and anode-cathode modes leads to an increase in porosity and roughness of coatings. Tests for electrical strength showed that all the test samples withstood a breakdown voltage of 600 V. The research results allow the use of the plasma growth model of oxide coatings as the basis for the development of a digital process twin of microarc oxidation. The obtained empirical results are appropriate use as training data for intelligent algorithms as a part of digital twin.

REFERENCES

1. **Mortazavi G., Jiang J., Meletis E.I.,** Investigation of the plasma electrolytic oxidation mechanism of titanium, Applied Surface Science. 488 (2019) 370–382.

2. **Moga S.G., Negrea D.A., Ducu C.M., Malinovschi V., Schiopu A.G., Coaca E., Patrascu I.,** The Influence of Processing Time on Morphology, Structure and Functional Properties of PEO Coatings on AZ63 Magnesium Alloy, Appl. Sci. 12 (2022) 12848.

3. **Mozafarnia H., Fattah-Alhosseini A., Chaharmahali R., Nouri M., Keshavarz M.K., Kaseem M.,** Corrosion, Wear, and Antibacterial Behaviors of Hydroxyapatite/MgO Composite PEO Coatings on AZ31 Mg Alloy by Incorporation of TiO_2 Nanoparticles, Coatings. 12 (2022) 1967.

4. **Jangde A., Kumar S., Blawert C.,** Evolution of PEO coatings on AM50 magnesium alloy using phosphate-based electrolyte with and without glycerol and its electrochemical characterization, Journal of Magnesium and Alloys. 8 (2020) 692–715.

5. **Golubkov P.E., Pecherskaya E.A., Gurin S.A., Alexandrov V.S., Artamonov D.V., Maksov A.A.,** Influence of process parameters on the properties of microarc oxide coatings, St. Petersburg State Polytechnical University Journal. Physics and Mathematics. 16 (3.1) (2023) 368–373.

6. **Xiaohui L., Shuaixing W., Nan D., Xinyi L., Qing Z.,** Evolution of the Three-Dimensional Structure and Growth Model of Plasma Electrolytic Oxidation Coatings on 1060 Aluminum Alloy, Coatings. 8 (2018) 105.

7. **Golubkov P.E., Pecherskaya E.A., Karpanin O.V., Shepeleva Y.V., Zinchenko T.O., Artamonov D.V.,** Automation of the micro-arc oxidation process, J. of Phys.: Conf. Ser. 917 (2017) 092021.

8. **Pecherskaya E.A., Golubkov P.E., Artamonov D.V., Melnikov O.A., Karpanin O.V., Zinchenko T.O.,** Intelligent Technology of Oxide Layer Formation by Micro-Arc Oxidation, IEEE Trans. Plasma Sci. 49 (9) (2021) 2613.

THE AUTHORS

MAKSOV Andrey A.
maksov.01@mail.ru
ORCID: 0009-0001-4255-1383

GURIN Sergey A.
teslananoel@rambler.ru
ORCID: 0000-0001-9602-7221

GOLUBKOV Pavel E.
golpavpnz@yandex.ru
ORCID: 0000-0002-4387-3181

PECHERSKAYA Ekaterina A.
pea1@list.ru
ORCID: 0000-0001-5657-9128

SHEPELEVA Julia V.
eduard.shepelev.67@mail.ru
ORCID: 0000-0001-5075-2727

ARTAMONOV Dmitriy V.
dmitrartamon@yandex.ru
ORCID: 0000-0002-3240-7222

Received 07.07.2024. Approved after reviewing 25.07.2024. Accepted 25.07.2024.

Conference materials
UDC 519.614
DOI: https://doi.org/10.18721/JPM.173.133

Comparative analysis of the effectiveness of transparent conductive coatings based on various materials

E.A. Pecherskaya [1] ✉, T.O. Zinchenko [1], A.E. Zhurina [1],
D.V. Artamonov [1], P.E. Golubkov [1]

[1] Penza State University, Penza, Russia
✉ pea1@list.ru

Abstract. Transparent conductive oxide materials, which are used mainly as transparent electrodes, but have also found applications in optics, photonics and instrumentation. The main material used in production is indium oxide, alloyed with tin. However, indium is a rather expensive material, as well as a rare one. In this regard, the analysis of alternative materials made of transparent conductive oxide is relevant. Transparent conductive oxide materials are mainly used as transparent electrodes, but have also found applications in optics, photonics and instrumentation. The main material used in production is indium oxide fused with tin. However, indium is a rather expensive material, as well as a rare one. In this regard, the analysis of alternative materials made of transparent conductive oxide is relevant. The materials under consideration are gallium oxide doped with indium and antimony, tin oxide doped with fluorine and antimony, zinc oxide doped with gallium and aluminum. The analysis of the main parameters of transparent conductive oxides is carried out, a method for evaluating the effectiveness of materials according to technical and economic criteria is proposed. The methodology is based on the Laplace criterion, the compilation of a matrix of the effectiveness of materials. According to the proposed methodology, taking into account the target effect and the cost of obtaining the studied films, the effectiveness of promising transparent conductive materials was evaluated.

Keywords: transparent conductive oxide, indium oxide, zinc oxide, tin oxide, effectiveness

Funding: The work was supported by the Russian Science Foundation (RSF grant 23-29-00343).

Citation: Pecherskaya E.A., Zinchenko T.O., Zhurina A.E., Artamonov D.V., Golubkov P.E., Comparative analysis of the effectiveness of transparent conductive coatings based on various materials, St. Petersburg State Polytechnical University Journal. Physics and Mathematics. 17 (3.1) (2024) 168–172. DOI: https://doi.org/10.18721/JPM.173.133

Материалы конференции
УДК 519.614
DOI: https://doi.org/10.18721/JPM.173.133

Сравнительный анализ эффективности прозрачных токопроводящих покрытий на основе различных материалов

Е.А. Печерская [1] ✉, Т.О. Зинченко [1], А.Е. Журина [1],
Д.В. Артамонов [1], П.Е. Голубков [1]

[1] Пензенский государственный университет, г. Пенза, Россия
✉ pea1@list.ru

Аннотация. Прозрачные проводящие оксиды – материалы, которые в основном используются в качестве прозрачного электрода, но также нашли применение в

оптике, фотонике и приборостроении. В качестве материалов рассмотрены оксид индия, легированный оловом, оксид олова, легированный фтором и сурьмой, оксид цинка, легированный алюминием и галлием, оксид галлия, легированный индием и сурьмой. Предложена методика обоснованного выбора оптимального прозрачного проводящего оксида как по наибольшей технологической эффективности, так и по технико-экономической эффективности с учетом технологических параметров и затрат на получение тонкопленочного покрытия.

Ключевые слова: прозрачные проводящие оксиды, оксид индия, оксид олова, оксид цинка, эффективность

Финансирование: Работа выполнена при поддержке Российского научного фонда (грант РНФ 23-29-00343).

Ссылка при цитировании: Печерская Е.А., Зинченко Т.О., Журина А.Е., Артамонов Д.В., Голубков П.Е. Сравнительный анализ эффективности прозрачных токопроводящих покрытий на основе различных материалов // Научно-технические ведомости СПбГПУ. Физико-математические науки. 2024. Т. 17. № 3.1. С. 168–172. DOI: https://doi.org/10.18721/JPM.173.133

Introduction

One of the promising and actively developing areas of electronics is thin-film electronics. Thin films have found application in many sectors of the semiconductor and optoelectronics industries [1, 2]. The segment of thin-film structures in the form of transparent conductive oxides requires special attention. The most common transparent conductive oxide (TCO) films are SnO_2, In_2O_3, GaO and ZnO [3–5]. At the present stage of technology development, indium tin oxide can be attributed to materials with the best functional properties. However, its high cost and scarcity indicate the relevance of choosing an alternative material for TCO [6, 7]. An important task is to achieve values of the transmittance of thin films in the visible range of the spectrum of more than 85%, resistivity – no more than 10^{-4} Ohm·cm.

Materials and Methods

The materials being compared are transparent conductive oxides, for which the main performance targets are coating resistance and throughput; other parameters indirectly affect these properties.

Properties were studied on coatings of the same thickness (250 nm ± 10 nm). The table shows a comparison of transparent conductive oxides according to the specified parameters.

Table 1

Comparison of materials used as transparent conductive oxides in terms of transparency and conductivity

Header	Samples of transparent conducting oxides						
	In_2O_3:Sn	SnO_2:F	SnO_2:Sb	ZnO:Ga	ZnO:Al	GaO:In	GaO:Sb
R (surface resistance), Ohm·cm	2.4×10^{-4}	5×10^{-4}	10^{-3}	10^{-3}	10^{-2}	2×10^{-3}	4×10^{-3}
D (transmittance), %	95	83	92	85	90	90	88

In addition, calculations of parameters such as concentration, mobility of charge carriers, and band gap were performed.

Table 2

Estimation of the band gap width, concentration and mobility of charge carriers

	In_2O_3:Sn	SnO_2:F	SnO_2:Sb	ZnO:Ga	ZnO:Al	GaO:In	GaO:Sb
Eg (band gap width), eV	4	4.41	3.75	3.59	3.52	–	–
n (concentration of charge carrier), cm^{-3}	1×10^{20}	4.6×10^{20}	2×10^{20}	10×10^{20}	4.7×10^{20}	4×10^{20}	3×10^{20}
μ (mobility of charge carriers) $cm^2/(s\times V)$	12	28	10	10	14.7	10	10

Based on the studies performed, it is advisable to conclude that the following are the optimal materials according to the criterion of the highest electrical conductivity: In_2O_3:SnO_2 and SnO_2:F. At the same time, from the point of view of optical application, In2O3:SnO2, SnO2:F and SnO_2:Sb can be singled out as priority materials. Based on the analysis, tin is a promising and currently undervalued material. In order to make a reasonable choice of a transparent conductive oxide, a matrix of the effectiveness of transparent conductive oxides has been compiled. The use of materials as a transparent conductive oxide dictates the need to ensure high transparency and conductivity, therefore, In_2O_3 materials: SnO_2 and SnO_2:Sb have found the greatest use to date, which is confirmed by the experimental data presented in the Tables 1, 2.

In order to determine the optimal material based on a set of significant technological parameters and cost factor, the authors propose a method for the reasonable selection of the optimal transparent conductive oxide both for the highest technological efficiency (excluding the cost factor for the technological process) and for technical and economic efficiency (taking into account technological parameters and costs). The methodology is based on the use of the Laplace criterion used in system analysis to select the optimal alternative. As essential technological parameters (by which technological efficiency is evaluated) the surface resistance and transmission coefficient are considered.

Initial data: alternative materials are available for the production of transparent conductive oxides. The indicators of surface resistance and transmittance, characterizing the target effect of using a transparent conductive oxide are known. The task is to choose the optimal material, which has the highest efficiency.

Results and Discussion

The compiled efficiency matrix is presented in Table 3, which also contains the values of the corresponding cost indicators. The dimensionless value of g_l is the cost ratio of obtaining a transparent conductive oxide to the maximum allowable costs; R_{il} is the ratio of the surface resistance to the maximum permissible (the maximum permissible surface resistance is 10^{-2} Ohm·cm), D_{il} is the ratio of the transmission coefficient to the maximum permissible.

Next, the efficiency of transparent conductive oxides is calculated and the efficiency of materials is compared based on the method based on the Laplace criterion.

For each materialal, it is necessary to calculate the efficiency $K(a_l)$ according to technological parameters (surface resistance and transmission coefficient) using the formula:

$$K(a_l) = p_1 \cdot \frac{1}{R_{il}} + p_2 \cdot \frac{1}{D_{il}}, \quad (1)$$

where p_1, p_2 is the coefficient that takes into account the priority of parameters $\frac{1}{R_{il}}$ or $\frac{1}{D_{il}}$ of the material.

The values of p_1, p_2 are determined by expert assessments. In the case under consideration, equal priority is given to the importance of the required values of surface resistance and transmission coefficient, that is, $p_1 = p_2 = 0.5$.

Table 3

Efficiency and cost matrix for materials used in software

Material	Material designation, a_1	$\frac{1}{R_{il}}$	$\frac{1}{D_{il}}$	g_1
In_2O_3:SnO_2	a_1	$\frac{1}{2.4\cdot10^{-2}}$	$\frac{1}{1.19}$	0.68
SnO_2:F	a_2	$\frac{1}{5\cdot10^{-2}}$	$\frac{1}{1.04}$	0.48
SnO_2:Sb	a_3	$\frac{1}{10^{-1}}$	$\frac{1}{1.15}$	0.43
ZnO:Ga	a_4	$\frac{1}{10^{-1}}$	$\frac{1}{1.06}$	0.45
ZnO:Al	a_5	1	$\frac{1}{1.125}$	0.49
GaO:In	a_6	$\frac{1}{2\cdot10^{-1}}$	$\frac{1}{1.125}$	0.59
GaO:Sb	a_7	$\frac{1}{4\cdot10^{-1}}$	$\frac{1}{1.1}$	0.49

Then $K_1 = 0.5\left(\frac{1}{2,4\cdot10^{-2}} + \frac{1}{1.19}\right) = 22.42$, similarly, K_2 = 10.48; K_3 = 5.43; K_4 = 5.47; K_5 = 0.94; K_6 = 2.94; K_7 = 1.7.

Then the optimal technological efficiency K_{opt} is determined as the largest value of seven values of $K(a_l)$. In the case under consideration K_{opt} = 22.42, therefore, according to the technological parameters (for the target effect), the optimal material, designated a1, In_2O_3:SnO_2 is taken.

To account the impact of the cost factor, the aggregating function $K(a_l, g_l)$ is defined as the ratio of efficiency $K(a_l)$ to the cost factor g_l:

$$K\left(a_l, g_l\right) = \frac{K\left(a_l\right)}{g_l}. \quad (2)$$

In the case under consideration, $K\left(a_1, g_1\right) = \frac{22.42}{0.68} = 32.97$, similarly, $K(a_2, g_2)$ = 21.83; $K(a_3, g_3)$ = 12.6; $K(a_4, g_4)$ = 12.15; $K(a_5, g_5)$ = 1.92; $K(a_6, g_6)$ = 4.58; $K(a_7, g_7)$ = 3.46.

Next, the optimal material is determined according to the target effect and cost factor $K(a_l, g_l)$, having:

$$K\left(a_l, g_l\right)_{opt} = max(l)\frac{K\left(a_l\right)}{g_l}. \quad (3)$$

In this case $K(a_l, g_l)_{opt}$ = 32.97, therefore, according to technical and economic indicators, the optimal material is In_2O_3:SnO_2.

Conclusion

A methodology is proposed for the reasonable selection of the optimal transparent conductive oxide both in terms of technological parameters and taking into account the cost of obtaining materials. The methodology is based on the Laplace criterion, takes into account the priority of

the importance of the parameters of materials (priority is determined by expert assessment and depends on the specific field of application of the material), depending on which efficiency is calculated according to technological parameters. In the case when, in addition to technological parameters, the cost of obtaining materials is decisive, then efficiency is calculated according to technical and economic parameters in the form of an aggregating function. The proposed technique has been tested to identify transparent conductive oxides with optimal technological parameters (surface resistance, transmission coefficient) and the lowest cost of obtaining them.

The result of the research is the identification of the most suitable materials for use in TCO, which are In_2O_3:SnO_2 and SnO_2:F. In this case, from the point of view of optical application, the priority materials can be In_2O_3:SnO_2, SnO_2:F and SnO_2:Sb. Based on the analysis, tin is a promising and undervalued material. The materials use as a transparent conductive oxide requires high levels of both transparency and conductivity, therefore the materials In_2O_3:SnO_2 and SnO_2:Sb have found the greatest application today, which is confirmed by the experimental data presented in the tables. Taking into account technical and economic indicators, the optimal material is In_2O_3:SnO_2.

REFERENCES

1. **Rakesh A., Sharma N., Madhuri Sh., Madhuri Sh.,** Transparent Conducting Oxide Films for Various Applications: A Review. Reviews on Advanced Materials Science. 53 (2019) 79–89.

2. **Sohn H.Y., Murali A.,** Plasma Synthesis of Advanced Metal Oxide Nanoparticles and Their Applications as Transparent Conducting Oxide Thin Films. Molecules. 2021 26 (2021) 1456.

3. **Muslih E.Y., Kim K.H.,** Preparation of Zinc Oxide (ZnO) Thin Film as Transparent Conductive Oxide (TCO) from Zinc Complex Compound on Thin Film Solar Cells: A Study of O_2 Effect on Annealing Process, IOP Conf. Ser.: Mater. Sci. 214 (2017) 012001.

4. **Zinchenko T.O., Pecherskaya E.A., Nikolaev K.O., Golubkov P.E., Shepeleva Y.V., Artamonov D.V.,** The study of the optical properties of transparent conductive oxides SnO_2:Sb, obtained by spray pyrolysis, Journal of Physics: Conference Series. 1410 (2019) 012090.

5. **Koida T., Ueno Yu., Shibata H.,** In_2O_3–Based Transparent Conducting Oxide Films with High Electron Mobility Fabricated at Low Process Temperatures, Physica Status Solidi (A) Applications and Materials. Vol. 215 (7) (2018) 201700506.

6. **Zinchenko T.O., Pecherskaya E.A., Novichkov M.D., Kozlov G.V., Karpanin O.V.,** Synthesis of thin-film structures of tungsten oxide by the spray-pyrolysis method, St. Petersburg State Polytechnical University Journal. Physics and Mathematics. 16 (3.1) (2023) 402–407.

7. **Elangovan E., Kandasamy R.,** A Study on Low Cost-High Conducting Fluorine and Antimony-Doped Tin Oxide Thin Films, Applied Surface Science. 249 (2005) 183–196.

THE AUTHORS

ZINCHENKO Timur O.
scar0243@gmail.ru
ORCID: 0000-0002-9342-9345

ARTAMONOV Dmitriy V.
dmitrartamon@yandex.ru
ORCID: 0000-0002-3240-7222

PECHERSKAYA Ekaterina A.
pea1@list.ru
ORCID: 0000-0001-5657-9128

GOLUBKOV Pavel E.
golpavpnz@yandex.ru
ORCID: 0000-0002-4387-3181

ZHURINA Angelina E.
gelya.zhurina@mail.ru
ORCID: 0000-0002-5076-3191

Received 08.07.2024. Approved after reviewing 12.08.2024. Accepted 13.08.2024.

Conference materials
UDC 621.382
DOI: https://doi.org/10.18721/JPM.173.134

Quantum state preparation with optical injection: Issue of intersymbol interference

I.S. Kudryashov [1, 2] ✉, R.A. Shakhovoy [1, 3]

[1] QRate, Moscow, Russia;

[2] Moscow Institute of Physics and Technology (National Research University), Dolgoprudny, Russia;

[3] Moscow technical university of communications and informatics, Moscow, Russia

✉ kudriashov.is@phystech.edu

Abstract. The dependence of the modulating signal on its history, which is referred in the literature to as intersymbol interference, may significantly affect the security of quantum key distribution. Here, we investigate the issue of intersymbol interference in the context of quantum state preparation with pulsed optical injection. Both experimental and theoretical study are presented.

Keywords: quantum key distribution, semiconductor lasers, pulsed optical injection, intersymbol interference

Citation: Kudryashov I.S., Shakhovoy R.A., Quantum state preparation with optical injection: Issue of intersymbol interference, St. Petersburg State Polytechnical University Journal. Physics and Mathematics. 17 (3.1) (2024) 173–177. DOI: https://doi.org/10.18721/JPM.173.134

Материалы конференции
УДК 621.382
DOI: https://doi.org/10.18721/JPM.173.134

Приготовление квантовых состояний с помощью оптической инжекции: проблема межсимвольной интерференции

И.С. Кудряшов [1, 2] ✉, Р.А. Шаховой [1, 3]

[1] ООО «КуРэйт», Москва, Россия;

[2] Московский физико-технический институт (национальный исследовательский университет), г. Долгопрудный, Россия;

[3] Московский технический университет связи и информатики, Москва, Россия

✉ kudriashov.is@phystech.edu

Аннотация. Зависимость модулирующего сигнала от его предыстории, называемая в литературе межсимвольной интерференцией, может существенно влиять на безопасность квантового распределения ключей. Настоящая работа посвящена вопросам межсимвольной интерференции в контексте подготовки квантовых состояний с помощью импульсной оптической инжекции как на основе теоретического анализа, так и в плане экспериментов.

Ключевые слова: квантовое распределение ключей, полупроводниковые лазеры, импульсная оптическая инжекция, межсимвольная интерференция

Ссылка при цитировании: Кудряшов И.С., Шаховой Р.А. Приготовление квантовых состояний с помощью оптической инжекции: Проблема межсимвольной интерференции

// Научно-технические ведомости СПбГПУ. Физико-математические науки. 2024. Т. 17. № 3.1. С. 173–177. DOI: https://doi.org/10.18721/JPM.173.134

Introduction

Various methods of state preparation for quantum key distribution (QKD) have been proposed in the literature. One of the most promising techniques is based on the use of optically injected semiconductor lasers [1–4], where the master is used as a phase preparation laser, and the slave is used as a pulse preparation laser. This method allows performing both phase and time-bin encoding, which makes it quite flexible. Moreover, a pulsed laser subjected to optical injection exhibits reduced chirp, suppressed relaxation oscillations and, consequently, provides improved laser pulse interference.

Here, we address the problem of intersymbol interference in case of quantum state preparation with optical injection. Both experimental results and simulations are provided, and possible solutions of the problem are discussed.

Materials and Methods

For the experiment, we used a couple of distributed feedback lasers connected via an optical circulator as shown in Fig. 1. A variable optical attenuator was installed in front of the slave laser to control the injected optical power. Both lasers operated in a gain-switching mode at wavelengths 1549.3 nm (master) and 1550.6 nm (slave). A WDM filter centered at 1549.32 nm (C35) was placed at the output of an optical circulator. Due to optical injection locking, the wavelength of the slave laser was shifted towards the master's wavelength when the pulse from the master came into the slave's cavity. Thereby, only those slave laser pulses whose frequency has been shifted by the master passed through the WDM filter (see Fig. 2).

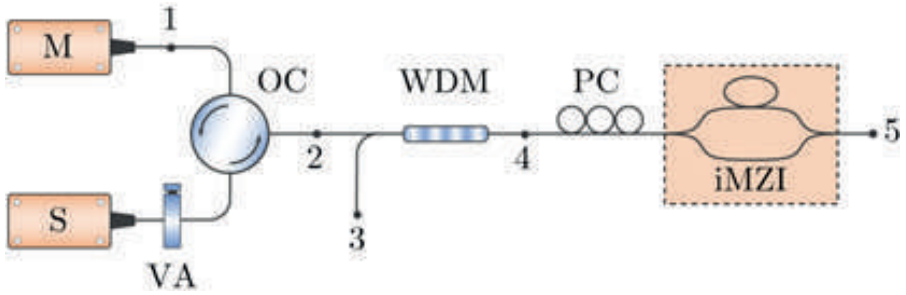

Fig. 1. The scheme of an experimental setup. M and S stand for master and slave lasers, VOA – variable optical attenuator, OC – optical circulator. PD –photodetector, PC – polarization controller, iMZI – integrated Mach-Zehnder interferometer. Optical signal was detected from points 1–5

The slave laser emitted short pulses at repetition rate of 1.25 GHz, whereas the master laser emitted two types of signals: short pulses with a duration of approximately 400 ps, and long pulses, which were approximately double the duration of short pulses. Short master pulses were used to prepare states in the Z-basis: when the pulse appeared in the early time slot, we assigned a bit value '1' to it (the Z_1-state), and when the pulse appeared in the late time slot, we assigned a bit value '0' to it (the Z_0-state). In the X-basis, we prepared only one state (X_0) by selecting the modulation current such that there is a phase difference $\Delta\varphi = 0$ between the corresponding pair of pulses.

Prepared quantum states were controlled with the thermostabilized integral imbalanced Mach-Zehnder interferometer (iMZI) with the delay line of 800 ps. In front of the interferometer, we installed a polarization controller to fine-tune the polarization state of the incoming signal. A Thorlabs PDA 8GS photodetector was used for the optical signal detection.

Results and Discussion

Experimental results on the state preparation using pulsed optical injection are shown in Fig. 2. Optical signal of the maser laser presented in Fig. 2, *a* was detected at point 1 of the optical scheme (see Fig. 1) and corresponds to the following cyclically repeated sequence of states: X_0, ∅, Z_1, X_0, Z_0, X_0, Z_1, ∅, where the "empty" state, ∅, was inserted intentionally. Significant distortions that can be clearly seen in the shape of master pulses are related to imperfections in the electrical signal from the driver. However, we note that this signal shape was quite stable (signal variations are highlighted in Fig. 2, *a* in yellow). It is also clear from Fig. 2, *a* that the shape of master laser pulses heavily depends on the prehistory, i.e. on which of the four states (Z_0, Z_1, X_0, or ∅) preceded the current pulse. Such dependence is generally referred to as intersymbol interference [5, 6].

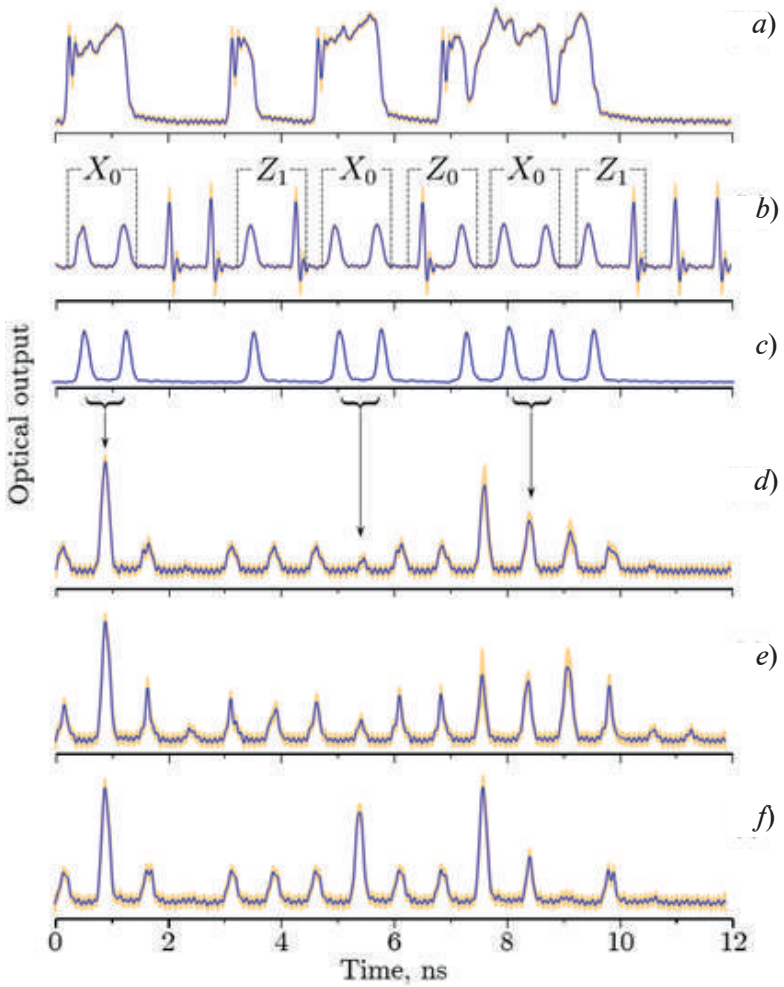

Fig. 2. Pulses emitted by the master laser (*a*), pulses that are coming out of the optical circulator (*b*), slave laser pulses that are coming out of the WDM filter (*c*), the result of the interference with different I_p values (*d*, *e*, *f*)

Figure 2, *b* demonstrates a sequence of slave laser pulses that corresponds to the master signal shown in Fig. 2, *a*. (This signal was recorded at point 2 of the scheme in Fig. 1.) One can see that pulses generated in the absence of optical injection are notably different from pulses appearing under emission of the master laser (the former are shorter and have a higher amplitude). Figure 2, *c* shows the same pulse sequence as in Fig. 2, *b* but recorded after the WDM filter at point 4 of the scheme. One can see that pulses of the slave laser emitted in the absence of master radiation are effectively filtered out. It is important to note that the shape of laser pulses in Fig. 2, *c* does not actually depend on the shape of master pulses, which means that intersymbol interference is less pronounced in the slave laser signal. Note, however, that this is true only for the *Z*-basis (see below).

Figures 2, *d*, *e*, *f* show the pulse sequences, corresponding to the interference of pulses from (Fig. 2, *c*) in the interferometer with the delay line of 800 ps. In (Fig. 2, *d*), the peak-to-peak value of the modulation current, I_p, was 34.4 mA; in (Fig. 2, *e*) and (Fig. 2, *f*) the value of I_p was set to 17.2 and 51.6 mA, respectively. Pulses that were "decoded" from X_0 states are marked with arrows. It can be seen that the intensity of the interference pulse is different in different places of the pulse sequence, which is due to intersymbol interference in the master signal. Thus, although the dependence of the shape of master pulses on the signal history does not seriously affect the shape of slave laser pulses in the *Z*-basis, it causes the significant intersymbol interference in the *X*-basis.

There are two possible reasons for the intersymbol interference in (Fig. 2, *a*). The first one relates to purely technical issues due to inaccuracies in laser driver design that lead to impedance mismatch in different parts of the electrical circuit. A more accurate design for the laser driver is required to remedy this issue. The second reason is purely physical and deals with the finite lifetime of carriers in the active layer of the laser diode. To check the latter impact, we have performed simulations of laser dynamics for the system shown in Fig. 1. Results are summed up in Fig. 3.

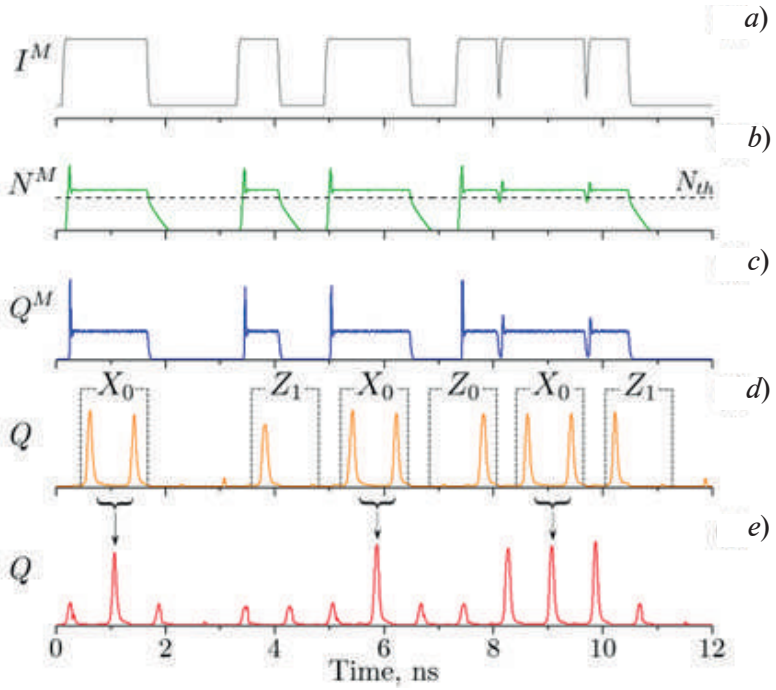

Fig. 3. Simulations of the sequence of quantum states. The master laser electric signal (*a*), charge carrier number dynamics (*a*), pulses coming from the master laser (*b*), slave laser pulses that are coming out of the WDM filter (*c*), the result of the interference (*d*)

We have used a standard model of stochastic rate equations [2] with the following set of laser parameters: master laser photon lifetime $\tau_{ph} = 1.0$ ps, slave laser photon lifetime $\tau_{ph} = 2.0$ ps, electron lifetime $\tau_e = 1.0$ ns, quantum differential output $\eta = 0.3$, transparency carrier number $N_{tr} = 4\times10^7$, threshold carrier number $N_{tr} = 5.5\times10^7$, spontaneous emission coupling factor $C_{sp} = 10^{-5}$, confinement factor $\Gamma = 0.12$, linewidth enhancement factor $\alpha = 5$, master gain compression factor $\chi = 30\text{W}^{-1}$, slave gain compression factor $\chi = 20\text{W}^{-1}$, master-slave detuning $\Delta\omega/2\pi = 100$ Hz. Figure 3, *a* shows the electrical signal $I^M(t)$ simulating the master's pump current, Fig. 3, *b* demonstrates time evolution of the carrier number $N^M(t)$ corresponding to this driving signal, Fig. 3, *c* depicts the master laser output intensity $Q^M(t)$, and Fig. 3, *d* shows the output intensity of the slave laser after spectral filtration (WDM filter was modelled with a second-order Butterworth filter). Finally, Fig. 3, *e* shows the result of the slave laser signal interfering with itself after an 800 ps shift.

In the above simulations, the dependences $Q^M(t)$ and $N^M(t)$ in the interval from 7 to 11 ns, which correspond to the sequence of states Z_0, X_0, Z_1, deserve attention. Here, the delay between

different master pulses is so small that the carrier number does not have enough time to fall considerably below threshold. Therefore, the master laser keeps operating in a quasi-continuous regime, and the laser pulses in the neighboring states turn out to be correlated in phase, which may lead to information leakage. However, this does not lead to significant distortions of the master signal and, consequently, to errors when encoding/decoding the signal in the *X*-basis. Therefore, we can conclude that the state preparation inaccuracy caused by the intersymbol interference shown in (Fig. 2, *d*, *e*, *f*), relates exclusively to inaccuracies in laser driver design.

Conclusion

We have demonstrated the case of intersymbol interference that occurs during optical-injection-based encoding. We also showed that the main cause of intersymbol interference in our case are inaccuracies in laser driver design. One of the possible solutions to minimize this effect (in addition to more accurate driver design) is to decrease the pulse repetition rate for the master laser.

REFERENCES

1. **Yuan Z.L., Frohlich B., Lucamarini M., Roberts G.L., Dynes J.F., Shields A.J.,** Directly phase-modulated light source, Phys. Rev. (6) (031044) (2016).

2. **Shakhovoy R., Puplauskis M., Sharoglazova V., Duplinskiy A., Zavodilenko V., Losev A., Kurochkin Y.,** Direct phase modulation via optical injection: theoretical study, Optics Express. (29) (9574) (2021).

3. **Paraiso T.K., De Marco I., Roger T., Marangon D.G., Dynes J.F., Lucamarini M., Yuan Z., Shields A.J.,** A modulator-free quantum key distribution transmitter chip, npj Quantum Information. (5) (42) (2019).

4. **Roberts G.L., Lucamarini M., Dynes J.F., Savory S.J., Yuan Z.L., Shields A.J.,** A direct GHz-clocked phase and intensity modulated transmitter applied to quantum key distribution, Quantum Sci. Technol. 3 (4) (045010) (2018).

5. **Makarov V., Abrikosov A., Chaiwongkhot P., et al.,** Preparing a commercial quantum key distribution system for certification against implementation loopholes. (2310) (20107) (2023).

6. **Sajeed S., Chaiwongkhot P., Huang A., et al.,** An approach for security evaluation and certification of a complete quantum communication system, Scientific Reports. (11) (5110) (2021).

THE AUTHORS

KUDRYASHOV Igor S.
kudriashov.is@phystech.edu

SHAKHOVOY Roman A.
r.shakhovoy@goqrate.com

Received 16.07.2024. Approved after reviewing 01.08.2024. Accepted 27.08.2024.

PHYSICAL ELECTRONICS

Conference materials
UDC 621.3
DOI: https://doi.org/10.18721/JPM.173.135

A compact MEMS switch for advanced radar systems

I.A. Belozerov [1] ✉, I.V. Uvarov [1]

[1] Valiev Institute of Physics and Technology of RAS, Yaroslavl Branch, Yaroslavl, Russia;
✉ belozerov.ftian@bk.ru

Abstract. MEMS switches are promising candidates for use in advanced radioelectronic systems. High RF performance combined with small size and low power consumption make them attractive for phased array antennas, aviation and space equipment. This work presents a switch based on a tiny cantilever with a length of 50 μm. Its working characteristics are compared with the calculation results. The advantages of the switch in comparison with previously developed products are demonstrated.

Keywords: MEMS switch, radar, cantilever, contact resistance, pull-in voltage

Funding: This work is supported by the program no. FFNN-2022-0017 of the Ministry of Science and Higher Education of Russia for Valiev Institute of Physics and Technology of RAS and by the Foundation for Assistance to Small Innovative Enterprises, grant No. 7GUP-KES18/91740, and is performed using the equipment of the Facilities Sharing Centre "Diagnostics of Micro- and Nanostructures".

Citation: Belozerov I.A., Uvarov I.V., A compact MEMS switch for advanced radar systems, St. Petersburg State Polytechnical University Journal. Physics and Mathematics. 17 (3.1) (2024) 178–181. DOI: https://doi.org/10.18721/JPM.173.135

Материалы конференции
УДК 621.3
DOI: https://doi.org/10.18721/JPM.173.135

Компактный МЭМС-переключатель для перспективных радиолокационных систем

И.А. Белозеров [1] ✉, И.В. Уваров [1]

[1] Ярославский филиал Физико-Технологического института РАН им. К.А. Валиева,
г. Ярославль, Россия;
✉ belozerov.ftian@bk.ru

Аннотация. МЭМС-переключатели представляют значительный интерес для перспективных радиоэлектронных систем. Высокие СВЧ характеристики в сочетании с малым размером и низким энергопотреблением делают их привлекательными для использования в фазированных антенных решетках, авиационных и космических радиосистемах. В этой работе представлен ключ на основе миниатюрного кантилевера длиной 50 мкм. Выполнено сравнение его рабочих характеристик с результатами расчетов. Продемонстрированы достоинства ключа в сравнении с ранее созданными изделиями.

Ключевые слова: МЭМС-переключатель, радиолокация, кантилевер, контактное сопротивление, напряжение срабатывания

Финансирование: Работа выполнена в рамках Государственного задания ФТИАН им. К.А. Валиева РАН Минобрнауки РФ по теме № FFNN-2022-0017 при

финансовой поддержке гранта Фонда содействия инновациям № 7ГУПКЭС18/91740 с использованием оборудования Центра коллективного пользования «Диагностика микро- и наноструктур».

Ссылка при цитировании: Белозеров И.А., Уваров И.В. Компактный МЭМС-переключатель для перспективных радиолокационных систем // Научно-технические ведомости СПбГПУ. Физико-математические науки. 2024. Т. 17. № 3.1. С. 178–181. DOI: https://doi.org/10.18721/JPM.173.135

Introduction

Switches fabricated using microelectromechanical systems (MEMS) technology are actively considered as a new element base for microwave devices [1]. They have lower insertion loss, higher isolation and lower power consumption than solid-state switches, which is critical for ultra-high frequency applications. These characteristics make them attractive for use in phased array antennas [2], aviation and space radar systems [3]. A conventional MEMS switch contains a cantilever suspended above the driving and signal electrodes. Applying voltage to the driving electrode creates an electrostatic force that bends the cantilever and brings it in contact with the signal electrode. When the voltage is turned off, the cantilever returns to its original position under the elastic force. MEMS switches are fabricated using microelectronic techniques and can be integrated with CMOS circuits.

MEMS switches have been developed since the 1990s, and the reliability of these devices remains a major unresolved problem [1]. One of the main reasons of poor reliability is high and unstable contact resistance. To solve this problem, the cantilever is replaced by complex structures with extended lateral size, which increases the contact force and thereby reduces the resistance. However, large size makes the switch sensitive to internal mechanical stresses, since even a small stress gradient significantly changes the gap between the electrodes. In addition, switching speed decreases, parasitic capacitance increases, and RF performance deteriorates. The complex shape of the electrodes makes it difficult to integrate the switch into a coplanar transmission line.

A cantilever-based switch has several advantages. The simple design allows both series and shunt configurations to be implemented. The small size of the device ensures resistivity to mechanical stress and short switching time. This paper presents a compact cantilever-based MEMS switch. Its pull-in voltage and contact resistance are measured. Experimental data are compared with the calculation results, and the advantages of the switch in comparison with previously created devices are revealed.

Materials and Methods

The switch is shown schematically in Figure 1, *a*. The movable electrode is an aluminum cantilever with the length of 50 μm, the width of 10 μm at the attachment sites and 40 μm at the free end (Fig. 1, *b*). The driving electrode surrounds the signal one in order to increase the area of electric field. The shape of the cantilever and electrodes was selected earlier to provide the highest contact force for the given footprint of the device [4]. The cantilever is 3.6 μm thick, and the contact bump height is of 0.5 μm. The gap between the cantilever and the electrodes is 1 μm. The natural frequency of the cantilever is 750 kHz, and the actuation time at a driving voltage of 90 V is 0.7 μs. The calculated pull-in voltage is of 85 V. More details on calculating performance characteristics can be found in [5].

The switch is fabricated on a thermally oxidized silicon wafer with a diameter of 100 mm using standard microelectronics techniques, namely photolithography, magnetron sputtering, plasma and wet etching. The fabrication procedure of the switch is described in detail in [4]. The contacts are made of ruthenium.

The switches are tested under standard laboratory conditions without packaging. The testing is carried out in the cold switching mode, in which mechanical contact is first made and then the switching signal is applied. The driving voltage is 90 V, while the switching signal is 1.5 V, and the

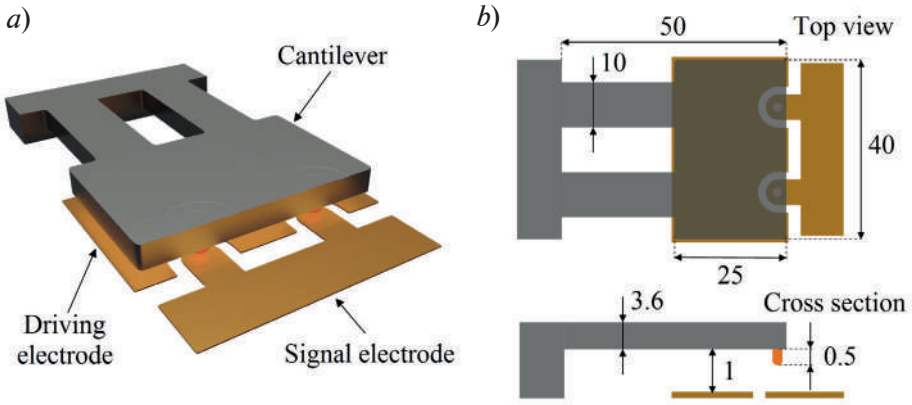

Fig. 1. Cantilever-based MEMS switch: 3D image (*a*); top view and cross section (dimensions are given in micrometers) (*b*)

actuation frequency is 7 Hz. At each switching cycle, the contact resistance is calculated using a resistive divider. The calculation is performed automatically using LabView software.

Results and discussion

The measured pull-in voltage is 64 V in average, which is 25% lower than the calculated value. The reason for the discrepancy is the bending of the cantilever under internal mechanical stresses. Due to the short cantilever length, this bending results only in a small change in the gap of 0.25 μm, which does not lead to the switch failure. The pull-in voltage decreases with the number of switching cycles and after 100 thousand cycles is on average 40 V. The voltage drop explains by plastic deformation of the cantilever, leading to a reduction in the air gap [6].

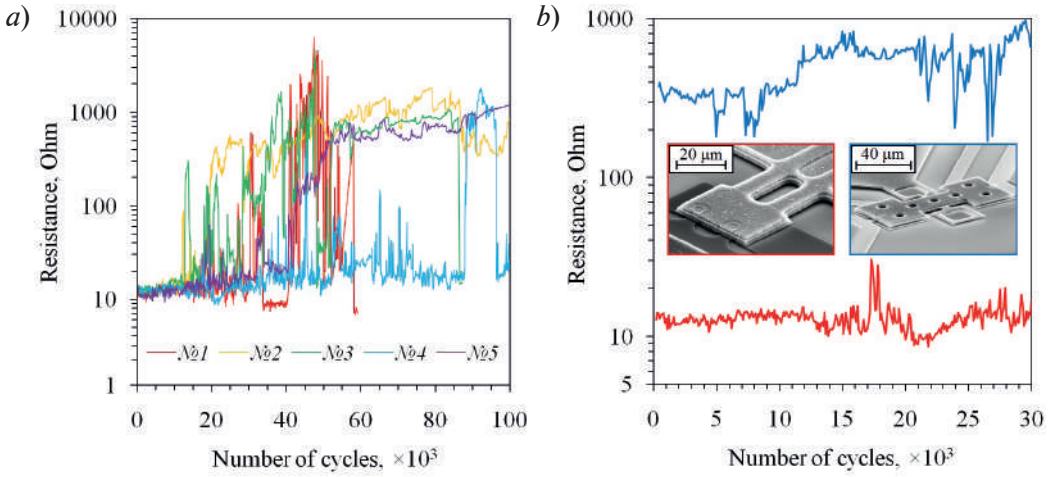

Fig. 2. Dependence of contact resistance on the number of switching cycles: for five cantilever-based samples (*a*); for a cantilever-based switch in comparison with a switch developed by the authors earlier (*b*)

The dependence of the contact resistance on the number of switching cycles for five samples is shown in Figure 2, *a*. During the first 10 thousand cycles, the switches demonstrate the resistance of 10–15 Ohms. Then it increases to several tens and hundreds of Ohms. The growth of resistance is explained by the formation of friction polymers on the surface of ruthenium contacts [7]. For the same reason, the resistance is unstable, increasing and decreasing several times during the test.

Figure 2, *b* shows the comparative test of the proposed switch (red curve) and a switch with an active opening mechanism, developed by the authors earlier [8] (blue curve). Both devices are fabricated using the technology described above, but the cantilever-based switch has 1–2 orders of magnitude lower resistance. The probable reason is the higher impact force of the cantilever that helps to break the contamination film on the contact surfaces.

Conclusion

This paper presents an electrostatic-type MEMS switch based on a compact aluminum cantilever. Its pull-in voltage is 64 V on average and is 25% lower than the calculated value due to cantilever bending under internal mechanical stress. The pull-in voltage decreases with increasing number of switching cycles because of plastic deformation of the cantilever. The contact resistance is of 10–15 Ohms for 10 thousand cold-switching cycles, and then it increases to several tens and hundreds of Ohms and becomes unstable due to contamination of the ruthenium contacts. However, the proposed switch has 1-2 orders of magnitude lower resistance compared to the previously developed device. Reliability testing under sealed conditions is planned for the presented MEMS switch.

REFERENCES

1. **Rebeiz G.M., Patel C.D., Han S.K., Ko C.-H., Ho K. M.J.,** The search for a reliable MEMS switch. IEEE Microw. Mag. 14 (2013) 57–67.

2. **Haupt R.L.,** Lanagan M., Reconfigurable antennas. IEEE Antennas Propag Mag. 55 (2013) 49–61.

3. **Daneshmand M., Mansour R.R.,** RF MEMS satellite switch matrices. IEEE Microw Mag. 12 (2011) 92–109.

4. **Belozerov I.A., Uvarov I.V.,** MEMS Switch Based on a Cantilever with Increased Contact Force. Russian Microelectronics. 52 (6) (2023) 475–482.

5. **Belozerov I.A., Uvarov I.V.,** Performance optimization of the cantilever-based MEMS switch. St. Petersburg State Polytechnical University Journal. Physics and Mathematics. 15 (3.2) (2022) 140–144.

6. **Do C., Lishchynska M., Delane, K., Fitzgerald P., Goggin R., Hill M.,** Model-based analysis of switch degradation effects during lifetime testing. 2012 IEEE 25th International Conference on Micro Electro Mechanical Systems (MEMS). (2012) 460–463.

7. **Czaplewski D.A., Nordquist C.D., Dyck C.W., Patrizi G.A., Kraus G.M., Cowan W.D.,** Lifetime limitations of ohmic, contacting RF MEMS switches with Au, Pt and Ir contact materials due to accumulation of 'friction polymer' on the contacts, J. Micromech. Microeng. 22 (10) (2012) 105005.

8. **Uvarov I.V., Marukhin N.V.,** A seesaw-type MEMS switch with enhanced contact force: the first results, Journal of Physics: Conference Series. IOP Publishing. 2086 (1) (2021) 012069.

THE AUTHORS

BELOZEROV Igor A.
belozerov.ftian@bk.ru
ORCID: 0000-0001-5620-0608

UVAROV Ilia V.
i.v.uvarov@bk.ru
ORCID: 0000-0002-6882-0625

Received 11.07.2024. Approved after reviewing 06.08.2024. Accepted 06.08.2024.

Conference materials
UDC 539.8:538.975
DOI: https://doi.org/10.18721/JPM.173.136

Microelectromechanical gas sensor of resistive type for detection of hydrogen sulphide low concentrations

I.A. Lazdin [1] ✉, A.S. Kondrateva [2, 1], I.M. Komarevtsev [2],
Ya.B. Enns [2], A.N. Kazakin [2], P.A. Karaseov [1]

[1] Peter the Great St. Petersburg Polytechnic University, St. Petersburg, Russia;
[2] Alferov University, St. Petersburg, Russia
✉ lazdin.ia@edu.spbstu.ru

Abstract. This article proposes a technology for manufacturing a microelectromechanical (MEMS) resistive gas sensor for detecting low concentrations of analytes and demonstrates the main technological characteristics of the device. MEMS contains a silicon substrate with nickel comb electrodes that act as a microheater. The distance between the teeth on the comb is about 300 microns, and the width of the heater tracks is 100 microns. As a sensitive layer, a thin (100nm) gas-sensitive layer of nickel oxide (NiO) is applied on top of the microheaters. The operating temperature of the sensitive layer in measurement mode is 130–205 °C. All applied meters are made on a silicon membrane of about 50 microns. The proposed work shows the effect of introducing H_2S into a gas mixture from 1 to 100 ppm on the conductivity of a gas sensor. The effective operating temperature of the heating elements was determined, at which the greatest response to the presence of hydrogen sulfide in the gas mixture is observed.

Keywords: microelectromechanical systems, gas sensor, nickel oxide, hydrogen sulfide

Funding: This work was performed within the framework of the State Task "Active Composite Materials and Analysis Techniques for (Bio)Sensorics" (Theme Code FSRM-2023-0009).

Citation: Lazdin I.A., Kondrateva A.S., Komarevtsev I.M., Enns Ya.B., Kazakin A.N., Karaseov P.A., Microelectromechanical gas sensor of resistive type for detection of hydrogen sulphide low concentrations , St. Petersburg State Polytechnical University Journal. Physics and Mathematics. 17 (3.1) (2024) 182–185. DOI: https://doi.org/10.18721/JPM.173.136

Материалы конференции
UDC 539.8:538.975
DOI: https://doi.org/10.18721/JPM.173.136

Микроэлектромеханический газовый датчик резистивного типа для определения низких концентраций сероводорода

И.А. Лаздин [1] ✉, А.С. Кондратьева [2, 1], И.М. Комаревцев [2],
Я.Б. Эннс [2], А.Н. Казакин [2], П.А. Карасев [1]

[1] Санкт-Петербургский политехнический университет Петра Великого,
Санкт-Петербург, Россия;
[2] Академический университет им. Ж.И. Алфёрова РАН, Санкт-Петербург, Россия
✉ lazdin.ia@edu.spbstu.ru

Аннотация. В работе предложена технология формирования резистивного МЭМС датчика сероводорода. В качестве газочувствительного материала выбран оксид никеля, способный к изменению своей проводимости при сорбции сероводорода, даже в присутствии паров воды. В работе показано влияние введения в исследуемый газовый поток от 1 до 100 ppm H_2S на электрический отклик МЭМС датчика.

Ключевые слова: микроэлектромеханическая система, газовый датчик, оксид никеля, сероводород

Финансирование: Работа выполнена в рамках Государственного задания «Активные композитные материалы и методики анализа для (био)сенсорики» (код темы FSRM-2023-0009).

Ссылка при цитировании: Лаздин И.А., Кондратьева А.С., Комаревцев И.М., Эннс Я.Б., Казакин А.Н., Карасев П.А. Микроэлектромеханический газовый датчик резистивного типа для определения низких концентраций сероводорода // Научно-технические ведомости СПбГПУ. Физико-математические науки. 2024. Т. 17. № 3.1. С. 182–185. DOI: https://doi.org/10.18721/JPM.173.136

Introduction

Microelectromechanical systems are used in a variety of applications from gyroscopes and accelerometers to air pollution detection systems [1, 2]. Of particular interest are MEMS gas sensors based on sensitive elements made of thin films of metal oxides. For such sensors, an urgent problem remains the study of the effectiveness of various sensitive layers for different gases and the search for designs that can increase their energy efficiency while maintaining the sensitivity parameter of the sensor.

P-type semiconductors are promising for reducing gases such as hydrogen sulfide due to the acceptor interaction mechanism. An inexpensive and efficient p-type semiconductor material is nickel oxide (NiO). The confirmed possibility of modifying the roughness of NiO films helps to increase the sensitivity of the active layer [3].

Thus, the goal of this work was to create a microelectromechanical gas sensor of a resistive type with a thin-film sensing element made of nickel oxide, suitable for detection in a gas mixture from 1 to 80 ppm H_2S.

Materials and Methods

The sensitive element is made of silicon with a thickness of 0.4 mm and has dimensions of 10×10 mm in the horizontal plane. In the central part, the silicon is thinned to a membrane thickness of about 50 microns. The membrane contains a heater and two nickel comb electrodes, separated by an insulating dielectric. The heater is made of Ni and has the form of a meander, the tracks of which pass between the teeth of the comb electrodes and is also covered with a protective dielectric on top, in contrast to the teeth of the electrodes [4]. The sensitive layer of 80 nm NiO is located on the membrane on top of all elements. The developed technological route is carried out using photolithography and magnetron sputtering methods.

Results and Discussion

NiO coatings obtained by magnetron sputtering were subjected to post-processing – annealing at atmospheric pressure. The effect of annealing on surface morphology was assessed using AFM, XRD and XPS.

AFM images of sensitive layer is shown on Fig. 1. It was found that annealing led to the formation of a pronounced grain structure and an increase in film roughness. The root-mean-square deviation of the surface profile from the average value before and after annealing was 0.7 nm and 1.94 nm. Such changes in morphology should have a positive effect on the sensitivity of the sensor, since the resulting microcracks serve as sites for the emergence of active centers for the addition gas.

X-ray diffraction studies were carried out to evaluate the crystallographic structure of nickel oxide films, shown on Fig. 2, *a*. Three peaks are observed corresponding to NiO (111), (200), (220). Annealing led to a significant increase in the intensity of the peak corresponding to NiO (200). The calculated value of crystallite sizes increased from 3 to 13.4 nm, the lattice

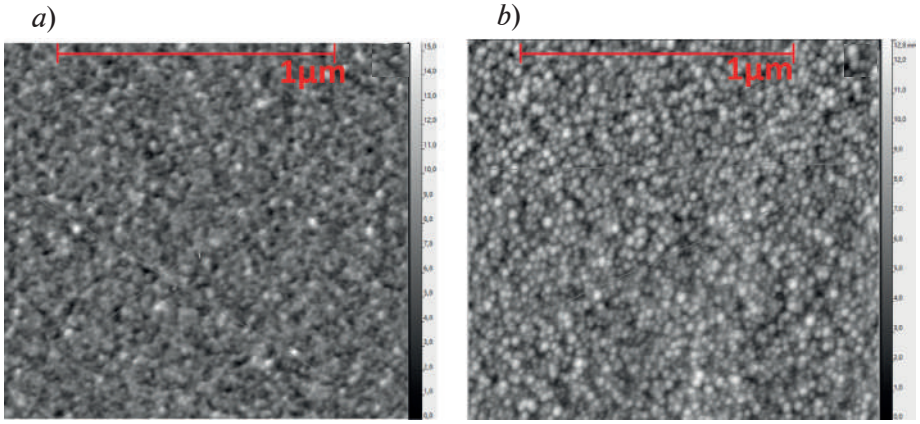

Fig.1. AFM image of NiO sensitive layer (*a*) before annealing, (*b*) after annealing

constant increased from 4.152 to 4.186 angstrom in the case of annealing in an atmosphere at comparison with unannealed samples.

Survey XPS spectra of the layer are shown in Fig. 2, *b*. The spectrum contains Ni $2p_{3/2}$ lines (868.6 ÷ 850 eV). The valency of nickel corresponds to two different oxidation states, so it can be concluded that highly defective nanocrystalline nickel oxide was used as a sensitive layer.

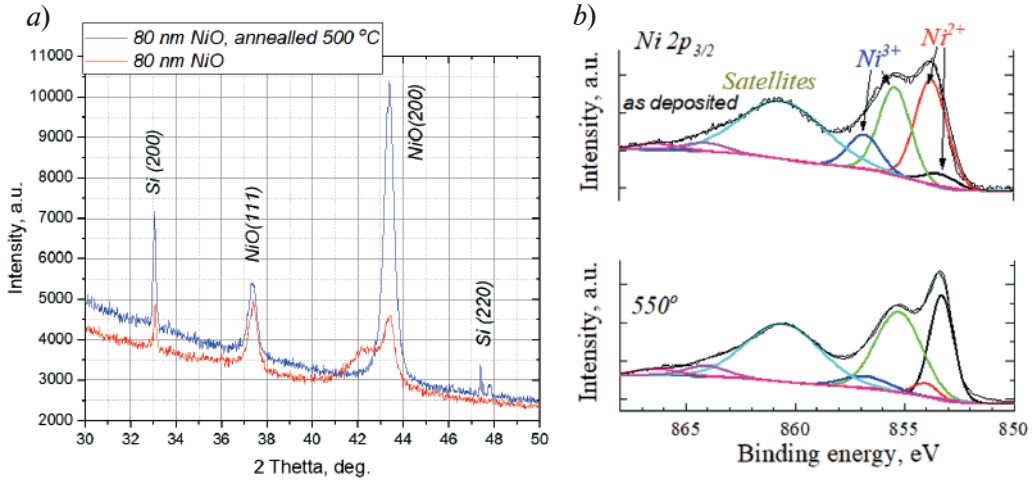

Fig.2. XRD spectrum of NiO films (80nm) before and after annealing (*a*), Ni $2p_{3/2}$ core level spectrum of NiO films (80 nm) before and after annealing (*b*)

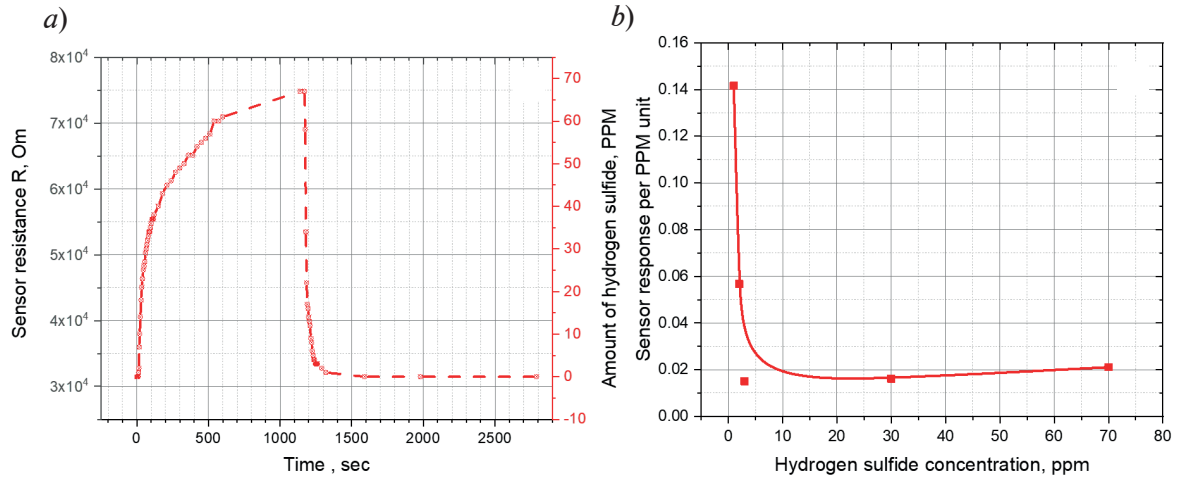

Fig. 3. Sensor response to the introduction of hydrogen sulfide vapor (*a*), sensor response per ppm unit at different H_2S concentrations (*b*)

The results of the study of the gas-sensitive properties of the MEMS sensor to the presence of hydrogen sulfide vapor are shown in Fig. 3 for a heater temperature of 205 °C in the range of hydrogen sulfide concentrations from 1 to 80 ppm. The determined parameter is the electrical response, defined for donor gases as the ratio of the resistance R_g measured in the presence of the substance being detected to the resistance in a pure model medium R at the same temperature. For acceptor gases, the inverse ratio is used [5]. The manufactured MEMS sensor makes it possible to determine the presence of hydrogen sulfide in the gas mixture under study with varying degrees of efficiency from 1 to 80 ppm. The operating power of the sensor was 1.5 W. The sensor response time ranged from 3 to 15 seconds, the recovery time was up to 30 minutes. The response speed increased with increasing operating temperature.

Conclusion

In this work, a technology for manufacturing MEMS hydrogen sulfide sensors with a sensitive layer of nickel oxide was proposed and tested. A sensitive layer of nickel oxide (NiO) deposited on the membrane showed sensitivity to hydrogen sulfide from 1 to 80 ppm, for annealed layer, the optimal operating temperature was 205 °C. This MEMS sensor is a resistive type with a self-heating thin NiO film is suitable for energy-efficient gas sensing applications, but requires selectivity testing and optimization temperature modes work.

Acknowledgments

Work was supported by the Ministry of Science and Higher Education (project No. FSRM-2023-0009).

REFERENCES

1. **Dong W., Gao Q., Zhou,** Anal Chim Acta, Characterization of the gas sensors based on polymer-coated resonant microcantilevers for the detection of volatile organic compounds. (671) (1–2) (20210) 85–91.

2. **Zampolli S.,** An electronic nose based on solid state sensor arrays for low-cost indoor air quality monitoring applications. Sens Actuators B Chem. (101) (1–2) (2004) 39–46.

3. **Chen H., Ma H., Zhu Y., Zhao M., Chen Z., Zhang L.,** Novel approach for improving electrochromic and mechanical properties of NiO film: Experiment and molecular dynamics simulation. Appl Surf Sci. (609) (2023).

4. **Lee C.Y., Hsieh P.R., Lin C.H., Chou P.C., Fu L.M., Chiang C.M.,** MEMS-based formaldehyde gas sensor integrated with a micro-hotplate. Microsystem Technologies. Microsystem Technologies. (349) (2006) 893–898.

5. **Kondrateva A.S., Bespalova P.G., Filatov L.A.,** Gas-sensitive properties of thin nickel oxide films. Russ J Appl Chem. (90) (2017) 846–852.

THE AUTHORS

LAZDIN Ilya A.
lazdin.ia@edu.spbstu.ru
ORCID: 0009-0002-0656-8433

ENNS Yakov B.
Ennsjb@gmail.ru
ORCID: 0000-0003-4396-2368

KONDRATEVA Anastasia S.
kondrateva_n@spbau.ru
ORCID: 0000-0003-3915-9329

KAZAKIN Alexei N.
Kazakin75@gmail.ru
ORCID: 0000-0001-8762-1587

KOMAREVTSEV Ivan M.
imk@spbstu.ru
ORCID: 0000-0001-5118-8152

KARASEOV Platon A.
platon.karaseov@spbstu.ru
ORCID: 0000-0003-2511-0188

Received 07.07.2024. Approved after reviewing 27.08.2024. Accepted 27.08.2024.

Conference materials
UDC 621.3
DOI: https://doi.org/10.18721/JPM.173.137

Combined resistive-capacitive MEMS switch for advanced communication systems

M.O. Morozov [1, 2] ✉, I.V. Uvarov [1]

[1] Valiev Institute of Physics and Technology of RAS, Yaroslavl Branch, Yaroslavl, Russia;
[2] P.G. Demidov Yaroslavl State University, Yaroslavl, Russia
✉ matvey19991@mail.ru

Abstract. The main characteristic of a capacitive microelectromechanical system (MEMS) switch is the ratio of capacitances in the open and closed states. In conventional switches, this ratio typically does not exceed ten and can be increased several times by using a floating potential electrode. The dependence of the capacitive characteristics, isolation and insertion loss of a switch with the "floating" electrode on the substrate material is investigated.

Keywords: MEMS switch, capacitance ratio, isolation, insertion loss, floating potential, finite element method

Funding: This work is supported by the program no. FFNN-2022-0017 of the Ministry of Science and Higher Education of Russia for Valiev Institute of Physics and Technology of RAS with the financial support of the Foundation for Assistance to Small Innovation Enterprises grant No. 18GUES18/91354.

Citation: Morozov M.O., Uvarov I.V., Combined resistive-capacitive MEMS switch for advanced communication systems, St. Petersburg State Polytechnical University Journal. Physics and Mathematics. 17 (3.1) (2024) 186–190. DOI: https://doi.org/10.18721/JPM.173.137

Материалы конференции
УДК 621.3
DOI: https://doi.org/10.18721/JPM.173.137

Комбинированный резистивно-емкостной МЭМС-переключатель для передовых систем связи

М.О. Морозов [1, 2] ✉, И.В. Уваров [1]

[1] Ярославский филиал Физико-технологического института РАН им. К.А. Валиева, Ярославль, Россия;
[2] Ярославский государственный университет им. П.Г. Демидова, Ярославль, Россия
✉ matvey19991@mail.ru

Аннотация. Основной характеристикой емкостного микроэлектромеханического (МЭМС) переключателя является отношение емкостей в замкнутом и разомкнутом состоянии. В стандартных изделиях это отношение обычно не превышает 10 и может быть увеличено в несколько раз за счет использования электрода с плавающим потенциалом. В работе исследуется зависимость емкостных характеристик, изоляции и вносимых потерь ключа с "плавающим" электродом от материала подложки.

Ключевые слова: МЭМС-переключатель, отношение емкостей, изоляция, вносимые потери, плавающий потенциал, метод конечных элементов

Финансирование: Работа выполнена в рамках государственного задания ФТИАН им. К.А. Валиева РАН Минобрнауки РФ по теме № FFNN-2022-0017 при финансовой поддержке гранта Фонда содействия инновациям №18ГУЭС18/91354.

Ссылка при цитировании: Морозов М.О., Уваров И.В. Комбинированный резистивно-емкостной МЭМС-переключатель для передовых систем связи // Научно-технические ведомости СПбГПУ. Физико-математические науки. 2024. Т. 17. № 3.1. С. 186–190. DOI: https://doi.org/10.18721/JPM.173.137

Introduction

MEMS switch is a micron-sized electromechanical relay fabricated by microelectronic techniques [1, 2]. It provides low insertion loss and high isolation, combined with small dimensions and virtually zero power consumption [3]. These features make MEMS switches attractive for advanced communication systems, radar equipment and other areas of radio electronics [4]. Recent growth of wireless communications and increased demands driven by 5G and 6G standards offer an ideal opportunity for MEMS switches.

The main characteristic of a capacitive switch is the ratio of capacitance in the down and up states of the movable beam C_{down}/C_{up}. In a conventional design, this ratio typically does not exceed 10 and does not ensure the required switching effect [5–7]. To increase this ratio, various methods have been suggested, such as using dielectrics with high dielectric constant, reducing the thickness of the dielectric layer or increasing the air gap [8, 9]. However, these methods have several drawbacks. For example, using non-standard dielectrics requires significant adjustments to the fabrication process, and enlarging the air gap increases the actuation voltage.

One of the most effective methods for increasing C_{down}/C_{up} is to use a floating potential electrode. This technique eliminates disadvantages mentioned above and allows one to vary the capacitance over a wide range without altering the design of the moving part. A metal electrode of the desired size is placed on the dielectric coating of the transmission line, creating a metal-to-metal connection between the beam and electrode. As a result, the switch becomes a resistive-capacitive device. This paper explores the performance of this type of switch, which is intended for use in advanced communication systems.

Materials and Methods

The proposed MEMS switch is schematically shown in Fig. 1, *a*. A movable electrode is an aluminum beam with a length of 100 μm, which is fixed on torsion suspensions. A transmission line is a coplanar waveguide running under the beam at a gap of 1 μm (Fig. 1, *b*). A thin metal electrode is formed on top of the dielectric layer. In the up state, the potential of the electrode is floating. The capacity of the beam-line system is small, so the signal passes from the input to the output with minimal loss. In the down state, the beam touches the electrode, and their potentials are equalized. The capacity between the beam and the transmission line increases significantly, so the switch shunts the line. The signal does not pass from the input to the output, and high isolation is achieved. Driving electrodes are located under both arms of the beam, so an additional restoring force may be applied in case of stiction. This design significantly improves the reliability of the switch compared to the classical cantilever structure.

The switch is simulated by the finite element method (FEM). The model includes a substrate with dimensions of 9.6×4.3 mm and a thickness of 460 μm, coated with a layer of SiO_2 with a thickness of 1 μm, as shown in Fig. 1, *c*. A transmission line with a length of 7.2 mm is formed on the insulating layer, with 1×1 mm contact pads for the central conductor and 1.4×1.4 mm pads for grounded conductors. The relatively large size of the pads is needed for welding electrical terminals. To speed the calculations up, the closure and opening of the switch was simulated by increasing the height of the contact bump, which has a cylindrical shape. The opposite signal electrode and driving electrodes were excluded from the model. At the same time, the model is located in a volume of air with the size 9.6×4.3×1 mm.

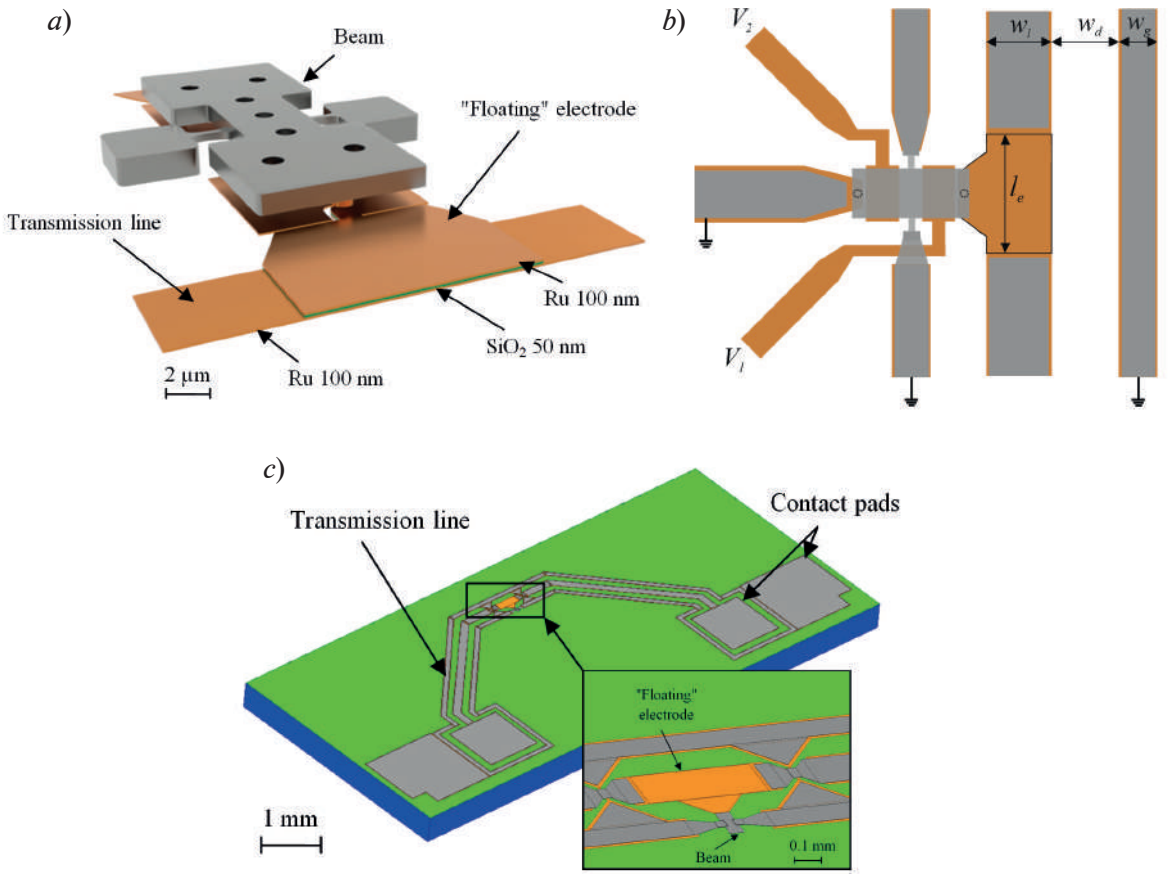

Fig. 1. A switch with a "floating" electrode: 3D view (*a*); top view of the switch built into the transmission line (*b*); a model of a chip (*c*)

Results and Discussion

The analytical calculation of the capacitance ratio is carried out using the formula (1), which was derived in our previous work [10]:

$$\frac{C_{down}}{C_{up}} = \varepsilon_r \frac{l_e w_l}{S} \frac{g - t_d - t_e}{t_d} = 1.5 \cdot 10^5, \quad (1)$$

where g is the air gap between the beam and the "floating" electrode, ε_r is the dielectric constant of the insulating material, w_l is the width of the transmission line, l_e is the length of the electrode that has a "floating" potential, S is the area of overlap between the beam and electrode, t_d is the thickness of the insulating material under the electrode, and t_e is the thickness of the "floating" electrode.

Expression (1) does not take into account the parasitic capacitance. Finite element simulation considers the real configuration of the transmission line and substrate properties. The dependence of the capacitance on the resistivity ρ of the silicon wafer is shown in Fig. 2. Increasing ρ reduces both C_{down} and C_{up} due to a decrease in the parasitic component. In turn, the drop of C_{up} increases the capacitance ratio. The maximum value is 7.4 at ρ = 50 kΩ·cm, which is significantly lower than the analytical prediction. The reason for the discrepancy is the relatively large C_{up} = 7 pF. Dielectric substrates significantly increase the capacitance ratio compared to silicon, see Table for details. The highest value of C_{down}/C_{up} = 46.1 is provided by borosilicate glass Borofloat 33. Sapphire substrate gives a capacitance ratio of 27.7. Thus, the proposed switch has a several times higher C_{down}/C_{up} in comparison to conventional capacitive switches.

Table

Material properties and simulation results for various substrates

Material	ε_r	ρ, Ω·cm	C_{down}, pF	C_{up}, pF	C_{down}/C_{up}
Low-resistivity silicon	11.7	12	120.89	74.25	1.6
High-resistivity silicon	11.7	$5 \cdot 10^3$	89.44	43.18	2.1
		$50 \cdot 10^3$	53.94	7.33	7.4
Sapphire	9.3	10^{16}	48.45	1.75	27.7
Borofloat 33	4.6	10^8	47.74	1.03	46.1

The next step is the estimation of insertion loss and isolation. These values are described by a single parameter S_{21} in the open and closed states of the switch:

$$|S_{21}|^2 = \frac{4}{\omega^2 C_{down}^2 Z_0^2}, \quad (2)$$

where Z_0 is the transmission line impedance, ω is the frequency of the switched signal. Measurements of these parameters were conducted in the frequency range of the switched signal ω from 1 to 20 GHz. Substrates made of glass, sapphire, and high-resistivity silicon (ρ = 5 kΩ·cm) were used in the calculations. Low-resistivity silicon was not considered, because it provides small capacitance ratio, while high-resistivity silicon (ρ = 50 kΩ·cm) was excluded due to its high cost and low availability.

For all the substrates, there is a trend towards decreasing isolation with the frequency, as shown in Fig. 3. Silicon and sapphire have similar isolation across the entire frequency range, while glass provides significantly better isolation in the 3–16 GHz range. As for insertion loss, silicon and sapphire provide similar results that do not exceed 0.8 dB across the entire range. However, the glass substrate has strong fluctuations in loss and large peak values of up to 1.6 dB. The acceptable S-parameter values are higher than 15 dB for isolation and less than 1 dB for insertion loss. The switch fabricated on the glass wafer ensures these characteristics over a frequency range from 1 to 12 GHz. The switches made from sapphire and silicon, on the other hand, have operating ranges of 1–10 GHz and 1–9 GHz, respectively.

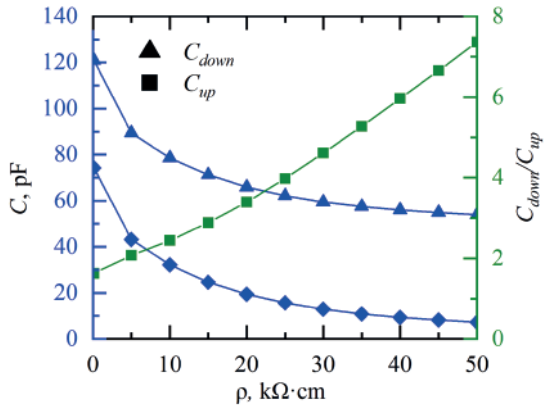

Fig. 2. The dependence of capacitive characteristics on the substrate resistivity

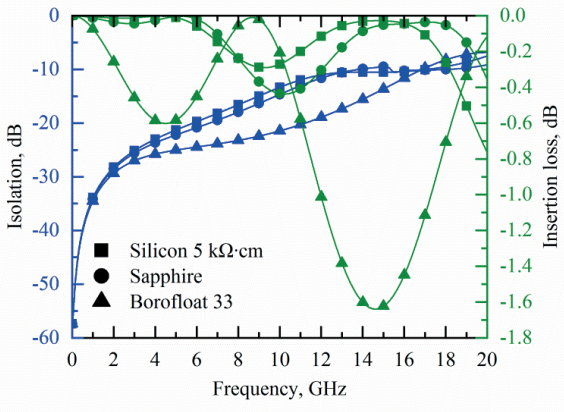

Fig. 3. The dependence of isolation and insertion loss on the signal frequency

Conclusion

The paper describes a combined resistive-capacitive MEMS switch equipped with a "floating" electrode that provides an enhanced capacitance ratio. The finite element method was used to calculate the capacitive characteristics, as well as the isolation and insertion loss in the 1–20 GHz frequency range. The use of low-resistivity silicon as the substrate material gives low capacitance ratio of 1.6. However, increasing the resistivity to 50 kΩ·cm increases C_{down}/C_{up} to 7.4. Even higher values can be achieved with dielectric substrates made of sapphire or borosilicate glass, which give ratios of 27.7 and 46.1, respectively. A switch on a sapphire substrate offers acceptable isolation of more than 15 dB and insertion loss lower than 1 dB in the 1–10 GHz range. The borosilicate glass substrate can extend the operating range up to 12 GHz.

REFERENCES

1. **Hindle P.,** The state of RF and microwave switches, Microwave J. 53(11) (2010) 20–36.

2. **Adonin A.S., Evgrafov A.Y., Minnebaev V.M., Ivashchenko N.G., Myakon'kikh A.V., Rogozhin A.E., Rudenko K.V.,** Electromagnetic modeling, technology, and production of microwave C3MOSHFET switches on AlGaN/GaN heterostructures, Russ. Microelectron. 46(6) (2017) 390–395.

3. **Majumder S., Lampen J., Morrison R., Maciel J.,** MEMS switches, IEEE Instrumentation & Measurement Magazine. 6 (1) (2003) 12–15.

4. **Haupt RL., Lanagan M.,** Reconfigurable antennas, IEEE Antennas Propag. Mag. 55 (2013) 49–61.

5. **Grichener A., Rebeiz G.M.,** High-reliability RF-MEMS switched capacitors with digital and analog tuning characteristics, IEEE Trans. Microw. Theory Techn. 58 (2010) 2692–2701.

6. **Yang H.H., Zareie H., Rebeiz G.M.,** A high power stress-gradient resilient RF MEMS capacitive switch, J. Microelectromech. Syst. 24 (2015) 599–607.

7. **Zareie H., Rebeiz G.M.,** High-power RF MEMS switched capacitors using a thick metal process, IEEE Trans. Microw. Theory Techn. 61 (1) (2013) 455–463.

8. **Tsaur J. et al.,** Broadband MEMS shunt switches using PZT/HfO_2 multi-layered high k dielectrics for high switching isolation, Sens. Acuators A: Phys. 121 (1) (2005) 275–281.

9. **Maninder K. et al.,** On characterization of symmetric type capacitive RF MEMS switches, Microsyst. Technol. 25 (2019) 729–734.

10. **Morozov M.O., Uvarov I.V.,** Performance Calculation for a MEMS switch with a Floating Electrode, Russ. Microelectron. 52 (6) (2023) 493–503.

THE AUTHORS

MOROZOV Matvey O.
matvey19991@mail.ru
ORCID: 0009-0005-3723-5924

UVAROV Ilia V.
i.v.uvarov@bk.ru
ORCID: 0000-0002-6882-0625

Received 11.07.2024. Approved after reviewing 26.07.2024. Accepted 29.07.2024.

Conference materials
UDC 621.382.2/.3; 537.312.54
DOI: https://doi.org/10.18721/JPM.173.138

Method for increasing of the voltage regulator radiation hardness

K.S. Pilipenko [1], E.A. Kulchenkov [1], S.B. Rybalka [1] ✉, A.A. Demidov [1]

[1] Bryansk State Technical University, Bryansk, Russia

✉ sbrybalka@yandex.ru

Abstract. For positive low-dropout linear voltage regulator the additional circuit elements have been developed in the output stage of voltage regulator, forming compensatory feedback and making it possible to increase voltage regulator radiation hardness.

Keywords: voltage regulator, total ionizing dose effects, X-ray irradiation

Funding: This study was supported by the Russian Ministry of Science and High Education (agreement with the Russian Ministry of Science and High Education of 9 February 2023 No. 075-11-2023-008) using state support measures provided by the Russian Federation Government's Decree of 9 April, 2010 No. 218.

Citation: Pilipenko K.S., Kulchenkov E.A., Rybalka S.B., Demidov A.A., Method for increasing of the voltage regulator radiation hardness, St. Petersburg State Polytechnical University Journal. Physics and Mathematics. 17 (3.1) (2024) 191–194. DOI: https://doi.org/10.18721/JPM.173.138

Материалы конференции
УДК 621.382.2/.3; 537.312.54
DOI: https://doi.org/10.18721/JPM.173.138

Метод для повышения радиационной стойкости стабилизатора напряжения

К.С. Пилипенко [1], Е.А. Кульченков [1], С.Б. Рыбалка [1] ✉, А.А. Демидов [1]

[1] Брянский государственный технический университет, г. Брянск, Россия

✉ sbrybalka@yandex.ru

Аннотация. Для линейного стабилизатора напряжения положительной полярности с низким падением напряжения IS-LS3-5V разработаны дополнительные элементы схемы выходного каскада стабилизатора напряжения, формирующие компенсационную обратную связь и позволяющие повысить радиационную стойкость стабилизатора напряжения.

Ключевые слова: стабилизатор напряжения, эффекты поглощенной дозы, рентгеновское излучение

Финансирование: Работа выполнена при финансовой поддержке Министерства науки и высшего образования РФ (соглашение с Министерством науки и высшего образования от 9 февраля 2023 г. № 075-11-2023-008) с использованием мер государственной поддержки, предусмотренных постановлением Правительства РФ от 9 апреля 2010 г. № 218.

Ссылка при цитировании: Пилипенко К.С., Кульченков Е.А., Рыбалка С.Б., Демидов А.А. Метод для повышения радиационной стойкости стабилизатора напряжения // Научно-технические ведомости СПбГПУ. Физико-математические науки. 2024. Т. 17. № 3.1. С. 191–194. DOI: https://doi.org/10.18721/JPM.173.138

Introduction

Today, the one of the main task is to increase the radiation hardness of electronic components to the effects of ionizing radiation [1, 2]. Therefore, the urgent question is to study a methods for increasing radiation hardness, especially, studying the response of individual elements of a linear voltage regulator IS-LS3-5V microcircuit, produced by JSC "GRUPPA KREMNY EL" (Bryansk) in framework of import substitution program, to total ionizing dose of ionizing radiation, using the developed hardware and software complex based on the X-ray research complex.

Materials and Methods

The positive low-dropout linear voltage regulator prototype IS-LS3-5V produced by JSC "GRUPPA KREMNY EL" (analogue of LM2937 type [3]) with output voltage of 5 V and made by epitaxial-planar bipolar technology. Investigation of the IS-LS3-5V voltage regulator for hardness to ionizing radiation by the effects of total ionizing dose were carried out using the developed hardware and software equipment based on an X-ray research complex XRRC-0401 (JSC "Specialized electronic systems" (SPELS) [4, 5]).

Results and Discussion

For increasing of voltage regulator's radiation hardness the additional circuit elements have been previously developed in the output stage of the linear voltage regulator, forming compensatory feedback, as a result of which the output voltage parameter of the voltage regulator remains within the limits established by the technical requirements at large values of the total ionizing dose [6]. This method can be implemented both at the stage of manufacturing a microcircuit chip, and as an external wiring diagram when using already produced serial products. Fig. 1 shows part of the electrical circuit of the IS-LS3-5V positive voltage regulator integrated circuit with additional elements where then the measurements were carried out.

In a known linear voltage regulator, the base of an additional n-p-n transistor is connected to the second inverted input of the operational amplifier, the collector of which is connected to the positive bus of the regulator, and the emitter is connected through the current generator to the

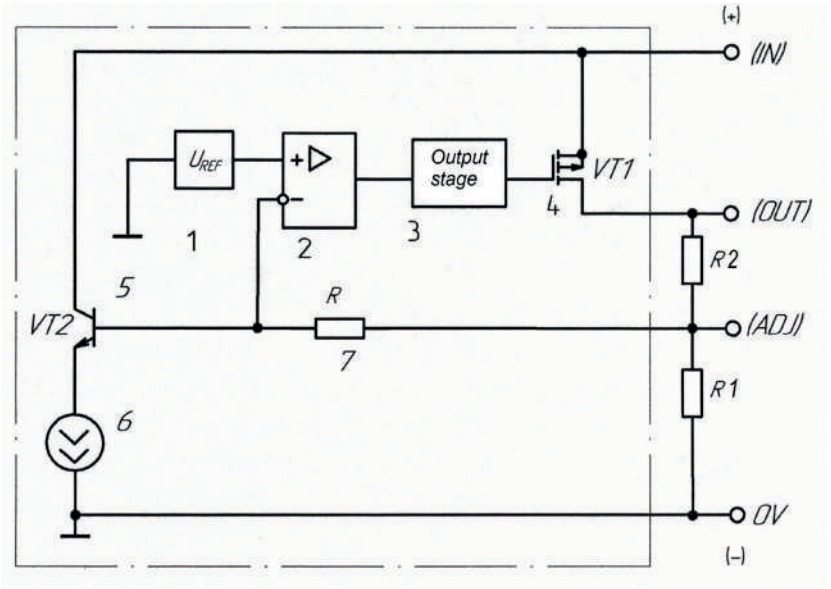

Fig. 1. Diagram of positive voltage regulator IS-LS3-5V: *1* – reference voltage source at the bandgap width; *2* – operational amplifier; *3* – output stage; *4* – output transistor; *5* – additional n-p-n transistor; *6* – current generator; *7* – additional resistor; 0V – positive bus; ADJ – feedback pin for adjusting the stabilization voltage; OUT – output of the voltage regulator; IN – positive bus; R1 and R2 – the stabilization voltage settings divider

negative bus of the regulator and a resistor is connected between the feedback pin and the second input of the operational amplifier, the value of which is determined by the formula:

$$R = \beta \Delta U_{REF} / I_G, \quad (1)$$

where β – the gain with the common emitter of the additional transistor after exposure to radiation; ΔU_{REF} – change in reference voltage from the nominal voltage after exposure to radiation; I_G – the magnitude of the generator current in the emitter circuit of the additional transistor. When exposed to radiation, the magnitude of the output voltage of the reference voltage source increases. An additional n-p-n transistor is a radiation dose sensor. The higher the radiation dose, the lower its gain in a common emitter circuit. At doses less than 200×10^3 un. (un. – the units of XRRC-0401), the gain of the n-p-n transistor changes slightly. Since the emitter current of the additional n-p-n transistor is set by the current generator and remains stable, when exposed to ionizing radiation, the current in the base circuit increases, the voltage drop across the resistor in the feedback circuit also increases, which leads to an increase in the potential at the inverted input of the operational amplifier. This causes the operational amplifier's output current to decrease, the output transistor to turn off, and the drain-to-source voltage drop to increase, thereby compensating for the drift of the output voltage due to the effect of ionizing radiation on the reference voltage source. In our case the calculated by equation (1) value of resistor R in the feedback circuit is 90 kΩ. In Fig. 2 presents the results of studies on the radiation hardness of voltage regulator without a compensation circuit (solid line) and using the method discussed above (dashed-line).

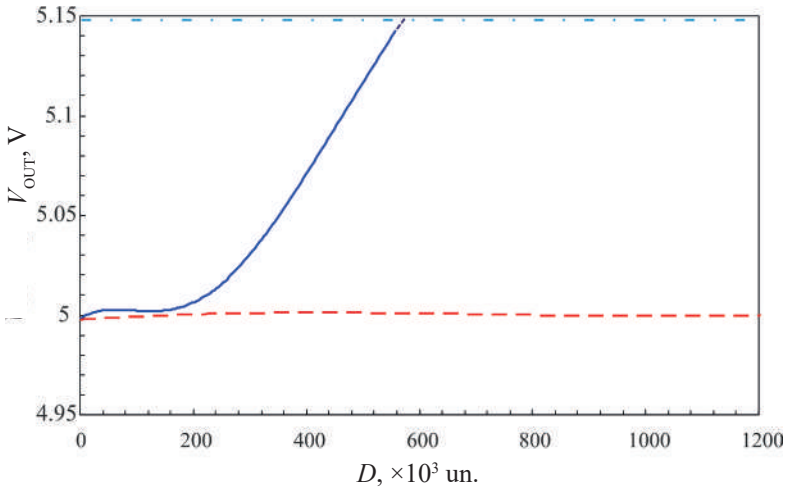

Fig. 2. The output voltage V_{OUT} dependence on total ionizing dose D for IS-LS3-5V voltage regulator: solid line – original voltage regulator integrated circuit, dashed-line – modified voltage regulator integrated circuit with additional circuit elements (dash-dot line – the upper limit of voltage regulator operation mode)

As can be seen from Fig. 2, the output voltage of the modified voltage regulator integrated circuit remains almost constant. Because of this, the output voltage V_{OUT} for nonmodified voltage regulator increase with increasing of total ionizing dose and reaches the upper limit of voltage regulator operation mode (5.15 V) at total ionizing dose equals of ~560×10^3 un. Therefore, using the above-mentioned additional circuit elements in the output stage of the linear voltage regulator leads to increasing of its radiation hardness more than two times.

Conclusion

The method of radiation hardness increasing to the positive low-dropout linear voltage regulator IS-LS3-5V (produced by JSC "GRUPPA KREMNY EL") with output voltage of 5 V has been developed. It is shown that additional circuit elements in the output stage of the linear voltage regulator form compensatory feedback and make it possible to increase its radiation hardness.

Acknowledgments

The results of the Research and Development have been achieved during the implementation of the project "Integrated microcircuits of analog signal converters in metal-polymeric package of various types: development and mastering of technology, replacement of imported analogs and organization of serial production" (agreement with the Russian Ministry of Science and High Education of 9 February 2023 No. 075-11-2023-008) using state support measures provided by the Russian Federation Government's Decree of 9 April, 2010 No. 218.

REFERENCES

1. **Gaul S.J., Vonno N., Voldman S.H., Morris W.H.,** Integrated Circuit Design for Radiation Environments, Wiley & Sons, Chichester, 2020.

2. **Volovich G.I.,** Circuit Technique of Analog and Analog-digital Electronic Devices, DMK Press, Moscow, 2018.

3. LM2937 500-mA Low Dropout Regulator, Texas Instruments, URL: http://www.ti.com/product/lm2937. Accessed May. 21, 2024.

4. JSC "Specialized electronic systems" (SPELS). URL: http://www.spels.ru. Accessed May. 21, 2024.

5. **Kulchenkov E.A., Rybalka S.B., Demidov A.A.,** Study of Radiation Hardness of Linear Voltage Regulator, Advances in Applied Physics. 5 (11) (2023) 445–454.

6. Patent RU 219091 U1, 2023. Authors: Derbunov I.V., Bryukhno N.A., Dantsev O.O., Kulchenkov E.A.

THE AUTHORS

PILIPENKO Kirill S.
www-kirill.pilipenko@yandex.ru
ORCID: 0000-0002-9806-0882

RYBALKA Sergey B.
sbrybalka@yandex.ru
ORCID: 0000-0002-7746-3009

KULCHENKOV Evgeny A.
ewgeniy2000@mail.ru
ORCID: 0000-0002-7294-7549

DEMIDOV Andrey A.
demandr@yandex.ru
ORCID: 0000-0002-8639-3575

Received 11.07.2024. Approved after reviewing 31.07.2024. Accepted 01.08.2024.

Conference materials
UDC 537.312.54; 621.382.2/.3
DOI: https://doi.org/10.18721/JPM.173.139

Radiation behaviour study of linear voltage regulator

S.B. Rybalka [1] ✉, A.A. Demidov [1], E.A. Kulchenkov [1], K.S. Pilipenko [1]

[1] Bryansk State Technical University, Bryansk, Russia

✉ sbrybalka@yandex.ru

Abstract. For positive low-dropout linear voltage regulator IS-LS1-3.3V it is established that the output voltage and consumption current change vary slightly in all studied total ionizing dose interval and do not fixed voltage regulator failure. The analytical dependencies of output voltage and consumption current on the total ionizing dose have been obtained.

Keywords: total ionizing dose effects, voltage regulator, X-ray irradiation

Funding: This study was supported by the Russian Ministry of Science and High Education (agreement with the Russian Ministry of Science and High Education of 9 February 2023 No. 075-11-2023-008) using state support measures provided by the Russian Federation Government's Decree of 9 April, 2010 No. 218.

Citation: Rybalka S.B., Demidov A.A., Kulchenkov E.A., Pilipenko K.S., Radiation behaviour study of linear voltage regulator, St. Petersburg State Polytechnical University Journal. Physics and Mathematics. 17 (3.1) (2024) 195–198. DOI: https://doi.org/10.18721/JPM.173.139

Материалы конференции
УДК 621.382.2/.3; 537.312.54
DOI: https://doi.org/10.18721/JPM.173.139

Исследование радиационного поведения линейного стабилизатора напряжения

С.Б. Рыбалка [1] ✉, А.А. Демидов [1], Е.А. Кульченков [1], К.С. Пилипенко [1]

[1] Брянский государственный технический университет, г. Брянск, Россия

✉ sbrybalka@yandex.ru

Аннотация. Для линейного стабилизатора напряжения положительной полярности с низким падением напряжения IS-LS1-3.3V установлено, что выходное напряжение и потребляемый ток незначительно изменяются во всем исследованном интервале ионизирующей дозы облучения и не зафиксировано отказа стабилизатора напряжения. Получены аналитические зависимости выходного напряжения и потребляемого тока IS-LS1-3.3V от поглощенной дозы.

Ключевые слова: эффекты поглощенной дозы, стабилизатор напряжения, рентгеновское излучение

Финансирование: Работа выполнена при финансовой поддержке Министерства науки и высшего образования РФ (соглашение с Министерством науки и высшего образования от 9 февраля 2023 г. № 075-11-2023-008) с использованием мер государственной поддержки, предусмотренных постановлением Правительства РФ от 9 апреля 2010 г. № 218.

Ссылка при цитировании: Рыбалка С.Б., Демидов А.А., Кульченков Е.А., Пилипенко К.С. Исследование радиационного поведения линейного стабилизатора

напряжения // Научно-технические ведомости СПбГПУ. Физико-математические науки. 2024. Т. 17. № 3.1. С. 195–198. DOI: https://doi.org/10.18721/JPM.173.139

Introduction

For development of industries such as cosmonautics, aircraft engineering, nuclear power, it is necessary to achieve reliable functioning of the electronic components such as voltage regulators that used under radiation conditions [1, 2]. Therefore, with taking into account, the main aim of this work is to study the radiation hardness to the effects of the total ionizing dose of the positive low-dropout linear voltage regulator IS-LS1-3.3V produced by JSC "GRUPPA KREMNY EL" (Bryansk) in framework of import substitution program, using the developed hardware and software complex based on the X-ray research complex.

Materials and Methods

As the object of research was the positive low-dropout linear voltage regulator prototype IS-LS1-3.3V produced by JSC "GRUPPA KREMNY EL" (analogue of LT1963 type [3]) with output voltage of 3.3 V and made by epitaxial-planar bipolar technology. Studies of the IS-LS1-3.3V voltage regulator for hardness to ionizing radiation by the effects of total ionizing dose were carried out using the developed hardware and software equipment based on an X-ray research complex XRRC-0401 (JSC "Specialized electronic systems" (SPELS) [4]). The schematic diagram of the developed hardware-software research complex is shown in Fig. 1. The X-ray research complex is an X-ray source RAP-100 with a maximum anode voltage of 80 kV and a maximum anode current of 0.3 mA, which installed in an X-ray protection chamber with a two-coordinate positioning system with a control step of 0.1 mm. The X-ray intensity was monitored using the X-ray comparator DRI-0401. The board of contact equipment is designed to place the sample in the radiation field and ensures its operation.

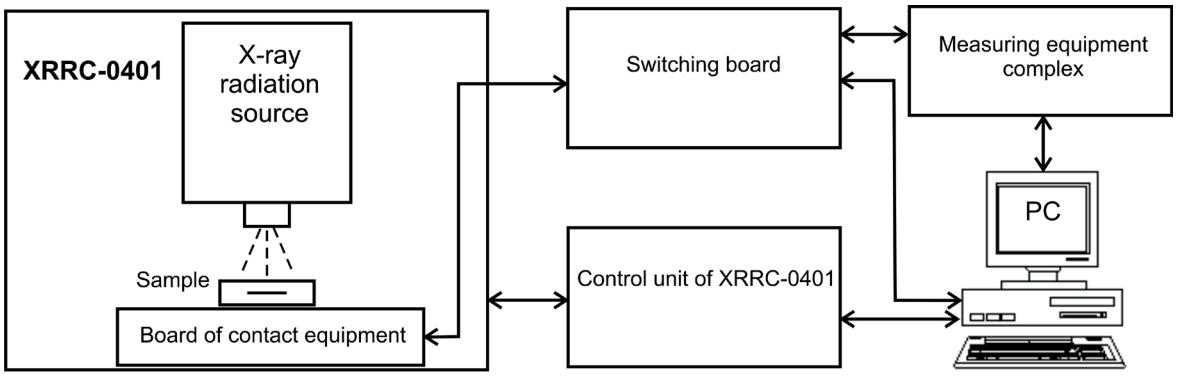

Fig. 1. The scheme of the hardware-software complex: XRRC-0401 – X-ray research complex; source of X-ray radiation; board of contact equipment; switching board; control unit of X-ray hardware-software complex; measuring equipment complex; PC – personal computer

The control unit of contact equipment sets the mode of X-ray source operation and duration of irradiation. The rate of dose of radiation exposure can be controlled by both the change in anode current and the distance from the window of the X-ray source to the sample being irradiated. The switching board specifies the electrical modes of testing sample, as well as the necessary connection of measuring equipment, power sources and loads. The measuring equipment complex includes: RIGOL DP832 power supply, Fluke 8845A multimeter, RIGOL DL3021 programmable electronic load and Keithley 6485 ammeter. The XRRC-0401 was controlled by specialized software developed in the LabView environment, which allows measuring monitored parameters after a given time

interval, and also provides the ability to set the electrical mode of operation of the voltage regulator during irradiation. The positive low-dropout linear voltage regulator IS-LS1-3.3V was connected to the board of contact equipment in accordance with typical scheme.

Results and Discussion

During the radiation experimental study of IS-LS1-3.3V positive low-dropout (LDO) linear voltage regulator the following operation mode was used for XRRC-0401: anode voltage of 70 kV, anode current of 150 μA. The distance from the window of the X-ray source equals of 40 mm and rate of radiation dose exposure equals of 35.3 un./s (un. – the units of XRRC-0401). In Fig. 2, *a* are shown experimental results for voltage regulator obtained during radiation experiment. As can be seen, the output voltage V_{OUT} slowly increase with increasing of total ionizing dose *D*. It is important to note that output voltage not reaches the lower and upper limit of voltage regulator operation mode (3.135–3.465 V). Thus, at value of total ionizing dose equals of 8×10^3 un. (that is equal of ~282 s) output voltage V_{OUT} equals of 3.29 V.

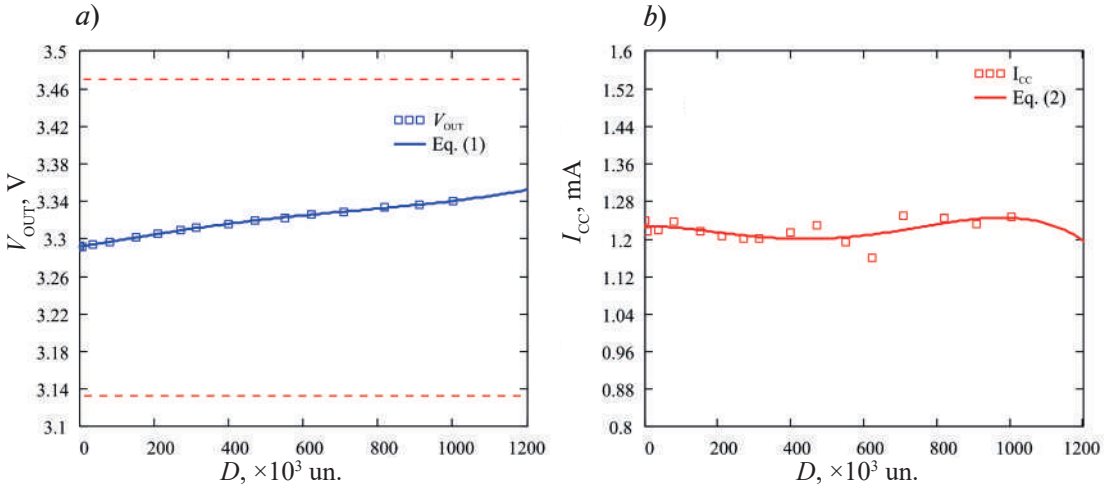

Fig. 2. The experimental (points) and theoretical (lines) data for output voltage dependence V_{OUT} (*a*) and consumption current I_{CC} (*b*) on total ionizing dose *D* for IS-LS1-3.3V voltage regulator (dashed-line curve – lower and upper limit of voltage regulator operation mode)

Further, during increasing of radiation dose exposure the output voltage V_{OUT} increase nonlinearly and at final value of total ionizing dose equals of 1002×10^3 un. (~35430 s) the output voltage value is 3.33 V ($\Delta V_{OUT} \approx 0.04$ V), i.e. in this case the voltage regulator scheme preserves a functional state without failure.

As follows from Fig. 2, *b* the consumption current I_{CC} varies slightly between 1.59 mA (622×10^3 un.) and 1.25 mA (707×10^3 un.) and reaches 1.246 mA at final value of total ionizing dose equals of 1002×10^3 un. (~35430 s). It should be noted that a similar results were detected in the similar type of positive LDO linear regulator designed specifically for space applications [5]. From a practical viewpoint, for engineering calculations it is important to know for voltage regulator the analytical dependence on the radiation dose. On the basis of above experimental data, analytical dependence of the output voltage V_{OUT} and consumption current I_{CC} on the total ionizing dose *D* for voltage regulator were calculated using mathematical processing methods of measurement results treatment, especially, the methods of regression analysis. The analytical dependence of the output voltage and consumption current on the total ionizing dose for voltage regulator (in active operating mode at input voltage of 24 V and load current of 5 mA) are following:

$$V_{OUT}=3.204\times10^{-14}D^4-4.435\times10^{-11}D^3-9.187\times10^{-9}D^2+7.041\times10^{-5}D+3.291, \quad (1)$$

$$I_{cc}=-6.276\times10^{-13}D^4+1.183\times10^{-9}D^3-5.368\times10^{-7}D^2-9.1\times10^{-7}D+1.226, \quad (2)$$

where *D* – the total ionizing dose (10^3 un.), V_{OUT} – the output voltage (V), I_{CC} – the consumption current (mA).

Consequently, the obtained equations can be used by developers-engineers in electronic circuit design for same parameters calculation of linear voltage regulator taking into account of radiation effect, for example, some type of the voltage regulator's that functioning in cosmic space.

Conclusion

The radiation hardness to the effects of the total ionizing dose of the positive low-dropout linear voltage regulator IS-LS1-3.3V produced in framework of import substitution program, has been studied using the developed hardware-software complex based on the X-ray research complex. It is established experimentally that the output voltage varies slightly from 3.29 up to 3.33 V ($\Delta V_{OUT} \approx 1.2\%$) in all total ionizing dose interval and preserves a functional state without failure. It is shown that the consumption current varies slightly between 1.59 mA and 1.25 mA. It is established that total ionizing radiation dose in investigated interval does not lead to the failure of the voltage regulator. For voltage regulator the analytical dependencies for the output voltage and consumption current on the total ionizing dose have been obtained.

Acknowledgments

The results of the Research and Development have been achieved during the implementation of the project "Integrated microcircuits of analog signal converters in metal-polymeric package of various types: development and mastering of technology, replacement of imported analogs and organization of serial production" (agreement with the Russian Ministry of Science and High Education of 9 February 2023 No. 075-11-2023-008) using state support measures provided by the Russian Federation Government's Decree of 9 April, 2010 No. 218.

REFERENCES

1. **Volovich G.I.,** Circuit Technique of Analog and Analog-digital Electronic Devices, DMK Press, Moscow, 2018.

2. **Kulchenkov E.A., Rybalka S.B., Demidov A.A.,** Study of Radiation Hardness of Linear Voltage Regulator, Advances in Applied Physics. 5 (11) (2023) 445–454.

3. LT1963A Series Low Noise, Fast Transient Response LDO Regulators, Analog Devices. URL: http://www.linear.com/LT1963A. Accessed May. 21, 2024.

4. JSC "Specialized electronic systems" (SPELS). URL: http://www.spels.ru. Accessed May. 21, 2024.

5. Ultra Low Dropout Positive Fixed Linear Regulator IRUH33P253A1M. URL: https://www.irf.com/product-info/datasheets/data/iruh33p253a1m.pdf. Accessed May. 21, 2024.

THE AUTHORS

RYBALKA Sergey B.
sbrybalka@yandex.ru
ORCID: 0000-0002-7746-3009

KULCHENKOV Evgeny A.
ewgeniy2000@mail.ru
ORCID: 0000-0002-7294-7549

DEMIDOV Andrey A.
demandr@yandex.ru
ORCID: 0000-0002-8639-3575

PILIPENKO Kirill S.
www-kirill.pilipenko@yandex.ru
ORCID: 0000-0002-9806-0882

Received 12.07.2024. Approved after reviewing 31.07.2024. Accepted 01.08.2024.

Conference materials
UDC 621.383.51
DOI: https://doi.org/10.18721/JPM.173.140

Gallium phosphide/black silicon heterojunction solar cells

E.A. Vyacheslavova [1] ✉, A.V. Uvarov [1], A.A. Maksimova [1, 2],
A.I. Baranov [1], A.S. Gudovskikh [1, 2]

[1] Alferov University, St Petersburg, Russia;
[2] St. Petersburg Electrotechnical University "LETI", St Petersburg, Russia
✉ cate.viacheslavova@yandex.ru

Abstract. A new type of heterojunction solar cell based on gallium phosphide/black silicon was considered. The nanostructured surface of black silicon (*b*-Si) was obtained by cryogenic etching in a SF_6/O_2 gas mixture. The average height of the *b*-Si structures varies from 1.4 to 2.1 μm. The heterojunction was fabricated by low temperature method such as plasma-enhanced atomic-layer deposition (PEALD). According to transmission electron microscopy, the thicknesses of the deposited GaP layer are fixed to be 30 nm. The layer consists of crystallites aligned along the crystal lattice direction, as well as their twins. This thin GaP layer allowed achieving a fill factor of 54.5% without transparent conductive oxide and with a test grid. The use of GaP layer as an emitter a broadening of the external quantum efficiency spectrum boundary in the short-wavelength region.

Keywords: black silicon, cryogenic etching, gallium phosphide, PEALD, heterojunction solar cell

Funding: The research was supported by the Russian Science Foundation Grant No. 23-29-00735, https://rscf.ru/project/23-29-00735/.

Citation: Vyacheslavova E.A., Uvarov A.V., Maksimova A.A., Baranov A.I., Gudovskikh A.S., Gallium phosphide/black silicon heterojunction solar cells, St. Petersburg State Polytechnical University Journal. Physics and Mathematics. 17 (3.1) (2024) 199–203. DOI: https://doi.org/10.18721/JPM.173.140

Материалы конференции
УДК 621.383.51
DOI: https://doi.org/10.18721/JPM.173.140

Гетероструктурные солнечные элементы на основе GaP/*b*-Si

Е.А. Вячеславова [1] ✉, А.В. Уваров [1], А.А. Максимова [1, 2],
А.И. Баранов [1], А.С. Гудовских [1, 2]

[1] Академический университет им. Ж.И. Алфёрова РАН, Санкт-Петербург, Россия;
[2] Санкт-Петербургский государственный электротехнический университет «ЛЭТИ» им. В.И. Ульянова (Ленина), Санкт-Петербург, Россия
✉ cate.viacheslavova@yandex.ru

Аннотация. Был рассмотрен новый тип гетероструктурного солнечного элемента на основе фосфида галлия/черного кремния. Наноструктурированная поверхность черного кремния (*b*-Si) была получена путем криогенного травления в газовой смеси SF_6/O_2. Средняя высота структур *b*-Si варьируется от 1.4 до 2.1 мкм. Гетеропереход был изготовлен с помощью низкотемпературного метода, такого как атомно-слоевое плазмохимическое осаждение (АСПХО). Согласно данным просвечивающей электронной микроскопии толщина нанесенного слоя фосфида галлия составляет 30 нм.

Слой состоит из кристаллитов, выровненных по направлению решетки, а также их двойников. Этот тонкий GaP слой позволил достичь фактора заполнения в 54.5% без прозрачного проводящего оксида и с использованием тестовой сетки. Использование слоя GaP в качестве эмиттера приводит к расширению границы спектра внешней квантовой эффективности в коротковолновой области.

Ключевые слова: черный кремний, криогенное травление, фосфид галлия, АСПХО, гетероструктурный солнечный элемент

Финансирование: Исследование выполнено за счет гранта Российского научного фонда № 23-29-00735, https://rscf.ru/project/23-29-00735/.

Ссылка при цитировании: Вячеславова Е.А., Уваров А.В., Максимова А.А., Баранов А.И., Гудовских А.С. Гетероструктурные солнечные элементы на основе GaP/*b*-Si // Научно-технические ведомости СПбГПУ. Физико-математические науки. 2024. Т. 17. № 3.1. С. 199–203. DOI: https://doi.org/10.18721/JPM.173.140

Introduction

The future global electricity generation will be largely powered by renewable energy sources. At the end of 2023, solar energy accounted for 73.1% of the renewable growth, with a capacity of 1.419 GW [1]. The overall growing solar cell market is dominated by silicon (Si) due to its availability, durability and cost-effectiveness. The technology of a solar cell production based on the amorphous/crystalline (*a*-Si:H/*c*-Si) silicon heterojunction is the main concept for a highly efficient Si solar cell. However, these heterojunction devices are limited by non-ideal optical and electronic properties. To reduce optical losses, an antireflection coating is used, as well as surface texturing (the formation of micron-sized pyramids). However, these approaches work effectively in a narrow range of wavelengths and angles of incidence. One of the effective methods of reducing optical reflectance in solar cells can be considered the use of a nanostructured black silicon (*b*-Si). Black silicon is a modification of silicon surface with extremely low reflectivity compared to the planar surface. The *b*-Si has excellent optical properties like low light reflection in both a wide wavelength range and incidence angles [2], and high absorption in the visible and infrared wavelength range [3]. It is worth noting, in the cases of a heterojunction based on *b*-Si, recombination at a nanostructured interface strongly affects efficiency. Gallium phosphide (GaP) can be a promising candidate for the passivating emitter layer of heterojunction cell. GaP has an indirect bandgap energy (2.27 eV) and a low lattice mismatch with Si, that provides to low parasitic absorption [4, 5]. Due to these properties, a conception based on GaP/*b*-Si heterojunction are an extremely promising solution for photovoltaic application.

Experimental section

Cryogenic etching (−150 °C) to obtain *b*-Si structures was carried out using p-type (1–20 Ω · cm) B-doped monocrystalline silicon (100). Before the etching process, the substrates were not cleaned of the native oxide (SiO_2). We used sulfur hexafluoride and oxygen (SF_6/O_2) mixture as process gases. At the beginning, accidental etching of the SiO_2 (ions and fluorine radicals F•) forms a rough surface. Isotropic etching of the Si surface by F• increases the roughness. Oxidation of the surface by O• radicals protects the roughness as Si etching occurs. A SiO_xF_y passivating layer is locally formed. Low temperatures and high oxygen content in the SF_6/O_2 (45/15 sccm) gas mixture lead to the formation of high-aspect structures.

After the etching, the samples were cleaned using the Shiraki technology [6]. To form thin GaP layers on the nanostructured *b*-Si surface, the PEALD method was used at a temperature of 380 °C [7]. This process consists of the exposure of precursors with the substrate surface in one assigned cycle. The cycle is repeated a set number of times. The trimethylgallium (TMG) metallic compound and phosphine (PH_3) gas were used as sources of Ga and P atoms. A pressure was 350 mTorr during deposition steps. The GaP layer was *n*-doped by silicon (SiH_4/H_2 gas mixture).

An aluminum (Al) layer was deposited on the backside of the samples to obtain ohmic contact. Further, the annealing of gallium phosphide was carried out for 1 minute in the rapid thermal annealing (RTA). The annealing temperature range was 600 to 700 °C. After that, a front contact in the form of a silver grid (1×1 cm) was formed. Figure 1 shows the design schematic of the GaP/*b*-Si heterojunction solar cell.

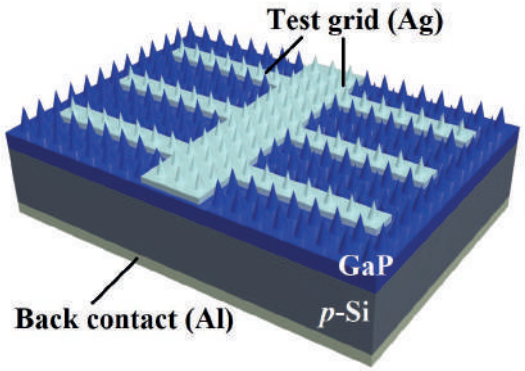

Fig. 1. Structure of the GaP/*b*-Si heterojunction solar cell

The current-voltage curves were measured using a solar simulator (Abet Technology SunLite) under AM1.5G and a Keithley 2400 electrometer with software control in a LabVIEW environment. The total reflection spectra were detected using an AvaSpec SensLine spectrometer with an integrating sphere. The external quantum efficiency (*EQE*) values were carried out with SLS M266 monochromator, a halogen lamp and a reference *c*-Si solar cell.

Results and Discussion

Surface morphology was characterized by a scanning electron microscopy (Supra 25 Zeiss). According to SEM, the etched silicon wafers consist of high density of *b*-Si structures (Fig. 2, *a*). The average height *b*-Si varies from 1.4 to 2.1 μm.

Transmission electron microscopy (TEM) were used to study the structural properties of the obtained GaP/*b*-Si structures. TEM images analysis showed that the GaP layer thickness was 30 nm. The layer consists of crystallites aligned along the crystal lattice direction, as well as their twins. The elemental composition was carried out directly in the TEM setup by the energy-dispersive X-ray (EDX) spectroscopy studies. The elemental mapping analysis indicated the uniform distribution of components (Ga and P) over the entire *b*-Si surface (Fig. 2, *b*). This indicates that there is no deficiency of either precursors in the structure during deposition.

The current density-voltage ($J-V$) curves of the heterojunction solar cells based on *b*-Si are shown in Figure 3, *a*. The measurements were obtained for an emitter coverage of ~80% using

a) *b*)

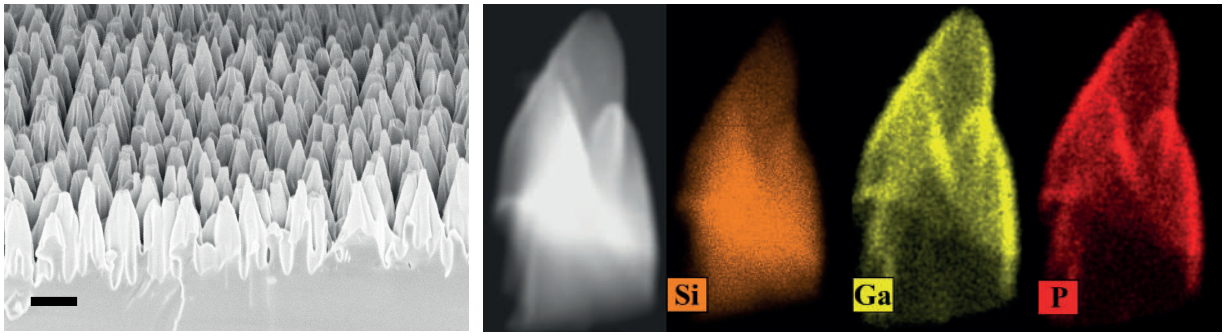

Fig. 2. SEM image (*a*), HAADF STEM image and EDX-elemental mapping analysis (*b*) of the *b*-Si coated with GaP. The bare scale is 1 μm

an aperture (area = 16 mm^2). The photovoltaic parameter values such as open circuit voltage (V_{OC}), short-circuit current density (J_{SC}), fill factor (*FF*) and power conversion efficiency (*PCE*) summarized in Table.

It is worth noting, samples were annealed at various temperatures (T_{RTA} = 600...700 °C) to activate the phosphorus dopant. At 600–650 °C, there is no diffusion of phosphorus atoms into the silicon substrate. At 700 °C, the phosphorus atoms start to diffuse into the silicon surface layer, thereby improving the lateral conductivity. Thus, for a sample based on *b*-Si with a height of 1.4 μm, an improvement in the J_{SC} from 28.7 to 33.7 mA/cm^2 is observed during annealing at 700 °C.

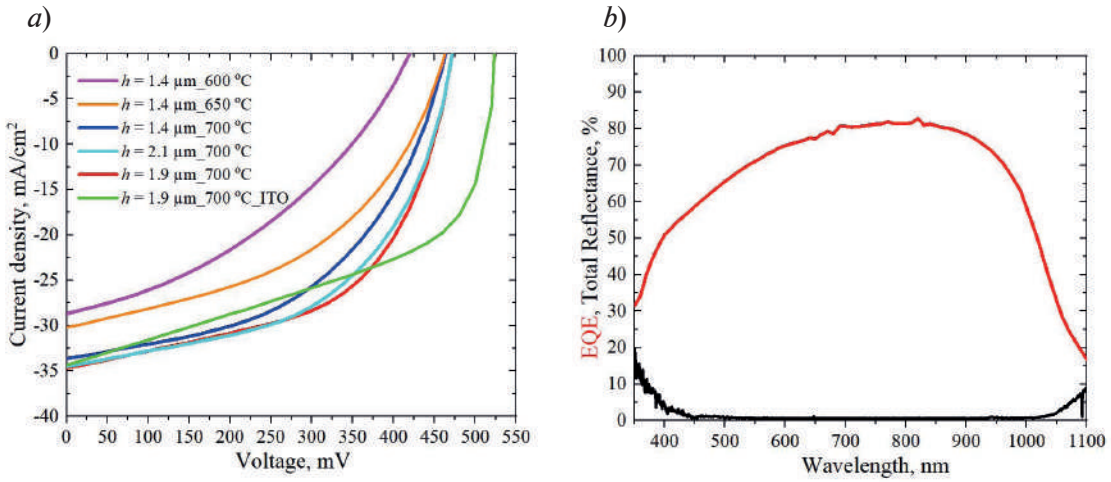

Fig. 3. *J*–*V* characteristics (*a*) and *EQE* spectrum (red line) (*b*) of the GaP/*b*-Si heterojunction solar cell

Table

Photovoltaic characteristics of the GaP/*b*-Si heterojunction solar cells

b-Si height, μm	T_{RTA} [°C]	ITO	V_{OC} [mV]	J_{SC} [mA/cm^2]	*FF* [%]	*PCE* [%]
~1.4	600	without	419	28.7	38.5	4.63
	650		463	30.2	46.5	6.5
	700		464	33.7	49.6	7.75
~2.1	700		472	34.5	52.6	8.56
~1.9	700		473	34.7	54.5	8.94
	700	with	530	34.3	50.5	9.19

The best GaP/Si heterojunction cell based on 1.9 μm height *b*-Si show a good performance achieving V_{OC} of 473 mV, J_{SC} of 34.7 mA/cm^2 and *FF* of 54.5% without transparent conductive oxide and with a silver (Ag) grid pitch of 2 mm. A power conversion efficiency of 9% was received. For the same solar cell with a layer of transparent conductive indium tin oxide (ITO), the V_{OC} was 530 mV. The magnetron sputtering process was used to formation of ITO thin film. However, there is a decrease in *FF* from 54.5% to 50.5% due to the shunt resistance.

Figure 3, *b* shows the total reflectance spectrum of black silicon coated with GaP. It can be seen that sample has total reflectance below 5% up to 1050 nm. The *EQE* spectrum was measured and is demonstrated in Figure 3, *b*. The maximum *EQE* value is 81.5% with shadowing with a silver grid. We can observe in the short-wavelength region a significant advantage of the GaP over *a*-Si:H on the *EQE* spectrum [8].

Conclusion

We have fabricated and investigated the GaP/*b*-Si heterojunction solar cells for the first time. The deposition of GaP layers on *b*-Si was carried out by the low temperature PEALD method. The elemental mapping analysis indicated the uniform distribution of components (Ga and P) over the entire black silicon surface. A GaP/*b*-Si solar cell efficiency of 9% was demonstrated. The *EQE* value is improving in the short-wavelength region through the lower light absorption of GaP layer.

Acknowledgments

The research was supported by the Russian Science Foundation Grant No. 23-29-00735, https://rscf.ru/project/23-29-00735/.

REFERENCES

1. A report by the International Renewable Energy Agency (IRENA) Renewable capacity statistics 2024.

2. **Hsu C.H., Wu J.-R., Lu Y.-T., et al.,** Fabrication and characteristics of black silicon for solar cell applications: An overview, Mater. Sci. Semicond. Processing. 25 (2014) 2–17.

3. **Zhao Z., Zhang Z., Jing J., et al.,** Black silicon for near-infrared and ultraviolet photodetection: A review, APL Mater. 11 (2023) 021107.

4. **Li T., Mastro M., Dadgar A.,** III-V Compound Semiconductors: Integration with Silicon-Based Microelectronics (CRC Press). (2010) 603.

5. **Corkish R.,** Some candidate materials for lattice-matched liquid-phase epitaxial growth on silicon, Sol. Cells. 31 (1991) 537–548.

6. **Ishizaka A., Shiraki Y.,** Low Temperature Surface Cleaning of Silicon and Its Application to Silicon MBE, Electrochem. Soc. 133 (1986) 666.

7. **Uvarov A.V., Gudovskikh A.S., Baranov A.I., Vyacheslavova E.A., et. al.,** Conformal growth of GaP on high aspect ratio Si structured surface via plasma-enhanced atomic layer deposition, Surface and Coatings Technology. 477 (2024) 130357.

8. **Vyacheslavova E.A., Uvarov A.V., Maksimova A.A., et. al.,** Heterojunction solar cells based on nanostructured black silicon, St. Petersburg Polytechnic University Journal. Physics and Mathematics. 16 (3.1) (2023) 434–438.

THE AUTHORS

VYACHESLAVOVA Ekaterina A.
cate.viacheslavova@yandex.ru
ORCID: 0000-0001-6869-1213

BARANOV Artem I.
itiomchik@yandex.ru
ORCID: 0000-0002-4894-6503

UVAROV Alexander V.
lumenlight@mail.ru
ORCID: 0000-0002-0061-6687

GUDOVSKIKH Alexander S.
gudovskikh@spbau.ru
ORCID: 0000-0002-7632-3194

MAKSIMOVA Alina A.
deer.blackgreen@yandex.ru
ORCID: 0000-0002-3503-7458

Received 18.07.2024. Approved after reviewing 12.08.2024. Accepted 12.08.2024.

Conference materials
UDC 621.382.323
DOI: https://doi.org/10.18721/JPM.173.141

Field plates design optimization to increase breakdown voltage of GaN HEMT

E.A. Kozlovskaya [1] ✉, D.M. Kurbanbaeva [1], K.A. Tsarik [1], A.V. Lashkov [1]

[1] National Research University of Electronic Technology, Moscow, Russia

✉ k89296190714@gmail.com

Abstract. This article presents the results of modeling the heterostructure of a normally-off n-channel transistor with various designs of field plates on electrodes. The use of field plates makes to possible to effectively control the distribution of the field in the channel and increases the breakdown voltage. The optimal design parameters of field plates to achieve maximum BV were determined by study of the current-voltage characteristics, the distribution of the field in the channel and the concentration of the majority carriers in the channel.

Keywords: GaN, power transistor, field plate, breakdown voltage

Funding: The work was supported by the Ministry of Education and Science in the framework of state task FSMR-2022-0004.

Citation: Kozlovskaya E.A., Kurbanbaeva D.M., Tsarik K.A., Lashkov A.V. Field plates design optimization to increase breakdown voltage of GaN HEMT, St. Petersburg State Polytechnical University Journal. Physics and Mathematics. 17 (3.1) (2024) 204–209. DOI: https://doi.org/10.18721/JPM.173.141

Материалы конференции
УДК 621.382.323
DOI: https://doi.org/10.18721/JPM.173.141

Оптимизация конструкции экранирующих электродов для повышения напряжения пробоя GaN HEMT

Е.А. Козловская [1] ✉, Д.М. Курбанбаева [1], К.А. Царик [1], А.В. Лашков [1]

[1] Национальный исследовательский университет «МИЭТ», Москва, Россия

✉ k89296190714@gmail.com

Аннотация. В данной статье представлены результаты моделирования гетероструктуры нормально закрытого n-канального транзистора с различными конструкциями экранирующих электродов. Использование экранирующих электродов позволяет эффективно управлять распределением поля в канале и повышает напряжение пробоя. С помощью исследования вольт-амперных характеристик, характера распределения электрического поля и концентрации основных носителей заряда в канале были определены оптимальные конструкционные параметры экранирующих электродов.

Ключевые слова: GaN, силовой транзистор, экранирующий электрод, напряжение пробоя

Финансирование: Работа выполнена в рамках Государственного задания FSMR-2022-0004.

Ссылка при цитировании: Козловская Е.А., Курбанбаева Д.М., Царик К.А., Лашков А.В. Оптимизация конструкции экранирующих электродов для повышения

напряжения пробоя GaN HEMT // Научно-технические ведомости СПбГПУ. Физико-математические науки. 2024. Т. 17. № 3.1. С. 204–209. DOI: https://doi.org/10.18721/JPM.173.141

Introduction

A breakdown in high electron mobility transistor (HEMT) is a critical event, as it can lead to irreversible damage to the device [1]. Therefore, when designing such transistors, special attention is paid to their ability to withstand high voltages. Over the past two decades, in the course of research in the field of GaN HEMT, experts have proposed and implemented design solutions that allow an order of magnitude increase in breakdown voltage (BV). For example, the use of field plates (FP) allows the electric field (EF) to be redistributed in the transistor channel between gate and drain. The shift of strong fields from critical areas to less significant areas of transistor leads to an increase in the BV [2, 3]. Due to the uniform distribution of the electric field, the FP helps reduce probability of occurrence of an avalanche breakdown, improve the thermal stability of the transistor, preventing local overheating, and also increase the reliability and durability of HEMT. The scientific community has proposed and studied various designs of field plates [2–4]. The variety of design approaches leads to the need for systematization and selection of the best. The geometric dimensions of multiple FPs have a huge number of combinations. Even the search for the optimal ratio of the sizes of dual FPs turns into a lengthy search of geometric parameters. A possible solution may be use of computer simulation, algorithms and artificial neural networks that optimize the design of complex FPs [5]. In the work, the effect of different FP designs on the BV of normally-off GaN HEMT was investigated by computer simulation.

Materials and Methods

The study was carried out by Sentaurus TCAD. The command file for modeling the electrophysical characteristics included a piezoelectric polarization model, drift-diffusion model, thermionic emission mechanism at heterojunctions, avalanche generation model, SRH recombination, etc. The equations were solved by Newton's iteration method. The 2D model mesh included 12,500 nodes densified in channel area. Drain voltage was limited to the range from 0 to 3000 V. The limit of current in the channel was 1 A/mm. The heterostructure design of GaN HEMT was taken from a previous study in which the optimal mole fraction of aluminum in the buffer layer was determined to achieve maximum BV [6]. The heterostructure consisted of a 50 nm AlN nucleation layer, a 2 μm $Al_{0.05}Ga_{0.95}N$ buffer layer, a 300 nm GaN channel layer, a 15 nm $Al_{0.25}Ga_{0.75}N$ barrier layer, a 1 nm AlN spacer layer and a 100 nm p-GaN cap layer (Fig. 1). Si_3N_4 was used as a dielectric. The heterostructure was located on a silicon substrate. The model took into account a background impurity (Si, 1×10^{15} cm^{-3}) in the heterostructure. The Mg concentration in the cap layer is 5×10^{17} cm^{-3}. The study of the influence of FPs on the BV was carried out for most common designs with FP-source, FP-gate, grating FP-gate, FP-drain, and dual FPs (Fig.1). The distance between source and drain is 21 μm, between source and gate 1 μm, between gate and drain 18 μm. The design of the FPs varied in length, height from the barrier layer, and presence of a trench. In GaN HEMTs with a gFP-gate, the distance from the gate edge to the edge of the last FP finger on the drain side is constant. The grating parameters satisfied the ratio L_{GG}:L_{GB} = 3:1, where L_{GG} is length of finger in the grate, L_{GB} is the distance between the FP fingers. The GaN HEMT without FPs in the design has a BV of about 311 V.

Results and Discussion

Modeling of GaN HEMT with FP-source (Fig. 1, *a*) demonstrated an increase in the BV with increasing FP-source length (L_S) due to the redistribution of the peak EF strength from the gate edge towards the drain (Fig. 2, *a*). However, a further increase in the L_S leads to a decrease in BV. Increasing the L_S reduces the dielectric layer between the drain edge and the FP edge, which causes breakdown through dielectric layer at lower drain voltages [7]. In addition, an

excessive field shift from the gate edge increases the EF peak at the drain edge, which can lead to an avalanche breakdown. Reducing the distance between barrier layer and FP-source leads to an increase in the efficiency of EF redistribution in the channel and an increase in BV. Since the minimum distance (1 μm) between FP-source and barrier layer (H_S) is limited by height of the gate (400 nm), a trench with a length of 4 μm was used on the FP-source edge, which reduced the distance between FP-source and barrier layer (H_{ST}) and increased the BV (Fig. 2, *a*). The optimal FP-source design to achieve maximum BV included L_S 9.5 μm and H_{ST} 50 nm. Similar field distributions were demonstrated in modeling of GaN HEMTs with FP-gate (Fig. 3). The BV and the nature of the BV versus L_G dependence were approximately the same as in the case of the FP-source (Fig. 2, *b*). It is worth noting that when the L_G reaches 6 μm and the trench at the FP-gate edge approaches the barrier layer (H_{GT}) to 50 nm, the BV drops, as a result of which the center of the "parabolic" dependence of the BV on the L_G acquires a valley. This is due to the fact that according to the reduction of H_{GT}, the EF peaks at the gate and drain edges are reduced, whereas the EF peak beneath the FP-gate edge increase [7]. Therefore H_{GT} or L_G to be selected so that the EF peaks at the gate and drain edges and the FP-gate edges are leveled. The optimal FP-gate design for leaving the valley and achieving maximum BV at H_{GT} of 50 nm and trench length of 0.9 μm requires L_G of 5 or 7 μm.

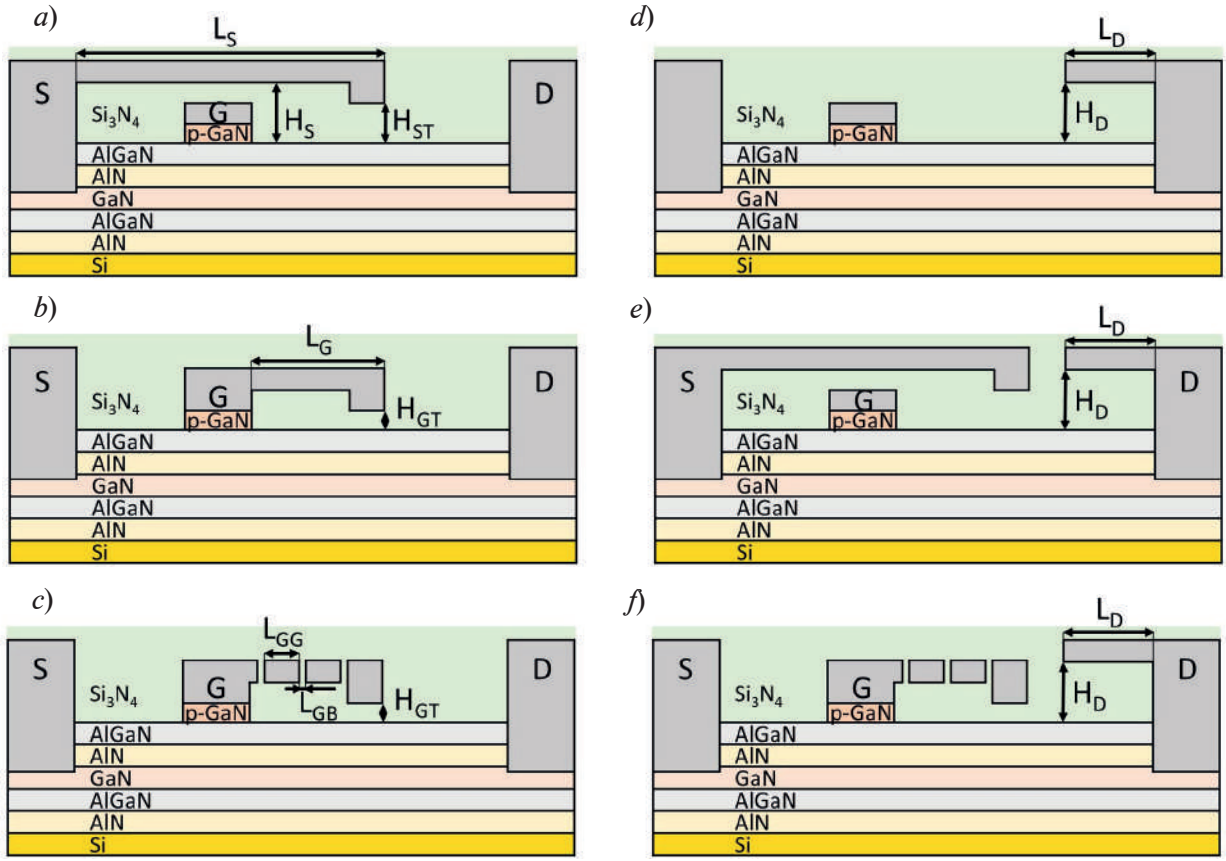

Fig. 1. Cross-section GaN HEMT with a FP-source (*a*), with a FP-gate (*b*), with a gFP-gate (*c*), with a FP-drain (*b*), with dual FPs: FP-drain and FP-source (*e*), with dual FPs: FP-drain and gFP-gate (*f*)

Converting FP-gate into grating FP-gate was applied to increase the BV (Fig. 2, *c*). The gFP-gate has more EF peaks due to charge induction between each finger. More points with electric charge located at the finger edges are generated, which redistribute and reduce the peak EF strength. The EF distribution in GaN HEMT with gFP-gate becomes smoother than in other designs. The maximum BV was achieved for gFP-gate length of 5 μm using a two-finger design and for gFP-gate length of 6 μm using a three-finger design (Fig. 2, *f*).

Reducing the H_{GT} to 50 nm leads to an increase in the BV in comparison with FP-gate, but does not allow one to overcome the valley at 6 μm. The optimal gFP-gate design to achieve

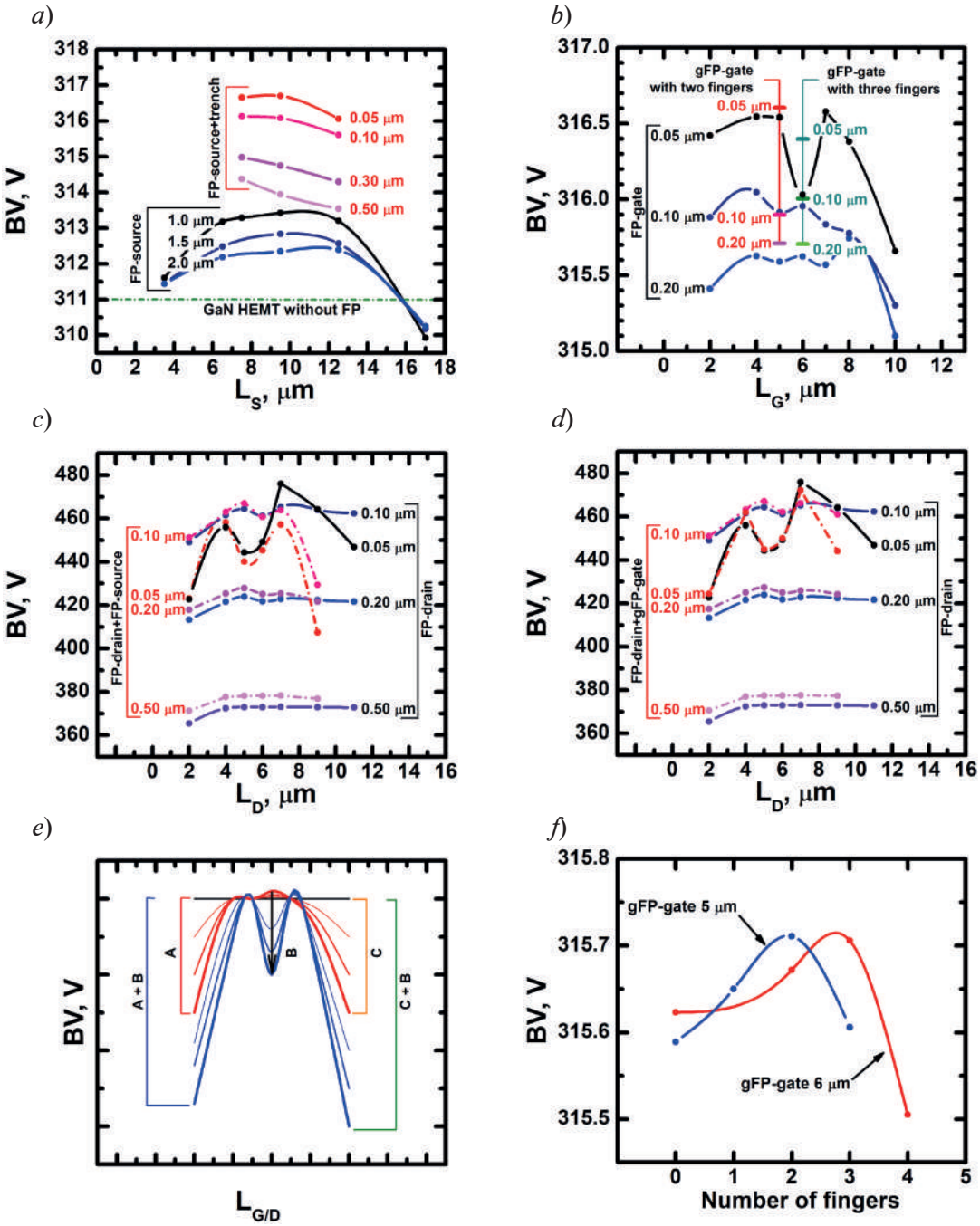

Fig. 2. Dependence of BV on length FP-source (*a*), FP-gate (*b*), FP-drain (dual FPs with FP-source) (*c*), FP-drain (dual FPs with gFP-gate) (*c*). The alleged influence of a close distance from FP edge to the own electrode (A) and to the opposite electrode (C) and peak states of the EF (B) on the dependence of BV on the FP length (*e*). The influence of the number of fingers in the gFP-gate on the BV (*f*)

maximum BV included two fingers, L_G 5 μm, L_{GG} 1.125 μm, L_{GB} 0.375 μm and H_{GT} 50 nm. The modulation of electric fields for GaN HEMT with FP-drain and gFP-drain is shown in Figure 3. As a result of the modeling, a significant increase in the BV was revealed when using a FP-drain in the GaN HEMT design (Fig. 2, *c*, *d*). The characteristic peak of the EF under the drain edge was significantly suppressed (Fig. 3). Similar to FP-source and FP-gate, the insufficient length of FP-drain leads to insignificantly shift the peak EF away from the source, and the excess length leads to a very close distance to the gate, which reduces the BV. Similar to FP-gate, the approach of FP-drain to the barrier layer leads to the appearance of a valley. Adding FP-source to GaN HEMT leads to a greater FP-drain length limitation than adding FP-gate. The previously found

optimal designs of FP-source and FP-gate were used to modeling GaN HEMT with dual FPs. The use of dual FPs makes it possible to increase the BV, but does not solve the problem of the appearance of a valley at small H_D. The optimal FP-drain design to achieve maximum BV included L_D 7 μm and H_D 50 nm. The optimal dual FPs design to achieve maximum BV was obtained at L_D of 5 μm and H_D of 100 nm.

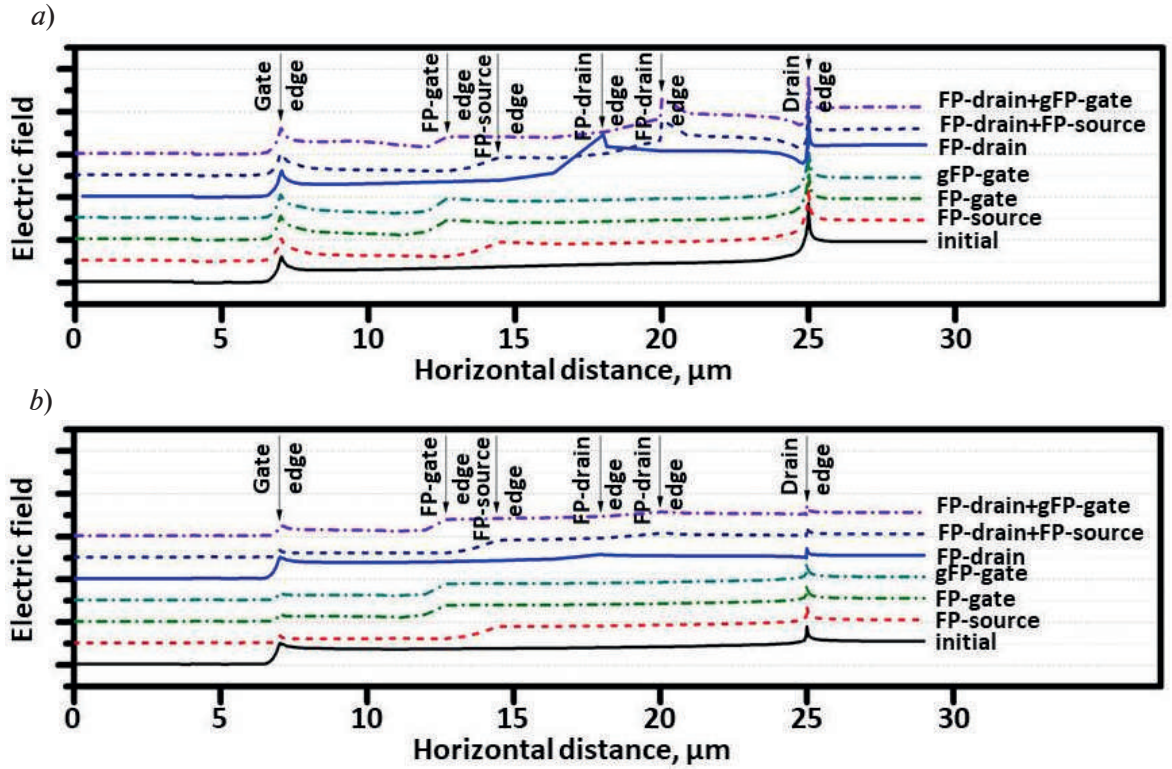

Fig. 3. The influence of different FP designs on field distribution in the GaN HEMT at BV (*a*) and 200 V (*b*). Field distribution is demonstrated for each type of FP with optimal dimensions and maximum BV

Conclusion

The work demonstrated the modeling results of GaN HEMT by Sentaurus TCAD. A characteristic change in the dependence of the BV on the FP length was established (Fig. 2, *e*). The close distance from the FP edge to the edge of its electrode (FP-gate and FP-drain) or to the edge of the gate (FP-source) leads to decrease of the BV due to increase of non-uniformity of EF (Fig. 2, *e*, A). The close distance of the FP edge to the edge of opposite electrode or FP leads to decrease of the BV due to breakdown through the dielectric layer between the FP edge and the opposite electrode. Thus, when designing the FP length, it is necessary to take into account the EF of an insulator breakdown and prevent excessive approaching of the elements of opposite electrodes. In addition, excessive field shift from the gate/drain edge increases the EF peak at the drain/gate edge, which can lead to avalanche breakdown (Fig. 2, *e*, C). Reducing the distance between the FP and the barrier layer increases the possibility of modulating the electric field, but contributes to the appearance of a valley with a low BV due to an increase in the EF peak at the FP edge (Fig. 2, *e*, B). The valley formation is not typical for a GaN HEMT with FP-source. Reducing the distance between the FP and the barrier layer at a minimum and maximum FP length leads to the overlap of two effects and a greater BV reduction (Fig. 2, *e*, A+B, C+B). Studying the influence of FPs design on BV made it possible to select the optimal FPs parameters to achieve maximum BV of GaN HEMT.

REFERENCES

1. **Wuerfl J., Bahat-Treidel E., Brunner F., Cho E., Hilt O., Ivo P., Knauer A., Kurpas P., Lossy R., Schulz M., Singwald S., Weyers M., Zhytnytska R.,** Reliability issues of GaN based high voltage power devices, Microelectronics Reliability. 51 (9-11) (2011) 1710–1716.

2. **Xia X., Guo Z., Sun H.,** Study of Normally-Off AlGaN/GaN HEMT with Microfield Plate for Improvement of Breakdown Voltage, Micromachines. 12 (11) (2021) 1318.

3. **Wang P., Deng C., Cheng H., Cheng W., Du F., Tang C., Geng C., Tao N., Wang Q., Yu H.,** Simulation of High Breakdown Voltage, Improved Current Collapse Suppression, and Enhanced Frequency Response AlGaN/GaN HEMT Using a Double Floating Field Plate, Crystals. 13 (1) (2023) 110.

4. **Saito W., Takada Y., Kuraguchi M., Tsuda K., Omura I.,** Recessed-gate structure approach towards normally off high-voltage AlGaN/GaN HEMT for power electronics applications, IEEE T Electron Dev. 53 (2) (2006) 356–362.

5. **Liu S., Duan X., Wang S., Zhang J., Hao Y.,** Optimization of dual field plate AlGaN/GaN HEMTs using artificial neural networks and particle swarm optimization algorithm, IEEE Transactions on Device and Materials Reliability. 23 (2) (2023) 204–210.

6. **Kurbanbaeva D.M., Lashkov A.V., Tsarik K.A.,** Investigation of the influence of the buffer layer design in a GaN HEMT transistor on the breakdown characteristics, Russian Microelectronics. Special issue based on the proceedings of the 15th International Conference "Micro and Nanoelectronics - 2023" (ICMNE-2023). 52 (1) (2023) S14–S19.

7. **Saito W., Kuraguchi M., Takada Y., Tsuda K., Omura I., Ogura T.,** Design optimization of high breakdown voltage AlGaN–GaN Power HEMT on an insulating substrate for $R_{ON}A$–V_B tradeoff characteristics, IEEE Transactions on electron devices. 52 (1) (2005) 106–111.

THE AUTHORS

KOZLOVSKAYA Ekaterina A.
k89296190714@gmail.com
ORCID: 0000–0003-0235-3101

TSARIK Konstantin A.
tsarik_kostya@mail.ru
ORCID: 0000-0002-8218-7774

KURBANBAEVA Diana M.
diana.kurbanbaeva.00@mail.ru
ORCID: 0000-0002-7012-1823

LASHKOV Andrey V.
lashkovav.miet@gmail.com
ORCID: 0000-0001-6794-8523

Received 15.07.2024. Approved after reviewing 12.08.2024. Accepted 12.08.2024.

Conference materials
UDC 546.26; 537.226.86
DOI: https://doi.org/10.18721/JPM.173.142

Influence of ambient humidity on the magnitude of the piezoelectric strain coefficient of nitrogen-doped carbon nanotubes for the creation of strain sensors

O.I. Soboleva [1] ✉, M.V. Il`ina [1], M.R. Polyvianova [1], A.A. Chefranov [1], O.I. Il`in [1]

[1] Institute of Nanotechnologies, Electronics and Equipment Engineering,
Southern Federal University, Taganrog, Russia
✉ osotova@sfedu.ru

Abstract. This paper establishes patterns of influence of ambient humidity on the piezoelectric strain coefficient and the magnitude of the current generated by nitrogen-doped carbon nanotubes (N-CNTs) during their deformation. It is shown that at humidity up to 60%, stable current generation is observed during the deformation of N-CNTs; at higher humidity, the instability of measurements increases and the spread of the generated current grows significantly, which is associated with a decrease in the N-CNTs piezoelectric strain coefficient.

Keywords: carbon nanotubes, nanopiezotronics, piezoelectric response, piezoelectric force microscopy, atomic force microscopy

Funding: This research was supported by the Ministry of Science and Higher Education of the Russian Federation in the framework of the state task in the field of scientific activity, grant number FENW-2022-0001.

Citation: Soboleva O.I., Il`ina M.V., Polyvianova M.R., Chefranov A.A., Il`in O.I., Influence of ambient humidity on the magnitude of the piezoelectric strain coefficient of nitrogen-doped carbon nanotubes for the creation of strain sensors, St. Petersburg State Polytechnical University Journal. Physics and Mathematics. 17 (3.1) (2024) 210–214. DOI: https://doi.org/10.18721/JPM.173.142

Материалы конференции
УДК 546.26; 537.226.86
DOI: https://doi.org/10.18721/JPM.173.142

Влияние влажности окружающей среды на величину пьезоэлектрического модуля легированных азотом углеродных нанотрубок для создания сенсоров деформации

О.И. Соболева [1] ✉, М.В. Ильина [1], М.Р. Полывянова [1],
А.А. Чефранов [1], О.И. Ильин [1]

[1] Южный федеральный университет,
Институт нанотехнологий, электроники и приборостроения, г. Таганрог, Россия
✉ osotova@sfedu.ru

Аннотация. В данной работе установлены закономерности влияния окружающей среды на пьезоэлектрический коэффициент деформации и величину тока, генерируемого углеродными нанотрубками, легированными азотом (N-УНТ), в процессе их деформации. Показано, что при влажности до 60% наблюдается стабильное генерирование тока при деформации N-УНТ, при более высокой влажности возрастает нестабильность измерений и значительно увеличивается разброс генерируемого тока, что связано со снижением пьезоэлектрического модуля N-УНТ.

Ключевые слова: углеродные нанотрубки, нанопьезотроника, пьезоэлектрический отклик, метод силовой микроскопии пьезоотклика атомно-силовой микроскопии

Финансирование: Данное исследование выполнено при поддержке Министерства науки и высшего образования Российской Федерации в рамках государственного задания в области научной деятельности, грант № FENW-2022-0001.

Ссылка при цитировании: Соболева О.И., Ильина М.В., Полывянова М.Р., Чефранов А.А., Ильин О.И. Влияние влажности окружающей среды на величину пьезоэлектрического модуля легированных азотом углеродных нанотрубок для создания сенсоров деформации // Научно-технические ведомости СПбГПУ. Физико-математические науки. 2024. Т. 17. № 3.1. С. 210–214. DOI: https://doi.org/10.18721/JPM.173.142

Introduction

At present, implantable electronics is an actively developing field of science. Basically, various types of materials with piezoelectric effect are used to transmit "tactile" sensations, effectively converting mechanical impact into an electrical signal [1]. At the same time, the efficiency of energy conversion in such sensors is mainly determined by two factors: the electromechanical properties of the piezoelectric material and the design of the sensor itself. In addition, such designs can be used to create highly sensitive strain gauges or microphones [2,3]. Piezoelectric materials can become electrically polarized when an external voltage is applied or deformed in response to electrical stimuli. Thus, sensors based on the piezoelectric effect can be used as versatile sensors. Compared to other sensors or monitoring methods, piezoelectric sensors have numerous advantages such as small size, light weight, low cost, availability in various formats, and high sensitivity [4]. Nitrogen-doped vertically aligned carbon nanotubes (N-CNTs) with anomalous piezoelectric properties can be one of the promising functional materials with high piezoelectric strain coefficient and mechanical strength [5]. However, for an instrument N-CNTs, it is important to understand how environmental parameters can affect the characteristics of the device and limit its scope of application. In particular, changes in atmospheric humidity can not only increase the parasitic capacitance, for example in pressure sensors, but also "glue" CNTs together, as well as affect the piezoelectric strain coefficient of the array. At the same time, many works have been devoted to studies of the influence of growth parameters on the properties of N-CNT [6, 7] However, there are no studies on the effect of environmental humidity on the piezoelectric strain coefficient N-CNTs in the literature. In view of this, this paper presents the results of a study of the influence of ambient humidity on the magnitude of the piezoelectric strain coefficient of nitrogen-doped carbon nanotubes to create strain sensors.

Materials and Methods

The experimental sample was an array of vertically aligned carbon nanotubes grown by plasma enhanced chemical vapor deposition method (C_2H_2 + NH_3). In this case, ammonia added during the growth process acts as a source of nitrogen defects. The growth was carried out at a temperature of 550 °C for 30 min and a pressure of 600 Pa. The plasma power was 40 W. Nickel (15 nm) deposited on a molybdenum sublayer was used as a catalyst. The piezoelectric properties of vertically aligned N-CNTs were studied by piezoelectric force microscopy (PFM) method of atomic force microscopy (AFM). The main difficulty in such experimental research is that the PFM method is a contact AFM technique, which leads to the CNTs detaching from the substrate near its base. The piezoelectric response of N-CNTs was measured by AFM piezoelectric force microscopy. A commercial NSG10 cantilever with a conductive TiN coating was used as an AFM probe.

Air humidity was changed by creating a confined ambient using a hermetic box. A container with hot water was placed under the hermetic box, as a result of hot water evaporation humidity increased and was controlled by a humidity sensor. The air humidity varied from 25 to 90%.

In the process of air humidity change, the probe was withdrawn from the N-CNT array to prevent sticking in the "N-CNT/probe" system. After reaching a certain humidity level, the container with water was removed.

The crystalline perfection of the grown N-CNTs was assessed by Raman spectroscopy on a Renishaw InVia Reflex (Renishaw plc, UK) with a wavelength of 532 nm. It was found that for the obtained N-CNT samples the positions of D-, G-peaks correspond to frequencies ~1365 and ~1593 cm^{-1}, which is characteristic of multilayer carbon nanotubes (Fig. 1). The ratio of I_D/I_G peaks intensity = 1.06 shows high defectivity of N-CNTs, which is associated with the introduction of nitrogen atoms into the CNT structure and the graphite lattice disordering, as well as with the peculiarity of the spectra acquisition technique, in which the laser beam is incident along the normal to the sample surface (i.e., parallel to the N-CNTs). The formation of bamboo-like bridge in the N-CNT structure causes symmetry violations of the graphite layer with sp2 hybridization of carbon atoms and leads to an increase in the intensity of the D-peak. There is also a 2D band (2550–2700 cm^{-1}) on the spectrum, which is characteristic of multi-wall CNTs and is associated with the occurrence of a second-order double resonance of two iTO phonons [8, 9]. In pure graphene, this band consists of a single narrow peak, while in multi-walled N-CNTs, the shape of the line is deformed due to the presence of defects in the lattice and the influence of many layers in the CNT structure. In this connection, the band broadening is observed in the range of 2250–3500 cm^{-1}. Additionally, the contribution of luminescence is visible, which does not allow us to unambiguously identify the position of the 2D band at the used laser irradiation frequency. Indirectly, for multi-wall CNTs, the displacement of the 2D band can carry information about the change in the value of the Young's modulus of CNTs.

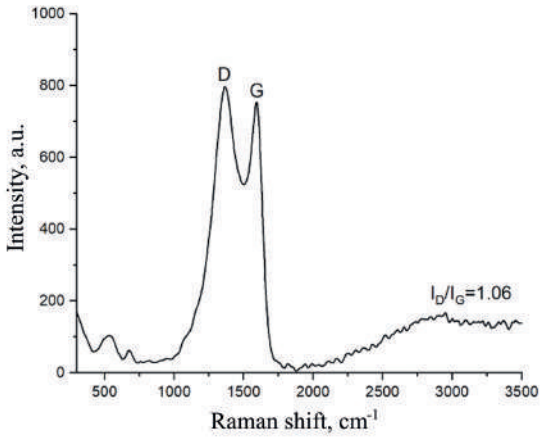

Fig. 1 Raman spectra of a N-CNT sample

Results and Discussion

The results of experimental studies showed that when the humidity increases from 30 to 60%, the value of the generated N-CNT current does not change significantly and is 7 ± 4 nA. With further increase in humidity up to 80%, the magnitude of the generated current increases to 12 ± 4 nA, and at 90% it decreases again to 5 ± 3 nA (Fig. 2, *a* and Fig. 3, *a*). This dependence is probably related to the change in the magnitude of the piezoelectric response of N-CNTs (Fig. 2, *b* and Fig. 3, *b*).

Thus, at a humidity of 30–55 %, the value of the piezoelectric strain coefficient of N-CNTs (Fig. 3, *b*) was 33 ± 14 pm/V, and then, when the humidity increased to 90%, it decreased to 0.5 pm/V. This pattern is probably due to the formation of an adsorption layer of water on the surface of N-CNTs, leading to a decrease in the magnitude of its polarization.

It is worth noting that the piezoelectric effect in N-CNTs differs from the classical volume effect and is surface [10, 11], which significantly affects the dependence of the piezoelectric strain coefficient of an N-CNT on the quality of its surface.

Thus, from Figure 3, it is found that at humidity above 60 %, unstable current generation with high spread of values is observed in the process of deformation of N-CNTs, as well as a significant decrease in the piezoelectric properties of N-CNTs.

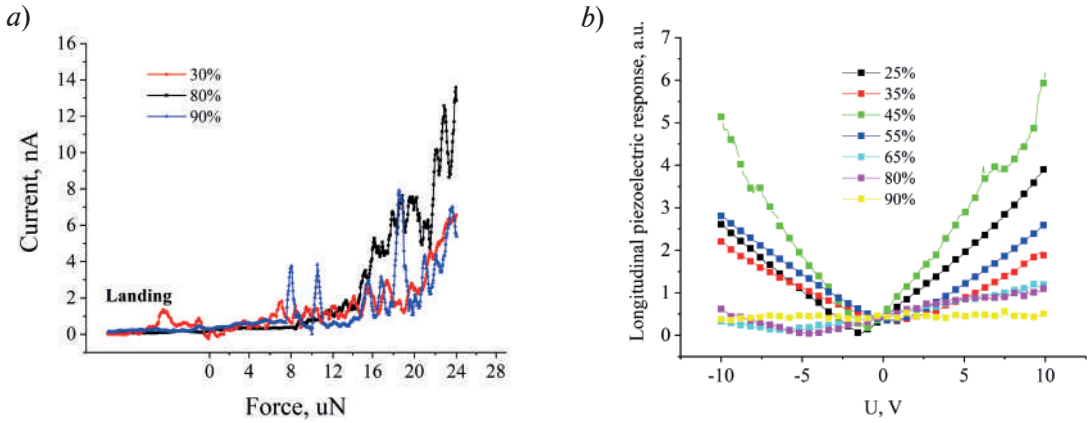

Fig. 2. The results of experimental studies of the influence of ambient humidity on the magnitude of the current generated by the N-CNT from the pressure force of the AFM probe (*a*) and the magnitude of the longitudinal piezoelectric response (*b*)

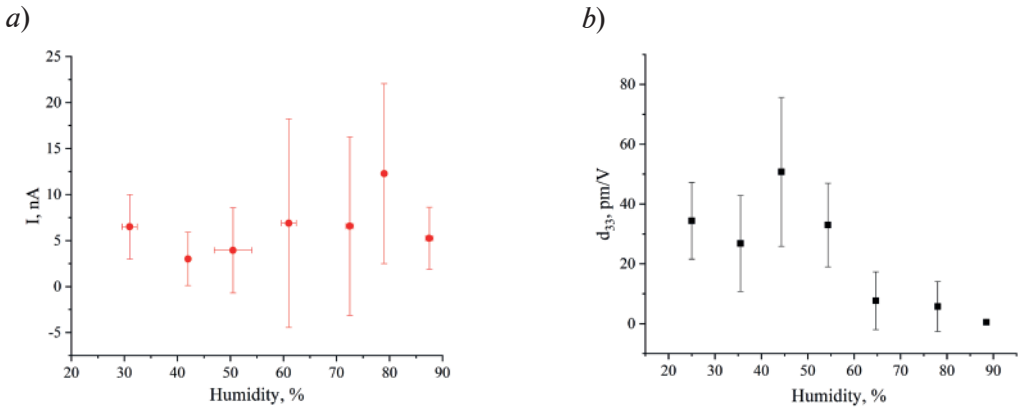

Fig. 3. Patterns of the influence of ambient humidity on the magnitude of the N-CNT-generated current at an AFM probe clamping force of 25 μN (*a*) and the magnitude of the N-CNT piezoelectric strain coefficient (*b*)

Conclusion

The paper establishes patterns of influence of ambient humidity on the piezoelectric strain coefficient and the magnitude of the current generated by N-CNTs during their deformation. It is shown that at humidity up to 60%, stable current generation is observed during the deformation of N-CNTs; at higher humidity, the instability of measurements increases, and the spread of the generated current grows significantly, which is associated with a decrease in the N-CNTs piezoelectric strain coefficient.

The research outcomes can be used in the development of mechanical energy converters: strain sensors or highly sensitive microphones.

REFERENCES

1. **Sawane M., Prasad M.,** MEMS piezoelectric sensor for self-powered devices: A review, Mater. Sci. Semicond. Process. 158 (2023) 107324.

2. **Ju M., Dou Z., Li J.W., Qiu X., Shen B., Zhang D., Yao F.Z., Gong W., Wang K.,** Piezoelectric Materials and Sensors for Structural Health Monitoring: Fundamental Aspects, Current Status, and Future Perspectives, Sensor. 23 (2023).

3. **Kwon S. ryung, Huang W., Zhang S., Yuan F.-G., Jiang X.,** A new type of microphone using flexoelectric barium strontium titnate, in: W. Ecke, K.J. Peters, N.G. Meyendorf, T.E. Matikas Eds. (2014) 90620Y.

4. **Sha F., Xu D., Cheng X., Huang S.,** Mechanical Sensing Properties of Embedded Smart Piezoelectric Sensor for Structural Health Monitoring of Concrete, Res. Nondestruct. Eval. 32 (2021) 88–112.

5. **Il'ina M.V., Il'in O.I., Guryanov A.V., Osotova O.I., Blinov Y.F., Fedotov A.A., Ageev O.A.,** Anomalous piezoelectricity and conductivity in aligned carbon nanotubes, J. Mater. Chem. C. 9 (2021) 6014–6021.

6. **Il'ina M.V., Soboleva O.I., Polyvianova M.R.,. Khubezhov S.A, Il'in O.I.,** Study of the Piezoelectric Properties of Nitrogen-Doped Carbon Nanotubes for the Development of Energy-Efficient Nanogenerators, Nanobiotechnology Reports. 18 (2023) 858–864.

7. **Il`ina M.V., Rudyk N.N., Soboleva O.I., Polyvianova M.R., Khubezhov S.A., Il`in O.I.,** Study of the Effect of Growth Temperature on the Properties of Nitrogen-Doped Carbon Nanotubes for Designing Nanopiezotronic Devices, Tech. Phys. 68 (2023) 871–877.

8. **Ferrari A.C., Robertson J.,** Interpretation of Raman spectra of disordered and amorphous carbon, Phys. Rev. B. 61 (2000) 14095–14107.

9. **Ferrari A.C., Meyer J.C., Scardaci V., Casiraghi C., Lazzeri M., Mauri F., Piscanec S., Jiang D., Novoselov K.S., Roth S., Geim A.K.,** Raman Spectrum of Graphene and Graphene Layers, Phys. Rev. Lett. 97 (2006) 187401.

10. **Kundalwal S.I., Meguid S.A., Weng G.J.,** Strain gradient polarization in graphene, Carbon N. Y. 117 (2017) 462–472.

11. **Il'ina M., Il'in O., Osotova O., Khubezhov S., Rudyk N., Pankov I., Fedotov A., Ageev O.,** Pyrrole-like defects as origin of piezoelectric effect in nitrogen-doped carbon nanotubes, Carbon N. Y. 190 (2022) 348–358.

THE AUTHORS

SOBOLEVA Olga I.
osotova@sfedu.ru
ORCID: 0000-0002-0487-7542

IL'INA Marina V.
mailina@sfedu.ru
ORCID: 0000-0002-8023-8283

POLYVIANOVA Maria R.
polyvianova@sfedu.ru
ORCID: 0009-0005-0152-1486

CHEFRANOV Alexander A.
chefranov@sfedu.ru

IL'IN Oleg I.
oiilin@sfedu.ru
ORCID: 0000-0002-1456-5139

Received 22.07.2024. Approved after reviewing 26.08.2024. Accepted 27.08.2024.

PHYSICAL OPTICS

Conference materials
UDC 535.8
DOI: https://doi.org/10.18721/JPM.173.143

Features of the implementation of optical superchannels in flexible optical networks

N.I. Popovskiy [1] ✉

[1] Bonch-Bruevich St. Petersburg State University of Telecommunications, St. Petersburg, Russia
✉ nikitanikita24@mail.ru

Abstract. This article examines the current problems of using fiber-optic communication systems for efficient long-distance data transmission. Special attention is paid to the concept of optical super channels, which combine several optical channels to increase transmission capacity and range. The article discusses the theoretical and practical aspects of the implementation of optical superchannels, including methods for generating multichannel signals, the use of optical precompensation of nonlinear effects and dispersion, as well as technologies for multiplexing orthogonal subcarrier channels. The prospects for the development of flexible optical networks to increase productivity and optimize the use of resources in modern telecommunications networks are considered.

Keywords: flexible optical networks, fiber-optic transmission system, dense wavelength division multiplexing, orthogonal frequency division multiplexing, transceiver.

Citation: Popovskiy N.I., Features of the implementation of optical superchannels in flexible optical networks, St. Petersburg State Polytechnical University Journal. Physics and Mathematics. 17 (3.1) (2024) 215–219. DOI: https://doi.org/10.18721/JPM.173.143

Материалы конференции
УДК 535.8
DOI: https://doi.org/10.18721/JPM.173.143

Особенности реализации оптических суперканалов в гибких оптических сетях

Н.И. Поповский [1] ✉

[1] Санкт-Петербургский государственный университет телекоммуникаций им. проф. М.А. Бонч-Бруевича, Санкт-Петербург, Россия;
✉ nikitanikita24@mail.ru

Аннотация. В статье рассматриваются проблемы использования волоконно-оптических систем связи для эффективной передачи данных на большие расстояния. Особое внимание уделяется концепции оптических суперканалов, которые объединяют несколько оптических каналов для увеличения пропускной способности и дальности передачи. В статье обсуждаются теоретические и практические аспекты реализации оптических суперканалов, включая методы формирования многоканальных сигналов, использование оптической предкомпенсации нелинейных эффектов и дисперсии, а также технологии мультиплексирования ортогональных поднесущих каналов. Рассматриваются перспективы развития гибких оптических сетей для повышения производительности и оптимизации использования ресурсов в современных телекоммуникационных сетях.

Ключевые слова: гибкие оптические сети, волоконно-оптическая система передачи, плотное мультиплексирование с разделением длин волн, ортогональное мультиплексирование с разделением частот, трансивер

Ссылка при цитировании: Поповский Н.И., Особенности реализации оптических суперканалов в гибких оптических сетях // Научно-технические ведомости СПбГПУ. Физико-математические науки. 2024. Т. 17. № 3.1. С. 215–219. DOI: https://doi.org/10.18721/JPM.173.143

Introduction

Superchannels represent an optimal solution for extending transmission reach and increasing channel speed in optical communication networks [1–3]. A super channel is essentially a composite channel that combines multiple carrier frequencies, often referred to as optical subcarriers. These subcarriers are closely spaced within the optical spectrum. By integrating super channels into optical networks, it becomes feasible to establish flexible and resilient optical infrastructures [4–5]. This capability allows for dynamic allocation and reallocation of bandwidth resources based on traffic demands and network conditions [6].

The method of implementing a superchannel in an optical line

The process of forming optical subcarrier waves within a superchannel typically occurs within a nonlinear or linear optical medium [5, 6]. Once these subcarrier waves are generated, they are separated using a splitter and subsequently modulated with information signals. These modulated subcarrier frequencies are then combined using an optical router based on a arrayed waveguide grating (Fig. 1).

The resulting superchannels are then combined by an optical multiplexer to form a coherent optical signal group with a protective band separating individual superchannels. For the subcarriers to maintain complete orthogonality, it's essential that the bandwidth of the data modulators matches the total bandwidth encompassing all subcarriers.

An important condition for minimizing crosstalk between subcarriers is the precise time alignment of signals entering each modulator. This alignment ensures that the frequency range of the subcarriers corresponds correctly to the symbol rate within each data channel, effectively reducing interference and optimizing signal integrity across the superchannel.

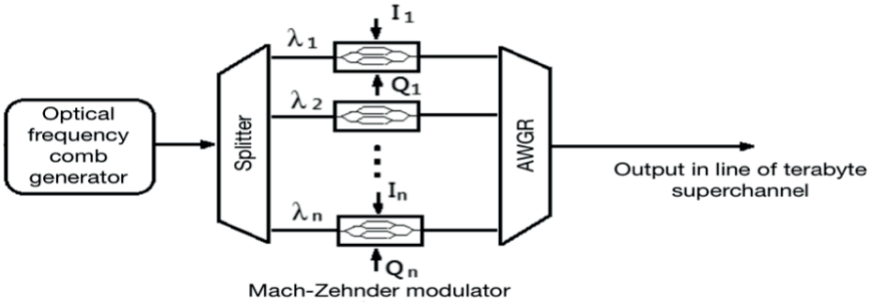

Fig. 1. Block diagram of an optical OFDM transmitter with four subcarriers

The transmitter design consists of three layers of plates. In the first layer, the function of a basic optical pulse divider is performed. The second layer functions as an inverse Fourier transform, introducing a series of phase shifts where each shift depends on a specific input waveguide and its corresponding output waveguide. Consequently, each waveguide receives a phase-weighted combination of signals from the four modulators' outputs. The third layer combines the signals from the second layer with different time delays. This process results in each input pulse being transformed into a sequence of eight output pulses. Each of these output pulses represents a phase-weighted combination of the outputs from all the modulators.

The signal entering the receiver input is partitioned into multiple equal segments, each segment experiencing a specific time delay. The difference in length ΔL between two waveguides

roughly corresponds to the time interval ΔT between successive counts, as described by formula 1. Furthermore, the divider matrix and the waveguide array function together to convert the serial signal into a parallel one (Fig. 2).

$$\Delta L \approx \Delta T \cdot \frac{c}{n_g}, \tag{1}$$

where c is the speed of light, n_g is the lattice index of the waveguide.

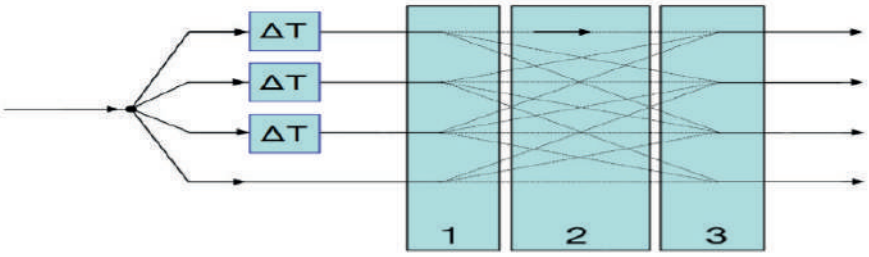

Fig. 2. Block diagram of an AWGR receiver with four subcarriers
(1. Matrix of splitters, 2. Matrix of phase delays, 3. Matrix of splitters)

The second layer, represented by a matrix of phase delays, is defined by equation 3, which expresses transmission coefficients between the outputs of waveguides with time delay m and the lattice outputs labeled n (carrying the subcarrier signal k). In equation 2, the phase shift matrix incorporates exponential terms, while the divider matrix executes summation operations for each subcarrier frequency. Together, these components facilitate the implementation of parallelization and phase adjustments crucial for signal processing within the transmitter system.

$$V_{sc,k} = \sum_{m=0}^{N-1} V_{in}(m) \cdot \exp\left(\frac{-2\pi jkm}{N}\right), \tag{2}$$

where $V_{in}(m)$ is the value of the input signal at the sample points m, N is the number of subcarriers.

$$\theta_{m,n} = 2\pi m \cdot \frac{n_s d}{\lambda R} n d_0, \tag{3}$$

where n_s is the lattice index, d is the distance between the waveguides, λ is the central wavelength, R is the focal length of the lattice, d_0 is the distance between the waveguides at the output.

Each output signal from the Arrayed Waveguide Grating Router (AWGR) is formed as a weighted sum of four consecutive samples of the input data. This operation effectively implements a discrete Fourier transform that operates on discrete samples over time. However, it's important to note that the inputs and outputs of the AWGR are continuous signals.

Therefore, the AWGR performs a sliding discrete Fourier transform, where the time intervals between successive transformations are infinitesimally small. To ensure valid output data, all input samples must belong to the same OFDM symbol. This necessitates that the AWGR output signal be sampled either in the optical domain or after conversion to the electrical domain. The assumption is that sampling is instantaneous, although any bandwidth limitations of the baseband will affect this process.

Experimental

To maintain orthogonality in an AWGR, it is crucial that the power transfer from the input to the output through any of the waveguides remains uniform. In a 4-waveguide device, achieving this uniformity is primarily dependent on balancing the power distribution between the external waveguides relative to the central waveguides, assuming some form of symmetry.

Figure 3 presents simulation results illustrating the Q factor values for four channels, which vary based on the unevenness of power distribution across the AWGR's waveguides. This unevenness can stem from various factors, including differences in bandwidth or inherent characteristics of the AWGR.

Typically, internal channels are more susceptible to crosstalk, regardless of whether this crosstalk arises due to bandwidth limitations or uneven power distribution within the AWGR structure. Maintaining uniform power transfer helps mitigate these issues and ensures the integrity of signal orthogonality and quality in optical communication systems utilizing AWGR technology.

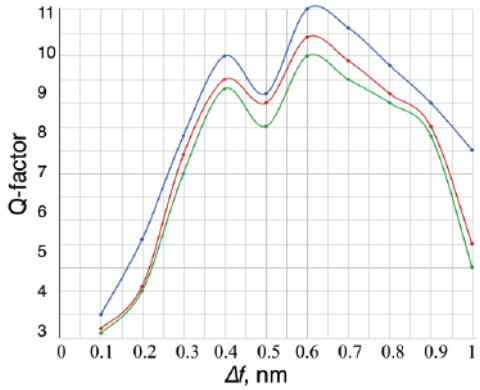

Fig. 3. The effect of AWGR bandwidth on Q. The electrical bandwidth of the signal is 25 GHz (blue), 50 HZ (red), 75 Hz (green)

Conclusion

The analysis has demonstrated that even with fewer waveguides and a narrower free spectral range, a standard AWGR can effectively multiplex and demultiplex subcarriers in an OFDM optical system. This capability hinges on ensuring that the electrical bandwidth in both the transmitter and receiver matches the total bandwidth of the combined subcarriers.

The AWGR functions as a serial-to-parallel converter, followed by a phase shift matrix, mirroring the digital implementation of Fourier transformation. To enhance transmitter bandwidth, modulators can be overloaded to achieve signal alignment, while receiver bandwidth can be reduced through optical sampling techniques.

Moreover, it is crucial for the AWGR design to guarantee uniform transmission regardless of the light path, ensuring consistent performance across all channels. This uniformity is essential for maintaining signal integrity and orthogonality, critical in optical communication systems employing AWGRs for efficient multiplexing and demultiplexing of subcarriers.

REFERENCES

1. **Konyshev V.A., Leonov A.V., Nanii O.E., Treshchikov V.N., Ubaidullaev R.R.,** Trends of and Prospects for the Development of Fiber-Optic Communication Systems, Bulletin of the Lebedev Physics Institute. 50 (2023) 435–450.

2. **Bourdine A.V., Demidov V.V., Dukelskii K.V., Tiwari M., Yin J.,** Six-Core GeO_2-Doped Silica Microstructured Optical Fiber with Induced Chirality Fibers. 11 (3) (2023) 28.

3. **Starykh D.D., Samodelkin L.A., Nanii O.E., Treshchikov V.N.,** Influence of Amplitude-Modulated Channels on Amplitude Phase Channels with Coherent Detection in Distributed Gain Fiber-Optic Communication Lines, Bulletin of the Lebedev Physics Institute. 50 (2023) 220–S226.

4. **Reznikov B.K., Stepanenkov G.V., Isaenko D.I., Vakorina D.V., Rodin S.A.,** Narrowband Lengthy Analogue Fiber Optic Communication Line for Telemetry Data Transmission. Proceedings of the 2023 Seminar on Networks, Circuits and Systems. (2023) 134–138.

5. **Popovskiy N.I.,** Development of OFDM Optical Signal Transceiver Based on AWGR, 2024 Conference of Young Researchers in Electrical and Electronic Engineering (ElCon) (2024), Saint-Petersburg. (2024) 741–744.

6. **Popovskiy N.I., Davydov V.V., Rud V.Y.,** Features of construction of fiber-optic communication lines with orthogonal frequency-division multiplexing, St. Petersburg Polytechnic University Journal. Physics and Mathematics. 15 (3.2) (2022) 178–183.

THE AUTHORS

POPOVSKIY Nikita I.
nikitanikita24@mail.ru
ORCID: 0000-0003-3457-0370

Received 07.07.2024. Approved after reviewing 12.08.2024. Accepted 12.08.2024.

Conference materials
UDC 621.383.526
DOI: https://doi.org/10.18721/JPM173.144

GaN based ultraviolet narrowband photodetectors

O.A. Sinitskaya [1] ✉, K.Yu. Shubina [1], D.V. Mokhov [1],
A.I. Baranov [1], A.M. Mizerov [1], E.V. Nikitina [1, 2]

[1] Alferov University, St. Petersburg, Russia;
[2] Ioffe Institute, St. Petersburg, Russia
✉ olesia-sova@mail.com

Abstract. In this work ultraviolet metal-semiconductor-metal photodetectors with semi-transparent Ni/Au interdigitated electrodes based on GaN/*i*-GaN/c-Al_2O_3 heterostructure were fabricated. The current-voltage, transient photoresponse on-off and spectral characteristics of the formed photodetectors were studied. It was found that the devices have a maximum responsivity at a wavelength of 364 nm with full width at half maximum of 11 nm, thus the presented PDs are narrowband.

Keywords: GaN, ultraviolet photodetector, narrowband photodetector, metal-semiconductor-metal

Funding: The work was supported by the Ministry of Education and Science (grant No. FSRM-2023-0006).

Citation: Sinitskaya O.A., Shubina K.Yu., Mokhov D.V., Baranov A.I., Mizerov A.M., Nikitina E.V., GaN based ultraviolet narrowband photodetectors, St. Petersburg State Polytechnical University Journal. Physics and Mathematics. 17 (3.1) (2024) 220–223. DOI: https://doi.org/10.18721/JPM.173.144

Материалы конференции
УДК 621.383.526
DOI: https://doi.org/10.18721/JPM.173.144

Узкополосные ультрафиолетовые фотодетекторы на основе GaN

О.А. Синицкая [1] ✉, К.Ю. Шубина [1], Д.В. Мохов [1],
А.И. Баранов [1], А.М. Мизеров [1], Е.В. Никитина [1, 2]

[1] Академический университет им. Ж.И. Алфёрова РАН, Санкт-Петербург, Россия;
[2] Физико-технический институт им. А.Ф. Иоффе РАН, Санкт-Петербург, Россия
✉ olesia-sova@mail.ru

Аннотация. В данной работе были изготовлены ультрафиолетовые фотодетекторы типа металл-полупроводник-металл с полупрозрачными Ni/Au встречно-штыревыми электродами на основе гетероструктуры GaN/*i*-GaN/c-Al_2O_3. Исследованы их вольтамперные характеристики, быстродействие и спектральные характеристики. Было обнаружено, что устройства имеют максимальную чувствительность на длине волны 364 нм с полной шириной на уровне половины высоты 11 нм, таким образом, представленные ФД являются узкополосными.

Ключевые слова: GaN, ультрафиолетовый фотодетектор, узкополосный фотодетектор, металл-полупроводник-металл

Финансирование: Работа выполнена при поддержке Министерства образования и науки (Государственное задание № FSRM-2023-0006).

Ссылка при цитировании: Синицкая О.А., Шубина К.Ю., Мохов Д.В., Баранов А.И., Мизеров А.М., Никитина Е.В. Узкополосные ультрафиолетовые фотодетекторы на основе GaN // Научно-технические ведомости СПбГПУ. Физико-математические науки. 2024. Т. 17. № 3.1. С. 220–223. DOI: https://doi.org/10.18721/JPM.173.144

Introduction

At present, ultraviolet (UV) photodetectors (PD) play a critical role in numerous technological applications, ranging from environmental monitoring and control of ultraviolet emitters to various alarm systems [1]. In recent years, there has been a growing demand for high-performance UV PDs with enhanced sensitivity, speed, reliability and high selective spectral responsivity. The latter characteristic is especially important for PDs used in optical communication and biophotonics applications [2].

The quest for efficient and reliable narrowband PDs has prompted significant research efforts aimed at exploring new materials and device architectures. In this context, GaN epitaxial layers have emerged as promising candidates owing to their unique properties, including a wide bandgap (3.4 eV), high electron mobility and excellent thermal and chemical stability [3].

Currently, there are various types of PDs designs. However, among them, the most attractive are the metal-semiconductor-metal (MSM) PDs, the advantages of which are fast operating speed, high sensitivity and simplicity of fabrication [1]. In this article narrowband UV MSM PDs fabricated on the GaN epitaxial layers are presented.

Materials and Methods

The 210 nm thick GaN epitaxial layers were grown by plasma-assisted molecular beam epitaxy (PA MBE) using Veeco GEN 200 industrial type MBE setup on *i*-GaN/c-Al_2O_3 templates pre-grown by metalorganic chemical vapour deposition. The synthesis occurred under conditions near unity ratio of gallium to nitrogen fluxes (slightly nitrogen-rich growth conditions). The surface morphology of the grown samples was examined using a scanning electron microscope (SEM). The conductivity type, concentration and mobility of charge carriers in the GaN epitaxial layers were assessed using Hall effect measurements based on the Van der Pauw four-point probe method.

Subsequently, MSM PDs with semitransparent Ni/Au (15 nm) interdigitated electrodes were fabricated using standard laser lithography technique, e-beam and thermal vacuum evaporation. Current-voltage (*I-V*), transient photoresponse on-off and spectral characteristics of the formed PDs were obtained.

Results and Discussion

SEM images (see Fig. 1, *a*, *b*) show that the obtained layers have a rough surface morphology, which may be due to slightly nitrogen-rich growth conditions. The rough surface morphology of epitaxial layers provides a large area of interaction between the active material and radiation, which can help increase the sensitivity of photodetectors based on them compared to detectors based on smooth epitaxial layers. As a result of Hall measurements, it was discovered that undoped synthesized layers have *n*-type conductivity, which is typical for III-N materials [4], with a carrier concentration of $n \sim 1.1\times10^{18}$ cm^{-3} and mobility of $\mu \sim 95$ cm^2/(V×s). This value of the charge carrier concentration can be associated with the 3-dimensional MBE growth of GaN layers (as can be seen from the surface morphology) and with a large number of defects in them. A photomicrograph of the formed PDs with semitransparent Ni/Au interdigitated electrodes is presented in Fig. 1, *c*.

The *I-V* characteristics of the UV PDs were measured both in the dark and under UV LED illumination (with a wavelength and power density of 365 nm and 12 mW/cm^2, respectively). It was noted that exposure to UV radiation resulted in an increase in current. However, it is evident from Fig. 2, *a*, that the PDs exhibit a very high dark current (6 mA at a bias of 1 V),

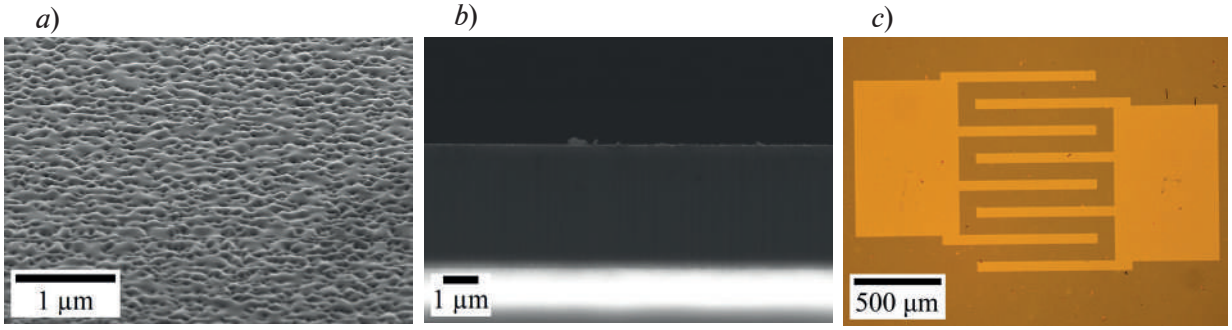

Fig. 1. SEM images of the GaN/*i*-GaN/c-Al_2O_3 epitaxial structure: isometry (*a*) and cross-section (*b*), photomicrograph of metal electrodes (*c*)

which may be attributed to the elevated defect density in the epitaxial GaN layers causing leakage channels [5]. The sensitivity of these photodetectors at a wavelength of 365 nm at a bias voltage of 1 V was 13.5 A/W.

The transient photoresponse on-off characteristics of the PDs were investigated at bias voltage of 1 V, under 365 nm rectangular light pulses with frequency 3 Hz and duty cycle 20% (see Fig. 2, *b*). The 10%–90% rise and fall times of the PDs were 1.4 and 84 ms, respectively. The PDs presented in this work demonstrate a faster response than the GaN-based PDs reviewed in other works [6]. The extended fall time primarily arises from the persistent photocurrent, where electrons have to pass through various trap states existing due to dislocations in order to recombine [7].

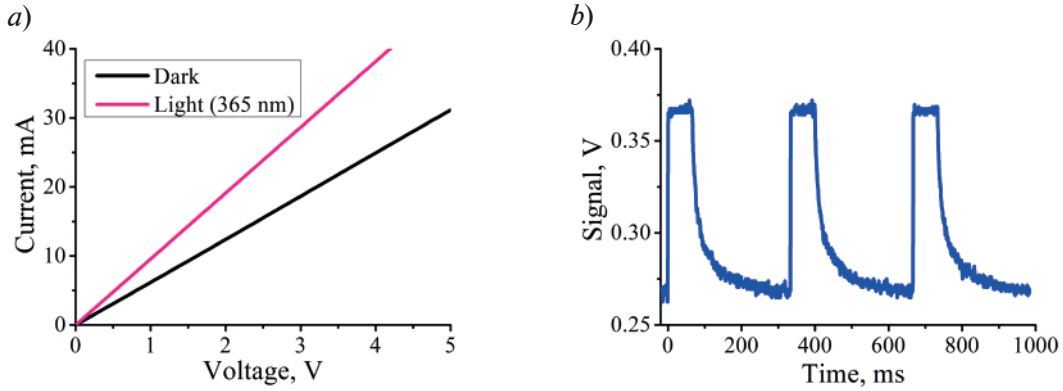

Fig. 2. *I-V* (*a*) and transient photoresponse on-off (*b*) characteristics of the formed PDs

The spectral response of the device over the wavelength range of 300–450 nm at 0.025 V bias is presented in Fig. 3. It can also be seen that the presented PDs have a narrowband detection configuration with a maximum at 364 nm and full width at half maximum (FWHM) of 11 nm. The observed characteristic could be linked to surface charges trapped at surface states or transitions associated with defect levels in GaN [8], but this requires further study.

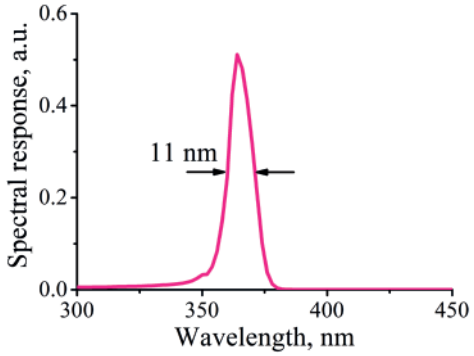

Fig. 3. Spectral response of the formed PDs

Conclusion

This report presents UV narrowband photodetectors based on GaN/*i*-GaN/c-Al_2O_3 heterostructures. These devices exhibit rapid response times of 1.4 ms. Furthermore, the fabricated devices achieve peak responsivity at a wavelength of 364 nm with a FWHM of 11 nm. Thus, PDs based on such GaN heterostructures, due to their high spectral selectivity, can be promising for use in communication systems and biophotonics.

REFERENCES

1 **Munoz E., Monroy E., Pau J.L., Calle F., Omnes F., Gibart P.,** III nitrides and UV detection, Journal of Physics: Condensed Matter. 13 (32) (2001) 7115.

2. **Wilson G.A., DeFreez R.K.,** Improving diode-laser-induced fluorescence detection of airborne biological particles by exciting multiple biofluorophores, Chemical and Biological Sensing V. – SPIE. 5416 (2004) 157–167.

3. **Bi W., Kuo H.-C., Ku P.-C., Shen B.,** Handbook of GaN semiconductor materials and devices, Boca Raton: Taylor & Francis, CRC Press, Abingdon, 2017.

4. **Monish M., Mohan S., Sutar D.S., Major S.S.,** Gallium nitride films of high n-type conductivity grown by reactive sputtering, Semiconductor Science and Technology. 35 (4) (2020) 045011.

5. **Chatterjee A., Khamari Sh. K., Kumar R., Dixit V.K., Oak S.M., Sharma T.K.,** Dislocations limited electronic transport in hydride vapour phase epitaxy grown GaN templates: A word of caution for the epitaxial growers, Applied Physics Letters. 106 (2) (2015).

6. **Wang T., Cao F., Ji X., Zhang Q.,** Study on tower-like GaN nanostructure: Growth, optical and fast UV sensing properties, Superlattices and Microstructures. 134 (2019) 106233.

7. **Calarco R., Marso M., Richter T., Aykanat A.I., Meijers R., Hart A.V.D., Stoica T., Luth H.,** Size-dependent photoconductivity in MBE-Grown GaN - nanowires, Nano Lett. 5 (2005) 981–984.

8. **Chatterjee A., Khamari S.K., Kumar R., Porwal S., Bose A., Raghavendra S., Dixit V.K., Sharma T.K.,** Ultranarrow Band UV Detection in GaN with Simple Device Architecture, physica status solidi (RRL)–Rapid Research Letters. (2022) 2200322.

THE AUTHORS

SINITSKAYA Olesya A.
olesia-sova@mail.ru
ORCID: 0000-0001-6561-0334

BARANOV Artem I.
itiomchik@yandex.ru
ORCID: 0000-0002-4894-6503

SHUBINA Kseniia Yu.
rein.raus.2010@gmail.com
ORCID: 0000-0003-1835-1629

MIZEROV Andrey M.
andreymizerov@rambler.ru
ORCID: 0000-0002-9125-6452

MOKHOV Dmitry V.
mokhov@spbau.ru
ORCID: 0000-0002-7201-0713

NIKITINA Ekaterina V.
mail.nikitina@mail.ru
ORCID: 0000-0002-6800-9218

Received 30.07.2024. Approved after reviewing 23.08.2024. Accepted 23.08.2024.

Conference materials
UDC 535.14
DOI: https://doi.org/10.18721/JPM.173.145

Influence of optical feedback on an optical pulse shape of a semiconductor laser

M.V. Boltanskii [1, 3], E.I. Maksimova [1], M.A. Fadeev [4, 5], R.A. Shakhovoy [1, 2, 6] ✉

[1] Limited Liability Company "QRate", Moscow, Russia;
[2] Moscow Technical University of Communications and Informatics, Moscow, Russia;
[3] Peoples' Friendship University of Russia, Moscow, Russia;
[4] Russian Quantum Center, Skolkovo, Moscow, Russia;
[5] ITMO University, St. Petersburg, Russia;
[6] NTI Center for Quantum Communications, National University of Science and Technology MISIS, Moscow, Russia
✉ m.boltanskiy@goqrate.com

Abstract. Gain-switched semiconductor lasers can produce pulses with naturally randomized phase, which makes them a convenient light source for quantum key distribution and random number generation. Nevertheless, semiconductor lasers are vulnerable to external optical feedback, a phenomenon, characterized by injection of a certain part of laser radiation into the laser's diode cavity. Although optical feedback may be used to decrease relaxation oscillations and chirp, it may have negative effect on laser pulses. Here, we study the influence of optical feedback on the pulse shape of a gain-switched laser.

Keywords: gain-switched laser, optical feedback, laser pulse interference

Citation: Boltanskii M.V., Maximova E.I., Fadeev M.A., Shakhovoy R.A., Influence of optical feedback on an optical pulse shape of a semiconductor laser, St. Petersburg State Polytechnical University Journal. Physics and Mathematics. 17 (3.1) (2024) 224–228. DOI: https://doi.org/10.18721/JPM.173.145

Материалы конференции
УДК 535.14
DOI: https://doi.org/10.18721/JPM.173.145

Влияние оптической обратной связи на форму оптических импульсов полупроводникового лазера

М.В. Болтанский [1, 3], Е.И. Максимова [1], М.А. Фадеев [4, 5], Р.А. Шаховой [1, 2, 6] ✉

[1] ООО «КуРэйт», Москва, Россия;
[2] Московский технический университет связи и информатики, Москва, Россия;
[3] Российский университет дружбы народов, Москва, Россия;
[4] Российский квантовый центр, Сколково, Москва, Россия;
[5] Университет ИТМО, Санкт-Петербург, Россия;
[6] Центр компетенций НТИ «Квантовые коммуникации» НИТУ МИСИС, Москва, Россия;
✉ m.boltanskiy@goqrate.com

Аннотация. Полупроводниковые лазеры в режиме усиления способны излучать импульсы со случайной относительной фазой, что делает их надежным источником энтропии для квантового распределения ключа и генерации случайности. Тем не менее, полупроводниковые лазеры уязвимы перед влиянием оптической обратной связи – явления, характеризуемого инжекции определенной доли лазерного излучения обратно в

полость лазерного диода. Хотя оптическая обратная связь может быть использована для подавления релаксационных колебаний и чирпа, она может иметь серьезный негативный эффект на лазерные импульсы. В этой работе мы изучаем влияние оптической обратной связи на форму импульса лазера в режиме переключения усиления.

Ключевые слова: лазер в режиме переключения усиления, оптическая обратная связь, интерференция лазерных импульсов

Ссылка при цитировании: Болтанский М.В., Максимова Е.И., Фадеев М.А., Шаховой Р.А., Влияние оптической обратной связи на форму оптических импульсов полупроводникового лазера // Научно-технические ведомости СПбГПУ. Физико-математические науки. 2024. Т. 17. № 3.1. С. 224–228. DOI: https://doi.org/10.18721/JPM.173.145

Introduction

External optical feedback (EOF) is known to have positive effect on a pulsed laser, e.g., it can reduce frequency chirp [1] and suppress relaxation oscillations [2], which can be useful in telecommunications. It also finds applications in range and velocity measurements [3]. However, optical feedback often causes certain unwanted effects, e.g. chaos dynamics [4] or increase of turn-on delay jitter [5]. In general, influence of EOF is stronger on lasers operating in continuous mode, meanwhile modulated lasers might avoid being impacted by EOF in case feedback radiation comes into a laser's cavity between modulation pulses [6]. Nevertheless, under certain circumstances, modulated laser pulses can be significantly affected by EOF as well [7]. Thereby, laser modules are often equipped with an optical isolator to prevent unwanted feedback. In this work, we studied the influence of optical feedback on a shape of optical pulses in a gain-switched distributed feedback (DFB) semiconductor laser.

Materials and Methods

The fiber-optic experimental scheme used to demonstrate the effect of optical feedback on a laser signal is shown in Fig. 1. It consisted of a semiconductor 1550 nm DFB laser diode (model SWLD-1554.94-FC/PC-05-PM) controlled by a laser driver based on a Texas Instruments ONET1151L chip, and a ring mirror (a looped beam splitter). The optical variable delay line (VDL) was installed in front of the mirror to control the length of the external cavity.

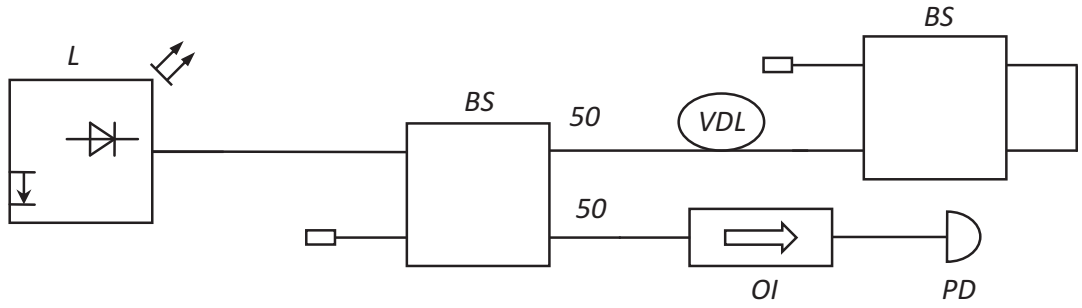

Fig. 1. The experimental scheme. *L* – laser module, *BS* – beam splitter, *OI* – optical isolator, *VDL* variable optical delay line, *PD* – photodetector

The experiment was conducted using a pulse train with pulses of duration 400 ps, pulse repetition rate of 1.25 GHz and average laser output power of 2.7 mW. During the experiment, we varied the delay line to change the length of the external resonator.

Results and Discussion

Figure 2 shows the waveforms of laser pulses at different VDL values. Each waveform in the figure is accompanied by a value of the delay introduced by the VDL in picoseconds modulo the pulse repetition period, where a 0 ps delay would mean that a reflected pulse completely overlaps a generated one. Hence, delay values describe a measure of time shifts of reflected pulses relative to generated ones. One can see that at positive delay values right parts of laser pulses are barely distorted, meanwhile first relaxation peaks are not changed at all. As we move on to the negative values, we can observe well-pronounced suppression of relaxation oscillations.

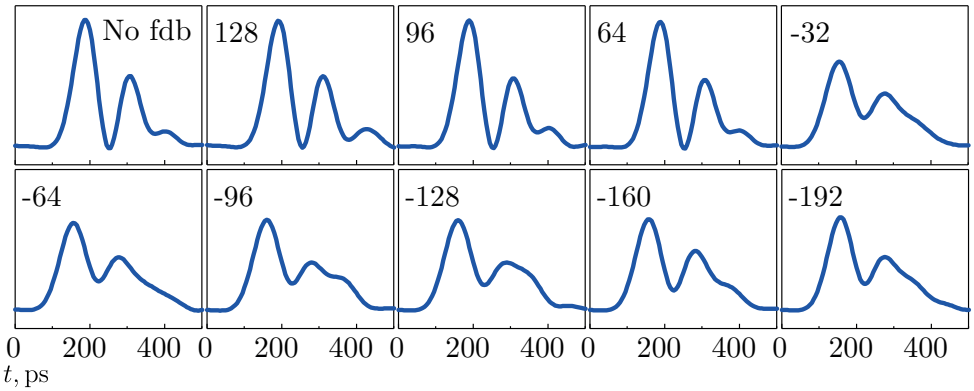

Fig. 2. Experimental laser pulse shapes at various optical feedback delay

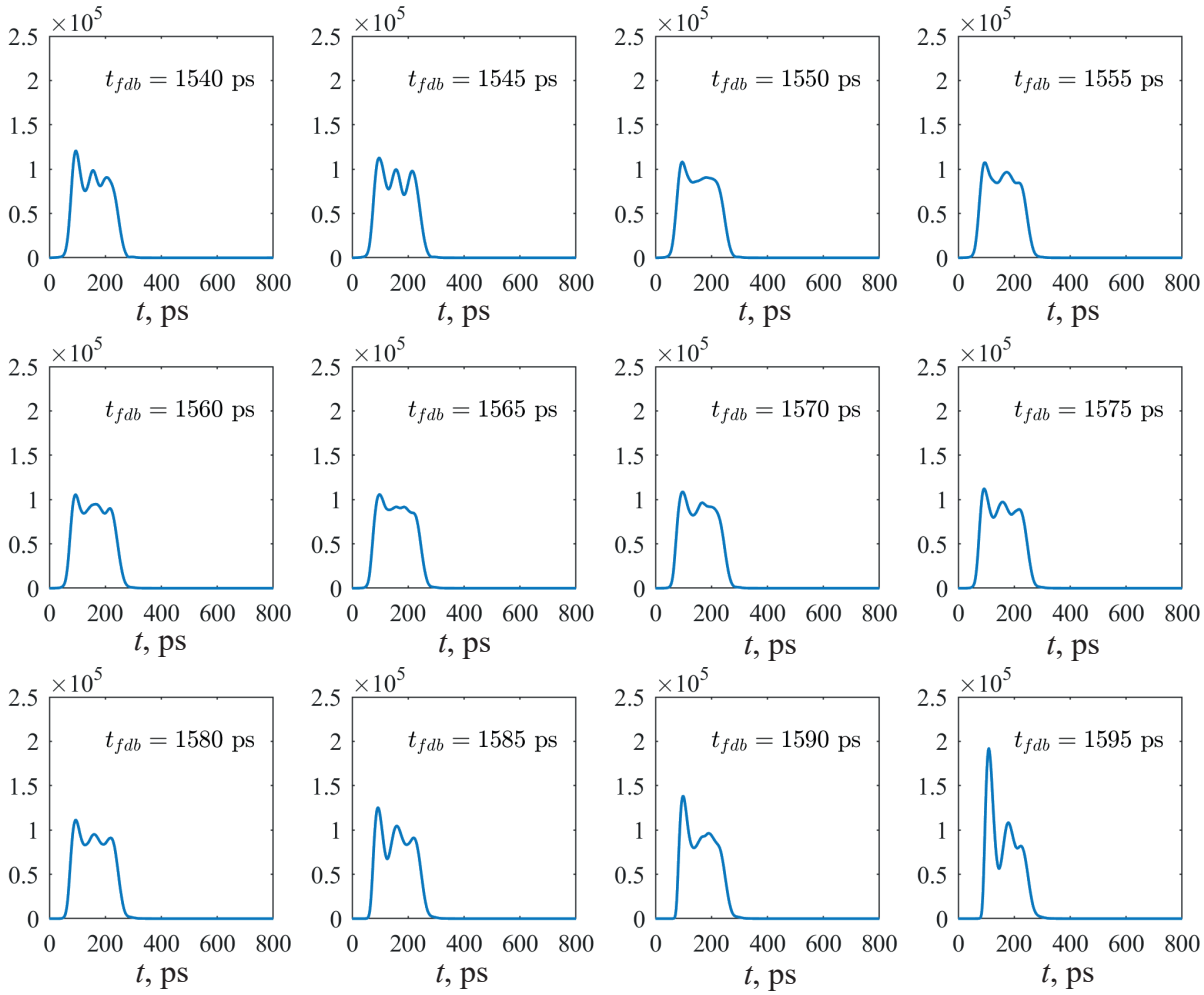

Fig. 3. Simulations of laser pulse shapes at various optical feedback delay

Figure 3 represents the results of computer simulations of a semiconductor laser diode with optical feedback, conducted with the commonly used rate equation model [8]. Simulation parameters are presented in Table. Simulations show that the influence of optical feedback on the waveform of laser pulses strongly depends on the arrival time of the reflected pulse. In particular, suppression of relaxation oscillations is more pronounced when the onset of lasing occurs under the quasi-stationary part of the reflected pulse, i.e. when the reflected pulse returns into the resonator earlier that the new pulse appears.

Table

Simulation parameters

Parameters	Values
Bias current $I_{b,}$ mA	6.0
Carrier lifetime τ_e, ns	1.0
Pulse width ω, ns	0.4
Central optical frequency ω_0, THz	193.548
Pulse repetition rate f_p, GHz	1.25
Confinement factor Γ	0.12
Threshold carrier number N_{th}	5.5·10e7
Transparency carrier number N_{tr}	4·10e7
Spontaneous emission factor C_{sp}	10e-5
Quantum differential output ϵ	0.3
Henry factor α	5
Feedback coupling factor κ_{fdb}, GHz	5

Conclusion

We performed an experimental and theoretical analysis to study the influence of optical feedback on an optical pulse shape of a gain-switched laser. It was shown that laser radiation reflected into the semiconductor laser diode's cavity may significantly change the pulse waveform at certain delay values, which is presented by our simulations, which are in a good agreement with the experimental results.

REFERENCES

1. **Lang R., Kobayashi K.,** Suppression of the Relaxation Oscillation in the Modulated Output of Semiconductor Lasers, IEEE Journal of quantum electronics. (12) (1976) 194–199.

2. **Grillot F., Provost J., Kechaou K., Thedrez B., Erasme D.,** Frequency Chirp Stabilization in Semiconductor Distributed Feedback Lasers with External Control, Optics Express. (20) (2012) 26062–26074.

3. **De Groot J.P.,** Applications of optical feedback in laser diodes, Laser-Diode Technology and Applications. (1219) (1990) 457–467.

4. **Al Bayati B., Ahmad A., Al Naimee K.,** Influence of optical feedback strength and semiconductor laser coherence on chaos communications, Journal of the Optical Society of America B. (35) (2018) 918–925.

5. **Langley L.N., Shore K.A.,** The effect of external optical feedback on timing jitter in modulated laser diodes, Journal of Lightwave Technology. (11) (1993) 434–441.

6. **Ryan A., Agrawal G., Gray G., Gage E.,** Optical-feedback-induced chaos and its control in multimode semiconductor lasers, IEEE Journal of Quantum Electronics. (30) (1994) 668–679.

7. **Clarke B.,** The effect of reflections on the system performance of intensity modulated laser diodes, Journal of Lightwave Technology. (9) (1991) 741–749.

8. **Shakhovoy R.A.,** Semiconductor laser dynamics, ELS «Лань», Saint-Petersburg. (404) (2024).

THE AUTHORS

BOLTANSKII Matvei V.
m.boltanskiy@goqrate.com

MAXIMOVA Elizaveta I.
e.maksimova@goqrate.com

SHAKHOVOY Roman A.
r.shakhovoy@goqrate.com

FADEEV Maxim A.
mfadeev2022@gmail.com

Received 04.07.2024. Approved after reviewing 31.07.2024. Accepted 31.07.2024.

Conference materials
UDC 535.42
DOI: https://doi.org/10.18721/JPM.173.146

Optical needle formation by subwavelength optical elements using high-performance computer systems

D.A. Savelyev [1] ✉

[1] Samara National Research University, Samara, Russia
✉ dmitrey.savelyev@yandex.ru

Abstract. The optical vortex diffraction on subwavelength optical elements with a standard and GRIN substrate using the finite difference time domain method was simulated in this paper. The possibility of increasing the light needle (up to 7.86λ) for input radiation with azimuthal and radial polarization was shown using a GRIN substrate and a subwavelength element with zones alternating in height.

Keywords: optical vortices, GRIN, subwavelength ring gratings, FDTD

Funding: This research was funded by the Russian Science Foundation (project No. 24-22-00044), https://rscf.ru/en/project/24-22-00044/.

Citation: Savelyev D.A., Optical needle formation by subwavelength optical elements using high-performance computer systems, St. Petersburg State Polytechnical University Journal. Physics and Mathematics. 17 (3.1) (2024) 229–232. DOI: https://doi.org/10.18721/JPM.173.146

Материалы конференции
УДК 535.42
DOI: https://doi.org/10.18721/JPM.173.146

Формирование оптических игл субволновыми оптическими элементами с использованием высокопроизводительных компьютерных систем

Д.А. Савельев 1✉

[1] Самарский национальный исследовательский университет им. академика С.П. Королева, г. Самара, Россия
✉ dmitrey.savelyev@yandex.ru

Аннотация. В работе методом конечных разностей во временной области проведено моделирование дифракции оптических вихрей на субволновых оптических элементах со стандартной и GRIN-подложкой. Показана возможность увеличения фокального светового отрезка для азимутальной и радиальной поляризации входного излучения при использовании GRIN-подложки и субволнового элемента с чередующимися по высоте зонами.

Ключевые слова: оптические вихри, GRIN, субволновые кольцевые решетки, FDTD

Финансирование: Работа выполнена при финансовой поддержке Российского научного фонда (проект № 24-22-00044, https://rscf.ru/project/24-22-00044/).

Ссылка при цитировании: Савельев Д.А. Формирование оптических игл субволновыми оптическими элементами с использованием высокопроизводительных компьютерных систем // Научно-технические ведомости СПбГПУ.

Физико-математические науки. 2024. Т. 17. № 3.1. С. 229–232. DOI: https://doi.org/10.18721/JPM.173.146

Introduction

Optical vortices are known for their use in various applications [1–5], among which are optical manipulation [2], sensing, optical information transmission, and sharp focusing [3, 5, 6]. Some optical structures can be used to generate optical vortices such as spiral phase plates [7], metasurfaces, and ring gratings [1, 6]. The ring gratings and diffraction axicons in various combinations are also used to obtain optical needles with a large depth of focus [6, 8].

Also currently well known is the use of materials with a gradient refractive index (GRadient Index, GRIN) to control the propagation of light, solve problems of optical communication, and light collimation [6, 9], in biology [10].

Thus, the study of the diffraction of Laguerre-Gaussian modes (optical vortices) on subwavelength ring gratings with a GRIN substrate was carried out in this paper to form an elongated focal segment (light needle).

Materials and Methods

The numerical simulations (3D) were carried out using the finite difference time domain (FDTD) method on an 900 Gflop computing cluster with using Meep software package [11]. This modeling parameters were considered: the wavelength λ of the input radiation was equal to 0.532 μm, space step – λ/35, time step – λ/(70c), where c is the speed of light. The size of the three-dimensional computational domain is 15.8 λ. The computational region was surrounded on all sides by an absorbing layer PML (with size 1.12 λ). The Laguerre-Gauss mode (1,0) (optical vortices of the first order, σ = 1.5 μm) with radial and azimuthal polarization were considered as input radiation.

The variable-height ring gratings with a standard substrate (refractive index $n = 1.47$) and a GRIN substrate were considered. The refractive index of GRIN substrate was varied uniformly from the maximum refractive index in the center ($n = 2.7$) to the minimum refractive index at the edges ($n = 1.47$). The GRIN substrate consisted of rings of the same width.

The refractive index of the relief was $n = 1.47$. The relief height of the elements h was chosen based on the phase jump π radians, respectively, for $n = 1.47$ the base height h was 1.06 λ (π). Next, the height of the odd (h_1) and even (h_2) relief zones of the elements was varied, also based on the phase jump π radians.

The production of such elements seems possible, since the possibility of producing a relief of optical elements with an aspect ratio of more than 1000 was previously shown [12].

Results and Discussion

The length of the light segment was estimated by the full length by the half maximum of the radiation intensity (DOF), similarly to the assessment of the focal spot on the optical axis – by the full width at half maximum (FWHM) of the intensity.

A diffraction axicon with a height of $h = 1.06$ λ (Fig. 1, *c*) with a standard substrate acted as a basic optical element for comparison. Increasing the height of the relief, as well as the use of a GRIN substrate, made it possible to increase the length of the light needle. Separately, cases were assessed when the height h1 was fixed (1.06 λ) and the height h_2 changed (Fig. 2) and the reverse case (Fig. 3).

It should be noted that an increase in height led to the formation of a powerful light needle for radial polarization, in contrast to the case of the same polarization for a standart axicon with a height $h_1 = 1.06$ λ (a minimum on the optical axis and the formation of a ring were observed).

The maximum light needle size was obtained for radial polarization at $h_1 = 5.32$ λ, $h_2 = 1.06$ λ (DOF = 7.86 λ), which is 3.19 times longer than in the case of the basic optical element.

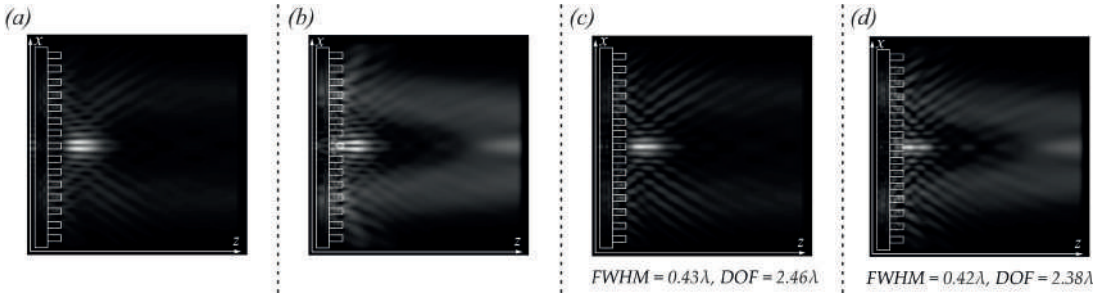

Fig. 1. The two-dimensional diffraction pattern (*xz* plane) of an optical vortex on ring gratings (total intensity), with relief height $h = 1.06\,\lambda$, radial polarization and (*a*) standard substrate, (*b*) GRIN substrate; azimuthal polarization and (*c*) standard substrate, (*d*) GRIN substrate

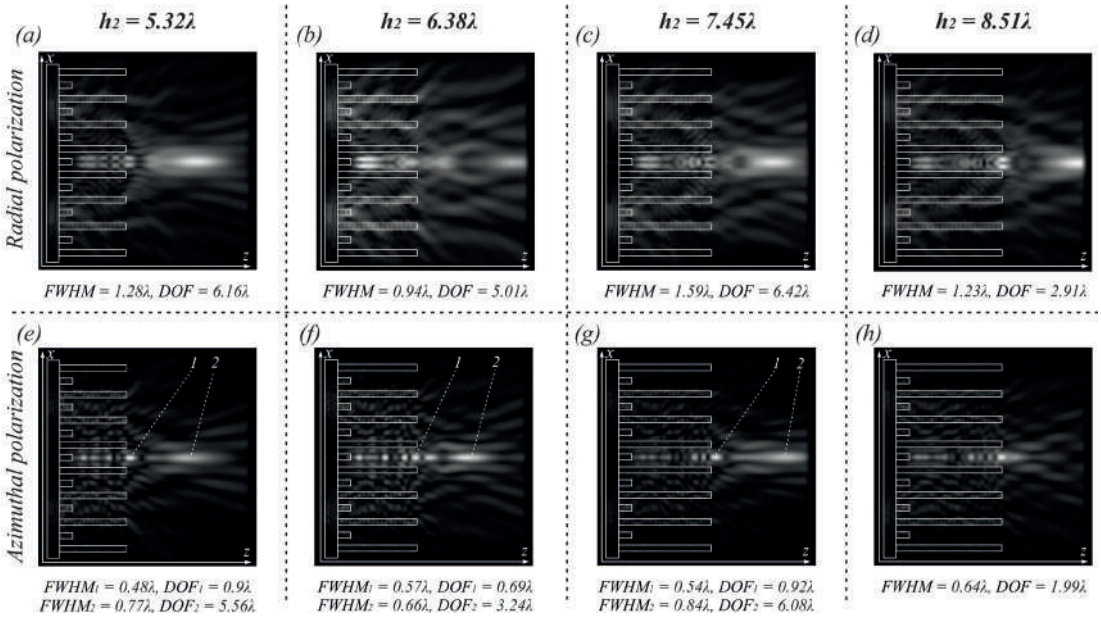

Fig. 2. The two-dimensional diffraction pattern (*xz* plane) of an optical vortex on ring gratings (total intensity, for fixed $h_1 = 1.06\,\lambda$), with radial polarization (*a*, *b*, *c*, *d*) and azimuthal polarization (*e*, *f*, *g*, *h*)

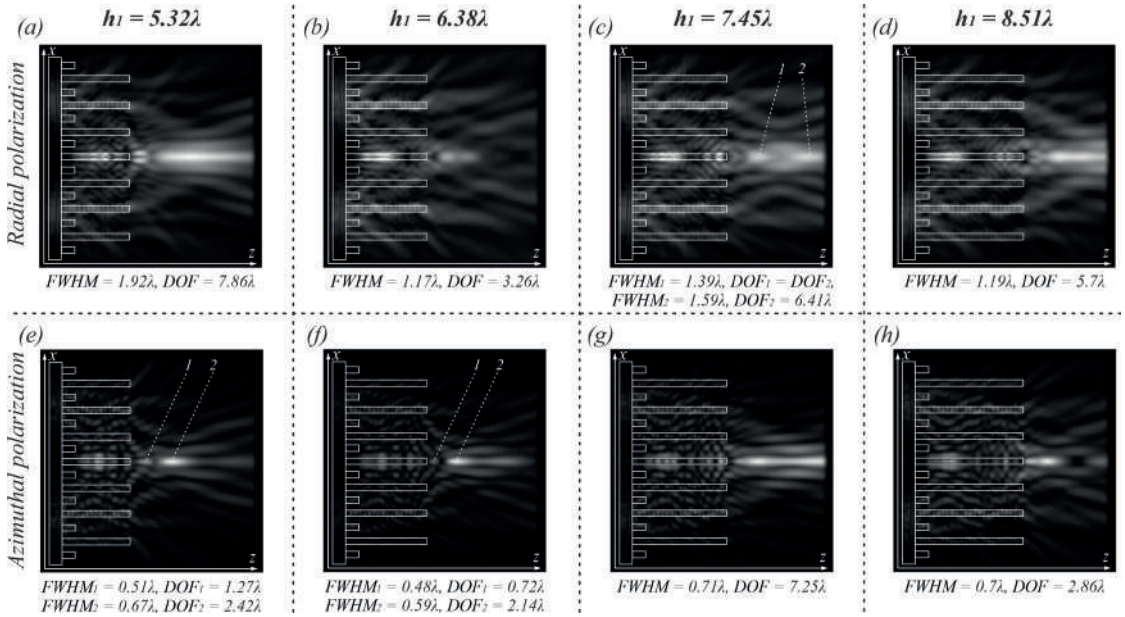

Fig. 3. The two-dimensional diffraction pattern (*xz* plane) of an optical vortex on ring gratings (total intensity, for fixed $h_2 = 1.06\,\lambda$), with radial polarization (*a*, *b*, *c*, *d*) and azimuthal polarization (*e*, *f*, *g*, *h*)

And for azimuthal polarization, the maximum size of the light segment was obtained for $h_1 = 5.32\,\lambda$, $h_2 = 1.06\,\lambda$ (DOF = $7.25\,\lambda$). An increase in the size of the light segments is accompanied by an increase in the size of the focal spots.

It should also be noted that for a number of cases considered, a set of maxima is formed on the optical axis (especially noticeable for azimuthal polarization at a fixed h_1 =1.06). The intensity oscillations on the optical axis were observed inside the element for the case with fixed h_2.

Conclusion

The diffraction of first-order optical vortices with azimuthal and radial polarization on subwavelength ring gratings of variable height with a GRIN substrate using the FDTD method was simulated in this paper.

The maximum light needle on the optical axis (DOF = $7.86\,\lambda$) was obtained for an element with alternating zones ($h_1 = 5.32\,\lambda$, $h_2 = 1.06\,\lambda$) with radial polarization of input radiation.

REFERENCES

1. **Shen Y., Wang X., Xie Z., Min C., Fu X., Liu Q., Gong M., Yuan X.,** Optical vortices 30 years on: OAM manipulation from topological charge to multiple singularities, Light: Science & Applications. 8 (1) (2019) 1–29.

2. **Wen, J., Gao, B., Zhu, G., Liu, D., Wang, L.G.,** Precise position and angular control of optical trapping and manipulation via a single vortex-pair beam, Optics and Lasers in Engineering. 148 (2022) 106773.

3. **Dong M., Zhao C., Cai Y., Yang Y.,** Partially coherent vortex beams: Fundamentals and applications, Science China Physics, Mechanics & Astronomy. 64 (2) (2021) 224201.

4. **Khonina S.N.,** Vortex beams with high-order cylindrical polarization: features of focal distributions, Applied Physics B. 125 (6) (2019) 100.

5. **Savelyev D.A.,** Features of a Gaussian beam near-field diffraction upon variations in the relief height of subwavelength silicon optical elements, Computer Optics. 47 (6) (2023) 938–947.

6. **Savelyev D.A., Karpeev S.V.,** Development of 3D Microstructures for the Formation of a Set of Optical Traps on the Optical Axis, Photonics. 10 (2) (2023) 117.

7. **Lightman S., Hurvitz G., Gvishi R., Arie A.,** Miniature wide-spectrum mode sorter for vortex beams produced by 3D laser printing, Optica. 4 (6) (2017) 605–610.

8. **Shi C., Xu Z., Nie Z., Xia Z., Dong B., Liu J.,** Sub-wavelength longitudinally polarized optical needle arrays generated with tightly focused radially polarized Gaussian beam, Optics communications. 505 (2022) 127506.

9. **Richardson K.A., Kang M., Sisken L., Yadav A., Novak S., Lepicard A., Martin I., Francois-Saint-Cyr H., Schwarz C.M., Mayer T.S., Rivero-Baleine C., Yee A. J., Mingareev I.,** Advances in infrared gradient refractive index (GRIN) materials: a review, Optical Engineering. 59 (11) (2020) 112602.

10. **Guo C., Urner T., Jia S.,** 3D light-field endoscopic imaging using a GRIN lens array, Applied Physics Letters. 116 (10) (2020) 101105.

11. **Srivastava P.R., Majumdar A., Menon R., Swartzlander G.A.,** High forward thrust metasurface beam-riding sail, Optics Express. 32 (2) (2024) 1756–1763.

12. **Zhang L., Jiang F., Wu B., Lv C., Wu M.,** A one-step synthesis of ultra-long silver nanowires with ultra-high aspect ratio above 2000 and its application in flexible transparent conductive electrodes, Nanotechnology. 32 (10) (2020) 105710.

THE AUTHORS

SAVELYEV Dmitry A.
dmitrey.savelyev@yandex.ru
ORCID: 0000-0003-2282-3895

Received 06.07.2024. Approved after reviewing 01.08.2024. Accepted 03.08.2024.

Conference materials
UDC 535.37
DOI: https://doi.org/10.18721/JPM.173.147

Study of planar microcavity structure with $In_{0.63}Ga_{0.37}As$ quantum dots and non-absorbing $Al_{0.2}Ga_{0.8}As/Al_{0.9}Ga_{0.1}As$ mirrors

A.V. Babichev [1], D.S. Papylev [2] ✉, S.D. Komarov [3], N.V. Kryzhanovskaya [3], S.A. Blokhin [1], V.N. Nevedomsky [1], A.G. Gladyshev [2], L.Ya. Karachinsky [2], I.I. Novikov [2], A.Yu. Egorov [2]

[1] Ioffe Institute, St. Petersburg, Russia;
[2] ITMO University, St. Petersburg, Russia;
[3] National Research University Higher School of Economics, St. Petersburg branch, St. Petersburg, Russia
✉ dspapylev@itmo.ru

Abstract. The planar microcavity structure based on non-absorbing $Al_{0.2}Ga_{0.8}As/Al_{0.9}Ga_{0.1}As$ mirrors was fully fabricated by molecular-beam epitaxy. Usage of $In_{0.63}Ga_{0.37}As$ quantum dots reveals room temperature emission near 1110 nm with emission bandwidth of about 80 meV. The determined spectral mismatch between peak position of gain region and reflectivity spectrum dip was about 115 meV at 290 K. The shift of the reflectance dip position along the whole wafer surface was less than 15 meV. The determined by defect inspection root mean square surface roughness was less than 1.3 nm for studied 8 μm thick planar microcavity structure.

Keywords: molecular-beam epitaxy, planar microcavity, gallium arsenide, InGaAs, Stransky-Krastanow growth mode

Funding: The authors from Ioffe Institute acknowledge support in part by the grant of the Russian Science Foundation No. 22-19-00221, https://rscf.ru/project/22-19-00221/ for the structure design, MBE epitaxy, transmission electron microscopy analysis and the study of photoluminescence spectra. The authors from HSE University acknowledge support in part by the Basic Research Program at the HSE University for support in the photoluminescence spectra analysis. The authors from ITMO University acknowledge support in part by the Ministry of Science and Higher Education of the Russian Federation, project no. 2019-1442 (project reference number FSER-2020-0013) for the analysis of surface defect and reflection spectra of a planar microcavity structure.

Citation: Babichev A.V., Papylev D.S., Komarov S.D., Kryzhanovskaya N.V., Blokhin S.A., Nevedomsky V.N., Gladyshev A.G., Karachinsky L.Ya., Novikov I.I., Egorov A.Yu., Study of planar microcavity structure with $In_{0.63}Ga_{0.37}As$ quantum dots and non-absorbing $Al_{0.2}Ga_{0.8}As/Al_{0.9}Ga_{0.1}As$ mirrors, St. Petersburg State Polytechnical University Journal. Physics and Mathematics. 17 (3.1) (2024) 233–237. DOI: https://doi.org/10.18721/JPM.173.147

Материалы конференции
УДК 535.37
DOI: https://doi.org/10.18721/JPM.173.147

Исследование планарной структуры микрорезонатора с квантовыми точками $In_{0.63}Ga_{0.37}As$ и непоглощающими зеркалами $Al_{0.2}Ga_{0.8}As/Al_{0.9}Ga_{0.1}As$

А.В. Бабичев [1], Д.С. Папылев [2] ✉, С.Д. Комаров [3], Н.В. Крыжановская [3], С.А. Блохин [1], В.Н. Неведомский [1], А.Г. Гладышев [2], Л.Я. Карачинский [2], И.И. Новиков [2], А.Ю. Егоров [2]

[1] Физико-технический институт им. А.Ф. Иоффе РАН, Санкт-Петербург, Россия;

[2] Университет ИТМО, Санкт-Петербург, Россия;

[3] Национальный исследовательский университет «Высшая школа экономики», Санкт-Петербургский филиал, Санкт-Петербург, Россия

✉ dspapylev@itmo.ru

Аннотация. Планарная структура вертикального микрорезонатора с непоглощающими распределенными брэгговскими отражателями $Al_{0.2}Ga_{0.8}As/Al_{0.9}Ga_{0.1}As$ была изготовлена методом молекулярно-пучковой эпитаксии. Квантовые точки, сформированные по механизму Странски-Крастанова из слоя $In_{0.63}Ga_{0.37}As$ демонстрируют фотолюминесценцию при комнатной температуре вблизи 1110 нм, с характерной полушириной пика около 80 мэВ. Величина спектрального рассогласования между положением пика фотолюминесценции активной области и провалом в спектре отражения составило около 115 мэВ при температуре 290 K. Сдвиг положения резонансной длины волны в спектре отражения при смещении от центра к краю пластины не превысил 15 мэВ. Оценочная величина шероховатости поверхности планарной структуры вертикального микрорезонатора толщиной 8 мкм не превысила 1.3 нм.

Ключевые слова: молекулярно-пучковая эпитаксия, планарный вертикальный микрорезонатор, арсенид галлия, InGaAs, механизм Странски-Крастанова

Финансирование: Авторы из ФТИ им. А.Ф. Иоффе выражают благодарность за частичную поддержку проекту РНФ № 22-19-00221, https://rscf.ru/project/22-19-00221/ в части разработки структуры, эпитаксии методом молекулярно-пучковой эпитаксии, анализ методом просвечивающей электронной микроскопии и исследование спектров фотолюминесценции. Авторы из НИУ ВШЭ благодарят за поддержку Программу фундаментальных исследований НИУ ВШЭ за поддержку в части анализа спектров фотолюминесценции. Авторы из Университета ИТМО выражают благодарность за поддержку Министерство науки и высшего образования Российской Федерации, проект тематики научных исследований № 2019-1442 (код научной темы FSER-2020-0013) в части анализа карт поверхностных дефектов и спектров отражения гетероструктуры вертикального микрорезонатора.

Ссылка при цитировании: Бабичев А.В., Папылев Д.С., Комаров С.Д., Крыжановская Н.В., Блохин С.А., Неведомский В.Н., Гладышев А.Г., Карачинский Л.Я., Новиков И.И., Егоров А.Ю. Исследование планарной структуры микрорезонатора с квантовыми точками $In_{0.63}Ga_{0.37}As$ и непоглощающими зеркалами $Al_{0.2}Ga_{0.8}As/Al_{0.9}Ga_{0.1}As$ // Научно-технические ведомости СПбГПУ. Физико-математические науки. 2024. Т. 17. № 3.1. С. 233–237. DOI: https://doi.org/10.18721/JPM.173.147

Introduction

The realization of optical reservoir computing (RC) based on micropillar lasers with optical pumping requires a high spectral uniformity and low threshold excitation powers in lasers array.

Recently, spectral uniformity about 190 μeV for 8×8 micropillar arrays and low threshold excitation power (about 1 mW for 5 μm diameter pillar) have been reported for microcavities with absorbing GaAs/$Al_{0.9}Ga_{0.1}As$ mirrors [1]. The maximal lasing temperature (~130 K) was limited by strong absorption of distributed Bragg reflector GaAs layers at excitation wavelength [2]. In opposite, the ultra-low threshold excitation power (about 30 μW for 5 μm pillar [3]) were reported for new microcavities with non-absorbing $Al_{0.2}Ga_{0.8}As/Al_{0.9}Ga_{0.1}As$ mirrors. Moreover, gain to cavity detuning, GCD (spectral mismatch between gain region maxima and microcavity reflectance dip position) strongly effect on the threshold excitation power versus temperature behavior as well [2, 4].

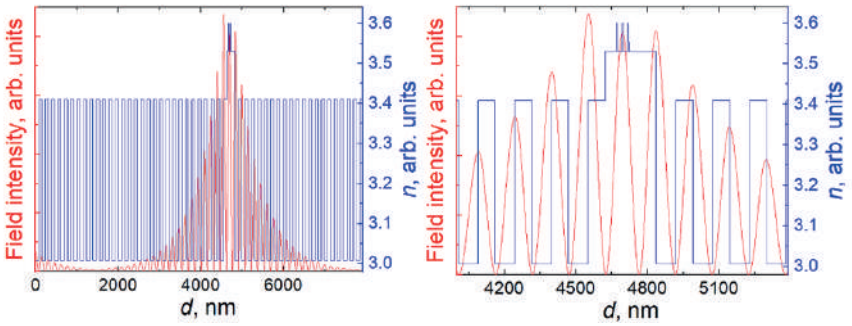

Fig. 1. Optical field intensity versus distance from the substrate. Right panel demonstrates the enlarged image of left panel

This paper is devoted to studies of the optical characteristics of planar microcavity structure with InGaAs/GaAs quantum dots (QDs) and non-absorbing $Al_{0.2}Ga_{0.8}As/Al_{0.9}Ga_{0.1}As$ mirrors.

Materials and Methods

The microcavity as well as QDs test heterostructure were grown by molecular-beam epitaxy. The one lambda thick microcavity was formed by non-absorbing (at 700–820 nm range of exciting laser wavelength) bottom and top mirrors consisted of 30 and 20 pairs of $Al_{0.2}Ga_{0.8}As/Al_{0.9}Ga_{0.1}As$ respectively. The gain region was positioned in E-field maxima and consisted of 3-fold stacked QDs layers separated by 20 nm thick GaAs barriers (cf. Fig. 1). The QDs were formed from $In_{0.63}Ga_{0.37}As$ layer by the Stransky-Krastanow growth mode. The thickness of $In_{0.63}Ga_{0.37}As$ layer was equaled to 2.6 monolayers. The QDs test structure includes the same three-stacked QDs layers that were applied as the gain region of microcavity structure.

The photoluminescence (PL) studies were carried out in the 77–290 K temperature range. The optical pumping of QDs test heterostructure was made by a Nd:YAG laser (with 532 nm wavelength excitation) with low CW excitation power density (54 mW/cm^2) aimed to compare with previously published results for structure grown by metal-organic chemical vapor deposition, MOCVD [5]. The reflection spectrum maps of the planar microcavity structure were analyzed by a VerteX PM2000 mapper system (Nanometrics Inc.). The transmission electron microscopy (TEM) studies were conducted using a JEM2100F electron microscope (Jeol Ltd.) at accelerating voltage of 200 kV. Surfscan defect inspection system (KLA Tencor Corp.) was used to measure the normal (with sizes in the range of 0.6–10 μm^2) and oval (with sizes in the range of 10–250 μm^2) defects distribution over the entire substrate surface.

Results and Discussion

The inhomogeneous broadening determined at 77 K for PL spectrum at 54 mW/cm^2 was about 99 meV. Temperature rise reveals to fall of the PL spectrum full width at half maximum (FWHM), with minimum value about 60 meV at 180 K. Room temperature (at 290 K) value of inhomogeneous broadening was 83 meV that is close to the previously mentioned value for MOCVD-grown single layer QDs (~80 meV [5]). Peak position of PL spectrum measured at 77 K was near 1030 nm. Rise of the temperature up to 290 K yields to shift of ground state emission to 1110 nm. This value is just above the previously mentioned for MOCVD structure (1014 nm [5]), due to the difference in QDs composition. To clarify the GCD the high-resolution reflectance spectrum was measured. The dip position of reflectance spectrum was located at 993 nm that

results GCD about 117 nm (~114 meV). Previously, the PL peak and reflectance dip position was 1100 nm and 1050 nm, respectively that yields GCD of about 50 nm (~54 meV) [5]. Using the value of FWHM of the reflectance spectra the quality-factor of planar microcavity structure was determined, which was ~1450. Aimed to clarify the spectral inhomogeneity of reflectance dip position over the whole wafer surface the map of reflectance spectra was measured. The change in the position of the reflection dip with a radial shift of approximately 25 mm from the center was about 3 meV, which is about 9 times less than for MOCVD-grown planar microcavity structure [1].

The images obtained by transmission electron microscopy are presented in Fig. 3. In general, "inverse Christmas tree" growth mode was realized due to indium segregation that cause dislocation formation in oversized QDs [6]. Moreover, due to different size of QDs in stacked layers increase the inhomogeneous broadening was observed for this gain region. Aimed to realize the uniform QDs, anticorrelation growth mode may be applied [7]. Herein, we have realized the QD seeding,

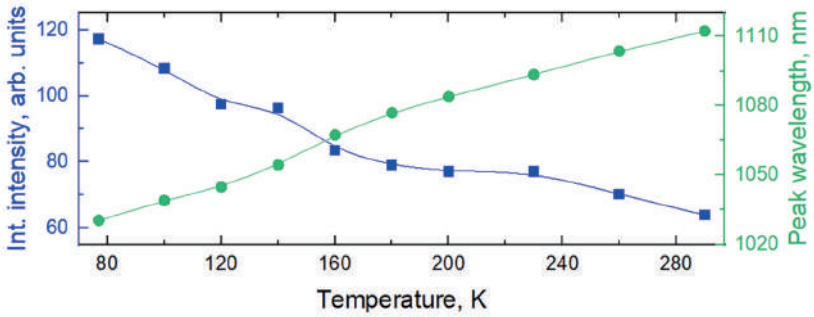

Fig. 2. Integrated intensity (left Y axis) and peak position of PL spectra (right Y axis) versus temperature behaviors for test structure with $In_{0.63}Ga_{0.37}As$ QDs

but without change of size for QDs located in different layers (cf. Fig. 3). As a result, the effect of increasing the inhomogeneous broadening due to the dispersion of QD sizes in different layers did not appear. The STEM image (Fig. 3) demonstrates that the DBR layers have good planarity and a constant period, and there are no defects in the area of the DBR/gain region boundaries.

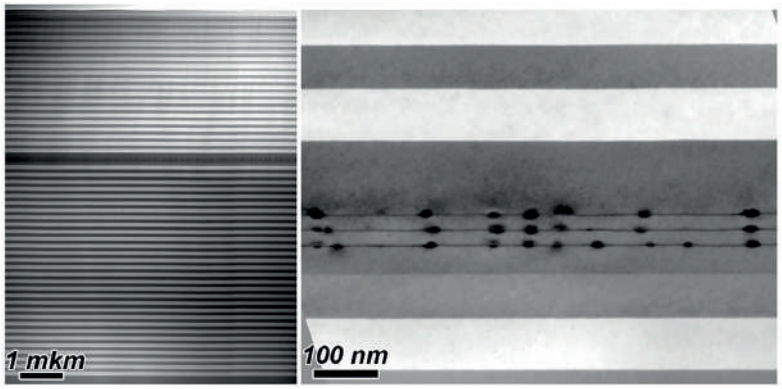

Fig. 3. STEM (left panel) and TEM (right panel) images of the microcavity heterostructure

The defects distribution over the entire substrate surface was analyzed as well. The density of normal and oval defects was 179 and 194 per cm^2, respectively. The average haze values were 412 and 388 ppm for normal and oval defects. As a result, the estimated root mean square (RMS) roughness of the surface was less than 1.3 nm.

Conclusion

MBE-grown $In_{0.63}Ga_{0.37}As$ quantum dots gain region were embedded in the one lambda length cavity based on 30 and 20 pairs $Al_{0.2}Ga_{0.8}As/Al_{0.9}Ga_{0.1}As$ DBR. The estimated from reflectance measurements quality-factor of this planar cavity was about 1450. The evaluated zero gain to cavity detuning was near the 230 K temperature. The small shift of reflectance dip value along

radius position reveals perspective of MBE-grown micropillar structure usage for fabrication of micropillars laser arrays with ultra-high spectral homogeneity.

REFERENCES

1. **Heuser T., Grose J., Holzinger S., Sommer M.M., Reitzenstein S.,** Development of highly homogenous quantum dot micropillar arrays for optical reservoir computing, IEEE J. Sel. Top. Quantum Electron. 26 (1) (2020) 1–9.

2. **Andreoli L., Porte X., Heuser T., Große J., Moeglen-Paget B., Furfaro L., Reitzenstein S., Brunner D.,** Optical pumping of quantum dot micropillar lasers. Opt. Express. 29 (6) (2021) 9084.

3. **Shih C.-W., Limame I., Krüger S., Palekar C.C., Koulas-Simos A., Brunner D., Reitzenstein S.,** Low-threshold lasing of optically pumped micropillar lasers with $Al_{0.2}Ga_{0.8}As/Al_{0.9}Ga_{0.1}As$ distributed Bragg reflectors. Appl. Phys. Lett. 122 (15) (2023) 151111.

4. **Gaur K., Shih C.-W., Limame I., Koulas-Simos A., Heermeier N., Palekar C. C., Tripathi S., Rodt S., Reitzenstein S.,** High-β lasing in photonic-defect semiconductor-dielectric hybrid microresonators with embedded InGaAs quantum dots. Appl. Phys. Lett., 124 (4) (2024) 041104.

5. **Kamiński B., Zielińska A., Musiał A., Shih C.W., Limame I., Rodt S., Reitzenstein S., Sęk G.,** Optical characteristics of cavity structures with $Al_{0.2}Ga_{0.8}As/Al_{0.9}Ga_{0.1}As$ distributed Bragg reflectors and $In_{0.37}Ga_{0.63}As$ quantum dots as the active region. Prz. Elektrotech., 1 (10) (2023) 296–299.

6. **Passaseo A., Rinaldi R., Longo M., Antonaci S., Convertino A. L., Cingolani R., Taurino A., Catalano M.,** Structural study of InGaAs/GaAs quantum dots grown by metalorganic chemical vapor deposition for optoelectronic applications at 1.3 μm. J. Appl. Phys. 89 (8) (2001) 4341–4348.

7. **Wang X.-D., Liu N., Shih C. K., Govindaraju S., Holmes A.L.,** Spatial correlation- anticorrelation in strain-driven self-assembled InGaAs quantum dots. Appl. Phys. Lett. 85 (8) (2004) 1356–1358.

THE AUTHORS

BABICHEV Andrey V.
a.babichev@mail.ioffe.ru
ORCID: 0000-0002-3463-4744

NEVEDOMSKY Vladimir N.
nevedom@mail.ioffe.ru
ORCID: 0000-0002-7661-9155

PAPYLEV Denis S.
dspapylev@itmo.ru
ORCID: 0009-0001-3683-5558

GLADYSHEV Andrey G.
glad@mail.ioffe.ru
ORCID: 0000-0002-9448-2471

KOMAROV Sergey D.
serega.komarow@mail.ru
ORCID: 0000-0002-7025-3527

KARACHINSKY Leonid Ya.
karach@switch.ioffe.ru
ORCID: 0000-0002-5634-8183

KRYZHANOVSKAYA Natalia V.
nkryzhanovskaya@hse.ru
ORCID: 0000-0002-4945-9803

NOVIKOV Innokenty I.
novikov@switch.ioffe.ru
ORCID: 0000-0003-1983-0242

BLOKHIN Sergei A.
blokh@mail.ioffe.ru
ORCID: 0000-0002-5962-5529

EGOROV Anton Yu.
anton@beam.ioffe.ru
ORCID: 0000-0002-0789-4241

Received 08.07.2024. Approved after reviewing 23.07.2024. Accepted 24.07.2024.

Conference materials
UDC 539.219.3
DOI: https://doi.org/10.18721/JPM.173.148

Memristive behavior of the system comprising Ag nanoparticles coated by HfO_x layer

Yu.O. Vasilevskaya [1, 2] ✉, P.O. Ksenofontova [2], K.I. Litvinova [3], A.I. Savitskiy [1]

[1] Scientific-Manufacturing complex "Technological Centre", Zelenograd, Russia;

[2] National Research University of Electronic Technology, Zelenograd, Russia;

[3] Institute of Nanotechnologies of Microelectronics of the RAS, Moscow, Russia

✉ fedorovauo@mail.ru

Abstract. Memristive systems promise energy-efficient computing and accelerated machine learning tasks by enabling simultaneous storage and processing of information within single device architecture. The research focuses on the analysis of percolation memristive systems based on silver nanoparticles in a hafnium oxide dielectric matrix. Conductivity in the nanoparticle network is achieved through atomic filament connections between adjacent particles. The systems exhibit hysteresis in I-V curves when a sawtooth electric voltage is applied. The hafnium oxide coating was used to provide sample stability and also to reduce the formation voltage due to the proposed additional mechanism of valence change during subsequent filament formation.

Keywords: silver nanoparticles, filament, percolation, neuromorphic computing

Funding: The work is supported by the Ministry of Science and Higher Education of the Russian Federation (project FNRM-2022-0008).

Citation: Vasilevskaya Yu.O., Ksenofontova P.O., Litvinova K. I., Savitskiy A.I., Memristive behavior of the system comprising Ag nanoparticles coated by HfO_x layer, St. Petersburg State Polytechnical University Journal. Physics and Mathematics. 17 (3.1) (2024) 238–242. DOI: https://doi.org/10.18721/JPM.173.148

Материалы конференции
УДК 539.219.3
DOI: https://doi.org/10.18721/JPM.173.148

Мемристивная динамика системы наночастиц серебра с покрытием HfO_x

Ю.О. Василевская [1, 2] ✉, П.О. Ксенофонтова [2], К.И. Литвинова [3], А.И. Савицкий [1]

[1] НПК «Технологический центр», г. Зеленоград, Россия;

[2] Национальный исследовательский университет «МИЭТ», г. Зеленоград, Россия;

[3] Институт нанотехнологий микроэлектроники РАН, Москва, Россия

✉ fedorovauo@mail.ru

Аннотация. Исследование сосредоточено на анализе перколяционных мемристивных систем на основе наночастиц серебра в диэлектрической матрице оксида гафния, где проводимость достигается за счет атомных связей между частицами. Системы демонстрируют гистерезис на кривых I-V при приложении пилообразного электрического напряжения. Покрытие оксидом гафния используется для стабилизации образца и снижения напряжения формирования.

Ключевые слова: серебряные наночастицы, филамент, перколяция, нейроморфные вычисления

Финансирование: Работа выполнена в рамках гос. задания Министерства науки и высшего образования РФ (проект FNRM–2022–0008).

Ссылка при цитировании: Василевская Ю.О., Ксенофонтова П.О., Литвинова К.И., Савицкий А.И. Мемристивная динамика системы наночастиц серебра с покрытием HfO_x // Научно-технические ведомости СПбГПУ. Физико-математические науки. 2024. Т. 17. № 3.1. С. 238–242. DOI: https://doi.org/10.18721/JPM.173.148

Introduction

Memristive systems offer the potential for energy-efficient computing and accelerated machine learning thanks to their unique ability to store and process information simultaneously within a single device architecture [1]. In some studies, memristive networks of nanoparticles (NPs) near the percolation threshold are investigated for their potential to exhibit brain-like activity related to critical dynamics [2, 3]. The percolation threshold refers to the point at which NPs begin to connect and form a continuous network. The functional synaptic plasticity, nonlinear dynamics, and decaying memory inherent in these systems make them suitable for neuromorphic computing [4]. The potential of metal oxide-based resistive random access memory (RRAM) offers new opportunities for creating more efficient memory devices due to its low power consumption, 3D integration, and compatibility with CMOS technology [5]. HfO_2, in particular, is a promising dielectric material for RRAM, with excellent resistive switching properties, including a large resistive window, a low set voltage, and good durability [6]. Previously, the authors studied percolation arrays of pure silver and gold nanoparticles and proposed the phase-field model qualitatively reproduce the memristive dynamics in such systems [7, 8]. In this study, we present the results of an investigation into the memristive properties of a percolative network consisting of silver nanoparticles coated with a dielectric matrix of HfO_x.

Materials and Methods

To study the electrical properties of Ag nanoparticle ensembles covered by HfO_x layer, planar structures of thermally oxidized silicon substrates (SiO_2 – 100 nm) were used. These structures featured two opposing gold electrodes arranged in an interdigital pattern, with pins measuring 12 μm in length and 10 μm in width, separated by a 2 μm gap (Fig. 1, *a*). Within this gap, an array of silver NPs was positioned using the vacuum thermal evaporation method. The size and density of these NPs were finely tuned by controlling the amount of material evaporated (Ag ~ 4.7 mg). After Ag deposition, a few samples were subjected to further vacuum annealing (230 °C). Next, a layer of hafnium oxide (layer thickness – 15 nm) was deposited using the atomic layer deposition method (process temperature 290 °C). As a source of Hf the organometallic precursor, TDMAH($Hf(N(CH_3)_2)_4$), was used. The morphology of the experimental samples was studied using an FEI Helios NanoLab 650i DualBeam electron-ion scanning microscope. The results of cyclic voltammetry were obtained on a Cascade Summit 2000 semi-automatic probe station at room temperature in air.

Results and Discussion

The main difference between samples (Fig. 1, *b*, *c*) lies in the main size of the particles in the array and the nature of particle size distribution. When the array is additionally annealed in a vacuum, the distribution of Ag particle sizes becomes more uniform, indicating that the nanoparticles have less variation in size around the average one. Also annealing makes the nanoparticles more spherical.

The memristive behavior is demonstrated using cyclic voltammetry (Fig. 2). The I-V curves show a reversible change in resistance between high and low states, accompanied by a notable increase in system conductance. When a sufficient potential difference is applied to the system (4–6 V for non-annealed Ag array, and 12–15 V for annealed), Ag atom electromigration is induced, that causes the formation of multiple local contacts between nanoparticles.

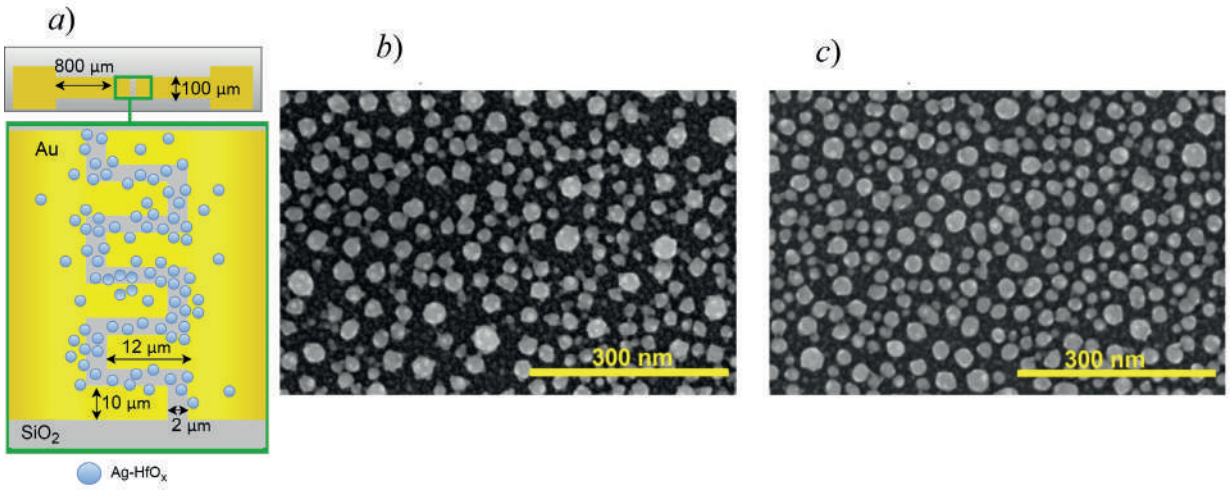

Fig. 1. Schematic view of experimental structure (*a*) with enlarged insert of gap between electrodes, and SEM images of the non-annealed (*b*) and annealed (*c*) array of Ag nanoparticles coated by HfO_x

Over time, this process forms a percolation cluster between the electrodes. This cluster, however, is apparently unstable and can dynamically rearrange with voltage variations. When the voltage is removed, the system gradually reverts back to its original state that is related to filament dissolution [7]. Comparing the authors' previous findings for pure nanoparticles (Fig. 3), we found that the switching dynamics persisted after the addition of an insulating matrix.

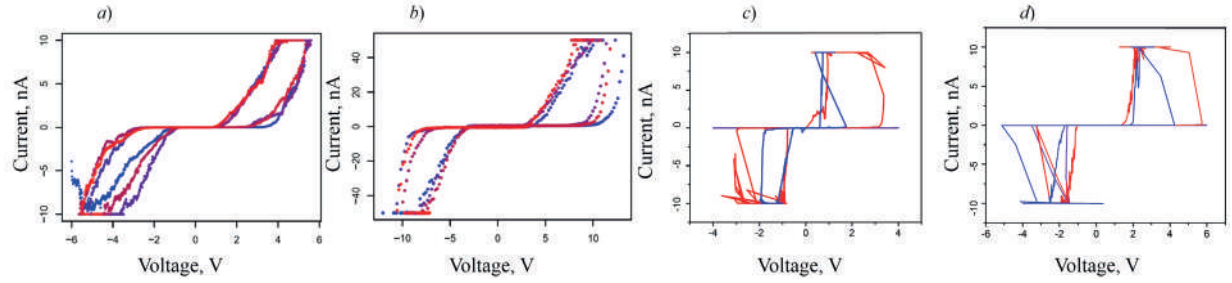

Fig. 2. Cyclic voltammograms for non-annealed (*a*) and annealed (*b*) Ag ensembles with coating, and data for the same structures, respectively, (*c*) and (*d*), measured 1 year later

Results show that in assemblies of non-annealed Ag nanoparticles, switching to the memristive state occurs at lower voltages compared to arrays of annealed ones. It is assumed that this is due to the nanoparticles shape in the gap, since the presence of "tips" on particles without annealing better promotes the growth of filaments due to locally higher field strength.

The temporal stability of the samples coated with hafnium oxide was confirmed a year later by repeating similar measurements of cyclic voltammetry (Fig. 2, *c*, *d*). Resistive switching is observed in the first case at voltages of approximately 4 V, while for annealed sample it occurred around 6 V. Despite the presence of fluctuations in the graphs, the structures replicate the memristive behavior. The results make the use of hafnium oxide coating suitable for increasing the stability of structures, however further development of the model is required to describe the internal dynamics in the Ag-HfO_x system.

To compare the temporal stability, the results for samples with pure Ag NPs array without coating are presented below.

As Figure 3 shows, the operating voltage for the silver NPs array, both without and with annealing, is lower compared to that for the coated samples (3 V and 8 V, respectively). In this case, the dynamics are similar to samples coated with hafnium oxide, however, over time, the operating voltage required for transition to the memristive state increases. It is worth noting that the width of the hysteresis "loop" in the case of pure nanoparticles expands that is associated with

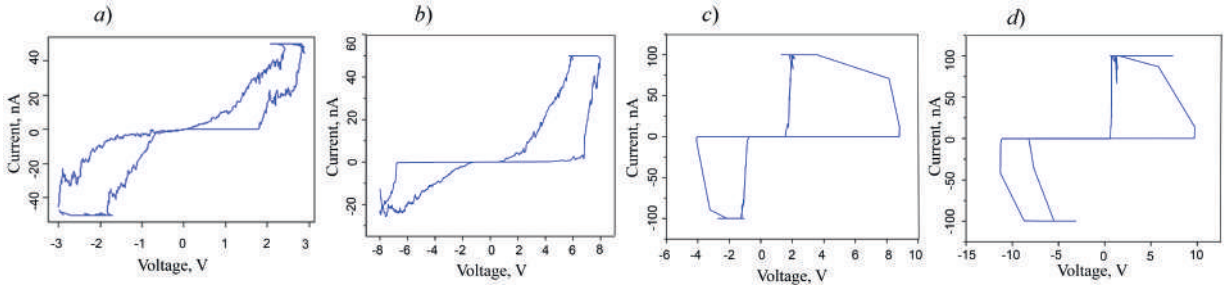

Fig. 3. Voltammograms for non-annealed (*a*) and annealed (*b*) Ag ensembles without coating, and data for the same structures, respectively, (*c*) and (*d*), measured 1 year later

the process in which neighboring NPs partially consolidated into larger clusters with increasing the distances between them. This assumption is based on the SEM results presented in Figure 4.

As can be seen for the sample of pure silver, the nanoparticles are formed into significantly larger "droplets" with sizes up to 100 nm compared to that with HfO_x layer, with higher distances between them; the coated sample is characterized by greater retention of particle morphology. Although such have been widely known [9], the results obtained require further in-depth research, since the effect of nanoparticle coalescence may force the percolation threshold affecting the conditions for a conductive path to form between the two electrodes.

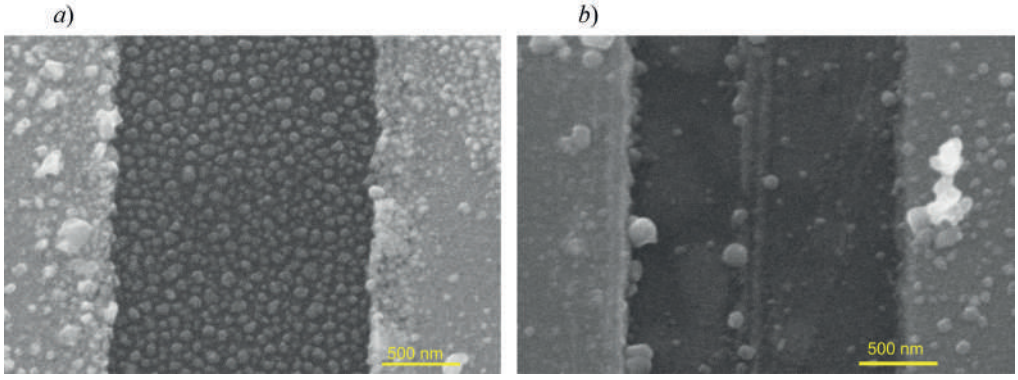

Fig. 4. SEM images of the non-annealed array of Ag nanoparticles in the gap without (*a*) and coated by HfO_x (*b*) measured 1 year later

Conclusion

HfO_x showed no negative effect on the memristive behavior of the nanoparticle ensemble and was used both to isolate the structure from environmental influences and prevent changes in the granulometric parameters of nanoparticles by stabilizing the array with a matrix coating (positive dynamics – decrease in operating voltage by ~1.5 times after a year). Studies of network dynamics in a matrix are essential, as encapsulating the network in an insulating medium is often an unavoidable step in the integration of electronic devices.

Acknowledgments

The authors are grateful to Lydia Volkova (Institute of Nanotechnology of Microelectronics of the Russian Academy of Sciences, Moscow) for the SEM studies of the experimental samples.

REFERENCES

1. **Gronenberg O., et al.,** In Situ Imaging of Dynamic Current Paths in a Neuromorphic Nanoparticle Network with Critical Spiking Behavior, Advanced Functional Materials. (2024) 2312989.

2. **Hesse J., Gross T.,** Self-organized criticality as a fundamental property of neural systems, Frontiers in systems neuroscience. 8 (2014) 166.

3. **Mallinson J.B., Steel J.K., Heywood Z.E., Studholme S.J., Bones P.J., Brown S.A.,** Experimental Demonstration of Reservoir Computing with Self-Assembled Percolating Networks of Nanoparticles, Advanced Materials. (2024) 2402319.

4. **Yang K., Joshua Yang, J., Huang R., Yang Y.,** Nonlinearity in memristors for neuromorphic dynamic systems, Small Science. 2 (1) (2022) 2100049.

5. **Shen Z., et al.,** Advances of RRAM devices: Resistive switching mechanisms, materials and bionic synaptic application, Nanomaterials. 10 (8) (2020) 1437.

6. **Pan J., He H., Dan Y., Lin Y., Yang S., Li M., Li T.,** HfO_2-Based RRAM with In Situ Conductive Channels Induced by Nanoparticles to Improve Stability, ACS Applied Electronic Materials. 6 (1) (2023) 406-414.

7. **Sibatov R.T., Savitskiy A.I., L'vov P.E., Vasilevskaya Y.O., Kitsyuk E.P.,** Self-Organized Memristive Ensembles of Nanoparticles Below the Percolation Threshold: Switching Dynamics and Phase Field Description, Nanomaterials. 13 (14) (2023) 2039.

8. **L'vov P.E., Sibatov R.T., Ryazanov R.M., Novikov D.V.,** Phase-field model of filament formation and growth in percolating memristive systems of nanoparticles, Materials Today Communications. (2024) 108464.

9. **Grammatikopoulos P., Sowwan M., Kioseoglou J.,** Computational modeling of nanoparticle coalescence, Advanced Theory and Simulations. 2 (6) (2019) 1900013.

THE AUTHORS

VASILEVSKAYA Yulia O.
fedorovauo@mail.ru
ORCID: 0000-0002-5183-6807

KSENOFONTOVA Polina O.
polina.ksenofontova.2002@mail.ru

LITVINOVA Kristina I.
litkristy@gmail.com

SAVITSKIY Andrey I.
savitskij-andrey@mail.ru
ORCID: 0000-0002-8137-4340

Received 09.07.2024. Approved after reviewing 31.07.2024. Accepted 01.08.2024.

Conference materials
UDC 681.7
DOI: https://doi.org/10.18721/JPM.173.149

Experimental study of the use of optical cables with different types of fibers in monitoring systems

V.E. Pylaev [1] ✉, E.I. Andreeva [1]

[1] Bonch-Bruevich Saint-Petersburg State University of Telecommunications, St. Petersburg, Russia

✉ me022@mail.ru

Abstract. A comparative study of the sensitivity to point vibration of a single-fiber optical cable with standard single mode optical fiber (SSMF) and with bend loss insensitive optical fiber (BLIF) was carried out. The measurement was carried out for a single vibration action – the fall of a kettlebell, and harmonic acoustic effects. During the experimental study, the advantage of the used optical cable with the bend loss insensitive optical fiber was revealed.

Keywords: fiber-optic reflectometers, optical fiber, Rayleigh scattering, DAS, fiber-optic acoustic distributed sensor

Citation: Pylaev V.E., Andreeva E.I., Experimental study of the use of optical cables with different types of fibers in monitoring systems, St. Petersburg State Polytechnical University Journal. Physics and Mathematics. 17 (3.1) (2024) 243–246. DOI: https://doi.org/10.18721/JPM.173.149

Материалы конференции
УДК 681.7
DOI: https://doi.org/10.18721/JPM.173.149

Экспериментальное исследование использования оптических кабелей с различными типами волокон в системах мониторинга

В.Е. Пылаев [1] ✉, Е.И. Андреева [1]

[1] Санкт-Петербургский государственный университет телекоммуникаций им. проф. М. А. Бонч-Бруевича, Санкт-Петербург, Россия

✉ me022@mail.ru

Аннотация. Представлены результаты сравнительного экспериментального исследования чувствительности к локальному вибровоздействию одноволоконного оптического кабеля со стандартным волоконным световодом и световодом с уменьшенными потерями на изгибах. Исследование проводилось для единичного вибрационного воздействия – падения гири и гармонического акустического воздействия. В ходе экспериментального исследования выявлено преимущество использования оптического кабеля с волоконным световодом с уменьшенными потерями на изгибах.

Ключевые слова: волоконно-оптические рефлектометры, волоконный световод, рэлеевское рассеяние, DAS, волоконно-оптический акустический распределенный датчик

Ссылка при цитировании: Пылаев В.Е., Андреева Е.И. Экспериментальное исследование использования оптических кабелей с различными типами волокон в системах мониторинга // Научно-технические ведомости СПбГПУ. Физико-математические науки. 2024. Т. 17. № 3.1. С. 243–246. DOI: https://doi.org/10.18721/JPM.173.149

Introduction

The distributed fiber-optic physical field sensors occupy a special place among sensor systems and represent the wide class of devices for the wide range of applications. The advantages of fiber-optic sensors over electrical ones are the possibility of the completely passive design, variety of shapes, immunity to electromagnetic interference and aggressive environments [1–5], small size and weight. As a result, they can be used in explosive atmospheres, flammable mixtures and strong electromagnetic fields [1–5]. Such fiber systems consist of the sensitive element - a conventional optical fiber - and the unit for generating an optical probing signal and analyzing the signal backscattered in the optical fiber. The operating principle is based on the time domain reflectometry technique (Optical Time Domain Reflectometer, OTDR). Local measurement of physical parameters using such sensors makes it possible to monitor in real time.

The purpose of this work is to study the influence of the choice of the optical fiber as part of the distributed sensor system on its parameters and the possibility of increasing spatial resolution when testing the object with the coherent reflectometer due to the optimal choice of the optical fiber.

Experimental study

At the test site, a trench was dug in the ground 120 cm deep, 30...40 cm wide, 30 m long. An optical cable was laid into the trench every 30 cm in height, starting from the bottom of the trench and covered with soil. After compacting the optical cable with soil, a period of 2 ... 3 weeks was maintained in the trench to stabilize the system parameters. The schematic block diagram of the measuring stand is shown in Fig. 1.

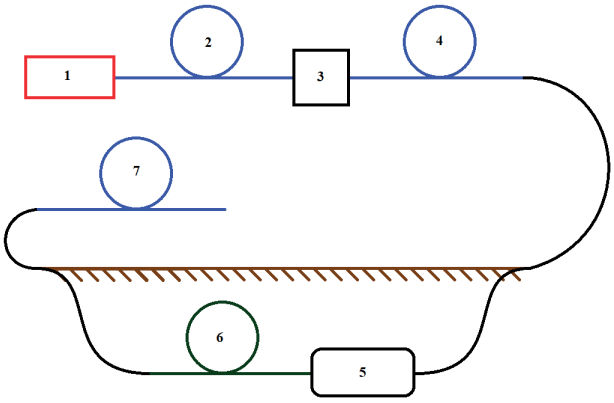

Fig. 1. Structural block diagram of the measuring stand: *1* – coherent optical reflectometer Danube, *2* – optical fiber, *3* – optical 19” cross-panel, *4* – multi-fiber optical cable, *5* – optical coupling for splicing a multi-fiber fiber-optic cable with test samples of optical cables in the trench, *6* – optical cable (segment) under test, *7* – optical fiber

The tested optical cable *6*, using an optical coupling *5*, was commutated with a multi-fiber trunk cable *4*, connected through a normalizing coil *3* to the coherent reflectometer *1*. An effect is made next to the cable: turning on sound at various frequencies from a reference frequency generator (Fig. 2).

To create a vibration-acoustic effect, an acoustic system was used, to which a harmonic signal was supplied. Signal frequencies varied from 5 Hz to 200 Hz

Results and Discussion

The tested optical cable samples differed in the type of optical fiber. In the first case, a standard optical fiber (SSMF, Standard Singlemode Fiber) was used, in the second case, a optical fiber with reduced bending losses (BLIF, bending-loss insensitive single-mode optical fiber) was used (Fig. 3, 4). Fiber parameters: dispersion D = 16.67 ps/nm/km (β_2 = 20 ps^2/km), loss 0.2 dB/km at operating wavelength λ = 1550 nm.

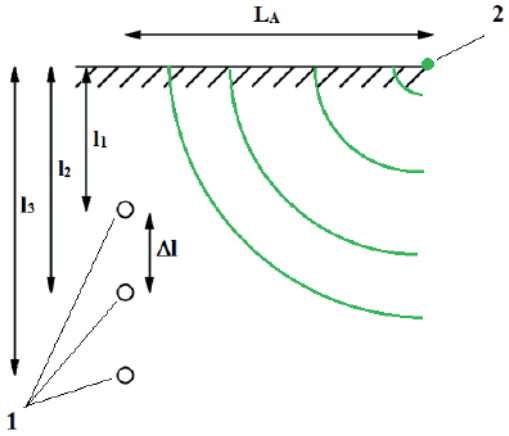

Fig. 2. Layout of the emitter and the optical cable under test: *1* – simplex optical cable, *2* – speaker

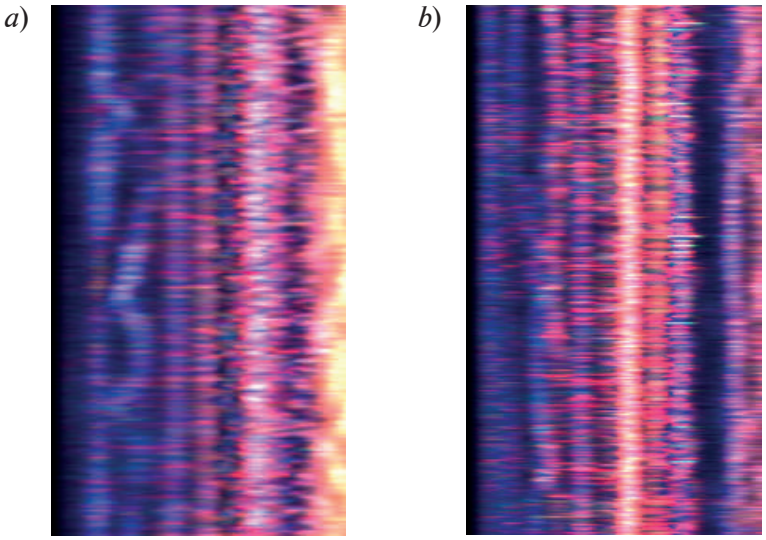

Fig. 3. "Waterfall" when recording vibration effects with an optical cable with a standard optical fiber (*a*) and with increased resistance to bending (*b*)

Table presents the results of measuring the response for the case of a weight (inert projectile) weighing 10 kg falling at a distance L_A = 10 m from the optical cable route.

Table

The effect of lens voltage on the structure size

Optical Fiber	Depth *l*, cm		
	l_1 =60 cm	l_2 = 90 cm	l_3 = 120 cm
SSMF	9.3	3.5	1.9
BLIF	9.4	7.0	5.6

The table shows that for the dumbbell weighing 10 kilograms, the signal energy is greater, therefore the effect is better discernible if the bend loss insensitive optical fiber is used as the sensor element.

The maximum permissible detection range is also longer for the optical cable with bend loss insensitive optical fiber.

Conclusion

The comparative study of the sensitivity to point vibration effects of a single-fiber optical cable with the standard optical fiber and bend loss insensitive optical fiber was carried out. The measurements were carried out for a single vibration impact - dropping the weight, and harmonic acoustic impact. An experimental study revealed the advantage of using an optical cable with the bend loss insensitive optical fiber.

REFERENCES

1. **Zhu H., Liu W., Wang T., Su J., Shi B.,** Distributed Acoustic Sensing for Monitoring Linear Infrastructures: Current Status and Trends, Sensors. (19) (22) (2022) 7550–7571

2. **Kharasov D.R., Fomiryakov E.A., Bengalskii D.M., Nikitin S.P., Nanii O.E., Treshchikov V.N.,** Distributed Acoustic Sensing over 146 km using Phase-sensitive Optical Time-domain Reflectometer assisted by bidirectional distributed Raman amplifier, 2022 International Conference Laser Optics (ICLO). IEEE, 2022.

3. **Nikitin S., Fomiryakov E., Kharasov D., Nanii O., Treshchikov V.,** Characterization of ultra-narrow linewidth lasers for phase-sensitive coherent reflectometry using eom facilitated heterodyning. Journal of Lightwave Technology. (38) (6) (2019) 1446–1453.

4. **Andreev D., Andreeva E., Podnikolenko A.,** Finding the Route of Laying the Optical Cable Using the Coherent Reflectometer. 2022 International Conference Laser Optics (ICLO). (2022) 1–1.

5. **Andy Lämmerhirt, Max Schubert, Bernd Drapp, Rene Zeilinger,** Fiber Optic Sensing for Railways – Ready to use?! SIGNAL + DRAHT. (114) (09) (2022) 60–69.

THE AUTHORS

PYLAEV Vadim E.
vadik.pylaev@mail.ru
ORCID: 0009-0002-4770-8738

ANDREEVA Elena I.
me022@mail.ru
ORCID: 0000-0002-1945-1050

Received 12.07.2024. Approved after reviewing 23.07.2024. Accepted 27.07.2024.

Conference materials
UDC 544.032.65
DOI: https://doi.org/10.18721/JPM.173.150

A study of laser cleaning of paper with fat-containing contaminations

A.D. Neelova [1] ✉, T.K. Lepekhina [1], D.V. Zhurba [2, 1],
V.I. Almiashev [1], V.A. Aseev [2], V.A. Parfenov [1]

[1] St. Petersburg Electrotechnical University "LETI", St. Petersburg, Russia;
[2] ITMO University, St. Petersburg, Russia
✉ angelina.neelova@gmail.com

Abstract. This paper is devoted to investigation of laser cleaning of paper with fat-containing contaminations. In recent years, laser technologies have been widely used in the preservation of Cultural Heritage (CH). One of the main fields of laser application in this area is the cleaning of CH objects from natural and anthropogenic contaminations. It is known that there exist two main approaches to the laser cleaning, e.g. dry cleaning and wet cleaning. We will present experimental results of wet laser cleaning with the Ytterbium fibre laser (wavelength of 1064 nm) of fat-containing contaminations from model samples and fragments of a real historical artefact such as XIXth century book.

Keywords: heritage science, laser application, laser cleaning

Citation: Neelova A.D., Lepekhina T.K., Zhurba D.V., Almiashev V.I., Aseev V.A., Parfenov V.A., A study of laser cleaning of paper with fat-containing contaminations, St. Petersburg State Polytechnical University Journal. Physics and Mathematics. 17 (3.1) (2024) 247–251. DOI: https://doi.org/10.18721/JPM.173.150

Материалы конференции
УДК 544.032.65
DOI: https://doi.org/10.18721/JPM.173.150

Исследование лазерной очистки бумаги от жиросодержащих загрязнений

А.Д. Неелова [1] ✉, Т.К. Лепехина [1], Д.В. Журба [2, 1],
В.И. Альмяшев [1], В.А. Асеев [2], В.А. Парфенов [1]

[1] Санкт-Петербургский государственный электротехнический университет «ЛЭТИ» им. В.И.Ульянова (Ленина), Санкт-Петербург, Россия;
[2] Университет ИТМО, Санкт-Петербург, Россия
✉ angelina.neelova@gmail.com

Аннотация. Данная работа посвящена исследованию лазерной очистки бумаги от жиросодержащих загрязнений. В последнее время лазерные технологии находят все более широкое применение в сохранении культурно-исторического наследия. Одним из главных направлений применения является лазерная очистка объектов культурно-исторического наследия от природных и антропогенных загрязнений. Известны два подхода к лазерной очистке: сухая очистка и влажная. В данной работе редставлены результаты использования технологии влажной лазерной очистки иттербиевым волоконным импульсным лазером с длиной волны 1064 нм модельных образцов и исторического артефакта такого, как книга XIX века.

Ключевые слова: культурно-исторические наследие, лазерная очистка, применение лазеров

Ссылка при цитировании: Неелова А.Д., Лепехина Т.К., Журба Д.В., Альмяшев В.И., Асеев В.А., Парфенов В.А. Исследование лазерной очистки бумаги от жиросодержащих загрязнений // Научно-технические ведомости СПбГПУ. Физико-математические науки. 2024. Т. 17. № 3.1. С. 247–251. DOI: https://doi.org/10.18721/JPM.173.150

Introduction

Laser technologies have recently begun to be widely embedded not only in industrial and scientific applications but also in the field of restoration and conservation of Cultural Heritage. Laser restoration of stone and metal monuments is the most well developed, while laser cleaning of CH objects made out of organic materials is still at the stage of experimental studies.

Studies conducted in the last decade have brought significant evidence that laser cleaning has a real potential for application in conservation of paper [1–3]. Laser irradiation could be used for treating various deteriorations such as dust, soot, fungi, foxings, etc.

Paper contaminations with fat-containing substances are highly widespread in conservation practice of books and documents on paper base. There could be found vegetable fat or animal fat, or a combination of both. For example, one of the most common contaminations of books and documents is “finger grip”, a trace of human skin oils. The removal of such contaminations by traditional conservation methods which imply using organic solvents that could be dangerous for the conservators is a laborious process. Moreover, such solvents could be damaging for the paper as well, which is unacceptable for rare CH objects on paper base. Thus, developing a novel approach to the described problem is an actual scientific task.

The authors of this work have already reported about laser cleaning of different kinds of paper using pulsed Ytterbium fibre laser with the wavelength of 1064 nm [3–5]. Earlier authors presumed that laser cleaning is suitable only for surface paper contaminations. However, it could be different in case of laser cleaning with the use of auxiliary liquid (for example distilled water), so called wet cleaning. The technology of wet laser cleaning is well-known in the field of cleaning stone and metal [6]. Wet laser cleaning is reported to serve not only for removing surface contaminations but also to clean contaminations that are in some depth of the material. Given technology also could be more delicate for the treated material.

The purpose of this work is to investigate the technology of wet laser cleaning of paper from fat-containing contaminations at 1064 nm with pulsed Ytterbium fibre laser performed on paper samples and real historical artefacts.

Experiment

During the experiment model paper samples as well as fragments of a real historical artefact were cleaned with laser irradiation and later studied. Model paper samples were purposefully prepared beforehand. To imitate fat contamination copy paper samples were soaked in olive and castor oils and then put into thermal cabinet with the temperature of 102–104 °C for 12 days. The latter was performed to simulate the process of paper ageing. Fragments of a real artefact, a book of religious content published in the XIXth century, were laser treated as well. Given fragments were contaminated with lamp oil, wax and traces of soot. In the process of wet laser cleaning 5% aqueous solution of sodium hydrogen carbonate ($NaHCO_3$) served as an auxiliary liquid, which is widely used in conservation practice for removing fat contaminations from paper. It is known that sodium hydrogen carbonate decomposes under the temperature higher than 60 °C into sodium carbonate, water and carbon dioxide. By using thermal processes that occur during laser ablation we can achieve such chemical reaction to “whip out” fat molecules from paper fibres.

In the work a laser system with the Ytterbium fiber laser source (1064 nm) was used. The “MiniMarker” laser apparatus is commercially available marking laser system produced by “Laser Center”, Ltd., Saint Petersburg.

To evaluate the results of wet laser cleaning of paper optical microscopy as well as scanning electron microscopy were used.

Results and Discussion

Preliminary study of reflectance of model paper samples contaminated with oils gave us information that dry laser cleaning could not give positive results due to the fact that on the working wavelength of laser (1064 nm) paper samples reflect nearly 90% of the irradiation. Reflection spectra of an artefact paper showed the same results. The fact was proved empirically on paper samples.

Since the dry laser cleaning was proved not to be an option the authors decided to consider the technology of wet laser cleaning. In case of wet laser cleaning, it was shown that use of laser irradiation with following parameters: wavelength of 1064 nm, pulse duration of 100 ns, peak power density from $1.4 \cdot 10^5$ W/cm^2 to $2.0 \cdot 10^5$ W/cm^2, the pulse repetition frequency of 20 kHz makes possible an effective removal of fat-containing contaminants. The laser system is equipped with the preinstalled scanning system. Scanning parameters for laser cleaning are as follows: beam scanning speed of 800 mm/s with the filling of 40 lines per millimetre. Wet laser cleaning performed on the model paper samples was a success, thus, it became possible to clean an artefact as well. Laser cleaning of fragments of the historical book showed positive results. As it could be seen in Fig. 1, *b* treated areas were considerably lightened in colour, which imply that the lamp oil was successfully removed. Moreover, it was noticed that wax contamination was removed as well (Fig. 1, *c*). There are no noticeable damages on the images by optical microscope.

Fig.1. Fragment of artefact book after laser cleaning (*a*). Cleaned areas are marked in red. Images by optical microscope of laser treated areas with lamp oil (*b*) and wax (*c*)

Images obtained by the means of scanning electron microscopy (SEM) proved that the laser cleaning of model samples from oils was efficient (Fig. 2). It could be noted that there are no damages to the paper structure of paper samples (Fig. 2, *b*).

On the left side of the SEM-image it could be noted that paper fibres are coated with contaminations whereas on the left deteriorated layer is removed. In addition, it could be noted that laser irradiation caused no damage to the paper fibres.

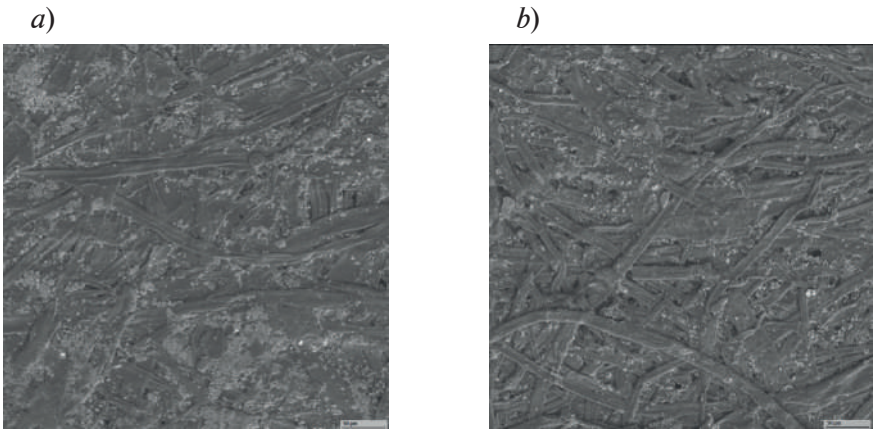

Fig.2. SEM-images of model samples before (*a*) and after laser cleaning (*b*) from fat-containing contaminations

SEM-images of laser treated fragment of the artefact proved that the laser cleaning was efficient (Fig. 3, *a*). On the left side of the SEM-image (Fig. 3, *a*, *b*) it could be noted that paper fibres are coated with contaminations consisted of oil and wax with traces of soot whereas on the left the deteriorated layer is removed. In addition, it could be noted in Fig. 3, *c* that laser irradiation caused no damage to the paper fibres and paper structure as a whole.

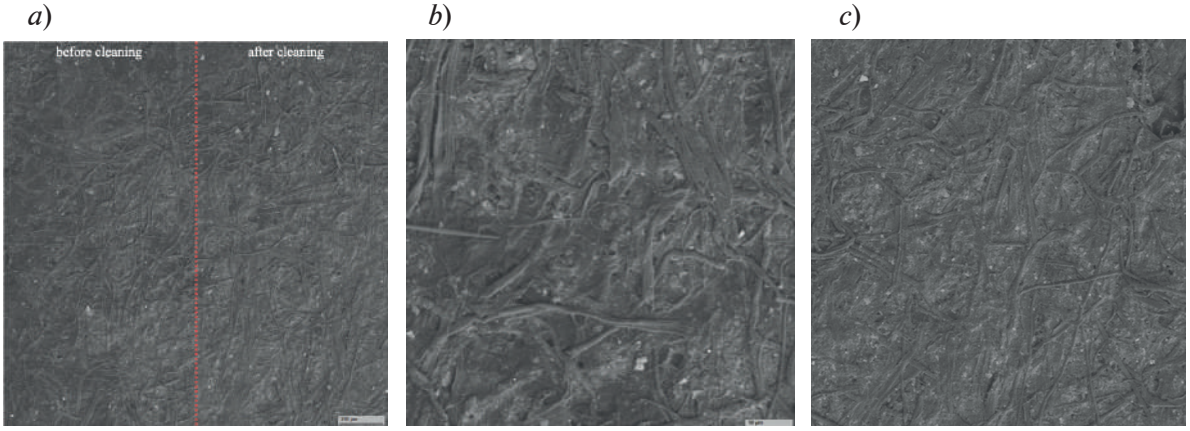

Fig.3. SEM-image of a fragment of the artefact book with the areas before (left) and after (right) laser cleaning (*a*) from fat-containing contaminations. It could be noted that fibres are coated with contaminated layer (*a* and *b*). Fragment of the book after laser treatment (*c*)

During the experiment FTIR spectroscopy was performed for the fragments of the artefact. By comparing spectra of laser treated fragments and non-treated it could be concluded that contaminated layer was removed successfully since there are no peaks that characterise the substances of contamination layer.

Conclusion

Removing fat-containing contaminations from paper showed the advantage of wet laser cleaning of paper in relation to the given task. Paper samples as well as fragments of an artefact were successfully cleaned from lamp oil and wax during the experiment with the use of 5% aqueous solution of sodium hydrogen carbonate as an auxiliary liquid. Investigation of laser treatment results by means of optical microscopy and scanning electron microscopy showed no damage to the paper structure and fibres after laser treatment. FTIR spectroscopy proved the efficacy of laser treatment.

To conclude, wet laser cleaning of paper from fat-containing contaminations is proven to be a novel and efficient solution to the very apparent problem in conservation practice. It showed that laser cleaning could be applied not only for surface contaminations but also to the ones that go deep into material such as fat-containing contaminations.

Nevertheless, further investigations of the application of wet laser cleaning for restoration and conservation of Cultural Heritage objects consisted of organic materials are needed as well as studies of the laser irradiation influence on such materials, their chemical and mechanical and other properties.

Acknowledgments

SEM studies were carried out in the electron microscopy laboratory of the Department of Electronic Instruments and Devices of St. Petersburg Electrotechnical University with the support of the Department of Physical Chemistry and a strategic partnership with the Federal state unitary entreprise “Alexandrov Research Institute of Technology”. The authors express their gratitude to N.N. Potrakhov D.Sc. for assistance in organasing the research.

REFERENCES

1. **Kautek W., Fotakis C., Anglos D., Zafiropulos V., et al.,** CRC Press, Taylor & Francis Group, Boca Rayton (USA), 2007.

2. **Mokrushin Yu.M., Parfenov V.A.,** Use of copper-vapor laser for restoration of artworks. Journal of Optical Technology. 7 (75) 2008, 476–477.

3. **Parfenov V., Galushkin A., Tkachenko T., Aseev V.,** Laser Cleaning as Novel Approach to Preservation of Historical Books and Documents on a Paper Basis. Quantum Beam Science. 3 (6) 2022, Pp. 23.

4. **Cooper M.,** Laser Cleaning in Conservation: An Introduction. Oxford: Butterworth-Heinemann. 1998.

5. **Neelova A.D., Shepilova E.M., Nosova E.I., Rongonen S.L., Parfenov V.A.,** A study of chemical and mechanical properties of paper under its laser cleaning, St. Petersburg State Polytechnical University Journal. Physics and Mathematics. 16 (3.2) (2023) 114–119.

THE AUTHORS

NEELOVA Angelina D.
angelina.neelova@gmail.com
ORCID: 0009-0004-8098-2055

ALMIASHEV Vyacheslav I.
vac@mail.ru
ORCID: 0000-0002-7376-2263

LEPEKHINA Tatiana K.
tanialep@mail.ru
ORCID: 0009-0009-8987-4698

ASEEV Vladimir A.
assev@oi.ifmo.ru
ORCID: 0000-0003-4098-2136

ZHURBA Danila V.
zhurba.danila306@ya.ru
ORCID: 0009-0001-6814-1737

PARFENOV Vadim A.
vadim_parfenov@mail.ru
ORCID: 0000-0002-2048-4677

Received 16.07.2024. Approved after reviewing 27.08.2024. Accepted 03.09.2024.

Conference materials
UDC 535.015
DOI: https://doi.org/10.18721/JPM.173.151

Investigation of the possibility of creating a broadband measuring source using the nonlinear properties of an optical fiber

E.I. Andreeva [1] ✉, D.P. Andreev [1, 2], M.A. Orlov [1], A.I. Isupov [1]

[1] Bonch-Bruevich St. Petersburg State University of Telecommunications, St. Petersburg, Russia;

[2] St. Petersburg Polytechnic University, St. Petersburg, Russia

✉ me022@mail.ru

Abstract. A computer simulation and experimental study of a broadband laser source for testing fiber-optic communication systems has been conducted. The study investigated the use of nonlinear optical effects in fiber to expand the spectrum of a laser source. Two types of fiber were compared: standard single-mode fiber (SSMF) and dispersion shifted fiber (DSF), to determine the best parameters for the source.

Keywords: fiber-optic communication system, Wavelength Division Multiplexing, optical fiber, nonlinear effects

Citation: Andreeva E.I., Andreev D.P., Orlov M.A., Isupov A.I., Investigation of the possibility of creating a broadband measuring source using the nonlinear properties of an optical fiber, St. Petersburg State Polytechnical University Journal. Physics and Mathematics. 17 (3.1) (2024) 252–256. DOI: https://doi.org/10.18721/JPM.173.151

Материалы конференции
УДК 535.015
DOI: https://doi.org/10.18721/JPM.173.151

Исследование возможности создания широкополосного измерительного источника с использованием нелинейных свойств оптического волокна

Е.И. Андреева [1] ✉, Д.П. Андреев [1, 2], М.А. Орлов [1], А.И. Исупов [1]

[1] Санкт-Петербургский государственный университет телекоммуникаций им. проф. М.А. Бонч-Бруевича, Санкт-Петербург, Россия;

[2] Санкт-Петербургский политехнический университет Петра Великого, Санкт-Петербург, Россия

✉ me022@mail.ru

Аннотация. Проведено компьютерное моделирование и экспериментальное исследование широкополосного измерительного лазерного источника для тестирования спектрально-селективных компонентов волоконно-оптических систем связи с мультиплексированием по длине волны. Показано, что за счет использования нелинейных эффектов в оптоволокне можно добиться многократного расширения спектра лазерного источника. Проведено сравнение параметров таких источников в случае использования стандартного одномодового волокна (SSMF) и волокна со смещенной дисперсией (DSF).

Ключевые слова: ВОЛС, мультиплексирование по длине волны, WDM, волоконный световод, нелинейные эффекты, спектр

Ссылка при цитировании: Андреева Е.И., Андреев Д.П., Орлов М.А., Исупов А.И. Исследование возможности создания широкополосного измерительного источника с использованием нелинейных свойств оптического волокна // Научно-технические ведомости СПбГПУ. Физико-математические науки. 2024. Т. 17. № 3.1. С. 252–256. DOI: https://doi.org/10.18721/JPM.173.151

Introduction

The development of fiber-optic communication systems with wavelength division multiplexing has led to the development and implementation of a wide class of passive spectral-selective devices for such systems [1-5]. Measurement sources such as ASE are traditionally used to measure the spectral bandwidth of spectrally selective passive elements of fiber-optics communication system. They provide a wide spectral band at a relatively high power of optical radiation. Broadband sources, complete with spectrally selective meters, such as an optical spectrum analyzer (OSA), allow you to visualize the results of measuring the bandwidth of the device under test. Narrow-band lasers, complete with broadband measuring power (OPM, Optical Power Meter) are used for accurate measurements of device operating parameters. In this case, the optical power meter must have either a smooth spectral sensitivity characteristic, or the possibility of considering its non-uniformity using calibration coefficients in each spectral range.

The aim of this work is to study the possibility of creating a broadband measuring source using a semiconductor laser and the nonlinear properties of an optical fiber.

Theory

Semiconductor lasers make it possible to obtain the high optical power pulses in the single-mode optical fiber; the Kerr nonlinearity effect makes it possible to achieve the significant broadening of their spectrum. Depending on the initial laser energy pulse parameters, the characteristics and length of the optical fiber, the broadband spectrum source can be obtained. Analytical description of nonlinear effects is possible only in some special cases. In this regard, of particular importance is the possibility of computer simulation of the effect of nonlinear broadening of the laser radiation spectrum in an optical fiber, considering optical power losses and group velocity dispersion.

The propagation equation in the case where losses can be neglected has the form of [1–2]

$$i\frac{\partial A}{\partial z} = \frac{1}{2}\beta_2 \frac{\partial^2 A}{\partial t^2} - \gamma |A|^2 A, \quad (1)$$

is the nonlinear Schrödinger equation, where $A(z, t)$ is the amplitude of the wave packet envelope, z, t are the spatial and time coordinates, β_2 is the value of the dispersion of group velocities, γ is the nonlinearity parameter in the case of self-phase modulation.

If the propagation distance $L \ll L_D$, but $L \gtrsim L_{NL}$, then in this case the effect of self-phase modulation determines the evolution of the pulse in the optical fiber, leading to spectral broadening of the pulse. The mode in which the nonlinearity dominates always takes place when

$$\frac{L_{NL}}{L_D} = \frac{|\beta_2|}{\gamma P_0 T_0^2} \ll 1, \quad (2)$$

In the approximation of the absence of group velocity dispersion ($\beta_2 = 0$) and optical power loss ($\alpha = 0$) for a pulse with a Gaussian envelope profile

$$A(0,t) = e^{\frac{t^2}{2\tau_0^2}}.$$

For a Gaussian pulse, the broadening of the spectrum caused by the self-phase modulation effect, $\delta\omega_{NL}$ is equal to

$$\delta\omega_{NL} = \sqrt{\frac{2}{e}}\frac{z}{L_{NL}}\Delta\omega_0.$$

The broadening coefficient of the pulse spectrum K can be determined by the approximate expression

$$K = \sqrt{\frac{2}{e}}\frac{z}{L_{NL}}.$$

Computer simulation

The computer simulation of the effect of nonlinear broadening of the laser spectrum in the optical fiber was made with considering optical power losses and group velocity dispersion. The optical simulation block diagram (Fig. 1) contains of the picosecond pulses source (*1*), optical preamplifier (booster) (*2*), standard single mode optical fiber (SSMF) or dispersion shifted fiber (DSF) (*3*), demultiplexer (*4*) (with $\Delta f = 100$ GHz, for example) and optical spectrum analyzer (5).

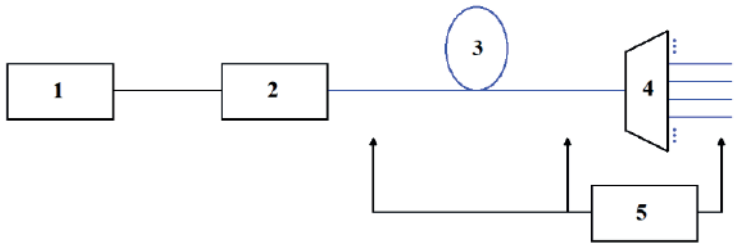

Fig. 1. The optical block diagram of the computer simulation: *1* – laser, *2* – optical amplifier, *3* – optical fiber, *4* – demultiplexer, *5* – optical spectrum analyzer

Picosecond pulses from the laser (*1*) after amplification (*2*) are fed to the input of the SSMF or DSF (*3*). The input power P_0 of the optical pulses was selected to be sufficient for the formation of a high-order soliton (Eq. 2). Such pulse undergoes self-compression with a significant broadening of the spectrum. The simulation was carried out under the condition of a slight change in the envelope of the optical pulse ($z < (L_D L_{NL})^{1/2}$) [2].

The spatial dynamics of the spectrum broadening as it propagates along the optical fiber is shown in Figure 2. The monotonic broadening of the initial spectrum corresponds to the calculations. Envelope of the optical pulse remained the same.

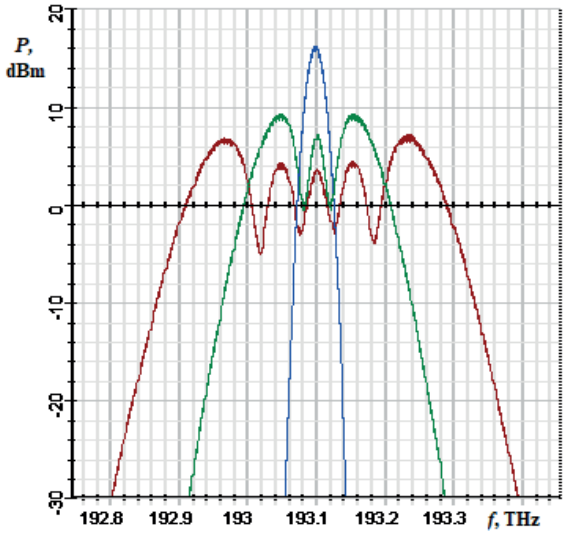

Fig. 2. The spectrum of the pulse at the entrance to the optical fiber (1) and after passing 1.2 km (2) and 2 km (3)

Thus, computer modeling has shown that the numerical estimates for K obtained in the approximation of the absence of dispersion of the second and higher order, as well as other nonlinear effects, can be used to qualitatively describe the broadening of the spectrum in an optical fiber.

Experimental Results and Discussion

The experimental setup included the laser source, the narrow-band filter, Er-amplifier, the standard optical fiber and the optical spectrum analyzer. Operating wavelength of the laser $\lambda = 1546.12$ nm (39th DWDM channel). Fiber optic parameters: dispersion $D = 16.67$ ps/nm/km ($\beta_2 = -20$ ps^2/km), Kerr nonlinearity coefficient $\gamma = 1.2$ W^{-1}km^{-1} loss 0.2 dB/km. The Previal erbium amplifier provided 24 dBm of optical power in the optical fiber. Results are presented at Fig. 3.

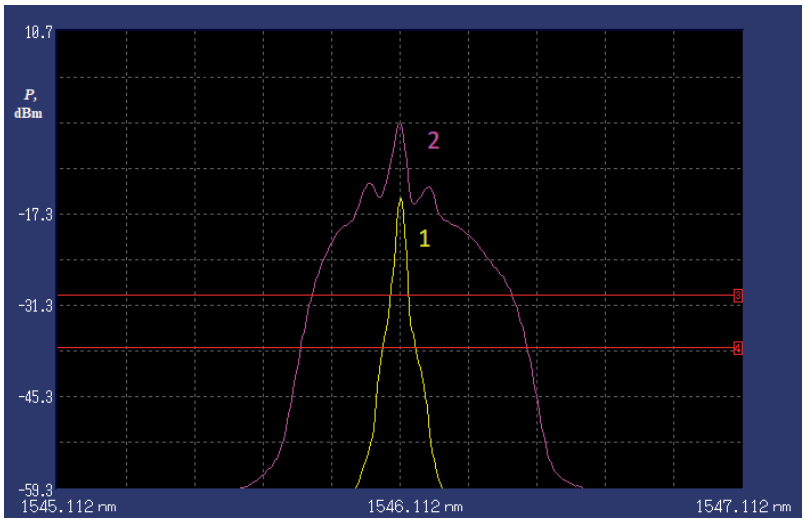

Fig. 3. Optical signal spectrum at the output of the optical fiber without an amplifier (1) and with an amplifier (2)

Studies have shown that to achieve greater spectral width at the output of the optical fiber, it is necessary to use a laser with a narrow spectrum to input radiation. Notch filters can be used to improve efficiency.

Conclusion

Thus, it has been shown that, due to the use of nonlinear effects in an optical fiber, it is possible to achieve a multiple broadening of the spectrum of a laser source.

Computer simulation confirmed the possibility of obtaining a broadband source. Spectrum broadening can be achieved by using a longer optical fiber. With a fixed optical fiber length, a wider spectrum is achieved with more input power. A smoother spectral response is achieved with DSF. With SSMF, a slightly higher optical signal power is required to achieve the same bandwidth as with DSF.

REFERENCES

1. **Agrawal G.,** Fiber-Optics Communication Systems, 5th Edition - New York. 2021.

2. **Agrawal G.,** Nonlinear Fiber Optics, / G. Agrawal // 6th Edition – Elsevier. 2019.

3. **Shcherbakov A.S., Andreeva E.I.,** Performance Data of Lengthy-Span Soliton Transmission System, Andreeva, Optical Fiber Technology. 2 (1) (1996) 127–133.

4. **Agrawal G.,** Nonlinear fiber optics: its history and recent progress, Opt. soc. Am. B.J. 28 (12) (2011) 1–10.

5. **Andreeva E.I., Bylina M.S., Glagolev S.F., Chaimardanov P.A.,** Properties of Temporary Optical Solitons in Optical Fibers and the Possibility of their Use in Telecommunications, Proceedings of Telecommunication Universities. 4 (1) (2018) 5–12.

THE AUTHORS

ANDREEVA Elena I.
e-andreeva-spb@yandex.ru
ORCID: 0000-0002-1945-1050

ANDREEV Dmitry P.
me022@mail.ru
ORCID: 0000-0001-8541-9916

ORLOV Mikhail A.
miha5033@yandex.ru
ORCID: 0009-0001-3075-9558

ISUPOV Alexander I.
is.alex60@gmail.com
ORCID: 0009-0006-2681-3562

Received 17.07.2024. Approved after reviewing 12.08.2024. Accepted 12.08.2024.

PHYSICAL MATERIALS TECHNOLOGY

Conference materials
UDC 535.342
DOI: https://doi.org/10.18721/JPM.173.152

Spectral and photocatalytic properties of Ag-AgCl nanostructures formed on surface of silicate glass by ion exchange

D.V. Marasanov [1] ✉, I.N. Litunovskiy [1], V.V. Pesnyakov [1],
Y.M. Sgibnev [1], N.V. Nikonorov [1]

[1] ITMO University, St. Petersburg, Russia
✉ dmitriymarasanov@bk.ru

Abstract. In this work, the spectral and photocatalytic properties of 3 silicate glasses with different chlorine concentrations from 0.5 to 1 mol. % were studied. Since photocatalysts require the presence of nanostructures on the glass surface, silver was introduced into silicate glass with chlorine by low-temperature Na^+-Ag^+ ion exchange. The synthesis of Ag-AgCl nanostructures occurred during heat treatment, after which a plasmonic absorption band in the visible range of the spectrum was revealed in the absorption spectra. The degree of decomposition of the aqueous solution of methyl orange dye increased from 80 to 92% with increasing chlorine concentration in the photocatalyst with Ag-AgCl nanostructures. Note that with increasing chlorine concentration, the concentration of nanostructures increases.

Keywords: ion exchange, nanostructures, nanocrystals, silver, absorption, photocatalysis

Funding: This study was funded by Russian Science Foundation grant No. 20-19-00559.

Citation: Marasanov D.V., Litunovskiy I.N., Pesnyakov V.V., Sgibnev Y.M., Nikonorov N.V., Spectral and photocatalytic properties of Ag-AgCl nanostructures formed on surface of silicate glass by ion exchange, St. Petersburg State Polytechnical University Journal. Physics and Mathematics. 17 (3.1) (2024) 257–260. DOI: https://doi.org/10.18721/JPM.173.152

Материалы конференции
УДК 535.342
DOI: https://doi.org/10.18721/JPM.173.152

Спектральные и фотокаталитические свойства наноструктур Ag-AgCl, сформированных на поверхности силикатного стекла ионным обменом

Д.В. Марасанов [1] ✉, И.Н. Литуновский [1], В.В. Песняков [1],
Е.М. Сгибнев [1], Н.В. Никоноров [1]

[1] Университет ИТМО, Санкт-Петербург, Россия
✉ dmitriymarasanov@bk.ru

Аннотация. В данной работе были исследованы спектральные и фотокаталитические свойства 3 силикатных стекол с разной концентрацией хлора от 0,5 до 1 мол. %. Так как для фотокатализаторов необходимо наличие наноструктур на поверхности стекла серебро в силикатное стекло с хлором вводилось низкотемпературным ионным обменом Na^+-Ag^+. Синтез наноструктур Ag -AgCl происходил в процессе термической обработки, после чего на спектрах поглощения выявлена плазмонная полоса поглощения в видимом диапазоне спектра. Степень разложения водного раствора красителя метилоранжа увеличивалась с 80 до 92% с увеличением концентрации хлора в фотокатализаторе

с наноструктурами Ag-AgCl. Отметим, что при увеличении концентрации хлора концентрация наноструктур растет.

Ключевые слова: ионный обмен, наноструктуры, нанокристаллы, серебро, поглощение, фотокатализ

Финансирование: Работа выполнена при финансовой поддержке Российского Научного Фонда (проект № 20-19-00559).

Ссылка при цитировании: Марасанов Д.В., Литуновский И.Н., Песняков В.В., Сгибнев Е.М., Никоноров Н.В. Спектральные и фотокаталитические свойства наноструктур Ag-AgCl, сформированных на поверхности силикатного стекла ионным обменом // Научно-технические ведомости СПбГПУ. Физико-математические науки. 2024. Т. 17. № 3.1. С. 257–260. DOI: https://doi.org/10.18721/JPM.173.152

Introduction

Currently, photocatalysts are being actively developed and used in various fields of science, technology and medicine. However, the quantum efficiency of modern photocatalysts is relatively low. This is mainly due to recombination processes between electrons in the conduction band and holes in the valence band, which arise under the influence of light. One of the most promising methods for suppressing recombination processes is the creation of noble metal nanoparticles in the photocatalyst matrix, which act as electron "suppressors".

The photocatalytic properties of Ag-AgBr and Ag-AgCl structures were previously studied by other authors [1–3]. Thus, according to [2], a photocatalyst with Ag-AgBr particles is capable of decomposing more than 80% of methyl orange dye in 2 minutes under solar radiation. However, the properties of Ag-AgCl photocatalyst based on sodium silicate glass have not yet been studied.

Since the presence of nanoparticles on the glass surface is important for photocatalytic applications, a promising tool for introducing silver into the glass composition is the ion exchange method. Ion exchange is a versatile and cost-effective method that allows for the precise incorporation of silver ions (Ag^+) into the glass matrix, followed by them in situ into Ag-AgCl nanostructures under controlled heat treatment conditions [4]. This method not only ensures uniform distribution of nanostructures but also enables the tuning of their size and density [5].

The aim of this paper is study of the spectral and photocatalytic properties of a photocatalyst with Ag-AgCl nanostructures in ion-exchange layers of sodium silicate glass.

Materials and Methods

The photocatalyst was created based on a matrix of sodium silicate glass Na_2O–ZnO–Al_2O_3–SiO_2–F doped with CeO_2, Sb_2O_3, Cl. The Cl concentration in the glass was 0.5, 0.75 and 1 mol. %. The 1 mm thick sample was carefully ground and polished.

The next step was to perform ion exchange on the sample in the $AgNO_3/NaNO_3$ melt (5 mol.%/95 mol.%, respectively). Ion exchange was carried out at 320 °C for 15 minutes.

The last stage of sample preparation was additional heat treatment of the sample above the glass transition temperature. The treatment temperature was 500 °C for 3 hours. After each stage, absorption spectra were measured.

The photocatalytic properties of the sample were then measured by measuring the absorption properties of an aqueous solution of methyl orange dye before and after irradiation. Its initial concentration was about 1 mg/100 ml of water. A laser with a wavelength of 405 nm was used to study the photocatalytic properties.

The solution together with the photocatalyst was subjected to broadband irradiation every 5 minutes. After each period, the absorption spectrum of the solution was measured. All spectra were measured using a Perkin-Elmer lambda 650 spectrophotometer.

The size of silver nanoparticles was calculated by Mie theory with using the following equation:

$$d = \frac{2v_F}{\Delta\omega}, \quad (1)$$

where d is the average diameter of silver nanoparticles, v_F is the Fermi velocity (1.39×10^8 cm/s for silver, $\Delta\omega$ is the half-width at half-height in the units of angular frequency.

Results and Discussion

To synthesize Ag-AgCl nanostructures, ion exchange was carried out on the surface of the sample, followed by heat treatment. Figure 1 shows the absorption spectra of the formed nanostructures. The position of this absorption peak (460 and 470 nm) of silver nanoparticles is slightly shifted to longer wavelengths relative to the spectrum of glass without chlorine from [3]. The displacement itself increases with increasing chlorine concentration to 0.75 mol.% and is caused by the growth of AgCl/NaCl shells around silver particles (Fig. 1, *a*). A further increase in concentration only leads to an increase in the absorption of nanostructures. The average diameter of the formed nanoparticles was calculated using the Mie theory (formula 1) and increased from 1.98 to 2.02 nm with increasing chlorine concentration. Note that there is a possibility of a growth in the size of the chlorine shell.

Note that during ion exchange, with increasing concentration, the depth of the layer itself increases due to the breaking of Si-O bonds by chlorine and, as a consequence, an increase in the diffusion coefficient of silver ions (Fig. 1, *b*).

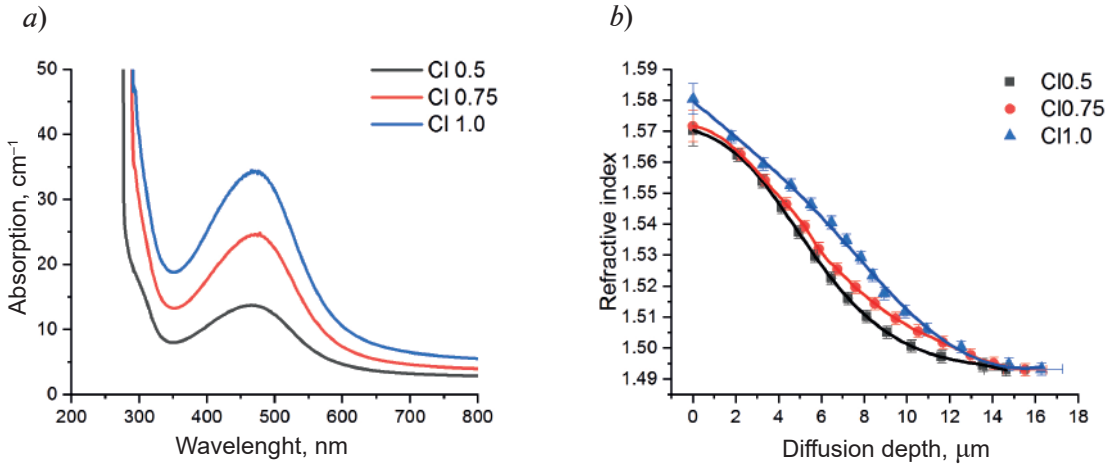

Fig. 1. Absorption spectrum for Ag-AgCl nanostructures in surface layer in silicate glass (*a*) and refractive index profiles of glasses with chlorine before heat treatment (*b*)

Figure 2 shows the dependence of the kinetics of degradation of an aqueous solution of methyl orange dye on the chlorine concentration. The amount of degradation of an aqueous solution of methyl orange dye was calculated from the ratio of the dye absorption amplitude after irradiation to the dye absorption amplitude before irradiation. The amount of degraded methyl orange dye increased with increasing chlorine concentration and amounted to 80 and 92%, respectively. The reason for the increase in the C/C_0 value is the formation of hot electrons on the surface of the sample due to the transfer of these charge carriers from silver chloride to silver nanoparticles, which enhance the effect of destruction of the dye molecule with increasing chlorine concentration. We also note that the low rate of photocatalytic reaction in samples with chlorine concentrations of 0.5 and 0.75 mol.% at the beginning of the experiment is possibly due to reabsorption of the dye on the surface. But further experiments are required to accurately interpret the data obtained.

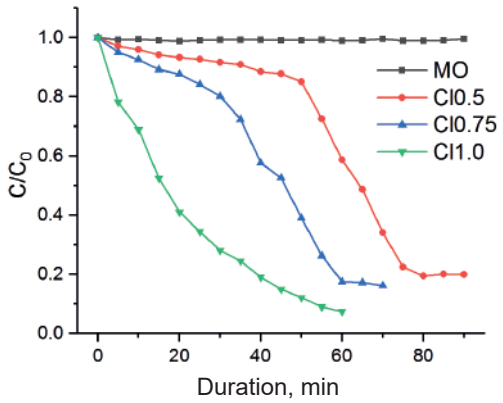

Fig. 2. The dependence of the kinetics of degradation of an aqueous solution of methyl orange dye on the chlorine concentration

Conclusion

The work assessed the photocatalytic degradation of an aqueous solution of methyl orange dye in the presence of a photocatalyst with Ag-AgCl nanostructures on the surface of silicate glass formed by the ion exchange method. It was shown that with increasing concentration of Ag-AgCl nanostructures, the C/C_0 ratio increases from 80% to 92%, associated with photocatalytic degradation of the dye.

REFERENCES

1. **Kuai L., Geng B., Chen X., Zhao Y., Luo Y.,** Facile subsequently light-induced route to highly efficient and stable sunlight-driven Ag–AgBr plasmonic photocatalyst, Langmuir. 26 (24) (2010) 18723–18727.

2. **Han L., Wang P., Zhu C., Zhai Y., Dong S.,** Facile solvothermal synthesis of cube-like Ag-AgCl: a highly efficient visible light photocatalyst, Nanoscale. 3 (7) (2011) 2931–2935.

3. **Li Q., Chang S., Wu D., Bao S., Zeng C., Nasir M., Tian B., Zhang J.,** Synthesis of cubic Ag-AgCl and Ag-AgBr plasmonic photocatalysts and comparison of their photocatalytic activity for degradation of methyl orange and 2, 4-dichlorophenol. Research on Chemical Intermediates. 44 (2018) 4651–4661.

4. **Marasanov D.V., Sgibnev Y.M., Nikonorov N.V.,** The Influence of Chlorides on the Spectral Properties of Ion-Exchange Layers of Photo-Thermo-Refractive Glass, Optics and Spectroscopy. 130 (6) (2022) 402–408.

5. **Sgibnev Y.M., Nikonorov N.V., Ignatiev A.I.,** High efficient luminescence of silver clusters in ion-exchanged antimony-doped photo-thermo-refractive glasses: Influence of antimony content and heat treatment parameters, Journal of Luminescence. 188 (2017) 172–179.

THE AUTHORS

MARASANOV Dmitriy V.
dmitriymarasanov@bk.ru

SGIBNEV Yevgeniy M.
sgibnevem@gmail.com

LITUNOVSKIY Igor N.
Litig2001@yandex.ru

NIKONOROV Nikolay V.
nikonorov@oi.ifmo.ru

PESNYAKOV Vladislav V.
v.pesnyackoff@yandex.ru

Received 06.07.2024. Approved after reviewing 12.08.2024. Accepted 12.08.2024.

Conference materials
UDC 539.216.1, 539.231, 543.424.2
DOI: https://doi.org/10.18721/JPM.173.153

Laser-stimulated tin-induced crystallization of silicon on flexible nonwoven substrates

A.M. Kartashova [1] ✉, A.A. Serdobintsev [1], L.D. Volkovoynova [1]

[1] Saratov State University, Saratov, Russia

✉ kartashovaam@sgu.ru

Abstract. The work is devoted to the formation of polycrystalline silicon coatings on electrospinned nonwoven polyacrylonitrile mats using a metal layer absorbing laser radiation. The results of experimental studies confirming the presence of crystallized silicon structures on nonwoven polymer substrates are presented. The efficiency of tin films with different thicknesses is compared when using them as upper laser-absorbing layers during laser-stimulated metal-induced crystallization of silicon. It was found out that during laser processing, the metal does not ablate completely and the remaining part of it is collected into particles, the size of which depends on the initial thickness of the metal film. It has also been established that during the laser annealing process expansion or glass transition of fibers can occur.

Keywords: nanofibrous nonwoven material, magnetron sputtering, laser-stimulated silicon crystallization, metal-induced silicon crystallization

Funding: This study was funded by the Russian Science Foundation (project No. 23-22-00047, https://rscf.ru/project/23-22-00047/).

Citation: Kartashova A.M., Serdobintsev A.A., Volkovoynova L.D., Laser-stimulated tin-induced crystallization of silicon on flexible nonwoven substrates, St. Petersburg State Polytechnical University Journal. Physics and Mathematics. 17 (3.1) (2024) 261–265. DOI: https://doi.org/10.18721/JPM.173.153

Материалы конференции
УДК 539.216.1, 539.231, 543.424.2
DOI: https://doi.org/10.18721/JPM.173.153

Лазер-стимулированная олово-индуцированная кристаллизация кремния на гибких нетканых подложках

А.М. Карташова [1] ✉, А.А. Сердобинцев [1], Л.Д. Волковойнова [1]

[1] Саратовский национальный исследовательский государственный университет им. Н.Г. Чернышевского, г. Саратов, Россия

✉ kartashovaam@sgu.ru

Аннотация. Работа посвящена получению поликристаллических кремниевых покрытий на нетканом нановолокнистом полимерном материале при помощи поглощающего лазерное излучение слоя олова. Приведены результаты экспериментальных исследований, подтверждающие наличие кристаллизованных кремниевых структур на нетканых полимерных подложках.

Ключевые слова: нановолокнистые нетканые материалы, магнетронное распыление, лазер-стимулированная кристаллизация кремния, металл-индуцированная кристаллизация кремния

Финансирование: Исследование выполнено за счет гранта Российского научного фонда № 23-22-00047 (https://rscf.ru/project/23-22-00047/).

Ссылка при цитировании: Карташова А.М., Сердобинцев А.А., Волковойнова Л.Д. Лазер-стимулированная олово-индуцированная кристаллизация кремния на гибких нетканых подложках // Научно-технические ведомости СПбГПУ. Физико-математические науки. 2024. Т. 17. № 3.1. С. 261–265. DOI: https://doi.org/10.18721/JPM.173.153

Introduction

Silicon (Si) is an affordable and well-studied material used in many fields of science and technology, for example, in micro- and nanoelectronics or solar energy harvesting. Devices using its polycrystalline (pc-Si) form are among the most promising. Recent research shows that pc-Si combines advantages such as efficiency close to that of crystalline Si (c-Si) and a relatively low cost of production [1]. Si films can be crystallized in various ways, but most of them are realized at sufficiently high temperatures. Metal-induced [2] or laser-stimulated [3, 4] crystallization methods are used to lower the crystallization temperature. However, both of these methods reduce the crystallization temperature of Si insufficiently for use bendable polymers as substrates. Combining the two approaches mentioned above allows minimizing the thermal effect on the substrate and opens up the possibility of using a larger range of materials [5]. Electrospinned nonwoven substrates are a unique basis for the production of nanostructures, since the diameter of their fibers initially lies in the range of hundreds of nm's.

Materials and Methods

Nonwoven nanofiber substrates were obtained by electrospinning from a solution of polyacrylonitrile (PAN) in dimethylformamide (0.661 g of dry matter and 5.046 ml of solvent). When the solution was ready, it was poured into a syringe fixed in a syringe pump. The distance from the end of the needle to the collector was set to 25 cm. The process lasted 15 minutes, while the voltage on the high-voltage power supply FUG HCP 140-65000 was equal to 53 kV, and the rate of extrusion of the solution from the syringe was set to 1 ml/h.

Thin films of Si and tin (Sn) were sequentially deposited to the obtained nonwoven substrates by magnetron sputtering using the Angstrom Nexdep setup. Four samples were obtained, differing in Sn thickness: I – 21 nm, II – 49 nm, III – 57 nm, IV – 76 nm. The Si thickness for all samples was equal to 190 nm.

On the obtained samples, 2×2 mm^2 squares were annealed with a pulsed laser (MiniMarker 2) with a wavelength of 1064 nm. Laser processing mode: laser radiation power 0.2 W; pulse duration 4 ns; frequency 60 kHz; laser beam scanning speed 1600 mm/s for samples I and II and 2700 mm/s for samples III and IV. The difference in the velocities of the laser beam for the samples is due to the different thicknesses of the Sn.

Crystallization was verified using Raman spectroscopy. The spectra were taken at the inVia (Renishaw) Raman microscope using a laser with a wavelength of 532 nm. The signal accumulation time was 10 s at each point at a radiation power of 1.25 μW; the laser spot size was 1.3 μm. The spectra were recorded at 16 points at distance of 15 μm.

Scanning electron microscopy (SEM) studies were carried out to observe changes occurring with nonwoven fibers and layers of Si and Sn after laser treatment.

Results and Discussion

Three of the four samples showed the evidence of crystallization, but even the peak of amorphous Si (a-Si) is missing from the spectra obtained from the sample with the thinnest Sn layer (Fig. 1, I). The absence of a-Si peak in the spectra of sample I indicates that not only metal, but also semiconductor ablation occurred during laser surface treatment. According to the remaining graphs (Fig. 1, II-IV), it can be seen that there is a clearly distinguishable peak in the spectra, close to the peak of c-Si (520 cm^{-1}).

Figure 2 shows the SEM images for each of the samples, as well as a snapshot of the original PAN fibers and deposited, but not yet laser-treated fibers.

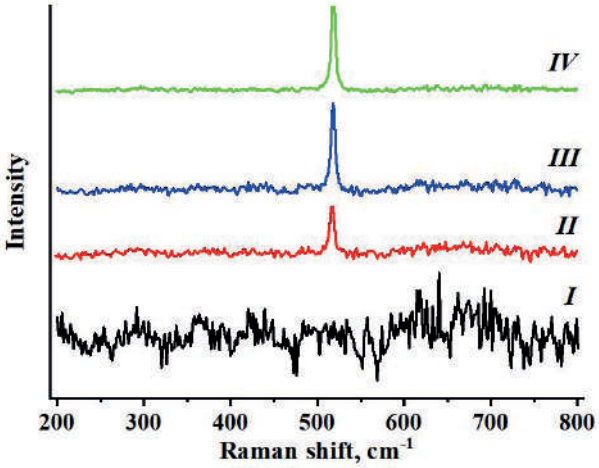

Fig. 1. Averaged Raman spectra of the samples

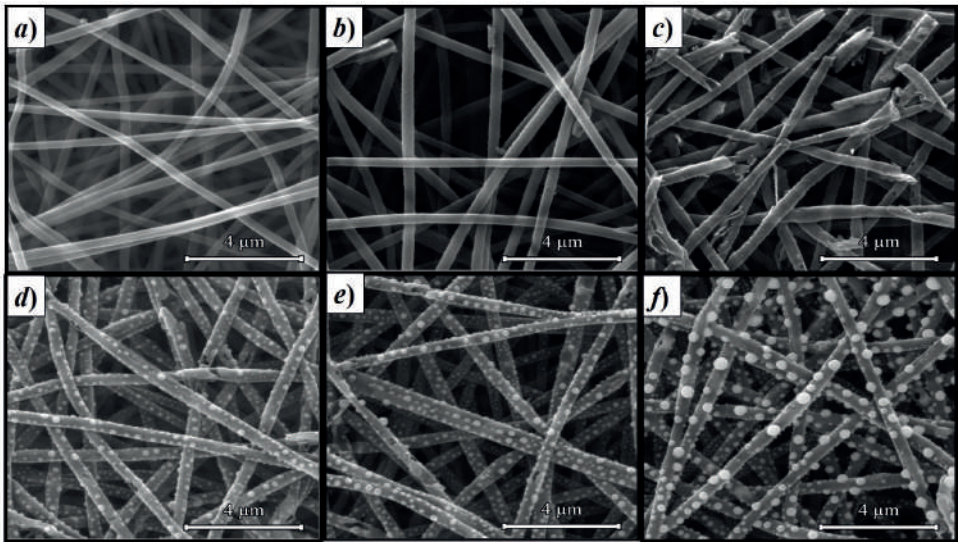

Fig. 2. SEM images of samples: (*a*) – initial PAN fibers; (*b*) – PAN fibers with deposited layers of Si and Sn that have not been subjected to laser treatment; (*c*) – I; (*d*) – II; (*e*) – III; (*f*) – IV

Initial PAN fibers and fibers with deposited layers of Si and Sn before laser treatment do not have much difference. For sample I besides the ablation of Sn and Si, the destruction of the substrate fibers also occurred. The fibers received enough heat for the glass transition (377 K [6]), and they lost their flexibility, becoming brittle. The images of samples II, III, IV also show damaged fibers, but their number is much smaller. The images clearly show also that after laser treatment, Sn is collected into particles, the size of which enlarges with increase of the thickness of the metal layer. In addition to the particles, the diameter of the filaments also grows (Table).

Initial PAN fibers have the smallest average diameter. It is then increased after deposition of Si and Sn layers. A further increase in the fibers diameter can be explained by their thermal expansion. It can be assumed that substrate heating rate slows down with increase of the thickness of the Sn, so the fibers do not have time to heat up to the glass transition temperature, but they manage to expand.

Additionally, the composition of samples II, III, IV was analyzed by the EDX before and after laser treatment. During laser treatment, an average of 13.5 at.% of Sn is removed, the remaining metal melts and collects into particles that are clearly visible in Figure 2.

Table

Data obtained during the investigation of samples by scanning electron microscopy

Sample	Average diameter of the fibers, nm	Average particle diameter, nm	Chemical composition				% of evaporated Sn
			Before laser treatment		After laser treatment		
			Sn, at.%	Si, at.%	Sn, at.%	Si, at.%	
Initial PAN	350.74 ± 0.49	–	–	–	–	–	–
PAN after deposition	389.30 ± 0.75	–	–	–	–	–	–
I	420.28 ± 0.75	–	–	–	–	–	–
II	465.03 ± 0.55	220.97 ± 0.45	15.71 ± 0.01	84.29 ± 0.01	13.29 ± 0.03	86.71 ± 0.03	15.40
III	450.51 ± 0.78	263.55 ± 0.48	21.02 ± 0.05	78.98 ± 0.05	18.45 ± 0.01	81.55 ± 0.01	12.23
IV	483.43 ± 0.84	415.29 ± 0.74	26.43 ± 0.01	73.57 ± 0.01	22.94 ± 0.01	77.06 ± 0.01	13.20

Conclusion

pc-Si structures on nonwoven nanofiber substrates using Sn as the upper absorbing layer were formed by laser-stimulated metal-induced crystallization. The effect of Sn layer thickness to the pc-Si formation was studied. For this purpose, Raman spectroscopy and SEM were used. It was found that the thinnest layer of Sn leads to full ablation of deposited layers and destruction of substrate fibers. Other samples exhibit a different behavior: Sn not only ablates during laser treatment, but also collects into particles. An average of 13.5 at.% of the Sn evaporates from the surface of the samples. Also it was found out that PAN fibers undergo thermal expansion during laser processing and the greater the thickness of the Sn, the more the fibers expand.

Acknowledgments

The authors express their gratitude to Demina P.A. and Savelieva M.S. for their help in creating nonwoven substrates and conducting research using scanning electron microscopy.

REFERENCES

1. **Abdurakhmanova B.M., Adilov M.M.,** Characteristics of Solar Cells Based on Polycrystalline Silicon, Doklady Physics. 67 (11) (2022) 439–441.

2. **Gestel D. Van et al.,** Metal induced crystallization of amorphous silicon for photovoltaic solar cells, Physics Procedia. 11 (2011) 196–199.

3. **Bronnikov K., Dostovalov A., Cherepakhin A., Mitsai E., Nepomniaschiy A., Kulinich S.A., Zhizhchenko A., Kuchmizhak A.,** Large-Scale and Localized Laser Crystallization of Optically Thick Amorphous Silicon Films by Near-IR Femtosecond Pulses, Materials. 13 (2020) 5296.

4. **Sanchari Chowdhury, Jinsu Park, Jaemin Kim, Sehyeon Kim, Youngkuk Kim, Eun-Chel Cho, Younghyun Cho, Junsin Yi,** Crystallization of Amorphous Silicon via Excimer Laser Annealing and Evaluation of Its Passivation Properties, Energies. 13 (13) (2020) 3335.

5. **Serdobintsev A.A., Kartashova A.M., Demina P.A., Volkovoynova L.D., Kozhevnikov I.O.,** Formation of crystalline silicon structures on nanofiber nonwovens using laser-stimulated metal-induced crystallization, Physics of the Solid State. 65 (12) (2023) 2132–2134.

6. **Khan W.S., Ceylan M., Jabarrania A., Saeednia L., Asmatulu R.,** Chemical and thermal investigations of electrospun polyacrylonitrile nanofibers incorporated with various nanoscale inclusions, Journal of Thermal Engineering. 3 (4) (2017) 1375–1390.

THE AUTHORS

KARTASHOVA Anastasia M.
nasty280801@gmail.com
ORCID: 0009-0007-7614-6734

VOLKOVOYNOVA Larisa D.
loris.volkoff@gmail.com
ORCID: 0000-0001-6780-9865

SERDOBINTSEV Alexey A.
SerdobintsevAA@sgu.ru
ORCID: 0000-0003-3281-8352

Received 08.07.2024. Approved after reviewing 29.07.2024. Accepted 30.07.2024.

Conference materials
UDC 53.043
DOI: https://doi.org/10.18721/JPM.173.154

Laser-induced switching of GST films using a spatial light modulator

E.V. Menshikov [1, 2] ✉, P.I. Lazarenko [3], D.Yu. Terekhov [3],
A.V. Dostovalov [4], A.Yu. Kokhanovskiy [1]

[1] ITMO University, St. Petersburg, Russia;
[2] University of Brescia, Brescia, Italy;
[3] National Research University of Electronic Technology, Zelenograd, Russia;
[4] Institute of Automation and Electrometry of the Siberian Branch of the RAS, Novosibirsk, Russia
✉ evgenii.menshikov@metalab.ifmo.ru

Abstract. One of the promising materials enabling tuning of optical response in photonic devices is the class of chalcogenide optical phase-change materials (oPCMs), such as GeSbTe (GST). These materials exhibit nonvolatile amorphous and crystalline phase states under normal conditions, while offering quick (ns-) phase switching and prominent optical contrast, which can be induced via laser irradiation. Direct laser modification of PCM films is usually realized through a point-by-point approach, by sequentially scanning a focused laser beam over the film surface. Although this technique is straightforward and easy to implement, it significantly limits potential fabrication speeds. In this work, we study a method of laser-induced switching of the phase state of GST films using a spatial light modulator. We demonstrate that this approach enables fast patterning of large areas of the material.

Keywords: phase-change materials, GeSbTe, laser imprinting, spatial light modulator

Funding: The study was funded by the grant of the Russian Science Foundation No. 20-79-10322, https://rscf.ru/project/20-79-10322/.

Citation: Menshikov E.V., Lazarenko P.I., Terekhov D.Yu., Dostovalov A.V., Kokhanovskiy A.Yu., Laser-induced switching of GST films using a spatial light modulator, St. Petersburg State Polytechnical University Journal. Physics and Mathematics. 17 (3.1) (2024) 266–270. DOI: https://doi.org/10.18721/JPM.173.154

Материалы конференции
УДК 53.043
DOI: https://doi.org/10.18721/JPM.173.154

Лазерно-индуцированное переключение фазового состояния пленок GST с помощью пространственного модулятора света

Е.В. Меньшиков [1, 2] ✉, П.И. Лазаренко [3], Д.Ю. Терехов [3],
А.В. Достовалов [4], А.Ю. Кохановский [1]

[1] Университет ИТМО, Санкт-Петербург, Россия;
[2] Университет Брешии, г. Брешия, Италия;
[3] Национальный исследовательский университет «Московский институт электронной техники», г. Зеленоград, Россия;
[4] Институт автоматики и электрометрии Сибирского отделения РАН, г. Новосибирск, Россия
✉ evgenii.menshikov@metalab.ifmo.ru

Аннотация. Перспективными материалами, позволяющих реализовать перестраиваемый оптический отклик в фотонных устройствах, является класс

халькогенидных оптических материалов с фазовой памятью (МФП), таких как GeSbTe (GST). Эти материалы стабильны при нормальных условиях, при этом обладают высокой скоростью переключения (нс-) и заметным оптическим контрастом, который может быть индуцирован лазерным излучением. В данной работе мы исследуем метод лазерно-индуцированного переключения фазового состояния пленок GST с помощью пространственного модулятора света. Этот подход позволяет быстро модифицировать большие участки материала, без механического сканирования образца или объектива.

Ключевые слова: материалы с фазовой памятью, GeSbTe, лазерная обработка, пространственный модулятор света

Финансирование: Исследование выполнено при финансовой поддержке гранта Российского научного фонда № 20-79-10322, https://rscf.ru/project/20-79-10322/.

Ссылка при цитировании: Меньшиков Е.В., Лазаренко П.И., Терехов Д.Ю., Достовалов А.В., Кохановский А.Ю. Лазерно-индуцированное переключение фазового состояния пленок GST с помощью пространственного модулятора света // Научно-технические ведомости СПбГПУ. Физико-математические науки. 2024. Т. 17. № 3.1. С. 266–270. DOI: https://doi.org/10.18721/JPM.173.154

Introduction

Optical phase-change materials (PCMs) enable variety of applications for tunable photonics, due to a unique combination of such properties as nonvolatality, ns-switching speeds and large refractive index contrast (e.g., $\Delta n = 2.24$ at 1550 nm) [1]. Additional feature of these materials is the possibility to induce the phase transition by thermal, electrical and laser stimuli, enabling mixed-operation photonic designs. Direct laser writing applied for PCMs appears to be a promising nanofabrication technique, as recently demonstrated for the direct imprinting and rewriting of photonic integrated circuits (PICs) [2] and the fabrication of metasurfaces [3]. This technique can be further advanced by replacing the point-by-point imprinting approach, in which the laser beam is sequentially scanned over the sample surface, with imprinting by modulated laser irradiation using a spatial light modulator (SLM). SLMs has been successfully applied for precision modulation in holographic displays, optical tweezers and lithography [4]. Possibility of using an SLM for the crystallization of thick 1 μm films of $Ge_2Sb_2Se_4Te$ (GSST, Se-substituted phase-change alloy) was demonstrated earlier [5]. In this work we focus on applications for integrated devices, studying the laser-induced modification of a thin (20 nm) film of $Ge_2Sb_2Te_5$ (GST-225, or just GST) deposited on top of a silicon nitride guiding layer. We show that using an SLM enables large-scale – up to tens of microns – crystallization of the PCM, through two approaches: direct imprinting of the full pattern and steering of multiple laser spots.

Materials and Methods

Amorphous $Ge_2Sb_2Te_5$ films with a thickness of 20 nm were deposited using a DC magnetron sputtering system on a thermally oxidized silicon wafers (2.6 μm thick SiO_2 layer) with a 450 nm thick stoichiometric low pressure chemical vapor deposited (LPCVD) silicon nitride (Si_3N_4) layer. The pressure of Ar ions during the GST deposition process was 4 mTorr, the sputtering power was 25 W. To prevent oxidation of GST, the films were covered with a 20 nm thick SiO_2 capping layer. The composition and distribution of elements for the GST films were controlled by the time-of-flight secondary ion mass spectrometry (IonTOF TOF SIMS 5) together with the Auger spectroscopy (PerkinElmer PHI-660).

Figure 1, *a* shows a schematic of the optical setup. We utilized emission of a Yb:KGW femtosecond laser system PHAROS, which operates at 1030 nm with a pulse duration of 290 fs, and a continuous wave (CW) laser that works at 1064 nm. The intensity of the laser emission was controlled by an attenuator, which consisted of a half-waveplate and a Glan polarizer. A beam expander was used to increase the beam size to match the vertical size of the SLM matrix, maximizing its illuminated area. Light modulation was realized with a reflective phase-only SLM Holoeye Pluto-2.

We used a 4*f* system with 20 cm focal length lenses to image the phase pattern, formed by the SLM onto the back focal plane of an objective. The modulated laser beam was focused on the sample with a Zeiss A-Plan 60× objective when using the CW laser and with a 20× Mitutoyo Plan Apo NIR objective with the fs-laser.

Phase masks for the SLM were calculated using the Fidoc algorithm [6]. To avoid modification of the patterns by the zero diffraction order, we summed the calculated masks with a blazed grating, shifting the patterns by approximately 3/4 of their characteristic size. The effective refractive indexes of the waveguide modes were calculated using COMSOL Multiphysics software.

Results and Discussion

We demonstrate that the switching of phase state of the GST film can be realized through two approaches. In the first approach, a desired pattern can be imprinted by forming a corresponding intensity distribution with an SLM using a single pre-calculated phase mask. In this case, the pattern can be imprinted all at once, using a fs-laser to provide fluence values sufficient for crystallization, which is approximately 5 mJ/cm^2 at 1030 nm. Figure 1, *b* shows a phase mask on the SLM matrix, corresponding to a 5×5 array of dots with a spacing of 10 μm. The phase mask irradiated with a fs-laser produces the pattern in the focal plane of the objective, leading to the crystallization of the material at the intensity maxima. An optical image of the pattern imprinted in the as-deposited amorphous GST film is shown in Figure 1, *c*. Here, the crystallized areas appear brighter due to the higher reflectivity of the crystalline phase ($R_{a\text{-}GST}/R_{c\text{-}GST}$ = 0.77 at 570 nm).

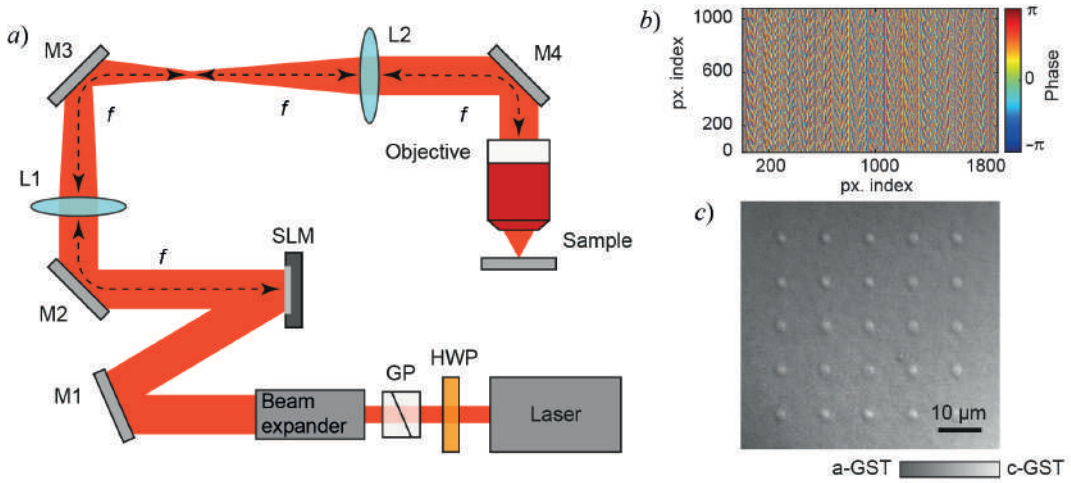

Fig. 1. Large-scale GST laser patterning. (*a*) schematic of the optical setup; here HWP – half-wave plate, GP – Glan polarizer, Mi – mirror, SLM – spatial light modulator, Li – lens with the focal length of f. (*b*) phase mask on SLM, corresponding to the array of dots, (*c*) optical image of the imprinted pattern

The second approach relies on splitting the pump laser beam with the SLM to steer multiple laser beams over the surface of the film in parallel. Here, the phase mask $\varphi_{tot}(m, n)$ presents a superposition of blazed diffraction gratings, calculated as follows [7]:

$$\varphi_{tot}(m,n) = \arg\left[\sum_{k}^{N} \exp(i\varphi_k(m,n))\right], \quad (1)$$

where $\varphi_k(m, n)$ is the blazed phase grating, corresponding to the *k*-th beam and *m*, *n* are the indexes of pixels of the phase mask in horizontal and vertical directions, respectively. The phase grating providing a given displacement x_k, y_k of the beam is

$$\varphi_k(m,n) = \frac{2\pi\Delta}{\lambda f_{obj}}(x_k m + y_k n)$$

where λ is the laser wavelength, f_{obj} is the focal length of the objective, and Δ is the pixel pitch (8 μm for our SLM matrix). The total phase mask $\varphi_{tot}(m, n)$ corresponds to the intensity

distribution of N laser spots, placed at given coordinates x_k, y_k. Due to the smaller instantaneous modification area, this approach can be implemented to increase the speed of the imprinting process, if there is a limitation on laser power.

Figure 2, *a* a shows phase masks, corresponding to the first $\varphi_1(m, n)$ and second $\varphi_2(m, n)$ laser spots (with coordinates of the ends of the arrows in Fig. 2, *b*, right pattern), and their superposition $\varphi_{tot}(m, n)$ calculated using equation (1). The gratings are dynamically updated to traverse the contour of the desired pattern by two CW-laser spots, as shown in Figure 2, *b*. Here, first, the spatial coordinates of the points of a pattern (the ITMO University logo and semicircles with a $\pi/4$ sector angle) were calculated. Next, the set of coordinates corresponding to two continuous fragments of the pattern was sequentially associated with the superposition of blazed gratings, shifting the laser spots to the corresponding coordinates. As one contour is imprinted, the formation of the next one starts immediately, allowing two beams to operate independently in parallel. Optical images of the completely imprinted patterns are shown in Figure 2, *c*.

Periodic modification of the effective refractive index of the waveguide mode by the changed phase state of the GST film ($n_{eff,\ am} = 1.67$ and $n_{eff,\ cr} = 1.73$ at 1550 nm, TM_0 mode), can be used as a tunable light coupling/decoupling structure (see Fig. 2, *c*, right pattern) [2]. By fine manipulation of the laser fluence during the formation process, it is possible to further advance this technique, forming patterns with intermediate crystallization states and achieving multilevel tuning of the optical response of the formed structure [8].

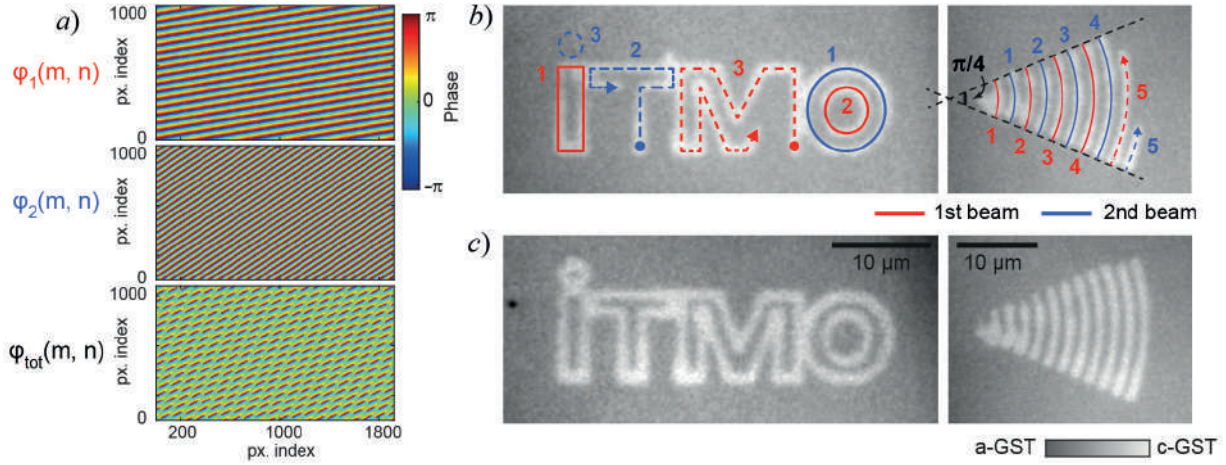

Fig. 2. Patterns imprinting by multibeam steering. (*a*) Phase gratings corresponding to the 1-st, $\varphi_1(m, n)$, and 2-nd, $\varphi_2(m, n)$, beams and the phase mask of their superposition, $\varphi_{tot}(m, n)$. The imprinting process is realized by two beams, forming the patterns in parallel (*b*), the numbers correspond to the order in which the continuous contours were imprinted; resulting patterns (*c*)

Conclusion

In this work, we have explored the large-scale phase modification of a thin GST film integrated with a silicon nitride planar waveguide, using a spatial light modulator. We have demonstrated the formation of binary phase patterns induced by CW- and fs-laser irradiation. The proposed method of phase switching opens the way for fast direct laser imprinting in PCMs for tunable PICs or holography.

Acknowledgments

The study was funded by the grant of the Russian Science Foundation No. 20-79-10322. The samples were fabricated with contributions from the research laboratory “Materials and devices for active photonics”.

REFERENCES

1. **Zheng C., Simpson R. E., Tang K., et al.,** Enabling active nanotechnologies by phase transition: From electronics, photonics to thermotics, Chemical Reviews. 122 (19) (2022) 15450–15500.

2. **Wu C., Deng H., Huang Y. S., Yu H., Takeuchi I., Rнos Ocampo C. A., Li M.,** Freeform direct-write and rewritable photonic integrated circuits in phase-change thin films, Science Advances. 10 (1) (2024) 1361.

3. **Bochek D.V., Samusev K.B., Yavsin D.A., et al.,** Fabrication of $Ge_2Sb_2Te_5$ metasurfaces by direct laser writing technique, Optics & Laser Technology. 141 (2021) 107124.

4. **Yang Y., Forbes A., Cao L.,** A review of liquid crystal spatial light modulators: devices and applications, Opto-Electronic Science. 2 (8) (2023) 230026–1.

5. **Driggers M., Rivero-Baleine C.,** Investigation of the crystallization behavior of laser-irradiated EXTREME pattern by Raman spectroscopy, International Journal of Applied Glass Science. 11 (3) (2020) 415–420.

6. **Pi D., Liu J., Wang Y.,** Review of computer-generated hologram algorithms for color dynamic holographic three-dimensional display, Light: Science & Applications. 11 (1) (2022) 231.

7. **Jones P. H., Maragò O. M., Volpe G.,** Optical tweezers: principles and applications, Cambridge University Press, England. 2015.

8. **Kunkel T., Vorobyov Y., Smayev M., Lazarenko P., Romashkin A., Kozyukhin S.,** Crystallization of GST225 thin film induced by a single femtosecond laser pulse: Experimental and theoretical study, Materials Science in Semiconductor Processing. 139 (2022) 106350.

THE AUTHORS

MENSHIKOV Evgenii V.
evgenii.menshikov@metalab.ifmo.ru
ORCID: 0009-0003-9168-2421

DOSTOVALOV Alexander V.
dostovalov@iae.nsk.su
ORCID: 0000-0002-9043-3197

LAZARENKO Petr I.
aka.jum@gmail.com
ORCID: 0000-0003-4309-3481

KOKHANOVSKIY Alexey Yu.
a.kokhanovskiy@metalab.ifmo.ru
ORCID: 0000-0002-1382-3589

TEREKHOV Dmitry Yu.
gsm.ads@yandex.ru

Received 10.07.2024. Approved after reviewing 27.08.2024. Accepted 27.08.2024.

Conference materials
UDC [621.785.3:539.216.2:(669.295+669.71)]::621.382.323
DOI: https://doi.org/10.18721/JPM.173.155

Low-temperature treatment of Al/Ti nanolayers to form solid solution in order to improve the ohmic contacts process formation

K.G. Nikitin [1] ✉, L.A. Barsukov [1], A.V. Romashkin [1],
A.Yu. Trifonov [1, 2], R.N. Mozhchil [3], S.G. Protasova [3]

[1] National Research University of Electronic Technology, Zelenograd, Moscow, Russia;
[2] National Research Centre "Kurchatov Institute", Moscow, Russia;
[3] Osipyan Institute of Solid State Physics, Russian Academy of Sciences, Chernogolovka, Russia
✉ halkwww@mail.ru

Abstract. Heat treatment of the Al, Al/Ti and Au/Ni/Al/Ti nanolayers at 450 °C was studied by measuring transparency, resistivity and also by SIMS (secondary ion mass spectrometry) and XPS (X-ray photoelectron spectroscopy). Heat treatment has led to the increase in transparency and in resistivity of Al/Ti films. On the contrary, the same treatment for the pure Al layer decreases resistivity but transparency increases due to the decrease in the unoxidized Al thickness. The upper Au/Ni layer has led to greater changes in resistivity and transparency but presumably due to a higher oxidation degree, that confirmed by XPS. Observed changes of the Al/Ti layer structure are assumed to be explained not only by oxidation, but also by the partial formation of a Ti-Al solid solution, confirmed by SIMS (Ti and Al redistribution in the layer). The suppression of oxidation, Ti-Al formation temperature reduction and, as a result, possibility to improve GaN HEMT ohmic contacts with such layers were studied.

Keywords: thin film, rapid thermal annealing, ohmic contact, TiAl compounds, transparency, Raman spectroscopy, SIMS, XPS

Funding: This research was supported by the Ministry of Science and Higher Education of the Russian Federation in the framework of state task FSMR-2023-0002.

Citation: Nikitin K.G., Barsukov L.A., Romashkin A.V., Trifonov A.Yu., Mozhchil R.N., Protasova S.G., Low-temperature treatment of Al/Ti nanolayers to form solid solution in order to improve the ohmic contacts process formation, St. Petersburg State Polytechnical University Journal. Physics and Mathematics. 17 (3.1) (2024) 271–277. DOI: https://doi.org/10.18721/JPM.173.155

Материалы конференции
УДК [621.785.3:539.216.2:(669.295+669.71)]::621.382.323
DOI: https://doi.org/10.18721/JPM.173.155

Низкотемпературная обработка нанослоев Al/Ti для формирования твердого раствора с целью улучшения процесса создания омических контактов

К.Г. Никитин [1] ✉, Л.А. Барсуков [1], А.В. Ромашкин [1],
А.Ю. Трифонов [1, 2], Р.Н. Можчиль [3], С.Г. Протасова [3]

[1] Национальный исследовательский университет «МИЭТ», Москва, г. Зеленоград, Россия;
[2] Национальный исследовательский центр «Курчатовский институт», Москва, Россия;
[3] ЦКП, Институт физики твердого тела им. Ю.А. Осипьяна РАН, г. Черноголовка, Россия
✉ halkwww@mail.ru

Аннотация. Исследована термообработка при 450 °C нанослоев Al, Al/Ti и Au/Ni/Al/Ti с анализом их прозрачности, удельного сопротивления, а также с применением ВИМС (вторично-ионная масс спектрометрия) и РФЭС (рентгеновская фотоэлектронная спектроскопия). Термообработка привела к увеличению прозрачности и сопротивления пленок Al/Ti. Аналогичная обработка чистого Al, напротив, снизила сопротивление, но увеличила прозрачность за счет частичного окисления. Верхний слой Au/Ni обусловливает более сильные изменения прозрачности и сопротивления, вероятно, из-за большей степени окисления, подтвержденной РФЭС. Однако общие изменения прозрачности и проводимости структуры слоев Al/Ti могут быть объяснены частично окислением, и частичным формированием твердого раствора Ti-Al, подтвержденным перераспределением Ti и Al по ВИМС. Таким образом, предложена возможность снижения температуры формирования, окисления и улучшения омических контактов к GaN HEMT для таких слоев.

Ключевые слова: тонкая пленка, быстрый термический отжиг, омический контакт, соединения TiAl, прозрачность, комбинационное рассеяние света, ВИМС, РФЭС

Финансирование: Работа выполнена при поддержке Минобрнауки России в рамках государственного задания FSMR-2023-0002.

Ссылка при цитировании: Никитин К.Г., Барсуков Л.А., Ромашкин А.В., Трифонов А.Ю., Можчиль Р.Н., Протасова С.Г. Низкотемпературная обработка нанослоев Al/Ti для формирования твердого раствора с целью улучшения процесса создания омических контактов // Научно-технические ведомости СПбГПУ. Физико-математические науки. 2024. Т. 17. № 3.1. С. 271–277. DOI: https://doi.org/10.18721/JPM.173.155

Introduction

The temperature of ohmic contacts formation of GaN HEMT during rapid thermal annealing (RTA) is caused by the necessity of the Ti atoms redistribution, that is crucial in the reactions between N and Ti, Al, with formed at the same time Ti-Al compounds solid solutions [1]. However, high temperature of RTA negatively affects the electrical parameters of the heterostructure, and reducing the RTA temperature is an important issue [2]. The temperatures > 800 °C are being used to form ohmic contacts in the traditional methods, e.g. RTA [1] or laser annealing, can affect the characteristics of the structure due to degradation of the GaN layer and oxidation of Ga and Al [3, 4]. It is proposed to use the nanolayers (< 3 nm), which melting point is lower [5], than the bulk material's one [6], to reduce the RTA temperature. Thus, it is possible to form an Al-Ti solid solution and activate processes, necessary for the ohmic contact formation at the lower temperatures. Low resistance contacts are formed at 500 °C [2]. This confirms that TiAl and TiN are formed at temperatures much lower than the Al-Ti melting points shown in the phase diagram [6]. The mechanism of this decrease in temperature remains unclear. The phase diagram shows that the formation of the Ti-Al alloy is both the cause and the necessary condition for the formation of ohmic contacts at temperatures below the melting point of pure Ti. RTA can cause the damage of AlGaN surface, which is one of the main reasons of GaN HEMT degradation and poor performance [3]. XPS analysis has shown that the damage to the AlGaN surface is associated with an oxidation reaction under high temperature. In this work, the problem of Ti-Al formation using nanolayers was investigated with low temperature process, slightly below the lowest temperature of ohmic contact formation for such layers [2], which was 450 °C. Such low temperature will avoid damage to the AlGaN surface and maintains the electrical characteristics stability of GaN HEMT, as well as reduces stress formation in the GaN on Si substrate during RTA.

Materials and Methods

Two structures deposited by electron-beam evaporation (0.25 Å/s) on Si substrates with 300 nm SiO_2 were studied: Al (11.2 nm)/Ti (2.3 nm)/Al (11.2 nm)/Ti (2.3 nm); and similar structure with

additional layers of Au (3 nm) and Ni (3 nm) on top Au (3 nm)/Ni (3 nm)/Al (9 nm)/Ti (2 nm)/Al (9 nm)/Ti (2 nm). Single layer of Al (~30 nm) was used as the reference structure. Thermal treatment was performed in a chamber in the Ar atmosphere with a flow rate of ~1 l/min at the annealing to 450 °C, rate of 20 °C/min. The resistivity of the metal layers was measured using the 4-probe method. The resulting transparency of the layers before and after heat treatment was investigated using Raman by comparing the signal (Centaur U HR, Nano Scan Technology) from Si with and without metal layers on top. Atomic force microscopy (AFM, Solver-Pro, NT-MDT) was used to monitor the thickness (to estimate oxide growth) and roughness of metal films. In addition, the elemental composition was analyzed using secondary ion mass spectrometry (SIMS, ToF.SIMS 5-100, Ion ToF) on the same samples of Au/Ni/Al/Ti/Al/Ti before and after annealing at 450 °C. An O_2^+ ion beam with an energy of 500 eV for sputtering and an analytical Bi^+ beam with an energy of 30 keV were used. When processing the SIMS data, the $^{58}Ni^+$, $^{54}Al_2^+$, and $^{49}Ti^+$. signals were normalized to the maximum current of each ion and then normalized to the total signal. An X-ray photoelectron spectroscopy (XPS, Kratos AXIS Ultra DLD, Research Facility Center at the Institute of Solid State Physics RAS) study with Ar^+ 5 keV ion etching was also performed for the same samples before and after annealing at 450 °C. XPS analysis shows the percentages of Ni, Al, Ti, Si, Au and O, also the contribution of SiO_2 has been subtracted that shown separately.

Results and Discussion

The total thickness of the Al/Ti sample after annealing increased from 29.5 nm to 31.8 nm: the thickness of the unoxidized Al layer decreased by 1.1 nm due to the partial oxidation (Fig. 1, *a*). Annealing of Al/Ti at 450 °C led to the increase in the film transparency from 14.1 to 23.5% (1.7 times, Fig. 2, *a*, *b*), as well as its resistivity – from 64 μΩ·cm (similar to the reference Al sample at 25 °C) up to 128 μΩ·cm (2 times) (Fig. 2, *c*). Similar measurements were performed for Al without a Ti layer. Due to the decrease in the thickness of unoxidized Al by 3.3 nm caused by partial oxidation (total layer thickness increased from 36.4 to 42.9 nm), the transparency increased from 18.9 to 23.2% (1.2 times), while the resistivity decreased from 75 μΩ·cm to ~27 μΩ·cm due to integration from initially formed clusters. Observed transparency changes align with the dependence of transparency on the thickness of unoxidized Al [7]. Significant Al sample thickness changes in the absence of Ti also indicates a difference in the oxidation mechanism of the upper Al layer (~11 nm) and an influence of the Ti sublayer. At the same time, the single Ti layer itself (~2.5 nm) is completely oxidized after 3 days in air without heating. The resulting TiO_2 (~4.5 nm) layer shows negligible presumably anti-reflective coating effect [8] as a slight increase of the Si Raman peak intensity (Fig. 2, *a*). Therefore, a higher oxidation depth increase was expected rather for Al/Ti than Al.

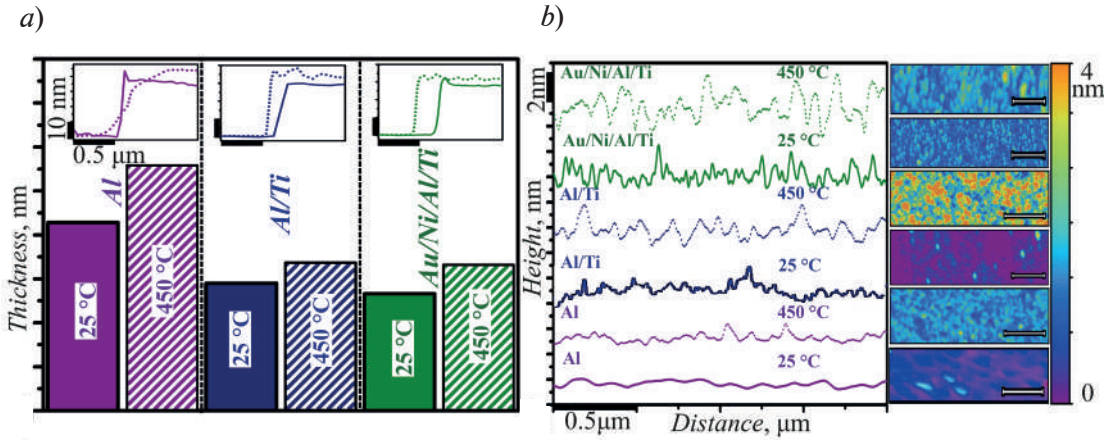

Fig. 1. AFM data of the layer thickness at the edge (*a*), AFM surface morphology and cross sections (*b*)

The roughness increase of Al/Ti compared to Al was observed (Fig. 1, *b*, all scale bars are 0.5 μm), which also indicates a difference in the layer's structure during annealing. The layers remained continuous even after annealing, so changes in the layer resistance cannot be explained by its

clustering. From the opposite changes in the resistivity of Al/Ti and Al, with co-directed changes in transparency with a greater change for Al/Ti, it can be assumed, that the Al Ti solid solution is partially formed, since the resistivity exceeds the reference sample of pure Al at 25 °C only in 2.2 times [9]). However, Ti-Al solid solutions can presumably form only at higher temperatures (480–520 °C), since the formation of ohmic contacts for such layers has been demonstrated [2], at which changes in the Ti layer are inevitable. However, noticeable changes in Al/Ti appear already at 450 °C. In the samples with Au/Ni top layers, there was a small difference in thickness (from 28.3 to 31.6 nm), indicating a small oxidation effect with annealing, but greater than one for the Al/Ti structure without a top layer (Fig. 1, *a*). For a sample with Au/Ni, transparency and resistance changed from 11.4 to 31.5% and from 27 to 183 μΩ·cm (Fig. 2). These changes are higher than for the Al/Ti and can be explained by the Au-Al, Ni-Al alloys formation (resistivity increase despite similar oxide fraction).

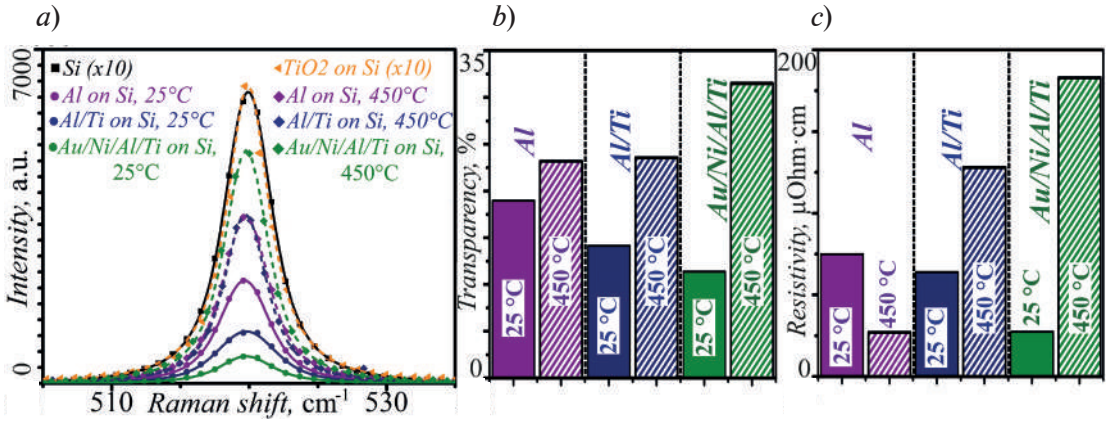

Fig. 2. Suppressing of the Raman of Si by metal (*a*) and estimated transmittance (*b*), resistivity (*c*)

Partial oxidation at a significant depth of the Ni-Al alloy was observed, due to it can be formed at the lower temperatures than Al-Ti [10]. Thus, the presence of Ni and Au in the depth demonstrates its low effectiveness as a protective layer, aligned with other results [1]. It is shown by SIMS that 1/4 of the depth of the structure is Ni/Al or Au/Al composite or alloy (Fig. 3, *a*). The Ni-Al alloy oxidizes at a significantly higher rate than Al-Ti [11, 12]. This explains the greater depth of oxidation and thickness changes. However, deep in the layer, where the contribution of Ni is negligible, SIMS has shown significant Ti redistribution, which directly confirms that at 450 °C layers start to change, which is important for the ohmic contacts formation. In contrast, for the sample at 25 °C the individual layers of Ti can be resolved (Fig.3, *a*). Presumably a Ti-Al compound with an elemental ratio similar to $TiAl_2$ or $TiAl_3$ was formed in areas where mainly Al was present before annealing, which is caused by the use of nanolayers (with clusters < 3 nm).

The presence of Ni in the deep layer of Ti even before the thermal treatment was caused by the non-uniformity of the etching rate in the studied area of 300×300 μm (with increased surface roughness). The sample without heat treatment contained up to ~10% Ni at the 1/4–1/3 of its depth (Fig. 3, *a*). The resistance of Al-Ti can differ from Al by 10 times [9]. However, even considering the contribution of Ni-Al or Au-Al, the resistance has increased only in 6 times, which indicates the partial formation of Al-Ti alloys in combination with the partial redistribution of Ti at 450 °C (this is not enough to achieve the minimum resistance of ohmic contacts, that obtained only at 500 °C [2]). The resistance of the Au-Al alloy is less than ~15 μΩ·cm [13], which is significantly less than the resistance of Al/Ti (about 50 μΩ·cm [9]). Thus, the formation of the Au-Al alloy is most likely a limiting factor for the growth of the resistance of the whole structure, as well as for the Ni-Al alloy [14]. Thus, these alloys' contribution to the increase in resistance is insignificant, considering their content and thickness (not more than 1/3). The increase in transparency and resistivity can be partially explained by the fact that the oxidation rate of $NiAl_3$ is an order of magnitude higher than that of $TiAl_3$, meaning that thin layers of Au/Ni are more likely to increase the contribution of oxidation compared to Al/Ti. The observed difference in transparency and resistivity for

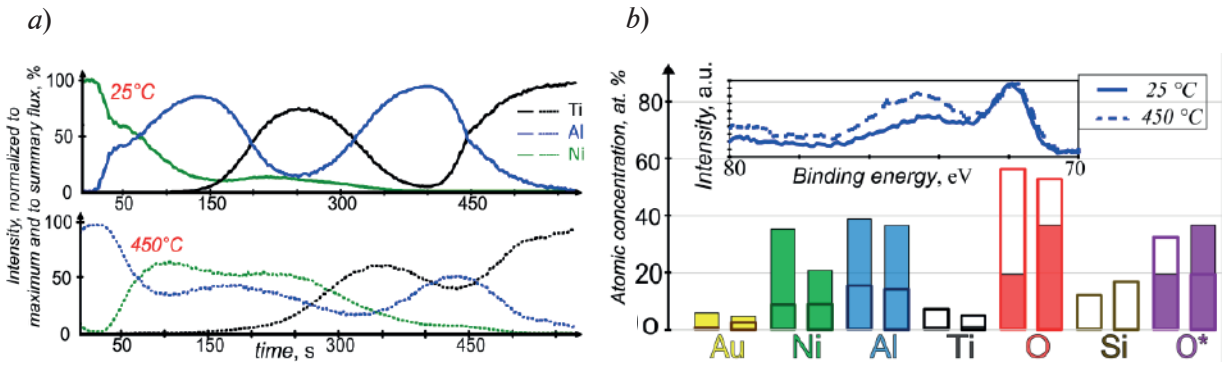

Fig. 3. Au/Ni/Al/Ti sample before and after annealing: SIMS profiles (*a*), XPS: left – 25 °C, right – 450 °C. Empty columns – elements in the depth of the layer (Ar^+ 500 s etching), and filled – in first ~1/4 in depth (100 s etching); * – oxygen not associated with Si; inset: Al 2p peak of 100 s etch (*b*)

Au/Ni/Al/Ti greatly differs from Al/Ti. The redistribution of Ni and Au can probably contribute to the redistribution of Ti and Al with the formation of Ti-Al over most of the layer thickness. Without an analysis of the oxides' contribution in layers it is impossible, even according to SIMS data, to entirely confirm the formation of the Al-Ti alloy. In the case of Ti/Al, the small thickness (up to 4 nm) of the oxide layer on Al limits further oxidation, in contrast to the possibility of deeper oxidation in Ni-Al layers. Thus, it is important to evaluate the oxides' contribution for Au/Ni/Al/Ti sample, which was performed by XPS. The sample after 450 °C shows a redistribution of Au and Ti in depth, but it similar to the one at 25 °C (Fig. 3, *b*). The presence of Ni, Ti, Al on XPS both after 100 s and 500 s of etching, combined with the presence of Si after 500 s, indicates that the initial homogeneity and structure of the layers' thickness have changed even for the sample without heat treatment. It indicates modification of the layer by Ar^+ ion beam during etching in XPS. In contrast, the redistribution and the formation of alloys in the depth of the layer, which is inhibited due to the parallel oxidation process [15], during sputtering with an O_2^+ ion beam in SIMS (with an energy of 500 eV), shows individual Ti layers at 25 °C (Fig. 3, *a*). An analytical Bi^+ beam etches in smaller area (30 μm diameter in contrast with 400 μm for XPS) during pulsed sputtering in SIMS, therefore there is less contribution of inhomogeneities in depth on that area, and the differences between 25 °C and 450 °C samples are significantly larger in contrast to the XPS data. The sample at 25 °C in the depth (at 500 s, when Si from the substrate appears) shows a high proportion of metal oxides, unbound with SiO_2 (~70 %), which can be explained by the oxidation of metals during sputtering of SiO_2 with an Ar^+. The sample after 450 °C has only ~45% share of metal oxides at both smaller and greater depths. It can be explained by the formation of $TiAl_3$, which has greater resistance to oxidation compared to NiAl [11, 12]. However, at the lesser depths (100 s, no Si signal) the proportion of oxides is ~20% for the 25 °C sample and ~45% for the sample after 450 °C (Fig. 3, *b*, in inset higher intensity above 73 eV with adjusted to intensity ca. 72 eV), which indicates that additional partial oxidation occurs during heat treatment. The equivalent thickness of a continuous unoxidized Al for a sample at 25 °C in terms of optical transparency is not ~16 nm (according to a quartz sensor during deposition), but 13 nm [7], corresponding to the measured transparency of ~11 % (Fig. 2, *b*), with 20% oxidation. However, the transparency of a 45% oxidized layer should be equivalent to a 8 nm layer, which corresponds to ca. 22% transparency. The Au/Ni/Al/Ti structure after 450 °C, has a transparency of 32% (Fig. 2, *b*), which is higher than the value estimated with a fraction of oxide from XPS data. This indicates that the observed transparency increase cannot be entirely explained only by the oxidation with residual oxygen processes during the heat treatment. The formation of Ni-Al, Au-Al compounds at the temperature lower than the Ti-Al one may precede and stimulate the formation of Ti-Al due to the redistribution of the materials. However, Au and Ni layers also lead to an oxidation contribution increase, caused by Ni-Al compounds formed at the temperatures lower, than the ones with Ti-Al.

Conclusion

Analysis of changes in thickness, resistivity, transparency, and elemental distribution, along with changes in the oxide proportion after 450 °C heat treatment according to SIMS and XPS data, indicates that nano-sized Al/Ti layers with 2–3 nm Ti can provide the $TiAl_3$ solid solution formation partially and also Ti redistribution. The addition of upper Au/Ni layers to the Al/Ti structure does not suppress the oxidation during heat treatment, but on the contrary, it can increase the oxide proportion, due to the formation of Al-Ni compounds, at the depths greater than the oxidation of the continuous Al layer. That explains the possibility of increasing the oxide proportion in Au/Ni/Al/Ti compared to the Al/Ti during heat treatment. However, changes in transparency and conductivity cannot be fully explained by oxidation, but can only be explained by the possibility of partial Ti-Al compound formation with the higher resistivity compared to Al. Similar processes of Ti redistribution and the Ti-Al alloys formation are important and necessary for the ohmic contacts formation using RTA in GaN HEMT structures. The features demonstrate the possibility to reduce the formation temperature, the oxidation processes and, as a result, the possibility to improve the ohmic contacts based on such layers.

REFERENCES

1. **Duffy S.J., Benbakhti B., Mattalah M., Zhang W., Bouchilaoun M., Boucherta M., Kalna K., Bourzgui N., Maher H., Soltani A.,** Low source/drain contact resistance for AlGaN/GaN HEMTs with high Al concentration and Si-HP [111] substrate, ECS Journal of Solid State Science and Technology. 6 (11) (2017) 3040–3043.

2. **Zhang L.Q., Wu X.L., Miao W.Q., Wu Z.Y., Xing Q., Wang P.F.,** Process of Au-free source/drain ohmic contact to AlGaN/GaN HEMT, Crystals. 12 (6) (2022) 826.

3. **Hou M., Xie G., Sheng K.,** Low surface damage during ohmic contact formation in AlGaN/GaN HEMT by selective laser annealing, Electronics Letters. 11 (55) (2019) 658–660.

4. **Hou M., Xie G., Sheng K.,** Mechanism of Al/Ti/Ni/Au ohmic contacts to AlGaN/GaN heterostructures via laser annealing, Chinese Physics B. 3 (28) (2019) 037302.

5. **Wang B., Wang G., Chen X., Zhao J.,** Melting behavior of ultrathin titanium nanowires, Physical Review. 67 (19) (2003) 193403.

6. **Zhang F., Chen S.L., Chang Y.A., Kattner U.R.,** A thermodynamic description of the Ti-Al system, Intermetallics 5 (6) (1997) 471–482.

7. **Hass G., Waylonis J.E.,** Optical constants and reflectance and transmittance of evaporated aluminum in the visible and ultraviolet, J. Opt. Soc. Am. 51 (7) (1961) 719–722.

8. **San Vicente G., Morales A., Gutierrez M.T.,** Preparation and characterization of sol–gel TiO_2 antireflective coatings for silicon, Thin Solid Film. 391 (1) (2001) 133–137.

9. **Wöltgens H. W., Friedrich I., Njoroge W.K., Theiß W., Wuttig M.,** Optical, electrical and structural properties of Al–Ti and Al–Cr thin films, Thin solid films. 388 (1-2) (2001) 237.

10. **Huang W., Chang Y.A.,** A thermodynamic analysis of the Ni-Al system, Intermetallics. 6 (6) (1998) 487–498.

11. **Wolf J.S., Evans E.B.,** Effect of Oxygen Pressure on Internal Oxidation of Nickel-Aluminum Alloys, Corrosion. 4 (18) (1962) 129t–136t.

12. **Umakoshi Y., Yamaguchi M., Sakagami T., Yamane T.,** Oxidation resistance of intermetallic compounds Al_3Ti and TiAl, Journal of materials science. (24) (1989) 1599–1603.

13. **Maldonado R.D., Oliva A.I., Corona J.E.,** Annealing effects on the electrical resistivity of AuAl thin films alloys, Materials Chemistry and Physics. 116 (2-3) (2009) 453–457.

14. **Miracle D.B.,** Overview No. 104 The physical and mechanical properties of NiAl, Acta metallurgica et materialia. 41 (3) (1993) 649–684.

15. **Bauer J., Frost F., Arnold T.,** Reactive ion beam figuring of optical aluminium surfaces, Journal of Physics D: Applied Physics. 8 (50) (2017) 085101.

THE AUTHORS

NIKITIN Konstantin G.
halkwww@mail.ru
ORCID: 0000-0002-0457-4568

BARSUKOV Leonty A.
leonty.barsukov@gmail.com
ORCID: 0000-0002-4802-0014

ROMASHKIN Alexey V.
romaleval@gmail.com
ORCID: 0000-0002-0101-6122

TRIFONOV Alexey Yu.
trif123456@yandex.ru
ORCID: 0000-0002-2976-9775

MOZHCHIL Rais N.
Mr_Mozhchil@mail.ru
ORCID: 0000-0002-8578-3977

PROTASOVA Svetlana G.
sveta@issp.ac.ru
ORCID: 0009-0007-7675-3876

Received 08.07.2024. Approved after reviewing 27.08.2024. Accepted 28.08.2024.

Conference materials
UDC 537.533.9
DOI: https://doi.org/10.18721/JPM.173.156

E-beam resist AR-N 7520 in the formation of the photonic structures

K.A. Fetisenkova [1, 2] ✉, A.E. Melnikov [1], A.V. Miakonkikh [1],
A.E. Rogozhin [1], A.A. Tatarintsev [1]

[1] Valiev Institute of Physics and Technology of RAS, Moscow, Russia;
[2] Moscow Institute of Physics and Technology, Moscow, Russia
✉ fetisenkova.ka@phystech.edu

Abstract. The study of plasma resistance of the AR-N 7520 was carried out. The selectivity of the reactive ion etching (RIE) of silicon through the mask of negative electron resist AR-N 7520 also was investigated. The dependence for selectivity was obtained at different fractions of SF6 in the feeding gas and at the different values of bias voltage. A high etching selectivity of 8.0 ± 1.8 was obtained for the etching process. The dependence of the resist line height on the exposure dose is presented. The optimal value for the line exposure dose was found to be 8200 pC/cm.

Keywords: electron-beam lithography; etching kinetic; novolak; reactive-ion etching, waveguide

Funding: This study was supported by Program no. FFNN-2022-0021 of the Ministry of Science and Higher Education of Russia for Valiev Institute of Physics and Technology of RAS.

Citation: Fetisenkova K.A., Melnikov A.E., Miakonkikh A.V., Rogozhin A.E., Tatarintsev A.A., E-beam resist AR-N 7520 in the formation of the photonic structures, St. Petersburg State Polytechnical University Journal. Physics and Mathematics. 17 (3.1) (2024) 278–282. DOI: https://doi.org/10.18721/JPM.173.156

Материалы конференции
УДК 537.533.9
DOI: https://doi.org/10.18721/JPM.173.156

Электронный негативный резист AR-N 7520 в процессах формирования фотонных структур

К.А. Фетисенкова [1, 2] ✉, А.Е. Мельников [2], А.В. Мяконьких [2],
А.Е. Рогожин [2], А.А. Татаринцев [2]

[1] Физико-технологический институт имени К. А. Валиева РАН, Москва, Россия;
[2] Московский физико-технический институт, Москва, Россия
✉ fetisenkova.ka@phystech.edu

Аннотация. Проведено исследование селективности плазмохимического травления кремния Si по отношению к маске из негативного электронного резиста AR-N7520 в зависимости от доли SF6 плазмообразующей смеси SF6/C4F8 и напряжения смещения. В оптимизированном процессе была получена высокая селективность травления 8.0 ± 1,8. Получено оптимальное значение дозы экспонирования для резиста AR-N 7520–8200 пКл/см.

Ключевые слова: электронно-лучевая литография, кинетика процессов травления, новолак, плазмохимическое травление, волновод

Финансирование: Работа выполнена в рамках Государственного задания ФТИАН им. К.А. Валиева РАН Минобрнауки РФ по теме № FFNN-2022-0021.

Ссылка при цитировании Фетисенкова К.А., Мельников А.Е., Мяконьких А.В., Рогожин А.Е., Татаринцев А.А. Электронный негативный резист AR-N 7520 в процессах формирования фотонных структур // Научно-технические ведомости СПбГПУ. Физико-математические науки. 2024. Т. 17. № 3.1. С. 278–282. DOI: https://doi.org/10.18721/JPM.173.156

Introduction

The study of the e-beam resist properties, optimization of the electron beam lithography (EBL) parameters, and the etching process are important for nanoelectronics and photonics because the resolution of EBL is defined by the properties of e-beam resist and by processes during development and exposure [1–3].

The negative e-beam resist AR-N 7520 belongs to the novolaks and has high contrast and high plasma etching resistance [4, 5]. Novolaks are polymers with a low molecular weight derived from phenols and formaldehyde [6]. In the processes of the reactive ion etching (RIE) selectivity (the ratio of their etching rates) values can be varied.

The study of EBL and RIE processes with AR-N 7520 will enable a technology for forming silicon waveguides and other photonic nanostructures with lower sidewall roughness and different aspect ratios.

Materials and Methods

A p-type silicon (100) wafers were pretreated in n-methylpyrrolidone and acetone. To promote adhesion, the silicon wafer was held in hexamethyldisilazane (HMDS) vapor at 85 °C for 10 minutes. The AR-N7520 with a concentration of 7.3% (PGMEA, 1-methoxy-2-propanol acetate) was spin-coated onto the surface using an SM-180 centrifuge (SAWATEC AG, Switzerland) at a centrifuge speed of 3000 rpm. The thickness of the resist layer was measured using a spectral ellipsometer M-2000X (J.A. Woollam Co., Inc., USA) and amounted to 100 ± 1nm. The exposure was carried out using EBL system Raith-150 (Raith, Inc., USA) with the e-beam energy of 30 keV, the beam current was 150 pA. The pattern of lines of 1 mm in length was formed. The line exposure dose ranged from 4000 to 16000 pC/cm with a step of 200 pC/cm. Development was performed in 25% tetramethylammonium hydroxide (TMAH) solution for 50 s at 21 °C.

RIE was performed on a Dual PlasmaLab 100 (Oxford Instruments Plasma Technology, UK) using an inductively coupled plasma (ICP) of the SF_6/C_4F_8 feeding gas. The wafers were segmented to obtain a set of samples with identical patterns of lines (60 lines per sample). Variation of the SF6 fraction in feeding gas in the range of 15% – 25% was investigated at 125 V DC bias. The effect of DC bias voltage on the etching process was studied in the range of 80 V – 150 V at a constant fraction of SF6 in feeding gas 22%. The etching process time was 30 s.

Images of the pattern of lines after etching and the thickness of the AR-N 7520 resist before and after the etching process, and the depth of silicon etching were obtained using a scanning electron microscope (SEM) Ultra 55 (Carl Zeiss AG, Germany).

The selectivity of the silicon RIE through the AR-N7520 mask was calculated as the ratio of the Si etching depth to the decrease in the height resist line during the etching process:

$$S = \frac{d_{\text{Si}}}{d_0 - d} \quad (1)$$

where d_{Si} is the depth of silicon etching, d_0 is the height of the resist line before etching and d is the height of the resist line after etching. The etching rate was calculated as the ratio of the etching depth to the etching time for each line.

Results and Discussion

The study of the samples after development was carried out to determine the dependence of the line height on the exposure dose. The dependence of the line height on the exposure dose is presented in Figure 1. It can be seen that the optimal value of the line exposure dose is 8200 pC/cm.

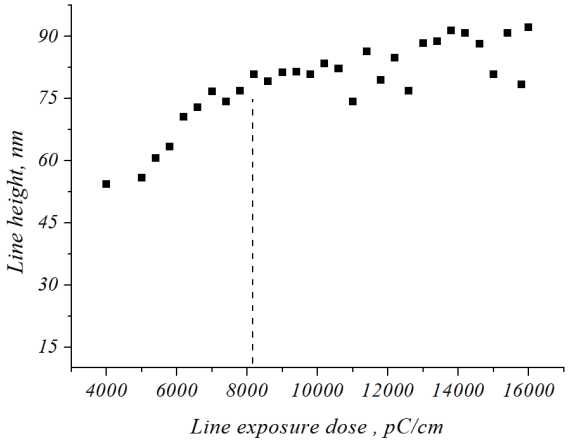

Fig. 1. Dependence of line height after development on the line exposure dose

The selectivity dependences on the fraction of SF6 in the feeding gas and bias voltage were obtained. Figure 2, *a* shows the dependence of the silicon etching rate (R_{Si}), etching rate of AR-N 7520 resist (R_{AR-N}), and selectivity (S) for the RIE at different SF_6 fractions in the feeding gas and constant bias voltage of 125 V. Figure 2, *b* shows the dependence of silicon etching rate (RSi), resist etching rate (R_{AR-N}), and selectivity (S) at the different values of bias voltage (−80 V, −100 V, −150 V) in the process of RIE and with a constant fraction of SF_6 in the feeding gas equal to 22%.

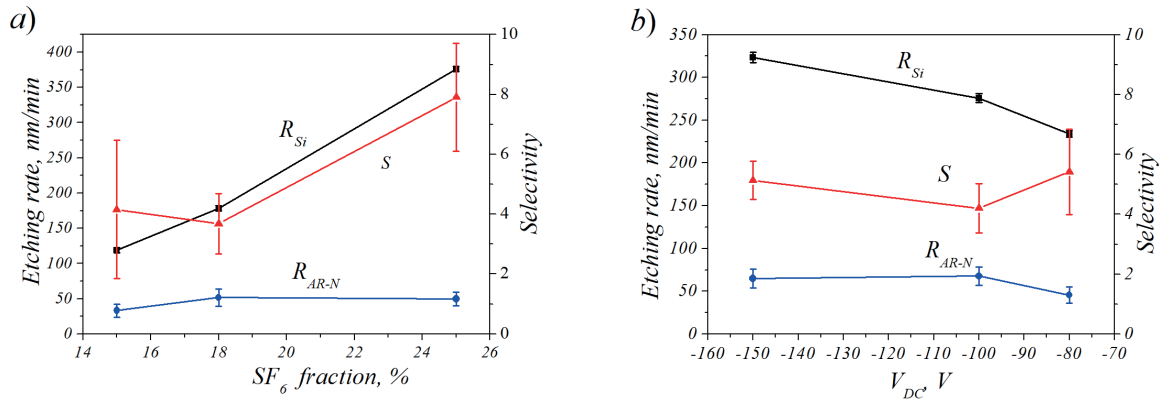

Fig. 2. Dependence of silicon etching rate, etching rate of AR-N 7520 resist, and selectivity on the SF_6 fraction in the feeding gas (*a*); dependence of silicon etching rate, etching rate of AR-N 7520 resist, and selectivity on the bias voltage (*b*)

The resist etching rate remains almost constant with an increasing fraction of SF_6 in the feeding gas, and the etching selectivity of silicon to the AR-N 7520 increases. The RIE process with a fraction of SF_6 in the feeding gas equal to 25% provides an etching selectivity of 8.0 ± 1.8. In the processes with the voltage in range from 100 V to 150 V the resist etching rate grows insignificantly. The process allows to obtain etching selectivity of 5.0 ± 1.4.

Figure 3 shows the dependence of the sidewall angle α on the SF_6 fraction in the feeding gas during RIE.

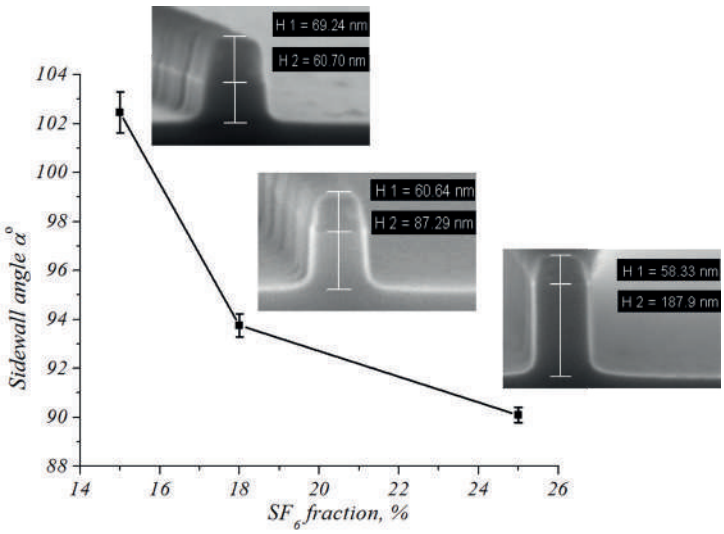

Fig. 3. Dependence of the sidewall angle of structures as a function of the SF_6 fraction in the feeding gas. SEM images of the lines also are shown (line width is about 60 nm)

Changing the ratio of the gas fraction in the feeding gas, it is possible to control the sidewall slope in the structure. Using the 25% fraction of SF_6 in the SF_6/C_4F_8 feeding gas allows us to obtain structures with a sidewall slope angle of $90.1 \pm 0.3°$

Conclusion

The RIE process with a fraction of SF6 in the feeding gas equal to 25% and a bias voltage of 125 V provides an etching selectivity of 8.0 ± 1.8. The optimum electron beam exposure dose for defining the mask was found to be 8200 pC/m at 30 keV. Selectivity does not depend on the exposure dose, at dose values over 4000 pC/cm.

REFERENCES

1. **Gao J., Zhang S., Cui X., Cong X., Guo X., Hu R., Wang S., Chen J., Li Y., Yang G.,** Effective Optimization Strategy for Electron Beam Lithography of Molecular Glass Negative Photoresist, Advanced Materials Interfaces. 10 (20) (2023) 2300194.

2. **Nedeljkovic M., Khokhar A.Z., Hu Y., Chen X., Penades J.S., Stankovic S., Chong H.M.H., Thomson D.J., Gardes F.Y., Reed G.T., Mashanovich G.Z.,** Silicon photonic devices and platforms for the mid-infrared, Optical Materials Express. 3 (9) (2013) 1205–1214.

3. **Gangnaik A.S., Georgiev Y.M., Holmes J.D.,** New generation electron beam resists: a review, Chemistry of Materials. 29 (5) (2017) 1898–1917.

4. **Grigorescu A.E., Hagen C.W.,** Resists for sub-20-nm electron beam lithography with a focus on HSQ: state of the art, Nanotechnology. 20 (29) (2009) 292001.

5. **Borzenko T., Fries P., Schmidt G., Molenkamp L. W., Schirmer M.,** A process for the fabrication of large areas of high resolution, high aspect ratio silicon structures using a negative tone Novolak based e-beam resist, Microelectronic engineering. 86 (4-6) (2009) 726–729.

6. **Hinsberg W.D., Wallraff G.M.** Lithographic Resists. Kirk-Othmer encyclopedia of Chemical Technology. (2005).

THE AUTHORS

FETISENKOVA Ksenia A.
fetisenkova@ftian.ru
ORCID: 0000-0003-3849-108X

MELNIKOV Alexander E.
Alexen96@gmail.com

MIAKONKIKH Andrey V.
miakonkikh@ftian.ru
ORCID: 0000-0002-9547-1619

ROGOZHIN Alexander E.
rogozhin@ftian.ru
ORCID: 0000-0002-9554-673X

TATARINTSEV ANDREY A.
tatarintsev@ftian.ru
ORCID: 0000-0002-4978-2280

Received 10.07.2024. Approved after reviewing 19.07.2024. Accepted 20.07.2024.

Conference materials
UDC 54.057
DOI: https://doi.org/10.18721/JPM.173.157

Formation of mesoporous silica coating on cores with different surface properties

D.A. Eurov [1] ✉, E.Yu. Stovpiaga [1], D.A. Kirilenko [1], D.A. Kurdyukov [1]

[1] Ioffe Institute, St. Petersburg, Russia

✉ edan@mail.ru

Abstract. An approach has been developed for the wet synthesis of mesoporous silica shell on the surface of various spherical composite particles with different zeta potential. It is demonstrated that the surface charge of the core particles influences the porous structure of the obtained shell. The proposed method allows obtaining a uniform layer of the same thickness on the surface of each core particle preventing their coalescence.

Keywords: spherical particles, core-shell nanostructures, silica, zeta potential, mesopores

Funding: This work was funded by the Russian Science Foundation, project no. 23-79-00018.

Citation: Eurov D.A., Stovpiaga E.Yu., Kirilenko D.A., Kurdyukov D.A., Formation of mesoporous silica coating on cores with different surface properties, St. Petersburg State Polytechnical University Journal. Physics and Mathematics. 17 (3.1) (2024) 283–287. DOI: https://doi.org/10.18721/JPM.173.157

Материалы конференции
УДК 54.057
DOI: https://doi.org/10.18721/JPM.173.157

Формирование оболочки мезопористого кремнезема на частицах с разными свойствами поверхности

Д.А. Еуров [1] ✉, Е.Ю. Стовпяга [1], Д.А. Кириленко [1], Д.А. Курдюков [1]

[1] Физико-технический институт им. А.Ф. Иоффе РАН, Санкт-Петербург, Россия

✉ edan@mail.ru

Аннотация. Разработан подход к покрытию сферических композитных частиц с различным дзета-потенциалом, находящихся в жидкой среде, оболочкой мезопористого кремнезема. Показано, что заряд поверхности частиц, выступающих в качестве ядра, оказывает влияние на пористую структуру формируемой оболочки. Метод позволяет осуществлять равномерное покрытие каждой частицы оболочкой одинаковой толщины, не приводя к коагуляции исходных ядер.

Ключевые слова: сферические частицы, наноструктуры ядро-оболочка, кремнезем, электрокинетический потенциал, мезопоры

Финансирование: Работа выполнена за счет гранта Российского научного фонда № 23-79-00018.

Ссылка при цитировании: Еуров Д.А., Стовпяга Е.Ю., Кириленко Д.А., Курдюков Д.А., Формирование оболочки мезопористого кремнезема на частицах с разными свойствами поверхности // Научно-технические ведомости СПбГПУ. Физико-математические науки. 2024. Т. 17. № 3.1. С. 283–287. DOI: https://doi.org/10.18721/JPM.173.157

Introduction

Nanotechnology has been a wide and growing field of research since the end of the last century. It deals with materials of various types at nanoscale level, where they demonstrate novel properties compared to their bulk counterparts. The synthesis, characterization, and applications of nanoparticles are among the most important sections of the wide range of nanotechnology areas [1]. To expand the functionality of this kind of materials researchers create not only single-composition nanoparticles, which are made from single substance, but also composite ones often possessing the so-called core-shell structure. The purpose of the coating can be varied, such as surface modification, increasing the functionality, stability, reduction in consumption of precious materials, and so on [1]. Core/shell nanoparticles are gradually attracting more and more attention, since they exhibit distinctive properties of the different materials applied together, which is especially important to meet the diverse application requirements. They are widely used in, for example, catalysis [2, 3], electronics [4, 5], biomedicine [6, 7]. For biomedical purposes silica shell is highly sought after, since silica is biocompatible (approved by FDA and EFSA), possess tunable surface functionalization, high adsorption capacity, and allows protecting healthy tissues from interaction with toxic drugs. Still the coating of various nanoparticle with silica shell may be challenging due to different surface properties especially zeta potential of the core particles, which is often not enough (in absolute value) to form stable suspension at neutral pH. As a result, the coagulation can occur hindering the formation of a uniform shell on the surface of each particle.

Materials and Methods

Materials. We used the following reagents: cetyltrimethylammonium bromide (CTAB, $C_{16}H_{33}N(CH_3)_3Br$), 99.99% (Acros Organics, Germany); aqueous ammonia (NH_3), 24 wt.%; ethanol (C_2H_5OH), 95.7 vol.%; deionized water (H_2O) with a resistance of 10 MΩ; tetraethoxysilane (TEOS, $Si(OC_2H_5)_4$), 99.9% (Acros Organics, Germany); gadolinium oxide (Gd_2O_3), 99.99% (Sigma-Aldrich, Germany); Iron (III) nitrate crystal hydrate ($Fe(NO_3)_3 \cdot 9H_2O$) ≥ 98% (Sigma-Aldrich, Germany); nitric acid (HNO_3), 70 wt.%; hydrochloric acid (HCl), 37 wt.%, ACS reagent grade; monosilane (SiH_4), electronic grade (Sigma-Aldrich, Germany). All the chemicals were of analytical purity grade commercially available. There was no need to additionally purify the reagents.

Methods. The core particles were obtained based on our previously developed methods for the synthesis of silica and various silica-based composite materials. In particular, the procedure for the synthesis of non-porous spherical silica particles ($nSiO_2$) was similar to that employed in [8, 9]. For the synthesis of spherical mesoporous silica ($mSiO_2$) particles filled with magnetite ($mSiO_2/Fe_3O_4$) we used the developed method for the filling of various silica matrices with iron oxides [10, 11]. Spherical mesoporous silica particles filled with gadolinium oxide ($mSiO_2/Gd_2O_3$) were synthesized based on the technique described in [12, 13]. For the synthesis of silicon within the pores of spherical mesoporous silica particles ($mSiO_2/Si$) we used the modified method of monosilane thermal decomposition [14, 15].

The synthesis of mesoporous silica shell was carried out via basic hydrolysis of TEOS in a water-ammonia-ethanol mixture containing organic pore-forming agent – CTAB. The molar ratio of the reagents $TEOS:H_2O:NH_3:C_2H_5OH:CTAB$ was 1:370:10:230:0.2. The core particles added to the reaction mixture acted as nucleation centers. TEOS was added dropwise under stirring to the resulting solution. After 6 h of further stirring, the particles obtained were washed in an alcoholic solution (0.01 M) of HCl, centrifuged, dried in air at 80 °C for 24 h, and calcined at 250 °C for 5 h.

Transmission electron microscopic measurements were performed using a Jeol JEM-2100F microscope (accelerating voltage 200 kV, point-to-point resolution 0.19 nm) equipped with Bruker XFlash 6T-30 energy dispersive X-ray (EDX) spectrometer. The nitrogen adsorption was performed using a Micromeritics 3FLEX at a temperature of 77 K. The specific surface area was calculated by the Brunauer – Emmett – Teller (BET) method, and the pore size distribution was found using the nonlocal density functional theory (NLDFT). The electrophoretic mobility of

the particles was determined by the method of electrophoretic light scattering at a temperature of 25 °C with a Zetasizer Nano (Malvern, UK). The electrokinetic potential was calculated using the built-in software package of the analyzer.

Results and Discussion

We used various spherical particles, namely $nSiO_2$, $mSiO_2/Si$, $mSiO_2/Fe_3O_4$ and $mSiO_2/Gd_2O_3$ possessing different surface properties as the cores for the covering with mesoporous silica shell. The results of the zeta potential measurements show (Fig. 1, *a*) that all the particles possess different surface charge almost in the whole range of pH values under study.

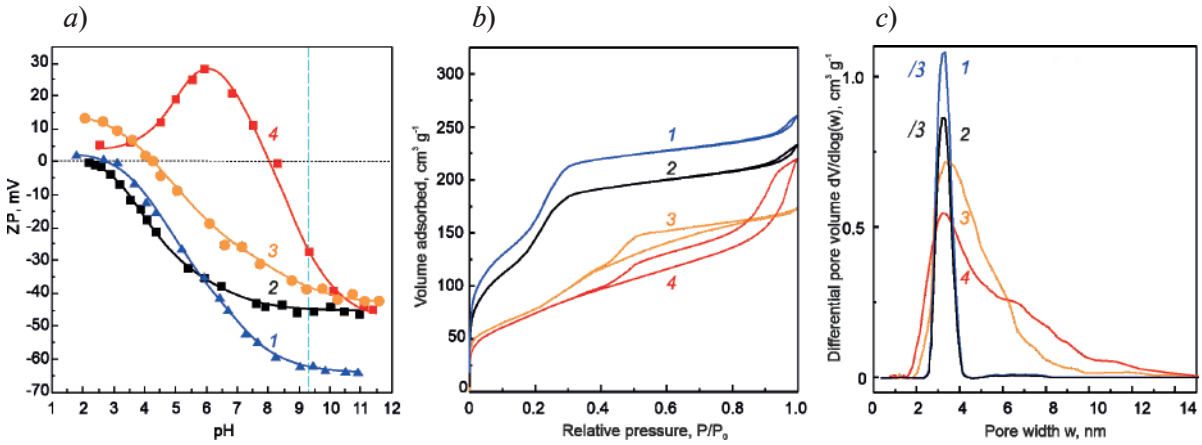

Fig. 1. Zeta potentials of $nSiO_2$ (*1*), $mSiO_2/Si$ (*2*), $mSiO_2/Fe_3O_4$ (*3*) and $mSiO_2/Gd_2O_3$ (*4*) particles at different pH (*a*); N_2 adsorption and desorption isotherms measured at 77 K (*b*) and NLDFT pore size distributions (*c*) for the same particles covered with a mesoporous silica shell. Blue vertical dashed line in panel (*a*) indicates pH of the reaction mixture used

As stated earlier the synthesis of mesoporous silica shell was carried out in the mixture of water, ammonia and ethanol containing core particles. After the addition of TEOS to the mixture the formation of mesoporous silica proceeds by an aggregative mechanism, when CTAB forms cylindrical micelles, which are covered, as a result of TEOS hydrolysis with a layer of amorphous SiO_2. Then, the 10-nm SiO_2/CTAB clusters coagulate with the formation of the shell on the surface of core particles [12]. Pores remain in place of CTAB after its removal by thermal annealing. The pH of the reaction mixture was adjusted to ~9.3 (marked by a blue dashed line in Fig. 1, *a*). At this value all the particles possess negative surface charge over −30 mV, which indicates their aggregative stability. This determines the fact that they do not coagulate and present in the solution as individual particles, which ensures the coating of each particle with a silica layer of the same thickness without their coalescence.

Fig. 1, *b* show the isotherms for the particles after coating with shell. It can be seen, that for the non-porous SiO_2 and $mSiO_2/Si$ particles possessing the highest in absolute value zeta potential the largest amount of the adsorbate is observed after the coating. The BET specific surface area (SSA) values calculated for these particles are 580 and 530 $m^2 g^{-1}$ respectively. The corresponding pore volumes are 0.41 and 0.37 $cm^3 g^{-1}$. The pore size distribution (Fig. 1, *c*) indicates the presence of one pronounced peak at 3.1 nm, which corresponds to the size of CTAB micelles. When the surface charge of core particles decreases in absolute value (in the case of $mSiO_2/Fe_3O_4$ and $mSiO_2/Gd_2O_3$ particles) isotherms of the particles after coating are lower indicating the lower BET SSA. Indeed, the corresponding values are 320 and 270 $m^2 g^{-1}$. This may be due to that CTAB molecules in the vicinity of surface with lower charge form the so-called platelet micelles, rather than cylindrical produced in the case of $nSiO_2$ and $mSiO_2/Si$ particles possessing higher negative surface charge, which leads to the formation of larger pores with lower SSA. This is confirmed by the pore size distributions (Fig. 1, *c*), which is substantially wider in this case. Note, the pronounced peak at 3.1 nm remains. Probably, larger pores are formed closer to the cores in the place of platelet CTAB micelles. Then, after a certain thickness the subsequent growth of the shell continues via coagulation of SiO_2/CTAB clusters consisting of cylindrical CTAB micelles, which determines

the formation of 3-nm pores. The obtained values of pore volume for $mSiO_2/Fe_3O_4$—shell and $mSiO_2/Gd_2O_3$—shell are 0.37 and 0.33 $cm^3\ g^{-1}$ respectively. The dependence of the zeta potential on pH for all the particles after coating is similar to that of $nSiO_2$ particles (Fig. 1, *a* curve *1*). Such values of the particles' surface charge ensure their aggregative stability at pH greater than 5, which is important from the practical point of view.

Fig. 2 shows TEM images of the obtained core-shell particles. The boundaries of the core and shell are clearly distinguishable. It can be seen that the covering of particles with mesoporous silica shell do not affect the morphology of the initial core particles, which remain spherical and do not coagulate. EDX elemental maps demonstrate that there is no redistribution of the core materials during silica shell synthesis. They are still homogeneously distributed within the cores of particles, and the shell in all the cases is fully composed of SiO_2. The TEM results are also confirmed the formation of a uniform mesoporous silica layer of the same thickness on the surface of cores. Note, the thickness of the shell can be controllably varied by the concentrations of reagents in the reaction mixture. The technique we developed allows obtaining shells with a thickness from tens of nanometers to several hundreds.

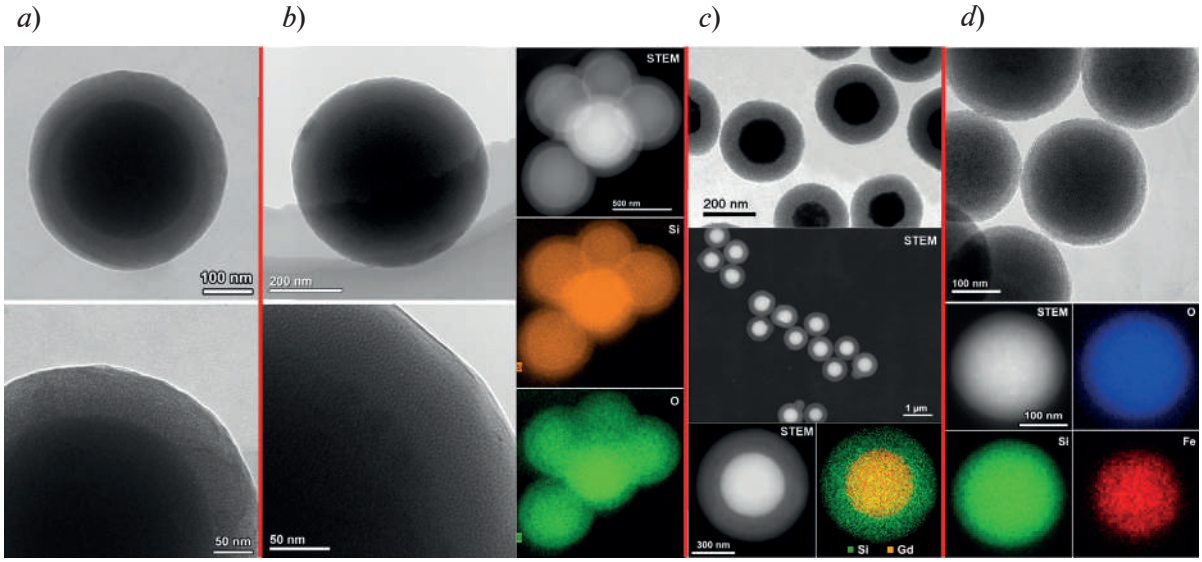

Fig. 2. TEM and STEM images and EDX elemental maps for the $nSiO_2$-shell (*a*), $mSiO_2$/Si-shell (*b*), $mSiO_2/Gd_2O_3$-shell (*c*) and $mSiO_2/Fe_3O_4$-shell (*d*) particles. There are no EDX maps for the $nSiO_2$-shell particles, since the core and the shell of the particles are made of the same material

Conclusion

An approach for the covering of various spherical particles having different surface charge with mesoporous silica shell possessing high SSA and pore volume is proposed. The synthesis of shell is carried out via basic hydrolysis of organosilane in a water-ammonia-ethanol mixture containing pore-forming agent. The synthetic conditions are selected in such a way that the cores are present in a form of aggregatively stable particles ensuring the formation of uniform layer of the same thickness on each particle. It is found that the lower the zeta potential of core is the wider the pore size distribution of the resulted shell is observed, however with the presence of a characteristic peak at 3.1 nm. The developed technique is a promising tool for the obtaining core-shell particles for biomedical applications that allows protecting the core and expanding the functionality of the particles.

Acknowledgments

The TEM study was carried out on equipment of the Federal Joint Research Center "Material science and characterization in advanced technology".

REFERENCES

1. **Chaudhuri R.G., Paria S.,** Core/Shell Nanoparticles: Classes, Properties, Synthesis Mechanisms, Characterization, and Applications, Chemical Reviews. 112 (2012) 2373–2433.

2. **Gawande M.B., Goswami A., Asefa T., Guo H., Biradar A.V., Peng D.-L., Zboril R., Varma R.S.,** Core–shell nanoparticles: synthesis and applications in catalysis and electrocatalysis, Chemical Society Reviews. 44 (2015) 7540–7590.

3. **Zhang X., Han S., ZhuB., Zhang G., Li X., GaoY., Wu Z., Yang B., Liu Y., Baaziz W.,Ersen O., Gu M., Miller J.T., Liu W.,** Reversible loss of core–shell structure for Ni–Au bimetallic nanoparticles during CO_2 hydrogenation, Nature Catalysis. 3 (2020) 411–417.

4. **Pajor-Świerzy A., Szczepanowicz K., Kamyshny A., Magdassi S.,** Metallic core-shell nanoparticles for conductive coatings and printing, Advances in Colloid and Interface Science. 299 (2022) 102578.

5. **Ghosh B., Sahu S., Pal A.J.,** Core-Shell Nanoparticles: An Approach to Enhance Electrical Bistability, Journal of Physical Chemistry C. 112 (2008) 11290–11294.

6. **Chatterjee K., Sarkar S., Rao K. J, Paria S.,** Core/shell nanoparticles in biomedical applications, Advances in Colloid and Interface Science. 209 (2014) 8–39.

7. **Lin C.-W., Chen J.-M., Lin Y.-J., Chao L.-W., Wei S.-Y., Wu C.-H., Jeng C.-C., Wang L.-M., Chen K.-L.,** Magneto-Optical Characteristics of Streptavidin-Coated Fe_3O_4@Au Core-Shell Nanoparticles for Potential Applications on Biomedical Assays, Scientific Reports. 9 (2019) 16466.

8. **Stöber W., Fink A., Bohn E.,** Controlled growth of monodisperse silica spheres in the micron size range, Journal of Colloid and Interface Science. 26 (1) (1968) 62–69.

9. **Stovpyaga E.Yu., Eurov D.A., Kurdyukov D.A., Yakovlev S.A., Kukushkina Yu.A., Golubev V.G.,** 3D photonic crystals with a hierarchical pore arrangement. Technical Physics Letters. 40 (2014) 224–227.

10. **Stovpiaga E.Yu., Eurov D.A., Kurdyukov D.A., Smirnov A.N., Yagovkina M.A., Grigorev V.Yu., Romanov V.V., Yakovlev D.R., Golubev V.G.,** The synthesis of clusters of iron oxides in mesopores of monodisperse spherical silica particles. Physics of the Solid State. 59 (2017) 1623–1628.

11. **Grudinkin S.A., Kaplan S.F., Kartenko N.F., Kurdyukov D.A., Golubev V.G.,** Opal-hematite and opal-magnetite films: lateral infiltration, thermodynamically driven synthesis, photonic crystal properties. Journal of Physical Chemistry C. 112 (2008) 17855–17861.

12. **Eurov D.A., Kurdyukov D.A., Kirilenko D.A., Kukushkina J.A., Nashchekin A.V., Smirnov A.N., Golubev V.G.,** Core–shell monodisperse spherical $mSiO_2/Gd_2O_3:Eu^{3+}$@$mSiO_2$ particles as potential multifunctional theranostic agents. Journal of Nanoparticle Research. 17 (2015) 82.

13. **Orekhova K.N., Eurov D.A., Kurdyukov D.A., Golubev V.G., Kirilenko D.A., Kravets V.A., Zamoryanskaya M.V.,** Structural and luminescent properties of Gd oxide doped with Eu^{3+} embedded in mesopores of SiO_2 particles. Journal of Alloys and Compounds. 678 (2016) 434–438.

14. **Bogomolov V.N., Golubev V.G., Kartenko N.F., Kurdyukov D.A., Pevtsov A.B., Prokof'ev A.V., Ratnikov V.V., Feoktistov N.A., Sharenkova N.V.,** Fabrication of regular three-dimensional lattices of submicron silicon clusters in an SiO_2 opal matrix. Technical Physics Letters. 24 (2017) 326–327.

15. **Kurdyukov D.A., Eurov D.A., Shmakov S.V., Kirilenko D.A., Kukushkina J.A., Smirnov A.N., Yagovkina M.A., Klimenko V.V., Koniakhin S.V., Golubev V.G.,** Fabrication of doxorubicin-loaded monodisperse spherical micro-mesoporous silicon particles for enhanced inhibition of cancer cell proliferation, Microporous Mesoporous Mater. 281 (2019) 1–8.

THE AUTHORS

EUROV Daniil A.
edan@mail.ru
ORCID: 0000-0002-7471-4028

KIRILENKO Demid A.
zumsisai@gmail.com
ORCID: 0000-0002-1571-209X

STOVPIAGA Ekaterina Yu.
kattrof@gvg.ioffe.ru
ORCID: 0000-0003-0434-5252

KURDYUKOV Dmitry A.
kurd@gvg.ioffe.ru
ORCID: 0000-0002-3041-9609

Received 15.07.2024. Approved after reviewing 22.07.2024. Accepted 24.07.2024.

Conference materials
UDC 537.226
DOI: https://doi.org/10.18721/JPM.173.158

Evolution of crystalline phases of P(VDF-TeFE) films filled with nanographite in various aprotic solvents

A.P. Khramov [1] ✉, N.G. Savinski [1], E.A. Grushevsky [1]

[1] Valiev Institute of Physics and Technology of RAS, Yaroslavl Branch, Yaroslavl, Russia

✉ artem.khramov.99.99@mail.ru

Abstract. The work under discussion describes the preparation and study copoly(vinylidene fluoride–tetrafluoroethylene) (P(VDF–TFE)) films filled with chemically exfoliated nanographite and crystallized by drying from various solvents. The content of α, β and γ phases of PVDF was estimated via Fourier transform infrared spectroscopy (FTIR) and supported by Raman spectroscopy and X-ray diffractometry. Experimental study revealed that films made from a solution of dimethyl sulfoxide (DMSO) have a higher content of the polar β-phase and films filled with nanographite showed increased degree of of β-phase content.

Keywords: poly(vinylidenefluoride–tetrafluoroethylene P(VDF-TeFE), dimethyl sulfoxide (DMSO), dimethylformamide (DMF), beta phase, FTIR, XRD, nanographite

Funding: The work was performed within the framework of the State program no. FFNN-2022-0018 of the Ministry of Science and Higher Education for Russia Yaroslavl branch of Valiev Institute of Physics and Technology of RAS.

Citation: Khramov A.P., Savinski N.G., Grushevsky E.A., Evolution of crystalline phases of P(VDF-TeFE) films filled with nanographite in various aprotic solvents, St. Petersburg State Polytechnical University Journal. Physics and Mathematics. 17 (3.1) (2024) 288–292. DOI: https://doi.org/10.18721/JPM.173.158

Материалы конференции
УДК 537.226
DOI: https://doi.org/10.18721/JPM.173.158

Эволюция кристаллических фаз в пленках сополимера поливинилиденфторида и тетрафторэтилена П(ВДФ-ТФЭ), наполненных нанографитом, в различных апротонных растворителях

А.П. Храмов [1] ✉, Н.Г. Савинский [1], Е.А. Грушевский [1]

[1] Ярославский филиал Физико-Технологического института РАН им. К.А. Валиева, г. Ярославль, Россия

✉ artem.khramov.99.99@mail.ru

Аннотация. Представленная работа описывает получение и исследование пленок сополимера поли (винилиденфторида–тетрафторэтилена) (П(ВДФ–ТФЭ)), заполненных электро-химически эксфолированным нанографитом и кристаллизованных из различных растворителей. Содержание α, β и γ-фаз в ПВДФ было оценено с помощью инфракрасной спектроскопии с преобразованием Фурье (ИКФС) и подтверждено методами рамановской спектроскопии и рентгеновской дифрактометрии. Было обнаружено, что пленки, изготовленные из раствора диметилсульфоксида (ДМСО), имеют более высокое содержание полярной β-фазы. Пленки, заполненные нанографитом, показали повышенную степень содержания β-фазы.

Ключевые слова: поли(винилиден-тетрафторэтилен) П(ВДФ-ТФЭ), диметилсульфоксид (ДМСО), диметилформамид (ДМФ), бета-фаза, ИК-спектроскопия, рентгенография, нанографит

Финансирование: Работа выполнена в рамках Государственной программы № FFNN-2022-0018 Министерства науки и высшего образования России по Ярославскому филиалу Физико-технического института им. К.А. Валиева РАН.

Ссылка при цитировании: Храмов А.П., Савинский Н.Г., Грушевский Е.А. Эволюция кристаллических фаз в пленках сополимера поливинилиденфторида и тетрафторэтилена П(ВДФ-ТФЭ), наполненных нанографитом, в различных апротонных растворителях // Научно-технические ведомости СПбГПУ. Физико-математические науки. 2024. Т. 17. № 3.1. С. 288–292. DOI: https://doi.org/10.18721/JPM.173.158

Introduction

The most prospective in terms of energy conversion are electroactive actuators, devices that transform electrical energy into mechanical one. They are increasingly being used in biological systems due to their promising properties. PVDF is extensively used in sensors and actuators, implantable devices and prostheses, energy harvesting power plants [1].

Currently, considerable attention in materials for actuators is focused on polyvinylidene fluoride (PVDF) and various composites based on it. PVDF can mainly be found in three crystalline phases: α, β and γ. Among the polar phases, the β phase is the most polar and, hence, have the strongest effect on the piezoelectric properties of PVDF. Fig. 1 shows crystalline phases of PVDF (Fig. 1, *a*) and dependency of the piezoelectric coefficient d_{33} on the β-phase content (Fig. 1, *b*) [2].

The purpose of this work is to assess the alteration in the content of the β phase of fluoroplast-42 filled with nanographite applying different solvents at different drying temperatures.

Materials and Methods

The copolymer of vinylidene fluoride and tetrafluoroethylene (fluoroplast grade F-42 mark B) is a crystalline polymer with a melting point of crystallites at 155–160 °C, having the chemical formula $[(-CF_2-CH_2-)n-(CF_2-CF_2-)m]k$ and containing 71% molar vinylidene fluoride (n) and 29% tetrafluoroethylene TFE(m). Electrochemically exfoliated nanographite was obtained in a two-electrode cell at a potential of 7 V in 0.6 M aqueous solution of ammonium peroxide sulfate obtained from graphite foil "Grapflex" RF 0.5 mm thick (with a carbon content of 99.5%, sulfur ≤ 0.12, chlorine ≤ 50 ppm). More details can found in our previous proceedings [3]. The crystallite size of the exfoliated nanographite (NG) was: thickness 14.86 nm; number of layers 44; basal size 17.08 nm. The next step, 0.25 g of the resulting powder was added into 95 g of aprotic solvent, DMSO or DMF. The solutions were mechanically dispersed using the FSH-2A unit at 2000 rpm for 1 hour and ultrasonically treated on the PS-30A unit at 180 Watts for 8 hours.

Fluoroplast-42, herein after referred to as F-42, was added to nanographite solutions in an amount of 5% by weight of the solution, and the nanographite content was 5% by weight relative to F-42. The solutions were alternately mixed at a temperature of 70 °C until F-42 was completely dissolved and treated with a mechanical dispersant FSH - 2A for 1.5 hours. Thus, 5% solutions of polymer F-42 filled with 5% of the mass of nanographite relative to the mass of F-42 were obtained. Further, solutions of F-42 were crystallized from DMSO and DMF at temperatures of 60 °C for 72 hours, 90 °C for 24 hours and 150 °C for 24 hours, respectively.

The study of F-42 films (50–450 μm) was perfomed by SEM Supra 40, Raman spectroscopy (Enspectr R532 spectrometer), infrared Fourier spectroscopy (Perkin-Elmer-TWO spectrometer), X-ray diffractometry (DRON 3M).

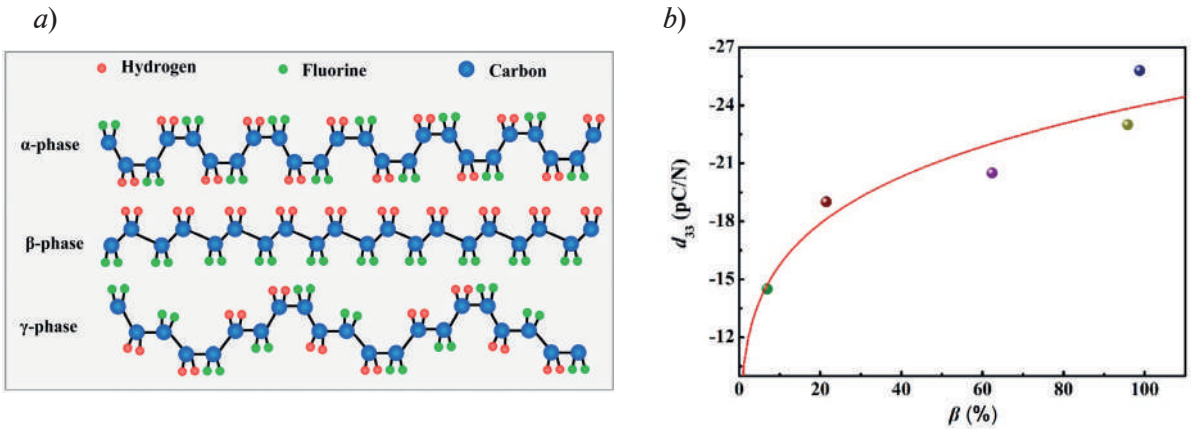

Fig.1. Crystalline phases of PVDF (*a*); dependence of the piezoelectric coefficient d_{33} on the β-phase content (*b*)

Results and Discussion

Figures 2, *a, b* show the typical FTIR spectra of F-42 samples and the fitting area for calculating the β-phase content. Peaks at 771 cm^{-1}, 840 cm^{-1}, 1234 cm^{-1} and 1275 cm^{-1} attribute to α-phase CF_2 bending, β or γ-phase CH_2 rocking, γ and β both to CF out-of-plane deformation vibrations respectively. The peak at 1251 cm^{-1}, as evidenced by [4] does not relate to either nanographite, PVDF or PTFE, but to the amorphous region of the copolymer as whole. The calculation of the β-phase is based on the ratio of the integral intensities of the decomposed peaks between the β- and γ- phases. The calculation based on the following equations for evaluation the content of the electroactive phase F_{EA}, polar β−phase $F(\beta)$ and γ−phase $F(\gamma)$ [5]:

$$F_{EA} = \frac{I_{EA}}{\frac{K_{840}}{K_{763}} I_{763} + I_{EA}} \times 100\% \quad (1)$$

$$F(\beta) = F_{EA} \times \left(\frac{I_{\beta}^{int}}{I_{\beta}^{int} + I_{\gamma}^{int}} \right) \quad (2)$$

where I_{EA} is the absolute peak intensity at 840 cm^{-1}, I_{763} is the absolute peak intensity at 763 cm^{-1}, K_{840} and K_{763} are extinction coefficients at the corresponding absorption frequencies equal to 7.7×104 and 6.1×104 cm^2/mol, respectively. I_{β}^{int} and I_{γ}^{int} are the integral areas of the peaks at 1275 cm^{-1} corresponding to the β−phase and at 1234 cm^{-1} corresponding to the γ−phase of F−42 in the spectral range of 1200−1300 cm^{-1}, after the peak separation procedure using the ACDLABS program.

Calculation given in [5] has no application for the current polymer, since there is a peak of the amorphous phase of the copolymer at 1250 cm^{-1}. To solve this problem, it is proposed to introduce spectrum processing in the 1200 cm^{-1}−1300 cm^{-1} region and subsequent peak deconvolution with calculation of integral peak intensities as replacement values in formula (2).

Figure 3 shows a diagram of the β-phase content of F-42 films under different manufacturing conditions. By making pairwise comparisons, it can be concluded that, compared with DMF, films crystallized from DMSO solution always have a higher β-phase content. Films filled with nanographite almost always have higher content of the β-phase. The alpha phase content fluctuates slightly from sample to sample and does not exceed 6%. Phase calculations were also performed based on XRD and Raman spectroscopy of the samples and the results in most cases correlate well with FTIR.

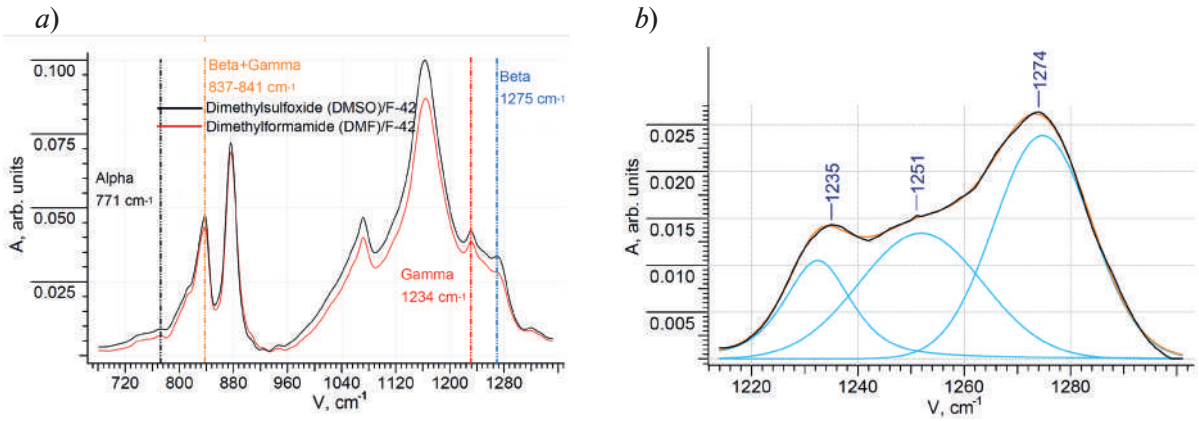

Fig.2. FTIR spectra of DMSO(DMF)/F-42 samples with nanographite at drying temperature 90 °C (*a*); FTIR fitting area for calculating the ratio of γ- and β-phases (*b*)

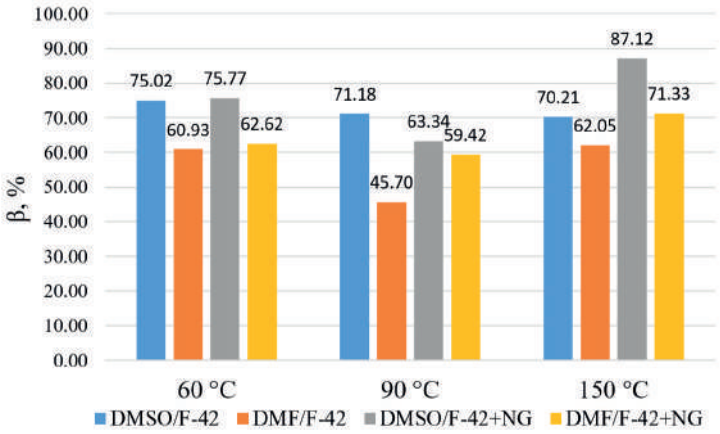

Fig. 3. Diagram of the beta phase content in F-42 films in different solvents, filling and drying conditions

Conclusion

Thus, DMSO is the best aprotic solvent for copolymer of vinylidene fluoride and tetrafluoroethylene F-42. Filling F-42 films with nanographite increases the beta phase content in the polymer. The alpha phase content does not exceed 6%, which indicates a large content of the electroactive phase as a whole. FTIR is sufficiently accurate to estimate the phase content in the polymer due to the simplicity of deconvolution of peaks in the region of 1200–1300 cm^{-1}.

REFERENCES

1. **Naumova O.V., Generalov V.M., Zaitseva E.G., Latyshev A.V., Aseev A.L., Pyankov S.A., Kolosova I.V., Ananko G.G, Agafonov A. ., Gavrilova E.V., Maksyutov R.A., Safatov A.S.,** Biosensors Based on SOI Nanowire Transistors for Biomedicine and Virusology, Russian Microelectronics. 50 (2021) 137.

2. **Li X., Wang Y., He T., Hu Q., Yang Y.,** Preparation of PVDF flexible piezoelectric film with high β-phase content by matching solvent dipole moment and crystallization temperature, Journal of Materials Science: Materials in Electronics. 30 (2019) 20174.

3. **Grushevski E., Savelev D., Mazaletski L., Savinski N., Puhov D.,** The scalable production of high-quality nanographite by organic radical-assisted electrochemical exfoliation, Journal of Physics: Conference Series. 2086 (2021) 012014.

4. **Haque R.I., Vié R., Germainy M., Valbin L., Benaben P., Boddaert X.,** Inkjet printing of high molecular weight PVDF-TrFE for flexible electronics, Flexible and Printed Electronics. 1 (2015) 015001.

5. **Cai X., Lei T., Sun D., Lin L.,** A critical analysis of the α, β and γ phases in poly (vinylidene fluoride) using FTIR, RSC advances. 7 (2017) 15382.

THE AUTHORS

KHRAMOV Artem P.
artem.khramov.99.99@mail.ru

GRUSHEVSKI Egor A.
yaregor@mail.ru

SAVINSKI Nikolay G.
savinski1@yandex.ru

Received 10.07.2024. Approved after reviewing 19.07.2024. Accepted 20.07.2024.

Conference materials
UDC 546.05; 538.975
DOI: https://doi.org/10.18721/JPM.173.159

Optical properties of the CuO-ZnO thin films

I.O. Ignatieva [1] ✉, A.P. Starnikova [2], V.V. Petrov [2], E.M. Bayan [1]

[1] Southern Federal University, Rostov-on-Don, Russia;

[2] Institute of Nanotechnologies, Electronics and Electronic Equipment Engineering, Southern Federal University, Taganrog, Russia

✉ iignateva@sfedu.ru

Abstract. In this work, we investigate the optical properties of CuO-ZnO thin films formed on quartz substrate. CuO-ZnO nanocomposite films were obtained by solid-phase pyrolysis with different atomic Cu:Zn ratios (1:99, 3:97, 5:95, 10:90) and annealed at a temperature of 600 °C. The crystal structure of the films was studied, and their optical transmission spectra were analyzed. It was found that transmittance is more than 84% for all materials in the range from 400 to 1000 nm.

Keywords: zinc oxide, copper oxide, composite, thin films, optical properties

Funding: The work was supported by Grant 4L/22-04-PISH carried out at the Southern Federal University.

Citation: Ignatieva I.O., Starnikova A.P., Petrov V.V., Bayan E. M., Optical properties of the CuO-ZnO thin films, St. Petersburg State Polytechnical University Journal. Physics and Mathematics. 17 (3.1) (2024) 293–296. DOI: https://doi.org/10.18721/JPM.173.159

Материалы конференции
УДК 546.05; 538.975
DOI: https://doi.org/10.18721/JPM.173.159

Оптические свойства тонких пленок CuO-ZnO

И.О. Игнатьева [1] ✉, А.П. Старникова [2], В.В. Петров [2], Е.М. Баян [1]

[1] Южный федеральный университет, г. Ростов-на-Дону, Россия;

[2] Институт нанотехнологий, электроники и приборостроения, Южный федеральный университет, г. Таганрог, Россия

✉ iignateva@sfedu.ru

Аннотация. В работе изучаются кристаллическая структура и оптические свойства тонких пленок CuO-ZnO, сформированных на подложках из кварцевого стекла. Нанокомпозитные пленки CuO-ZnO получали методом твердофазного пиролиза с молярным соотношением Cu:Zn (1:99, 3:97, 5:95, 10:90). Установлено, что коэффициент пропускания составляет более 84% для материалов в диапазоне длин волн 400-1000 нм.

Ключевые слова: оксид цинка, оксид меди, тонкие пленки, оптические свойства

Финансирование: Работа выполнена при поддержке гранта 4L/22-04-ПИШ в Южном федеральном университете.

Ссылка при цитировании: Игнатьева И.О., Старникова А.П., Петров В.В., Баян Е.М. Оптические свойства тонких пленок CuO-ZnO // Научно-технические ведомости СПбГПУ. Физико-математические науки. 2024. Т. 17. № 3.1. С. 293–296. DOI: https://doi.org/10.18721/JPM.173.159

Introduction

Nowadays, special attention is being paid to the development of multifunctional materials that can be used in various industries. One of these materials is zinc oxide, is a wide-band n-type conductor (E_g = 3.37 eV) [1]. Materials based on it are used in electronic and optoelectronic devices such as semiconductor lasers and LEDs in the ultraviolet (UV) region of the spectrum [2], solar cells [3] and gas sensors [4].

There are many physical and chemical synthesis methods, such as pulsed laser deposition [5], magnetron sputtering [6], sol-gel [7] and spray pyrolysis [8]. It is known that the creation of a p-n heterojunction has a beneficial effect on various properties of the materials obtained. Thus, the combination of ZnO with p-type semiconductors such as CuO, NiO, Co_3O_4 and Cr_2O_3 allows the use of chemical sensors, magnetic drives and optical devices [9].

The article [10] reports on the production of CuO-ZnO thin films by radio frequency sputtering. Based on the optical transmission spectra, it was found that the transmission coefficient and the band gap decrease with increasing film thickness and CuO content, which is explained by hybridization between CuO and ZnO to form a composite material.

In this paper, we report on the structural and optical properties of CuO-ZnO thin films obtained by solid-phase pyrolysis. The results showed that the obtained materials are promising candidates for creation of the optical devices.

Materials and Methods

Zinc (II) acetate dihydrate, copper (II) acetate dihydrate and organic acid $C_{20}H_{30}O_2$ were used to produce thin CuO-ZnO films by solid-phase pyrolysis. The process of forming thin films consisting of two stages conducted according to the previously described method [11, 12]. The films were annealed at 600 °C during 2 h. We have studied the phase composition of the film materials and crystalline quality by X-ray phase analysis (XRD) on an ARL'XTRA diffractometer, Cu-Kα radiation. The optical properties of obtained thin films were studied using an optical transmittance spectrum obtained on a UV-1100 spectrophotometer.

Results and Discussion

Fig. 1, *a* demonstrates X-ray diffraction patterns of CuO-ZnO thin films with different atomic Cu:Zn ratios (1:99, 3:97, 5:95, 10:90) in the 2 theta range 20–80°.

The obtained materials are polycrystalline in nature and two-phase. In addition to the peaks of the hexagonal structure of wurtzite of zinc oxide, there are peaks characteristic of tenorite CuO, having a monoclinic crystal structure. Diffractograms of the obtained materials were compared with standard sample ZnO and CuO from the database. Moreover, the intensity of the peaks of zinc oxide wurtzite is much more pronounced than the peaks of copper oxide. No other phases were found in the synthesized materials, which indicates the purity of the obtained material.

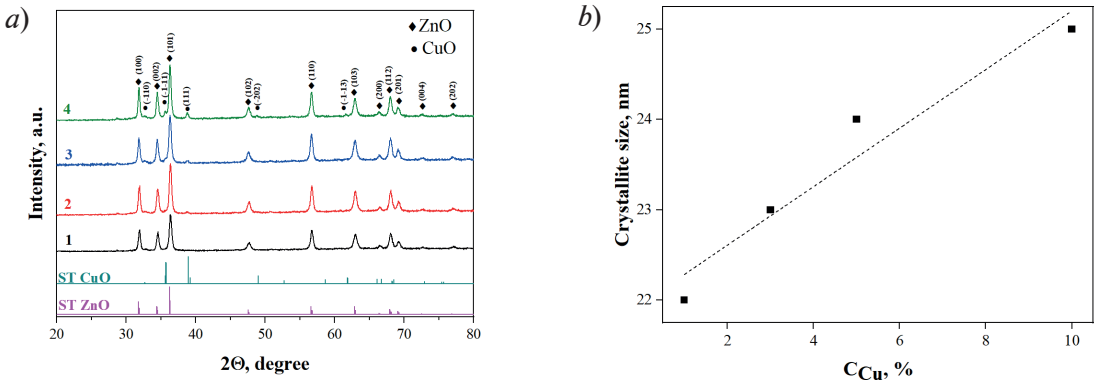

Fig. 1. X-ray images of CuO-ZnO films with Cu:Zn of 1:99 (1), 3:97 (2), 5:95 (3), 10:90 (4) and standard sample from the database (curve ST ZnO and ST CuO) (*a*) and dependences of the crystallite size on the CuO content (*b*)

The particle size was estimated with the Scherrer equation (Fig. 1, *b*). The crystal sizes range from 22–25 nm. The ZnO particle size increases with increasing CuO content in the film.

Optical transmittance spectra are shown in Fig. 2. It was determined that the obtained materials are optically transparent in the range from 400 to 1000 nm with a transmittance of more than 84%. Thin film with an atomic ratio Cu:Zn = 3:97 has the least transmittance in the visible light range, and the highest transmittance in the UV light range of 94%.

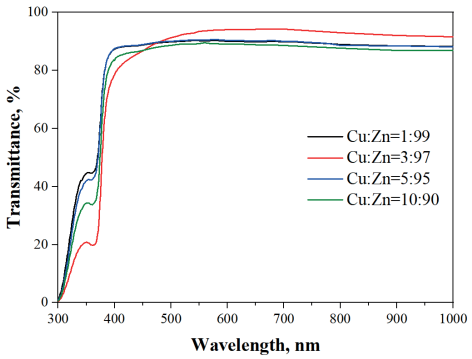

Fig. 2. Optical transmittance spectra of CuO-ZnO films of various composition

Based on the measured optical absorption spectra, Tauck graphs were obtained: $\alpha^2 = f(h\nu)$ and $\alpha^{1/2} = f(h\nu)$ and the optical absorption boundary characterizing the band gap was determined [13]. The assessment took into account the fact that indirect interband transitions can occur in complex semiconductors, which include metal oxides. Table shows the values of the band gap for direct and indirect crossings.

Table

The band gap of the CuO-ZnO thin films

Composition	$E_g(\alpha^2)$, eV	$E_{g1}(\alpha^{1/2})$, eV	$E_{g2}(\alpha^{1/2})$, eV
Cu:Zn of 1:99	4.00	3.18	3.45
Cu:Zn of 3:95	3.98	3.12	3.34
Cu:Zn of 5:97	3.98	3.14	3.40
Cu:Zn of 10:90	3.98	3.12	3.38

The value of the band gap for direct transitions $E_g(\alpha^2)$ CuO-ZnO thin films is significantly higher than that of pure ZnO obtained by solid-phase pyrolysis technology and equal to 3.30 eV. The obtained values of $E_g(\alpha^2)$ are close to the values of the band gap of Co_3O_4-ZnO films obtained in [12]. This can be explained by the fact that a large concentration of charge carriers is observed in the conduction band, leading to an observed increase in the energy of direct transitions. Two levels of indirect transitions $E_{g1}(\alpha^{1/2})$ and $E_{g2}(\alpha^{1/2})$ are also present on the Tauck graphs, the energies of which are significantly lower than the value of $E_g(\alpha^2)$. The values of $E_{g1}(\alpha^{1/2})$ correspond to the values of the band gap of $Zn_{1-x}Cu_xO$ films ($x = 0.01$ or 0.02) obtained in [14]. At the same time $E_{g2}(\alpha^{1/2})$ are close to the values of the band gap of zinc oxide ZnO [1].

Conclusion

CuO-ZnO thin films were obtained by solid-phase pyrolysis on quartz substrate. The material is two-phase, which is confirmed by the presence of peaks characteristic of ZnO and CuO. The particle size increase with increasing the copper oxide content. Transmittance is more than 84% for all materials in the range 400–1000 nm. The obtained materials can be used as optical devices.

Acknowledgments

The work was supported by Grant 4L/22-04-PISH carried out at the Southern Federal University.

REFERENCES

1. **Cranton W.M., Kalfagiannis N., Hou X., Ranson R., Koutsogeorgis D.C.,** Enhanced electrical and optical properties of room temperature deposited Aluminium doped Zinc Oxide thin films by excimer laser annealing, Optics and Lasers in Engineering. 80 (2016) 45–51.

2. **Makino T., Chia C. H., Segawa Y., Kawasaki M., Ohtomo A., Tamura K., Matsumoto Y., Koinuma H.,** High-throughput optical characterization for the development of a ZnO-based ultraviolet semiconductor-laser, Applied surface science. 189 (3-4) (2002) 277–283.

3. **Wibowo A., Marsudi M.A., Amal M.I., Ananda M.B., Stephanie R., Ardy H., Diguna L.J.,** ZnO nanostructured materials for emerging solar cell applications, RSC advances. 10 (70) (2020) 42838–42859.

4. **Zhu L., & Zeng W.,** Room-temperature gas sensing of ZnO-based gas sensor: A review, Sensors and Actuators A: Physical. 267 (2020) 242–261.

5. **Tsoutsouva M.G., Panagopoulos C.N., Papadimitriou D., Fasaki I., Kompitsas M.,** ZnO thin films prepared by pulsed laser deposition, Materials Science and Engineering: B. 176 (6) (2011) 480–483.

6. **Xiong D.P., Tang X.G., Zhao W.R., Liu Q.X., Wang Y.H., Zhou S.L.,** Deposition of ZnO and MgZnO films by magnetron sputtering, Vacuum. 89 (2013) 254–256.

7. **Hashim A.J., Jaafar M.S., Ghazai A.J., & Ahmed N.M.,** Fabrication and characterization of ZnO thin film using sol–gel method, Optik. 124 (6) (2013) 491–492.

8. **Tarwal N.L., Rajgure A.V., Inamdar A.I., Devan R.S., Kim I.Y., Suryavanshi S.S., Ma Y.R., Kim J.H., Patil P.S.,** Growth of multifunctional ZnO thin films by spray pyrolysis technique, Sensors and Actuators A: Physical. 199 (2013) 67–73.

9. **Moumen A., Kumarage G.C., & Comini E.,** P-type metal oxide semiconductor thin films: Synthesis and chemical sensor applications, Sensors. 22 (4) (2022) 1359.

10. **Abdel-wahab M.S., Wassel A.R., Hammad A.H.,** Characterization of CuZnO nanocomposite thin films prepared from CuO-ZnO sputtered films, Journal of Electronic Materials. 49 (12) (2020) 7179–7186.

11. **Petrov V.V., Ivanishcheva A.P., Volkova M.G., Storozhenko V.Y., Gulyaeva I.A., Pankov I.V., Volochaev V.A., Khubezhov S.A., Bayan E.M.,** High gas sensitivity to nitrogen dioxide of nanocomposite ZnO-SnO_2 films activated by a surface electric field, Nanomaterials. 12 (12) (2022) 2025.

12. **Petrov V.V., Sysoev V.V., Ignatieva I.O., Gulyaeva I.A., Volkova M.G., Ivanishcheva A.P., Khubezhov S.A., Varzarev Y.N., Bayan E.M.,** Nanocomposite Co_3O_4-ZnO thin films for photoconductivity sensors, Sensors. 23 (12) (2023) 5617.

13. **Bayan E.M., Petrov V.V., Volkova M.G., Storozhenko V.Y., Chernyshev A.V.,** SnO_2–ZnO nanocomposite thin films: The influence of structure, composition and crystallinity on optical and electrophysical properties, Journal of Advanced Dielectrics. 11 (05) (2021) 2160008.

14. **Asadov M.M., Mustafaeva S.N., Guseinova S.S., Lukichev V.F.,** Ab initio calculations of electronic properties and charge transfer in $Zn_{1-x}Cu_xO$ with wurtzite structure, Phys. Solid State. 64 (5) (2022) 528–539.

THE AUTHORS

IGNATIEVA Irina O.
iignateva@sfedu.ru
ORCID: 0000-0002-8528-4537

PETROV Victor V.
vvpetrov@sfedu.ru
ORCID: 0000-0003-3725-6053

STARNIKOVA Alexandra P.
starnikova@sfedu.ru
ORCID: 0000-0002-3779-8242

BAYAN Ekaterina M.
ekbayan@sfedu.ru
ORCID: 0000-0002-8445-9139

Received 11.07.2024. Approved after reviewing 31.07.2024. Accepted 01.08.2024.

Conference materials
UDC 547.458:[539.264+539.25]
DOI: https://doi.org/10.18721/JPM.173.160

Supramolecular ordering of thin glycerohydrogel plates of chitosan L- and D-aspartate

O.S. Ushakova [1], T.N. Lugovitskaya [2], A.B. Shipovskaya [1] ✉

[1] Saratov State University, Saratov, Russia;

[2] Ural Federal University named after first president of Russia B.N. Yeltsin, Yekaterinburg, Russia

✉ Shipovskayaab@yandex.ru

Abstract. The supramolecular ordering of thin glycerohydrogel plates of chitosan L- and D-aspartate was studied using small-angle X-ray scattering (SAXS) and transmission electron microscopy (TEM). At the nanolevel of supramolecular organization of the objects under study, two forms of scattering inhomogeneities were revealed, namely: nanospheres and nanorods. In CS·L-AspA-based plates, larger scattering nanoaggregates and their less symmetrical ordering in the solid-phase state of the polymeric substance were found.

Keywords: chitosan, L- and D-aspartic acid, glycerohydrogel plates, small-angle X-ray scattering, microscopy

Funding: This research was funded by a grant from the Russian Science Foundation No. 24-16-00172, https://rscf.ru/project/24-16-00172/.

Citation: Ushakova O.S., Lugovitskaya T.N., Shipovskaya A.B., Supramolecular ordering of thin glycerohydrogel plates of chitosan L- and D-aspartate, St. Petersburg State Polytechnical University Journal. Physics and Mathematics. 17 (3.1) (2024) 297–301. DOI: https://doi.org/10.18721/JPM.173.160

Материалы конференции
УДК 547.458:[539.264+539.25]
DOI: https://doi.org/10.18721/JPM.173.160

Надмолекулярное упорядочение тонких глицерогидрогелевых пластин L- и D-аспарагината хитозана

О.С. Ушакова [1], Т.Н. Луговицкая [2], А.Б. Шиповская [1] ✉

[1] Саратовский национальный исследовательский государственный университет им. Н.Г. Чернышевского, г. Саратов, Россия;

[2] Уральский федеральный университет им. первого Президента России Б.Н. Ельцина, г. Екатеринбург, Россия

✉ Shipovskayaab@yandex.ru

Аннотация. Методами малоуглового рассеяния рентгеновских лучей (SAXS) и просвечивающей электронной микроскопии (TEM) исследовано надмолекулярное упорядочение тонких глицерогидрогелевых пластин L- и D-аспарагината хитозана. На наноуровне надмолекулярной организации исследуемых объектов выявлены две формы рассеивающих неоднородностей: наносферы и нанопалочки.

Ключевые слова: хитозан, L- и D-аспарагиновая кислота, глицерогидрогелевые пластины, малоугловое рентгеновское рассеяние, микроскопия

Финансирование: Работа выполнена при финансовой поддержке Российского научного фонда № 24-16-00172, https://rscf.ru/project/24-16-00172/.

Ссылка при цитировании: Ушакова О.С., Луговицкая Т.Н., Шиповская А.Б. Надмолекулярное упорядочение тонких глицерогидрогелевых пластин L- и D-аспарагината хитозана // Научно-технические ведомости СПбГПУ. Физико-математические науки. 2024. Т. 17. № 3.1. С. 297–301. DOI: https://doi.org/10.18721/JPM.173.160

Introduction

Nanostructured hydrogel composites based on chitosan (CS), a biodegradable polymer of natural origin, are promising for designing flexible thin-film materials for biodegradable electronics and sensors, including low-cost disposable products. E.g., film sol–gel composites of CS and copper nanowires are characterized by flexibility, transparency and good electrical properties [1]. CS nanocomposites with graphene oxide exhibit the properties of ohmic-type semiconductors [2]. Hydrogel composites based on CS, ordered colloidal silica and a spatial sol–gel network of the product of hydrolysis and condensation of tetraethyl orthosilicate exhibit selective expansion of the SiO_2 photonic crystal lattice depending on the pH of the medium [3]. In many cases, the characteristics of the considered chitosan-containing nanocomposites are superior to those of transparent nanocomposites based on synthetic polymers filled with inorganic nanoparticles [4].

It should be noted that, as a rule, acetic acid solutions of high-molecular-weight CS or aqueous solutions of oligomeric CS are used to form nanostructured chitosan-containing systems, followed by the introduction of nanoparticles into the polymer system. In this work, L-(D-)aspartic acid (AspA) was used to prepare CS solutions [5]. The starting point for choosing this dissolving medium was the effect we discovered of counterionic condensation with phase segregation of chitosan aspartate (CS·AspA) at the nanoparticle level [6]. In this regard, we believe that the use of CS solutions in L-(D-)AspA may facilitate the one-step preparation of chitosan-containing nanocomposites with introducing no inorganic nanoparticles into the polymeric system.

In this work, the supramolecular ordering of thin glycerohydrogel plates of chitosan L- and D-aspartate was studied using SAXS and TEM. To make them, we used an approach previously tested in the formation of shape-stable thin-film plates of CS L- and D-ascorbates [7]. It consists in the formation of a system of interpenetrating spatial networks of organic and inorganic nature in a polymeric sample. The organic network is represented by a physical gel of CS and an inert structure former, whose –OH groups act as a template for the synthesis of an inorganic chemical network of silicon polyolate (~–Si–O–Si–~). Since a glycerol solution of silicon tetraglycerolate ($Si(OGly)_4 \cdot GlyOH$) is the precursor of the inorganic phase, the sol–gel synthesis is accompanied by the formation of polymeric glycerohydrogels.

Materials and Methods

The starting reagents were CS with a viscosity-average molecular mass $\bar{M}_\eta = 200$ kDa, a degree of deacetylation 82 mol %, and a moisture content of $W = 8 \pm 1$ wt% (Bioprogress Ltd., Russian Federation); glucomannan with $\bar{M}_\eta = 1100$ kDa (Uspekh LLC, RF); L-AspA (JSC Bioamid, RF); D-AspA (Vekton Corp., RF); $Si(OGly)_4 \cdot 3\,GlyOH$ (58.7 wt%, Ural Branch of Russian Academy of Sciences, Institute of Organic Synthesis named after I.Ya. Postovsky, RF); distilled water (Milli-Q, pH = 6.0); ethyl alcohol (C_2H_5OH, 95.6%, Baza Khimreaktivov Corp, RF).

To obtain glycerohydrogel plates, aqueous solutions of CS·L-AspA or CS·D-AspA with a concentration of 0.6 $g \cdot dL^{-1}$ (polymer) and 0.4 $g \cdot dL^{-1}$ (acid), an 0.2 $g \cdot dL^{-1}$ aqueous glucomannan solution and a glycerol $Si(OGly)_4$ solution were mixed in a mass ratio of components 1 : 1 : 0.5 and thoroughly homogenized with a glass rod for 1–2 min. The finished mixture composition was transferred onto a horizontal glass substrate (preliminarily defatted with C_2H_5OH) at a rate of 0.4 $mL \cdot cm^{-2}$ and kept at room atmosphere for ~72 h until gelation was completed.

Small-angle X-ray scattering (SAXS) measurements were carried out on a D8 Discover small-angle diffractometer (Bruker) with CuK_α radiation and a LynxEye solid-state position-sensitive detector in 0D mode, the slit width in front of the detector was 0.2 mm. The scattering intensity

I_q was recorded in the range of the modulus of the scattering wave vector q = 0.2–7.1Å^{-2}, where $q = 4\pi \sin\theta \cdot \lambda^{-1}$, 2θ being the scattering angle (deg), λ the radiation wavelength (1.542 Å). Scattering intensity dependences were plotted in both standard $I = f(q)$ and double logarithmic coordinates $\ln I = f(\ln q)$, as well as in Guinier coordinates $\ln I_q = q^2$ (to calculate the average radius of gyration R_n of phase inhomogeneities) and Kratky ones $q^2 I = f(q)$. The structural parameter n, which characterizes the morphology of scattering particles, was determined from the tangent of the slope of the straight sections of the scattering curve $\ln I = f(\ln q)$. The assignment of n to the shape of scattering inhomogeneities and the approximated functions of the Kratky curve was carried out according to Refs [8] and [9], respectively.

TEM images were acquired on a Jeol JEM 2100 transmission electron microscope at an accelerating voltage of 200 kV. Sample preparation was as follows: 5 μl of the test object was placed onto a copper grid coated with a carbon film (10–100 nm), dried for 15 min in air, then 10 min in the airlock vacuum chamber of the microscope.

Results and Discussion

The SAXS curves of our glycerohydrogel CS·L-AspA and CS·D-AspA plates in standard coordinates $I = f(q)$ were identical and differred only in the intensity value at small scattering angles (Fig. 1, *a*).

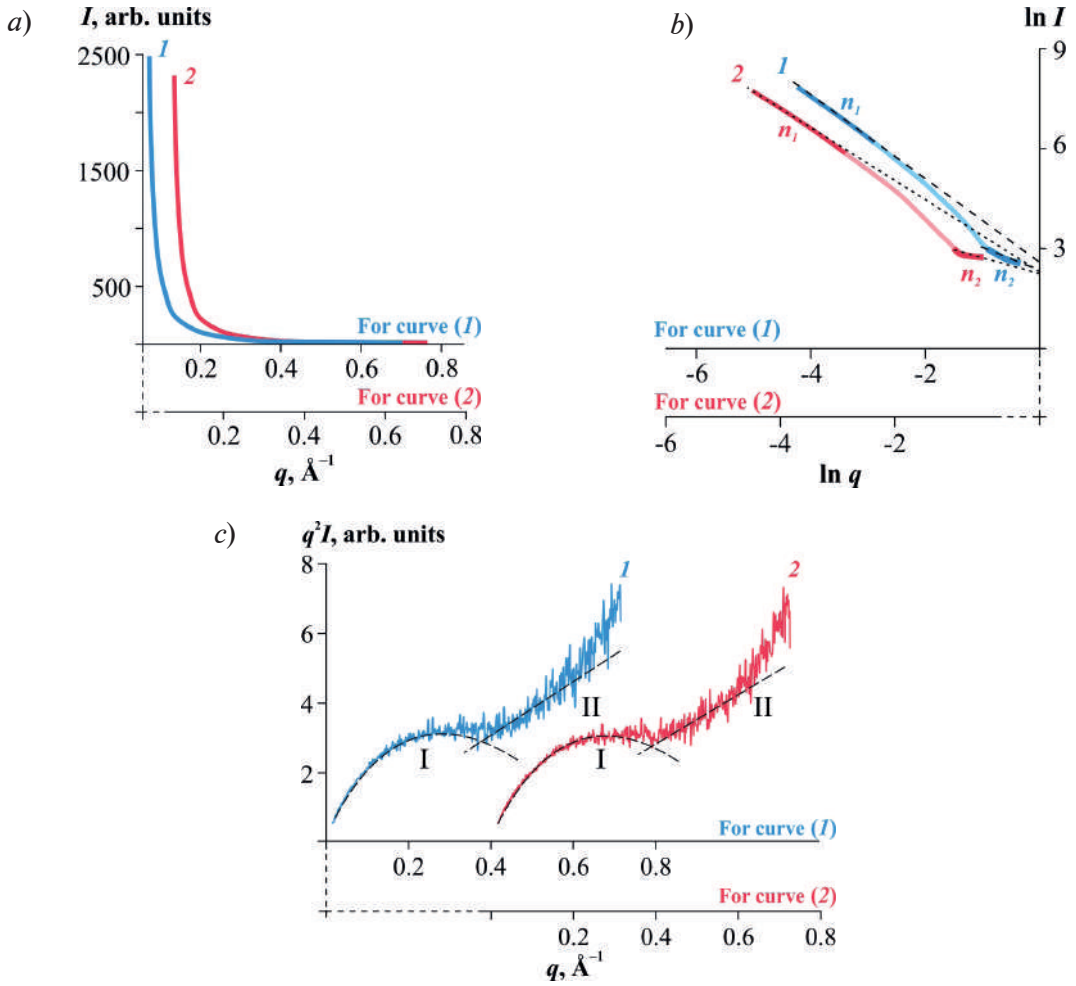

Fig. 1. Small-angle X-ray scattering (SAXS) curves of thin-film glycerohydrogel plates based on CS·L-AspA (*1*) and CS·D-AspA (*2*): experimental curve in standard coordinates (*a*), double logarithmic coordinates to estimate the structural parameter $n = \Delta(\ln I)/\Delta(\ln q)$ (*b*) and plot in Kratky coordinates to identify the shape of phase inhomogeneities: I – region of scatterers as hollow spherical particles $I(q) \sim q^{-4}$, II – as rods $I(q) \sim q^{-1}$ (*c*)

The highest values of I were observed for the CS·L-AspA-based sample. Plotting scattering curves in double logarithmic coordinates ln $I = f(\ln q)$ revealed two straight sections with a monotonic decrease in intensity, corresponding to different values of the modulus of the scattering vector: q = 0.02–0.06 and 0.5–0.7 Å^{-1} (Fig. 1, *b*). Linearization of these intervals by straight lines with angular coefficients n_1 and n_2 equal to 1.2 and 0.5 for CS·L-AspA, 1.3 and 0.3 for CS·D-AspA, respectively, showed the presence of two types of scattering structures. According to Ref. [8], the values of $n \sim 1$ indicate the presence of scattering volumetric domains in the form of hollow spheres in the spatial network of our glycerohydrogel, while $n < 1$ correspond to rod-shaped scattering inhomogeneities. The average radius of gyration R_n of spherical scattering particles, calculated from the dependence in Guinier coordinates ln $I_q = q^2$, was 30 Å and 25 Å for glycerohydrogel CS·L-AspA and CS·D-AspA, respectively.

To check the disclosed morphostructural features of the scatterers, the dependences $I = f(q)$ were replotted in Kratky coordinates $q^2 I = f(q)$, which make it possible to characterize the shape of phase inhomogeneities with sufficiently high accuracy (Fig. 1, *c*). The approximation (dashed lines), as well as the values of n_1 and n_2, show that the spectral contour of the experimental dependences of scattering intensity is due to the overlap of two functional dependences corresponding to different forms of scatterers, namely: spherical compact particles (possibly hollow spheres) – parabolic peak I in the range $q \approx 0.02–0.36$ Å^{-1} [9, 10] and rod-shaped (fibrillar) particles – line (II) at $q \approx 0.36–0.65$ Å^{-1} [11, 12]. There is a small straight section between regions I and II, probably corresponding to flat scattering supramolecular formations.

We were able to visualize the shape of the scatterers predicted by SAXS using TEM. Dried microsamples of CS·L-(D-)AspA solutions used to obtain glycerohydrogel plates consist of densely packed spherical nanoparticles (well visualized on a scale of 20–200 nm), separated by fibrillar (rod-shaped) structures (Fig. 2). The geometry and topological characteristics of the anisodiametric structures in the CS·L-AspA and CS·D-AspA samples are significantly different. E.g., CS·L-AspA is characterized by an asymmetric ordering of branched fibrils of a dendrite-like type, whilst CS·D-AspA is characterized by an almost symmetric ordering of fibrils with no branches. The length and width of the fibrillar structures in the sample based on CS·L-AspA were greater than those in CS·D-AspA.

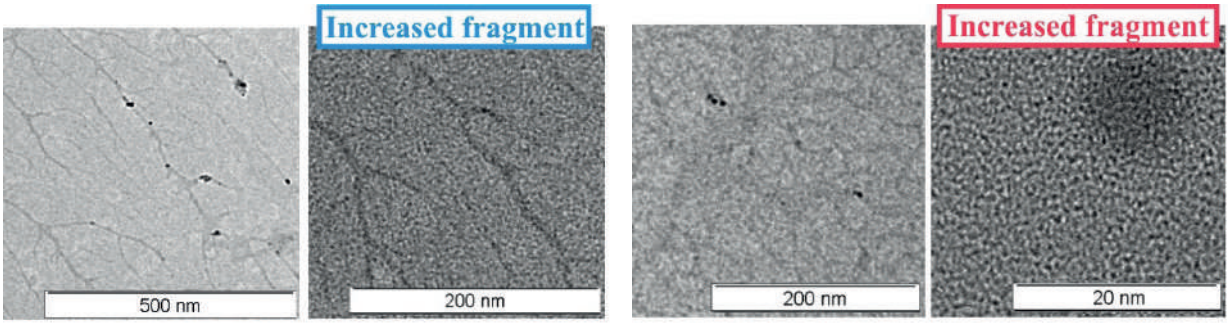

Fig. 2. TEM images of microsamples of CS·L-AspA (*a*) and CS·D-AspA (*b*) solutions dried on a copper grid

Conclusion

Using SAXS and TEM methods, structural diagnostics of the supramolecular ordering in thin glycerohydrogel CS·L-(D-)AspA plates in the nanometer range was carried out. It has been established that phase inhomogeneities in the structure of the polymeric substance are represented by two types of scattering structures, namely: hollow spheres and rod-shaped particles, whose morphological features and dimensional characteristics depend on the enantiomeric form of AspA. The objects based on CS·L-AspA reveal larger scattering nanoaggregates (both spherical and fibrillar morphology) and less symmetrical ordering in the solid state of the polymer substance than those based on CS·D-AspA. Note that a similar effect of the organic acid isomer used to dissolve CS on the dimensional characteristics of scattering objects and their fractal organization in the supramolecular structure of the hydrogel phase was discovered CS for L-(D-)ascorbate plates [7].

Good shape stability, nanocomposite ordering, and biodegradability of the components will determine the prospects for using CS·L-(D-)AspA glycerohydrogel plates in solving fundamental and applied problems of electronics and sensorics, including the development of disposable materials. The use of CS solutions in L-(D-)AspA will make it possible to develop a one-step method for the production of chitosan-containing nanocomposites.

REFERENCES

1. **Yu S. H., Liu Z., Zhao L., Li L.,** Degradable, ultra-flexible, transparent and conductive film made of assembling CuNWs on chitosan, Optical Materials. 123 (2022) 111752.

2. **Dhayal V., Hashmi S.Z., Kumar U., Choudhary B.L. , Kuznetsov A.E., Dalela S., Kumar S., Kaya S., Dolia S.N., Alvi P.A.,** Spectroscopic studies, molecular structure optimization and investigation of structural and electrical properties of novel and biodegradable chitosan-GO polymer nanocomposites, Journal of Material Science. 55 (2020) 14829–14847.

3. **Ryan C.C., Delezuk J.A.M., Pavinatto A., Oliveira O.N.J., Fudouzi H., Pemble M.E., Bardosova M.,** Silica-based photonic crystals embedded in a chitosanTEOS matrix: preparation, properties and proposed applications, Journal of Material Science. 51 (2016) 5388–5396.

4. **Yu S.H., Liu X.Y., Wu M.Y., Dong H.L., Wang X.H., Li L.X.,** All-solution-processed molybdenum oxide-encapsulated silver nanowire flexible transparent conductors with improved conductivity and adhesion, ACS Appllied Materials & Interfaces. 13 (2021) 14483–14491.

5. **Singh J., Dutta P.K.,** Preparation, circular dichroism induced helical conformation and optical property of chitosan acid salt complexes for biomedical applications, International Journal of Biological Macromolecules. 45 (2009) 384–392.

6. **Lugovitskaya T.N., Shipovskaya A.B., Shmakov S.L., Shipenok X.M.,** Formation, structure, properties of chitosan aspartate and metastable state of its solutions for obtaining nanoparticles, Carbohydrate Polymer. 277 (2022) 118773.

7. **Shipovskaya A.B., Gegel N.O., Babicheva T.S.,** Comparative analysis of nanosized structures in thin hydrogel plates of chitosan L- and D-ascorbate–hydrochloride, St. Petersburg Polytechnic University Journal. Physics and Mathematics. 15 (3.3) (2022) 111–117.

8. **Simonova N.B., Tuzikov F.V., Khramov R.N., Tuzikova N.A., Tuzikov M.F., Vakshtein M.S.,** Study of CdSe/CdS quantum dots in solutions and gels by the small-angle method X-ray scattering, Surface. X-ray, synchrotron and neutron studies. 2 (2011) 27–34.

9. **Valentini E., Kikhney A.G., Previtali G., Jeffries Cy M., Svergun D.I.,** SASBDB, a repository for biological small-angle scattering data, Nucleic Acids Research. 43 (D1) (2015) D357–D363.

10. **Jacques D.A., Guss J. M., Svergun D.I., Trewhella J.,** Publication guidelines for structural modelling of small-angle scattering data from biomolecules in solution, Acta Crystallographica Section D Biological Crystallography. 68(6) (2012) 620–626.

11. **Svechnikov N.Yu., Stankevich V.G., Kolbasov B.N., Zubavichus Y.V., Veligzhanin A.A., Somenkov V.A., Sukhanov L.P., Lebedev A.M., Menshikov K.A.,** Cluster-type structure of amorphous smooth hydrocarbon CDx films (x~0.5) from T-10 tokamak, J. Surface Investigation: X-ray, Synchrotron and Neutron Techniques. 11 (2017) 1208–1215.

12. **Braun A., Huggins F.E., Seifert S., Ilavsky J., Shah N., Kelly K.E., Huffman G.P.** Size-range analysis of diesel soot with ultra-small angle X-ray scattering, Combustion and Flame. 137(1-2) (2004) 63–72.

THE AUTHORS

USHAKOVA Olga S.
olgakol4ina777@yandex.ru
ORCID: 0009-0005-6189-4567

SHIPOVSKAYA Anna B.
Shipovskayaab@yandex.ru
ORCID: 0000-0003-1916-4067

LUGOVITSKAYA Tatyana N.
tlugovitskaja@mail.ru
ORCID: 0000-0002-8286-0711

Received 19.07.2024. Approved after reviewing 22.07.2024. Accepted 24.07.2024.

Conference materials
UDC 541.145
DOI: https://doi.org/10.18721/JPM.173.161

Photocatalytic properties of Ag-AgBr nanostructures formed by ion-exchange in photo-thermo-refractive glass for water-dye degradation

V.V. Pesnyakov [1] ✉, D.V. Marasanov [1], Y.M. Sgibnev [1], N.V. Nikonorov [1]

[1] ITMO University, St. Petersburg, Russia

✉ vvpesnyakov@itmo.ru

Abstract. In this paper Ag-AgBr nanostructures photocatalytic properties were studied. Hybrid nanoparticles were grown in photo-thermo-refractive glass during the ion exchange in $AgNO_3$ solution and subsequent heat treatment. XRD study demonstrated the growth of Ag nanoparticles with increase of bromine concentration. Water-dye degradation rate shows that with increase of bromine concentration photocatalytic properties of glass are also increases.

Keywords: photocatalysis, PTR glass, silver nanoparticles, semiconductor nanoparticles

Funding: The research was supported by the Russian Science Foundation grant No. 20-19-00559.

Citation: Pesniakov V.V., Marasanov D.V., Sgibnev Y.M., Nikonorov N.V., Photocatalytic properties of Ag-AgBr nanostructures formed by ion-exchange in photo-thermo-refractive glass for water-dye degradation, St. Petersburg State Polytechnical University Journal. Physics and Mathematics. 17 (3.1) (2024) 302–305. DOI: https://doi.org/10.18721/JPM.173.161

Материалы конференции
УДК 541.145
DOI: https://doi.org/10.18721/JPM.173.161

Фотокаталитические свойства наноструктур Ag-AgBr, сформированных методом ионного обмена в фото-термо-рефрактивном стекле, для разложения водных красителей

В.В. Песняков [1] ✉, Д.В. Марасанов [1], Е.М. Сгибнев [1], Н.В. Никоноров [1]

[1] Университет ИТМО, Санкт-Петербург, Россия

✉ vvpesnyakov@itmo.ru

Аннотация. В данной работе исследованы фотокаталитические свойства наноструктур Ag-AgBr. Гибридные наночастицы были сформированы в фото-термо-рефрактивном стекле в процессе ионного обмена в растворе $AgNO_3$ и последующей термообработки. Рентгеновское исследование продемонстрировало рост серебряных наночастиц с увеличением концентрации брома. Скорость разложения водного красителя показывает, что с увеличением концентрации брома фотокаталитические свойства стекла также возрастают.

Ключевые слова: фотокатализ, фото-термо-рефрактивное стекло, наночастицы серебра, полупроводниковые наночастицы

Финансирование: Исследование выполнено при поддержке гранта Российского научного фонда № 20-19-00559.

Ссылка при цитировании: Песняков В.В., Марасанов Д.В., Сгибнев Е.М., Никоноров Н.В. Фотокаталитические свойства наноструктур Ag-AgBr, сформированных

методом ионного обмена в фото-термо-рефрактивном стекле, для разложения водных красителей // Научно-технические ведомости СПбГПУ. Физико-математические науки. 2024. Т. 17. № 3.1. С. 302–305. DOI: https://doi.org/10.18721/JPM.173.161

Introduction

Carbon free fuel is one of the main long-term goal which humanity need to achieve as fast as possible. For that purpose, it is already done many steps, such as widespread implementation of wind power plants and solar cells, development of geothermal power plants and even fusion reactors. However, in the field of carbon-free fuel there is not much steps were done. The most promising fuel to replace the traditional petrol is hydrogen [1]. It was estimated that it is the highest clean energy carrier, which can be used in almost any energy applications such as transportation and electricity generation [2]. Notably, the sole byproduct of hydrogen combustion is water, rendering it a supreme candidate for displacing incumbent fossil fuels. The main obstacle on the way of its widespread use is the fact that hydrogen is practically never found on Earth in its pure [3]. That leads us to the main scientific field of research of development of the commercially profitable ways of extracting it from other compounds using various chemical methods. However, many of them have disadvantages like having greenhouse gases during its process. One of the possible method without significant disadvantages is to extract it from the water during photocatalysis. This is the way of water decomposition using just a semiconductor and a photon with energy higher than its energy bandgap to produce an electron – hole pair. This process can be described as following: semiconductor $+h\nu \rightarrow h\nu_{VB}^{+} + e_{CB}^{-}$, where $h\nu_{VB}^{+}$ is a hole in valence band and e_{CB}^{-} is an electron in a conductive band. Then these electron-hole pairs interact with water molecules adsorbed on its surface: $H_2O + 2h^{+} \rightarrow 2H^{+} + 1/2\ O^2$ and after that: $2H^{+} + 2e^{-} \rightarrow H^2$.

In this investigation, we delve into the characterization of Ag-AgBr hybrid nanoparticles encapsulated within a glass matrix, synthesized via an ion exchange technique.

Materials and Methods

In this research, PTR glasses with Na_2O-ZnO-Al_2O_3-SiO_2-F-Sb_2O_3-CeO_2-Ag_2O-Br matrix with different concentrations of Br were studied: GBr0.5 (Br = 0.51 mol.%), GBr0.7 (Br = 0.76 mol.%) and GBr2.1 (Br = 2.1 mol.%). Ion exchange was held in 5% $AgNO_3$ / 95% $NaNO_3$ solution. After that, thermal treatment took place for 3 hours in a muffle furnace at a temperature of 560 C°. The size of nanoparticle was calculated based on the X-ray diffraction data by the Scherrer formula [4]: $d = K\lambda / (\beta \cos\theta)$, where K is a Scherrer constant, λ is the X-ray radiation wavelength, β – peak width at half maximum and θ is the diffraction angle. To see the methyl orange dye (MO) degradation rate 405 nm laser was used. To calculate the degradation rate of MO C/C_0 first the absorption spectra of initial water dye solution was obtained using spectrophotometer Lambda 650 (PerkinElmer). Then after sample irradiation in a solution for a fixed period of time, absorption spectra were obtained again. The deference of the absorption on a 600 nm and 450 nm is C for that time interval and C_0 is for initial solution.

Results and Discussion

First, to obtain the particles size XRD method was applied. XRD spectra are shown in Figure 1. According to Scherrer formula, average Ag particle sizes are 45 nm in GBr0.5, 47 nm in GBr0.7 and 56 nm in GBr2.1.

It can be clearly seen the one peak located at 38°2θ correlated to silver 111 crystal.

It should be noted that despite the fact that XRD spectra does not show any peaks correlated to AgBr, it is reliably known from the previous studies that Ag-AgBr hybrid nanoparticles with Ag core and AgBr shell grow in this glass under these conditions [5]. Absence of any AgBr peaks can be explained by the fact that silver-core is much bigger than the AgBr-shell. For instance, the AgBr shell can be 2–5 nm while the Ag core nanoparticle is 47 nm.

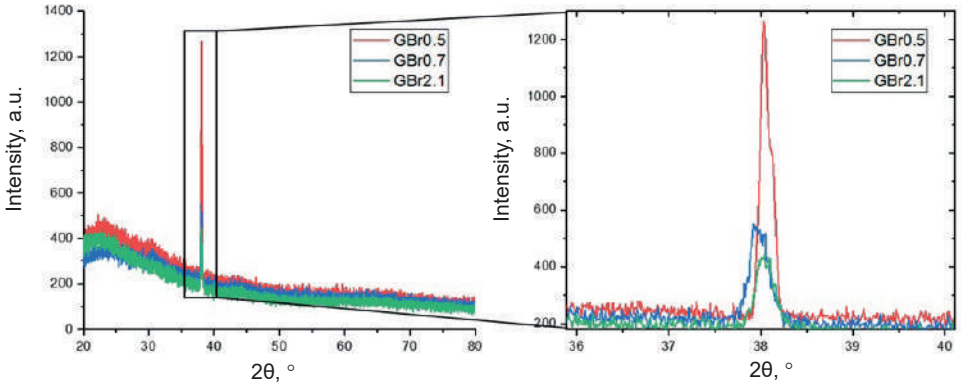

Fig. 1. XRD spectra of studied glasses

Figure 2 demonstrates different MO degradation curves using different glass samples.

Degradation of MO dye curves show that glass with the least Br concentration (GBr0.5) exhibit the worst photocatalytic MO degradation which stops at 0,14 C/C_0. While the glass with the biggest Br concentration (GBr2.1) shows the fastest MO dye degradation rate as well as the maximum degradation point of 0.08 C/C0. It can be concluded that with increase of Br concentration the photocatalytic properties are also increases. That fact can be explained by the growth of semiconductor AgBr shell on silver nanoparticle.

Last, on Figure 3 comparison of different kinds of glass samples' MO dye degradation rate is presented, where Gag contain only silver nanoparticles without any AgBr shell, GAgBr contain only semiconductor AgBr without Ag nanoparticle shell and GAg-AgBr is a sample with discussed above Ag-core and AgBr shell nanoparticles.

Degradation rate shows significant improvements in photocatalytic MO dye degradation of GAg-AgBr in comparison with samples containing only Ag or AgBr nanoparticles separately.

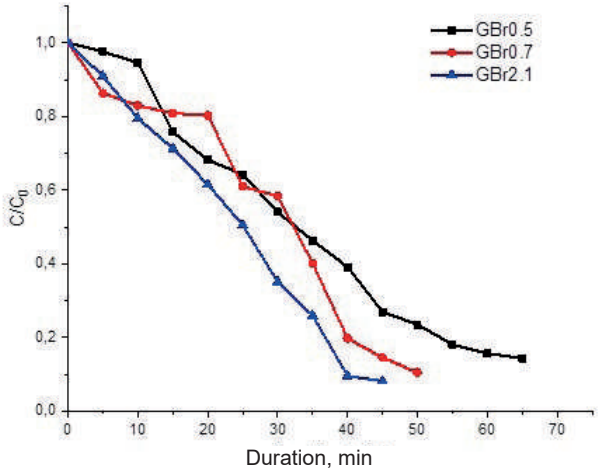

Fig. 2. Photocatalytic degradation of MO water solution with different glass samples with different Br concentration (GBr0.5 (0.51 mol.% Br), GBr0.7 (0.76 mol.% Br) and GBr2.1 (2.1 mol.% Br)

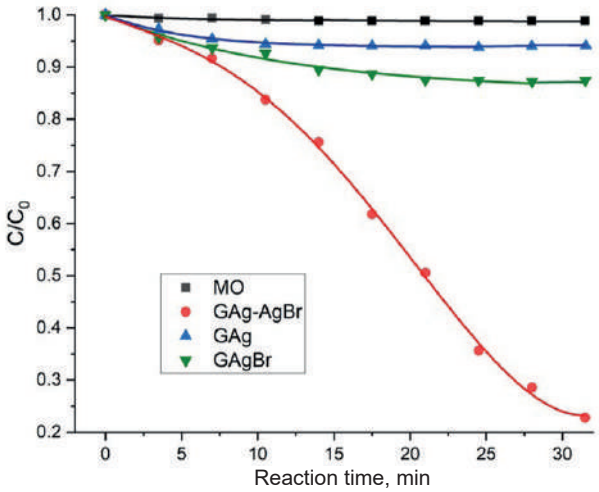

Fig.3. Photocatalytic degradation of MO water solution with different glass samples: GAg contains only Ag nanoparticles, GAgBr contains only AgBr and GAg-AgBr contains nanoparticles with Ag core and AgBr shell

Conclusion

Photocatalytic degradation of MO demonstrates that glass with Ag-AgBr nanoparticles exhibit better photocatalytic activity in comparison to samples with Ag or AgBr nanoparticles separately, which explains by the fact that AgBr shell increases electron lifetime. While higher concentration

of Br shows better dye-degradation rate. That can be explained by the growth of the nanoparticle's AgBr shell. XRD spectra also shows the increase of Ag nanoparticle, however, there is no peaks correlated to the AgBr. That can happen due to the small AgBr shell of nanoparticles which is not enough to distinguish its XRD peaks.

Acknowledgments

The research was supported by the Russian Science Foundation grant No. 20-19-00559.

REFERENCES

1. **Takanabe K.,** Photocatalytic water splitting: quantitative approaches toward photocatalyst by design., Acs Catalysis. 7 (11) (2017) 8006–8022.

2. **Hosseini S.E., Mazlan A.W.,** Hydrogen from solar energy, a clean energy carrier from a sustainable source of energy. International Journal of Energy Research. 44 (6) (2020) 4110–4131.

3. **El-Shafie M., Shinji K., Yukio H.,** Hydrogen production technologies overview. (2019).

4. **Patterson A.L.,** The Scherrer formula for X-ray particle size determination, Physical review. 56 (10) (1939) 978.

5. **Sgibnev Y.M., Marasanov D.V., Smetanin I.V., Uskov A.V., Kuzmenko N.K., Ignatiev A.I., Nikonorov N.V., Baryshev A.V.** A comparative study of photocatalytic activity of Na+–Ag+ ion-exchanged glass-ceramics with metallic Ag, semiconductor AgBr, and hybrid Ag–AgBr nanoparticles. Dalton Transactions. 52 (36) (2023) 12661–12667.

THE AUTHORS

PESNIAKOV Vladislav V.
v.pesnyackoff@yandex.ru

SGIBNEV Yevgeniy M.
sgibnevem@gmail.com

MARASANOV Dmitriy V.
dmitriymarasanov@bk.ru
ORCID: 0000-0001-8480-2016

NIKONOROV Nikolay V.
nvnikonorov@corp.ifmo.ru

Received 18.07.2024. Approved after reviewing 31.07.2024. Accepted 31.07.2024.

Conference materials
UDC 535.3
DOI: https://doi.org/10.18721/JPM.173.162

Influence of the wet-chemical treatment on the optical and structural properties of core-shell InGaN nanowires

T. Shugabaev [1, 2] ✉, V.O. Gridchin [1, 3], A. Kuznetsov [4], A.S. Kulagina [1, 2], A.I. Khrebtov [1, 2], V.V. Lendyashova [1, 2], R.R. Reznik [1], G.E. Cirlin [1, 3, 5]

[1] St. Petersburg State University, St. Petersburg, Russia;
[2] Alferov University, St. Petersburg, Russia;
[3] Institute for Analytical Instrumentation RAS, St. Petersburg, Russia
[4] Center for Photonics and 2D Materials, Moscow Institute of Physics and Technology, Dolgoprudny, Russia
[5] ITMO University, St. Petersburg, Russia
✉ talgashugabaev@mail.ru

Abstract. We study the influence of the shell in InGaN nanowires with spontaneously formed core-shell structure on their optical and morphological properties. It is shown that removing the shell from the initial nanowires induces the photoluminescence enhancement and changes their spectrum emission. Our research shows that etching the shell of these nanowires nanocrystals leads to their deviation from the vertical position.

Keywords: core-shell InGaN nanowires, etching of nanowires, photoluminescence enhancement, molecular beam epitaxy

Funding: The samples growth was done under the support of the Ministry of Science and Higher Education of the Russian Federation (state task No 0791-2023-0004). A.K. acknowledges support of the optical experiments by the Russian Science Foundation (grant No. 24-12-00225). For the morphological properties studies of grown samples the authors acknowledge Saint-Petersburg State University for a research project 87465891. Carrying out chemical etching procedures were supported by the Ministry of Science and Higher Education of the Russian Federation, research project no. 2019-1442 (project reference number FSER-2020-0013).

Citation: Shugabaev T., Gridchin V.O., Kuznetsov A., Kulagina A.S., Khrebtov A.I., Lendyashova V.V., Reznik R.R., Cirlin G.E., Influence of the wet-chemical treatment on the optical and structural properties of core-shell InGaN nanowires, St. Petersburg State Polytechnical University Journal. Physics and Mathematics. 17 (3.1) (2024) 306–309. DOI: https://doi.org/10.18721/JPM.173.162

Материалы конференции
УДК 535.3
DOI: https://doi.org/10.18721/JPM.173.162

Влияние химического травления на оптические и структурные свойства нитевидных нанокристаллов InGaN ядро-оболочка

Т. Шугабаев [1, 2] ✉, В.О. Гридчин [1, 3], А. Кузнецов [4], А.С. Кулагина [1, 2], А.И. Хребтов [1, 2], В.В. Лендяшова [1, 2], Р.Р. Резник [1], Г.Э. Цырлин [1, 3, 5]

[1] Санкт-Петербургский государственный университет, Санкт-Петербург, Россия;
[2] Академический университет им. Ж.И. Алфёрова РАН, Санкт-Петербург, Россия;
[3] Институт аналитического приборостроения РАН, Санкт-Петербург, Россия;
[4] Центр фотоники и двумерных материалов МФТИ, г. Долгопрудный, Россия;

[5] Университет ИТМО, Санкт-Петербург, Россия
✉ talgashugabaev@mail.ru

Аннотация. В данной работе исследуется влияние химического травления нитевидных нанокристаллов InGaN со спонтанно-сформированной структурой ядро-оболочка на их оптические и структурные свойства. Продемонстрировано, что удаление оболочки у исходных нитевидных нанокристаллов приводит к увеличению интегральной и пиковой интенсивностей фотолюминесценции. Проведенные исследования показывают, что травлением оболочки данных нитевидных нанокристаллов, приводит к их отклонению от вертикального положения.

Ключевые слова: нитевидные нанокристаллы InGaN, ядро-оболочка, травление нитевидных нанокристаллов, усиление фотолюминесценции, молекулярно-пучковая эпитаксия

Финансирование: Экспериментальные образцы были синтезированы при поддержке Министерства науки и высшего образования Российской Федерации (госзадание № 0791-2023-0004). А.К. выражает благодарность Российскому научному фонду (грант № 24-12-00225) за поддержку экспериментов по исследованию оптических свойств синтезированных образцов. Исследования морфологических свойств выращенных образцов были выполнены при поддержке СПбГУ, шифр проекта 87465891. Процедуры химического травления были проведены при поддержке Министерства науки и высшего образования Российской Федерации, проект тематики научных исследований № 2019-1442 (код научной темы FSER-2020-0013).

Ссылка при цитировании: Шугабаев Т., Гридчин В.О., Кузнецов А., Кулагина А.С., Хребтов А.И., Лендяшова В.В., Резник Р.Р., Цырлин Г.Э. Влияние химического травления на оптические и структурные свойства нитевидных нанокристаллов InGaN ядро-оболочка // Научно-технические ведомости СПбГПУ. Физико-математические науки. 2024. Т. 17. № 3.1. С. 306–309. DOI: https://doi.org/10.18721/JPM.173.162

Introduction

InGaN nanowires (NWs) are prospective candidates for fabrication ultra-high resolution micro- and nano- light-emitting devices over a wide range of wavelengths [1, 2]. InGaN NWs can be grown on lattice-mismatched substrates without forming structural defects, in particular on cheap and available Si substrates [3]. The synthesis of ternary InGaN compounds in the morphology of nanowires allows to obtain nanostructures with necessary emission wavelength in the visible range due to all possible variations in the In content [4, 5]. Moreover, orange and red-emitting InGaN nanocolumns with a high density of localized states due to large In fluctuation was shown to potential achieve high luminescence efficiency [6].

Recently, it was shown that InGaN NWs grown by plasma-assisted molecular beam epitaxy spontaneously formed with the core-shell structure [5], where the core contains 35–40 % indium ($In_{0.35\text{-}0.40}Ga_{0.65\text{-}0.60}N$), and the shell is almost pure GaN with 0–4 % In content. In this work, for the first time, we study the influence of the shell of the NWs on their photoluminescence (PL) properties. We determine that a decrease in the diameter of core-shell InGaN nanowires induced by the wet-chemical treatment leads to their deviation from the vertical position.

Materials and Methods

The InGaN NWs were grown directly on p-type Si(111) substrates using Riber Compact 12 molecular beam epitaxy setup, equipped with Ga, In effusion cells, and a nitrogen plasma source. Prior to growth, the substrates were heated up to a temperature of 920 °C and annealed for 20 min to remove the native oxide. The residual pressure in the chamber was $7 \cdot 10^{-8}$ Torr. Then, the substrate temperature was decreased and a plasma source was turned on. After reaching the temperature of 650 °C, gallium and indium shutters were opened simultaneously. The growth time of InGaN NWs was 20 hours.

We subjected the initial NW arrays to chemical treatment. Wet chemical etching was carried out in the solution KOH:H_2O (1:5) at a temperature of 75 °C to remove the GaN shell. The etching time varied from 20 to 80 seconds.

The morphology of the samples was studied by scanning electron microscopy (SEM Supra 25 Zeiss). The NW array was investigated with the use of micro-photoluminescence (PL) spectroscopy. The measurements were carried out on Jobin Yvon Horiba LabRAM HR 800 spectrometer equipped with a 100× magnification objective (N.A. = 0.9), camera and a stage with piezoelectric controllers for precise positioning of the laser beam. The source of optical excitation was a 532 nm laser, operating in a continuous mode. The optical system focuses the excitation into the beam with a diameter of about 1 μm.

Results and Discussion

Figure 1, *a* demonstrates schematical image of initial NWs (before etching). The typical SEM images of the grown NWs are presented in Fig. 1, *b*. It is clearly seen that the array contains both separated and coalesced NWs with an average height of about 2.7 μm. The spatially separated part of NWs have a core-shell structure with a shell thickness of about 20–30 nm and core diameter d_3 30–40 nm [5, 7]. The core-shell NW diameters are not constant and decrease from 100–130 nm (d_1) at the substrate surface up to 55–65 nm (d_2) at the tops of NWs.

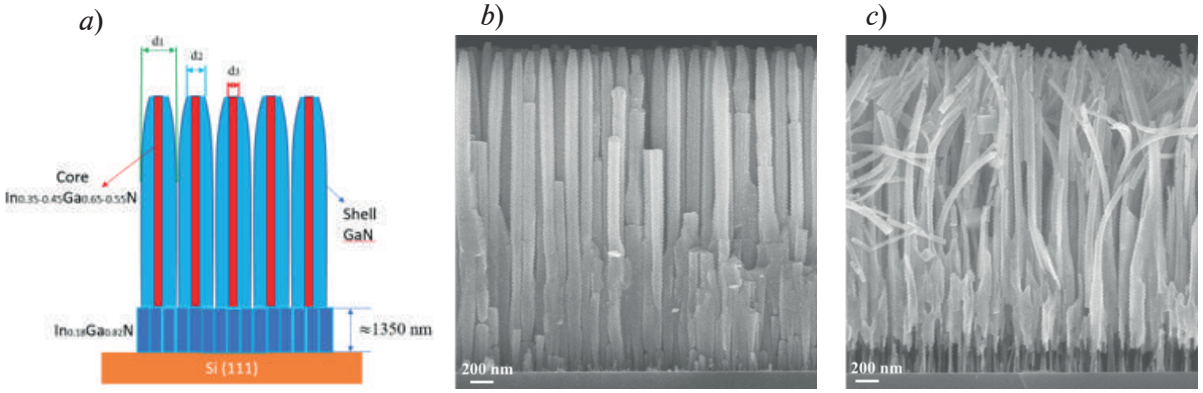

Fig. 1. Schematic image of the NW array before etching (*a*); typical cross-section SEM images of initial InGaN NWs (*b*) and after 50 s of etching (*c*)

The average values of d1 and d_2 decreased to 66 nm and 42 nm, respectively, after 60 seconds of etching (Fig. 1, *c*). Note that this value of d_2 is close to the core diameter d_3 30–40 nm. In addition, we observe a deviation of NWs from the growth direction in the range from 0 to 60 degrees that induced by the thinning of the shells.

Figure 2 demonstrates room-temperature PL spectra of sample with different etching times:

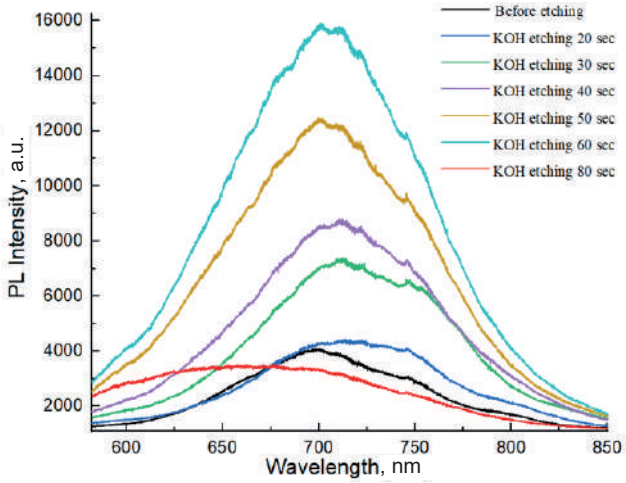

Fig. 2. Room-temperature PL spectra of the NW array with different etching times

The grown NWs have a noticeable PL in the range of 600–800 nm. We attribute the relatively broad PL spectrum to the compositional fluctuations of the indium content within the NWs. Figure 2 shows an increase in peak and integral PL intensity by a factor of 3.5 with increasing etching time from 0 to 60 seconds. Noticeable PL quenching and a shift of the PL peak to short wavelengths are observed after 80 seconds of etching that is explained by the sufficient core etching. Detailed mechanisms and reasons for the PL enhancement as a result of InGaN core-shell NWs etching will be presented in further studies.

Conclusion

This work should be useful for understanding the influence of shell on the luminescent properties of core-shell InGaN NWs. The PL intensity enhancement was observed in the case of etched NWs. Moreover, our results showed that a decrease in the diameter of core-shell NWs induced by treatment leads to their deviation from the vertical position. The results obtained can be useful for fabrication efficient LEDs based on molecular beam epitaxy growth InGaN NWs.

REFERENCES

1. **Pandey A., Reddeppa M., Mi Z.,** Recent progress on micro-LEDs, Light: Advanced Manufacturing. 4 (2024) 519–542.

2. **Bi Z., Gustafsson A., Samuelson L.,** Bottom-up approaches to microLEDs emitting red, green and blue light based on GaN nanowires and relaxed InGaN platelets, Chinese Physics B. 32 (2023) 018103.

3. **Tabata T., Paek J., Honda Y., Yamaguchi M., Amano H.,** Growth of InGaN nanowires on a (111) Si substrate by RF-MBE, Physica Status Solidi. 9 (2012) 646–649.

4. **Roche E., Andre Y., Avit G., Bougerol C., Castelluci D., Réveret F., Gil E., Médard F., Leymarie J., Jean T.,** Circumventing the miscibility gap in InGaN nanowires emitting from blue to red, Nanotechnology. 29 (2018) 465602.

5. **Gridchin V.O., Kotlyar K.P., Reznik R.R., Dragunova A.S., Kryzhanovskaya N.V., Lendyashova V.V., Kirilenko D.A., Soshnikov I.P., Shevchuk D.S., Cirlin G.G.,** Multi-colour light emission from InGaN nanowires monolithically grown on Si substrate by MBE, Nanotechnology. 32 (2021) 335604.

6. **Shimosako N., Inose Y., Kinjo K., Nakaoka T., Oto T., Kishino K., Ema K.,** Carrier density dependence of localized carrier recombination dynamics in orange-emitting InGaN/GaN nanocolumns, Journal of Applied Physics. 128 (2020).

THE AUTHORS

SHUGABAEV Talgat
talgashugabaev@mail.ru
ORCID: 0000-0002-4110-1647

KHREBTOV Artem I.
khrebtovart@mail.ru
ORCID: 0000-0001-5515-323X

GRIDCHIN Vladislav O.
gridchinvo@gmail.com
ORCID: 0000-0002-6522-3673

LENDYASHOVA Vera V.
erilerican@gmail.com
ORCID: 0000-0001-8192-7614

KUZNETSOV Alexey
alkuznetsov1998@gmail.com
ORCID: 0000-0001-7143-6686

REZNIK Rodion R.
moment92@mail.ru
ORCID: 0000-0003-1420-7515

KULAGINA Anastasia S.
a.s.panfutova@gmail.com
ORCID: 0000-0002-9668-6398

CIRLIN George E.
george.cirlin@mail.ru
ORCID: 0000-0003-0476-3630

Received 23.07.2024. Approved after reviewing 31.07.2024. Accepted 01.08.2024.

Conference materials
UDC 535.372
DOI: https://doi.org/10.18721/JPM.173.163

Luminescent properties of glasses activated by $CsPbBr_3$ perovskite nanocrystals and europium ions

A.D. Ratova [1], A.N. Babkina [1] ✉, R.D. Kharisova [1], K.S. Zyryanova [1]

[1] ITMO University, St. Petersburg, Russia

✉ babkina@itmo.ru

Abstract. A series of borogermanate glasses with $CsPbBr_3$ perovskite nanocrystals and Eu^{3+} ions is synthesized. At low concentrations of Eu_2O_3 in glass, Eu^{3+} ions play the role of crystallization centers for the nucleation of perovskite nanocrystals. At high concentrations of Eu_2O_3 in glass, $CsPbBr_3$ nanocrystals nucleate only during additional heat treatment. The lifetime of Eu^{3+} luminescence increases from 1.58 to 1.69 msec along with an increase in the Eu_2O_3 concentration. Along this, a slight distortion of the Eu^{3+} environment occurs in the glass matrix, resulting in a slight redistribution of the characteristic luminescence bands.

Keywords: perovskite nanocrystals, borogermanate glasses, trivalent europium

Citation: Ratova A.D., Babkina A.N., Kharisova R.D., Zyryanova K.S., Luminescent properties of glasses activated by $CsPbBr_3$ perovskite nanocrystals and europium ions, St. Petersburg State Polytechnical University Journal. Physics and Mathematics. 17 (3.1) (2024) 310–314. DOI: https://doi.org/10.18721/JPM.173.163

Материалы конференции
УДК 535.372
DOI: https://doi.org/10.18721/JPM.173.163

Люминесцентные свойства стекол, активированных нанокристаллами перовскита $CsPbBr_3$ и ионами европия

А.Д. Ратова [1], А.Н. Бабкина [1] ✉, Р.Д. Харисова [1], К.С. Зырянова [1]

[1] Университет ИТМО, Санкт-Петербург, Россия

✉ babkina@itmo.ru

Аннотация. Синтезирована серия боргерманатных стекол с нанокристаллами перовскита $CsPbBr_3$ и добавкой ионов Eu^{3+}. С изменением концентрации ионов Eu^{3+} наблюдается изменение люминесцентных свойств стекол в видимом диапазоне, при этом время жизни люминесценции Eu^{3+} увеличивается с 1,58 до 1,69 мс.

Ключевые слова: нанокристалл перовскита, борогерманатное стекло, ионы европия

Ссылка при цитировании: Ратова А.Д., Бабкина А.Н., Харисова Р.Д., Зырянова К.С. Люминесцентные свойства стекол, активированных нанокристаллами перовскита $CsPbBr_3$ и ионами европия // Научно-технические ведомости СПбГПУ. Физико-математические науки. 2024. Т. 17. № 3.1. С. 310–314. DOI: https://doi.org/10.18721/JPM.173.163

Introduction

Optical materials based on perovskite lead halide cesium nanocrystals are promising due to their unique optical, optoelectronic and photoelectric properties[1]. Due to the large absorption coefficient, high carrier mobility and emission efficiency, enabling perovskite to become ideal materials for combining with silicon photodetectors [2]. In addition, it has been widely used in initial solar cells, high-energy ray detection, light-emitting diode, lasers, and other fields in the span of an only few years. The rare-earth Eu^{3+} ion-doped $CsPbX_3$ nanocrystals can achieve a higher photoluminescent quantum yield due to the energy transfer from excitons to Eu^{3+} ions [3], thus improving the response of photodetectors. Herein, a series of borogermanate glasses co-doped with $CsPbBr_3$ perovskite nanocrystals and Eu^{3+} ions was synthesized, and its luminescent properties were studied.

Materials and Methods

The composition of the glasses under study was as follows: 4.97 ZnO – 4.83 Na_2O – 4.3 PbO – 6.17 Cs_2O – 19.94 B_2O_3 – 48.37 GeO_2 – 3.06 K_2O – 5.19 Br – 1.66 TiO_2 – 0.98 P_2O_5 – x Eu_2O_3, where x = 0.5; 1; 2 wt.%. Glass synthesis was carried out in an air atmosphere at a temperature of 950 °C in closed glass crucibles. After synthesis, the glasses were inertially annealed at a temperature of 470 °C. In glass composition with 0.5 wt.% Eu_2O_3, the nucleation of $CsPbBr_3$ perovskite nanocrystals occurred spontaneously during the annealing process. In the remaining compositions, the nucleation of perovskite crystals occurred only after additional heat treatment at temperatures above glass transition temperature (470 °C). The glass absorption spectra were measured by a Lambda 650 spectrophotometer (Perkin Elmer) in the spectral range of 200–900 nm. For the luminescence and excitation spectra recording, as well as for the luminescence decay measurements the LS-55 spectrofluorimeter (Perkin Elmer) was used.

Results and Discussion

Fig. 1 shows the absorption spectra of the glass samples under study. Since in glass with 0.5 wt.% Eu_2O_3 spontaneous precipitation of $CsPbBr_3$ nanocrystals occurred; a characteristic band corresponding to the absorption of semiconductor crystals is visible in the absorption spectrum in the region of 500 nm [4]. The intensity of the absorption band was only 1 cm^{-1}, which indicated a low concentration of the crystalline phase. This prevented confirmation of the nanocrystals' nucleation by X-ray diffraction. Absorption spectra of glass samples with 1 wt.% Eu_2O_3 and 2 wt.% Eu_2O_3 had a high scattering level and contained low-intensity absorption bands of Eu^{3+} ions, corresponding to the transitions: 1 – $^7F_0 \rightarrow {}^5L_6$, 2 – $^7F_0 \rightarrow {}^5D_2$. In the region of 562 nm, a defect was observed in the spectra due to the measurement method and the low absorption intensity.

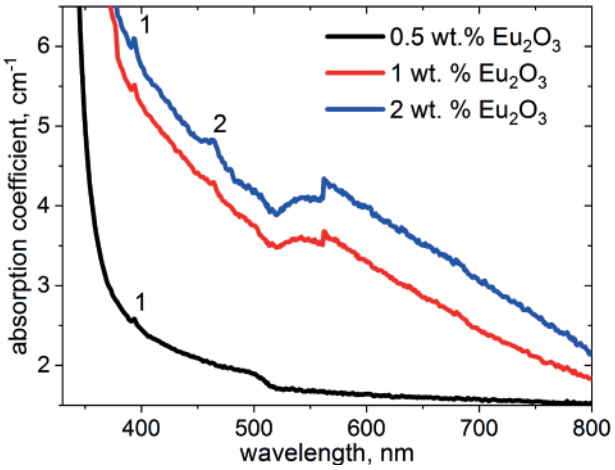

Fig. 1. Absorption spectra of the glasses under study

Fig. 2, *a* shows the luminescence spectra of glasses under study in the range of 375–730 nm under the excitation of 395 nm. For the glass with 0.5 wt.% Eu_2O_3 a narrow band with the maximum at 535 nm, corresponding to $CsPbBr_3$ perovskite nanocrystals, was observed [4]. Luminescence spectra of the glass with 1 wt.% Eu_2O_3 possessed two bands at 450 and 500 nm. The long-wavelength band also corresponded to the luminescence of perovskite nanocrystals, while the etymology of the short-wavelength band was not yet clear and required additional research. At this point, it can be assumed that broad blue luminescence may belong to $CsPbBr_3$ crystals of a very small subcritical size. In the region of 615 nm, both spectra also contained a Eu^{3+} luminescence band corresponding to the $^5D_0 \rightarrow {}^7F_2$ transition [5], but its intensity was 1000 and 100 times lower than the nanocrystals' luminescence intensity for compositions with 0.5 and 1 wt.% Eu_2O_3 respectively. Luminescence spectrum of glass with 2 wt.% Eu_2O_3 represented the bands of Eu^{3+} ions, the designation of the main bands is shown in Fig. 2, *d*. However, in addition to them, the luminescence spectrum also contained low-intensity bands at 558, 537 nm, which can be attributed to the $^5D_1 \rightarrow {}^7F_3$ and $^4D_1 \rightarrow {}^7F_2$ transitions in Eu^{3+} ions [6].

Excitation spectrum of the composition with 0.5 wt.% Eu_2O_3 exhibited a shape quite characteristic of semiconductor crystals. However, in the photoluminescence excitation spectrum of glass containing 1 wt.% Eu_2O_3 at wavelengths corresponding to the most intense absorption transitions in Eu^{3+} ions (398 and 467 nm), dips were observed. It is worth noting that the excitation spectrum for luminescence with a maximum at 450 nm in the same sample was very different from that for nanocrystals, which once again confirmed the presence of another luminescent center in the material. Excitation spectrum of glass with 2 wt.% Eu_2O_3 consisted of characteristic bands of Eu^{3+} ions; their correspondence to electronic transitions is indicated in Fig. 2, *d* [5].

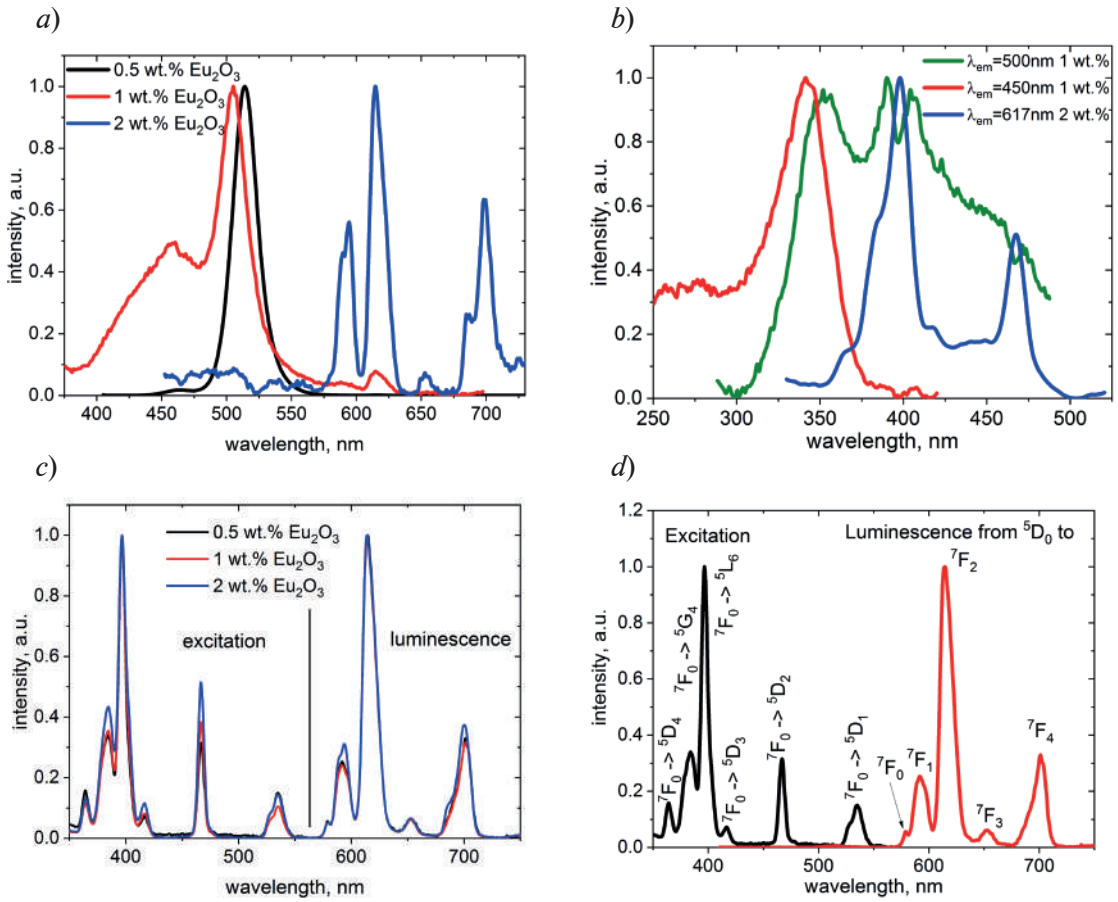

Fig. 2. Luminescence spectra of the glasses under study (λ_{ex} = 395 nm) (*a*), photoexcitation spectra for different glass and different luminescence wavelengths (*b*), luminescence spectra of the glasses under study with the delay of 0.05 msec (λ_{ex} = 395 nm) (*c*), luminescence and corresponding excitation spectra for glass with 0.5 wt.% Eu_2O_3, recorded with the delay of 0.05 msec (*d*)

In two of the three glass compositions, the nanocrystals' luminescence significantly exceeded the Eu^{3+} luminescence, even though the intensity of the $CsPbBr_3$ exciton absorption band was minimal or absent altogether. The luminescence lifetime of $CsPbBr_3$ is limited to 30 ns [7], and the luminescence lifetime of europium ions in glasses can reach 2 ms [8]. The luminescence spectra of the material were recorded in the presence of a delay between the exciting pulse and signal detection of 0.05 ms (Fig. 2, *c*, *d*). This delay completely neutralized the influence of the $CsPbBr_3$ luminescence on the spectra, leaving only Eu^{3+} bands. The luminescence intensity ratio (R) between intensities of $^5D_0 \rightarrow {}^7F_2$ and $^5D_0 \rightarrow {}^7F_1$ transitions' bands measures the interaction strength between the host matrix and the dopant ions. The symmetry local site without inversion center around Eu^{3+} ion leads to a higher value of R (R > 1), the opposite would lead to 1 > R > 0 [5]. The increase of the Eu_2O_3 content led to R decrease from 4.2 to 3.2, which indicated a slight change in the symmetry of the ligand field around Eu^{3+} ions.

Using time-resolved luminescence spectroscopy, the luminescence lifetimes of Eu^{3+} ions were obtained separately. Luminescence decay kinetics at 615 nm for glasses with 0.5 wt.% Eu_2O_3 and 1 wt.% Eu_2O_3 was approximated by a single exponential with decay times of 1.58 and 1.69 ± 0.02 ms, respectively. Luminescence decay kinetics at 615 nm in a composition with 2 wt.% Eu_2O_3 was approximated by two exponential components with lifetimes of 0.17 and 1.65 ms.

Conclusion

As a result of the work, borogermanate glasses with $CsPbBr_3$ perovskite nanocrystals and different concentrations of Eu_2O_3 were synthesized. At low concentrations Eu^{3+} ions played the role of crystallization centers for the nucleation of perovskite nanocrystals. At a high concentration of Eu^{3+} ions, perovskite crystals nucleated only during additional heat treatment. The decay time of Eu^{3+} luminescence increased along with an increase in the Eu_2O_3 content in glass. Along this, a slight distortion of the environment around Eu^{3+} ions occurred.

REFERENCES

1. **Bispo-Jr A.G., de Morais A.J., Calado C.M.S., Mazali I.O., Sigoli F.A.,** Lanthanide-doped luminescent perovskites: A review of synthesis, properties, and applications, J. Lumin. 252 (2022) 119406.

2. **Chen Y., Wu Z., Liang X., Nan D., Xu W., Xiang W.,** Sm^{3+}-doped $CsPbCl_2Br1$ nanocrystal glasses facilitating high ultraviolet performance of silicon photodetectors, Ceram. Int. 49 (2023) 14017–14023.

3. **Timkina Y.A., Tuchin V.S., Litvin A.P., Ushakova E.V., Rogach A.L.,** Ytterbium-Doped Lead–Halide Perovskite Nanocrystals: Synthesis, Near-Infrared Emission, and Open-Source Machine Learning Model for Prediction of Optical Properties, Nanomaterials. 13 (2023) 744.

4. **Zhang H., Jin M., Liu X., Zhang Y., Yu Y., Liang X., Xiang W., Wang T.,** The preparation and up-conversion properties of full spectrum $CsPbX_3$ (X = Cl, Br, I) quantum dot glasses, Nanoscale. 11 (2019) 18009–18014.

5. **Binnemans K.,** Interpretation of europium(III) spectra, Coord. Chem. Rev. 295 (2015) 1–45.

6. **Klimesz B., Lisiecki R., Ryba-Romanowski W.,** Thermal and optical properties of oxyfluorotellurite glasses doped with europium ions, J. Alloys Compd. 704 (2017) 180–186.

7. **Nedelcu G., Protesescu L., Yakunin S., Bodnarchuk M.I., Grotevent M.J., Kovalenko M.V.,** Fast Anion-Exchange in Highly Luminescent Nanocrystals of Cesium Lead Halide Perovskites ($CsPbX_3$, X = Cl, Br, I), Nano Lett. 15 (2015) 5635–5640.

8. **Mariselvam K., Kumar R.A., Karthik S.,** Optical and luminescence characteristics of europium doped barium lithium fluoroborate glasses, Chem. Phys. 525 (2019) 110379.

THE AUTHORS

RATOVA Anastasiya D.
ratova.anastasia@mail.ru
ORCID: 0009-0009-6573-0841

KHARISOVA Rufina D.
harisovarufina@gmail.com
ORCID: 0000-0002-9146-8519

BABKINA Anastasiia N.
babkina.anastasya@bk.ru
ORCID: 0000-0003-0784-1585

ZYRYANOVA Ksenia S.
ms.z.k.s@mail.ru
ORCID: 0000-0001-6733-1443

Received 23.07.2024. Approved after reviewing 31.07.2024. Accepted 01.08.2024.

BIOPHYSICS AND MEDICAL PHYSICS

Conference materials
UDC 621.317
DOI: https://doi.org/10.18721/JPM.173.164

Using Monte-Carlo based randomisation for stabilisation of data fitting in bioimpendance spectroscopy: Proof-of-concept

N.A. Boitsova [1] ✉, A.A. Abelit [1], N.A. Verlov [2], D.D. Stupin [1]

[1] Alferov University, St. Petersburg, Russia;

[2] Petersburg Nuclear Physics Institute named by B.P. Konstantinov of NRC "Kurchatov Institute", St. Petersburg, Russia

✉ natab2002@yandex.ru

Abstract. Nowadays, a lot of bioimpedance devices are proposed and signal processing for them is still under intensive development. In this study, we improved the complex non-linear least squares (CNLS) protocol for non-stationary bioimpedance data analysis. To be specific, we tested different Monte-Carlo applications for choosing starting point for CNLS approximation – an essential step for every non-linear problem. As a result, we have proved that symbiosis approach with usage of the CNLS-solution of the previous spectra as starting point and global Monte-Carlo searching of the starting point is the promising powerful combination for such a task.

Keywords: bioimpedance, CNLS, Monte-Carlo

Funding: The work was supported by the Ministry of Science and Higher Education of the Russian Federation (FSRM-2024-0001).

Citation: Boitsova N.A., Abelit A.A., Verlov N.A., Stupin D.D., Using Monte-Carlo based randomisation for stabilisation of data fitting in bioimpendance spectroscopy: Proof-of-concept, St. Petersburg State Polytechnical University Journal. Physics and Mathematics. 17 (3.1) (2024) 315–319. DOI: https://doi.org/10.18721/JPM.173.164

Материалы конференции
УДК 621.317
DOI: https://doi.org/10.18721/JPM.173.164

Использование рандомизации Монте-Карло для стабилизации обработки данных в биоимпедансной спектроскопии: пилотное исследование

Н.А. Бойцова [1] ✉, А.А. Абелит [1], Н.А. Верлов [2], Д.Д. Ступин [1]

[1] Академический университет им. Ж.И. Алфёрова РАН, Санкт-Петербург, Россия;

[2] Петербургский институт ядерной физики им. Б.П. Константинова НИЦ «Курчатовский институт», Санкт-Петербург, Россия

✉ natab2002@yandex.ru

Аннотация. Сегодня активно создаются все новые биоимпедансные устройства и совершенствуются методы получаемых с их помощью данных. В этом исследовании мы улучшили комплексный нелинейный метод наименьших квадратов (CNLS) для анализа нестационарных биоимпедансных спектров. В частности, мы протестировали различные приложения метода Монте-Карло для выбора начальной точки CNLS-аппроксимации – важного шага для решения любой нелинейной задачи. В результате мы показали, что симбиоз использования результатов CNLS-обработки предыдущих спектров в качестве

начальной точки и применения глобального поиска начальной точки методом Монте-Карло является перспективной комбинацией для таких аппроксимаций.

Ключевые слова: биоимпеданс, CNLS, Монте-Карло

Финансирование: Работа выполнена при поддержке Министерства науки и высшего образования Российской Федерации (госзадание FSRM-2024-0001).

Ссылка при цитировании: Бойцова Н.А., Абелит А.А., Верлов Н.А., Ступин Д.Д. Использование рандомизации Монте-Карло для стабилизации обработки данных в биоимпедансной спектроскопии: Пилотное исследование // Научно-технические ведомости СПбГПУ. Физико-математические науки. 2024. Т. 17. № 3.1. С. 315–319. DOI: https://doi.org/10.18721/JPM.173.164

Introduction

Today, bioelectronics is one of the most quickly expanding science fields [1, 2]. A lot of interest from researchers aimed at developing multipurpose bioelectronic devices for the need of healthcare and practical biology, for example, bioimpedance cytosensors. Although hardware for such apparatus is well-developed, signal processing still is in need of improvement [1]. In particular, almost all commercially available bioimpedance sensors use the Cell Index measure for the estimating cells state [3]. This approach is intuitive and easy in programming implementation, yet it cannot be used for reliable studying of the various biophysical phenomena due to the indirect relationship between such effects and Cell Index. An alternative approach for impedance analysis is to match impedance spectra with some theoretical models like equivalent schemes by using complex non-linear least squares technique (CNLS) [4]. Contrary to Cell Index, this approach allows us to separate different biophysical effects, although it requires an addition of mathematical processing. Namely, like most of the non-linear problems CNLS solution is obtained in an iterative manner, so choosing the starting point for the first iteration is also relevant for it. For non-stationary impedance spectra data, which is commonly used in cell research, this issue has one obvious solution: using the result of the previous spectra approximation as starting point for the new one. At the same time, this strategy has one significant drawback: if approximation for one spectrum fails, then risk of incorrect CNLS-processing of the next spectra will be higher [5].

In this paper, we aimed to overcome this issue by using Monte-Carlo methods (MC), which helps an iterative algorithm with jumping out from the failed approximation point. We have proposed two strategies for it, namely, local Monte-Carlo, which is based on the strategy of choosing the starting point randomly nearly the previous CNLS-approximation result, and global Monte-Carlo, which chooses the starting point randomly in the CNLS parameters' reasonable space. As a result, we discover that in the experiments with living cells the global Monte-Carlo approach provides the more stable inline CNLS-approximation.

Materials and Methods

In order to obtain bioimpendance data, we have used a multielectrode array 60StimMEA200/30 (MultiChannels Systems, Germany), which contained living cells. To perform FFT-based impedance measurement a setup was used, described in Ref. [1], Fig. 6. The spectra were collected in the frequency range from 20 Hz to 40 kHz with 2-Hz step.

As to validate our MC approach, we used HeLa cells, obtained from Institute of cytology of RAS. The cells were grown in multielectrode array in DMEM medium (Biolot, Russia) at 37 °C and 5% CO_2. Before bioimpedance measurements, the cells medium in multielectrode array was replaced by phosphate buffered saline (PBS, Biolot, Russia). The rhodamine 6G based home-made dye ABDS (cells membrane staining, green pseudo-color) was used to visualise cells. Microscopic photographs were made by Leica 4000 DM B fluorescence microscope (Leica, Germany). As biological stimulus during experiment we have used trypsin-Versene solution (1:4, Biolot, Russia), which decrease cell/electrode impedance due to cells de-adhesion process.

The impedance data was analyzed in the MatLab package by using NELM software (available by request). This algorithm is based on CNLS method of impedance approximation, namely

$$\sum_n |Y_m(\omega_n, \vec{p}) - Y(\omega_n)|^2 = \min, \quad (1)$$

where Y_m is model admittance, Y is experimental admittance, ω is angular frequency, and $\vec{p}$ is the vector of the scheme tuning parameters (resistance, capacitance, *etc.*). In the current study, we have used the series RL-CPE circuit as a model admittance Y_m. Consequently, the parameters vector $\vec{p} = [R, L, W, \alpha]$, where R is resistance, L is inductance (Op-Amp artifact [2]), W and α are parameters of the CPE element, which admittance is $W(i\omega)^{\alpha}$. In order to achieve a minimum of (1), we used simplex Nelder-Mead method [6].

To stabilize CNLS-approximation, in this paper two types of Monte-Carlo randomization were used: local, that generate starting point near the previous approximation of spectra $\vec{p}_{last}$, and global, which generate starting point near "universal" origin point $\vec{p}_{glb}$ given before calculations by the user of the program. Thus, the three strategies for getting initial $\vec{p}$ – value were examined: (i) no MC, $\vec{p} = \vec{p}_{last}$; (ii) Local MC, $\vec{p} = \vec{p}_{last} + \vec{r}$; (iii) Global MC, $\vec{p} = \vec{p}_{glb} + \vec{r}$. Here $\vec{r}$ is a random vector, which allows to vary $\vec{p}$ -values in the range of 100%. For MC processing (items ii and iii), for each spectrum we have provided 11 randomized simulations and one simulation which used previous approximation results as a starting point. Further, the $\vec{p}$ -value which gives the lowest CNLS-error was selected as equivalent scheme estimation.

Results and Discussion

The results obtained from applying different strategies of choosing starting point are presented in Fig. 1. It can be seen that if approximation was performed without MC, all spectra did not

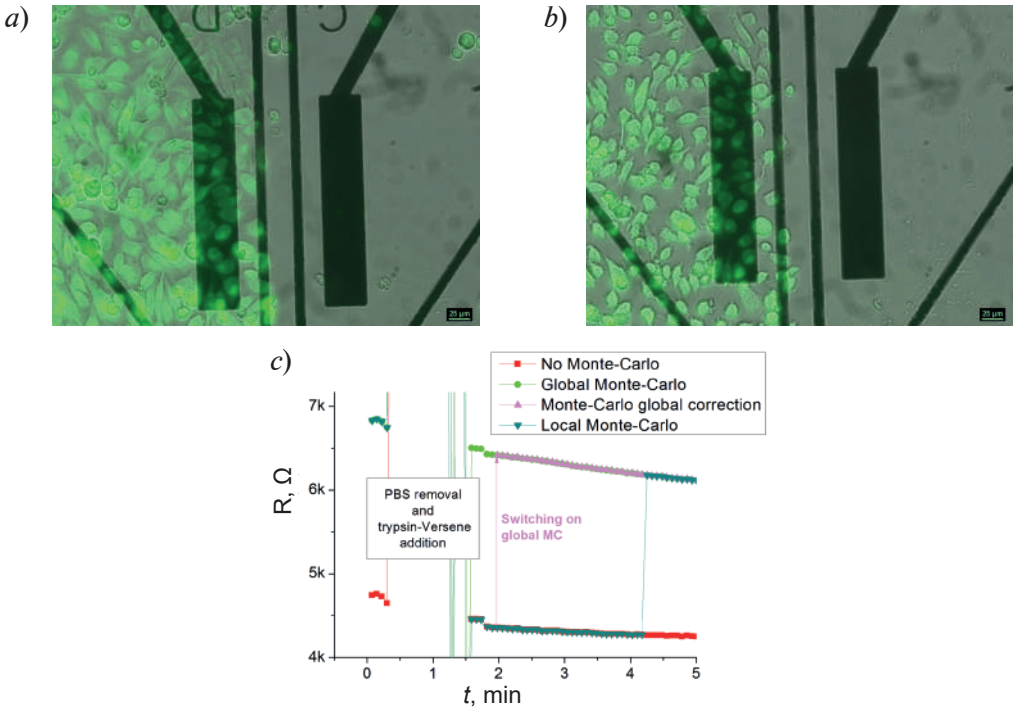

Fig. 1 Comparison of different CNLS processing strategies. (*a*) and (*b*) Photographs of the cells before and after trypsin-Versene addition respectively; (*c*) evolution of CNLS obtained resistance for different strategies of choosing starting point. Here and in Fig. 2, red color corresponds to no usage of MC (strategy i), green – usage of global MC (strategy iii), dark cyan – usage of local MC (strategy ii), magenta – global MC correction. It can be seen that addition of trypsin-Versene leads to cells de-adhesion (*a*) and (*b*). However, resistance, obtained with different strategies (*c*), varies greatly, and only the global MC approximation spectra completely match with the experimental one, this claim being justified by Fig. 2. Moreover, this approximation is one that behaves in accordance with the Giæver-Keese model [1]

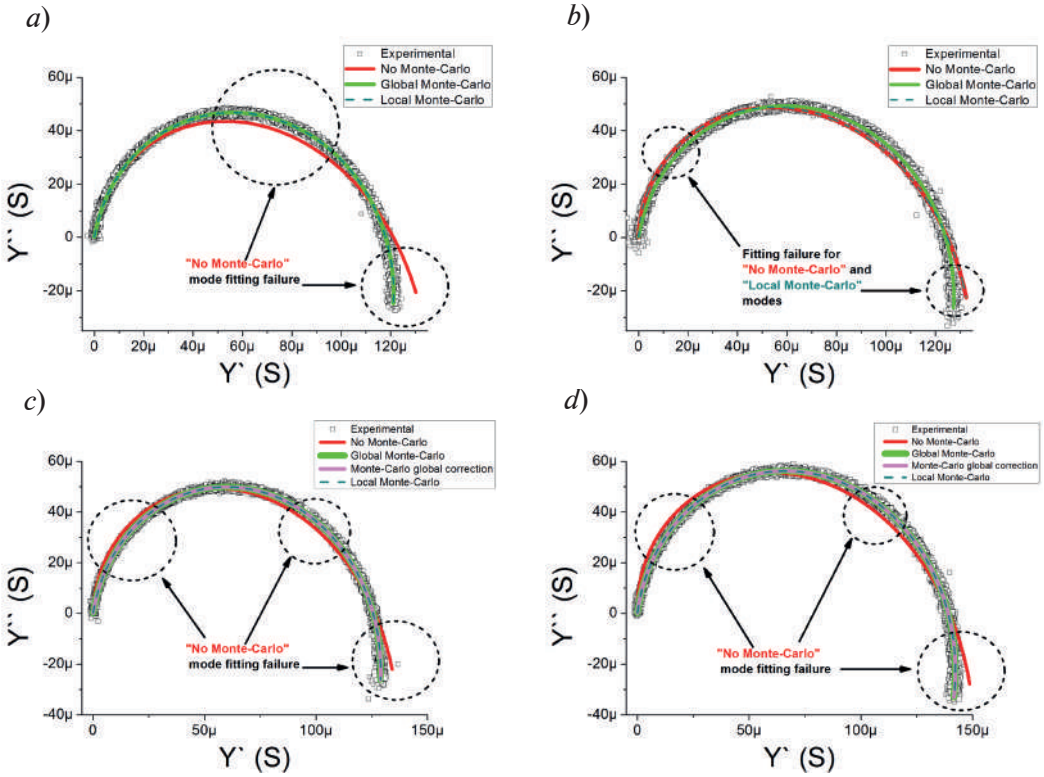

Fig. 2 Comparison of admittance loci of the cell/electrode interface for different CNLS processing strategies for the different time moments: (*a*) 0 min, (*b*) 1.5 min, (*c*) 2 min, and (*d*) 5 min. Squares scatter plot corresponds to experimental data, other line types are similar to Fig. 1. Dashed circles are highlighting spectrum parts with significant difference between CNLS approximation and experimental data. It can be seen that addition of trypsin-Versene leads to corresponding change of the spectra (compare loci with Fig. 1). Also, in the beginning local MC and global MC is indistinguishable, but, after PBS removal, global MC is the only one that match with experimental spectra. Moreover, after start of global MC correction, both global MC coincide with each other

match with the experimental one. In case of local MC strategy, starting spectra did match, but, after some manipulation with medium and as a result vastly different impedance signal, spectra stopped matching and approximation started behaving similarly to the strategy without MC. In the end, the local MC was able to find the minimum of the working function (Eq. 1) and provide an exact approximation. On the contrary, the global MC strategy did not only match experimental spectra all the way, but it also was able to succeed with a starting point, taken from failed local MC approximation, proving its supremacy.

Thus, the obvious strategy with using the result of the previous spectra approximation presents itself as not a stable one, due to the fact that change in the impedance was too large for the Nelder-Mead alone to be able to go back to the previous level. Even usage of local Monte-Carlo, which allowed us to run several simulations simultaneously in the search of the minimum, did not prove itself useful. Moreover, because in the end local MC was able to find exact approximation, usage of such a strategy led to the incoherent evolution of the resistance, which is showing sudden change in the state of the cells where in fact there is none. In a situation like that it is important to not only rely on the approximation of the previous spectra, but also have a universal starting point, located near the supposed minimum of the working function Eq. (1).

Conclusion

In this paper, we considered three different approaches to choosing a starting point for CNLS approximation and tested them on the bioimpendance experimental data. The strategy of not using Monte-Carlo showed itself as the most unreliable one; local Monte-Carlo was more stable, but still failed on some spectra; global Monte-Carlo was proved to be the most promising one out of them, being able to make accurate approximation for the whole duration of the experiment.

Thus, the combined approach, which consists of ruining several simulations using a universal starting point and the result of the previous approximation, was found out to be useful method for choosing a starting point. We believe that the results of this study will help in the development of new, more reliable devices for the needs of healthcare and modern biology.

Acknowledgments

Authors express their gratitude Yakovleva L.E., Dubina M.V. for comprehensive assistance and support and Tischenko Y.V., Kraevskya A.A., Fedorova I.S. for valuable advice.

REFERENCES

1. **Stupin D.D., Kuzina E.A., Abelit A.A., Emelyanov A.K., Nikolaev D.M., Ryazantsev M.N., Koniakhin S.V., Dubina M.V.,** Bioimpedance spectroscopy: basics and applications, ACS Biomaterials Science & Engineering. 7 (2021) (6) 1962–1986.

2. **Stupin D.D., Koniakhin S.V., Verlov N.A., Dubina M.V.,** Adaptive filtering to enhance noise immunity of impedance and admittance spectroscopy: Comparison with Fourier transformation. Physical Review Applied. 7 (2017) (5) 054024.

3. **Ning K., Wang X., Xu X., Abassi Y.A.,** The xCELLigence system for real-time and label-free monitoring of cell viability. Mammalian Cell Viability: Methods and Protocols. (2011) 33–43.

4. **Ross M.J., Schoonman J., Lehnen A.P.,** Applicability and power of complex nonlinear least squares for the analysis of impedance and admittance data. Journal of Electroanalytical Chemistry and Interfacial Electrochemistry. 131 (1982) 77–95.

5. **Bondarenko A.S.,** Analysis of large experimental datasets in electrochemical impedance spectroscopy. Analytica chimica acta. 743 (2012) 41–50.

6. **Lagarias J.C., Reeds J.A., Wright M.H., Wright P.E.,** Convergence properties of the Nelder–Mead simplex method in low dimensions. SIAM Journal on optimization. 9 (1) (1998) 112–147.

THE AUTHORS

BOITSOVA Natalia A.
natab2002@yandex.ru
ORCID: 0009-0006-2524-7618

VERLOV Nikolai A.
verlov_na@pnpi.nrcki.ru
ORCID: 0000-0002-3756-0701

ABELIT Anna A.
anna.abelit@gmail.com
ORCID: 0000-0003-3859-6981

STUPIN Daniil D.
stu87@ya.ru
ORCID: 0000-0002-5470-9301

Received 09.07.2024. Approved after reviewing 31.07.2024. Accepted 31.07.2024.

Conference materials
UDC 621.317
DOI: https://doi.org/10.18721/JPM.173.165

Autostainer feature for multielectrode arrays: proof-of-concept

D.D. Stupin [1], N.A. Boitsova [1] ✉, P.M. Dubina [1], N.A. Verlov [2], A.A. Abelit [1]

[1] Alferov University, St. Petersburg, Russia;

[2] Petersburg Nuclear Physics Institute named by B.P. Konstantinov of NRC "Kurchatov Institute", St. Petersburg, Russia

✉ natab2002@yandex.ru

Abstract. Today, bioelectronics technologies are opening new horizons and paving the way for future development using a wide range of materials. For example, numerous purely electronic materials, such as silicon, textolite and various polymer masks, are very promising for the purposes of cellular bioelectronics in vitro, but their optical properties limit their use, since modern microscopic control is still the most reliable tool for live cell diagnostics. This problem can be solved with the help of special dyes, however the staining procedure requires reagents and time, which on an industrial scale will lead to costs and a slowdown in the production process. Here we propose a solution to this issue based on the fabrication of cell-based bioelectronic devices that automatically stain cells without any additional sample manipulation.

Keywords: MEA, autostainer, Hoechst, silicon, PETG

Funding: The study was supported by the Ministry of Education and Science of the Russian Federation (Project FSRM-2024-0001).

Citation: Stupin D.D., Boitsova N.A., Dubina P.M., Verlov N.A., Abelit A.A., Autostainer feature for multielectrode arrays: proof-of-concept, St. Petersburg State Polytechnical University Journal. Physics and Mathematics. 17 (3.1) (2024) 320–324. DOI: https://doi.org/10.18721/JPM.173.165

Материалы конференции
УДК 621.317
DOI: https://doi.org/10.18721/JPM.173.165

Автоматическая покраска клеток в мультиэлектродных матрицах: пилотное исследование

Д.Д. Ступин [1], Н.А. Бойцова [1] ✉, Ф.М. Дубина [1], Н.А. Верлов [2], А.А. Абелит [1]

[1] Академический университет им. Ж.И. Алфёрова РАН, Санкт-Петербург, Россия;

[2] Петербургский институт ядерной физики им. Б.П. Константинова НИЦ «Курчатовский институт», Санкт-Петербург, Россия

✉ natab2002@yandex.ru

Аннотация. Сегодня в направлении биоэлектроники (БиоЭл) открываются все новые горизонты благодаря внедрению в ее технологии последних достижений из области материаловедения. Тем не менее, ряд перспективных для БиоЭл материалов, таких как кремний, текстолит и различные полимерные маски, до сих пор применяются в ней ограниченно для *in vitro* исследований, поскольку такие материалы непрозрачны и поэтому несовместимы с классической микроскопической диагностикой клеток в режиме проходящего света. Данную проблему можно решить с помощью использования специальных красителей, однако сама процедура покраски клеток достаточно

трудозатратна и в промышленных масштабах экономически неэффективна. В настоящей работе мы предлагаем решение вышеочерченной проблемы, которое заключается во внедрении в БиоЭл приборы блока автоматической покраски клеток.

Ключевые слова: мультиэлектродные матрицы, Hoechst, кремний, PETG

Финансирование: Российское Министерство Образования и Науки, номер гранта FSRM-2024-0001.

Ссылка при цитировании: Ступин Д.Д., Бойцова Н.А., Дубина Ф.М., Верлов Н.А., Абелит А.А. Автоматическая покраска клеток в мультиэлектродных матрицах: пилотное исследование // Научно-технические ведомости СПбГПУ. Физико-математические науки. 2024. Т. 17. № 3.1. С. 320–324. DOI: https://doi.org/10.18721/JPM.173.165

Introduction

The bioelectronics (BE) industry today covers a wide range of applications such as biosensing, neuroprosthetics, laboratory disease monitoring, living cell research *in vitro* etc [1–3]. One of the challenges facing BE device development is choice of materials that must be biocompatible, inexpensive, easy to usage, and compatible with modern biocharacterization methods. For these reasons, some promising electronic industry materials, such as the classical semiconductors silicon and germanium or insulators such as textolite, are today used much less frequently in cellular biosensors than glass or transparent polymers, due to their incompatibility with microscopic transfer-light techniques that are usually utilized to check the number of cells and their state. Thus, to include opaque materials in the BE arsenal, it is necessary to use staining methods that require time, reagent consumption, and additional manipulations [4] with the cell, i.e. this approach is invasive and economically ineffective.

One possible solution to this problem is to simplify or eliminate the stage of manipulation with cell staining through the use of specially prepared additional parts of the BE device. Here we propose to use the second approach, which is very useful for BE devices such as multielectrode arrays (MEAs). Each MEA consists of a substrate with planar electrodes and a Petri dish ring, the function of which is typically to maintain the cellular medium on the MEA electrodes. However, we can increase the functionality of such a ring by treating it with highly adhesive dyes such as Hoechst [5]. Thus, the ring treated in this way will become a source of dye, and cells cultured with it in MEA will be automatically stained without any additional cell preparation steps. Therefore, in this article, we will provide a proof-of-concept of this approach to create an MEA with autostaining feature.

Materials and Methods

To test the ring auto-staining technique, we assembled an MEA-like device from silicon wafer [Si (100) doped with sulfur, surface coated with natural SiO_2], PDMS Sylgard 184 (DowCorning, Germany, 10/1 PDMS/hardening agent ratio), and a 3D-printed ring of polyethylene terephthalate glycol (PETG). The technological process is shown in Fig. 1. First, the surface of the silicon and rings was cleaned with ethanol and dried with compressed air. A small amount of PDMS was then applied to the bottom of the rings, after which silicon chips were glued to them (Fig. 1,a). Next, the resulting structures were baked at a temperature of 65 °C for 30 minutes in a bottom-up position (Fig. 1, *b*). Such manipulations (small amount of PDMS and bottom-up baking) are necessary to prevent leakage of PDMS onto the MEA prototype dish bottom. It should also be emphasized that the use of PDMS at this stage is aimed at ensuring a sealed contact between the silicon substrate and the ring, and not at creating a strong bond between them. After the first hardening step, PDMS was applied a second time to the outer part of the ring to ensure a strong connection between the ring and the substrate, after which the sample was hardened again at a temperature of 65 °C for 30 minutes (Fig. 1, *c*).

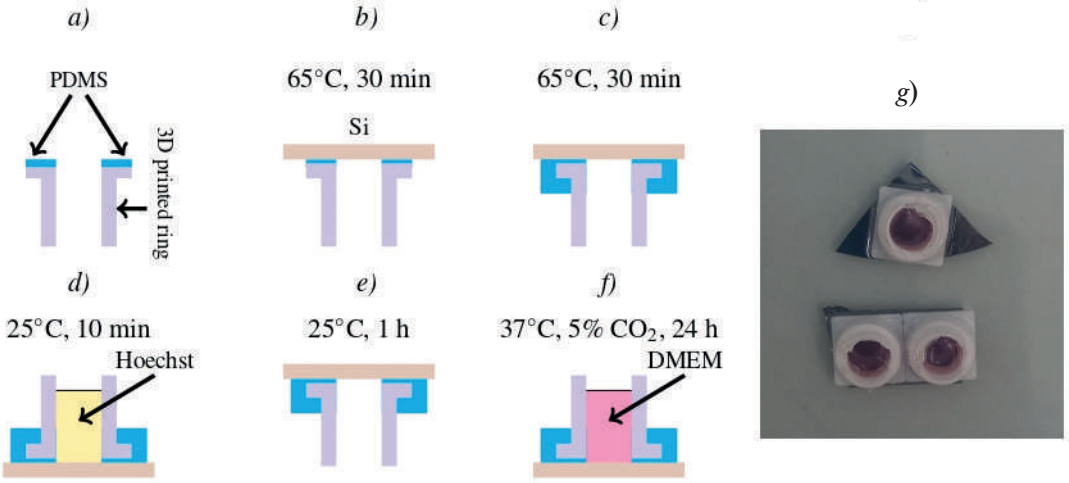

Fig. 1. MEA prototype with autostainer feature fabrication process. PDMS deposition (*a*), formation of the hermetic contact between silicon and ring (*b*), formation of the strength joint between silicon and ring (*c*), exposing device by Hoechst (*d*), washing and drying MEA prototype (*e*), seeding and culturing cells in MEA prototype (*f*), top-view photograph of the obtained MEA-like devices (*g*)

The resulting prototype MEA was then washed with soap and water, rinsed with deionized water, and sterilised with ethanol. Finally, a Hoechst solution (ThermoFisher, USA, 1:1000 dilution in PBS) was added to the obtained MEA prototype for 10 min (Fig. 1, *d*), after which the sample was washed, sterilised again and dried in a bottom-up position (Fig. 1, *e*). For the control sample of the MEA prototype, the step shown in (Fig. 1, *d*) (Hoechst processing) has been omitted. The external view of the obtained devices is shown on (Fig. 1, *g*). As a sample for autostainer's test the HeLa cells were used. The cells were obtained from bank of the cell cultures from Institute of Cytology RAS. One day before experiment the cells were seeded onto MEA prototypes and cultivated at 37 °C and 5% CO_2 in DMEM medium (Biolot, Russia) with 5% FBS (Sigma Alrich, USA) and 1.5% gentamicine (Biolot, Russia) (Fig. 1, *f*). Immediately before experiment the cells' medium was replaced by PBS with propidium iodide dye (PI, ThermoFisher Scientific, USA) for checking cells viability. The microphotographs of the cells were made using Leica 4000 DM B fluorescence microscope (Leica, Germany).

Results and Discussion

The results obtained from testing the autostainer-MEA prototype are presented in Fig. 2. It can be seen that control (Fig. 2, *a*) and autostaining samples (Fig. 2, *b*, *d*, *e*, *f*) allow diagnosing cells in the non-fluorescent mode of bright reflected light in the case when the microscope lens looks at the center of the Petri dish, where optical distortions caused by the meniscus of the cellular medium are minimal. It should also be noted that the cell viability of all samples is high (Fig. 2, PI channel). However, the UV-pumped Hoechst-images (Fig. 2, *a*) and (Fig. 2, *b-f*) are significantly different. More precisely, the control sample (Fig. 2, *a*) not treated with Hoechst dye exhibits a weak cell autofluorescence signal, making it very difficult to isolate individual cells.

In contrast, cells incubated in the Hoechst-treated device (Fig. 2, *b-f*) showed very clear nuclear fluorescence, which can be used to count cells and determine their location.

Looking at the brightfield images Fig. 2, one might get the impression that the use of fluorescent dyes is not necessary. However, this misconception immediately disappears in the case of studying cells located in the immediate vicinity of the edge of the Petri dish ring (Fig. 2, *c*). Indeed, one of the significant but not obvious differences between microscopic examination of cells on transparent substrates (where the microscope lens can be placed *under a flat* Petri dish) and opaque substrates (where the lens must be placed *above* the Petri dish) is the existence of a meniscus near the rings border of the Petri dish, which causes optical distortion of the microscopic top-view image (see left photograph on Fig. 2, *c*). This effect reduces photographs resolution due to optical smoothing of the image, resulting in the inability to distinguish individual cells within populations using reflected light alone.

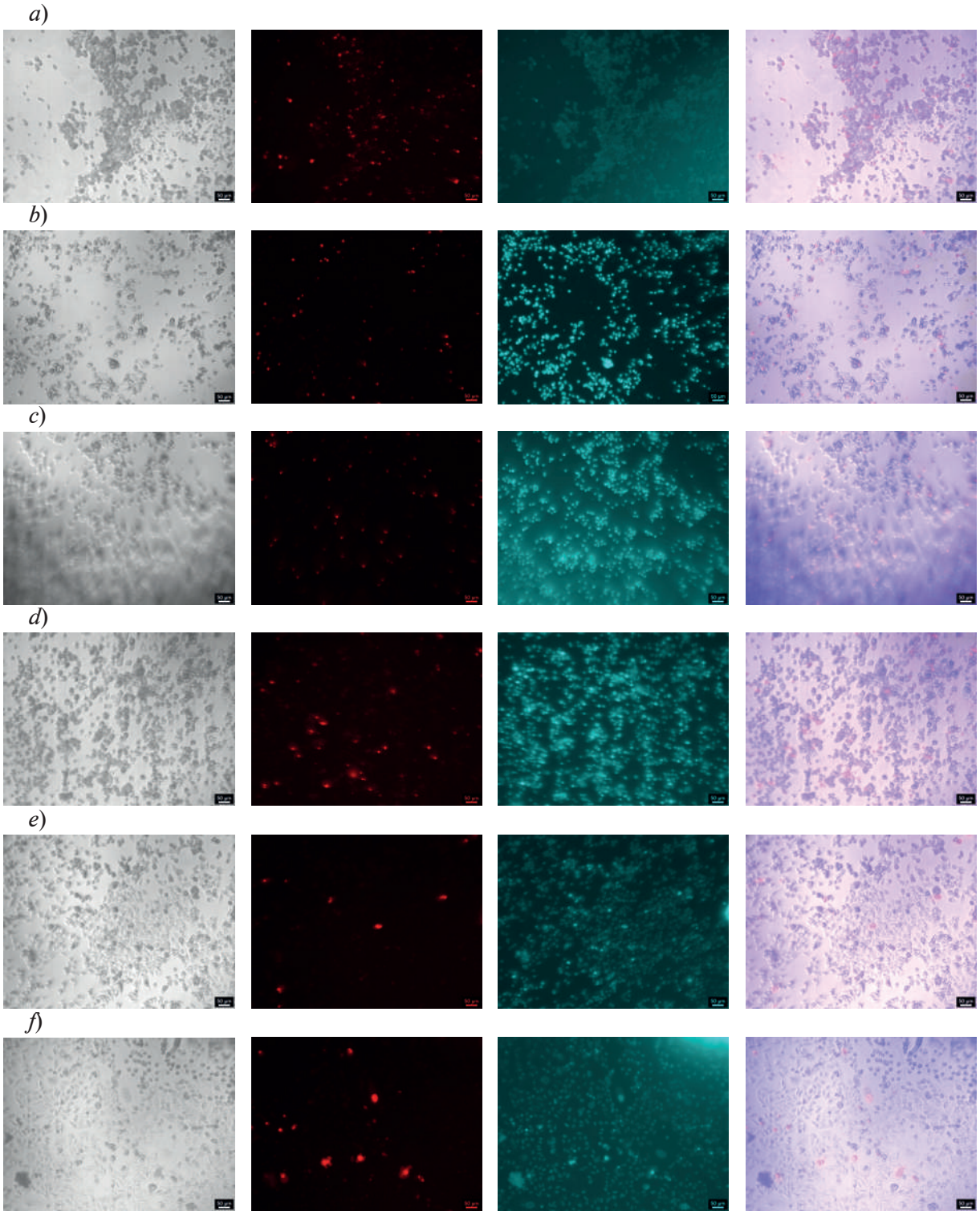

Fig. 2. Demonstration of the auto-staining effect. A photograph of the control MEA prototype is shown in panels (*a*), and other panels corresponds to MEA prototype with autostaining function as follows: (*b*) and (*c*) shows MEA after 2 washing/cells seeding procedures, (*d*, *e*, *f*) corresponds to 3, 4, and 5 washing/cells seeding cycles, respectively. Scalebar corresponds to 50 μm

For MEAs using the Lab-on-Chip concept, this effect is very negative because when developing such devices, engineers try to use the entire available area of the Petri dish, and the inability to monitoring the electrodes near the Petri dish ring can lead to the loss of part or all of the biosignal.

The clear advantage of using fluorescent dyes is shown in Fig. 2, *c*), from which it can be seen that near the edge of the ring the brightfield image is completely distorted, but the fluorescent channels still work perfectly, transmitting information about the number of cells and their position. This phenomenon can be explained by the selective staining property of dyes. Because cell nuclei are smaller than a whole cell, and therefore the distance between nuclei is greater than the distance between cells, the drop in resolution caused by meniscus optical distortion does not affect their images as significantly as on bright-field images of cells, which resulting in sharpness nuclei photographs in fluorescence mode. During experiments we also observed that silicon MEA with PETG ring conserve autostaining effect up to five cells seeding procedures.

Conclusion

In this paper, we demonstrated how the autostaining feature can be implemented in MEA devices and how it can be used to monitor cells *in vitro* in opaque MEAs. More precisely, we showed that MEAs pretreated with Hoechst dye, even after five wash cycles, still stain cell nuclei without any additional manipulation by the MEA user. We also demonstrated the advantage of our autostaining method over brightfield methods by taking photographs near the edge of the MEA, where brightfield methods are not applicable due to image distortion caused by meniscus, but the fluorescence methods in such case still works correctly. We believe that the results of our work open up new prospects for the creation of bioelectronic devices from modern electronic opaque materials, which will increase the versatility of such devices and, thereby, allow solving current problems in biosensing, healthcare and cytology.

Acknowledgments

Authors express their gratitude Mozharov A.M., Filatov N.A., and Dubina M.V. for comprehensive assistance.

REFERENCES

1. **Stupin D. Daniil et. al.,** Bioimpedance spectroscopy: basics and applications, ACS Biomaterials Science & Engineering. (7) (6) (2021) 1962–1986.

2. **Neroev V.V., Astakhov Yu.S., Lobanova M.M., Stupin D.D., et. al.,** Artificial vision: advances, topical issues, and prospects, Russian Ophthalmological Journal. (11) (3) (2018) 3–27.

3. **Jiang Wen G., ed.,** Electric cell-substrate impedance sensing and cancer metastasis. Springer Science & Business Media. (17) 2012.

4. **Matsumoto B.,** Cell biological applications of confocal microscopy. Elsevier. (70) 2003.

5. **Bucevičius J., Lukinavičius G., Gerasimaitė R.,** The use of hoechst dyes for DNA staining and beyond. Chemosensors. (6.2) (2018) 18.

THE AUTHORS

STUPIN Daniil D.
stu87@ya.ru
ORCID: 0000-0002-5470-9301

VERLOV Nikolai A.
verlov_na@pnpi.nrcki.ru
ORCID: 0000-0002-3756-0701

BOITSOVA Natalia A.
natab2002@yandex.ru
ORCID: 0009-0006-2524-7618

ABELIT Anna A.
anna.abelit@gmail.com
ORCID: 0000-0003-3859-6981

DUBINA Phillip M.
filipp.dubina@gmail.com
ORCID: 0009-0009-3972-777X

Received 11.07.2024. Approved after reviewing 29.07.2024. Accepted 29.07.2024.

Conference materials
UDC 004.852
DOI: https://doi.org/10.18721/JPM.173.166

Solder based on nanoparticles with metallic properties for laser reconstruction of blood vessels

V.V. Suchkova [1, 2] ✉, D.I. Ryabkin [1, 2], P.A. Varlamova [2], A.Yu. Gerasimenko [1, 2]

[1] I.M. Sechenov First Moscow State Medical University, Moscow, Russia;

[2] National Research University of Electronic Technology MIET, Zelenograd, Moscow, Russia

✉ suchkova_v_v@staff.sechenov.ru

Abstract. Laser blood vessel reconstruction is a modern, non-invasive method of blood vessel closure. Until now, most previous work has used protein and dye-based solders (laser absorbers) to form welds. However, the addition of nanoparticles to the solder, which have outstanding bactericidal properties and the ability to accelerate wound epithelialisation, has the potential to improve the efficiency of optical wound healing. The aim of the study was to experimentally investigate the physicochemical properties of dispersed solders including antibacterial nanoparticles of metals Ni, Al, Fe_3O_4 and carbon nanotubes with metallic properties, biopolymer – albumin, and dye localizing laser radiation in the area of wound dissection – indocyanine green, the formation of a biological tissue compound and the study of their mechanical properties. The selected nanoparticles have a high absorption coefficient of laser radiation, which provides high efficiency of laser energy utilization and allows recovery with minimal losses. The effectiveness of solders with different metal nanoparticles was experimentally tested in cattle vessels. Tissue reconstruction was performed by diode laser with a wavelength of 810 nm. The suture was formed within 1 minute. The laser exposure temperature was 55 °C for each particular specimen. The results showed that the highest tensile strength was in the specimen with carbon nanotubes. The achieved strength with carbon nanotubes was 950 kPa.

Keywords: vessel reconstruction, nanoparticles, laser soldering

Funding: The work was supported by the Ministry of Education and Science of the Russian Federation (project FSMR-2024-0003).

Citation: Suchkova V.V., Ryabkin D.I., Varlamova P.A., Gerasimenko A.Yu., Solder based on nanoparticles with metallic properties for laser reconstruction of blood vessels, St. Petersburg State Polytechnical University Journal. Physics and Mathematics. 17 (3.1) (2024) 325–329. DOI: https://doi.org/10.18721/JPM.173.166

Материалы конференции
УДК 004.852
DOI: https://doi.org/10.18721/JPM.173.166

Припой на основе наночастиц с металлическими свойствами для лазерного восстановления кровеносных сосудов

В.В. Сучкова [1, 2] ✉, Д.И. Рябкин [1, 2], П.А. Варламова [2], А.Ю. Герасименко [1, 2]

[1] Первый Московский государственный медицинский университет им. И.М. Сеченова, Москва, Россия;

[2] Национальный исследовательский университет «Московский институт электронной техники», г. Зеленоград, Москва, Россия

✉ suchkova_v_v@staff.sechenov.ru

Аннотация. Исследование направлено на изучение физико-химических свойств диспергированных припоев с антибактериальными наночастицами различных металлов и углеродных нанотрубок, а также на оценку их механических свойств.

Проведенные эксперименты на сосудистых моделях показали, что биополимерный припой, содержащий углеродные нанотрубки, обеспечивает наивысшую прочность на разрыв.

Ключевые слова: восстановление сосудов, наночастицы, лазерная пайка

Финансирование: Работа выполнена в рамках Государственного задания «Биоинтегрированная электроника на основе углеродных нанотрубок и графена» (Проект FSMR-2024-0003).

Ссылка при цитировании: Сучкова В.В., Рябкин Д.И., Варламова П.А., Герасименко А.Ю. Припой на основе наночастиц с металлическими свойствами для лазерного восстановления кровеносных сосудов // Научно-технические ведомости СПбГПУ. Физико-математические науки. 2024. Т. 17. № 3.1. С. 325–329. DOI: https://doi.org/10.18721/JPM.173.166

Introduction

Laser reconstruction of biological tissues is a modern method of wound healing, which is a non-invasive alternative to traditional methods. Laser tissue reconstruction is based on the reversible change in the molecular structure of tissues under the thermal influence of laser radiation. To prevent thermal necrosis of tissues, solder is applied to the area of dissection, which is an aqueous dispersion of protein – albumin and dye – indocyanine green [1]. The addition of nanoparticles to the solder, which have outstanding bactericidal properties and the ability to accelerate wound epithelialization, can potentially increase the efficiency of the optical method of wound healing [2, 3].

The aim of the study was to experimentally investigate the physicochemical properties of dispersed solders incorporating antibacterial metal nanoparticles Ni, Al, Fe_3O_4, and carbon nanotubes (CNT) formed the connection of biological tissues and to study their mechanical properties. Aluminum nanoparticles as the most budget-friendly and easily obtainable were chosen in two sizes: 50 nm and 100 nm.

Materials and Methods

Solder manufacturing. All solders were an aqueous dispersion of bovine serum albumin at a concentration of 25 wt.%, indocyanine green 0.1 wt.%, and the corresponding nanoparticles at concentrations ranging from 0.001 wt.% to 0.1 wt.%. A total of 28 different solders were prepared, varying in the type and concentration of nanoparticles. All solders were produced using the same technology. Metal nanoparticle powder was added to distilled water until the desired concentration was achieved. The resulting mixture was processed with a submersible ultrasonic homogenizer until the medium became homogeneous. Then, with continuous stirring, indocyanine green and bovine serum albumin were added to the dispersed medium. The resulting solder was treated in an ultrasonic bath until the protein was completely dissolved.

Laser soldering system. The laser system included an emission unit, laser guidance system, and temperature feedback. The system was capable of emitting radiation with two wavelengths: $\lambda = 810$ nm and $\lambda = 970$ nm. A laser with wavelength $\lambda = 810$ nm was used for laser soldering. To transmit laser radiation, the laser system was equipped with a 600 μm diameter optical fiber. The utilization of temperature feedback facilitated precise regulation of heating within the dissection zone, thereby mitigating thermal injury to adjacent tissues. Monitoring of the temperature within the laser-soldering region was achieved through an infrared sensor interfaced with a microcontroller. A proportional-integral-derivative (PID) controller was employed to modulate the laser radiation power in order to uphold the designated temperature. Visual representation of temperature variations was graphically depicted utilizing specialized software compatible with standard personal computers. The temperature control system exhibited a nominal error margin of 0.5 °C, a level of precision deemed suitable for the delicate process of biological tissue soldering.

Solder research methods. The following were selected as the main characteristics of solders affecting the strength of the laser connection of vessels: optical characteristics (absorption and transmittance), solder viscosity, studies of agglomerate sizes using the method of dynamic light scattering, and solder density.

Formation of laser welds. The effectiveness of solders with different nanoparticles was experimentally tested on bovine vessels. The welds were formed within 1 minute. The laser exposure temperature was 55 °C for each specific specimen [4, 5]. The heating temperature of the irradiated area was monitored by an MLX90614 infrared temperature sensor, which was installed directly above the collimator on the body of the surgical pen. When the desired surface temperature was reached, the temperature feedback system reduced the power of the radiation to maintain a stable temperature in the soldering area. After soldering, the tensile strength of the welds was determined using a testing machine.

Results and Discussion

Spectral characteristics of the solder. The study of the spectral characteristics of the solder makes it possible to determine the degree of localization of laser radiation in the solder application zone. In order to trace the absorption ability of the nanoparticles themselves, the first group of solders excluded the addition of dye – indocyanine green. The measurement results show strong absorption in the UV region provided by the spectral properties of the proteins. The addition of nanoparticles in all cases provides an increase in absorption over the entire range in the visible and infrared spectra, but there are no pronounced absorption peaks. The addition of carbon nanotubes (CNT) at a concentration of 0.05 wt.% results in complete absorption of radiation over the entire range under study (Fig. 1, *a*).

The results of the study demonstrate that the addition of indocyanine green to all types of solders leads to the formation of a pronounced absorption peak at a wavelength of 800 nm, which corresponds to the wavelength of the selected laser radiation (Fig. 1, *b*).

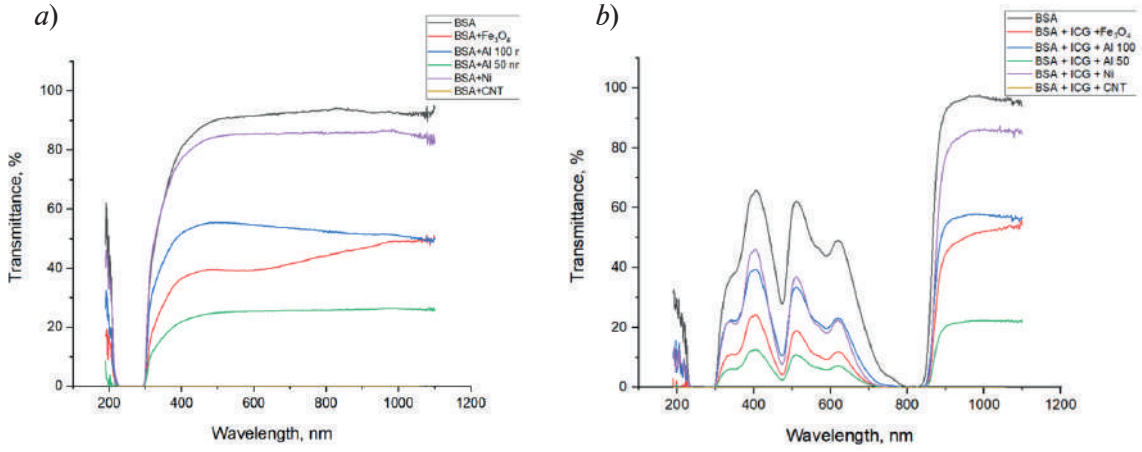

Fig. 1. Transmittance of solders: without ICG (*a*), with ICG (*b*)

Physical and chemical characteristics of solder. The density and viscosity of solder determines the consistency of solders their stability and ability to pre-glue the wound edges. The results of the studies are presented in Table. Carbon nanotubes provide the highest viscosity because they have higher surface energy and the ability to form a structure in the solder, which leads to an increase in viscosity.

The radii of the nanoparticles were determined by dynamic light scattering method. They are presented in Table. In general, for metal solders, it was observed that when dispersed in albumin, a protein shell is formed on the surface of the nanoparticles, increasing the particle size by 30% of the initial particle size. The size of nickel particles increased twice as much as the initial particle size. The structure of nickel nanoparticles itself is more prone to aggregation and formation of larger particles than other metals

Mechanical testing of welds. The effectiveness of solders with different metal nanoparticles was experimentally tested on ex vivo vessels and skin. Tissue reconstruction was performed with

Table

Study of physical and chemical characteristics of solder

Characteristics	Nanoparticles				
	Fe_3O_4	Al 100	Al 50	Ni	CNT
Viscosity, mPa*s	3.08	3.28	3.31	3.91	5.96
Density, g/cm	1.057	1.076	1.083	1.083	1.086
Particle size, nm	170 ± 60	145 ± 40	71 ± 15	159 ± 25	–

a diode laser with a wavelength of 810 nm. The suture was formed within 1 minute. The laser exposure temperature was 55 °C for each specific sample. The mechanical test results are shown in Figure 2. Solder based on carbon allows to localize the radiation as much as possible in the area of the joint formation and increases the strength of the formed welds by 10 times in comparison with solder without nanoparticles. In the case of aluminum nanoparticles, the size of the nanoparticles is critical on the strength of the welds. The strength of solders with the addition of 100 nm aluminum nanoparticles showed strength values equivalent to that of carbon nanotubes, while stable fabric bonding could not be achieved with 50 nm aluminum nanoparticles.

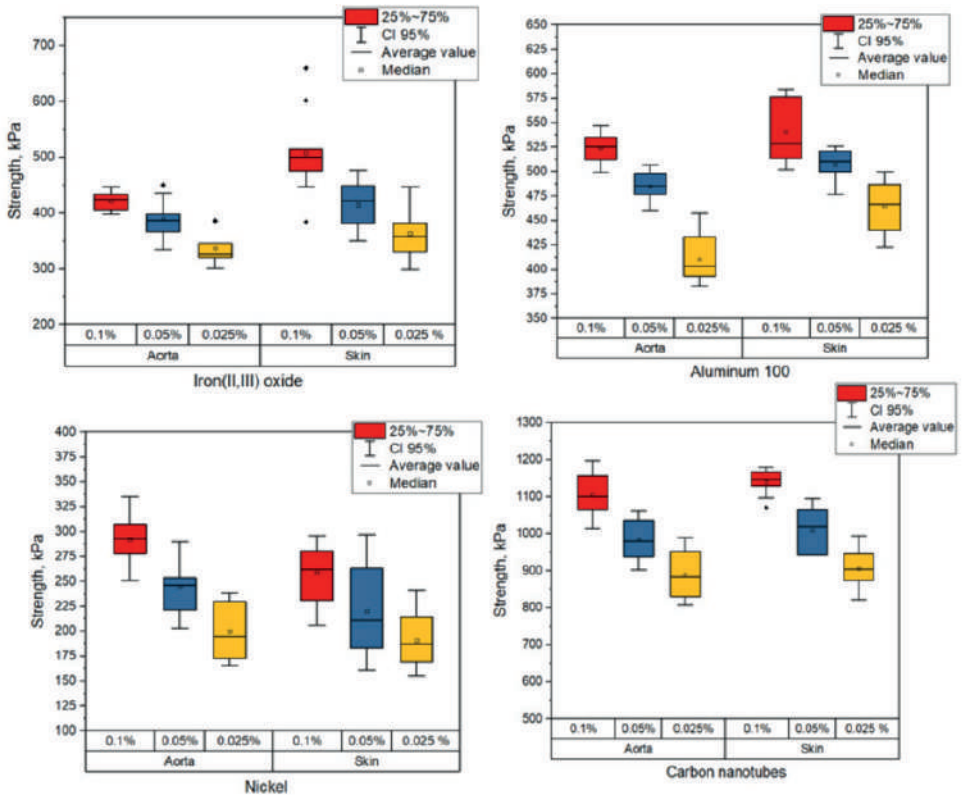

Fig. 2. Investigation of the strength of reconstructed welds

Conclusion

A new approach based on the high efficiency of laser energy and the excellent bactericidal properties of nanoparticles may lead to accelerated epithelialization of wounds and improved healing. The results of experiments on bovine aorta suggest that the use of solders with metal nanoparticles and carbon nanoparticles with metallic properties may be promising for the development of laser tissue reconstruction methods.

REFERENCES

1. **Gomes D.F., Galvana I., Ramos Loja M.A.,** Overview on the Evolution of Laser Welding of Vascular and Nervous Tissues, Applied sciences. 9 (2019) 9102157.

2. **Gerasimenko A.Y., Morozova E.A., Ryabkin D.I.,** Reconstruction of soft biological tissues using laser soldering technology with temperature control and biopolymer nanocomposites, Bioengineering. 9 (6) (2022) 238.

3. **Ratto F., Matteini P., Rossi F.,** Photothermal effects in connective tissues mediated by laser-activated gold nanorods, Nanomedicine: Nanotechnology, Biology and Medicine. 5 (2) (2009)143–151.

4. **Ryabkin D.I., Suchkova V.V., Gerasimenko A.Yu.,** Modelling of laser welding of biological tissues using focused radiation, St. Petersburg State Polytechnical University Journal. Physics and Mathematics. 16 (3.2) (2023) 344–348.

THE AUTHORS

SUCHKOVA Victoria V.
molodykh1999@gmail.com
ORCID: 0000-0002-3207-7622

RYABKIN Dmitrii I.
ryabkin@bms.zone
ORCID: 0000-0002-1327-5690

VARLAMOVA Polina A.
polina.var_20@mail.ru

GERASIMENKO Alexander Yu.
gerasimenko@bms.zone
ORCID: 0000-0001-6514-2411

Received 12.07.2024. Approved after reviewing 21.08.2024. Accepted 23.08.2024.

Conference materials
UDC 621.37
DOI: https://doi.org/10.18721/JPM.173.167

Reducing the error in measuring bioimpedance when studying body composition

V.V. Antipenko [1] ✉, E.A. Pecherskaya [1], D.V. Yakushov [1],
D.V. Artamonov [1], O.V. Karpanin [1], Yu.V. Shepeleva [2]

[1] Penza State University, Penza, Russia;
[2] Penza State University of Architecture and Construction, Penza, Russia
✉ v.antipenko7@yandex.ru

Abstract. Automated bioimpedance measurement systems are part of modern medicine because they provide the ability to determine body composition and provide performance parameters. Bioimpedance analysis has the advantage of being able to test non-invasively, and accuracy and availability continue to improve every year. Currently, when assessing bioimpedance parameters, special attention is paid to the methods and accuracy of measurements. This article discusses key aspects of bioimpedance determination related to measurement errors. Various approaches to reducing errors in bioimpedance measurements are also presented.

Keywords: impedance, measurement, Cole model, error, object

Citation: Antipenko V.V., Pecherskaya E.A., Yakushov D.V., Artamonov D.V., Karpanin O.V., Shepeleva Yu.V., Reducing the error in measuring bioimpedance when studying body composition, St. Petersburg State Polytechnical University Journal. Physics and Mathematics. 17 (3.1) (2024) 330–334. DOI: https://doi.org/10.18721/JPM.173.167

Материалы конференции
УДК 621.37
DOI: https://doi.org/10.18721/JPM.173.167

Уменьшение погрешности измерения биоимпеданса при исследовании состава тела

В.В. Антипенко [1] ✉, Е.А. Печерская [1], Д.В. Якушов [1],
Д.В. Артамонов [1], О.В. Карпанин [1], Ю.В. Шепелева [2]

[1] Пензенский государственный университет, г. Пенза, Россия;
[2] Пензенский государственный университет архитектуры и строительства, г. Пенза, Россия
✉ v.antipenko7@yandex.ru

Аннотация. Биоимпедансные диагностические системы являются неотъемлемой частью современной медицины, поскольку они предоставляют уникальную возможность исследовать состав тела и ключевые физиологические параметры. Они являются золотым стандартом в области неинвазивного тестирования, и их точность и доступность продолжают улучшаться с каждым годом. В настоящее время при оценке параметров биоимпеданса особое внимание уделяется методам и точности измерений. В данной статье обсуждаются ключевые аспекты определения биоимпеданса, связанные с ошибками измерений. Также представлены различные подходы к снижению погрешностей при измерении биоимпеданса.

Ключевые слова: импеданс, измерение, модель Коула, погрешность, объект

Ссылка при цитировании: Антипенко В. В., Печерская Е. А., Якушов Д. В., Артамонов Д.В., Карпанин О. В., Шепелева Ю. В. Уменьшение погрешности измерения биоимпеданса при исследовании состава тела // Научно-технические ведомости СПбГПУ. Физико-математические науки. 2024. Т. 17. № 3.1. С. 330–334. DOI: https://doi.org/10.18721/JPM.173.167

Introduction

Automated bioimpedance measurement systems being developed offer a simple and rapid method for assessing body composition by measuring physiological parameters that are important indicators of physical health [1]. These systems have advantages over analogues in terms of technical and economic indicators, they are portable and do not require specialized training for use. Many modern devices for measuring bioimpedance use an alternating current with a constant amplitude, applied to the sample through two electrodes. The resulting voltage between the other two electrodes serves to determine the characteristic. To obtain the most accurate results, the current excitation system must provide operation in a wide frequency range, determined by the excitation method and the external device. The impedance measurement is then performed and equivalent electrical parameters are derived from the model of the sample being compared [2].

For the research, we used a developed software and hardware complex for measuring bioimpedance with a modernized symmetrical current source capable of carrying out measurements in a wide frequency range from 300 Hz to 2000 kHz. This ensures high repeatability of measurement results and brings bioimpedance analysis closer to a reliable method for diagnosing human health [3, 4].

Bioimpedance measurement and results analysis

In order for the measurements to be reliable, it is important to calibrate the measuring unit using a calibration resistor. In this work, a 910 ohm calibration resistor is used. Calibration creates a table of complex coefficients to measure a known resistance at all frequencies in a given range. The dependence of the impedance modulus and phase angle tangent on frequency is shown in Figure 1.

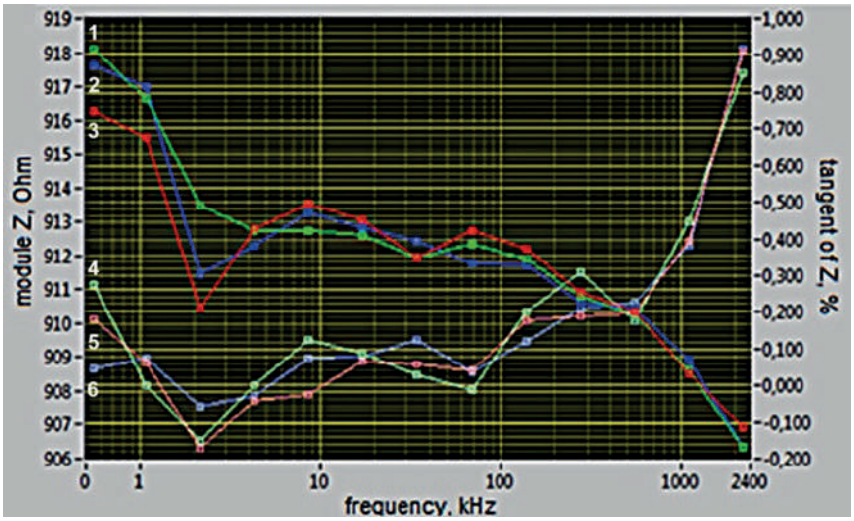

Fig. 1. Frequency response R = 910 Ohm, after calibration using a 910 Ohm resistor

Figure 1 shows the frequency response on the left along the ordinate on a logarithmic scale, the total impedance module is displayed, on the right – the phase shift angle in percentage. The X-axis displays frequency.

Notation: 1, 2, 3 – indicate the impedance modulus; 4, 5, 6 – indicate the phase shift angle

The graph clearly shows that the maximum absolute resistance deviation is 8 ohms. The maximum relative deviation is 0.87%, which indicates a slight change in this parameter. In turn, the maximum absolute deviation phase shift angle is –0.9%, which indicates the stability of this indicator.

If one takes a resistor of a different value, for example 300 Ohms, and take measurements using the previously obtained calibration table of coefficients, the dependence graph will turn into a curve. The resistor imitates the parasitic parameters of the human electrode-cell transition, and subsequently, during measurements, these parameters no longer affect the measurements. A prerequisite is to connect the cabling resistor and electrodes to the connector using the same (or identical) connecting cables. Calibration coefficients are recorded in the device's memory and saved. It is known that the active component of the impedance does not depend on frequency (Fig. 2).

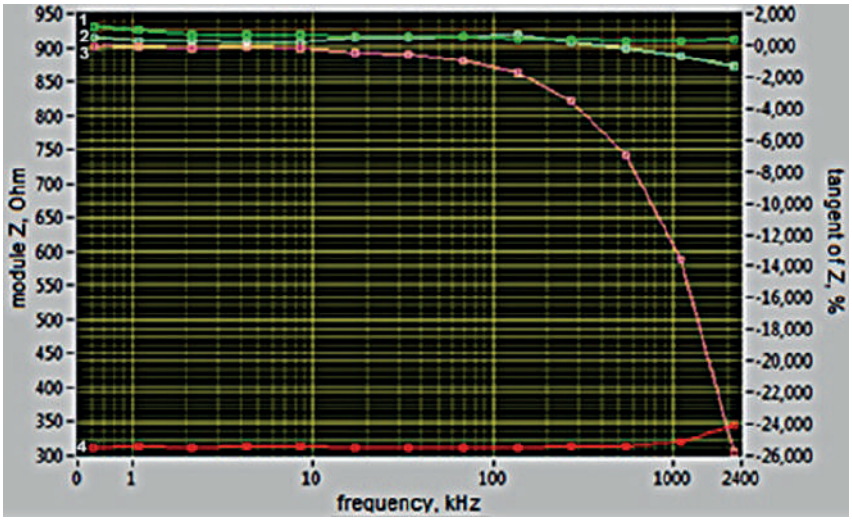

Fig. 2. Frequency response R = 300 Ohm and R = 910 Ohm, after calibration with a 910 Ohm resistor.

Notation: 1, 4 – indicate the impedance modulus; 2, 3 – indicate the phase shift angle

Next, we calculate the maximum absolute and relative error of resistance from the dependence graph (Fig. 1), it is respectively equal to $\Delta R = 45$ Ohm and $\delta = 13.1\%$. The absolute error of the tangent of the phase angle was $\Delta \mathrm{tg}\varphi = 26\%$.

Continuing the study of impedance measurements, significant discrepancies were revealed on a resistor with a resistance of 300 ohms from the calibration one. At high frequencies, the complex impedance changes sharply, which is caused by a discrepancy between the measured impedance and that taken into account during calibration.

Next, measurements are carried out, and the resulting spectral characteristic is visualized using a Bode diagram, reflecting the dependence of the module of the complex impedance and the tangent of the phase angle on frequency, after which it must be converted to the Nyquist format. Based on this information, it is necessary to establish the characteristics of the equivalent and mathematical models [5–7].

The measurement procedure produces a graph showing the frequency response of the impedance (Fig. 3).

To obtain active and reactive components of resistance, it is necessary to use formula (1) and (2):

$$R = |Z| \cdot \cos(\mathrm{arctg}\varphi), \tag{1}$$

$$X_c = |Z| \cdot \sin(\mathrm{arctg}\varphi). \tag{2}$$

Next, it is necessary to approximate the experimental data by a circle using the least squares method (Fig. 4). As a result, a circle with a radius of 140 Ohms is formed, the center of which lies at the point (570; –65).

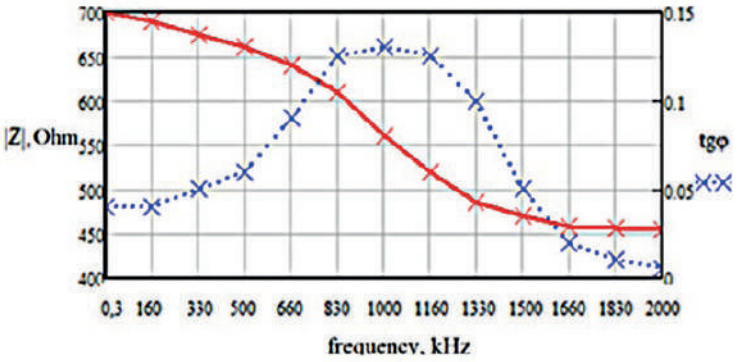

Fig. 3. Experimental frequency dependence of impedance

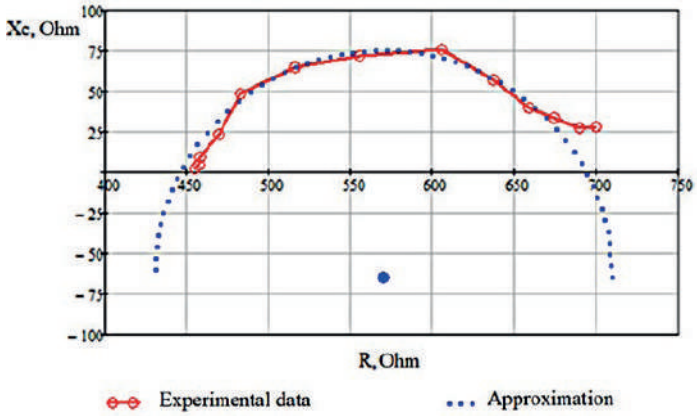

Fig. 4. Approximation of experimental data

Formula (3) opens up the possibility of determining the parameters of the Cole model, which describes the electrical properties of various materials.

$$\overline{Z} = R_{\infty} + \frac{R_0 - R_{\infty}}{1 + \left(J \cdot \omega \cdot \tau_z\right)^{\alpha}}. \tag{3}$$

These parameters include resistance at infinite high frequency (R_{∞}), resistance at zero frequency (R_0), dimensionless parameter (α), time constant (τ_z) and circular frequency (ω). From the graph shown in Figure 4, we determine R_{∞} = 445 Ohm, R_0 = 690 Ohm. We take α = 0.7, ω = 40 Hz. The time constant is defined as:

$$\tau = \frac{1}{2 \cdot \pi \cdot \omega} = 3.98[ms]. \tag{4}$$

Figure 5 shows a plot of the resulting Cole model.

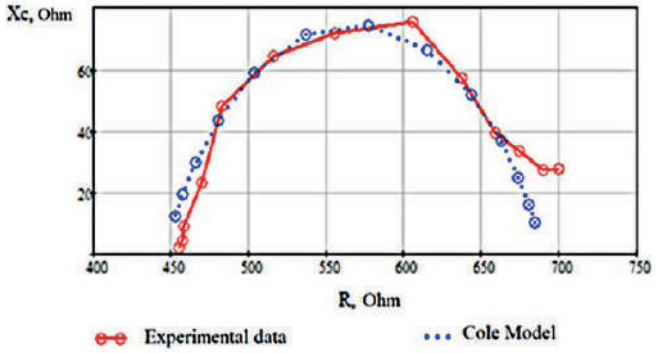

Fig. 5. Cole Model

Therefore, we can conclude that measuring different resistances of objects using the same calibration coefficients leads to measurement inaccuracy. The value of the resistance or measurement object must be selected close to the calibration value.

Conclusion

In this work, impedance measurements were carried out in the frequency range from 300 Hz to 2000 kHz. Thanks to repeated measurements and subsequent software and mathematical data processing and selection of the correct nominal value of the relative calibration resistance, the relative measurement error will be reduced to a minimum.

REFERENCES

1. **Dutra D., Bertemes-Filho P.,** Extracting parasite effects of electrical bioimpedance measurements, J. Electr. Bioimp. 9 (2018) 115–122.

2. **Qin E.S., Mindy M.J., Chen W.F.,** Diagnostic accuracy of bioimpedance spectroscopy in patients with lymphedema: A retrospective cohort analysis, Journal of Plastic, Reconstructive & Aesthetic Surgery. 71 (2018) 1041–1050.

3. **Antipenko V.V., Pecherskaya E.A., Tuzova D.E., Yakushov D.V., Artamonov D.V.,** Development of an automated system for measuring bioimpedance for the study of body composition, St. Petersburg State Polytechnical University Journal. Physics and Mathematics. 16 (3.2) (2023) 294–300.

4. **Antipenko V.V., Pecherskaya E.A., Zinchenko T.O., Artamonov D.V., Spitsina K.Yu., Pecherskiy A.V.,** Development of an automated bioimpendance analyzer for monitoring the clinical condition and diagnosis of human body diseases, J. Phys. Conf. Ser. 1515 (5) (2020) 052075.

5. **Sindeeva L.V., Kazakova G.N.,** Anthropometry and bioimpedansometry: parallels and divergences, Medical Sciences. 9 (2013) 476–480.

6. **Freeborn T.J., Crircher S.,** Threshold and Trend Artifacts in Localized Multi-Frequency Bioimpedance Measurements, IFAC PapersOnLine. 54–15 (2021) 55–60

7. **Anamika P., Mukesh R.,** Bioimpedance analysis of vascular tissue and fluid flow in human and plant body: A review, Biosystems engineering. 197 (2020) 170–178.

THE AUTHORS

ANTIPENKO Vladimir V.
v.antipenko7@yandex.ru
ORCID: 0000-0003-0274-7004

PECHERSKAYA Ekaterina A.
pea1@list.ru
ORCID: 0000-0001-5657-9128

YAKUSHOV Dmitriy V.
hammer.fate@yandex.ru
ORCID: 0009-0005-0892-312X

ARTAMONOV Dmitriy V.
dmitrartamon@yandex.ru
ORCID: 0000-0002-3240-7222

KARPANIN Oleg V.
karpanino@mail.ru

SHEPELEVA Yulia V.
eduard.shepelev.67@mail.ru
ORCID: 0000-0001-5075-2727

Received 15.07.2024. Approved after reviewing 31.07.2024. Accepted 31.07.2024.

MATHEMATICAL PHYSICS

Conference materials
UDC 004.032.26
DOI: https://doi.org/10.18721/JPM.173.168

Improving compliance of brain MRI studies with the atlas using a modified TransMorph neural network

N.A. Nefediev [1] ✉, N.E. Staroverov [2], R.V. Davydov [3]

[1] Alferov University, St. Petersburg, Russia;

[2] St. Petersburg Electrotechnical University "LETI", St. Petersburg, Russia;

[3] Peter the Great St. Petersburg Polytechnic University, St. Petersburg, Russia

✉ Nikolay-Nefedev@yandex.ru

Abstract. The work carried out a study on modifying the architecture of the TransMorph neural network by integrating an input data preprocessing unit. The goal was to achieve better similarity scores between studies in the dataset and the reference atlas. The data was assessed based on the structure similarity metric. The results suggest that the use of a Sobel filter can lead to improvement.

Keywords: DIR, TransMorph, brain segmentation, MRI, neural network, AI in medicine

Citation: Nefediev N.A., Staroverov N.E., Davydov R.V., Improving compliance of brain MRI studies with the atlas using a modified TransMorph neural network, St. Petersburg State Polytechnical University Journal. Physics and Mathematics. 17 (3.1) (2024) 335–339. DOI: https://doi.org/10.18721/JPM.173.168

Материалы конференции
УДК 004.032.26
DOI: https://doi.org/10.18721/JPM.173.168

Улучшение соответствия МРТ исследований головного мозга атласу при помощи модифицированной нейронной сети TransMorph

Н.А. Нефедьев [1] ✉, Н.Е. Староверов [2], Р.В. Давыдов [3]

[1] Академический университет имени Ж.И. Алфёрова РАН, Санкт-Петербург, Россия;

[2] Санкт-Петербургский государственный электротехнический университет «ЛЭТИ» им. В.И. Ульянова (Ленина), Санкт-Петербург, Россия;

[3] Санкт-Петербургский политехнический университет Петра Великого, Санкт-Петербург, Россия

✉ Nikolay-Nefedev@yandex.ru

Аннотация. В работе проведено исследование по модифицированию архитектуры нейронной сети TransMorph путем встраивания блока предобработки входных данных. Целью было достижение лучших показателей схожести между исследованиями из набора данных и эталонным атласом. Оценка данных проводилась на основе метрики structure similarity. Результаты позволяют сделать выводы, что применение фильтра собеля может привести к улучшению.

Ключевые слова: DIR, TransMorph, сегментация мозга, МРТ, нейронные сети, искусственный интеллект в медицине

Ссылка при цитировании: Нефедьев Н.А., Староверов Н.Е., Давыдов Р.В. Улучшение соответствия МРТ исследований головного мозга атласу при помощи модифицированной нейронной сети TransMorph // Научно-технические ведомости СПбГПУ. Физико-

математические науки. 2024. Т. 17. № 3.1. С. 335–339. DOI: https://doi.org/10.18721/JPM.173.168

Introduction

Deformable image registration (DIR) is an important task in the field of image processing. In general, DIR is the spatial correlation of objects in one image (displaced) to another image (fixed or reference). From a practical point of view, this task is one of the fundamental tasks in the field of medical image processing, especially where there are series of images (computer tomography like research).

When working with diagnostic radiology studies, especially with MRI and CT studies, a situation often arises when a specialist receives a deformed series of images. Deformations of CT and MRI studies often occur due to shifts in the patient's position relative to the positioning of the specialist or the urgency of the study, when it is not possible to perform the correct positioning. Such cases contribute to the fact that the output series contains rotations of the patient relative to the standard placement or unclear boundaries of internal structures due to random movements.

One solution to the problem of image deformation is the use of classical image registration algorithms. The principle of operation of such algorithms is to process two images, solve the problem that is the basis of the algorithm and, based on the solution found, change the target image relative to the reference one. The main advantage of solutions of this kind is that they work based on clear and easily interpreted rules, and, unlike neural networks, they do not require training. The main disadvantage of this approach is the high cost of calculations and, therefore, the speed of their operation. Despite the attempt to transfer calculations to the GPU, solving the DIR problem using most classical algorithms can take minutes or even more. When solving a problem for multi-slice CT or MRI studies, this together can lead to significant processing time for the entire series. This significant drawback greatly complicates the application of solutions based on classical algorithms in real practice.

An alternative to classical algorithms are solutions created on the basis of neural networks. The field of medicine was no exception. In the context of interaction with MRI and CT series, advanced results are achieved using algorithms based on neural networks. The main problem in the use of neural network algorithms for analyzing research in medicine most often lies in the fact that training occurs on a set of studies with unclear semantics, and when processing a deformed study, various types of errors may occur.

To eliminate biases, the study uses image registration algorithms. Among neural network algorithms, two subtypes can be distinguished, namely neural networks that learn with and without a teacher. To train the first type of networks, a ground truth data set is required, which acts as a reference result of the processed research: at each stage, the option predicted by the network is compared with the ground truth and based on this comparison, the error is calculated, and a decision is made to direct the further training step. Often in this approach, a set of ground truths is created using classical algorithms. For unsupervised learning, only a rule is required by which the error metric will be calculated. During the learning process, the network itself will select the optimal rules for changing the image to minimize errors. Currently, algorithms based on unsupervised learning show state of the art results in solving the DIR problem. We explored the possibility of using a modified TransMorph architecture to improve brain MRI data [1].

Materials and methods

For solving the DIR problem, algorithms solve a typical energy optimization problem between two images:

$$E(I_m, I_f, \phi) = E_{sim}(I_m \circ \phi, I_f) + \lambda R(\phi), \quad (1)$$

where I_m и I_f is shifted and fixed image, ϕ is deformation field, which distorts the shifted image (i.e. $I_m \circ \phi$), $R(\phi)$ ensures the smoothness of the deformation field, λ is the regularization

hyperparameter that determines the tradeoff between image similarity and deformation field regularity.

This equation reduces to solving the optimization problem:

$$\hat{\phi} = \arg\min_{\phi} E(I_m, I_f, \phi), \tag{2}$$

The DIR reference study was the brain atlas. The atlas also served to calculate the structural similarity index measure (SSIM) for the studies under consideration [2, 3]. SSIM is one of the methods for assessing the similarity of two images and displays the structural changes of one image relative to the reference:

$$SSIM(x, y) = \frac{(2\mu_x\mu_y + c_1)(2\sigma_{xy} + c_2)}{(\mu_x^2 + \mu_y^2 + c_1)(\sigma_x^2 + \sigma_y^2 + c_2)}, \tag{3}$$

where μ_x and μ_y are mean x and mean y respectively, σ_x^2 and σ_y^2 are variance x and variance y respectively, σ_{xy} is the covariance between x and y. $c_1 = (k_1 L)^2$, $c_2 = (k_2 L)^2$ – two variables, in which L is the dynamic range of the pixel-values (k_1 = 0.01, k_2 = 0.03 by default).

When working with images, in addition to approaches based on the use of algorithms (classical or neural network), image filtering is often used. This approach is based on applying a filter kernel to an image to obtain a new one. Depending on the filter settings, the new image can have various properties, i.e. highlighting edges, suppressing noise, changing sharpness, as well as changing parameters such as brightness and contrast, as well as aligning their values. The processed image can be better perceived by a specialist (for example, in the medical field) or participate in a further pipeline. It is worth noting that there are a huge variety of filters for image processing that allow you to highlight target features in the input data. In our work, we used the Sobel filter, which allows us to find the boundaries of image objects, and the operating principle is based on calculating local changes in the pixel area.

In our work, we used the open dataset "Information eXtraction from Image" – IXI [4]. The dataset contains about 600 MRI studies performed in T1, T2, PD-weighted images. To carry out our work, we used T2 studies.

The first step was to study the structural correspondence of the existing studies in the dataset to the reference atlas. The SSIM metric was used to calculate structural fit. The next step was to align studies from the existing dataset against the atlas and recalculate the SSIM for the processed dataset and atlas. We used the TransMorph architecture, which is based on the idea of using Swin Transform as an encoder [5]. In Transmorph, SWIN Transform blocks have been configured, which adapts the self-attention mechanism for the DIR task and improves the usefulness of the method relative to conventional self-attention. An increase in the metric was obtained.

The next step was to modify the TransMorph network and apply its modified version to the dataset. To modify the architecture, the original architecture with trained weights was taken from the TransMorph authors' github repository. We have built into the architecture a convolutional layer for processing input data with parameters of 128×128×32, a customized convolution kernel according to the Sobel filter. The modified architecture is shown in Figure 1, the internal structure of two successive swin transformer blocks is shown in Figure 2.

In the modified network, the input data first passes through the convolutional layer, from where it is transferred to the original TransMorph part. The resulting displacement field is applied to the original input data. An example of data after the convolutional layer is given in the next section.

Results and Discussion

Figure 3 shows data from the dataset in the form of single slices before pre-processing by the convolutional layer (top row original) and after the convolutional layer (bottom row after filter).

The impact of the original and modified versions of TransMorph was assessed on 20 randomly selected studies from the IXI dataset. The evaluation was carried out using the SSIM metric, which was calculated at the research step. The results obtained are shown in Figure 4.

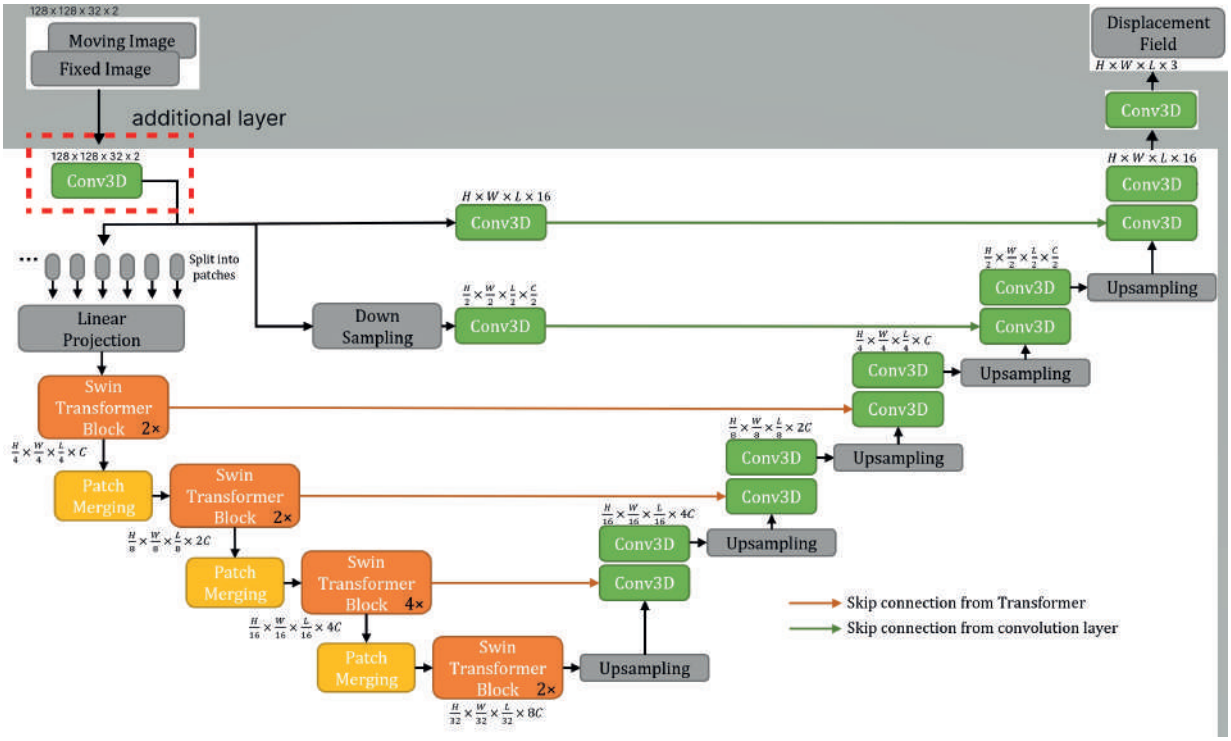

Fig. 1. Modified TransMorph architecture

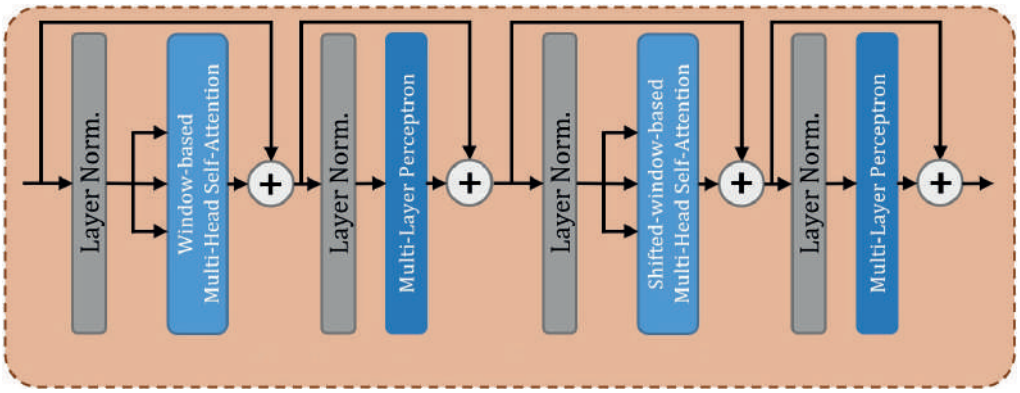

Fig. 2. Internal structure of two successive swin transformer blocks

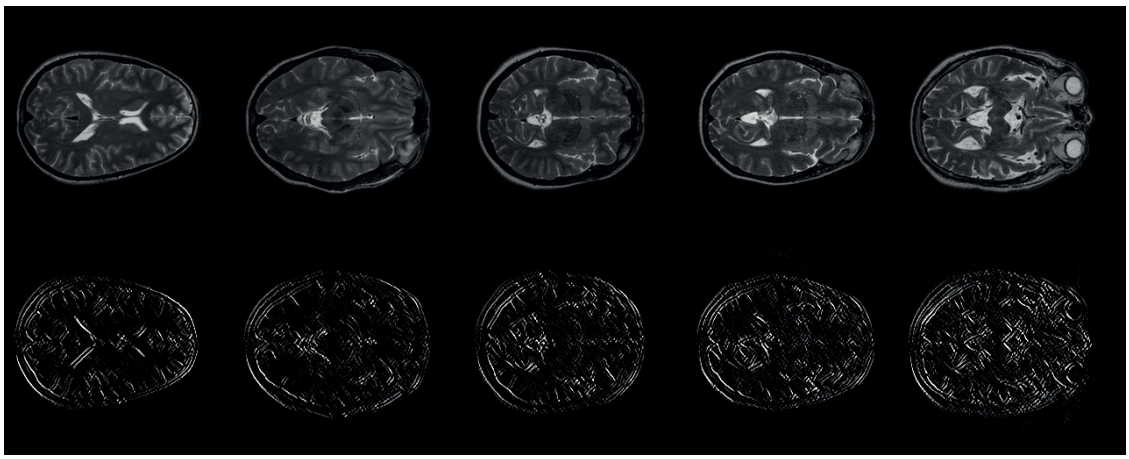

Fig. 3. A single slice of the series after additional layer

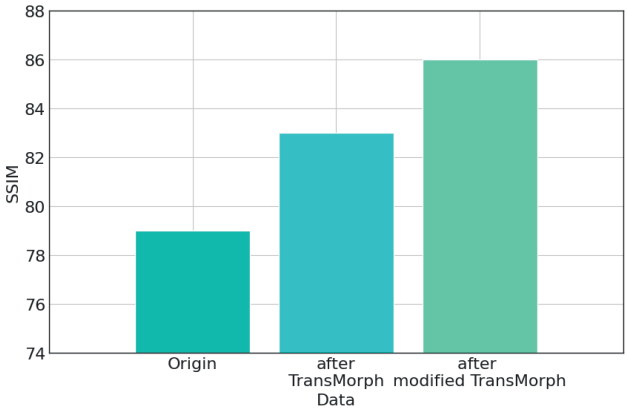

Fig. 4. SSIM metric value on original data and after applying TransMorph and modified version

Conclusion

The research work carried out shows the prospects for using data preprocessing for DIR. If positive results are obtained on a more variable dataset, the next step is to use the processed data to train segmentation networks and analyze MRI studies of the brain.

REFERENCES

1. **Rigaud B., Simon A., Castelli J., Lafond C., de Crevoisier R.,** Deformable image registration for radiation therapy: principle, methods, applications and evaluation. Acta Oncologica. 58 (9) (2019) 1225–1237.

2. **Chen J., Frey E. C., He Y., Segars W. P., Li Y., Du Y.,** TransMorph: Transformer for unsupervised medical image registration, Medical Image Analysis. (82) (102615) (2022).

3. **Chen J., Li Y., Du Y., Frey E.C.,** Generating anthropomorphic phantoms using fully unsupervised deformable image registration with convolutional neural networks. Med Phys. 47(12) (2020) 6366–6380.

4. Brain Development. URL: https://brain-development.org/ixi-dataset/ (accessed 2.11.2023).

5. **Tang Y., Dong Y., Wenqi L., Holger R.R., Bennett L., Daguang X., Vishwesh N., Ali H.,** Self-supervised pre-training of swin transformers for 3d medical image analysis. In Proceedings of the IEEE/CVF conference on computer vision and pattern recognition. (2022) 20730–20740.

THE AUTHORS

NEFEDIEV Nikolay A.
Nikolay-Nefedev@yandex.ru
ORCID: 0009-0004-6601-8884

DAVYDOV Roman V.
davydovroman@outlook.com
ORCID: 0000-0003-1958-4221

STAROVEROV Nikolay E.
nik0205st@mail.ru
ORCID: 0000-0002-4404-5222

Received 14.07.2024. Approved after reviewing 27.08.2024. Accepted 28.08.2024.

MECHANICS

Conference materials
UDC 62-83
DOI: https://doi.org/10.18721/JPM.173.169

A fast and strong microactuator powered by explosion of a hydrogen-oxygen mixture

P.S. Shlepakov [1] ✉, I.V. Uvarov [1], V.B. Svetovoy [2]

[1] Valiev Institute of Physics and Technology of RAS, Yaroslavl Branch, Yaroslavl, Russia;
[2] A.N. Frumkin Institute of Physical Chemistry and Electrochemistry RAS, Moscow, Russia
✉ p.shlepakov@bk.ru

Abstract. An electrochemical actuator is demonstrated that uses the periodic explosions of hydrogen and oxygen gases in a microchamber with a volume of 3.1 nl. The gases are generated in the form of nanobubbles during alternating polarity electrolysis. The device operates at a frequency of up to 10 Hz. The stroke of the membrane can reach 100 μm, which is an order of magnitude larger than the deflection in the non-explosive mode. No significant wear of the device is observed after 40 000 explosions in the chamber. The output force is measured by loading the membrane with different objects. The actuator develops a force at least 0.5 N, significantly outperforming other actuators in terms of force density.

Keywords: electrochemical actuator, membrane, alternating polarity electrolysis, nanobubbles, explosion, force

Funding: This work is supported by the program no. FFNN-2022-0017 of the Ministry of Science and Higher Education of Russia for Valiev Institute of Physics and Technology of RAS.

Citation: Shlepakov P.S., Uvarov I.V., Svetovoy V.B., A fast and strong microactuator powered by explosion of a hydrogen-oxygen mixture, St. Petersburg State Polytechnical University Journal. Physics and Mathematics. 17 (3.1) (2024) 340–344. DOI: https://doi.org/10.18721/JPM.173.169

Материалы конференции
УДК 62-83
DOI: https://doi.org/10.18721/JPM.173.169

Быстрый и сильный микроактюатор на основе взрыва водород-кислородной смеси

П.С. Шлепаков 1 ✉, И.В. Уваров [1], В.Б. Световой [2]

[1] Ярославский Филиал Физико-технологического института им. К.А. Валиева РАН, г. Ярославль, Россия
[2] Институт физической химии и электрохимии им. А.Н. Фрумкина РАН, Москва, Россия
✉ p.shlepakov@bk.ru

Аннотация. Исследованы рабочие характеристики быстрого электрохимического актюатора, использующего взрыв стехиометрической смеси водорода и кислорода в закрытой камере объемом 3.1 нл. Ход мембраны составляет около 100 мкм и на порядок превышает отклонение при работе без взрыва. Актюатор развивает силу 0.5 Н и существенно превосходит актюаторы других типов по этому параметру.

Ключевые слова: электрохимический актюатор, мембрана, электролиз переменной полярности, нанопузыри, взрыв, усилие

Финансирование: Работа выполнена в рамках Государственного задания ФТИАН им. К.А. Валиева РАН Минобранауки РФ по теме № FFNN-2022-0017.

Ссылка при цитировании: Шлепаков П.С., Уваров И.В., Световой В.Б. Быстрый и сильный микроактюатор на основе взрыва водород-кислородной смеси // Научно-технические ведомости СПбГПУ. Физико-математические науки. 2024. Т. 17. № 3.1. С. 340–344. DOI: https://doi.org/10.18721/JPM.173.169

Introduction

The development of microfluidic technology has opened up new possibilities in various fields, including chemical analysis, cellular research, rapid disease diagnosis, and other areas of biology and medicine. These systems can deliver drugs directly to affected organs or tissues, minimizing side effects and enhancing treatment efficacy [1]. A key component of these microfluidic devices is the drug delivery module, which consists of a micropump that dispenses fluid from an integrated reservoir to the body. The pump uses an actuator to create a back-and-forth motion of the membrane, which is essential for accurate and efficient drug delivery. The actuator must be small, generate a significant force, and can be manufactured using conventional microelectronic techniques. Electrochemical actuators are well-suited for this purpose, as they consist of a chamber containing two electrodes immersed in an electrolyte solution. During electrolysis, gas bubbles form in the chamber, pushing the membrane and causing it to move back and forth.

Conventional electrochemical actuators have a long response time due to the slow gas recombination process. Recently, a new type of actuator has been developed that can operate at much higher frequencies than conventional actuators [2]. This new actuator is capable of delivering an ultra-precise dosage of 0.14 nl/cycle, but it has a relatively low pumping rate [3]. However, by using a novel mode of operation that involves the merging of hydrogen and oxygen nanobubbles into a larger microbubble, the flow rate can be significantly increased. In this study, we investigate the performance of this actuator when it operates in this explosive mode.

Materials and Methods

The actuator is schematically illustrated in Figure 1. It is fabricated on a 460 μm thick silicon substrate coated with a 1 μm thick thermally grown SiO_2 layer. On the dielectric layer, bilayer electrodes are formed by magnetron sputtering. The lower layer is a 500 nm thick aluminum layer that reduces the resistance of the electrodes, and the top layer is 150 nm thick ruthenium layer that guaranties resistivity to mechanical action of nanobubbles. The electrodes are located inside the working chamber with a diameter of 500 μm, and the chamber walls are made of SU-8 photoresist with a thickness of 16 μm. The chamber is closed by a flexible membrane made of 30 μm thick polydimethylsiloxane.

The operation principle is the following. One electrode is grounded, and a series of voltage pulses of alternating polarity with a frequency of 500 kHz is applied to the second electrode. The amplitude of pulses is chosen so that the concentration of H_2 and O_2 nanobubbles reaches a critical value. Densely packed nanobubbles merge into a microbubble containing a stoichiometric mixture of gases and electrolyte nanodroplets. Due to these nanodroplets, a combustion reaction is spontaneously ignited, leading to an explosive expansion of the bubble and a rapid upward movement of the membrane. During the reaction, the gases rapidly turn back into water causing the membrane to return to its initial position after the explosion.

The exploding microbubble leads to a sharp decrease in the current flowing through the electrodes. This drop is detected by the special electronics built into the pulse generator. When an explosion occurs, the generator stops sending the driving signal to prevent secondary, less powerful explosions and the accumulation of gas in the chamber. The movement of the membrane stroke is monitored by a video camera attached to an optical microscope. At the exact moment of the explosion, the generator sends a triggering pulse that initiates the process of taking pictures.

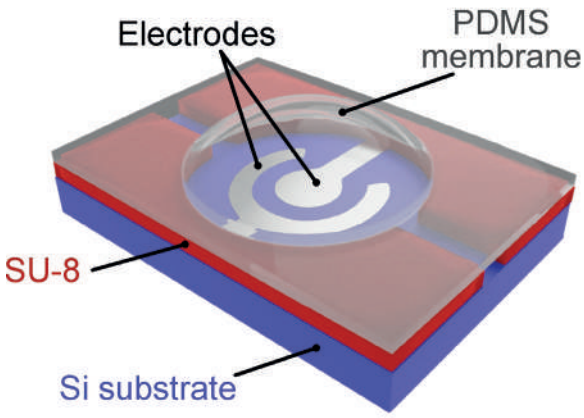

Fig. 1. Design of the actuator

To measure the output force, a metal ball with a diameter of 1.05 mm and a mass of 4.1 mg and a metal plate with a size of 3.9×2.0×0.6 mm and a mass of 35 mg are placed on the membrane. The movement of the load is recorded at a rate of 240 frames per second.

Results and Discussion

A photograph of the membrane after it has been deflected by an explosion is shown in Figure 2. Due to the rapid motion of the membrane, the image appears blurred. The average deflection of the membrane is about 100 μm, which is significantly larger than the deflection in the non-explosive regime.

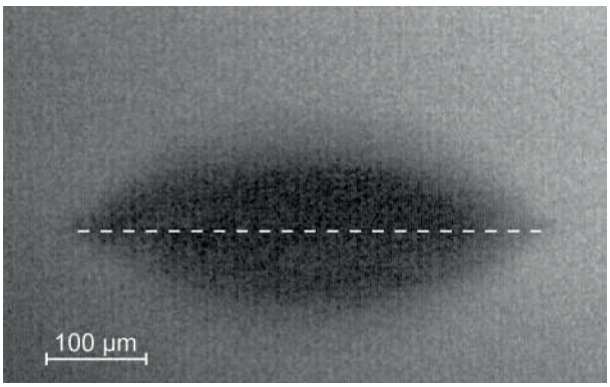

Fig. 2. A photograph of the membrane during the explosion, side view. The dotted line marks the initial position

Interrupting the series of pulses after the explosion reduces the amount of residual gas in the chamber, allowing for cyclic operation at a frequency of up to 10 Hz, which is in order of magnitude higher than the previous value [4]. The explosions may damage the sample due to cavitation. For electrodes located in unconfined space filled with the electrolyte, several thousand explosions can cause cracks and material detachment as shown in Fig. 3, *a*. However, for the actuator confined in the chamber no signs of wear even after 40 000 explosions, as shown in Fig. 3, *b*. The reason is related to the asymmetric position of the microbubble relative to the center of the chamber. Thus, the actuator is able to operate in the explosive mode for a long time.

The actuator throws the loading ball to a height h up to 29 mm and delivers the energy $E = m \cdot g \cdot h = 1.2$ μJ, where m is the ball mass. The initial velocity of the ball is $v = (2 \cdot g \cdot h)^{1/2} = 0.75$ m/s. According to the current waveform, the membrane deflects to its maximum for $t_0 \approx 10$ μs. Thus, the initial acceleration is estimated $a \approx v/t_0 \approx 7\,700$ g, and the output force is $F = m \cdot a \approx 0.31$ N. The actuator is able to move a heavy plate with a force of 0.5 N. Therefore, the micron-sized actuator under investigation is able to move macroscopic objects 11 000 times heavier than itself.

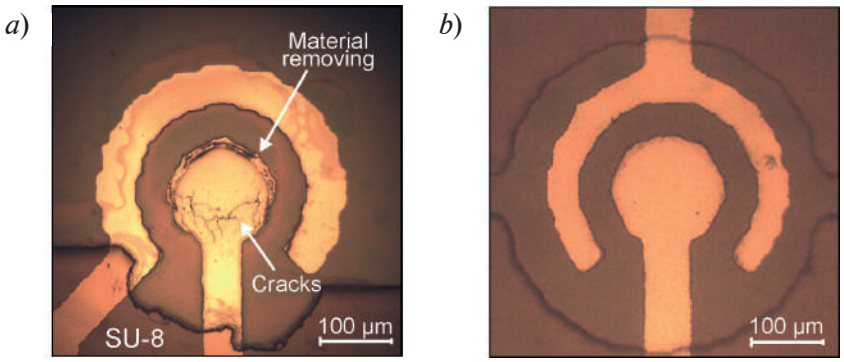

Fig. 3. Top view photographs of the electrodes: electrodes outside the chamber after 3 000 explosions (*a*); electrodes in the chamber after 40 000 explosions (*b*)

It is reasonable to compare various actuators using the force density, which is a ratio of an output force to an effective volume of the device. Electrostatic, thermal, and piezoelectric actuators are the strongest [4–6]. They can generate specific force up to several Newtons per cubic millimeter. The proposed actuator has a force density of 150 N/mm^3 that is at least one order of magnitude higher.

Conclusion

The operation of a fast electrochemical actuator in explosive mode is investigated. After the explosion, a series of pulses are interrupted, providing cyclic operation of the actuator at a frequency up to 10 Hz. The actuator can withstand more than 40,000 explosions without degradation. The membrane stroke is 100 μm, which is an order of magnitude higher than in the non-explosive mode. When a load is applied to the membrane, the actuator generates a force up to 0.5 N, which is several orders of magnitude greater than devices of comparable size can produce. The force density of the actuator is 150 N/mm^3, which is significantly higher than the most powerful devices.

REFERENCES

1. **Pons-Faudoa F.P., Ballerini A., Sakamoto J., Grattoni A.,** Advanced implantable drug delivery technologies: transforming the clinical landscape of therapeutics for chronic diseases, Biomedical microdevices. 21 (2019) 1–22.

2. **Uvarov I.V., Lokhanin M.V., Postnikov A.V., Melenev A.E., Svetovoy V.B.,** Electrochemical membrane microactuator with a millisecond response time, Sensors and Actuators B: Chemical. 260 (2018) 12–20.

3. **Uvarov I.V., Shlepakov P.S., Abramychev A.M., Svetovoy V.B.,** Fast Electrochemical Micropump for Portable Drug Delivery Module, Russian Microelectronics. 52 (3) (2023) 186–194.

4. **Uvarov I.V., Shlepakov P.S., Svetovoy V.B.,** A Fast and Strong Microactuator Powered by Internal Combustion of Hydrogen and Oxygen, Advanced Materials Technologies, (2024), 2400690

5. **Felder J., Lee E., DeVoe D.L.,** Large vertical displacement electrostatic zipper microstage actuators, Journal of Microelectromechanical Systems. 24(4) (2014) 896–903.

6. **Li Q., Liu C., Lin Y.H., Liu L., Jiang K., Fan S.,** Large-strain, multiform movements from designable electrothermal actuators based on large highly anisotropic carbon nanotube sheets, ACS nano. 9 (1) (2015) 409–418.

7. **Oldham K.R., Pulskamp J.S., Polcawich R.G., Dubey M.,** Thin-film PZT lateral actuators with extended stroke. Journal of Microelectromechanical Systems. 17(4) (2008) 890–899.

THE AUTHORS

SHLEPAKOV Pavel S.
p.shlepakov@bk.ru
ORCID: 0000-0002-1255-791X

SVETOVOY Vitaly B.
svetovoy@yandex.ru
ORCID: 0000-0002-9649-5663

UVAROV Ilia V.
i.v.uvarov@bk.ru
ORCID: 0000-0002-6882-0625

Received 11.07.2024. Approved after reviewing 22.07.2024. Accepted 22.07.2024.

RADIOPHYSICS

Conference materials
UDC 621.396.42
DOI: https://doi.org/10.18721/JPM.173.170

Subterahertz circularly polarized 1k-pixel reflective surface for 6G applications

A.A. Razakova [1, 3] ✉, A.N. Prikhodko [1, 2, 4], A.V. Lvov [1, 2],
A.S. Shurakov [1, 2, 3], G.N. Gol'tsman [1, 2, 4]

[1] Moscow Pedagogical State University, Moscow, Russia;
[2] HSE University, Moscow, Russia;
[3] National University of Science and Technology "MISIS", Moscow, Russia;
[4] Russian quantum center, Skolkovo, Moscow, Russia
✉ aa_razakova@student.mpgu.edu

Abstract. Wireless communication is a hot topic of research and development at this moment. The need of increasing data transfer rates and connection stability within vast digitalization of people interactions sets new tasks for scientific community. One of them is the utilization of higher operating frequencies in range of 140–150 GHz. This is an obvious way to obtain bigger channel capacity. However, for line-of-sight wireless channels, it may potentially lead to severe propagation losses, including absorption in water-containing atmospheric environments and scattering off static or dynamic objects. In this work, we report on the development of a technologically robust reflective surface that can be used in the sixth-generation reflection-aided data links. The proposed reflective surface has 36×36 spiral metallic elements implemented on top of a thin back-metalized quartz plate. The fabricated prototype was designed for 50° deflections from specular propagation paths at angles of incidence within ±75° and successfully used for a non-distorting reflection of a 6ϵ wide Gaussian beam at 145 GHz. It supports both linear and circular polarizations and exhibits cross-polarization level of approximately –25 dB.

Keywords: subterahertz, reflectarray antenna, wireless channel, 6G communication

Funding: This study was funded by the Russian Science Foundation grant number 22 79 10279, https://rscf.ru/project/22-79-10279/.

Citation: Razakova A.A., Prikhodko A.N., Lvov A.V., Shurakov A.S., Gol'tsman G.N., Subterahertz circularly polarized 1k-pixel reflective surface for 6G applications, St. Petersburg State Polytechnical University Journal. Physics and Mathematics. 17 (3.1) (2024) 345–348. DOI: https://doi.org/10.18721/JPM.173.170

Материалы конференции
УДК 621.396.42
DOI: https://doi.org/10.18721/JPM.173.170

Субтерагерцовая 1к-пиксельная отражающая поверхность с круговой поляризацией для технологий 6G

А.А. Разакова [1, 3] ✉, А.Н. Приходько [1, 2, 4], А.В. Львов [1, 2],
А.С. Шураков [1, 2, 3], Г.Н. Гольцман [1, 2, 4]

[1] Московский Педагогический Государственный Университет, Москва, Россия;
[2] Национальный исследовательский университет «Высшая школа экономики», Москва, Россия;

[3] Национальный исследовательский технологический университет «МИСИС», Москва, Россия;
[4] Российский квантовый центр, Сколково, Москва, Россия
✉ aa_razakova@student.mpgu.edu

Аннотация. Поиск новых решений в сфере беспроводных сетей является актуальной областью проблематики науки и техники. Потребность общества в повышении скорости и надежности беспроводной передачи данных ставит перед научно-техническим сообществом новые задачи, в частности разработки решений для работы в субтерагерцовом диапазоне частот. Для данного диапазона крайне актуальной является задача разработки устройств маршрутизации в каналах беспроводной связи. В данной работе мы представляем результаты разработки и экспериментального исследования антенной решетки отражательного типа 36×36 элементов на основе массива логарифмических спиральных антенн для диапазона частот 140–150 ГГц.

Ключевые слова: субтерагерцовый диапазон, отражательная антенная решетка, беспроводной канал, 6G связь

Финансирование: Исследование выполнено за счет гранта Российского научного фонда № 22-79-10279, https://rscf.ru/project/22-79-10279/.

Ссылка при цитировании: Разакова А.А., Приходько А.Н., Львов А.В., Шураков А.С., Гольцман Г.Н. Отражающая поверхность субтерагерцового диапазона для сетей 6G с круговой поляризацией и разрешением 1 килопиксель. // Научно-технические ведомости СПбГПУ. Физико-математические науки. 2024. Т. 17. № 3.1. С. 345–348. DOI: https://doi.org/10.18721/JPM.173.170

Introduction

New solutions in wireless communication technologies are of great interest in modern scientific and industrial considerations. Development of novel applications and services imposes high data rate and stability requirements on wireless networks [1]. The migration of operating frequencies into the subterahertz (sub-THz) band, on the way of increasing baud rates, is accompanied by the appearance of new signal attenuation factors leading to ultra-directional data links in the sixth generation (6G) wireless networks. Thus, line-of-sight communication channels are potentially exposed to the effects of dynamic blockages, micromobility and scattering off obstacles [2]. Reflection-aided data links with either static, semi-static or dynamically reconfigurable reflective surfaces [3] are among novel solutions to avoid this problem. In this work, we report on a static reflective surface (RS) that can be used for handling of few degrees wide Gaussian beams (GBs) during the first deployment stage of 6G wireless networks. It utilizes 36×36 spiral metallic elements [4] as antenna array implemented on top of a thin back-metalized quartz wafer and is designed for non-specular channels operating at 140–150 GHz.

Materials and Methods

The development of the electromagnetic (EM) model is the first step in the workflow. The modeling is done via computer-aided system utilizing finite element method. The elementary cell of the RS is modeled using Floquet port analysis to obtain in-reflection phase shifts for different spiral arm lengths. As a result, we obtained the geometry-dependent data. From the calculations we select three length values conforming the following principle: phase shifts between two of three adjacent cells with corresponding phases φ_1, φ_2, φ_3 must be equal 120°, i.e. $\varphi_2 - \varphi_1 = \varphi_3 - \varphi_2 = \varphi_1 - \varphi_3 = 120°$.

After the determination of spiral arm lengths with corresponding phase shifts, we constructed the array of 36×36 cells within the multibeam interference theory by the array factor method [5]. The construction utilizes quartz as a substrate. A metallic screen is implemented on the bottom side to provide non-specular reflection of the incident beam. As shown in Fig. 1,*a* the normally incident GB is reflected by angle θ, which is equal to 50° in the RS under study (here $\vec{E_0}$ is the

electric field strength vector, $\vec{k}$ is the wave vector). Spiral stop angle defines the arm length of spiral antenna in each elementary cell. The phase shifting is dependent on the spiral stop angle as shown in Fig. 1, *b*.

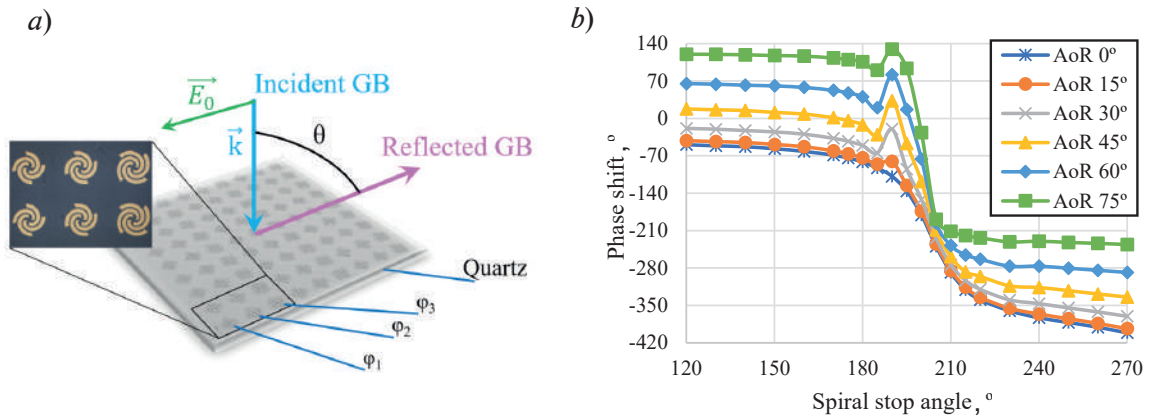

Fig.1. Scheme of the proposed reflective surface in action and (*a*), dependencies of phase shifts on spiral stop angle with different angles of reflection (AoR) (*b*)

The developed RS prototype is fabricated in a cleanroom process. The technological route includes forming a metallic spiral antenna array on a 140 μm thick quartz wafer using lift-off lithography process. The substrate is covered with AZ1512 photoresist using centrifuge, then exposed with maskless laser-beam aligner machine MLA150. The sample is developed in 0.7% KOH after the exposure and chemically hardened by chlorobenzene. To implement metallization of the array, 5 nm Ti and 400 nm Au layers are made via thermoresistive evaporation with VUP-5M machine. The titanium is used as a sorbent layer for improving adhesive characteristics. The lift-off removal of the unexposed regions is performed in heated acetone bath. The back-side metallization is implemented by attaching a 400 μm thick sapphire wafer entirely covered by Ti/Au (5/400 nm) evaporated thin film.

Results and Discussion

To measure beam profiles of the fabricated device, we developed experimental setup (Fig. 2, *a*). It includes a continuous wave microwave synthesizer, 12× frequency multiplier, voltage-controlled attenuator (VCA), horn antennas, envelope detector based on Schottky diode and lock-in amplifier. The carrier frequency is 145 GHz. The VCA is used for amplitude modulation and synchronized with lock-in amplifier. During the measurement, Rx is rotated around its axis with 1° step. The data is then acquired from the lock-in amplifier. Three types of experiments are conducted: measurements in E- and H-planes and cross-polarization measurement.

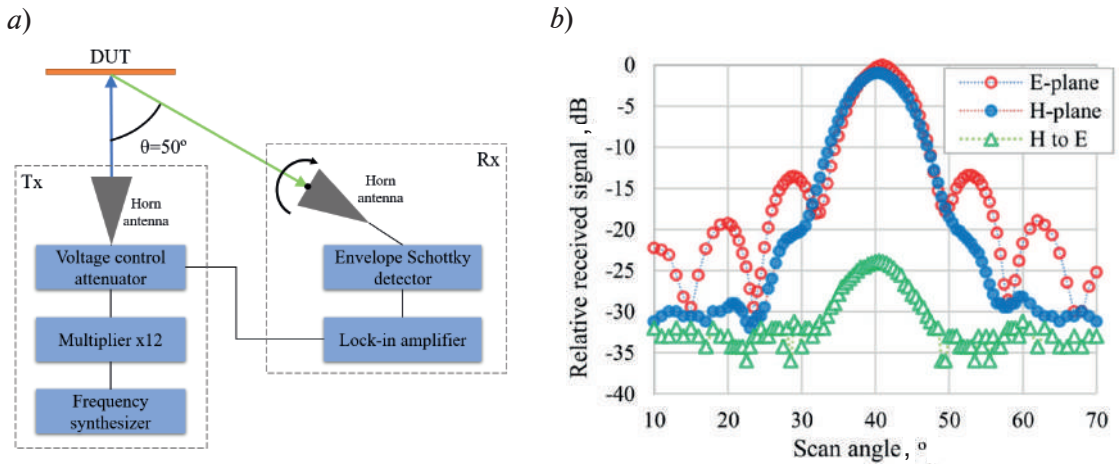

Fig. 2. Scheme of the measurement setup (*a*) and measured BP of the fabricated prototype (*b*)

Results of the RS prototype beam profiles (BP) measurements are presented in Fig. 2,*b*. The prototype is successfully used for a non-distorting reflection of a 6ϵ wide GB at 145 GHz. It supports both linear and circular polarizations and exhibits cross-polarization level of approximately −25 dB.

Conclusion

We presented development and fabrication process of the subterahertz circularly polarized 1k-pixel reflective surface for 6G applications and its characteristics, obtained experimentally. The prototype is represented by an array of scaled spiral antennas on the low loss quartz substrate. Spiral antennas have three variants of spiral arm length to provide 120° phase shift between adjacent elementary cell in row. The prototype was fabricated utilizing clean room processes that are necessary to provide accuracy of geometrical dimensions. The prototype under test shows the reflection of normally incident beam by the expected 50° angle. It is capable of static beamforming and disrupt geometrical optics law of reflection. It also demonstrates the support of both s- and p-polarizations. We believe that our findings should be interesting to developers of the next generation wireless systems operated at 140−150 GHz.

REFERENCES

1. **Yeh C., Do Jo G., Ko Y. J., Chung H.K.,** Perspectives on 6G wireless communications, ICT Express. 9 (1) (2023) 82−91.

2. **Moltchanov D., Sopin E., Begishev V., Samuylov A., Koucheryavy Y., Samouylov K.,** A tutorial on mathematical modeling of 5G/6G millimeter wave and terahertz cellular systems. IEEE Communications Surveys & Tutorials. 24(2) (2022) 1072−1116.

3. **Yang F., Pitchappa P., & Wang N.,** Terahertz reconfigurable intelligent surfaces (RISs) for 6G communication links. Micromachines. 13 (2) (2022) 285.

4. **Xue F., Wang H., Yi M., Liu G., Dong X.,** Design of a broadband single-layer linearly polarized reflectarray using four-arm spiral elements., IEEE Antennas and wireless propagation letters. 16 (2016) 696−699.

5. **Balanis C.A.,** Antenna theory: analysis and design, John Wiley & Sons, Hoboken, New Jersey, 2016.

THE AUTHORS

RAZAKOVA Anita A.
aa_razakova@student.mpgu.edu
ORCID: 0009-0008-9982-8022

SHURAKOV Alexander S.
alexander@rplab.ru
ORCID: 0000-0002-4671-7731

PRIKHODKO Anatoliy N.
anprihodko@hse.ru
ORCID: 0000-0002-4859-8975

GOLTSMAN Grigory N.
goltsman@rplab.ru
ORCID: 0000-0002-1960-9161

LVOV Andrey V.
alvov@hse.ru
ORCID: 0000-0002-2969-7695

Received 03.07.2024. Approved after reviewing 23.07.2024. Accepted 24.07.2024.

Conference materials
UDC 621.396.42
DOI: https://doi.org/10.18721/JPM.173.171

A mm-wave dielectric antenna with symmetric beam compatible with PCB machinery

M.I. Ershova [1] ✉, A.N. Prikhodko [1, 2, 4], A.S. Shurakov [1, 2, 3], G.N. Goltsman [1, 2, 4]

[1] Moscow Pedagogical State University, Moscow, Russia;
[2] National Research University Higher School of Economics, Moscow, Russia;
[3] National University of Science and Technology "MISIS", Moscow, Russia;
[4] Russian Quantum Center, Skolkovo, Moscow, Russia
✉ mi_ershova@student.mpgu.edu

Abstract. The current decade is associated with the start of active deployment and use of fifth generation networks, while the ongoing developments in the sixth generation communication technologies should be finalized in the upcoming decade. It is forecasted that sufficiently directive wireless transceivers will become integral parts of the next generation wireless communication systems. In this study, we report on the development of a low-cost millimeter wave dielectric antenna with nearly symmetric beam. The antenna makes use of a dual-stage dielectric multimode interference power divider terminated by 16 dielectric tapers with flare angles of 6–12°. It is designed for operation at frequencies of 50–77 GHz. The design is developed for fabrication by the means of printed circuit board prototyping machinery from high-permittivity laminates and, therefore, is compatible with the Si platform for solid-state electronics and integrated photonics. The fabricated antenna samples exhibit half-power beamwidths of 27° with corresponding side lobe levels of approximately −10 dB, as measured at 52 GHz.

Keywords: millimeter wave, dielectric rod antenna, antenna array, high-permittivity laminate, direct machining

Funding: This study was funded by the Russian Science Foundation grant number No. 21-72-10119, https://rscf.ru/project/21-72-10119/.

Citation: Ershova M.I., Prikhodko A.N., Shurakov A.S., Goltsman G.N., A mm-wave dielectric antenna with symmetric beam compatible with PCB machinery, St. Petersburg State Polytechnical University Journal. Physics and Mathematics. 17 (3.1) (2024) 349–353. DOI: https://doi.org/10.18721/JPM.173.171

Материалы конференции
УДК 621.396.42
DOI: https://doi.org/10.18721/JPM.173.171

Диэлектрическая антенна миллиметрового диапазона с симметричным пучком, совместимая с оборудованием для печатных плат

М.И. Ершова [1] ✉, А.Н. Приходько [1, 2, 4], А.С. Шураков [1, 2, 3], Г.Н. Гольцман [1, 2, 4]

[1] Московский педагогический государственный университет, Москва, Россия;
[2] Национальный исследовательский университет «Высшая школа экономики», Москва, Россия;
[3] Национальный университет науки и технологий «МИСиС», Москва, Россия;
[4] Российский квантовый центр, Сколково, Москва, Россия
✉ mi_ershova@student.mpgu.edu

Аннотация. Текущее десятилетие связано с началом активного развертывания и использования сетей пятого поколения, при этом текущие разработки в области коммуникационных технологий шестого поколения должны завершиться в ближайшее десятилетие. Прогнозируется, что достаточно направленные беспроводные приемопередатчики станут неотъемлемой частью систем беспроводной связи следующего поколения. В этом исследовании мы сообщаем о разработке диэлектрической антенны миллиметрового диапазона волн с почти симметричным пучком. В антенне использован двухкаскадный диэлектрический делитель мощности на основе многомодовой интерференции, оканчивающийся 16 диэлектрическими конусами с углами раствора 6–12°. Антенна предназначена для работы на частотах 50–77 ГГц. Конструкция разработана посредством прототипирования печатных плат из ламината с высокой диэлектрической проницаемостью и, следовательно, совместима с кремниевой платформой для твердотельной электроники и интегральной фотоники. Изготовленные образцы антенн имеют ширину пучка по полуспаду мощности 27° с соответствующими уровнями боковых лепестков примерно −10 дБ, измеренные на частоте 52 ГГц.

Ключевые слова: миллиметровые волны, диэлектрическая стержневая антенна, антенная решетка, ламинат с высокой диэлектрической проницаемостью, прямая механическая обработка

Финансирование: Исследование выполнено за счет гранта Российского научного фонда № 21-72-10119, https://rscf.ru/project/21-72-10119/.

Ссылка при цитировании: Ершова М.И., Приходько А.Н., Шураков А.С., Гольцман Г.Н. Диэлектрическая антенна миллиметрового диапазона с симметричным пучком, совместимая с оборудованием для печатных плат // Научно-технические ведомости СПбГПУ. Физико-математические науки. 2024. Т. 17. № 3.1. С. 349–353. DOI: https://doi.org/10.18721/JPM.173.171

Introduction

Currently, science and technology are interested in the development of low-cost, efficient, and compact modules capable of transmitting and receiving of millimeter wave (mmWave) signals. Wireless channels of the fifth and sixth generation (5/6G) communication networks require sufficiently directive transceivers as their crucial elements [1]. Moreover, novel mmWave antenna solutions are in demand by such applications as radar systems or atmospheric monitoring within the context of meteorological and climatological remote sensing [2, 3], etc.

In this study, we report on the development of a low-cost mmWave integrated dielectric rod antenna (DRA) array. Our design makes use of a dual-stage dielectric multimode interference power divider (MMIPD) [4] terminated by a 4×4-element planar array of dielectric tapers [5] with flare angles of 6–12°. Such a design can be easy tuned for efficient operation at any desired frequency within 50–77 GHz. It is developed for fabrication by the printed circuit board (PCB) prototyping machinery from high-permittivity laminates and, therefore, is naturally compatible with solid-state electronics and integrated photonics based on Si platform. Results of the simulations and detailed performance analysis of the developed antenna structures are to be presented further in the text of the article.

Results and Discussion

Figure 1, *a* provides a photograph of the fabricated completely dielectric DRA arrays with flare angles α of 6° and 12°. The main dimensions of a dual-stage MMIPD and DRA arrays are presented in Table and shown in Figure 1, *b*. They are developed for operation at 52 GHz, and their MMIPDs are equipped with input taper interfaces for coupling with rectangular metallic waveguides of a constant waveform source and power detector during beam profile measurements. The DRA array samples are fabricated by the means of direct machining from a high-permittivity PCB laminate (FSD1020T series). This material possesses relative permittivity of 10.2 and a loss

tangent of 0.002 at 10 GHz according to the specifications provided by the manufacturer, and its dielectric properties at 130–160 GHz are briefly reported in [6]. A similar type of one-dimensional antenna from another series of PCB laminates, along with a more detailed description of the technological process, is provided in [7]. The first and the second stages of the samples' MMIPDs are attached through dielectric holders made from a low-permittivity material by a 3-dimensional (3d) printing.

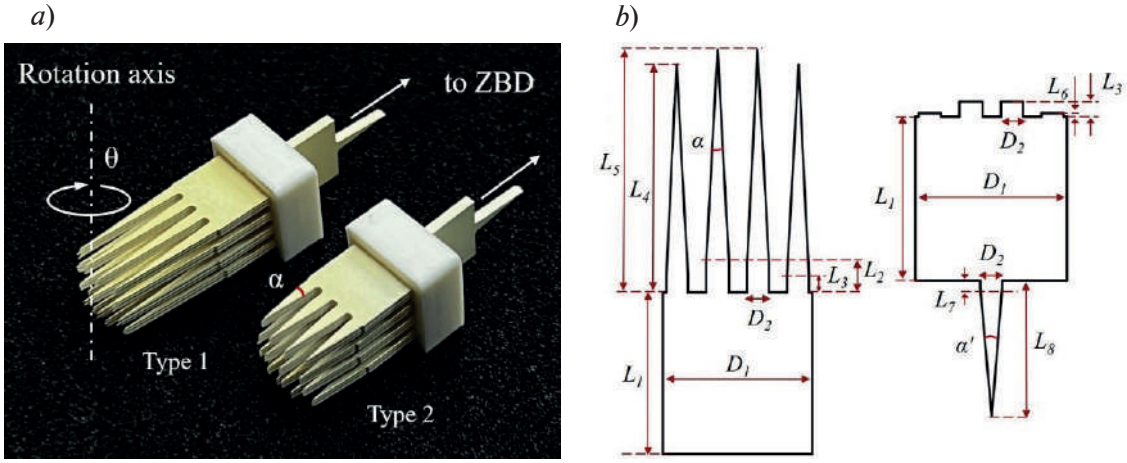

Fig. 1. Photograph of the fabricated DRA arrays (*a*); Geometry of the fabricated DRA arrays (*b*)

Table

Dimensions of the antenna array key elements

Array type	Geometric parameter											
	α, °	α', °	L_1, mm	L_2, mm	L_3, mm	L_4, mm	L_5, mm	L_6, mm	L_7, mm	L_8, mm	D_1, mm	D_2, mm
1	6	10	12	1.3	0.25	15.99	17.04	1.15	0.51	9.94	11.1	1.65
2	12	10	12	1.3	0.25	8.1	9.15	1.15	0.51	9.94	11.1	1.65

The fabricated DRA array samples are further experimentally studied. Experimental setup (Fig. 2, *a*) for the far-field radiation pattern measurements mainly makes use of a 50–77 GHz backward-wave oscillator (BWO) and a zero-biased Schottky diode detector (ZBD). The distance between Tx and Rx in the measurements significantly exceeds the Fraunhofer distance (DF). ZBD voltages are registered with aid of selective nanovoltmeter.

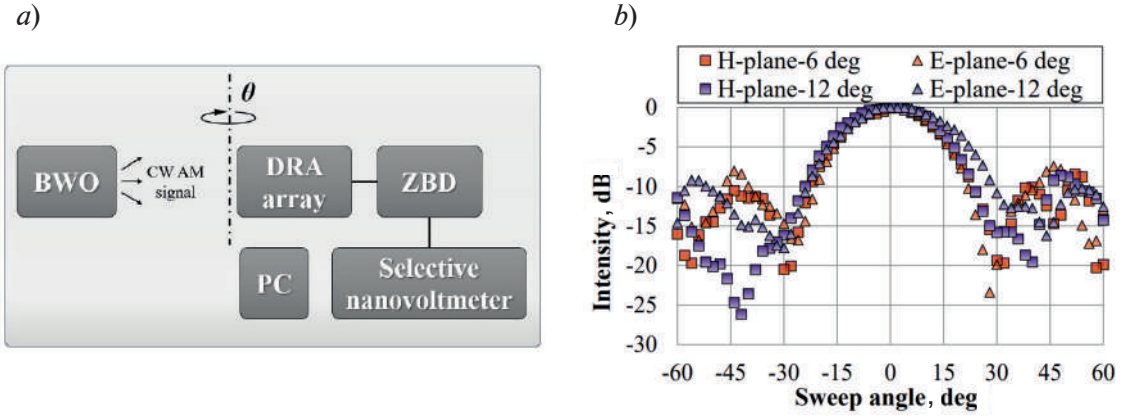

Fig. 2. Scheme of the experimental setup for measuring the beam profiles in H- and E-planes (*a*); H- and E-plane beam profiles of the fabricated samples measured at 52 GHz (*b*)

We use the 3D EM finite element method to simulate the beam profiles. Measured half-power beamwidths (*HPBW*) of 27° and side lobe levels (SLL) of −10 dB for both designs are qualitatively consistent with the calculated *HPBW* of 24° and SLL of −15 dB. Comparing the results of the manufactured dual-stage structure with the one-dimensional ones given in [7, 8], it is possible to identify an increase in the symmetry of the beam due to the cross-orientation of the power dividers.

The DRA gain weakly depends on the geometry of the flare angle. Thus, fabrication tolerance is relieved, and potential errors in fabrication of the most mechanically vulnerable elements, i.e., dielectric tapers, do not compromise performance of the integrated dielectric structure. In our study devices with 6−12° flare angles demonstrate decent performance at 52 GHz and can be tuned to any frequency within 50−77 GHz. Given that the proposed antenna design is naturally compatible with Si platform.

Conclusion

We propose the design of DRA arrays integrated with dual-stage MMIPD at the ends of which 16 tapered rod antennas are implemented. This work provides a detailed description of the fabrication and study of the main characteristics of the antennas. In direct machining, we use low-cost PCB laminate with high permittivity, so fabrication of DRA arrays becomes a simple and cheap process. As part of the study, radiation patterns of DRA arrays are measured at a carrier frequency of 52 GHz and show the half-power beamwidths of 27°, with corresponding side lobe levels of −10 dB for both designs. The corresponding calculated values of 24° and −15 dB are consistent with the experiment. Proposed DRA arrays are compatible with Si platform and can be used in solid-state electronics and integrated photonics in the millimeter wave range. The compact transceivers equipped with them can be used in 5/6G wireless communication modules, as well as in radar systems and atmospheric monitoring instruments due to their advantages.

REFERENCES

1. **Boulogeorgos A., Alexiou A., Merkle T., Schubert C., Elschner R., Katsiotis A., Rodrigues F.,** Terahertz Technologies to Deliver Optical Network Quality of Experience in Wireless Systems Beyond 5G. IEEE Communications Magazine. 56 (6) (2018) 144−151.

2. **Michler F., Scheiner B., Reissland T., Weigel R., Koelpin A.,** Micrometer Sensing With Microwaves: Precise Radar Systems for Innovative Measurement Applications. IEEE Journal of Microwaves. 1 (1) (2021) 202−217.

3. **Westwater E., Crewell S., Matzler C.,** A review of surface-based microwave and millimeter-wave radiometric remote sensing of the troposphere, September 2004URSI Radio Science Bulletin. 310 (2004) 59−80.

4. **Soldano L., Pennings E.,** Optical multi-mode interference devices based on self-imaging: principles and applications. Journal of Lightwave Technology. 13 (4) (1995) 615−627.

5. **Prikhodko A., Yaropolov T., Shurakov A., Gol'tsman G.,** Parametric model of a dielectric rod antenna array for terahertz applications. Proceedings of the 34th European Modeling & Simulation Symposium (EMSS 2022).

6. **Prikhodko A., Belikov I., Lvov A., Shurakov A., Gol'tsman G.,** Millimeter wave photonic crystal waveguides fabricated via direct machining, St. Petersburg Polytechnic University Journal. Physics and Mathematics. 15 (3.3) (2022).

7. **Lyubchak A., Prikhodko A., Andreev V., Shurakov A., Goltsman G.,** A mmWave rod antenna array compatible with a PCB prototyping technology, St. Petersburg State Polytechnical University Journal. Physics and Mathematics. 15 (3.3) (2022) 340−344.

8. **Shurakov A., Belikov I., Prikhodko A., Ershova M., Goltsman G.,** Superconducting Electronic−Photonic Platform for HEB-Based Terahertz Spectrometers. Appl. Sci. 13 (2023) 5892.

THE AUTHORS

ERSHOVA Margarita I.
mi_ershova@student.mpgu.edu
ORCID: 0009-0009-6785-4389

SHURAKOV Alexander S.
alexander@rplab.ru
ORCID: 0000-0002-4671-7731

PRIKHODKO Anatoliy N.
anatprikh1995@yandex.ru
ORCID: 0000-0002-4859-8975

GOLTSMAN Grigory N.
goltsman@rplab.ru
ORCID: 0000-0002-1960-9161

Received 04.07.2024. Approved after reviewing 08.08.2024. Accepted 08.08.2024.

Conference materials
UDC 537.86
DOI: https://doi.org/10.18721/JPM.173.172

Wireless power transfer in magnetic resonance imaging with a detuned birdcage coil

O.I. Burmistrov [1] ✉, N.A. Olekhno [1]

[1] ITMO University, Saint Petersburg, Russia

✉ oleg.burmistrov@metalab.ifmo.ru

Abstract. In this work, we develop an application of a transmit birdcage coil for wireless power transfer during the receive phase within a magnetic resonance imaging (MRI) scanner. The study includes numerical simulations and an experimental verification of a numerical model with a clinical birdcage coil. We simulate numerically magnetic fields inside the magnetic resonance imaging scanner with a phantom, the specific absorption rate distributions with a human voxel model, and the resulting voltage on receiving system coils. Therefore, we characterize possible distortions in MR images, demonstrate safety of the setup for a patient, and evaluate the RF-RF efficiency numerically, respectively. Finally, we outline potential devices placed in MRI bore which can provide a wireless power supply with the detuned birdcage coil and receive system.

Keywords: MRI, magnetic resonance imaging, birdcage coil, WPT, wireless power transfer, resonators

Funding: This work was supported by the Russian Science Foundation (Project No. 21-79-30038).

Citation: Burmistrov O.I., Olekhno N.A., Wireless power transfer in magnetic resonance imaging with a detuned birdcage coil, St. Petersburg State Polytechnical University Journal. Physics and Mathematics. 17 (3.1) (2024) 354–357. DOI: https://doi.org/10.18721/JPM.173.172

Материалы конференции
УДК 537.86
DOI: https://doi.org/10.18721/JPM.173.172

Беспроводная передача энергии в магнитно-резонансной томографии с использованием отстроенного резонатора типа «птичья клетка»

О.И. Бурмистров [1] ✉, Н.А. Олехно [1]

[1] Университет ИТМО, Санкт-Петербург, Россия

✉ oleg.burmistrov@metalab.ifmo.ru

Аннотация. В данной работе рассмотрена концепция беспроводной передачи энергии с помощью отстроенного резонатора типа «птичья клетка» для магнитно-резонансной томографии (МРТ) во время фазы приёма сигнала от ядер атомов. Было проведено численное моделирование, а также верификация численной модели в эксперименте с помощью резонатора от клинического аппарата МРТ. В частности, рассчитаны картины магнитного поля для такого резонатора с фантомом, распределения удельного коэффициента поглощения электромагнитной энергии внутри воксельной модели человека, а также напряжение на системе приёмных антенн. В результате, оценены возможные искажения на МР-изображениях, безопасность такой системы, а также

коэффициент полезного действия. Разработанная схема беспроводной передачи энергии может быть использована внутри тоннеля аппаратов МРТ со встроенным резонатором типа «птичья клетка» и системой приёма энергии, что позволит обеспечивать электроэнергией большинство видов приёмных локальных катушек (ближнепольных антенн с предусилителями и системой отстройки), а также медицинских датчиков.

Ключевые слова: МРТ, магнитно-резонансная томография, резонатор типа «птичья клетка», БПЭ, беспроводная передача энергии, резонаторы

Финансирование: Работа выполнена в рамках гранта Российского Научного Фонда (проект номер 21-79-30038).

Ссылка при цитировании: Бурмистров О.И., Олехно Н.А. Беспроводная передача энергии в магнитно-резонансной томографии с использованием отстроенного резонатора типа «птичья клетка» // Научно-технические ведомости СПбГПУ. Физико-математические науки. 2024. Т. 17. № 3.1. С. 354–357. DOI: https://doi.org/10.18721/JPM.173.172

Introduction

Magnetic resonance imaging (MRI) is an important method of medical diagnostics for the diseases including cancer and injuries. Near field antennas (called local coils) are used in MRI bore to enhance the functionalities of an MRI scanner and require a wire connection to the scanner during the scanning process. However, wire connection of local coils has many disadvantages, including patient discomfort, lowered speed of the patient positioning by medical staff, periodic replacement required by connectors and wires, and wrong cable positioning within MRI bore which can cause an additional heating of the patient [1]. The cable provides data transfer and power supply.

These issues can be resolved with wireless power transfer [2, 3]. Power supply without any cables between a local coil and an MRI scanner can be realized with energy harvesting at the scanning (Larmor) frequency, and with wireless power transfer at the frequency, different from Larmor frequency [4]. The main drawback of energy harvesting is low transmitted power (above 500 mW) [5, 6] which can supply only limited types of receive local coils. However, wireless power transfer requires an additional antenna [7–10]. Otherwise, the power transfer takes place during a very limited time of the nuclei excitation (the excitation phase) [11], which is much lower than the time of receiving the signal from the nuclei (the receive phase). As we demonstrate, this problem can be solved by performing wireless power transfer during the receive phase without an additional transmitting antenna. In particular, we use Siemens Avanto Body Coil with a modified detuning system as the transmitting structure.

Materials and Methods

We apply CST Microwave Studio 2022 software package for numerical simulations. The numerical model includes a birdcage coil with a modified detuning system, a radio frequency (RF) screen, a receive system, and a phantom or the human voxel model. The Gustav voxel model from CST Bio models library which was used for numerical simulations consists of $2\times2\times2$ mm^3 voxels with permittivity, conductivity, permeability, density, and heat capacity corresponding to those of specific human tissues and organs (for example, grey matter of the brain, skin, bones, etc.), making it possible to study the specific absorption rate (SAR). The numerical model of the birdcage coil is based on Siemens Avanto Body Coil with two ports and includes a matching circuit. Moreover, the diodes in the birdcage coil model are replaced by inductors to implement the detuning system. The RF screen is modelled as a cylinder surface made of an annealed copper. The receive system consists of two identical orthogonal loop coils with a port including a matching circuit in each of them. The body phantom is implemented as a cylinder with the diameter of 300 mm and the length of 500 mm filled with a salted water.

The voltage on the dummy load and the magnetic fields within the birdcage coil are simulated with the frequency domain solver (implementing a modified finite element method), while the time domain solver (a modified finite difference time domain method) was used to obtain the (SAR) of the voxel human model.

The permittivity and conductivity of the Siemens Test Phantom liquid for 1.5 T MRI scanners used in numerical simulations were measured by SPEAG DAK 12 probe and Planar S5048 vector network analyser. Besides, Planar S5048 was used for measuring the scattering parameters of Siemens Avanto Body Coil.

Results and Discussion

For numerical simulations, we measured the permittivity of 80 and the conductivity of 1 Sm/m for Siemens Test Phantom for 1.5 MRI scanners. Then, we verified our numerical model by comparing the scattering parameters of the Siemens Avanto Body Coil and the model. When converting the scattering parameters into Z-parameters, we obtained that the difference between the frequencies in the numerical model and the experiment for five modes does not exceed 4%. After that, we added a detuning system with inductors to the model, and calculated scattering parameters (Fig. 1) of the birdcage coil. We obtained the resonance frequency of the fundamental mode (59 MHz), and higher-order modes (41 MHz, 31 MHz, 26 MHz) after converting the scattering parameters into Z-parameters. We convert the real and imaginary parts of the S-parameter of the first port (S11) to Z-parameters. The resulting frequency dependence of impedance features a maximum whose position corresponds to the frequency of a certain mode. Finally, for all studied modes (59 MHz, 41 MHz, 31 MHz, 26 MHz) we characterize the safety, the RF-RF efficiency, and the distortion of MR-images by calculating the specific absorption rate for the voxel human model, the voltage on dummy load within the receive coils, and the magnetic fields, respectively. We established that the optimal mode for wireless power transfer is the one at the frequency 31 MHz with RF-RF efficiency of 49%. Safety is the key limiting factor for the birdcage coil input power since a human body is heated during scanning. The heating for any part of the human body must be less than 2 W/Kg [12]. However, the received power (116 W) is sufficient for supplying many types of receiving local coils and medical sensors, while providing the safety of the scanning procedure. Moreover, the magnetic fields do not demonstrate any considerable distortion at Larmor frequency (63.6 MHz) within the phantom volume, facilitating that the proposed wireless power transfer system with a detuned birdcage coil will not decrease the MR-images quality.

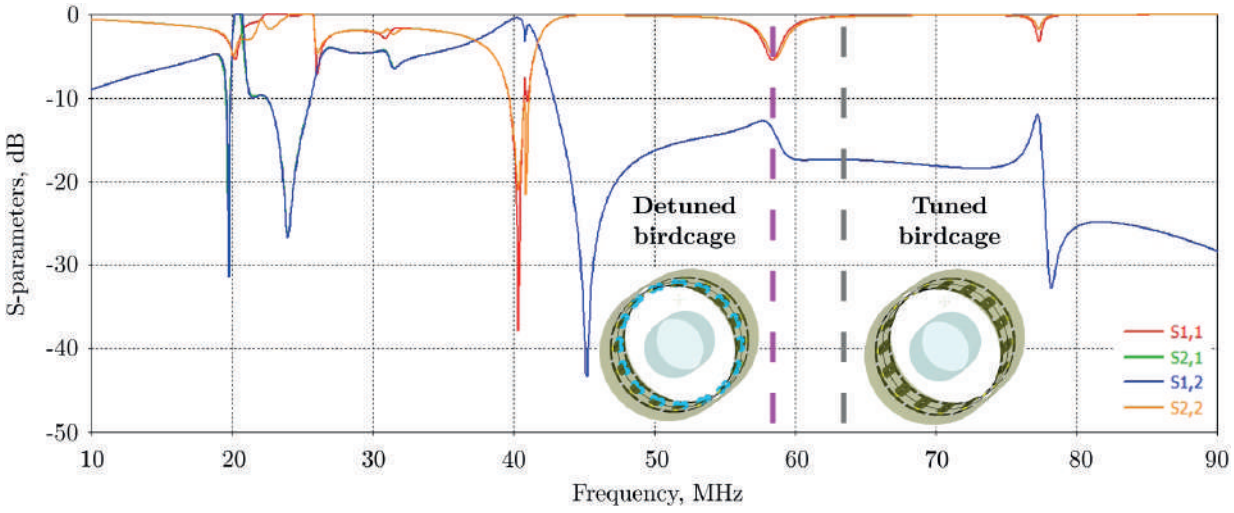

Fig. 1. S-parameters of the birdcage coil. Grey dashed line indicates the fundamental mode frequency 63.6 MHz of the tuned coil (right inset). Purple dashed line shows the fundamental mode frequency of the detuned coil (left inset). Blue markers in the inset indicate inductors used for detuning

Conclusion

In this work, we demonstrated a principle of wireless power transfer with a detuned birdcage coil, which allows providing power supply wirelessly during the phase of receiving the signal from atomic nuclei. It allows power transfer with minimal pauses (tens of ms during several seconds). For this purpose, a numerical model of the Siemens Avanto Body Coil has been developed and verified. Then, a detuning system and a receiving antenna system were added to the model. Magnetic field profiles for several birdcage modes were obtained, which facilitate that higher-order modes, rather than the fundamental one, should be used for wireless power transfer since their fields are concentrated on the surface of the phantom instead of its bulk. We demonstrate that the optimal mode for wireless power transfer has the frequency of 31 MHz. Simulations with a human voxel model show that the efficiency of wireless power transfer is 49%, and the maximal transmitted power is 116 W, which is sufficient supply the majority of modern multichannel receive coils and medical sensors. The developed system can be implemented in Siemens Avanto setups, and the principle itself can be used for any MRI scanners with a birdcage coil.

Acknowledgments

The work is supported by Russian Science Foundation (project 21-79-30038).

REFERENCES

1. **Dempsey M., et al.,** Thermal Injuries Associated with MRI, Clin. Radiol. 56 (457) (2001).
2. **Wei J., et al.,** A realization of digital wireless transmission for MRI signals based on 802.11b, J. Magn. Reson. 186 (358) (2007).
3. **Aggarwal K., et al.,** A millimeter-wave digital link for wireless MRI, IEEE Trans. Med. Imaging. 36 (2017) 574–583.
4. **Nohava L., et al.,** Perspectives in wireless radio frequency coil development for magnetic resonance imaging, Front. Phys. 8 (11) (2020).
5. **Seregin P., Burmistrov O., et al.,** Energy-Harvesting Coil for Circularly Polarized Fields in Magnetic Resonance Imaging, Phys. Rev. Appl. 17, 044014 (2022).
6. **Ganti A., et al.,** A novel energy harvesting circuit for RF surface coils in the MRI system, IEEE Trans. Biomed. Circuits Syst. 15 (791) (2021).
7. **Byron K., et al.,** An RF-gated wireless power transfer system for wireless MRI receive arrays, Concepts Magn. Reson. Part B Magn. Reson. Eng. 47B, e21360 (2017).
8. **Byron K., et al.,** An MRI compatible RF MEMs controlled wireless power transfer system, IEEE Trans. Microw. Theory Tech. 67 (1717) (2019).
9. **Ganti A., et al.,** Achieving electromagnetic compatibility of wireless power transfer antennas inside MRI system, Wirel. Power Transf. 6 (138) (2019).
10. **Ullah S., et al.,** Wireless, battery-free, and fully implantable micro-coil system for 7 T brain MRI, IEEE Trans. Biomed. Circuits Syst. 16 (430) (2022).
11. **Burmistrov O., et al.,** Wireless power transfer in magnetic resonance imaging at a higher-order mode of a birdcage coil, Phys. Rev. Appl. 21, 014047 (2024).
12. International Electrotechnical Commission, et al., Medical Electrical Equipment: Particular Requirements for the Basic Safety and Essential Performance of Medical Beds, (International Electrotechnical Commission, 2015).

THE AUTHORS

BURMISTROV Oleg I.
oleg.burmistrov@metalab.ifmo.ru
ORCID: 0000-0003-0083-6409

OLEKHNO Nikita A.
nikita.olekhno@metalab.ifmo.ru
ORCID: 0000-0002-9437-3320

Received 09.07.2024. Approved after reviewing 31.07.2024. Accepted 05.08.2024.

Conference materials
UDC 004.032.32
DOI: https://doi.org/10.18721/JPM.173.173

Development of an excitation signal generation system for a rubidium frequency standard

A.P. Valov [1, 2] ✉, E.V. Isupova [3], D.V. Zaletov [2]

[1] The Bonch-Bruevich Saint-Petersburg State University of Telecommunications, St. Petersburg, Russia;

[2] JSC "Obukhovskiy zavod", St. Petersburg, Russia;

[3] Peter the Great Saint-Petersburg Polytechnic University, St. Petersburg, Russia

✉ tony.valov2015@yandex.ru

Abstract. In the digital age, information transmission systems, telecommunications and satellite navigation systems, as well as metrology services play an important role. However, the development of these technologies leads to the need to constantly improve the frequency standards used for signal synchronization. To improve the stability of the signal produced by the frequency standard, a new system has been proposed for generating a microwave signal with a frequency that matches the frequency of the atomic transition of rubidium-87 atoms.

Keywords: frequency standard, atomic clock, phase-locked loop, frequency synthesizer, stabilization

Citation: Valov A.P., Isupova E.V., Zaletov D. V., Development of an excitation signal generation system for a rubidium frequency standard, St. Petersburg State Polytechnical University Journal. Physics and Mathematics. 17 (3.1) (2024) 358–362. DOI: https://doi.org/10.18721/JPM.173.173

Материалы конференции
УДК 004.032.32
DOI: https://doi.org/10.18721/JPM.173.173

Разработка системы формирования сигнала возбуждения рубидиевого стандарта частоты

А.П. Валов [1, 2] ✉, Е.В. Исупова [3], Д.В. Залетов [2]

[1] Санкт-Петербургский государственный университет телекоммуникаций им. проф. М.А. Бонч-Бруевича, Санкт-Петербург, Россия;

[2] АО «Обуховский завод», Санкт-Петербург, Россия;

[3] Санкт-Петербургский политехнический университет Петра Великого, Санкт-Петербург, Россия

✉ tony.valov2015@yandex.ru

Аннотация. В эпоху цифровых технологий важную роль играют системы передачи информации, телекоммуникационные и спутниковые навигационные системы, а также метрологические службы. Однако развитие этих технологий приводит к необходимости постоянного совершенствования стандартов частоты, используемых для синхронизации сигналов. Для повышения стабильности сигнала, вырабатываемого стандартом частоты, предложена новая система формирования СВЧ-сигнала с частотой, соответствующей частоте атомного перехода атомов рубидия-87.

Ключевые слова: стандарт частоты, атомные часы, фазовая автоподстройка частоты, синтезатор частоты, стабилизация

Ссылка при цитировании: Валов А.П., Исупова Е.В., Залетов Д.В. Разработка системы формирования сигнала возбуждения рубидиевого стандарта частоты // Научно-технические ведомости СПбГПУ. Физико-математические науки. 2024. Т. 17. № 3.1. С. 358–362. DOI: https://doi.org/10.18721/JPM.173.173

Introduction

In today's world, accurate measurement of time and frequency is critical for conducting numerous experiments in various scientific fields, such as atomic physics, exploration of the earth's surface or outer space. Without highly stable frequency and time sources, normal operation of communication equipment and metrological services is impossible. A slight frequency deviation can lead to significant errors, especially when transmitting large amounts of data.

Quantum frequency standards (QFS) occupy a special place among devices for determining frequency and time. On the one hand, expanding the range of tasks for which satellite navigation systems are used requires increasing the accuracy of determining the position of objects to 0.5 meters. On the other hand, the development of scientific and technological progress leads to changes in the composition of the electronic equipment used, which also requires constant modernization of the QFS.

Therefore, existing systems are most often upgraded to improve their characteristics, such as reducing size and weight, reducing energy consumption and increasing metrological accuracy. It is important to note that modernization can concern both the entire design of the QFS and its individual components or blocks [1–7].

Materials and Methods

The operating principle of QFS on rubidium-87 atoms is based on optical pumping of rubidium-87 atoms [1, 5], and one of the key elements of this system is a crystal oscillator capable of generating a stable frequency. The crystal oscillator is tuned to the frequency of the quantum transition of rubidium-87 atoms.

The process of tuning the frequency of a quartz oscillator to the quantum-frequency transition of rubidium-87 atoms (6.8347 GHz) is performed by using a microwave signal that is supplied from a frequency synthesizer (FS) to an atomic discriminator. Block diagram of RFS is presented on Fig. 1 [1].

When the frequency of the microwave signal coincides with the quantum transition frequency of excited rubidium-87 atoms, the photodetector records the maximum signal-to-noise ratio (S/N). If the frequency of the microwave signal deviates from the frequency of the resonant transition, the S/N ratio decreases and the electronic circuit is triggered, which generates an error signal.

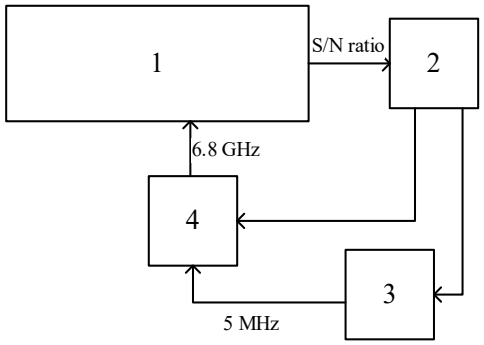

Fig. 1. Block diagram of RFS: 1 – atomic discriminator; 2 – automatic frequency control system; 3 – highly stable crystal oscillator; 4 – frequency synthesizer

Based on this error signal, the frequency of the crystal oscillator is adjusted by automatic frequency control system [1, 5] and tuned frequency is supplied to FS.

Therefore, one of the important aspects of the operation of atomic clocks is the formation of a high-frequency microwave signal, taking into account various requirements for its characteristics. This process is carried out in a frequency synthesizer block, which must ensure high frequency accuracy, minimal presence of side amplitude components in the spectrum of the output signal, as well as stability of the output frequency and amplitude when temperature changes.

Having examined in detail the principle of microwave signal formation, we can highlight a number of disadvantages of this system. The main disadvantage is the lack of direct control of the frequency of the generated microwave signal. This complicates control and requires assessing frequency coincidence using indirect signs. Another disadvantage is the difficulty of matching the signal mixture with the multiplying diode of the atomic discriminator.

In the current version, frequency synthesis in RFS works using the direct digital synthesis DDS method and multiplying the frequency to the frequency of the atomic transition of rubidium-87. The use of DDS allows to tune quite accurately the frequency signal, however, the multiplication cascade reduces this effect and does not allow for better frequency stability [4].

Results and Discussion

The above disadvantages limit the possibilities for improving system performance. An analogue of a microwave signal generation system is considered to overcome these limitations.

The generation system being developed must synthesize an intermediate signal with a frequency of 100 MHz and a microwave signal with a frequency of 6.8347 GHz.

It is proposed to synthesize the required signal frequency using a multi-loop phase-locked loop (PLL) circuit, the main elements of which are a voltage-controlled oscillator (VCO), a phase detector (PD) and a low-pass filter (LPF) (Fig. 2).

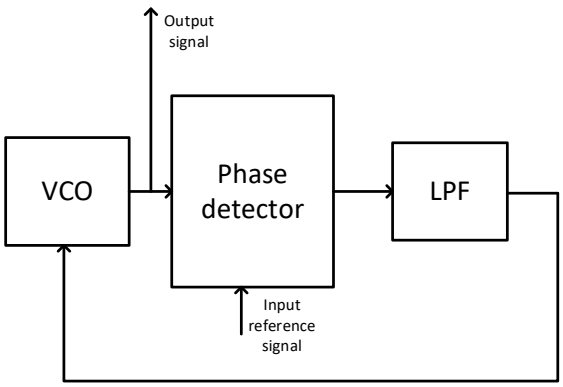

Fig. 2. Block diagram of PLL

This method allows to reduce the power spectral density of the phase noise of the carrier signal to the power spectral density of the phase noise of a highly stable crystal oscillator.

The 100 MHz phase-locking circuit uses a 100 MHz tunable crystal oscillator, a frequency synthesizer chip that operates as a phase detector, and is fed a 5 MHz signal from the rubidium frequency standard. The 5 MHz signal is converted into a square wave signal using an amplifier system and a Schmitt trigger, since the frequency synthesizer chip used only works with a square wave signal as a reference. The frequency synthesizer then compares the phases of the 5 MHz and 100 MHz signals, producing a signal about the phase difference between these signals. Next, this signal is converted into a control voltage for a 100 MHz generator and its frequency is adjusted.

A PLL circuit layout for 100 MHz was developed and experimental studies were carried out on the output characteristics of the power spectral density of a 100 MHz signal with and without a PLL loop (Fig. 3).

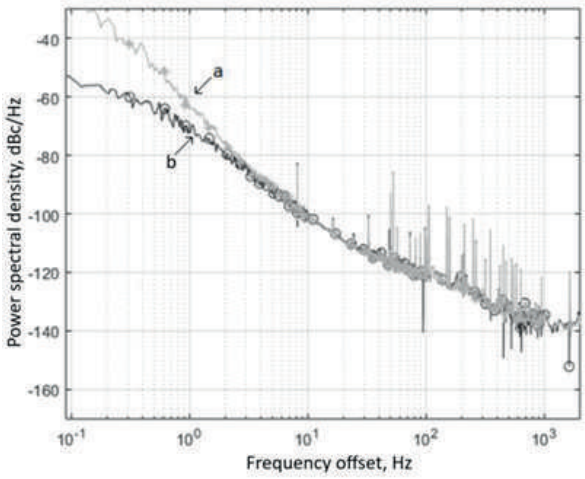

Fig. 3. Power spectral density of 100 MHz signal: signal without PLL system (*a*); signal with PLL system (*b*)

Based on experimental studies, PLL loop works only for detuning frequencies less than 10 Hz, however, this system could be upgraded for detuning frequencies up to 1kHz.

Conclusion

An experimental study of the resulting circuit made it possible to verify the operability of the circuit for detuning frequencies less than 10 Hz. To improve the operation of the PLL loop for detuning more than 10 Hz, it is proposed to refine the low-pass filter and replace the voltage-controlled oscillator with a more stable oscillator and with lower phase noise characteristics.

REFERENCES

1. **Riehle F.,** Frequency standard. Basic and applications, WILEY-VCH Verlag CmbH Co. KGaA: New-York. 2008.

2. **Arinushkina K., Grevsteva A., Valov A., Lukashev N.,** Development of the Controllable C-field Current Stabilizer for the Atomic Beam Tube of the Cesium Atom Clock. Springer Proceedings in Physics. 268 (2022) 589–596.

3. **Valov A.P., Dmitriev R.A., Davydov V.V., Shavshin A.V.,** Investigation of a method for improving phase noise in the frequency standard generator block, St. Petersburg State Polytechnical University Journal. Physics and Mathematics. 16 (3.2) (2023) 434–438.

4. **Petrov A. A., Shabanov V. E., Zalyotov D. V., Bulyanitsa A. L., Shapovalov D.V.,** Modernization of the frequency synthesizer of cesium atomic clock, IEEE International Conference on Electrical Engineering and Photonics, EExPolytech. (8564389) (2018) 52–55.

5. **Davydov V.V., Ermak S.V., Karseev A.U., Nepomnyashchay H.K., Petrov A.A. Velichko E.N.,** Fiber-optic super-high-frequency signal transmission system for sea-based radar station, Lecture Notes in Computer Science (including subseries Lecture Notes in Artificial Intelligence and Lecture Notes in Bioinformatics) LNCS. (8638) (2014) 694–702.

6. **Blinov I.Y., Boiko A.I., Domnin Y.S., Kostromin V.P., Kupalova O.V., Kupalov D.S.,** Budget of Uncertainties in the Cesium Frequency Frame of Fountain Type. Measurement Techniques. 60 (1) (2017) 30–36.

7. **Davydov V.V., Sharova N.V., Fedorova E.N., Gilshteyn E.P., Malanin K.Y., Fedotov I.V., Vologdin V.A., Karseev A.Yu.,** Fiber-Optics System for the Radar Station Work Control, Lecture Notes in Computer Science (including subseries Lecture Notes in Artificial Intelligence and Lecture Notes in Bioinformatics). (9247) (2015) 712–721.

THE AUTHORS

VALOV Anton P.
tony.valov2015@yandex.ru

ZALETOV Dmitriy V.
tony.valov2015@yandex.ru

ISUPOVA Ekaterina V.
isupova.e24@mail.ru
ORCID: 0000-0002-0963-5497

Received 15.07.2024. Approved after reviewing 23.08.2024. Accepted 26.08.2024.

Conference materials
UDC 621.396.42
DOI: https://doi.org/10.18721/JPM.173.174

Polyethylene-on-quartz platform for subterahertz reconfigurable reflective surfaces

P.V. Rozhkova [1] ✉, A.N. Prikhodko [1, 2, 4], A.S. Shurakov [1, 2, 3], G.N. Goltsman [1, 2, 4]

[1] Moscow Pedagogical State University, Moscow, Russia;
[2] HSE University, Moscow, Russia;
[3] National University of Science and Technology "MISIS", Moscow, Russia;
4 Russian quantum center, Skolkovo, Moscow, Russia;
✉ pv_rozhkova2@student.mpgu.edu

Abstract. Subterahertz frequency band is preallocated for the deployment of sixth generation wireless networks. Mastering of this band is challenging and requires development of appropriate hardware and software. The properties of components used should be authentically known for the purpose of accurate designing and prototyping. This research focuses on the radiophysical properties of a polyethylene-on-quartz sandwich as a potential dielectric platform for the implementation of reconfigurable reflective surfaces. The sandwich is exposed to spectral studies, statistical analysis of feasible fabrication tolerances and compatibility with cleanroom metal deposition and patterning processes. Its technological robustness is assessed upon prototyping of a 16-element planar reflectarray designed for operation in specular and non- specular reflection regimes at 155 GHz and 120 GHz, respectively. Using the measured value of quartz permittivity of a 3.55 and the loss tangent of a 0.001, we calculate the reflectarray reflection losses of approximately 1.5 dB. The calculations agree well with the results of its radiation pattern measurements conducted at 155 GHz. This hints that the developed passive platform is suitable for integration with A3B5 active layers with nonlinear elements ensuring fast beam steering in the subterahertz band.

Keywords: subterahertz, polyethylene-on-quartz, permittivity, reconfigurable reflective surface, reflection loss, 6G network

Funding: This study was funded by the Russian Science Foundation grant number 22-79-10279, https://rscf.ru/project/22-79-10279/.

Citation: Rozhkova P.V., Prikhodko A.N., Shurakov A.S., Goltsman G.N., Polyethylene-on-quartz platform for subterahertz reconfigurable reflective surfaces, St. Petersburg State Polytechnical University Journal. Physics and Mathematics. 17 (3.1) (2024) 363–366. DOI: https://doi.org/10.18721/JPM.173.174

Материалы конференции
УДК 621.396.42
DOI: https://doi.org/10.18721/JPM.173.174

Платформа полиэтилен-на-кварце для субтерагерцовых реконфигурируемых отражающих поверхностей

П.В. Рожкова [1] ✉, А.Н. Приходько [1, 2, 4], А.С. Шураков [1, 2, 3], Г.Н. Гольцман [1, 2, 4]

[1] Московский Педагогический Государственный Университет, Москва, Россия;
[2] Национальный исследовательский университет «Высшая школа экономики», Москва, Россия;
[3] Национальный исследовательский технологический университет «МИСиС», Москва, Россия;
[4] Российский квантовый центр, Сколково, Москва, Россия;
✉ pv_rozhkova2@student.mpgu.edu

Аннотация. Это исследование сосредоточено на радиофизических свойствах бислоевой структуры полиэтилен-на-кварце как потенциальной диэлектрической платформы для реализации реконфигурируемых отражающих поверхностей. Структура подвергается спектральным исследованиям, статистическому анализу возможных технологических допусков и совместимости с процессами осаждения металла и формирования рисунка в чистой комнате. Расчеты хорошо согласуются с результатами измерений диаграммы направленности, проведенных на частоте 155 ГГц. Это указывает на то, что разработанная пассивная платформа пригодна для интеграции с активными слоями A3B5 с нелинейными элементами, обеспечивающими быстрое управление пучком в субтерагерцовом диапазоне.

Ключевые слова: субтерагерцовый диапазон, полиэтилен-на-кварце, диэлектрическая проницаемость, реконфигурируемая отражающая поверхность, потери на отражение, сеть 6G

Финансирование: Грант РНФ «Интеллектуальная отражающая поверхность миллиметрового волнового диапазона для систем связи нового поколения» № 22-79-10279.

Ссылка при цитировании: Рожкова П.В., Приходько А.Н., Шураков А.С., Гольцман Г.Н. Платформа полиэтилен-на-кварце для субтерагерцовых реконфигурируемых отражающих поверхностей // Научно-технические ведомости СПбГПУ. Физико-математические науки. 2024. Т. 17. № 3.1. С. 363–366. DOI: https://doi.org/10.18721/JPM.173.174

Introduction

Subterahertz (sub-THz) frequency band is pre-assigned for the deployment of wireless networks of the sixth generation (6G). Mastering of corresponding carrier frequencies is laborious due to some specifics. Therefore, there appears a necessity to develop appropriate hardware and software. The properties of components that are used should be reliably known. So that it leads to the increasing accuracy of design and implementation of 6G wireless modules and systems. This research is focused on the radiophysical properties of a metallization-equipped polyethylene-on-quartz platform potentially suitable for the implementation of reconfigurable reflective surfaces. A series of measurements of the reflection spectra of a 140 μm thick quartz substrate in both *s*- and *p*-polarizations is carried out at 130–160 GHz. The quartz substrate is exposed to V/Cu (5/200 nm) and Ti/Au (10/300 nm) deposition and patterning on the front and rear sides. Its front side is further coated by a 100 μm thick polyethylene layer, whose surface is exposed to V/Cu (5/400 nm) deposition and patterning at the later stage. The resulting structure has a nominal geometry identical to that reported by us earlier in [1], yet the actual linear and angular dimensions differ from their nominals due to fabrication errors. The unit cell model of the reflectarray [2] is accordingly adjusted, and its simulated performance is further experimentally justified.

Materials and Methods

In our spectral studies intended to distinguish exact relative permittivity of the chosen quartz substrate potentially ranging from 3.5 to 4.5 [3], the quartz material under the test (MUT) is represented by a two-inch diameter wafer. The thickness of the MUT is 140 μm. In order to evaluate the permittivity of the MUT, we assess the reflective properties of the material. The experimental setup along with the employed methods are described by us in details elsewhere [4]. The optical paths between 130–160 GHz transmitter (Tx) and receiver (Rx) with respect to MUT are identical and equal to Fraunhofer distance (FD).

Once the dielectric and conducting properties as well as the actual geometry of the developed V/Cu / polyethylene / V/Cu / quartz / Ti/Au reflectarray structure are assessed, we measure its radiation pattern in the far-field and evaluate reflection losses at 155 GHz. The same set up is used as well. In order to analyze the losses the radiation pattern of the array-sized mirror is also measured in the similar manner.

Results and Discussion

We conduct measurements for the angles of incidence θ equal to 30, 45, 60 deg and consistently acquire MUT's complex permittivity of 3.55 (1 + 0.001*i)* for both transverse electric (TE) and transverse magnetic (TM) waves. Note that the angle θ equal to 60 deg is close to the Brewster's angle. Using the characteristic matrix (CM) [5] based fitting of the experimental spectral data, we achieve measurement accuracy of approximately 10−20%. The CM fit-functions are compared with the predictions of Fresnel equations (FE). CM was implemented due to the thickness of the sample as FE are not applicable for thin-layered media. Our findings are summarized in (Fig. 1, *a*, *b*) and (Fig. 2, *a*).

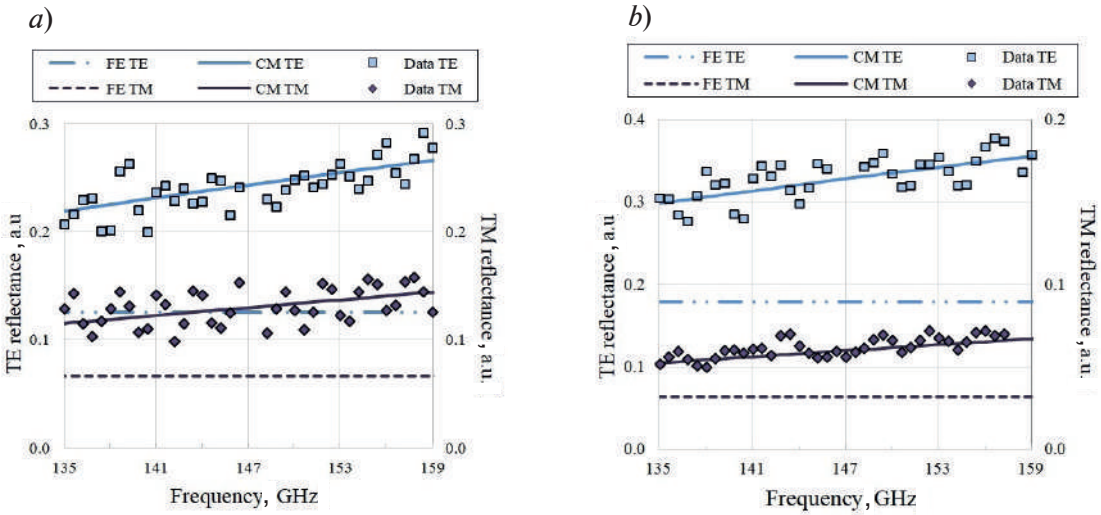

Fig. 1. Reflection spectra of the quartz substrate at θ = 30 deg (*a*); reflection spectra of the quartz substrate at θ = 45 deg (*b*)

As far as properties of the substrate of reflectarray are assessed we measure the far-field radiation pattern of the structure at a carrier frequency 155 GHz. We are interested in this frequency as the electromagnetic (EM) modeling predicts the reflection losses of approximately 1.5 dB and the mirror-like behavior of the reflectarray structure with adjusted parameters of quartz wafer. To confirm the accuracy of EM modeling and to evaluate the reflection losses we also analyze the pattern of the array-sized mirror measured in the same setup. Signal intensity drops obtained in the radiation pattern are due to the geometry of the device with corresponding additional losses introduced by layers into the structure.

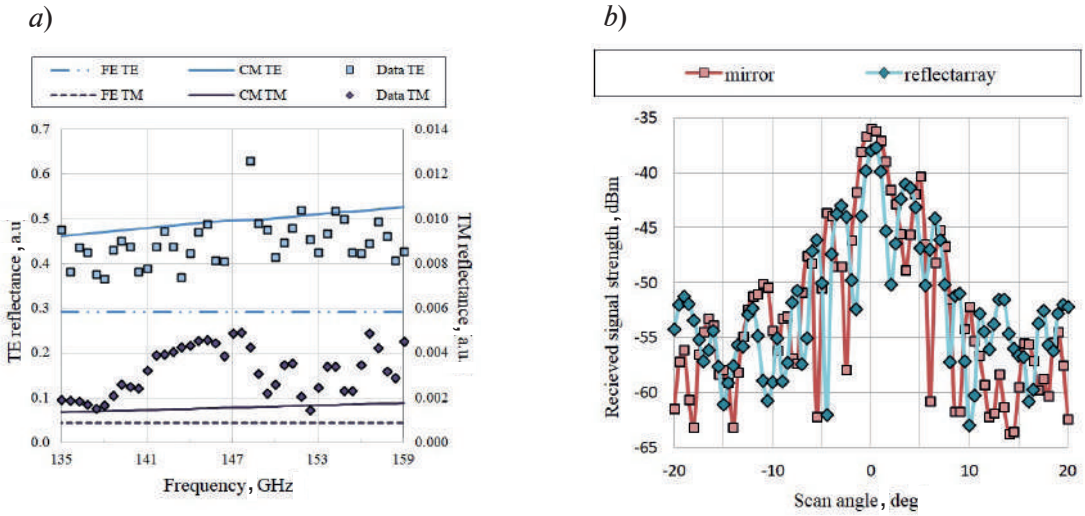

Fig. 2. Reflection spectra of the quartz substrate at θ = 60 deg (*a*); far-field radiation patterns of the fabricated reflectarray and the array-sized mirror measured at 155 GHz (*b*)

Experiments reveal excessive losses of 1.5–2 dB as compared to those of mirror. Our findings are summarized in (Fig. 2, *b*).

Both experiments and simulations consistently validate relevance of the reflectarray design in terms of radiophysics and hint its technological robustness in terms of fabrication tolerances and compatibility with cleanroom processes.

Conclusion

In this paper, we report on the reflective and refractive properties of quartz wafer as a substrate for reflectarray and the reflection losses of the fabricated reflectarray. An appropriate measurement setup is developed. The experimental value of dielectric permittivity of quartz is $3.55 + 0.0035i$. The measured reflectarray losses of approximately 1.5–2 dBm at 155 GHz are consistent with one calculated. Overall, we can conclude that the developed passive platform is suitable for integration with A3B5 active layers with nonlinear elements ensuring fast beam steering in the sub-THz band. This should be interesting to developers of reconfigurable reflective surfaces for reflection-aided 6G wireless channels.

REFERENCES

1. **Shurakov A., Prikhodko A., Belikov I., Razakova A., Goltsman G.,** Integrated Circuit of an Intelligent Reflecting Surface for sub-THz Wireless Communication, In 2023 IEEE 18th International Conference on Nano/Micro Engineered and Molecular Systems (NEMS). (2023) 183–187.

2. **Prikhodko A., Yaropolov T., Shurakov A., Gol'tsman G.,** Unit cell model of a terahertz intelligent reflecting surface with Schottky microcontacts, In Proceedings of the 35th European Modeling & Simulation Symposium (EMSS). (2023) 019.

3. **Lamb W.,** Miscellaneous data on materials for millimetre and submillimetre optics, International Journal of Infrared and Millimeter Waves. 17 (12) (1996) 1997–2034.

4. **Shurakov A., Rozhkova P., Khakimov A., Mokrov E., Prikhodko A., Begishev V., Koucheryavy Y., Komarov V., Goltsman G.,** Dynamic Blockage in Indoor Reflection-Aided Sub-Terahertz Wireless Communications, IEEE Access. 11 (2023) 134677–134689.

5.**Born M., Wolf E.,** Principles of Optics, Cambridge University Press. 2019.

THE AUTHORS

ROZHKOVA Polina V.
pv_rozhkova2@student.mpgu.edu
ORCID: 0009-0005-6258-9353

SHURAKOV Alexander S.
alexander@rplab.ru
ORCID: 0000-0002-4671-7731

PRIKHODKO Anatoliy N.
anatprikh1995@yandex.ru
ORCID: 0000-0002-4859-8975

GOLTSMAN Gregory N.
Goltsman@rplab.ru
ORCID: 0000-0002-1960-9161

Received 18.07.2024. Approved after reviewing 26.08.2024. Accepted 29.08.2024.

THEORETICAL PHYSICS

Conference materials
UDC 530.145.83.
DOI: https://doi.org/10.18721/JPM.173.175

Thermal entanglement in the three-qubit Tavis-Cummings model with many-photon transitions

A.R. Bagrov [1] ✉, E.K. Bashkirov [1]

[1] Samara National Research University, Samara, Russia
✉ alexander.bagrov00@mail.ru

Abstract. In this paper, we consider the model consisting of an isolated qubit and two qubits trapped in a lossless cavity and interacting with cavity thermal field via many-photon transitions. We obtain the exact solution of the model under consideration. On its basis we calculate the negativity as a measure of pair qubits entanglement. It is shown that, for many-photons processes entanglement is stronger than for that in the linear one-photon processes and can suppress the sudden death of qubit-qubit entanglement. The pairwise entanglement transfer between qubits pairs are also observed.

Keywords: qubits, thermal field, entanglement, many-photon transitions, sudden death of entanglement, cavity

Citation: Bagrov A.R., Bashkirov E.K., Thermal entanglement in the three-qubit Tavis-Cummings model with many-photon transitions, St. Petersburg State Polytechnical University Journal. Physics and Mathematics. 17 (3.1) (2024) 367–371. DOI: https://doi.org/10.18721/JPM.173.175

Материалы конференции
УДК 530.145.83.
DOI: https://doi.org/10.18721/JPM.173.175

Тепловая перепутанность в трехкубитной модели Тависа-Каммингса с многофотонными переходами

А.Р. Багров [1] ✉, Е.К. Башкиров [1]

[1] Самарский национальный исследовательский университет им. академика С.П. Королёва, г. Самара, Россия
✉ alexander.bagrov00@mail.ru

Аннотация. В этой статье мы рассматриваем модель, состоящую из изолированного кубита и двух кубитов, заключенных в резонатор без потерь и взаимодействующих с тепловым полем резонатора посредством многофотонных переходов. Мы получаем точное решение рассматриваемой модели. На его основе мы вычисляем отрицательность как меру перепутанности пар кубитов. Показано, что для многофотонных процессов перепутанность сильнее, чем для линейных однофотонных процессов, и может подавлять мгновенную смерть кубит-кубитной перепутанности. Также наблюдается попарный переход перепутанности между парами кубитов.

Ключевые слова: кубиты, тепловое поле, перепутанность, многофотонные процессы, мгновенная смерть перепутывания, резонатор

Citation: Багров А.Р., Башкиров Е.К., Тепловая перепутанность в трехкубитной модели Тависа-Каммингса с многофотонными переходами // Научно-технические

ведомости СПбГПУ. Физико-математические науки. 2024. Т. 17. № 3.1. С. 367–371. DOI: https://doi.org/10.18721/JPM.173.175

Introduction

In recent years, much attention has been paid to the development of efficient quantum information processing (QIP) systems capable of performing quantum computing and quantum communications tasks [1–3]. The use of natural atoms (Rydberg atoms, ions in magnetic trap and molecules) and artificial atoms (superconducting circuits, spins in solid, quantum dots etc.) has allowed to realize such unique quantum devices as quantum computers and quantum networks [4]. A significant breakthrough in the role of artificial atomic systems in the field of QIP was achieved when these qubits, especially superconducting qubits and spins in solids, were embedded in superconducting microwave cavities [4, 5]. In contrast to natural atoms, artificial atoms have much stronger coupling with cavity fields. It has been shown that such an architecture can be effectively used to control, entangle, and read out the states of qubits. The quantum entanglement is now seen as a necessary resource to help with QIP tasks. Two-qubit and multi-qubit entangled states enable for quantum computation and other QIP [6]. Therefore, the investigations of entanglement dynamics of the qubits interacting with selected modes of the cavity electromagnetic fields is the topical problem of the QIP.

At present there are a number of theoretical and experimental papers devoted to investigation of the properties of entangled states. But the quantitative entanglement criteria are currently only defined for two-qubit states. For many-qubit system, the situation is more involved as there exist several inequivalent classes of entanglement. For the simplest case of three-qubit system, all pure and mixed states are classified into three types. They are separable, biseparable and genuine entangled GHZ- and W-states [7]. The genuine entangled GHZ- and W-states are not equivalent under the stochastic local operations and classical communication (SLOCC). As a universal alternative to two-qubit gates, three-qubit gates based on three-qubit systems, such as Toffoli or Fredkin gates are possible produce the QIP. Three-qubit entangled states types were subsequently realized experimentally for superconducting qubits as well as for spins in solids and ions in traps (see references in [8–10]).

The QIP require maximally entangled states. However, through interaction with environment the decoherence usually occurs. However, it has recently been shown that the opposite effect can also occur: the environment can produce entanglement. In particular, the thermal noise of the cavity can act as such an environment. Kim and co-author showed that a chaotic field of the cavity can entangle two qubits [11]. Later a number of authors investigated the entanglement induced by a thermal cavity in two-qubit (see refs. in [12]) and three-qubit systems [13]. In [14] the authors considering the dynamics of two-qubit two-photon Tavis-Cummings model (TCM) showed that the entanglement induced by nonlinear interaction is larger than that induced by linear one-photon interaction. This result motivated us to focus our attention on studying the thermal three-qubit JCM with many-photon transitions. Since it is not possible to simply generalize the useful tools used in the bipartite case to the multipartite case, it is of particular interest to study the dynamics of three-qubit systems in a cavity for pure biseparable initial qubit states. In this case the three-qubit state is separable under some bipartition of the three qubits.

In this paper we will consider three partite system consisting of an isolated qubit and two qubits trapped in a lossless cavity and interacting with one-mode cavity field via many-photon transitions based on many-photon TCM (see refs. in [15]). We will investigate the dynamics of pairwise entanglement for biseparable initial qubits states and thermal state of the cavity field. As the measure of the pairwise qubits entanglement we will use the negativity. In the following, we shall pay our main attention to the influence of the photon transition multiples on the occurrence conditions of entanglement sudden death (ESD) phenomenon and entanglement transfer between pair of qubits in the process of the system evolution.

Model and its solution

We consider a system consisting of three identical qubits *A*, *B* and *C*. Two qubits *B* and *C* resonantly interact with the quantized electromagnetic field of the cavity via many-photon transition. The qubit *A* can move freely outside the cavity. The Hamiltonian of the interaction of such a system in the dipole approximation and the rotating wave approximation can be written as

$$\hat{H}_{Int} = \sum_{j=B}^{C} \hbar\gamma(\hat{R}_j^{+}\hat{b}^{k} + \hat{R}_j^{-}\hat{b}^{+k}), \tag{1}$$

where $\hat{R}_j^{+} = |2\rangle_{jj}\langle 1|$ and $\hat{R}_j^{-} = |1\rangle_{jj}\langle 2|$ are the transition operators between the excited $|2\rangle_j$ and the ground $|1\rangle_j$ states in the *j*-th qubit ($j = B, C$), $\hat{b}^{+}$ and $\hat{b}$ are the creation and the annihilation operators of the photons, γ is the qubit-photon coupling and *k* is the photon transition multiple.

The initial qubits state is assumed to be biseparable such as

$$|\Psi_1(0)\rangle_{ABC} = \cos\vartheta\,|2,1,1\rangle + \sin\vartheta\,|1,2,1\rangle \tag{2}$$

or

$$|\Psi_2(0)\rangle_{ABC} = \cos\vartheta\,|2,1,2\rangle + \sin\vartheta\,|1,2,2\rangle. \tag{3}$$

The initial cavity field state is assumed to be thermal with density matrix

$$\wp_{Field}(0) = \sum\nolimits_p \lambda_p\,|p\rangle\langle p|,$$

where $\lambda_p = \overline{p}^{\,p}/(1+\overline{p})^{p+1}$ and $\overline{p}$ is the mean thermal photon number $\overline{p} = \left(\exp\left[\hbar\omega/k_BT\right]-1\right)^{-1}$, k_B is the Boltzmann constant and *T* is the cavity temperature.

We obtained the exact formula for unitary operator of the system (1) under consideration. On it basis we derived the exact solution of the quantum Liouville equation for whole density matrix $\wp_{A,B,C,Field}(t)$. To obtain the pairwise negativity selected pair of qubits one can obtain the reduced qubit-qubit density matrixes. These can be produce by averaging the whole density matrix over the field and third qubit variables

$$\wp_{ij} = Tr_k Tr_{Field}\wp_{A,B,C,Field}\left(i \neq j \neq k, i, j, k = A, B, C\right).$$

We found the exact formulas for reduced qubit-qubit density matrix for all pairs of qubits and calculated on its basis the pairwise negativities which was defined by standard manner

$$\xi_{ij} = -2\sum_l \mu_{ijl}^{-},$$

where μ_{ijl}^{-} is the negative eigenvalues of partial transpose of a reduced atomic density matrix $\wp_{ij}^{T_1}$. The exact expressions for negativities are too cumbersome to present in this article.

Results and Discussion

In Fig. 1 we plot the time-dependence of negativities ξ_{AB}, ξ_{AC} and ξ_{BC} for initial qubits state (2) with $\vartheta = \pi/4$, fixed values of mean photon number and different values of photon multiple. One can see from Fig. 1 that at some times the entanglement disappears abruptly ($\xi_{ij} \leq 0$) for small values of photon multiple *k* and remains zero for a finite time before being revived. This means that there is an sudden death of entanglement effect. The sudden death of entanglement is the disappearance of entanglement of qubits at times less than the time of energy dissipation, phase, etc. The entanglement sudden death (ESD) phenomenon disappears for large values of the mentioned parameter *k*. At initial time qubits 1 and 2 are in maximally entangled Bell type state. The initial entanglement between qubits 1 and 3 and 2 and 3 are absent. One can see that for small multiples *k* the negativity ξ_{AB} in process of evolution reach zero at such interval of moment for which firstly qubits 2 and 3 become entangled. At subsequent time instants, the states of qubits 2 and 3 are disentangled (with the states of qubits 1 and 2 still being separable), but qubits 1 and 3 are entangled. At subsequent time interval, the states of qubits 2 and 3 are disentangled (the states of qubits 1 and 2 still being separable), but qubits 1 and 3 are entangled. Further, the processes of entanglement and disentanglement of qubit states are repeated. This result can be

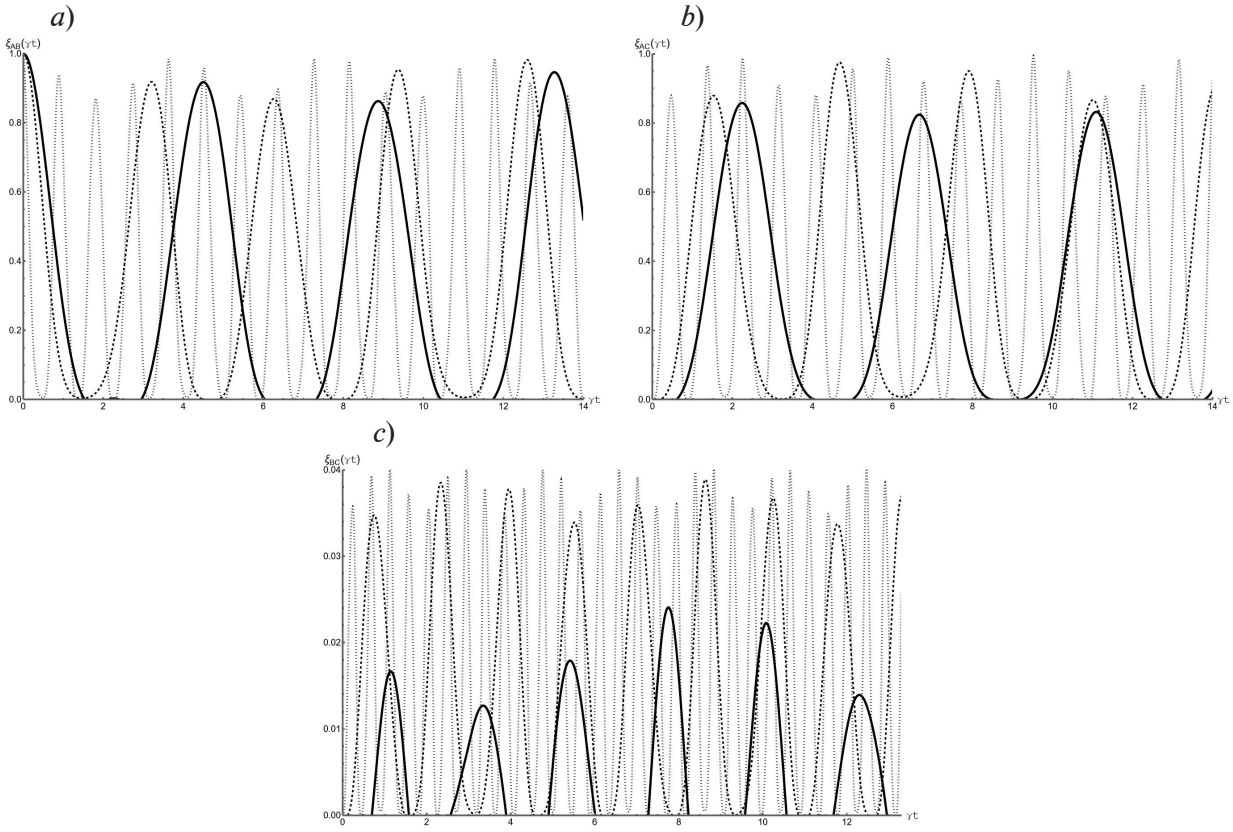

Fig. 1. The negativity criterion ξ_{AB} (*a*), ξ_{AC} (*b*) and ξ_{BC} (*c*) vs scaled time γt for initial biseparable qubits state $\cos\vartheta\,|2,1,1\rangle + \sin\vartheta\,|1,2,1\rangle$ with $\vartheta = \pi/4$. The photon multiple $k = 1$ (solid), $k = 2$ (dashed), $k = 4$ (dotted). The mean photon number $\overline{p} = 0.1$

interpreted as transition of entanglement from one pair of qubits to another pair of qubits. The numerical calculations of pairwise negativity for another biseparable initial state (3) showed that the time behavior of and ξ_{AC} is similar to that for bisparable state (2). But the behavior of pairwise negativity of qubits 2 and 3 ξ_{BC} is quite unexpected. The thermal field (or the vacuum field when $\overline{p} \to 0$) does not induce entanglement between qubits 2 and 3 for all values of model parameter *k*.

Conclusion

In this paper, we studied the dynamics of a system of three identical qubits, one of which is isolated, and the other two are trapped in an ideal cavity and interact resonantly with the one mode of the electromagnetic field of this cavity through many-photon transitions. The biseparable states of qubits and thermal state of field were in the focus of our attention. We derived the exact solution of the model under consideration. To investigate the entanglement of the pair of qubits we calculated the negativity. For biseparable states ESD effect takes place for small values of multiples and disappears for large values of mentioned parameter. The transition of entanglement from one pair of qubits to other pairs of qubits in the evolution process are also observed.

REFERENCES

1. **Kurizki G. et al.,** Quantum technologies with hybrid systems, Proc. National Acad. Sci. 112(13) (2015) 3866–3873.

2. **Blais A., Girvin S.M., Oliver W.D.,** Quantum information processing and quantum optics with circuit quantum electrodynamics, Nature Phys. 16(3) (2020) 247–256.

3. **Chen J.,** Review on quantum communication and quantum computation, J Phys: Conf. Ser. 1865 (2021) 022008.

4. **Li G.-Q., Pan X.-Y.,** Quantum information processing with nitrogen–vacancy centers in diamond, Chin. Phys. 27 (2018) 020304.
5. **Chia C. et al.,** Hybrid Quantum Systems with Artificial Atoms in Solid State, Adv. Quantum Technol. 7 (2024) 2300461.
6. **Souza A.M., Sarthour R.S., Oliveria L.S., Vedral V.,** Entanglement in many body systems. Rev. Mod. Phys. 653 (2023) 414511.
7. **Dur W., Cirac J.I.,** Classification of multiqubit mixed states: Separability and distillability properties, Phys. Rev. A. 61 (2000) 0423149.
8. **Neely M. et al.,** Generation of Three-Qubit Entangled States using Superconducting Phase Qubits, Nature. 467 (2010) 570–573.
9. **Roos C.F. et al.,** Control and Measurement of Three-Qubit Entangled States, Science. 304 (2004) 1478-1480.
10. **Takeda K. et al.,** Quantum tomography of an entangled three-qubit state in silicon, Nature Nanotech. 16 (2021) 965–969.
11. **Kim M.S., Lee J., Ahn D., Knight P.L.,** Entanglement induced by a single-mode heat environment, Phys. Rev. A. 65 (2002) 040101(R).
12. **Bashkirov E.K.,** Thermal entanglement in Tavis-Cummings models with Kerr media, SPIE Proc. 12193 (2022) 121930Q.
13. **Cai J.-F., Liu H.-P.,** Entanglement in Three-Atom Tavis Cummings Model Induced by a Thermal Field, Commun. Ther. Phys. 43 (2005) 427-431.
14. **Zhou L., Song H.S.,** Entanglement induced by a single-mode thermal field and criteria for entanglement, J. Opt. B. 4 (2002) 425-429.
15. **Dong Z., Zhang G., Wu A.-G., Wu R.-B.,** On the Dynamics of the Tavis-Cummings Model, IEEE Trans. Autom. Control, 68(4) (2023) 2048–2063.

THE AUTHORS

BAGROV Alexander R.
alexander.bagrov00@mail.ru
ORCID: 0000-0002-1098-0300

BASHKIROV Evgeniy K.
bash@ssau.ru
ORCID: 0000-0001-8682-4956

Received 04.07.2024. Approved after reviewing 31.07.2024. Accepted 31.07.2024.

Journal

ST. PETERSBURG STATE POLYTECHNICAL UNIVERSITY JOURNAL: PHYSICS AND MATHEMATICS

Vol. 17, No. 3.1, 2024

Founder and publisher: Peter the Great St. Petersburg Polytechnic University

The journal is registered with the Federal Service for Supervision of Communications, Information Technology and Mass Media (Roskomnadzor).
Certificate ПИ ФС77-51457 issued 19.10.2012.

All papers presented are final author versions
Peer review is under responsibility of the Organizing Committee

Phone 8 (812) 294-22-85

Website https://physmath.spbstu.ru/

E-mail: physics@spbstu.ru

Typesetting by *N.A. Bushmanova*, *A.S. Kolgatina*

Published 30.10.2024. Format 60x84/8. Digital print.

Printer's sheets 43,36. Print circulation 1000. Order ID № 4904.